REPUBLIQUE DU CAMEROUN
Paix - Travail – Patrie
****
UNIVERSITE DE YAOUNDE I
****
CENTRE DE RECHERCHE ET DE FORMATION DOCTORALE EN SCIENCES, TECHNOLOGIES ET GEOSCIENCES
****
UNITE DE RECHERCHE ET DE FORMATION DOCTORALE PHYSIQUE ET APPLICATIONS
B.P. : 812 Yaoundé
E-mail : crfd_stg@uy1.uninet.cm

REPUBLIC OF CAMEROON
Peace - Work – Fatherland
****
THE UNIVERSITY OF YAOUNDE I
****
POSTGRADUATE SCHOOL OF SCIENCE, TECHNOLOGY AND GEOSCIENCES
****
RESEARCH AND POSTGRADUATE TRAINING UNIT FOR PHYSICS AND APPLICATIONS
Po Box : 812 Yaounde
E-mail : crfd_stg@uy1.uninet.cm

LABORATOIRE DE PHYSIQUE DE L'ENVIRONNEMENT TERRESTRE
LABORATORY OF THE EARTH ENVIRONMENT'S PHYSICS

EVIDENCES OF CRUSTAL STRUCTURES BASED ON GEOPHYSICAL DATA INTEGRATION IN THE NKOLAFAMBA- SANGMELIMA AREA (SOUTH CAMEROON)

A thesis defended for the award of the degree of Doctor of Philosophy (PhD) in Physics
Speciality: Geophysics and Geoexploration

By:

ASSEMBE Stéphane Patrick
MSc. Geophysics
Matricule: 00V145

Thesis Publicly defended on the 22 March 2021 before the Jury made up of:

President:	**NDJACKA Jean Marie Bienvenu**, *Professor, University of Yaounde I*
Rapporteur:	**NDOUGSA MBARGA**, *Professor, University of Yaounde I*
Members:	**NJANDJOCK NOUCK Phillipe**, *Professor, University of Yaounde I*
	NOUAYOU Robert, *Professor, University of Yaounde I*
	BEN-BOLIE Hubert Germain, *Professor, University of Yaounde I*
	MOUANGUE Ruben, *Associate Professor, University of Ngaoundere*

Year 2021

UNIVERSITÉ DE YAOUNDÉ I
THE UNIVERSITY OF YAOUNDE I

FACULTÉ DES SCIENCES
FACULTY OF SCIENCE

DÉPARTEMENT DE PHYSIQUE
DEPARTMENT OF PHYSICS

ATTESTATION DE CORRECTION DE LA THÈSE DE DOCTORAT/Ph.D

Nous, Professeur **Pr BEN-BOLIE Germain Hubert** et Professeur **NDJAKA Jean Marie Bienvenu**, respectivement Examinateur et Président du jury de la Thèse de Doctorat/Ph.D de Monsieur **ASSEMBE Stéphane Patrick**, Matricule **00V145**, préparée sous la direction du Professeur **NDOUGSA MBARGA Théophile,** intitulée : « **Evidences of crustal structures based on geophysical data integration in the Nkolafamba-Sangmelima area (South Cameroon)**», soutenue le **Lundi, 22 Mars 2021**, en vue de l'obtention du grade de Docteur/Ph.D en Physique, Spécialité **Physique de l'Environnement Terrestre,** Option **Geophysique et Geoexploration**, attestons que toutes les corrections demandées par le jury de soutenance ont été effectuées.

En foi de quoi, la présente attestation lui est délivrée pour servir et valoir ce que de droit.

Fait à Yaoundé le ..01 JUN 2021.....

Examinateur

Pr BEN-BOLIE Germain Hubert

Le Chef de Département de Physique

UNIVERSITE DE YAOUNDE I
FACULTE DES SCIENCES
Le Chef de Département
DEPARTEMENT DE PHYSIQUE

Pr NDJAKA Jean-Marie Bienvenu

Le Président du jury

Pr NDJAKA Jean-Marie Bienvenu

DEDICATIONS

To my children, may this work inspire them in the future

To, my mothers

AND

In the loving memory of:

Assembe Ernest. Etienne, my father

Essoundou Jean. Hervé, my brother

Ebalé Christian. Brice, my nephew and friend

ACKNOWLEDGMENTS

I address thanks to Professor Théophile NDOUGSA MBARGA who initiated and supervised this work in the Geophysics & Geoexploration unit, Laboratory of Earth Environment Physics, University of Yaoundé I. Your availability despite your multiple occupations, your scientific rigor and devotion to work, your remarks and especially your advices as parent are the keystones to the completion of this project. Accept my timeless gratitude.

To Professor Luc Calvin. OWONO OWONO, Head of the Physics and Applications Research and Training Unit, Postgraduate School of Science, Technology and Geoscience at the University of Yaoundé I, who enabled the completion of this study. I am very thankful to you.

Credit to Professors TABOD Charles TABOD, Robert NOUAYOU, Philippe NJANDJOCK NOUCK, Marie Louise C. OWONO ANGUE who nurtured in me the essence of geophysics in the Geophysics & Geoexploration unit, Laboratory of Earth Environment Physics.

Professors Ute WECKMANN, Paul DIRKS and Colin REEVES provided interesting research materials and explanatory advises; Professors Germain H. BEN BOLIE and Bertrand BODO, endeavoured to overcome many obstructive difficulties towards the completion of this study; Professor Dieudonné BISSO and Mr. Christophe AVA offered the logistics for the Audiomagnetotelluric field campaign. Please receive my deep gratitude.

I extend my gratitude to the members of the Jury for all the precious time they will be sacrificing in order to examine this work; and to all the reviewers whose commitment will contribute into the improvement of this dissertation.

Special thanks to Professors Arsène MEYING, Jean L. NSOUANDELE and Jean G. TAMBA; and Doctors Francoise ENYEGUE A NYAM, Daniel GOUET, Paul NGOUMOU, Alain ZANGA, Marcelin BIKORO Bi ALOU, William TEIKEU ASSATSE, Olivier U. OWONO AMOUGOU, Serge POKAM KEGNI, Augustin D. PEPOGO MANVELE and Alain R. NZEUGA, for their indefectible support.

To Jean D. NGOH, Gaetan. ENEME, Fabrice EMBOLO and all the graduate researchers working alongside me, I appreciate your collaboration.

My endless thanks to my mothers Valentine NNOMO, Martine NGONO and Anne M. NGO NGUIMBOUS; to Serge ASSEMBE, Philemon ESSI, Charles ASSEMBE, Guy MEVELE, Stephanie S. ZE MEMANE, Veronique LAISIN, Pauline ELOMO, all my siblings, and my friends mainly Pierre C. NGA, Cyrille DJANG, Mr and Mrs ETOUNDI, for their timeless and indefectible supports throughout. My regrads to whosoever, unnamed, contributed in any manner to the completion of this program.

ABSTRACT

An integrated study combining the tensor audiomagnetotellurics (AMT), aeromagnetics, remote sensing and field geological data is used to better understand the structural geology in the Nkolafamba-Sangmelima region, a southern portion of the North Equatorial Fold (Panafrican) Belt -Congo Craton transition zone located between latitudes 02º45'N-04º00'N and longitudes 11º30'E-12º15'E. The lithology of the area comprises (i) the Yaounde Group (southern member of the Panafrican belt) represented by the Yaounde series (made up of migmatised gneisses, micaschists) and the Mbalmayo series; (ii) the Congo Craton, also referred to as the Ntem complex, which is made up of various granites and charnokites of the Tonalite-Trondheimite-Granodiorite suites. Three (or four) syn-, late to post-Panafrican deformation stages are identified in the NEFB whereas three stages supposedly related to pre-, syn to post Panafrican events affect the Congo Craton.

The AMT data have been collected along 6 profiles striking N135º. From data analyses, the phase and apparent resistivity pseudosections revealed or confirmed that folding and many discontinuities affected the Yaounde series, showing that the area underwent intense tectonics and that the subsurface is made up of a mixture of both Panafrican belt and Congo Craton formations. The discontinuities have been interpreted as faults and/or fractures on geoelectrical sections; active faults being related to the conductive discontinuities. The highlighted faults correlate many fractures and faults observed on outcrops from Yaounde, Nkolafamba and Loum 2. They form a network of parallel faults symptomatic of NE-SW strike-slips in the area initially assumed to be coeval to the Central Cameroon Shear Zone. Field data confirm the results and aeromagnetics is used to check the south and east continuity of this strike-slips system.

Aeromagnetics covers a contiguous area south and east of the AMT surveyed zone. The data deriving from a nationwide survey carried out in years 70s, have been provided as digital total magnetic intensity map at 1:50000 scale. The reduction to the magnetic equator highlighted a main NE-SW channel of strongly magnetised anomalies which presume the dominance of the NE-SW structural direction in the area. These anomalies are interpreted as lineaments, mafic to ultramafic or subcrustal intrusions affecting both the Yaounde Group and the Ntem complex. Analytic signal outlines magnetic domains sometimes matching known formations, potential mineral host including inferred greenstones belts relics. The difference in the anomalies (lineaments) density, due to difference in their nature of rocks, enabled to differentiate the Panafrican belt from the Ntem complex on the first vertical derivative map. Some lineaments are

interpreted either as faults or contacts, including the faults outlining the Congo Craton/Panafrican belt thrust limit. The dominant directions of lineaments are NE-SW to ENE-WSW, WNW-ESE to NW-SE and E-W. The multiscale edge analysis using the horizontal gradient magnitude isolates the major faults and contacts; these faults are vertical to sub-vertical and extend to depth located from 621 to 4000 m (or deeper) by the Euler 3D deconvolution method. The magnetic foliation map depicts folding subsequent to E-W, NNW-SSE and N-S compressions and various shear zones affecting the study area. The faults' geometry is consistent with both vertical movements (related to basement's collapses) and horizontal movements (wrenches) in both the Congo Craton and the Panafrican Belt. Vertical movements and the faults' geometry has been confirmed by geophysical 2.75 modelling which neatly locates the Congo craton/Panafrican belt between Latitudes 03º20'N and 03º15'N eastward. Magnetic study corroborates the existence of NE-SW strike-slips south of the AMT investigated area and is validated by remote sensing.

Remote sensing involves Landsat 8 OLI data over the entire study area; it is particularly efficient in lineaments detection, and serves as a validation tool. The remotely sensed lineaments interpreted as faults or contacts (total of 863) maintain the dominance of the NE-SW, NW-SE and N-S directions. However, an analysis based on length classified the NE-SW, NNW-SSE to WNW-ESE among the major lineaments, forming many shear zones and strike-slips. Remote sensing analysis validate the magnetic and the AMT faults, and establishes the continuity within the findings of the study which henceforth highlights a unique sinistral NE-SW shear zone affecting both the Panafrican belt and the Congo Craton as a result of pre-Neoproterozoic events followed by syn- and post-Neoproterozoic reactivations in a continent-continent convergence setting actually marked by WNW-ESE transpressions in the two units.

The study correlate and upgrade the number of greenstones relics and the faults mapped in the Yaounde region, thus, it improves the geological map of the southern Cameroon and the information on the Panafrican belt/Congo Craton transition with positive moods for mineral exploration. Also, the integration of geosciences methods and data reveals to be consistent in investigation areas with a non-uniform geophysical surveying coverage.

Keywords: Tensor audiomagnetotellurics; aeromagnetics; remote sensing; Panafrican belt; Congo Craton; faults; strike-slips

RESUMÉ

Afin de mieux appréhender la géologie structurale de la region de Nkolafamba-Sangmelima, située entre les latitudes 02º45N-04º00N et les longitudes 11º30E-12º15E dans la zone de transition entre la Chaine Panafricaine d'Afrique Centrale et le Craton du Congo, une approche combinant les données audio-magnétotelluriques tensorielles, aéromagnétiques, les images satellites et des données géologiques de terrain a été adoptée dans le cadre des présents travaux. La lithologie de la zone comprend (i) la série de Yaoundé représentée par les gneiss migmatisés, les micaschistes et les schistes de Mbalmayo ; (ii) le Craton du Congo, comprenant des granites divers et des charnockites de la série Tonalite-Trondheimite-Granodiorite. Trois (ou quatre) épisodes de déformation syn- à post-Pan-Africain sont identifiés dans la Chaine Panafricaine tandis qu'ils sont pré-, syn. à post-Pan-Africain dans le Craton Congo.

Les données AMT ont été collectés suivant six profiles de direction N135º (NO-SE). Les pseudos sections de phase et de résistivité apparente révèlent dans le sous-sol la zone d'étude, des plissements et de nombreuses discontinuités interprétées dans les sections géoélectriques comme des failles ou des fractures ; et un mélange des formations issues à la fois du Craton du Congo et du Panafricain. Certaines failles, de par leur faible conductivité, sont supposées actives. Les failles mise en exergue et confirmées par des observations de terrain à Nkolafamba, Yaounde et Loum 2, forment un réseau de failles parallèles suggérant l'existence dans la zone d'une ligne décrochements majeurs NE-SO corrélable au Cisaillement Centre Camerounais et donc Des données magnétiques aideraient à vérifier la continuité dans le reste de la zone cible.

La portion investiguée par la méthode aéromagnétique est dans le prolongement sud et est de la portion couverte par l'AMT. Les données utilisées, collectées lors d'une campagne nationale dans les années 70, nous ont été fournies sous forme de carte de champ total au 1/50000^{e} en version numérique. La réduction à l'équateur révèle un couloir NE-SO composé d'anomalies à fortes intensités, traduisant la prépondérance de la direction NE dans la zone d'étude. Ces anomalies majeures seraient liées à des linéaments ou à des apports mafiques à ultra mafiques ou sub-crustaux sous le Panafricain et le Craton du Congo. Le signal analytique définie des domaines magnétiques coïncidant parfois avec de sformations, des cibles minières connues et des reliques probables de roches vertes. L'individualisation respective du Craton du Congo et du Panafricain issue desdits domaines est renforcée par la première dérivée verticale, suivant la densité (liée à leurs natures distinctes), très élevée au sud, des linéaments identifiés. Certains des linéaments interprétés comme failles ou contacts marquent la ligne de chevauchement

Craton/Panafricain. De la multitude des directions observées, seuls les groupes NE-SO à ENE-OSO, ONO-ESE à NO-SE et NO-SE sont prépondérants. L'analyse multi-échelle impliquant le gradient horizontal souligne des failles majeures et des contacts subverticaux à verticaux dont les profondeurs selon la deconvolution d'Euler 3D se situent ente 621 et 4000 m. La foliation magnétique quant à elle relève des axes de compression E-O, N-S et NNO-SSE traduisant des plissements et des cisaillements. La géométrie des failles traduit des mouvements verticaux (effondrements du socle) et horizontaux (décrochements) que confirme la modélisation 2.75 qui par ailleurs affine la localisation de la limite Craton/Panafricain d'est en ouest entre 03º20'N et 03º15'N. Cette étude corrobore l'existence au sud d'un cisaillement NE-SO souligné en amont par l'AMT et validé par télédétection. Les failles dans le Craton seraient pré-Neoprotérozoiques mais connaissent des réactivations syn- à tardi- et post-Neoprotérozoiques. Ces failles réactivées sont donc contemporaines de la fracturation dans le Panafricain mise en évidence par l'AMT.

La télédetection par imagerie Landsat 8 dans l'ensemble de la zone d'étude, s'avere efficace dans la cartographie des linéaments et sert d'outils de validation aux autres methodes. Les linéaments interprétés comme des failles ou des contacts (863) suivent les directions majeures NE-SO, NO-SE et N-S. Selon la longueur, les failles d'orientations NE-SO, NNO-SSE à ONO-ESE sont des linéaments majeurs marquant des cisaillements et des décrochements. Dans l'ensemble, l'étude met en évidence un couloir de cisaillements NE-SO affectant à la fois le Craton du Congo et la Chaine Panafricaine, en réponse a une tectonique pré-panafricaine (dans le Craton du Congo d'abord) suivie de rajeunissements syn- et post-panafricain dans une convergence continent/continent et actuellement soulignée par des transpressions ONO-ESE dans les deux unités lithostructurales.

Le présent travail contribue donc par la cartographie de nouvelles failles et de reliques de ceintures roches vertes, à l'amélioration de la carte géologique du sud Cameroun et de la connaissance de la zone de transition Craton/Panafricain, ce qui devrait à coup sûr réorienter significativement l'exploration minière dans la zone. Par ailleurs, l'approche utilisée dans le cadre de ces travaux dans l'intégration de plusieurs méthodes et données géoscientifiques, se révèle efficace dans l'étude des zones impliquant une juxtaposition des méthodes géophysiques.

Mots clés : méthode audiomagnétotellurique tensorielle ; méthode aéromagnétique ; télédétection ; CPAC ; CC ; failles ; décrochements

TABLE OF CONTENTS

Table, figure and photo captions

List of tables

List of figures

List of photos

LIST OF SYMBOLS, ABBREVIATIONS AND ACRONYMS

$\vec{E}$: Electric field vector

mV/km: millivolt per kilometre

$\vec{H}$:Magnetic field vector

A/m: Ampere per metre

$\vec{j}$: Current density vector (A/m^2)

μ_o : Magnetic permeability of vacuum ($\mu_o=4\pi.10^{-7}$ U.S.I)

1-D: One dimension

2-D: Two dimensions

3-D: Three dimensions

A: Magnetic potential

f : Frequency

Hz: hertz

F_e :Total field

D: Declination

$\vec{D}$: Electric displacement field

$\vec{B}$: Magnetic induction

AFMAG: Audio-frequency magnetic

AMT: Audio-Magnetotelluric

NEFB: North Equatorial Fold Belt

BE: Beguele 1

BG: Beguele 2

CC: Congo Craton

CCSZ: Central Cameroonian Shear Zone

CSAMT: Controlled Source Audio-Magnetotelluric

DC: Direct current

E: East

ENE: East North-East

FVD: First Vertical Derivative

h : Penetration depth

km: kilometre

I: Inclination

Lm: Loum

k: magnetic susceptibility

KB: Kamba

M: Magnetic field intensity

Ma: Millions of years

MT.: Magnetotelluric

N: North

NE: North-East

NNE: North North-East

NK: NKol-Afamba

nT: nanoTesla

NW: North-West

NNW: North-North-West

OS: Ossol

PAB: Panafrican Belt

R: Earth Radius

s: second

S: South

SE: South-East

SSE: South-South-East

SW: South-West

SSW: South South-West

T: Period

TDEM: Time Domain Electromagnetic Methods

v: Velocity

W: West

WSW: West South-West

WNW: West North-West

$\mathbf{X_e}$: Horizontal north,

$\mathbf{Y_e}$: Horizontal east

γ: Unit of magnetic field intensity

δe: Skin depth

ε: Permittivity

μ: Magnetic permeability

ρ : Resistivity

ρ_a : Apparent Resistivity

Ω.m: Ohm metre

σ : Conductivity

S/m: Siemens per metre

Φ : Phase

°: Degree

ω: Electromagnetic wave pulsation

rad/s: radian per second

GENERAL INTRODUCTION

"Understanding the present to explain the past", there can be the fundamental objective of geosciences, but the reconstruction of the past environments and the associated processes, based on present-days' data is challenging because these data need to be first understood in their extant context before serving as evidences of past events or environments. In this quest, geology that primarily relied only on direct observations of landforms and outcrops is now getting a more valuable support from geophysics through indirect observations of the Earth's crust or shallow subsurface. Geophysical investigation of the crust involves at or near surface measurements to assess the space-variations of its physical properties. The multiplicity of physical parameters implies the existence of various survey methods. The contribution of geophysics to geosciences spans from lithological characterisation to structures delineation and mapping with direct applications in mineral exploration, civil engineering, geology and environment.

The current study applies various geophysical methods in order to investigate subsurface structures in the Nkolafamba-Sangmelima area. Its objective is to improve the understanding of geological history of the transition zone of Central Africa with particular attention on Cameroon. Within this frame, the specific objectives are: (1) to ameliorate the geological and mineral information on south Cameroon; and (2) to propose an approach that enables to investigate an area with a juxtaposition of geophysical methods. The study area is located in south Cameroon; it encompasses both the Mobile zone represented by the Yaounde series and Mbalmayo schists (Nedelec et al., 1986; Nzenti et al., 1984a, 1988) thrusting onto the northern edge of the Congo Craton referred to as the Ntem Complex (Maurizot et al., 1986; Nedelec et al., 1990). Globally, many studies have been achieved on the Mobile zone in Cameroon. These studies revealed an E-W deep tectonic accident marking the suturing line between the Congo Craton and the Central Africa Panafrican Belt at the latitude N04° and many NE oriented structures (Manguelle Dicoum et al., 1992; Mbom-Abane, 1997; Meying et al., 2009, 2013; Tadjou et al., 2009; Ndougsa-Mbarga et al., 2010) often supposed to be Neoproterozoic or Phanerozoic. Some of these structures form the Central Cameroon Shear Zone, whose nearby known member is the Sanaga Fault (Ngako et al., 2008). Despite the disputed models proposed to explain the geodynamic setting and evolution at the northern margin of the Congo Craton (e.g. Toteu et al., 2006, 2007; Mvondo et al., 2007a; Ngako and Njonfang, 2008, 2018; Ngako et al., 2009; Mvondo-Ondoa et al., 2009; Nkoumbou et al., 2014; Tchakounté Numbem et al., 2018a, 2017, 2018b; Houketchang Bouyo, 2018), a collision involving the Congo Craton and the NEFB is commonly agreed. Since these models are mainly based on geological inputs, contributions from geophysics may help

solving that dispute by proposing a unifying model. Moreover, convergent settings in general host various deposit types; based on the present known mineral potential of southern Cameroon, addressing the issue above would enable to upgrade its significance. This study involves an integration of field geological and geophysical data. Geophysical works consist in the application of tensor audiomagnetotellurics to investigate structures in a portion of the study area; check their continuity in the remain, using aeromagnetics (the study area has been divided into two adjacent portions) and further, apply remote sensing (Landsat 8 OLI) for validation purposes over the entire study area.

This dissertation is subdivided into three chapters:

Chapter one describes firstly, the global geodynamic evolution leading to the formation and dislocation of Gondwana; summarizes the geology of Cameroon, then presents the study area. The section reviews the deformations and tectonic processes that occurred in Africa until the South Atlantic Ocean's opening in the Cretaceous. Besides, focus is given to lithological constitution and structural features encountered through a literature review of past geoscience works carried on the Mobile zone in Cameroon, out of which the research questions and the awaiting goals of the study will be defined.

The second chapter presents the *instrumentum labores* of the study. Indeed, the fundamentals and key applications of the geophysical methods as well as remote sensing used in the current study are herein presented, emphasis being given to the audiomagnetotellurics and aeromagnetics. Besides, a description of the materials and the entire work methodology is presented herein.

The third chapter initially presents progressively, the audiomagnetotelluric, aeromagnetic and remote sensing results. Secondly, these results are summarised, cross-validated (validation in-between methods) and validated with field and existing geological data along with remote sensing analyses), then discussed. Some implications to the findings are also stated.

A general conclusion ends the dissertation by outlining the main objectives, the outputs and perspectives that swamp out of the study.

CHAPTER ONE: THE LITERATURE REVIEW

INTRODUCTION

"*Understanding the present to explain the past*", that is the mission to be fulfilled by this study in Central Africa with respect to southern Cameroon. Although geophysics has become very important in geological modelling, mastering of the geological setting of a studied area remains critical. Therefore, describing the study area's geology in the framework of a regional geodynamic setting would be a vital constraint to geophysical models. This first chapter aims at presenting the regional and local settings in regards of the recent geoscience literature, starting from the Precambrian evolution of the to induct readers with global tectonics.

1.1. GEODYNAMICS FROM PRECAMBRIAN TO THE PHANEROZOIC AGES

The Precambrian history is documented on all the actual continents though the events are not everywhere of the same ages. This matches two main eras, the Archaean and the Proterozoic.

1.1.1. The Archaean evolution (3800-2500 Ma)

1.1.1.1. The Archaean evolution: general facts

The Archaean in one sense, is the timeframe of first amalgamation processes of lithospheric fragments and terrains accretions (Scotese, 2009; Weckmann, 2012; Heine et al., 2013; Piper, 2013; Pérez-Díaz and Eagles, 2014) leading to the formation of major Precambrian plates and continents such as the Congo continent (Meert and Powell, 2001; Scotese 2009). Before the amalgamations, great terrain accretions led to the increase of the earth crust budget. The Archaean continental crust accretions occurred at various ages. The Pilbara Craton in Australia, formed at ca 3800 Ma, provides a good example of oldest Archaean terrains. The formation of continental crust nuclei and their subsequent accretion are the witnesses of many Archaean orogenies e.g. the Superior Province formed at ca 2740-2640 Ma, resulted from the accretion of many 3100 Ma to 2670 Ma continental blocks to form the largest Archaean cratons.

In the midst of theories on the mechanisms of the Archean tectonics, the first emerging ideology relates plate amalgamation origines to present-days'style subduction tectonics (e.g. Kato and Nakamura, 2003; Fumes et al., 2007; references therein) while the second ideology controversially favours plume-dominated and crustal delamination processes during vertical motions (Foley *et al.* 2003, references therein). However, recent studies (e.g. Moyen and Hunen, 2012; Roberts et al., 2015; Vezinet et al., 2018) confirm hypothetically short-lived subduction

processes to pertain on Archaean tectonics; i.e. arc magmatism dominantly contributed to the increase of the crust's budget. In addition, both schools agree on the existence of prior lithospheric blocks whose amalgamation formed continental landmasses after various tangential or vertical movements during several extension and compression episodes (e.g.Cawood et al., 2006b, 2016; de Wit et al., 2008), *as per* the Wilson cycle concept. Restricting the explanation of tectonics in these terms can be misguiding. The process implies alternative openings and closures of paleo-oceans along weakness zones between the landmasses where earth materials constantly rejuvenate and experience rifting.

1.1.1.2. The Archaean evolution of Central Africa

Africa Plate present-day look results only from recent tectonic activities as Archaean geodynamics essentially led to the formation between ca 3800-2550 Ma (Neoarchean to paleo Proterozoic), of the seven cratons which frame it. These continental nuclei are the Man shield, the Reguibat shield, the Sahara Metacraton, the Kaapvaal Craton, the Zimbabwe Craton, the Tanzania Craton and the Congo Craton (van Hinsbergen et al., 2011). Further some of these blocks merged to form three major cratons referred to as the West Africa, Central Africa (Congo-Tanzania) and Southern Africa (Zimbabwe-Kaapvaal) Cratons (Dirks et al., 2008).

The Congo-Tanzania Craton is a region of pre 2500 Ma continental crust located in Central Africa, which resulted from the amalgamation of the Tanzania and the Congo Cratons (van Hinsbergen et al., 2011). The Congo Craton particularly, is formed by many blocks which the Kasai block in NE Angola and S DR Congo; the Congo block in W-Uganda and NE-DR Congo and the Chaillu-Gabon block. The Chaillu-Gabon craton underlies SW-Equatorial Guinea, Gabon, Congo and S-Cameroon, where it is referred to as the Ntem Complex (e.g. Nedelec et al., 1990). Feybesse et al. (1998) describe this block as made up of ca 3190-3120 Ma (Mesoarchean) rocks affected by high-grade metamorphisms. These are post-associated by calk-alkaline tonalites and granites, felsic volcanics and ultrabasic rocks before the stabilisation of the block in Neoarchean, similarly to other major African cratons.

The available records infer many orogenic cycles and the setting of structures affecting the Earth's crusts; all these witnessed in many present-days continents. In Africa, a ca 2600-2500 Ma orogenic cycle (Neoarchean), the Liberian orogeny, reported by several authors (e.g. (Tchameni 1997; Shang *et al.* 2010; references therein), probably marks the transition to the Proterozoic in the Ntem Complex. In fine, the Archaean evolution mainly corresponds to continental crust's formation. Indeed, most of the continental crust budget balance was realised

through this period; this is particularly the case of the nuclei of the actual continents: the shields or Cratons. However, the amazing history was not yet to end with the Archaean.

1.1.2. The Proterozoic evolution

The Proterozoic, subdivided into three periods: The Paleoproterozoic (2600-1800 Ma), the Mesoproterozoic (1800-1000 Ma) and the Neoproterozoic (1000-540 Ma); is the most known Precambrian eon in the earth's geologic evolution saga. It provides a wide interval (ca 2060 Ma) of long and everlasting geodynamic and tectonic processes dominated by the making and demaking of supercontinents (de Wit et al., 2008; Weckmann, 2012; Fairhead et al., 2013a) leading to the actual continents.

1.1.2.1. The Paleo-Mesoproterozoic evolution

a. The pre-Neoproterozoic evolution: the global view

The evolution of supercontinents is the essential of the pre-Neoproterozoic history thanks to its link with the major accretionary events, continental crust augmentation and orogenic cycles. Herein, one psrticular supercontinent history requires some attention. In the late Mesoproterozoic, following the breakup of the Columbia Paleoproterozoic supercontinent (Scotese 2009), the Congo continent and the Rodinia supercontinent constituted the essential of the earth's landmasses. According to Scotese (2009), the Congo continent was constituted by the Congo-Sao Francisco Craton and the Sahara shield minus the West African Craton and the Hijaz island arcs (Sudan, Egypt and Arabia). Besides, in its final configuration, the Rodinia had two halves, the North Rodinia and South Rodinia (Rowell et al., 1993; Pisarevsky et al., 2003a; Zhao et al., 2006; Cawood et al., 2016a). North-Rodinia was constituted by East Gondwana, Cimmeria, Sibumasu and Kalahari/Mozambique (including East Arabia) Cratons; while. South-Rodinia comprised the Laurentia, Amazonia, Siberia, West Africa and Baltica Cratons (J Brendan Murphy and Nance, 1991; Meert and Powell, 2001; Schettino and Scotese, 2005; Cawood et al., 2007; Moulin et al., 2010; Heine et al., 2013; Pérez-Díaz and Eagles, 2014). The Grenville orogeny ended the formation of the Rodinia or *mother of all continents* at ca 1100 Ma (Piper, 2000; Schettino and Scotese, 2005; Li et al., 2008; Liu et al., 2015).

The paleoenvironment reconstruction by Scotese (2009) puts the Congo continent west from Rodinia, beyond the Pharusian/Mozambique paleo-ocean to the north, and the Adamastor (Panafrican) paleo-ocean to the south. This assumed the existence of a circum-Congo continuous subduction zone (The connection of the Mozambique Belt and the Pharusian–Adamastor subduction zones formed a continuous zone surrounding the Congo continent (Scotese et al., 1999) which played a major role in the geodynamic evolution of the Rodinia, by forcing its

convergence towards the Congo continent, so, causing the Panafrican thermo-tectonic event (Stewart, 2007). Scotese et al. (1999), Stewart (2007) and Scotese (2009); including references, provide comprehensive information about the supercontinents' evolution from Rodinia to modern continents.

The pre-Neoproterozoic evolution acknowledged many orogenies and riftings. Some of the resulting faults were probably related to the relaxation and earth's compensation after magmatic upwells. Examples of Paleo- to Mesoproterozoic orogenic systems are the Svecofennian system in Europe, the Trans-Hudson and the Grenville systems in North America and the Eburnean and the Kibaran systems in Africa.

b. Pre-Neoproterozoic activity in Africa

In Africa, the Eburnean and Kibaran orogeneses are the main orogenic cycles characterising the pre-Neoproterozoic period: The Eburnean occurring in the Paleoproterozoic (ca 2200-2000 Ma), met the growth and stabilisation of West Africa Craton (Ennih and Liégeois, 2008). Alongside, the Congo and Tanzania Cratons merged into Central Africa Craton along with passive margin development and orogeny at the west margin of the central and southern Africa cratons (Fernandez-Alonso et al., 2010).

The Kibaran event occurred in Mesoproterozoic, after the convergence of the Central Africa Craton to the north toward the southern Africa Craton between 1400 and 1000 Ma (Tack et al., 2008). Coeval formations have been reported in SE DR Congo, SW Nigeria and Cameroon (Ennih and Liégeois, 2008). The end of the Kibaran (ca 1000 Ma) corresponds to the final individualisation of the Congo continent and the development of a circum-Congo subduction zone that triggered the Congo continent / Rodinia collision.

1.1.2.2. The Neoproterozoic evolution

a. The global geodynamic evolution: The Pannotia supercontinent

The Neoproterozoic is characterised by the formation of the greater Gondwana supercontinent from 800 to 542 Ma (Cawood et al., 2001, 2007, 2016). The greater Gondwana or Pannotia (Dalziel, 1997) resulted from the suturing of continental blocks derived from Rodinia breakup. Scotese (2009) suggested that the collision of the Congo continental block with Rodinia triggered that breakup (**Figure 1.1-1**). The driving force of this process was generated by the circum-Congo subduction zone that forced the convergence of Rodinia onto the Congo continent. Fernandez-Alonso et al. (2010) assumed that the collision of the Central Africa (Congo) continent and the Kalahari Craton (Kibaran orogeny) is the premise in the Mesoproterozoic of the Rodinia/Congo continent's collision. As summarised in Scotese (2009), once the Congo continent collided and sutured with Rodinia (800-750 Ma), the former

continuous circum-Congo subduction zone divided by two. This led to the creation of the north (Hijaz-Mozambique) and the south (Pharusian-Adamastor) subduction zones at the rims of Congo. The differential plate tectonic stress created consequently tore Rodinia into two halves (N-Rodinia and S-Rodinia) and finally splited and dismembered it.

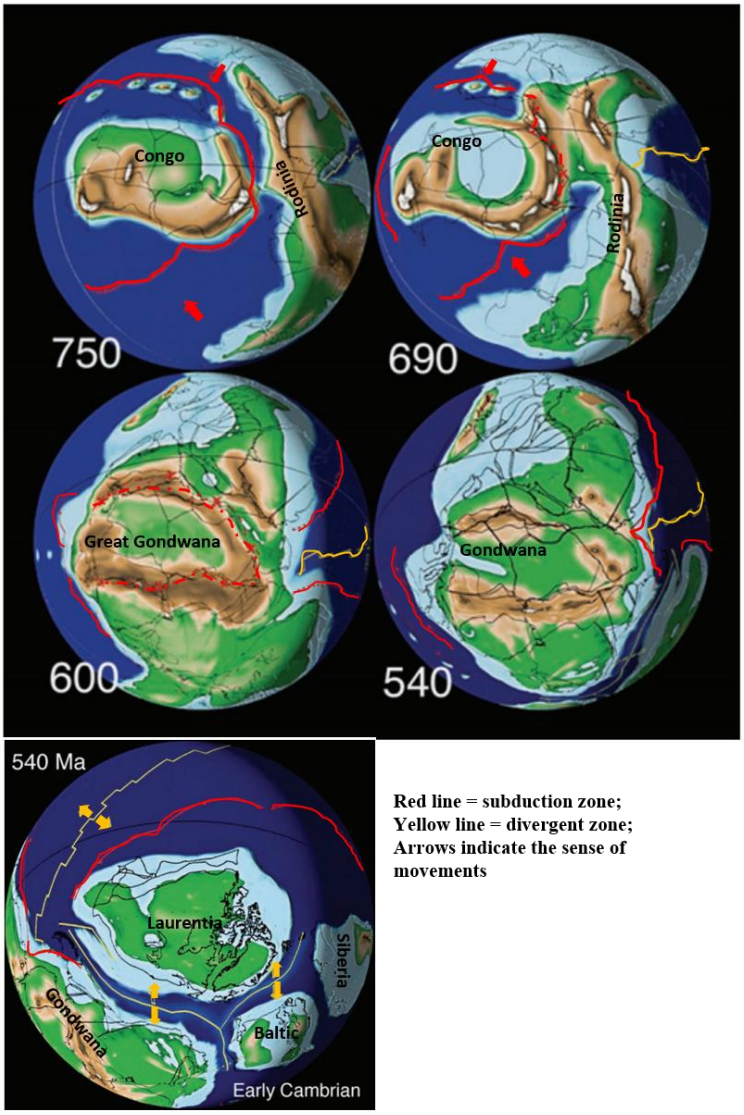

Figure 1.1-1 : Graphical summary of the Neoproterozoic evolution (Scotese, 2009)

The forces generated by the two formed subduction zones at the rims of Congo caused an anticlockwise of N-Rodinia toward the Hijaz-Mozambique subduction zone, leading to the formation of Mozambique belt as a consequence of progressive accretion of Hijaz arc shields north of the continent. Similarly, S-Rodinia rotated (**Figure 1.1-1**) clockwise, N-converging toward S-Congo. This caused the closure of the Adamastor Ocean and the formation of the Panthalassa rift (which later evolved into the Panthalassa Ocean). From this diachronous rotation of the Rodinia halves against Congo continent resulted the amalgamation of Pannotia at ca 600-540 Ma (Piper, 2000). This placed the Congo continent at the core of Pannotia (Cawood et al.,

2001, 2007; Scotese, 2009; and references therein). The final suturing of Pannotia around 540 Ma characterises the end of the Neoproterozoic era; but soon after its amalgamation, Pannotia broke-up into four main continents: Baltic, Gondwana, Laurentia and Siberia (Cocks and Torsvik, 2002, references therein) in the early Cambrian.

b. The Panafrican orogeny: definitions

The term 'Panafrican' initially, defined a system of orogenic belts mainly reported in Africa, Brazil and Eastern Antarctica that were formed during ca 540 Ma ago. The concept was then extended to describe tectonic, magmatic, and metamorphic activities the crust that was once part of Gondwana from Neoproterozoic to earliest Paleozoic age (Kröner and Stern, 2004), resulting in two main types of constructions. The first type consisted of predominantly Neoproterozoic supracrustal and magmatic assemblages, many of juvenile origin, with structural and metamorphic geneses that are similar to those in the Phanerozoic collision and accretion belts. The second type consisted of polydeformed high-grade metamorphic assemblages, exposing middle to lower crustal levels, whose origin, environment of formation and structural evolution are more difficult to reconstruct.

The Panafrican orogenic cycle corresponds to the Rodinia/Congo continent collision, then the breakup of Rodinia and the final amalgamation and suturing, from late Neoproterozoic to early Phanerozoic, of Pannotia or greater Gondwana (Spalletti et al., 2010; Piper, 2013).

c. The Panafrican system in Central Africa

The Panafrican system, sometimes referred to as North Equatorial Fold Belt (Nzenti et al., 1988, references therein) covers in Central Africa Cameroon, Chad and the Central African Republic; and the south western part of Nigeria known as the Ife–Ilesha schist belt (Caby and Boesse, 2001). According to Abdelsalam et al. (2002), the North Equatorial Fold Belt represents an E-W orogene that marks the suture between the Sahara Metacraton and the Congo Craton (CC). The Panafrican episode in Central Africa is represented by rejuvenated magmatic and metamorphic rocks (essentially migmatites and granites) originating from several Precambrian epochs (Ngako et al., 1991; Penaye et al., 1993).

Southwards in Cameroon, Ngako et al. (2008) described three main geotectonic units within the Panafrican concept:

- The Poli Group corresponding to an early Neoproterozoic back-arc basin formed between 830 and 665 Ma (Ngako, 1986; Toteu et al., 2006b), that includes: detrital and volcanoclastic deposits, metavolcanics (tholeitic basalts and calk-alkaline rhyolites), and pre-, syn- to late-tectonic calk-alkaline intrusions (diorites, granodiorites and granites) emplaced between 660 and 580 Ma (Toteu et al., 1987, 2001).

- The Adamawa domain including huge Panafrican batholiths and large scale Paleoproterozoic remnants that were metamorphosed during the Panafrican event (Toteu et al., 2001; Tchakounté Numbem et al., 2017).

- The Yaoundé Group comprising the Mbalmayo-Bengbis, the Ayos and the Yaoundé series (Nedelec et al., 1986; Mvondo et al., 2007c), is represented by a syntectonic basin and a Neoproterozoic belt.

1.1.3. The Phanerozoic evolution

1.1.3.1. The geological evolution of Gondwana

The Phanerozoic eon, also called "Cambrian explosion" by several authors (e.g. Meert and Libermann 2004, 2007; Canfield et al., 2007), is related to the development and diversification of life on Earth. Additionally, this corresponds to the period through which the final resurfacing processes of the planet took place yielding what we see nowadays. Indeed, the Panafrican events caused the split of Rodinia, then the amalgamation of Pannotia from late Neoproterozoic to early Phanerozoic followed by short after with ist break up into four major landmasses including the Gondwana in the early Cambrian (Spalletti et al., 2010; Piper, 2013).

The Gondwana comprises the West-Gondwana (South-America, Africa) and East-Gondwana (Australia, East-Antarctica, India). Despite its blurry absolute age, the suture between West and East Gondwana was defined along the East African Orogen (Meert and Lieberman 2008, references therein). Studies by Dirks et al. (2008) revealed that the Hercinian orogeny between 450-250 Ma at the NW and S margins of the African plate; and the ongoing Alpine orogeny caused by the subduction of Africa beneath the Eurasia plate.

1.1.3.2. The African rifts and shear zones: imprints of the post-Panafrican evolution

Collisional or divergent orogenic systems are both accompanied by the setting of brittle structures, generally shear zones and faults or joins characterising either compressional or extensional environments (Masterton et al., 2012). The well documented African rifts and shear zones are the East African (EARS), the West African (WARS) and the Central Africa Rift Systems (CARS). These features are mainly related to stress accommodation in the African plate during the Cretaceous-Albian evolution (Fairhead, 2009; Masterton et al., 2012; Fairhead et al., 2013a) characterised by the growth of the Atlantic Ocean and the individualisation of the Somalian plate. These rifts systems probably developed along earlier weakness zones between major shields that constitute the African plate. Illustratively, the CARS formed in pre-Panafrican extensional setting (Vicat and Moloto-a-Kenguemba, 2001). The development of these lineaments had enabled to consider the African plate as subdivided in sub-plates (NW-Africa, S-

Africa and E-Africa) which are allowed to move relative to each other, rather than a rigid plate; making it possible for intra-plate deformations to occur within Africa (Masterton et al., 2012).

Amongst the regional lineaments above mentioned, the WARS and the CARS are of great importance for this study. According to Fairhead (2009) and Fairhead et al. (2013), they form a unique system, the West Central Africa Rift System (WCARS) which constitutes the sub-plate boundary between NW Africa and S Africa. The WCARS runs from the Atlantic to the Indian oceans throughout the Central Africa, including Cameroon, hence its importance to this study. Additional details on African rift systems in de Wit et al. (2008).

1.2. PRESENTATION OF THE STUDY AREA AND RESEARCH QUESTION

1.2.1. Summary of Cameroon's geology

1.2.1.1. Lithology

Cameroon is constituted of a basement complex and superficial terrains.

a. The basement or basal complex

The basal complex is essentially made up of Precambrian magmatic and metamorphic rocks rejuvenated during the Panafrican orogeny (Penaye et al., 1993; Mvondo et al., 2007c; Olinga et al., 2010). It is composed of metamorphosed and granitised rocks that form the metamorphic complex (gneisses, quartzites, migmatites and charnockites), and platforms formations. Oldest basement units represent the Cameroonian part of the Congo Craton (CC) in the south (Regnoult, 1986).

b. The superficial terrains

Superficial terrains include volcanic formations and a sedimentary overburden. The sedimentary overburden is represented in the north and south respectively, by Cainozoic and Mesozoic rocks, and recent sedimentary layers like the lower Cretaceous sedimentary formations of the Benue trough, the Mamfé and Bida Gulfs (Genik, 1992). The sedimentary overburden lies on the Precambrian basement. The volcanic formations are represented by volcanic structures related to the Cameroon Volcanic Line. They include some cambro-ordovician (550-500 Ma) plutons and younger granites locally called hossérés (Nyoré, Gouna, Peské, etc.) which belong to the Adamaoua basement (Regnoult, 1986). The trachybasalts of Mount Cameroon prove the ongoing volcanism ignited in the late Eocene (Bessoles and Lasserre, 1977).

The Cameroon's territory is generally divided into three structural domains: the southern, the central and the northern domains (**Figure.1.2-1**). The southern domain corresponds to the CC or Ntem Complex. It is a set of formations which are assumed to have not been affected by the Panafrican thermo-tectonic event (Meying 2011, references therein). The central and northern domains correspond to the North Equatorial Fold Belt (NEFB), an E-W orogenic zone made up

of terrains which have been rejuvenated during the Panafrican episode, which extends to the east in Sudan (Ngako et al., 1991; Rolin, 1992, 1995) and to the west in NE-Brazil (van Schmus et al., 2008).

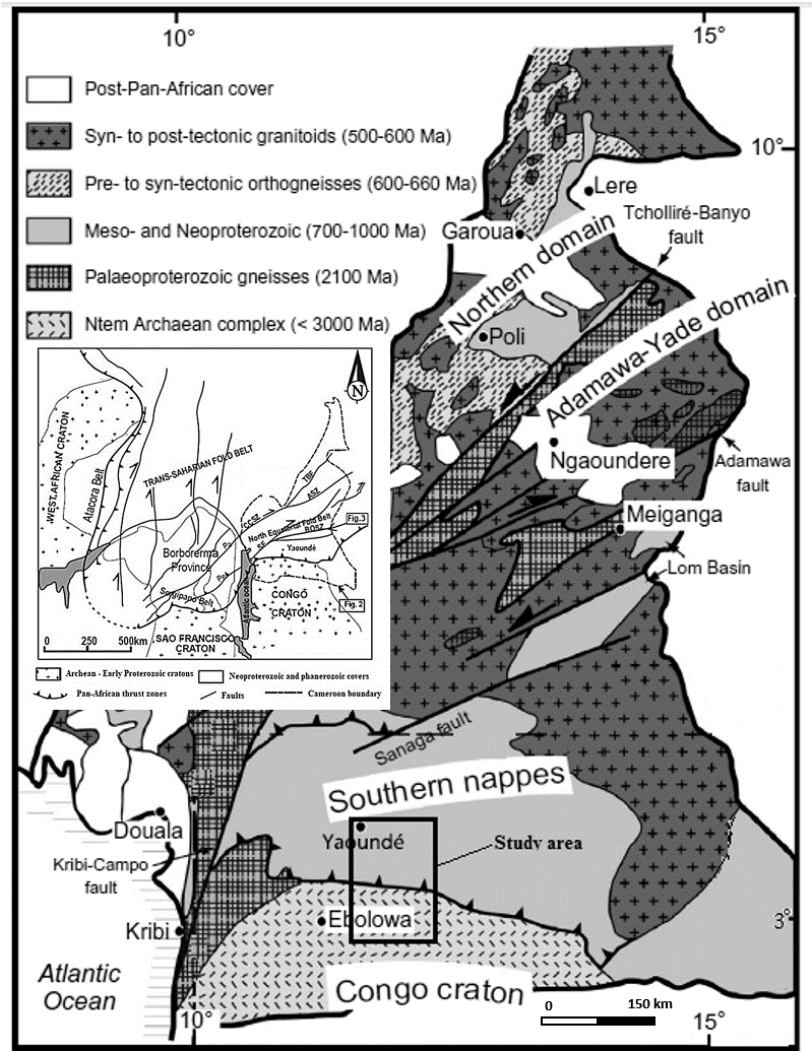

Figure 1.2-1 : Geological map of Cameroon (Toteu et al., 2001, modified)

1.2.1.2. Tectonic history

The tectonic history in the Mobile zone is more documented in the Panafrican chain than in the Craton which was hitherto assumed steady. At the regional scale, Mobile zones underwent at least three main deformation stages termed D1 to D2 which differ respectively in the north and the south of the Panafrican domain as revealed by Ngako et al. (2003) and Olinga et al. (2010). According to Ngako *et al.* (2006) and Olinga et al. (2010), the D1 stage is associated to a W and SW complex overthrust affecting the Eburnean bedrock in the north, while it occurs in the southern edge without any tangential deformation with an indefinite regional significance. The D2 stage occurs in the south with tangential tectonics marked by the setting up of the Yaoundé nappe oriented south towards the CC. Meanwhile, this stage in north is marked by N-S to E-W

en echelon or right folds and overfolds related to senestrial strike-slips which are transposed by a D3 stage marked by dextral strike-slips and shear movements along the Central Cameroon Shear Zone (Ngako et al., 1991, 2003; Njonfang et al., 2008; Olinga et al., 2010).

1.2.2. Presentation of the study area

1.2.2.1. Physiography

The study area stretches from the E11°30' to E12°15' longitudes; and, the N02°45' to N04°00' latitudes (**Figure 1 2-2**). This corresponds to an average area of 11,551 km^2. The study area spans over the Centre and the South Regions; and four (04) administrative divisions. The main localities are Yaoundé, Mbalmayo, Mfou, Nkolafamba, Metet, Sangmelima and Zoetele. There are many paved and unpaved roads that cross the entire area.

The area belongs to the south Cameroon plateau. Its global flat topography raises between 600 and 700 m with some peaks from 900 to 1000 m observed around Yaoundé where they form rounded hills stretching in the E-W direction. The climate is equatorial with four seasons (two dryers and two rainy). The temperature rate and annual average rainfall are 24°C and 1480 mm, respectively. The tropical vegetation is always green but presents a deterioration facies in the northern part of the study area while it is denser to the south.

The hydrographical system is dominated by the Nyong River (the main collector) which flows nearly NE-SW to ENE-WSW. Its main tributaries are Ato'o and So'o Rivers, respectively in the north and the south banks, fed up by many streams. In the south, the main river is Lobo, a tributary of Dja. The drainage is generally dendritic, but sometimes locally trellis or radial.

1.2.2.2. Geological context

The lithology of the study area is dominated by the North Equatorial Fold Belt (NEFB) and the Congo Craton (CC) formations, hereafter detailed, northwards (**Figure 1.2-2**).

a. Lithology

The NEFB in the study area is represented by the Yaounde and Mbalmayo series.

i). The Yaounde series

The Yaounde series (YS) forms the basal complex of the northern half of the study area. It is made up of old granitised and metamorphosed sediments in the high pressure granulite facies (Nkoumbou et al., 2014; references therein). Initially seen as the heart of the Panafrican thrust (Nedelec et al., 1986; Nzenti et al., 1988), its rock assemblage includes migmatites (dominant) mainly represented by garnetiferous and migmatised gneisses; and ectinites represented by gneisses associated to micaschists (Champetier de Ribes and Aubague, 1956). These formations are hereafter described.

- ***Gneisses associated with micaschists:***

- *Garnetiferous micaschists:*

They are foliated, made up of quartz, biotite, muscovite and garnets (commonly almandine), with few types of feldspar. They present some quartzite breaks containing muscovite and some garnets (Champetier de Ribes and Aubague, 1956).

- *Micaschist garnetiferous gneisses with two micas*

They contain more feldspars than those above. They are made up of oligoclases, biotite, muscovite, garnets and kyanite. They are fine grained with some biotite and muscovite rich quartzite breaks.

- ***Garnetiferous and migmatised gneisses***

- *Migmatised garnetiferous micaschists*

Their main pattern is the presence of coarse K-feldspars crystals inside micaschists and the development of pegmatite lenses.

- *Two micas embrechites or with biotite solely*

They are dominant, dense and banded. They are made up of: (1)- a framework composed of biotite, quartz and garnets soaked up with feldspars (microcline, oligoclase and albite) and kyanite; (2)- Drift lenses or veins made up of fine grained biotite, garnets and quartz grains elongated in the schistosity strike (Olinga et al., 2010; references therein). Beside the above described formations, there are many mica-quartzite formations that are encountered both in ectinites and migmatites. The economic minerals present are graphite and titanium iron oxides.

ii). The Mbalmayo series

The Mbalmayo series (MS) is the southernmost member of the YG (**Figure 1.2-2**). The MS lays discordant onto the CC and possibly corresponds to the sole of the Yaounde nappe which was exhumed after the collision and thrust of YG onto the CC (Toteu et al., 2004; Olinga et al., 2010). It outcrops as flattened domes without any vegetation in Mbalmayo and Metet. The MS formations are schists and quartz-sericite which slightly dip to the east and rest discordant to gneisses and embrechites; and some volcanic relics reported in Metet (Maurizot et al., 1986; Regnoult, 1986). Its mineralogy is mainly quartz, chlorite, tourmaline, zircon and iron oxides.

To sum up, the Yaounde domain corresponds to a vast anticlinorium where pelitic and volcanoclastic sediments were deposited, recrystallized and thrust onto the Congo Craton (Toteu et al., 2001; Olinga et al., 2010; Ngnotue et al., 2012a; Nkoumbou et al., 2014).

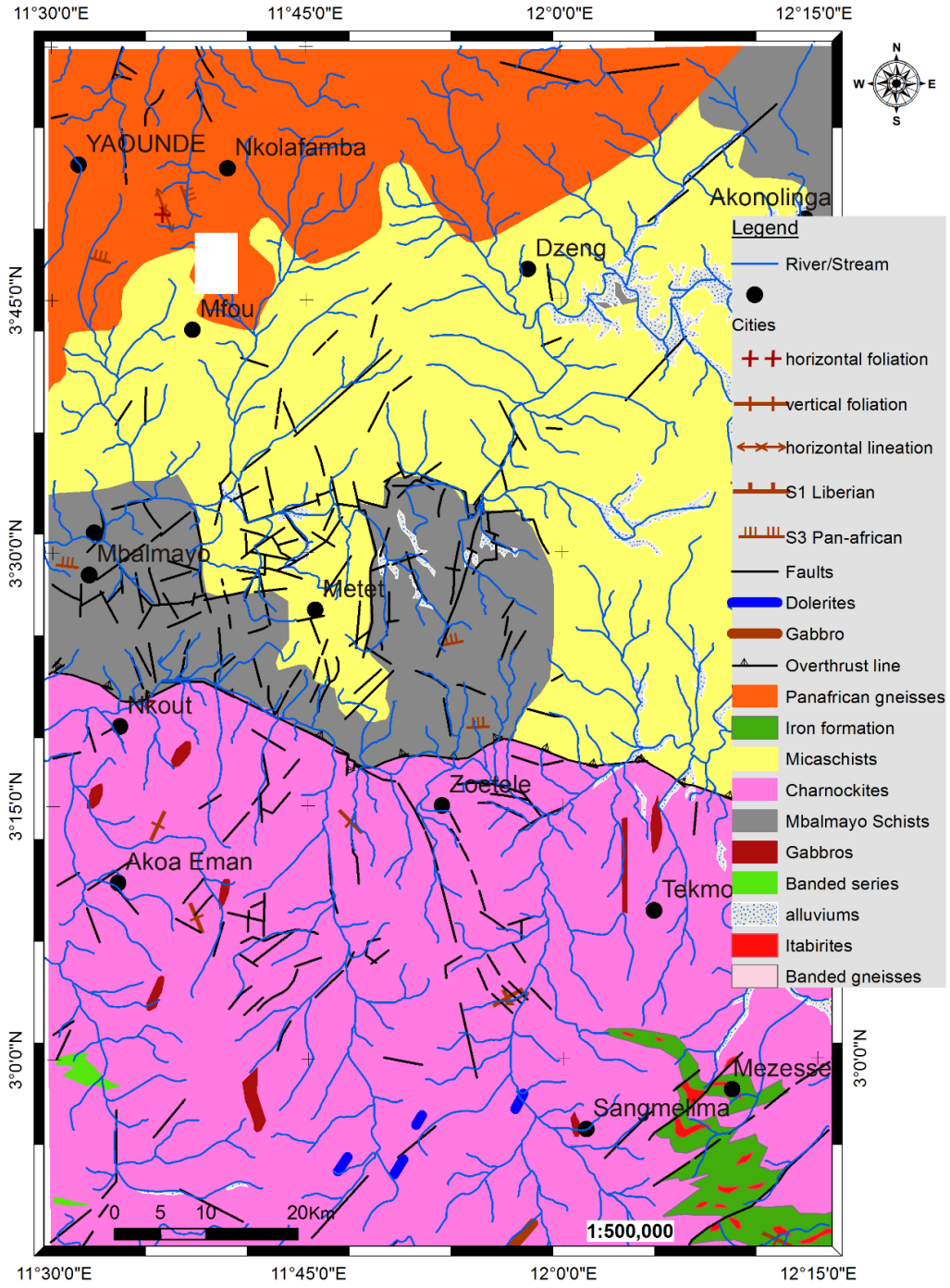

Figure 1.2-2 : Geological map of the study area (Maurizot, 1986 modified).

iii). The Congo Craton (CC)

The Congo Craton (CC) or Ntem complex seats in the southern part of the study area (**Figure 1.2-2**); its formations mainly result from a magmatic activity that ended in the Eburnean (Meso-Proterozoic). According to the geological studies, the main rock budget of the Ntem complex is formed by tonalite-tronghemite-granodiorite (TTG) and K-rich granitoids (Shang et al., 2007, 2010; Tchameni et al., 2010; references therein). Members of the TTG suite include charnockitic rocks, tonalites and granodiorites (Shang et al., 2004a). The tonalitic suite (early

known as Soo granites) essentially exposed to the north, is strongly mylonitized and retrogressed along the fault boundary with the NEFB, while granodioritic suite massifs form distinct bodies within the dominantly charnockitic southern zone (Nedelec et al., 1993; Shang et al., 2004a, 2004b; references therein). Charnockites crop out as xenoliths within TTG massifs and TTG-type veins also occurring charnockite massifs thus portraying relative chronology for these granitoids. Exposures of supracrustal rocks (banded iron formations, sillimanite-bearing paragneisses, garnet bearing amphibolites and pyroxenites) representing ca. 3100 Ma greenstone belts remnants are also present (Maurizot et al., 1986; Tchameni et al., 2004). Late- to post-tectonic granitoids and calc-alkaline to alkaline syenites which clearly postdate the major crust forming episode intrude the TTG (Nedelec et al., 1990; Tchameni et al., 2000, 2001; Shang et al., 2004a, 2007). Meanwhile, the magmatic activity contributing to the crust budget in the Ntem complex is witnessed by post-Archean doleritic dykes affected by Eburnean (2050 Ma) high-grade metamorphism (Toteu et al., 1994; Vicat and Moloto-a-Kenguemba, 2001).

b. Tectonics

The belonging of the study area to both the NEFB and the CC, imposes a description of tectonics as per domain.

i). Tectonics in the Panafrican domain

The evolution of the Yaounde basin and the its subsequent formations has been described by various models which are sometimes anatagonists; but globally, the deformations affecting the Panafrican domain in Cameroon are aged from the late Meso- to post Neoproterozoic. According to Ngako and Njonfang, (2011), that evolution started with a back-arc development which resulted in the opening of the Yaounde basin at the northern margin of the CC, which was later affected and shaped by that four events. The NEFB evolution involved (i) subduction and back-arc basin and range setting to the north of the CC (1000–640 Ma); (ii) collision leading to thickening, emplacement of early nappes (e.g. Yaounde and Bafia groups) and high-pressure granulite-facies metamorphism (640–630 Ma); (iii) protracted crustal shortening with migmatisation and exhumation of the southern metasediments (Yaounde granulites) in ca. 600 Ma; and (iv) conjugate wrench movements associated to delamination of the lithospheric mantle (585–570 Ma) leading to dextral shearing and widespread granitisation (CCSZ, Adamawa granitoids). Extensional tectonics at northern margin of the CC have been confirmed by many recent studies (e.g. Ngnotue et al., 2012; Nkoumbou et al., 2014; Tchakounté Numbem et al., 2017) despite their different implications on the evolution of the NEFB/CC transition zone.

The literature on the YS reveals that its position as a sheet on the northern edge of the CC resulted from sub-horizontal tangential deformations (Nzenti et al., 1988; Ngako et al., 2008a;

references therein). Detailed studies (Mvondo et al., 2003, 2007c; Olinga et al., 2010; Mbola-Ndzana et al., 2014) around Yaounde show that the textures of rocks correlate with four deformation stages. The D1 event preceding the calc-alkaline diorites mineralization is responsible of the nappe formation that led to the granulitic metamorphism of soft sediments. These nappes were reprinted during symmetrical extension D2 (that generated flat regional textures), probably associated to large scale foliation boudinages, gneissic domes formation, and intensive sub-superficial magmatic deposits. These formations were after upraised by unclassified D3 and D4 folding, defining a vertical constriction accompanied by an E-W to NW-SE major narrowing colinear to that of the D1 stage of thrust nappes piling. Olinga et al., (2010) summarised tectonics into alternative E-W to NW-SE contractions and N-S to NE-SW parallel orogenic stretches; all charactyerised by the thrusting of the Yaounde nappe onto the CC; and strike-slip shears in ductile to brittle-ductile conditions (characterized by N or S dipping penetrative foliation), an associated E-W to NW-SE stretching lineation and N-S to NE-SW folding due to the Trans-saharan collision.

ii). Tectonics in the Ntem Complex

The Ntem complex is mix-up of 3200-1800 Ma terrains evolving at the NW margin of the CC (Lasserre and Soba, 1976; Toteu et al., 1994) which recorded several tectonic events in the Archaean, the Paleoproterozoic and Neoproterozoic eras. The Archaean evolution mainly dominated by the Liberian orogeny (Lasserre and Soba, 1976) witnessed the development of greenstone belts and late diapiric intrusions of charnokitic (or not) TTG (Regnoult, 1986) and late anatexite K-granitoids (Tchameni, 1997). Structural events correspond to syn-metamorphic deformation D1-M1 characterised by E-W subvertical foliation and structures (Tchameni, 1997; Shang et al., 2001) associated with high to low-grade metamorphism (Takam et al., 2009).

The Eburnean orogeny mainly characterises the Paleo-Proterozoic of the CC (Toteu et al., 1994; Tchameni, 1997). This event corresponded to the emplacement of alkaline syenites and dolerites; and the prevalence of a D2-M2 deformation associated to a prograde metamorphism from amphibolite to granulite facies at ca. 2050 Ma (Tchameni et al., 2000, 2001). The deformations are characterised by the development of NNE-SSW lineaments (including dextral or sinistral shear zones) NW (**Figure 1.2-1**) of the Ntem complex (Lerouge et al., 2006; Shang et al., 2007; references therein) probably reactivated during the Panafrican episode. Penaye et al., (2004) linked the Eburnean corresponds to the Sao-Francisco-Congo collision. In opposition to the previous, the Neoproterozoic cycle is very diffuse in the Ntem complex albeit the records near the contact zone with the Yaounde Group (**Figure 1.2-2**). Some studies (Toteu et al., 1994;

Vicat et al., 1998) related it to the emplacement of dolerites at ca 1000 Ma, nepheline syenites around 570 Ma and a low grade metamorphism.

c. Synthesis of the geological evolution of the study area

Without timing investigations, Maurizot et al., (1986) highlighted N-S, NE-SW, E-W and NNW-SSE (**Figure 1.2-2**) lineaments corresponding to faults and strike-slips, in the Ntem complex. More recently, Akame et al., (2013) evidenced NE dolerite dykes; N-S to NNW-SSE and NNE-SSW sinistral shears affecting the granodiorites near Sangmelima. These features show that the Ntem complex is mostly affected by brittle tectonics. The Yaounde Group besides, underwent both ductile and brittle-ductile tectonics dominated by syn to post-Panafrican overprints. The major structural directions displayed are NE-SW to NNE-SSW, NW-SE to NNW-SSE, E-W to ESE-WNW and N-S. Among these, the NE-SW to NNE-SSW and E-W to ESE-WNW directions are related to strike-slips and wrench movements resulting from alternative compressions and orogenic stretches (Olinga et al., 2010; Mbola-Ndzana et al., 2014). Thus, the study area underwent a multistage tectonics activity causing the development of several structural features including foliation, faults and fractures which have been permanently overprinted or reactivated, from the Archaean to the Precambrian, as previously described. In regards with the global tectonics pertaining in the Mesozoic, changes in the African plate movements induced new stress/strain conditions. The accommodation to these led to the reactivation of many faults (Kirkpatrick et al., 2013; Katumwehe et al., 2015) and the development of the CARS, a member of the regional WCARS (Fairhead, 2009; Gaina et al., 2013; Heine et al., 2013). The NEFB accommodates well with the rift's development (see the CCSZ) contrarily to the CC which broke up again at ca. 140 Ma (Pérez-Díaz and Eagles, 2014).

1.2.2.3. Geophysical data

Inactive in early geoscience studies, geophysical investigations have significantly improved the geological information in Cameroon during the last two decades. Many of these studies concern the CC/NEFB transition zone which encompasses our study area.

a. Gravity studies

The gravity is the most ancient and widely used geophysical method for geological investigation in Cameroon. Analysis of heritage gravity data (Collignon, 1968) revealed an E-W zone characterised by strong anomaly gradients in the Akonolinga/Ayos/Nguelemendouka/Abong-Mbang area; interpreted around latitude N04 by Mbom-Abane, (1997) as a major E-W tectonic accident corresponding to the CC/NEFB limit; and in the Mengueme/Abong-Mbang area as an E-W normal fault (Ndougsa Mbarga et al., 2003). These was confirmed by Shandini et al., (2010, 2011) and Basseka et al., (2011) who

further highlighted NE-SW and NW-SE basement lineaments related to faulting at the northern edge of the CC as a consequence of a continent-continent collision (Shandini and Tadjou, 2012; Zanga-Amougou et al., 2013) involving the NEFB and the CC. Additional contributions (Owona Angue et al., 2013) highlighted N-S to NNE-SSW faults (Kribi Fault System) that limit the CC to the west in south-western Cameroon.

b. Magnetic studies

The initial studies involving magnetics realised in Cameroon used of airborne data collected in years 70s. The preliminary interpretation of the related maps over south Cameroon by Paterson Grant and Watson Ltd (1976) revealed minor magnetic anomalies attributed to metamorphic structures. The reinterpretation of some of these aeromagnetic maps by Feumoe et al. (2012) and Feumoe (2014) demonstrated the south extension of the Panafrican formations below latitude N03 and they highlighted WNW-ESE and ENE-WSW lineaments that affect both the CC and the Panafrican in the area. Additional studies in the same area (Ndougsa-Mbarga et al., 2012) imaged ENE-WSW and NE-SW buried Eburnean faults in the CC basement reactivated during the initiation of the CCSZ. Assembe et al. (in preparation) through a local study, correlate these results and associate faulting to collapse of basement below both the Mbalmayo series and the Sôo granites (Ntem complex) in the Yaounde-Sangmelima region.

c. Resistivity studies

The resistivity studies carried out for structural purposes involved mainly Magnetotellurics (MT). Indeed, MT revealed in the Akono outskirts, the NEFB's thrust line onto the CC corresponding to the Eseka-dja faults line (Manguelle-Dicoum, 1988) and a major E-W trending lineament corresponding to the CC/NEFB boundary and secondary ENE-WSW to NNW-SSE lineaments at Ayos, in the southern edge of the NEFB (Manguelle-Dicoum et al., 1992). Later, Tadjou et al., (2008) confirmed the interpretation of the E-W lineament as the CC/NEFB boundary and additionally inferred subsidence within the basement, associated with intrusions of low resistive materials beneath the NEFB domain in the Abong-Mbang/Akonolinga area, east from our study area. Recent applications of audiomagnetotellurics in the CC/NEFB transition zone confirmed the E-W CC/NEFB boundary and associated it to some faults, while theys related the NNW-SSE to ENE-WSW faults to post-collision tectonics (Meying et al., 2009, 2013; Ndougsa-Mbarga et al., 2010) including imprints of active extensional movements in the Yaounde series.

d. Remote sensing studies

A recent use of satellite remote sensing in the region by Akame et al. (2013, 2014) detailed many N-S to NNW-SSE and NNE-SSW fractures and faults that affected the Ntem Complex basement around Sangmelima (south Cameroon). The same technique was used by Teikeu et al. (2016) in the Yaoundé area to map N-S, NW–SE and NE–SW post-orogenic relaxation fractures in Panafrican basement of the Neoproterozoic Yaounde series to north, aligned with those in the Archaean domain to the south (Akame et al., 2013, 2014).

1.3. RESEARCH QUESTION AND INTERESTS

1.3.1. Research question and study objectives

1.3.1.1. Research question

Past and recent studies reveal a multi-staged evolution at the northern margin of the Congo Craton, including its flanking NEFB. Despite the various attempts to explain that evolution, divergences in the proposed explanatory geodynamic model (Penaye et al., 1993; Ngnotue et al., 2012, 2000; Mvondo et al., 2003, 2007a, 2007b, 2009; Pouclet et al., 2006; Toteu et al., 2006a, 2007; Ngako and Njonfang, 2008, 2011, 2018; Mbola-Ndzana et al., 2014; Nkoumbou et al., 2014; Tchakounté Numbem et al., 2017, 2018a, 2018b; Houketchang Bouyo, 2018) maintain the issue unsolved, especially in regards with the recent advances in defining the pre-Neoproterozoic setting at the northern margin of the CC and the global geodynamic evolution within which these models must fit, like the evolution of supercontinents (e.g. Murphy and Nance, 1991; Dalziel, 1997; Chatterjee and Scotese, 1999; Scotese et al., 1999; Piper, 2000, 2013; Pisarevsky et al., 2003b; Cawood et al., 2006, 2016; Scotese, 2009). Moreover, geophysics brought very worthy contributions by evidencing many structures (faults mainly) at various scale, but made few attempts toward geodynamic interpretion (Goussi et al., 2018) of these structures; keeping the debate pending. So, *using geophysics to produce a unifying model that would suitably explain the geodynamic evolution at the northern margin of the Congo Craton is the concern of this work.*

1.3.1.2. Objectives of the study

The current study aims at bringing more light into the understanding of the evolution of transition domain north of Congo Craton in Central Africa, with a reference on the Nkolafamba-Sangmelima region (southern Cameroon), by realising an updated geological map with a related improved mineral potential. Specifically, two objectives are targeted:

(1) The study supports the continent-continent collisional model; therefore, it will endeavour at seizing structural evidences that can validate that hypothesis.

(2) In the absence of geologic observations, geophysics is a good tool to solve geologic problems. But, access to data is the most complicated problem faced by geophysicists in less developed countries. Data, when available, may be from dirrent source, sparse and/or random. This study intends to propose an operational geophysical solution to handle this issue, particularly in the case of juxtaposition of geophysical data sources.

1.3.2. Research interests

From the main objectives above, some interests can exhale if expectations are fulfilled. Those interests are not scientific solely as the study might also influence the nation's wealth.

- The scientific interest comes out here on two aspects: (1) the amelioration of the structural and geodynamic evolution of the CC/NEFB transition zone; and (2) design of a new methodology in applying geophysics.
- At the economic level, by contributing to the amelioration of the geological map of this portion of southern Cameroon, this study can upgrade the mineral potential then increase the mineral exploration activity in this area by attracting more investors.
- The building constructions and groundwater exploitation are booming in some areas of the targeted region due to the increase of the population. This raises some social and environmental concerns (e.g. groundwater availability and pollution, soil stability, sinkholes monitoring, etc.) that the present study may help to mitigate.

Conclusion

The position of Cameroon in the West Central Africa is of great importance in regard to the geological evolution of both Africa and West Gondwana. Various-scales geoscience studies improved the geological information on the Cameroon territory in general and on its southern domain particularly. Geophysics on its own helped to map major structural features affecting the S-Cameroon region, among these are the Congo Craton/Panafrican limit and relays of the CCSZ. Despite the increasing number of geophysical studies carried over the Congo Craton/Panafrican transition zone, complete explanation of interplays between these two major litho-structural units (the CC and the NEFB) either at local or at regional scale remains limited. Also, linking the mapped structural features to the Precambrian supercontinents remain hazy (if not inexistent) till date, making it not possible for geophysics to the arbitrate on the debate about the geodynamic evolution of the Mobile Zone north of the CC. This study temptatively solve these issues by looming initially evidences to the CC/NEFB collision model then drawing sights of neotectonics in the actual global context.

CHAPTER TWO: MATERIALS AND METHODS

Introduction

Geophysics has become an important toolbox for earth sciences, in that it allows screening below the levels where no eye can reach for direct observations. It is the eye that brings the earth scientists beyond the limits they thought they would never go to perform their observations. However, efficient use of this toolbox requires a good understanding of how the tools within (methods and/or techniques) work. In other words, understanding the principles of each geophysical method is vital for their good application. Hence this chapter mainly aims at describing the methods to be used by the current study, starting from audiomagnetotellurics.

2.1. THE AUDIOMAGNETOTELLURIC METHOD

2.1.1. Basic concepts

The fundamental theory for electromagnetic (EM) fields behaviour has been established in the 19th century by James Maxwell through a system of four equations. Recently, Zhdanov, (2009) using the property of differential forms revealed that it is more suitable to consider electric and/or magnetic flux and work as major characteristics of the electromagnetic field, rather than the conventional vector representations. This other approach of Maxwell's equations spines electromagnetic geophysical experiments.

2.1.1.1. Maxwell's equations

Maxwell's equations below (Zhdanov, 2009) are mathematical formulation of laws describing EM fields behaviour, used to develop the electrical prospecting theory. These are:

$$\nabla \times \boldsymbol{H} = \boldsymbol{j} + \frac{\partial \boldsymbol{D}}{\partial t} \quad (1.a)$$

$$\nabla \times \boldsymbol{E} = -\frac{\partial \boldsymbol{B}}{\partial t} \quad (1.b)$$

$$\nabla \cdot \boldsymbol{B} = 0 \quad (1.c)$$

$$\nabla \cdot \boldsymbol{D} = \boldsymbol{q} \quad (1.d)$$

where $\boldsymbol{H}$, $\boldsymbol{B}$, $\boldsymbol{E}$ and $\mathbf{D}$ are respectively, the magnetic, the induction, the electric and the displacement fields vectors. j and q are the conduction current and the electrical charge densities, respectively.

The completeness of these equations comes with the so-called constitutive equations:

$$\boldsymbol{D} = \varepsilon \boldsymbol{E} \quad (2.a)$$

$$\boldsymbol{B = \mu H} \quad (2.b)$$

where, ε and μ are the permittivity and the magnetic permeability of the medium, respectively.

2.1.1.2. Electromagnetic field models

In electrical prospecting, two models for EM fields behaviour mainly used are the static and the quasi-stationary models. The first model governs Direct Current methods while the second is the frame of EM methods.

The quasi-stationary model is obtained by removing the term $\frac{\partial \boldsymbol{B}}{\partial \boldsymbol{t}}$ that is, neglecting effects of displacement current. The EM fields behaviour is then described by the diffusion equations:

$$\boldsymbol{\nabla^2 E - \mu\sigma E = 0} \quad (3.a)$$

$$\boldsymbol{\nabla^2 H - \mu\sigma H = 0} \quad (3.b)$$

where $\boldsymbol{\sigma}$ is the conductivity of the medium.

Equations (3.a & b) describe the propagation of EM fields into conductive media as *electromagnetic diffusion*. This supposes that in quasi-stationary regime, electromagnetic fields are independent of the dielectric properties of the medium (Zhdanov, 2009).

2.1.1.3. The monochromatic electromagnetic field

In the case of a monochromatic electromagnetic field, assuming that the time dependence is expressed by the term $\boldsymbol{e^{-\omega t}}$ in the equations above lead to complex expressions (Zhdanov, 2009).

$$\boldsymbol{\nabla^2 E + i\omega\mu\sigma E = 0} \quad (4.a)$$

$$\boldsymbol{\nabla^2 H + i\omega\mu\sigma H = 0} \quad (4.b)$$

Introducing the wave number k, equations (4.a & b) can be written in the form:

$$\boldsymbol{\nabla^2 E + k^2 E = 0} \quad (5.a)$$

$$\boldsymbol{\nabla^2 H + k^2 H = 0} \quad (5.b)$$

And then $\boldsymbol{k = (i\omega\mu\sigma)^{1/2} = (i)^{1/2}(\omega\mu\sigma)^{1/2}}$

To satisfy the condition Re(k)>0 and Im(K)<0, we will consider the positive square root of i: $\boldsymbol{(i)^{1/2} = e^{i\pi/4}}$ and according to the approximation $\boldsymbol{\mu \approx \mu_0}$ we obtain the expression of the wave number (equation 6):

$$\boldsymbol{k = e^{i\pi/4}(\omega\mu_0\sigma)^{1/2}} \quad (6)$$

Where $\boldsymbol{\mu_0}$ is the free-space magnetic permeability ($\boldsymbol{\mu_0 = 4\pi \cdot 10^{-7} \Omega \cdot s/m}$). Defining the parameter λ such as: $\frac{2\pi}{\lambda} = (\omega\mu_0\sigma)^{1/2}$ and recognizing that:$\boldsymbol{\omega = \frac{2\pi}{T}}$, where T is the period oscillation in seconds; and $\boldsymbol{\sigma = \frac{1}{\rho}}$, we deduce equation (7):

$$\boldsymbol{\lambda} = (\mathbf{10^7 \rho T})^{1/2}\text{m} \qquad (7)$$

λ is the wavelength and it is of extreme importance in electrical sounding as it permits to define the depth of penetration of the EM field into the earth, sometimes referred to as skin depth (δe).

$$\boldsymbol{\delta_e = \frac{\lambda}{2\pi} \approx 0.159(10^7 \rho T)^{1/2}}\ \text{m} \qquad (8)$$

2.1.2. The Audio-magnetotelluric (AMT) method

2.1.2.1. Overview

The premises of the EM methods have been laid by Rikitake (1948), but the development of the magnetotelluric (MT) method started first with Tikhonov (1950) and then by Cagniard (1953). The essence of the MT method is to observe the subsurface impedance over a spectrum of frequencies to determine conductivity (or resistivity) as function of depth, based on the recognition that the depth reached by a field depends on its attenuation (Telford et al., 1990). Further, a high-frequencies MT (or Audiomagnetotelluric (AMT)) application was developed (Niblett and Sayn-Wittgenstein, 1960; Vozoff, 1972; Strangway et al., 1973; Goldstein and Strangway, 1975) and applied to various fields such as geological surveys, mineral and petroleum explorations.

The MT/AMT method uses naturally occurring time-varying EM-fields generated by solar winds interaction with the magnetosphere or worldwide thunderstorms (spherics) to investigate the electrical conductivity of the Earth's structures (Vozoff, 1991; Garcia and Jones, 2000a). These time-varying magnetic fields induce electric fields within the Earth's. Thus, observations of the temporal and spatial variations of electric and magnetic fields at the Earth's surface contain information about the distribution of the electrical conductivity within the Earth. The conductivity, which depends on such things as rock composition and water content, may be related to geological structures, economic mineral, hydrocarbon and water-bearing formations. The typical range of the electrical conductivity of earth material varies widely from 10^{-5} to 10^{2} usi (Parasnis, 1986; Palacky, 1988; Telford et al., 1990).

2.1.2.2. Simplifying hypotheses

The development of the MT theory lies on the assumption of some hypotheses:

Firstly, the subsurface is assumed to be tabular. Then, the magnetotelluric wave is a plane wave propagating downwards along (O,z) and is polarized (**Figure 2.1.1**) so that electric field E and magnetic field H are directed along (O,x) and (O,y) axes, respectively, in the (O,x,y,z) Cartesian reference system.

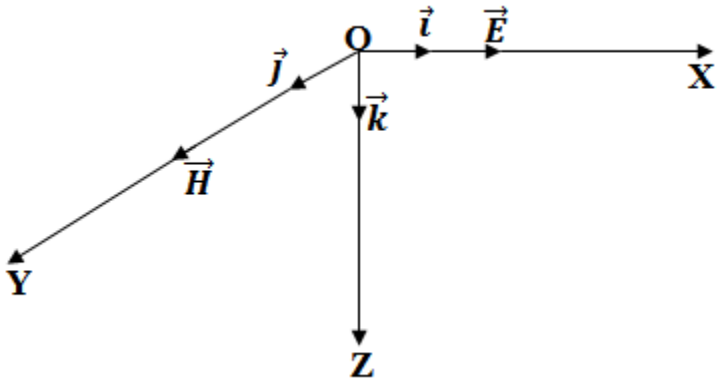

Figure 2.1-1 : Cartesian reference system in AMT/MT theory.

Secondly, displacement current effects are neglected. This supposes that electromagnetic fields are independent of the dielectric properties of the medium. Hence equations (5a), (5b) and (6) are valid.

Horizontal gradients of magnetic and telluric field vectors are insignificant compared to the vertical gradients, and that time variations are periodic (Niblett and Sayn-Wittgenstein, 1960; Dmitriev and Berdichevsky, 1979; Vozoff, 1990a; Chave et al., 2012) it results in following relations:

$$\frac{\partial}{\partial x} = \frac{\partial}{\partial y} = 0 \quad \text{and} \quad \frac{\partial}{\partial t} = -\frac{2\pi i}{T} \qquad (9)$$

Where variables are expressed in terms of Cartesian coordinates (x, y, z) and T is the period. These hypotheses suggest that the electrical conductivity is a function of depth only, and field variation sources are so that horizontal extension of phenomena at the surface are greater than their penetration depth.

2.1.2.3. The Tensor-Audiomagnetotelluric method

Modern AMT systems record variations of both the electric and magnetic fields in two orthogonal directions then calculate the subsurface impedance at a measurement site. The scalar subsurface impedance defined as:

$$Z_{ij} = \frac{E_i}{H_j} \qquad (10)$$

is easier to calculate but its weakness resides in its ability to vary with the direction of the source fields. A tensor formulation would better account for this variations (Bailey and Groom, 1987, n.d.; Bahr, 1988; Groom and Bailey, 1989; Vozoff, 1990a; Weaver et al., 2000). Indeed, the surface tensor impedance Z is complex, frequency-dependent, and, because of the presence of noise and the earth structures. The surface impedance tensor $\bar{\bar{\mathbf{Z}}}(\boldsymbol{\omega})$ should be thought helpfully as a two input, two output linear system where the inputs are the magnetic field components and the outputs are the electrical field components, as shown by equation (11) (Mcneice and Jones, 2001)

$$\bar{\mathbf{E}}(\boldsymbol{\omega}) = \bar{\bar{\mathbf{Z}}}(\boldsymbol{\omega}) \cdot \bar{\mathbf{H}}(\boldsymbol{\omega}) \text{ or } \begin{cases} \mathbf{E_x} = \mathbf{Z_{xx}H_x} + \mathbf{Z_{xy}H_y} \\ \mathbf{E_y} = \mathbf{Z_{yx}H_x} + \mathbf{Z_{yy}H_y} \end{cases} \qquad (11)$$

This tensor formulation is preferred over the scalar formulation because, when the source fields are nearly plane waves, the impedance elements $\boldsymbol{Z_{ij}}$ are time-invariant and permits a two- or three-dimensional (2-D or 3-D) study (Vozoff, 1990; Garcia and Jones, 2002; Ledo et al., 2002; Zhdanov, 2009). The surface impedance is usually expressed as apparent resistivity and impedance phase, calculated from the surface impedance components as (Zhdanov, 2009) (Geometrics, 2000):

$$\boldsymbol{\rho_{ij}} = \frac{\mathbf{1}}{\boldsymbol{\omega\mu_0}} \left|\mathbf{Z_{ij}}\right|^2 = \mathbf{0.2T}\left|\mathbf{Z_{ij}}\right|^2 \qquad (12.a)$$

$$\text{and } \boldsymbol{\emptyset_{ij}} = \mathbf{tan^{-1}}\left(\frac{\mathbf{Im(Z_{ij})}}{\mathbf{Re(Z_{ij})}}\right) \qquad (12.b)$$

The AMT method entails simultaneous measurements of electric and magnetic fields over the frequency range 10 Hz to 10 kHz. However, signals are generally weak in the frequency range 1 kHz to 5 kHz called the AMT dead band (Garcia and Jones, 2000) and data acquisition then requires a controlled source system or transmitter (Zonge and Hughes, 1991; Goldstein and Strangway, 1975; Vozoff, 1990). For valid interpretations, measurements site must be sufficiently distant from the transmitter to be located in the transmitter's far field, so as to enable the plane wave assumption (Zonge and Hughes, 1991; references therein).

2.1.3. AMT data acquisition and interpretation

2.1.3.1. Data acquisition

a. The equipment

The AMT data for our study have been collected with the Stratagem EH4 resistivity-meter made by EMI and Geometrics Inc (**figure 2.1-2**). This system uses a combination of natural and hybrid MT signals. Any available natural background signals are used in the entire frequency band while a transmitter is used to provide additional high-frequency signals in the

range of 1 kHz to 70 kHz where natural signals are weak. To optimise high/low frequency data collection, the operator can select the frequency bands and the number of time series "stacks" for data collection (Geometrics, 2000).

The EH4 transmitter, powered by a 12V DC battery, consists of a dual-loop antenna, transmitter's electronics, and a controller. It provides non-polarised source fields which allow for true tensor measurements of ground resistivity. This provides more accurate interpretation of true resistivity than conventional single-dipole transmitter source signals. The resolution depth is more than 1km but, in general, depth to which a target can be imaged depends on the earth's resistivity/conductivity at the survey site and the lowest frequency for which there are reliable data (Geometrics, 2000; McPhee et al., 2006, 2008).

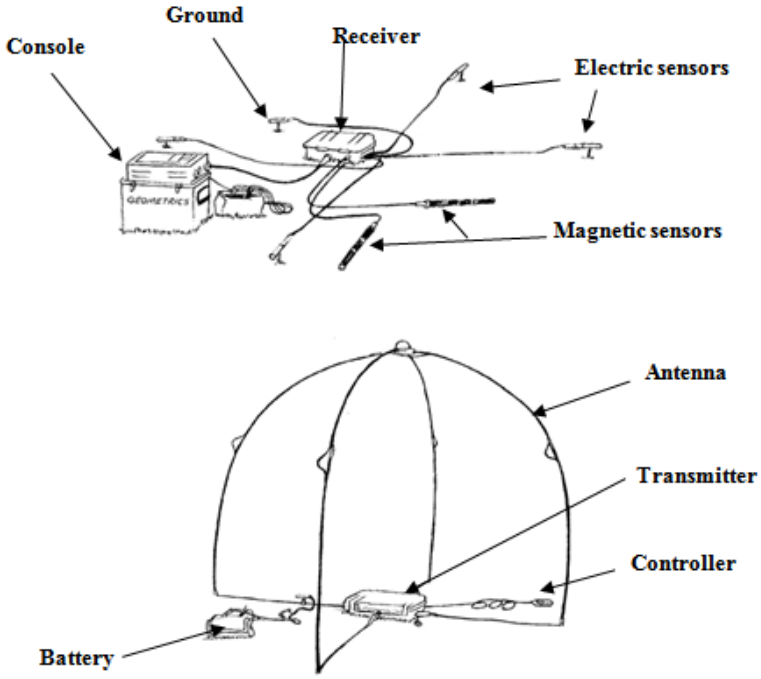

Figure 2.1-2 : Standard EH4 equipment layout (Geometrics, 2000).

Along with the EH4 system, standard field instruments were used. These are, a Garmin 60s GPS to record the stations location data; a compass; a water level to check the horizontality of coils; a 50 m tape to measure the length of dipoles.

b. Description of profiles

Generally, in geophysical surveys, profiles must be directed perpendicularly to the a priori geologic strike of a given area. The approximate orientation of profiles is N135, as the SW-NE strike supposedly controls the regional geology. AMT data were collected with a Stratagem EH4 kit during two field campaigns achieved progressively in August 2011 then August 2012 for a total of 35 stations and 6 profiles, two by two parallel. The first five profiles have an inter-station distance of 100m and a profile length of 500 m; each profile comprising six

stations (the second profile is 400 m length with five stations). Besides, profile 6 is 1500 m length with a mean stations spacing of 300 m.

The profile 1 to profile 4 forms a set of four profiles which were realised in the Nkolafamba subdivision while the second set (profiles 5 and 6) was realised in the Mfou subdivision, nearly 20 km away on bird's wing southeast from the first site. Except on profile 1 where x and y dipoles lengths are 50 m and 25 m, respectively, these lengths are equal (25 m) for the five remaining profiles.

c. Measurement sites

Generally, measurement sites were away from human activity (**photo 1**), in quiet places to avoid cultural noise revealed by signals distortion. Distortion of signals can be caused by the interaction between a near EM and the magnetotelluric fields. This happens when a measurement site is located near of power generation or consumption sites, noisy sources and mechanical activity sites. Noisy sources include power lines, electric fences, radio transmitters, pipelines with cathodic protection, proximity to large metal clumps, flowing water or wind vibration, etc.

Photo 1 : Recording of AMT data in a remote area (Profile 1).

The transmitter-antenna unit was sometimes set to improve signal strength. Geographical coordinates of the stations are given in the appendices. Data acquisition was done by recording several passes individually composed of one or more time-series segments in a particular band. Signals are processed into time series from electric and magnetic fields, which are converted into frequency domain measurements (spectral data) by Fast Fourier Transform.

2.1.3.2. Data processing

Tensor-AMT data recorded in the frequency domain are transformed into EM transfer functions from which apparent resistivity and phase tensors are estimated. The data are

processed within the stratagem EH4 using the Bostick transform (Sims et al., 1971; Boehl et al., 1977; Bostick, 1977) that links the apparent resistivity to the phase using the Hilbert transform.

a. Signals' correlation

Stratagem EH4 records the EM field through four channels representing electric and magnetic fields components. For electric and magnetic field are coupled, this must be the same for their components; thus, the signal response for transverse complementary components must be similar (**Figure 2.1-3**). This supposes that, the phase and amplitude of E_x should resemble those of H_y and so for E_y and H_x. The operator should be aware if, for example, at least one channel is constantly out of scale or doesn't correlate with the others.

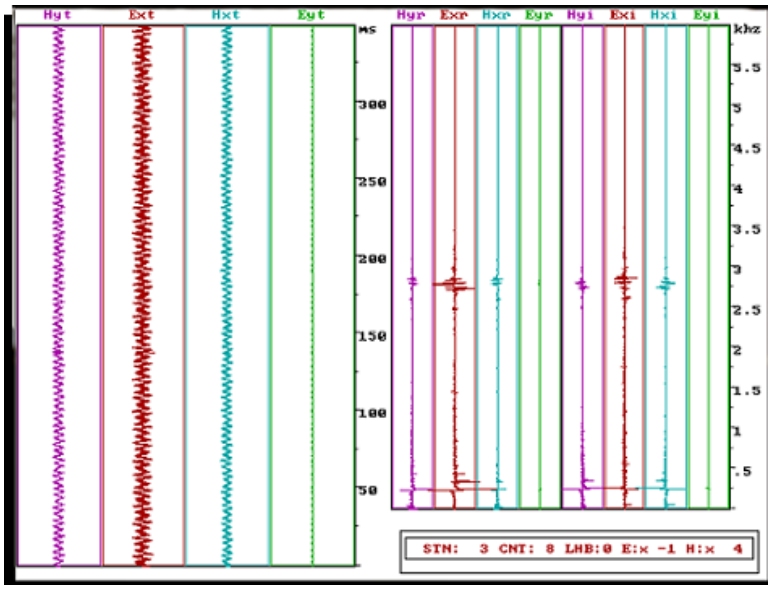

Figure 2.1-3 : Signal's correlation display (Ossol, station 3). Disturbances are observed in the same frequency ranges for all the signal components at the right of the display, meaning a good correlation of signals.

b. Impedance components' correlation

The correlation of impedance components ensures the validity of a sounding. When they correlate, we should observe a dip in the phase response when apparent resistivity increases with the period (or frequency decreases), and contrariwise for a period's decrease. This phenomenon is expected according to the relationship between impedance components:

$$\emptyset = \frac{\pi}{4}\left(1 - \frac{\partial(log\rho_a)}{\partial(logT)}\right) \qquad (13)$$

Slight departures from equation (13) are expected because of the normal low-level scatter in the data but when an important portion of the sounding curve fails to obey it, then cultural noise sources may have introduced a bias.

c. Data coherency

Typically, the correlation of EH4 data is expressed in terms of coherency (Geometrics, 2000). Since electric field values can be estimated from those of the magnetic field, the

coherency between predicted electric field values and those measured is the signal on noise ratio. In the Stratagem EH4 system, acceptable data are those for which the coherency is above 0.5.

2.1.3.3. Data interpretation.

Data interpretation consist in equating the resistivity imaging to a hypothetical subsurface geology of an area. The steps followed are (1) analysing resistivity and phase pseudo sections and (2) earth-modelling through geoelectrical sections; both after the dimensionality analysis.

a. Dimensionality analysis

Dimensionality refers to the subsurface geoelectrical structure or spatial distribution of the electrical resistivity, classified either as 1-D, 2-D or 3-D (Bailey and Groom, 1987; Zhang et al., 1987; Vozoff, 1991; Parker, 2011). In a 2-D earth, the conductivity is constant along one horizontal direction while changing both along the vertical and the other horizontal direction. The direction along which the conductivity is constant is known as the geo-electric strike (Vozoff, 1991; Chave et al., 2012). The Stratagem EH4 system performs simultaneous measurement of the EM field along two orthogonal directions which enable to decouple the impedance tensor components in to a TE and TM and to assume that the geoelectrical structure is at least 2-D (Geometrics, 2000; Simpson and Bahr, 2005; McPhee et al., 2006). Moreover, Groom and Bailey (1989) empirically established that dimensionality can be assessed by observing the behaviour of the resistivity curves in both TE and TM modes when plotted on the same graph. They found that when the ground structure is at least 2D, the TE and TM resistivity curves generally once coinciding depart from each other at low frequencies.

b. Apparent resistivity and phase pseudo sections

Pseudo-sections are contour plots with distance on the horizontal scale and frequency (log of) on the vertical. They picture how resistivity or phase varies with depth (lower frequency is equivalent to greater depth). The phase has the advantage of being non-sensitive to the effects of shallow subsurface anomalies, so it is particularly useful for the detection of deep structures (Caldwell et al., 2004; Weaver et al., 2006). Pseudo-sections enable to highlight lateral discontinuity zones which appear with strong horizontal resistivity gradient, thus contrasting with tabular zones where isoresistivity lines are horizontal (Vozoff, 1972). In this work pseudo-sections ploted with Surfer 13™.

c. Geoelectrical section

The geoelectrical section or 2-D resistivity is a model of the subsurface resistivity structure (Zhdanov, 2009), so as to give the hypothetical lithological arrangement beneath a

profile (Zhdanov, 2009; Chave et al., 2012; Meying et al., 2013).. The model assumes a tabular layering and that a resistivity contrast defines each layer.

2.1.3.4. Ancillary

The AMT data processing and interpretation were done with Imagem an EH4 built-in program which transforms the time-series into impedance data finally stored as apparent resistivity, phase, and as 2-D resistivity data. These processed data are visualised with plot2D, a program designed to view and print the 2D results produced by Imagem (Geometrics, 2000). However, for clarty pseudo sections are displayed with Surfer v.13 ™. Before any interpretation, the electrical structure has been assessed using ZondMT2D™.

2.2. THE MAGNETIC METHOD

The magnetic effect is far most the earliest physical parameter that seized the human though. Questioning the mutual attraction of lodestones has been traced back to the Greek philosopher Thales era, in the sixth century B.C. Additionally, the tendency of lodestones to align preferentially in certain directions, observed in early Christian era was apparently the first recognition that the earth is associated with a property that affects magnetic objects, thus opening the door to geomagnetic studies (Blakely, 1996). As geological applications of magnetics began as early as 1930, the World War II favoured the advent of aeromagnetics (Blakely, 1996).

2.2.1. The fundamentals

2.2.1.1. The geomagnetic field

a. The nature of the geomagnetic field

Historically, the Chinese invention of the compass is the main evidence of the earth's magnetic (or geomagnetic) field whose components were summarised by Campbell, (1997):

- The main field originates from the inner Earth and varies slowly. It results from convection currents in the outer core and the planet's rotation (dynamo effect). Considered as a dipolar field of about 50 000 nT, it contributes about 80-90 % of the geomagnetic field.
- The external field, smaller than the main field, is caused by spherics and all particles and radiations from the space and the sun (ionized flow in the upper atmosphere).
- The crustal field, also smaller than the main field, originates from ferromagnesian rocks and/or near-surface crustal heterogeneities seated where temperatures are sufficiently low, i.e., less than about 580◦C (Curie temperature of magnetite). This region is confined to the upper 20‑30 km of the crust. The crustal field is related to the distribution of

magnetic minerals within the crust, and the information this relation provides about exploration targets make the philosophy of magnetic exploration method.

The figure 2.2-1. gives two representations of the geomagnetic field and its components.

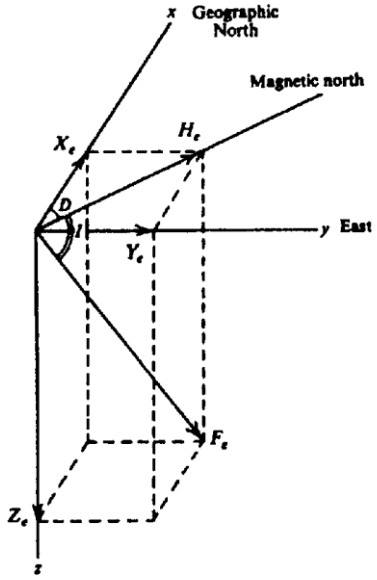

Figure 2.2-1 : Representation of the total magnetic field Fe.

The total magnetic field vector may be defined either (a) by its three orthogonal components (horizontal north $\mathbf{X_e}$, horizontal east $\mathbf{Y_e}$ and vertical $\mathbf{Z_e}$) or (b) by the scalar magnitude of the total field, $\mathbf{F_e}$ and two angles, the inclination from the horizontal, I and the declination from true (geographic) north, D. The second definition pertains to geophysics, since only the scalar magnitude Fe is generaly measured.

b. The International Geomagnetic Reference Field (IGRF)

The IGRF (Peddie, 1983) corresponds to the standardised value of the geomagnetic field at any point on the Earth's surface. It is published by the International Association of Geomagnetism and Aeronomy (IAGA) on a five-yearly basis, using a mathematical model which best fits all the actual observational data from geomagnetic observatories, satellites and other approved sources for a given epoch. The model is defined by a set of spherical harmonic coefficients to degree and order 13 (Campbell, 1997). The value of F_e worldwide at the epoch of the model (e.g. for 1995) and the annual rate of change in these coefficients for the following five years (e.g. 1995-2000) are computed, a software which permits the use of these coefficients to calculate IGRF values over any chosen survey area is available (Reeves, 2005). The values currently in use are based on the IGRF 2015 and its tentative extrapolation (prediction) to 2020. Eventually, a definitive model until 2020 will be adopted with an extrapolation to 2025, and so

on. The IGRF coefficients are published and freely availed by IAGA at http://www.iugg.org/IAGA/iaga_pages/pubs_prods/igrf.htm.

Magnetic field in SI units is defined in terms of the flow of electric current needed in a coil to generate that field. Thus, its units are volt-second per square metre or Weber/m2 or Tesla (T). Since the magnitude of the Earth's magnetic field is only about 5 x 10^{-5} T, the convenient SI unit of measurement in geophysics is the nanoTesla (nT = 10^{-9} T).

2.2.1.2. Magnetic properties of earth materials

a. Types of magnetisation

The inner earth magnetism originates from two main types of magnetisation, the induced or normal magnetisation and the remnant or permanent magnetisation.

- ***Induced magnetisation:***

Normal (or induced) magnetisation J_i is due to the induction of the Earth's magnetic field. When a magnetic material is placed in a magnetic field, the material becomes magnetised and the external magnetising field is reinforced by the magnetic field induced in the material itself. The direction and amplitude is proportional (the proportionality constant is the magnetic susceptibility) to the applied field (Reeves, 2005).

- ***Remnant magnetisation:***

Remnance is a type of permanent magnetisation J_r, which prevails in some rock types more than others, and contributes to the total magnetisation. When the external field is cancelled, the induced magnetisation disappears at once, but some materials retain a permanent or remnant magnetisation whose direction will be fixed within the specimen in the direction of the inducing field. Remnant magnetisation is complex and can be due to several causes including the thermo-remnant magnetisation, which happens when magnetic materials are cooled down to the Curie point (temperature above which magnetic properties theoretically vanish) in the presence of an external field (Hinze et al., 2013, references therein). Very old rocks shew that the remnant magnetisation vector can remain unchanged, regardless of any subsequent changes in the ambient field (see Clark and Emerson, (1991) for further reading on magnetisation).

Simply, it follows that any rock in situ may now be expected to have two magnetisations, one induced and one remnant. The induced component, J_i, is parallel to the Earth's present field, while the remnant component, J_r, may reasonably have any direction. As vector quantities, their sum is a vector giving the total magnetisation of the rock in situ. For simplifications, the Koenigsberger ratio, Q, defined by equation (14) is preferred in geophysicis.

$$\boldsymbol{Q = J_r / J_i} \qquad (14)$$

Very often, it is necessarily assumed that the value of Q is small, i.e. that all significant magnetisation in the rocks is induced and in the direction of the present day Earth's field.

b. The magnetic susceptibility

Clearly, all crustal rocks find themselves situated within the geomagnetic field. They are therefore likely to display induced magnetisation. The magnitude of the magnetisation they acquire, J_i, is proportional to the strength of the Earth's field, $\boldsymbol{F_e}$, in their vicinity. The constant of proportionality, k, is, by definition, the rock's magnetic susceptibility (Reeves, 2005; Lowrie, 2007):

$$\boldsymbol{J_i = kF_e} \qquad (15)$$

Magnetic susceptibility in SI units is a dimensionless ratio with values less than 1 for most rocks, as illustrated by the **figure 2.2-2** below from Clark and Emerson (1991).

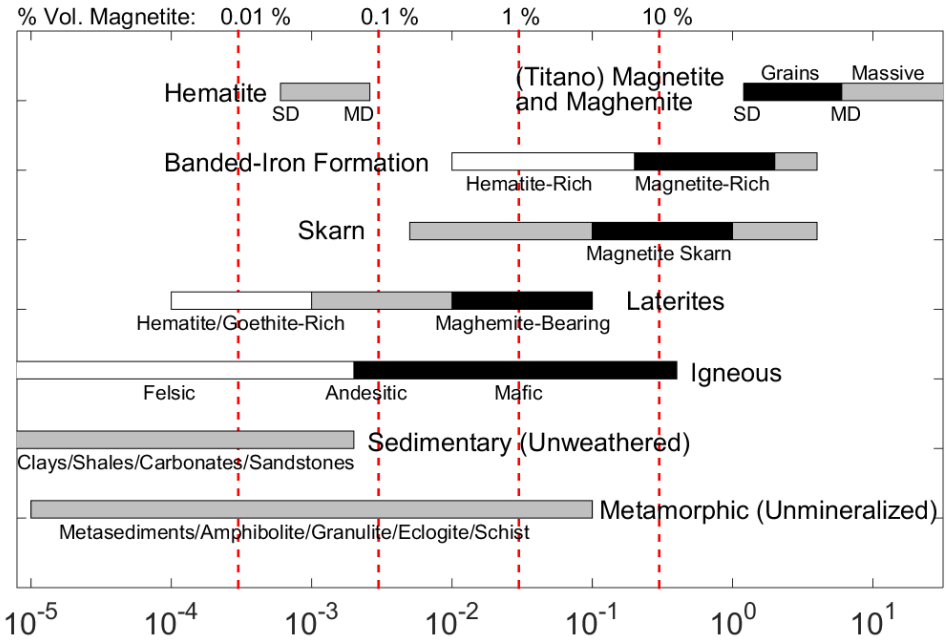

Figure 2.2-2 : Magnetic susceptibility scale for common minerals (Clark and Emerson, 1991).

c. The magnetic domains and minerals

- ***Magnetic domains or groups***

In general, solid materials are classified as diamagnetic, paramagnetic, ferromagnetic and anti-ferromagnetic. The first two types of magnetic property have been usually considered as insignificant in magnetic anomaly mapping; rocks having only these properties are often classed as ***non-magnetic***, since their magnetisation is orders of magnitude less than that of common sources of magnetic anomalies. Ferromagnetic materials, by contrast, contain magnetic "domains" which magnetise very easily, whereas anti-ferromagnetic materials have domains which cancel each other out to give zero magnetisation. Most magnetic materials of geological

significance are imperfectly anti-ferromagnetic, for which class the term ferrimagnetic is used. In fact, only a rather small number of minerals display significant magnetic properties are mixed oxides of iron, titanium, manganese plus one sulphide mineral, pyrrhotite (Reeves, 2005).

- ***Magnetic minerals***

The minerals that normally cause observable magnetic effects in mineral eexploration are (Redford, 2014 personal communication):

- Magnetite (Fe_3O_4): the most magnetic mineral, generally with neglectible remanence.
- Monoclinic Pyrrhotite (FeS): only the monoclinic form is magnetic and frequently has remnant magnetisation an order of magnitude greater than its induced magnetisation– the susceptibility of pyrrhotite is circa 1/10 that of magnetite.
- Hematite (Fe_2O_3): at times having strong remanence, it can show weak magnetic responses due to induced magnetisation.
- Ilmenite/Titanohematite ($Fe^{2+}TiO_3$/ $(Fe, Ti)_2O_3$): it can give weak but observable magnetic responses. Titanohematite is an intergrowth richer in hematite.
- Maghemite (Fe_2O_3): it is a weathering product of spinels containing ferrous oxides (usually magnetite or titano-magnetite) which can have strong magnetic responses.

2.2.2. Aeromagnetic surveying

2.2.2.1. The principles

The high-order terms in the energy density spectrum of the geomagnetic field are related to the magnetization of crustal rocks. Magnetic investigations then, can yield important data about geological structures. By analogy with gravity, a magnetic anomaly is defined as the local difference between the measured (and suitably corrected) magnetic field of the Earth and that which would be expected from the IGRF (Lowrie, 2007). This anomaly results from the contrast in magnetization when rocks with different magnetic properties are adjacent to each other; e.g. when a strongly magnetic basaltic dike intrudes a less magnetic host rock (Paterson and Reeves, 1985; Telford et al., 1990; Nabighian et al., 2005). The stray magnetic field surrounding the dike locally disturbs the geomagnetic field and can be measured with sensitive magnetometers. Equation (16) summarising these statements is part of the magnetic data reduction (Paterson and Reeves, 1985; Campbell, 1997; Nabighian et al., 2005; Reeves and Korhonen, 2007; Hinze et al., 2013) :

$$\mathbf{M} = \mathbf{F_e} - \mathbf{F_{IRGF}} \qquad (16)$$

Where $\mathbf{F_e}$, $\mathbf{F_{IGRF}}$ and $\mathbf{M}$ are respectively the total, the reference and the reduced magnetic fields.

2.2.2.2. Surveying procedures

In the airborne magnetic surveying, the procedures and stages are common to ground and marine magnetic surveying methods hereafter presented.

a. Data acquisition

Aeromagnetic meseaurements are usually made either through helicopter (bird) or plane (stinger). alsmost same patterns are required and the same equipment are used to collect data. Interested readers can nurture themselves on aeromagnetics, with the literature from Reeves et al. (1997), Reeves (2005); Boyd and Isles (2007), and Hinze et al. (2013). The aeromagnetic survey specifications are as follow:

- The traverse or survey line spacing is chosen regarding the desired resolution and size of the structures to image;
- The traverse trend is defined according to the known strike of geological structures in the area;
- The tie or cross line are perpendicular to traverse. Their spacing is 5 to 10 times the traverses' spacing;
- The flight height or survey elevation is either according to sea level or constantly above ground level (terrain clearance).

b. Data correction and reduction

The data correction stage involves some calculations to remove diurnal variations in the field due to the part of geomagnetic field that originates from ionosphere, position and altitude corrections (Brodie, 2002). Generally, these tasks are partly performed by the contractors (Hinze et al., 2013) who provide data as total magnetic field intensity (with raw data as well). Later, a reduced field strength's value (local field) is obtained by subtracting the IGRF from the total field measurements. This corresponds to the removal of the non-geologic or regional effects from the total field measurements to leave the magnetic anomaly (local geologic-residual information clearly visible for the interpreter) subsequently used for data analysis and interpretation through many filtering and transform operations.

2.2.2.3. Data processing and interpretation

Once reduced, data are presented as total magnetic intensity anomaly field map requiring several additional transforms and filtering depending on specific interpretations. However, initial care shall be given whereas the surveyed area's location is close to the poles or the equator. At low latitudes (the case of the current study), the reduction to the magnetic equator is the first data transformation applied. All the computer works done in Geosoft ® Oasis Montaj v.8.4.

a. Reduction to magnetic equator (RTE) and noise filtering

Generally, on a magnetic map, anomalies are shifted away from the location of their causative bodies, but application of the Reduction to the poles transform (Baranov and Naudy, 1964; Blakely, 1996) helps solving this matter by bringing back the anomaly at the apex of its source. In equatorial regions where inclination is less than 15°, the Reduction to the poles transform is generally unstable thus a similar operation, the Reduction to the magnetic equator (RTE) is applied instead (Hinze et al., 2013, references therein). The application of the RTE transform requires the knowledge of the inclination ***I*** (-6.2°**)** and declination ***D*** (-18.2°) of the geomagnetic field at the time of data acquisition (IGRF model of January 1970) -6.2°.

On magnetic anomaly grids, noise is often related to high frequency signals. Various noise suppression techniques exist (Blakely, 1996; Reeves, 2005) with different fortunes, but the upward continuation (described further in this paper) to a height of 125 m has been adopted for noise filtering. This distance (125 m) has been chosen so as to be comprised between half the flight height and the sixth of the lines spacing, to avoid subsequent reduced noise or Nyquist effects on signals (Drury, 2001; Hinze et al., 2013). Since data were collected along 750 m distant flight paths flown at 235 m height, the 125 m distance chosen is nearly the half of 235 and the sixth of 750. The resulting RTE map (**Figure 3.2-1)** while usable for regional appraisal of the area, also serves as input for further filtering and interpretations.

b. Analytic signal (Total gradient)

The analytic signal (AS) amplitude combines the horizontal and vertical gradients of a given field. Magnetic and gravity applications of the AS have been introduced by Nabighian (1972, 1974) to determine the depth and position of the anomaly source in the 2D case, since the form of the AS anomaly over causative bodies depends only on the locations of the bodies but not on their directions of magnetization. The technique has been improved with the Hilbert transform (Nabighian, 1984) then extended to 3D problems with gridded data (Roest et al., 1992) as formulated by equation (17):

$$\boldsymbol{A}(\boldsymbol{x},\boldsymbol{y},\boldsymbol{z}) = \frac{\partial \boldsymbol{M}}{\partial \boldsymbol{x}}\boldsymbol{i} + \frac{\partial \boldsymbol{M}}{\partial \boldsymbol{y}}\boldsymbol{j} + \frac{\partial \boldsymbol{M}}{\partial \boldsymbol{z}}\boldsymbol{k} \qquad (17)$$

where ***A (x, y, z)*** is the analytic signal vector; ***i, j, k*** are the unit vectors in the *x, y,* and *z*, directions, respectively; *M* being the anomaly field intensity.

With gridded data, the AS is used either as a mapping and depth-to source technique or as a way to learn about the nature of the causative magnetization (MacLeod et al., 1993; Reeves, 2005). Mapping applications have been clearly demonstrated by in recent mineral exploration plays, where the AS served as a geochemical tool for lithological units outlining (Geosoft, n.d.).

c. The First vertical derivative (FVD)

The application of first vertical derivative (FVD) is equivalent to observing the vertical gradient directly with a magnetic gradiometer. The FVD both enhances shallow sources while suppressing deeper ones and gives a better resolution of closely-spaced sources (Reeves, 2005). The FVD expressed by **equation (18)**, is filtering technique particularly useful in highlighting structural features like lineaments (Boyd and Isles, 2007; Feumoe et al., 2012; Fairhead et al., 2017), mostly the shallow ones.

$$\mathbf{FVD} = \frac{\partial \mathbf{M}}{\partial \mathbf{z}} \qquad (18)$$

where *M* is the magnetic field anomaly.

The FVD is generally much more responsive to local influences than to regional effects. Therefore, it tends to give sharper pictures than the total field intensity on maps.

d. Horizontal gradient

The horizontal gradient filtering (Blakely, 1996; references therein) is in many ways the simplest approach to estimate contact locations of the bodies (Anderson et al., 2013; Hinze et al., 2013; Feumoe, 2014), thanks to its low sensitivity to noise in the data because it only requires calculation of the two first-order horizontal derivatives of the field. If $\boldsymbol{M}$ is the magnetic field, then its horizontal gradient magnitude (HGM) is given by:

$$\boldsymbol{HGM}\,(\boldsymbol{x},\boldsymbol{y}) = \sqrt{\left(\frac{\partial \mathbf{M}}{\partial \mathbf{x}}\right)^{\mathbf{2}} + \left(\frac{\partial \mathbf{M}}{\partial \mathbf{y}}\right)^{\mathbf{2}}} \qquad (19)$$

$\frac{\partial \mathbf{M}}{\partial \mathbf{x}}$ and $\frac{\partial \mathbf{M}}{\partial \mathbf{y}}$ are horizontal gradients of the field *M* in the *x* and the *y* directions, respectively.

The HGM function gives a peak anomaly above magnetic contacts under the following assumptions (Feumoe, 2014): (1) the regional magnetic field is vertical, (2) the magnetizations are vertical, (3) the contacts are vertical, (4) the contacts are isolated, and (5) the sources are thick. Violations of the first four assumptions would shift peaks away from the contacts, while for the fifth it would produce secondary peaks parallel to contacts (Feumoe, 2014).

e. The upward continuation

Based on the Green's third identity, the upward continuation (UC) is an operation that enables to transform a potential field from a surface it was measured to a field that would had been measured to another surface farther from all sources (Blakely, 1996; Nabighian et al., 2005; Lowrie, 2007). The UC transform in the Fourier is given by:

$$\boldsymbol{UC} = \boldsymbol{M}\boldsymbol{e}^{-\Delta \boldsymbol{z}|\boldsymbol{k}|},\ \Delta \boldsymbol{z} > \mathbf{0} \qquad (20)$$

$\Delta \boldsymbol{z}$ is the distance used for the continuation in ground units and $|\boldsymbol{k}|$ is the wave number.

Clearly from **equation (20)**, the UC attenuates all wave numbers except $|\boldsymbol{k}| = \mathbf{0}$. The degree of attenuation increases with the continuation distance.

In practice, the UC acts as a low-pass filter by attenuating short wavelengths (or high frequencies) anomalies corresponding to shallow geological effects while accentuating high wavelength sources effects due to deep sources. Thus enabling to outline deep regional geological or basement structures (Blakely, 1996; Nabighian et al., 2005; Lowrie, 2007; Hinze et al., 2013; Fairhead et al., 2017). The combination of the upward continuation of magnetic field data at several heights and the detection of the peaks of their respective horizontal gradient magnitude grids (Blakely and Simpson, 1986) provides a pseudo 3D view of the geometry of deep magnetic sources. This approach known as the multiscale edge analysis (Archibald et al., 1999) has been applied in many studies (Basseka et al., 2011; Anderson et al., 2013; Owona-Angue et al., 2013).

f. The 3D Euler deconvolution method

Thompson (1982) proposed a 2D technique, the Euler deconvolution, to analyse magnetic profiles based on the Euler's homogeneity equation. The technique uses first-order x, y and z derivatives to determine location and depth for various targets, assuming an a priori information (at least the geometry) referred to as structural index (N). Reid et al. (1990) extended the technique to 3D data by applying the Euler operator to gridded data sets (see equation (21)):

$$\boldsymbol{N\,(B-M)} = \boldsymbol{(x-x_0)\frac{\partial M}{\partial x} + (y-y_0)\frac{\partial M}{\partial y} + (z-z_0)\frac{\partial M}{\partial z}} \qquad (21)$$

Where **B** is the regional field, (x0, y0, z0) is the position of the magnetic source producing the field M at (x, y, z). Theoretically, N=0 (practical values between 0.25 and 0.5 are preferred) for contacts and faults.

g. Geophysical inversion ($2^{3/4}$ modelling)

The modelling consists in designing and calculating the response of a theoretical geological model; then using the Marqardt algorithm to invert and linearize the solutions. The $2^{3/4}$ modelling particularity is that the source bodies are assigned fixed extensions across the profile. The modelling approach assumes that the anomalies are due to various sources (including both supra-basement and intrabasement responses) using local geology as model constraint (Prieto, 1996). The $2^{3/4}$ modelling is executed with GM-SYS ™ extension in Geosoft ® Oasis Montaj v.8.5.

2.2.2.4. The materials

a. Origin of data

The magnetic data used in this study were collected by the Survair Ltd in 1970s. The flight paths were flown N-S with a line spacing of 750 m a constant fly height of 235 m. The data were corrected and processed by Paterson, Watson and Grant Ltd, a consulting service that released data initially as 1: 50,000 total intensity contour maps to the Cameroonian government. The portion covered by this study has been availed in 2015 by the Directorate of Geology from the Ministry in charge of mines, in Cameroon.

b. Data preparation and materials

Dataset was provided as scanned-images of contour maps printed on paper. Once scanned-images of maps are acquired and viewed on the computer screen, then georeferenced. The georeferencing step is followed by the digitisation of data by capturing the x and y coordinates values along each flight line with the mouse's cursor. The total field value (z value) at each x, y location is entered and recorded in an output XYZ-file, leading to the compilation of a new digitally acquired survey database. The georeferencing and digitization tasks resulting into the new database were realised on Esri ® ArcGIS v.10.6. The final task in data preparation is gridding. Gridding is a contouring procedure herein done with a 250 x 250 m cell. The cell size (1/3 of the line spacing-750m) has been chosen to avoid aliasing effects (Reeves, 2005; Hinze et al., 2013). The gridding algorithm used was the minimum curvature (Briggs, 1974) implemented in Oasis montaj ™ platform.

2.3. THE REMOTE SENSING METHOD

Remote sensing is the process of detecting and monitoring the physical characteristics of an area by measuring its reflected and emitted radiation at a distance, using on-board airborne or space borne platforms (USGS, 2016). Remotely sensed imagery ensures rapid structural analyses by mapping regional or local lineaments and circular features (Liu and Mason, 2009).

2.3.1. Theoretical principles

2.3.1.1. Electromagnetic energy

The electromagnetic (EM) spectrum is the continuous range of electromagnetic radiation, extending from gamma rays (highest frequency and shortest wavelength) to radio waves (lowest frequency and longest wavelength) including visible light. The EM spectrum can be divided into seven different regions: gamma rays, X-rays, ultraviolet, visible light, infrared, microwaves and radio waves (**Figure 2.3-1)**. Remote sensing involves the measurement of energy in many parts of the EM spectrum (NASA, 2015).

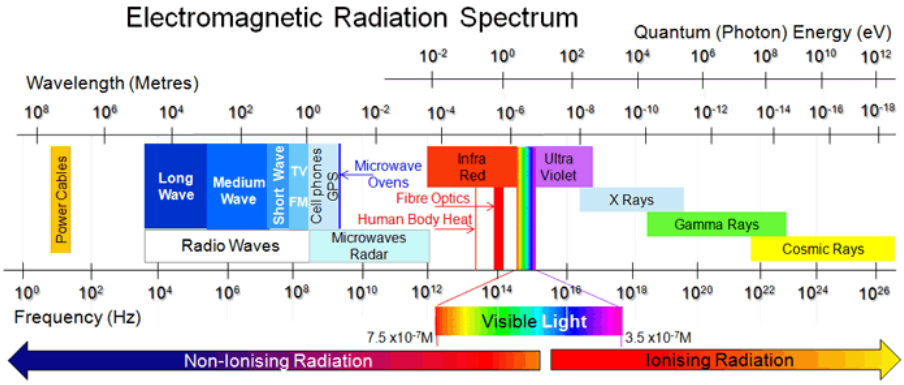

Figure 2.3-1 : EM spectrum

2.3.1.2. Reflection and absorption

The physical principle governing the remote sensing method is that when radiation from the Sun reaches the surface of the Earth, some of the energy at specific wavelengths is absorbed and the remaining is reflected by the surface materials. The only two exceptions (very rare in the natural world) to this situation are if the surface of a body is a perfect reflector or a true black body (Schowengerdt, 2007; Liu and Mason, 2009).

2.3.1.3. Reflectance-spectral signature-spectral band

Remote sensing involves the measurement of the EM radiations that is reflected back from the Earth's surface materials. Soil, water and vegetation exhibit different patterns of reflectance and absorption over different wavelengths. The reflectance of radiation from one type of surface material, such as soil, varies over the range of wavelengths in the EM spectrum. This is known as the spectral signature of the material, corresponding to its radiometrical response for a given set of wavelengths. Each surface feature, including minerals, vegetation, dry soil, water, and snow, has a unique spectral reflectance or signature. The measurement of the radiations takes place in spectral bands (or colours which are discrete intervals of the EM spectrum).

2.3.2. The remote sensing surveying

2.3.2.1. Satellite remote sensing principles

Satellites are equipped with sensors looking down to the earth which constantly observe the earth as they go round in predictable orbits. These sensors are designed to measure responses within particular spectral bands to enable the discrimination of the major Earth surface materials (see **Figure 2.3-2)**. The radiations are mainly recorded in the the visible and the infrared regions, corresponding to the wavelengths region extending from the visible and near-infrared (VNIR) to the short-wave infrared (SWIR).

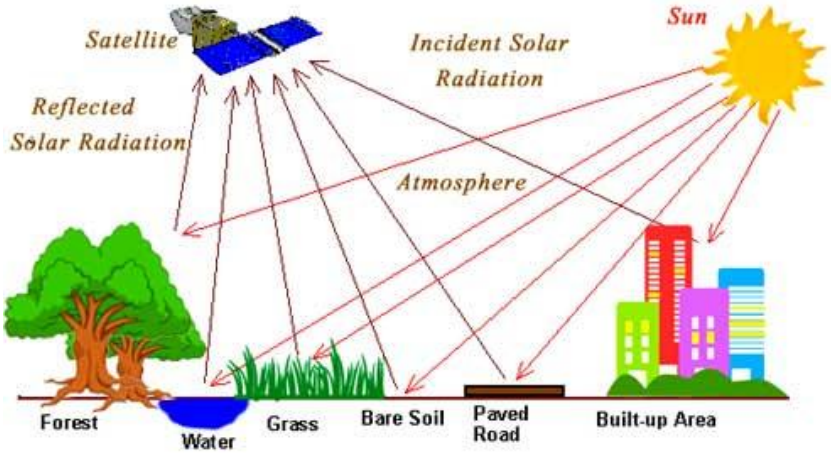

Figure 2.3-2 : Principle of satellite remote sensing (NASA, 2016)

2.3.2.2. Data description

The Remote sensing data of interest have been measured by the Operational Land Imager (OLI), a sensor on-board of the Landsat-8 satellite launched in February 2013 (http://earthexplorer.usgs.gov/). Landsat-8 (OLI) images scanned in nine bands categorised into multispectral (band 1 to 7), Panchromatic (band 8) and Cirrus (band 9). These spectral bands are presented in **table 1**. The approximate scene size is 185 km north-south by 180 km east-west. These data are freely available from the Global Land Cover Facility homepage (http://earthexplorer.usgs.gov/). USGS (2016) provides any interested reader with Landsat-8 products specifications.

Table 1 : Characteristics of a Landsat 8/ OLI data (USGS, 2016)

Band Number	Spectral range (µm)	Spectral band	Resolution
1	0.43 - 0.45	Coastal blue	30 m
2	0.45 – 0.51	Blue	30 m
3	0.53 – 0.59	Green	30 m
4	0.64 – 0.67	Red	30 m
5	0.85 – 0.88	NIR	30 m
6	1.57 – 1.65	SWIR-1	30 m
7	2.11 – 2.29	SWIR-2	30 m
8	0.50 – 0.68	Panchromatic	30 m
9	1.36 – 1.38	Cirrus	30 m

The data used in the current study have been recorded on the 12th January 2015. These are to two adjacent scenes whose respective path/row identifications are 185/057 and 185/058 (**Figure 2.3-3**). The Landsat-8 products used are standard L1T1 i.e. geometrically corrected data.

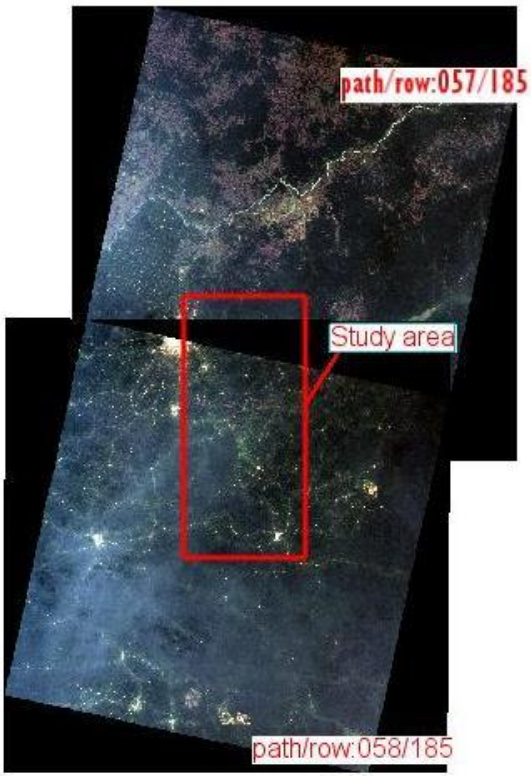

Figure 2.3-3 : True-colors Landsat 8 scenes used in this study.

2.3.2.3. Data processing and analyses

a. Data pre-processing

OLI data are level 1-T images, i.e. they are terrain-corrected (geometrical correction). However, these images necessitate additional pre-processing, starting with the radiometric calibration.

- ***The radiometric calibration:***

The radiometric calibration is a two-steps procedure which permits to transform digital numbers (DN) contained in one image into physical parameters i.e. radiance and reflectance, progressively for each band. The parameters values required for calculations are given in the metafile accompanying images:

Calculation of the radiance*:* The radiance is a measure of the energy radiated by an object. The operation (equation 21) corresponds to the transformation of digital number (DN) of each scene for a given band of wavelength λ to radiance at sensor L_λ, using the formula below:

$$L_\lambda = M_L * Q_{cal} + A_L \qquad (21)$$

With: L_λ = spectral radiance in $Wm^{-2}\ sr^{-1}\ \mu m^{-1}$; $\mathbf{Q_{cal}}$ = quantized calibrated pixel value in DN; M_λ and A_L = radiance multiplicative and additive scaling factors, respectively for the band.

***Calculation of the top of atmosphere (ToA) reflectance**:* The reflectance ρ is the measure of the ration of outgoing to incoming energy. The ToA is calculated using equation (22):

$$\boldsymbol{\rho_\lambda = [M_\rho * Q_{cal} + A_\rho]/sin\vartheta} \quad (22)$$

With: $\boldsymbol{\rho_\lambda}$ = ToA reflectance (unitless); $\mathbf{Q_{cal}}$ = quantized calibrated pixel value in DN; $\boldsymbol{M_\rho}$ and $\boldsymbol{A_\rho}$ = reflectance multiplicative and additive scaling factors, respectively for the band; $\boldsymbol{\vartheta}$ solar elevation angle. After the radiometric correction, the scenes are mosaicked then, spatially subset to the size of the study area before the next pre-processing step.

- ***Vegetation suppression:***

Vegetation suppression (Crippen and Bloom, 2011) removes the vegetation's spectral signature from multispectral and hyperspectral imagery, using information from red and near-infrared bands (**Figure 2.3-4**). This method helps to better interpret geologic and urban features in medium spatial resolution (as for Landsat-8) imagery.

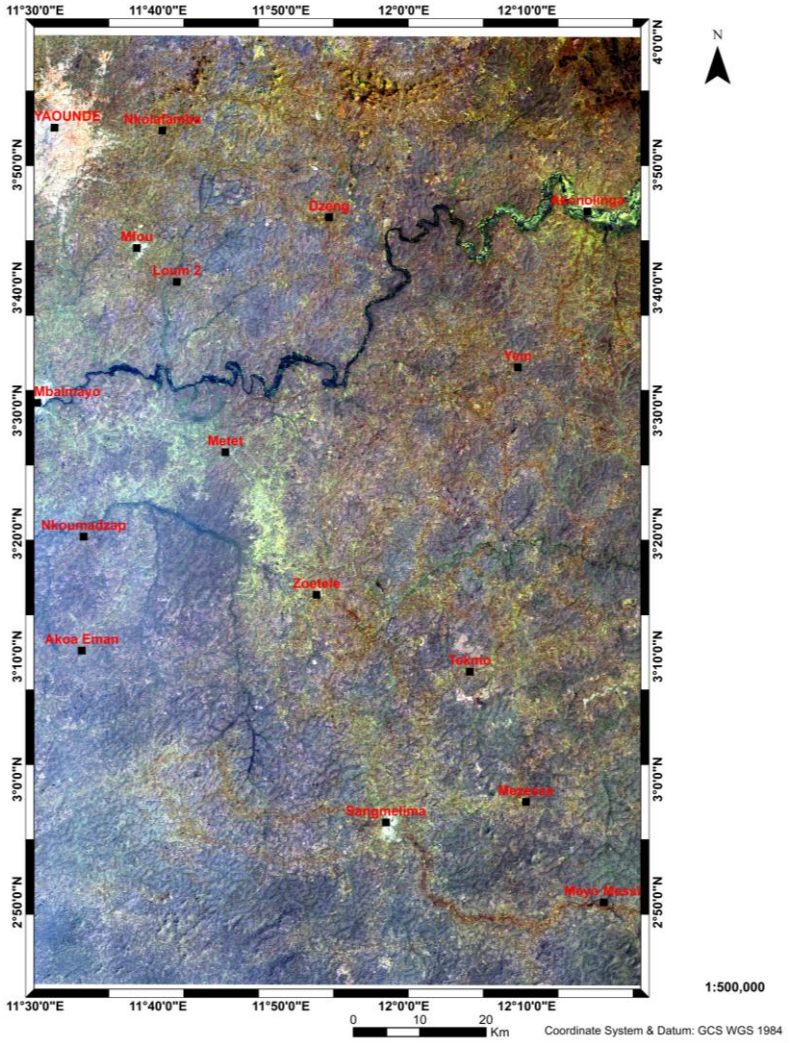

Figure 2.3-4 :Mosaicked image subset to the study area after the suppression of vegetation.

The algorithm models the amount of vegetation per pixel by calculating the relationship of each input band with vegetation, then decorrelating the vegetative component of the total signal on a pixel-by-pixel basis for each band. The result (**figure 2.3-4**) is useful for qualitative analysis, primarily for linear feature enhancement hidden by closed canopies.

b. Image enhancement: Principal components analysis (PCA)

The purpose of image enhancement is to highlight lithological features (Schowengerdt, 2007; Liu and Mason, 2009). The chosen image enhancement technique is the principal components analysis (PCA). This transform uses the variance to segregate noise components and to reduce the dimensionality of datasets, by finding a new set of orthogonal axes that have their origin at the data mean and that are rotated so that the data variance is maximized (Liu and Mason, 2009). The variance S_j^2 or second order momentum quantifies the spread of a distribution; it is given by the relation:

$$S_j^2 = \frac{1}{n}\sum_{i=1}^{n}\left(x_i^j - \overline{x^j}\right)^2 \qquad (23)$$

Where n is the number of bands, x_i^j is the jth vector of the ith band and $\overline{x^j}$ is the central mean of the j values which is defined as:

$$\overline{x^j} = \frac{1}{n}\sum_{i=1}^{n} x_i^j \qquad (24)$$

PCA seeks a linear combination of variables such that the maximum variance is extracted from the variables. It then removes this variance and seeks a second linear combination which explains the maximum proportion of the remaining variance, and so on till it produces orthogonal (uncorrelated) bands. The PCA is particularly useful because multispectral data bands are often highly correlated. The last PC bands appear noisy because they contain very little variance, much of which is due to noise in the original dataset (**figure 2.3-5)**. The preprocessing and image enhancement tasks have been realised with ENVI 5.3 ® software.

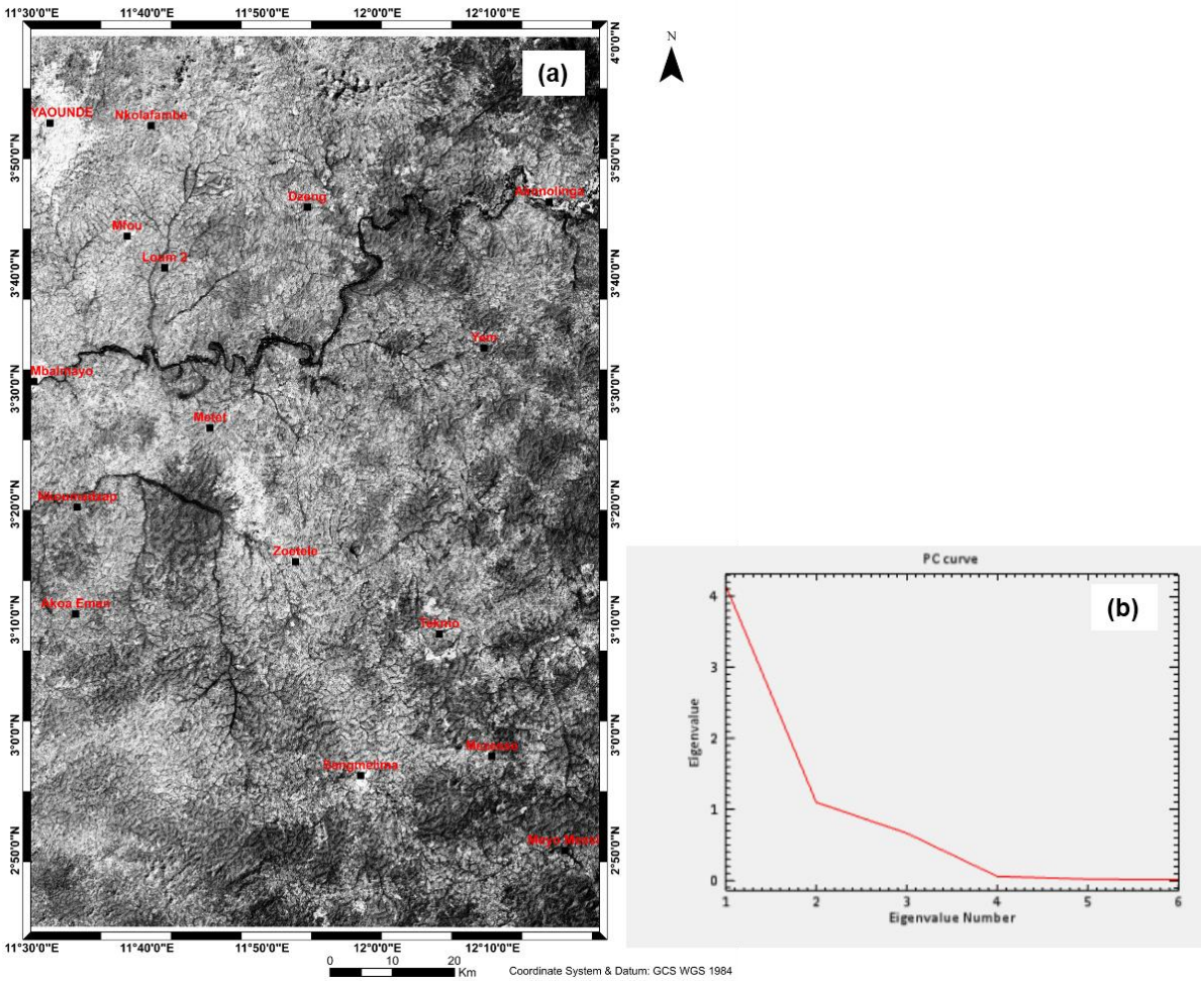

Figure 2.3-5 : Principal component analysis (PCA)from fig.2.3-4. (a) The PCA1 image over the study area; (b) PCA analysis graph showing that thePCA1 contains almost all the information from to the target area.

c. Lineament filtering and extraction

Filtering process involved the application of directional filter for lineaments detection. For the case, the Sobel filter have been applied to the greyscaled PCA1 image along four directions (N-S, NE-SW, E-W and SE-NW) using a 7 x 7 built-in window on ENVI 5.3 platform. The Sobel filter is an edge detector, particularly useful to delineate lithological contacts, faults, fractures or joints (Mwaniki et al., 2015; Teikeu et al., 2016; references therein).

The lineaments extraction involved a semi-supervised classification that consists in (1) merging the Sobel's filtered images into a unique image; (2) extracting lineaments automatically, using the LINE module in PCI ® Geomatica v.9.0 (**see Figure 3.3-1**); then, (3) removing manually the anthropic lineaments within the output after underlaining image from (1) by the digital elevation model generated from the SRTM data of the area; and applying the photo-geological approach to interpret structural lineaments based on visual continuity and hydrography. The tasks are performed with Esri® ArcGIS 10.6. (for map editing) and Rockworks 16 ™ (to compute lineaments statistics).

2.4. JUSTIFICATION OF THE STUDY APPROACH AND WORK METHODOLOGY

2.4.1. Justification of the approach

Geophysical investigation in least-developed countries like Cameroon remains very challenging. For scientists and researchers, the main challenge to overcome is the access to data because of the lack of geophysical equipment, and the lack of funding for data collection or data purchase. In this study, the coverage of the entire study area has been ruled by the data availability. In fact, because of the absence of funding, the AMT survey initially planned for the entire study area has been interrupted and thus restricted to the portion covering Yaounde-Nkolafamba-Mfou zone. Later access to aeromagnetic data enabled to cover the remaining space but the flight ban above Yaounde (the country's city-capital) made it impossible to have magnetic data in the AMT-surveyed zone. As a result, the space is divided into two adjacent sub study areas depending on the geophysical method. The northwestern area covered by the tensor-AMT survey while aeromagnetics prevails in the remaining domain. This led to a new approach in geophysical studies departing from usual superposition of methods over a same study area, as explicated in the next section.

2.4.2. Workflow methodology

The study is a juxtaposition of geophysical methods over the study area for regional structural study. It chiefly consisting in:

(a) Juxtaposing two differents methods (tensor-AMT and aeromagnetics) in two adjacent subsets areas, each serving to highlight structural features but the magnetic study additionnally aims verifying the south-continuity of structural features outlined by the tensor-AMT study, then possibly outline the lithology.

(b) Remote sensing the entire study area using Landsat-8 OLI data. The remote sensing herein mainly serves to correlate both AMT and magnetic outputs in order to (1) validate the spatial extension of the lineaments outlined all over the study area and (2) validate magnetic feature mapping.

(c) Cross-validating and integrating the three methods (two by two) by merging their outputs to form a unique study's final output.

(d) Validating the geophysical results from (c) with both existing geological results from previous studies and the geological information collected during field campaigns.

Conclusion

To fulfil the purposes of this thesis, researches were initially based on AMT and aeromagnetics. The insufficiency of ground controls and the coverage of the area by each of

these methods led to the integration of remote sensing to link them. The **figure 2.4-1** shows the coverage of the study area by each used geophysical prospecting method and the field geological investigation. Usually, studies rather involve the superposition of methods above the same area; departing from this approach, a new methodology capable of solving geological problems by juxtaposing geophysical methods is proposed. Since physical laws cannot entirely explain the Earth's behaviour as geologic complexities are above simple explanation, geophysical models always contain valuable information that can be extracted as errors using inadequate data are much less than those using no data at all.

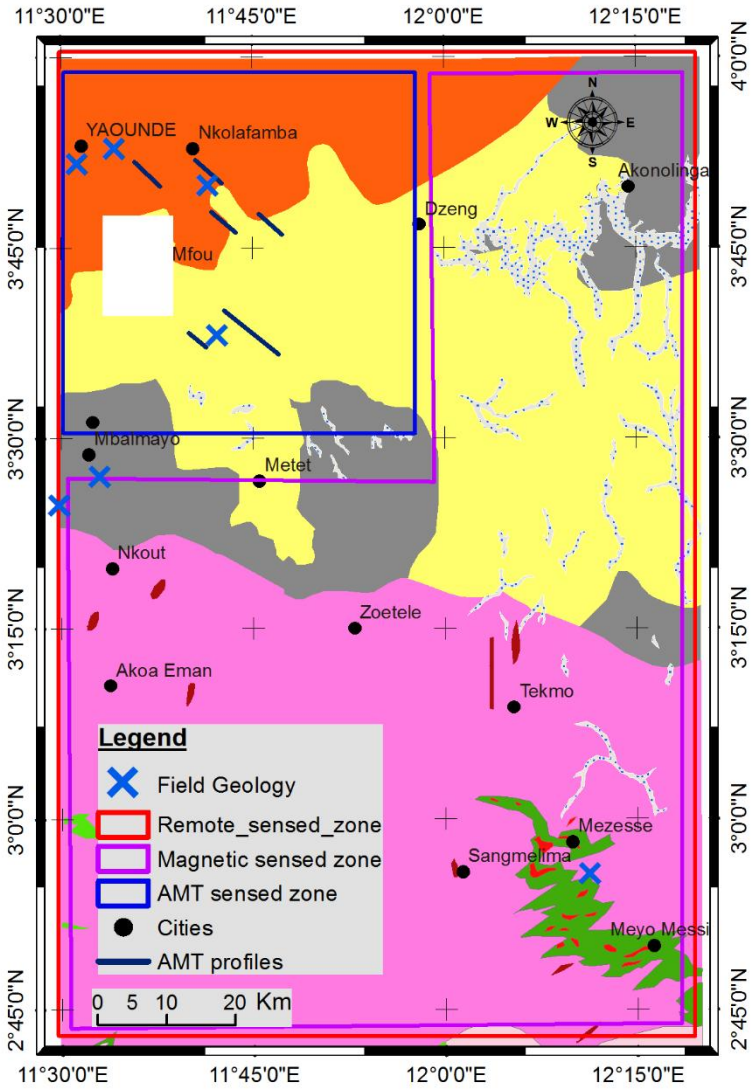

Figure 2.4-1 : Distribution of area coverage according to each method.

CHAPTER THREE: RESULTS AND DISCUSSIONS

Introduction

In geological investigation, the contribution of geophysics is merely at locating and determining the orientation of various structural elements and probable lithology. Inspite of being right or wrong, a geophysical model can also be irrelevant; hence the need of ground controls to constrain it. Alternatively, multiple geophysical techniques can be used as it follows.

3.1. AUDIOMAGNETOTELLURIC DATA INTERPRETATION

Though empirical means exist to assess the geoelectrical structure (Groom and Bailey, 1986) and despite the operational assumptions of the stratagem, a dimensional analysis has been carried out before any interpretation of AMT data.

3.1.1. Geoelectrical structure of resistivity anomalies

The dimensionality or geoelectrical structure of AMT data in the study area has been determined using ZondMT2D™ (**figure 3.1-1**). The dimensionality is evaluated by observing the behaviour of the impedance along a given profile. In general, the resistivity structure in the area is 2D; the 2D character is recognisable by the two petal flower shape observed at each sounding station (**Figure 3.1-1**).

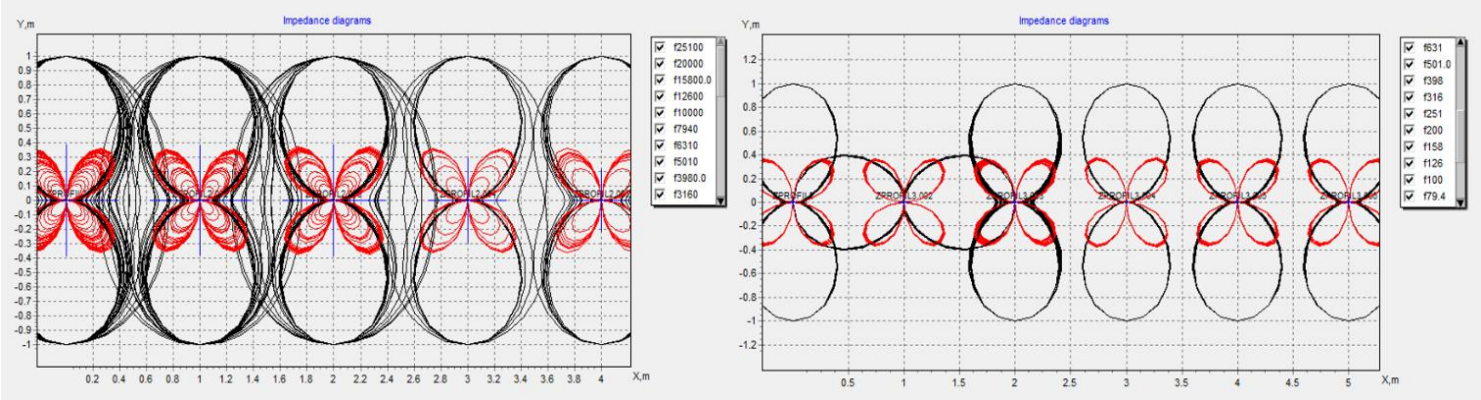

Figure 3.1-1 : Dimensionality analyses Nkolafamba data. The results presented for profile 2 (left) and profile 3 (right) show that the electrical structure is at least 2D.

The subcircles surrounding some flowers (**Figure 3.1.1 left**) show that the structure can be 2d or 3D, or either suffer some galvanic distortion. This is partly overcomed by the rotation of data within the Stratagem system, providing the best electrical strike of the impedance (Geometrics, 2000; McPhee et al., 2006). Based on that inferred two-dimensionality, AMT data interpretation is limited to the analysis of phase and apparent resistivity pseudo-sections, and geoelectrical sections.

3.1.2. Profile 1 (Ossol)

3.1.2.1. Phase pseudo section

The observation of the phase pseudo section plot (**Figure 3.1-2**) shows three (03) main features. The first is characterised by a mean phase value of 45°. It appears from surface to middle depth (frequencies greater than 1200 Hz) along the whole profile and at depth, below station OS5 and station OS6 (frequencies less than 80 Hz).

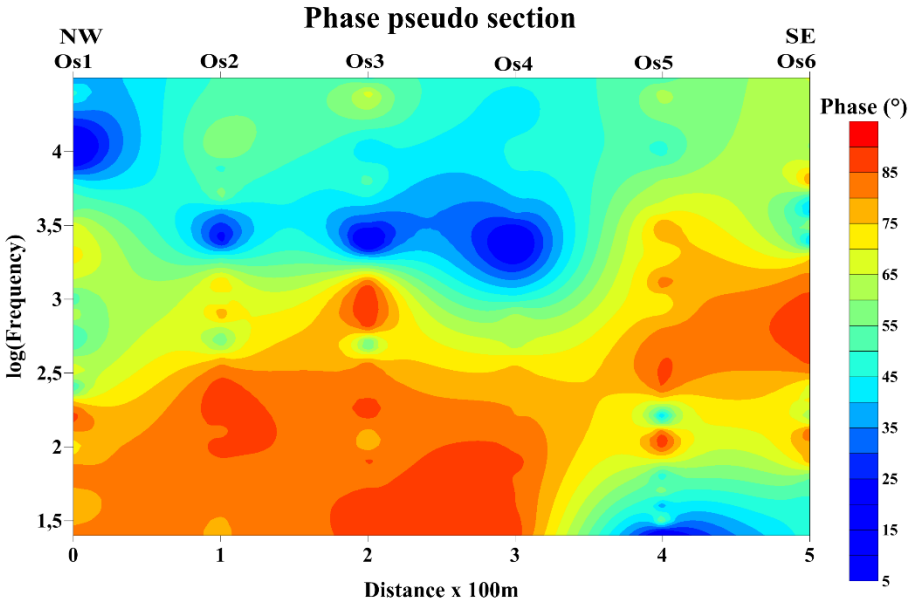

Figure 3.1-2: Phase pseudo section of profile 1 (Ossol). One of the most highlights is the high-phase values channel with a mean value of 85°.

The second feature is characterised by a mean phase value of 85°. It is displayed like an oblique channel along the whole section from the lower left to the middle (or the upper right in another view) right border. The third group of features is characterised by elliptical isophase anomalies at middle depth from OS2 to OS4, at near surface beneath OS1 and at depth under station OS5. These anomalies are characterised by a mean phase value of 14°. The phase pseudo-section (**Figure 3.1-2**) suggests a conductive shallow subsurface in the area. Some vertical to subvertical curve lines are also observed in various part of the pseudo section, particularly between 250 m and 350 m.

3.1.2.2. Apparent resistivity pseudo section

The apparent resistivity pseudo section (**Figure 3.1-3**) of profile 1 shows three concentric resistivity anomalies from depth to surface. These anomalies have a mean resistivity value of 193.0 Ω.m and they form a conductive channel located between stations OS3 and OS5, corresponding to a probable upwell or intrusion of conductive materials. The plot also portrays a conductive entire near surface and an anomalous resistant structure centred at OS3 and evolving

downwards. Another subcircular resistive anomaly is observed downward from mid-depth beneath stations OS5 and OS6.

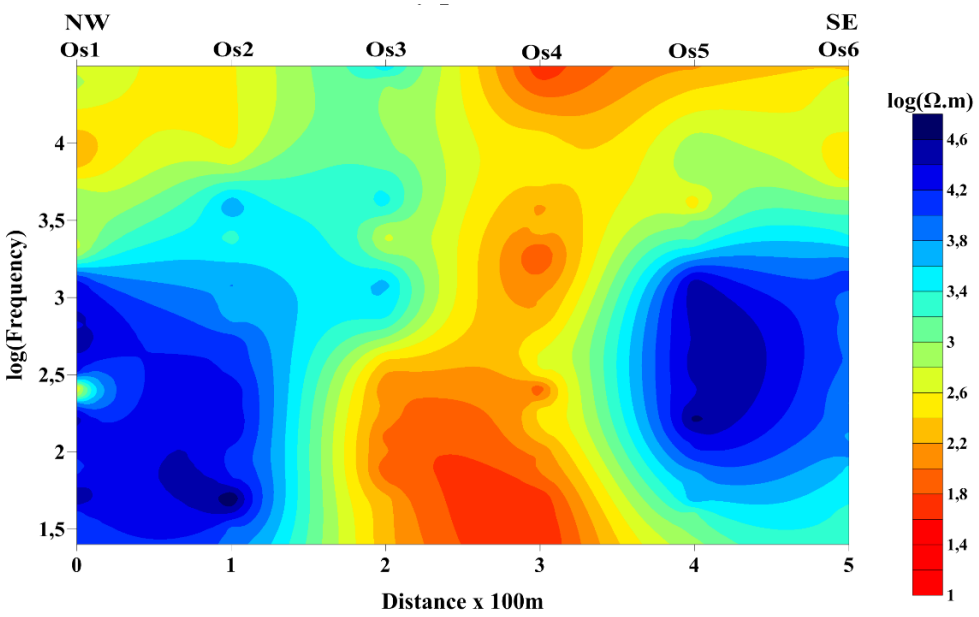

Figure 3.1-3 : Resistivity pseudo section of profile 1 (Ossol).A SW-NE conductive channel (reddish coloured) cross-cut the subsurface, probably a NE active fault.

The apparent resistivity pseudo section (Figure 3.1-3) of profile 1 (Ossol) shows irregular distribution and shapes of isoresistivity contours lines corresponding to variations of the resistivity. These variations along with the vertical to subvertical disposition of resistivity contour lines (beneath stations OS2 and OS5) may infer some geological discontinuities. The curling of these contours suggest that the area may have undergone a folding process. Discontinuities detected could be interpreted as faults or some geological major contacts. These facts (shapes of isoresistivity contour lines, curling, discontinuities, etc.) are inferrences of an intense tectonic activity in Ossol.

The pseudo-sections (**Figures 3.1-2** and 3.1-3) show irregularly shaped iso-contours shapes at all. They both exhibit dislocation patterns of blocks on one hand, and on another, they show that conductive formations are encountered both on surface and at depth.

3.1.2.3. Geoelectrical section

The analysis of the geoelectrical section (Figures 3.1.4 and 3.1.5) suggests that the Ossol subsurface lithology is broadly made up of five (05) formations. The following facts are noticeable, looking downwards:

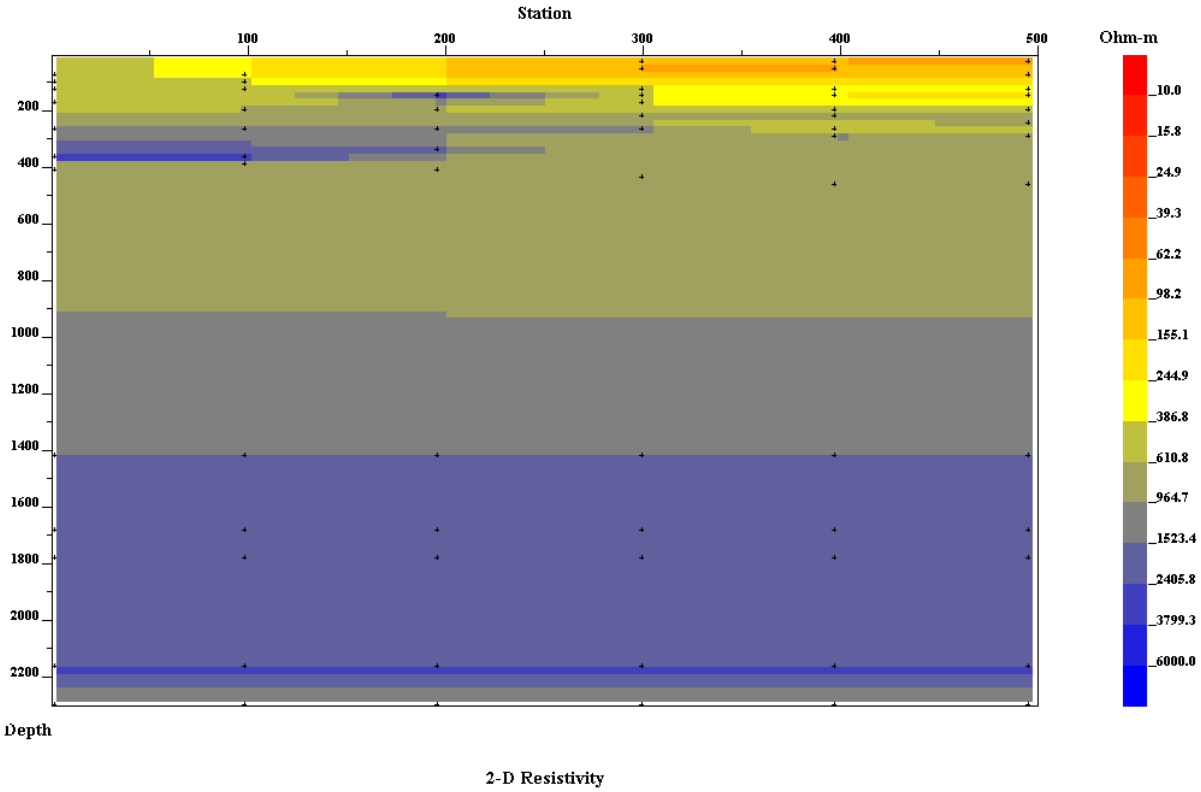

Figure 3.1-4 : Geoelectrical section of profile 1 (Ossol) from 0 to 2200 m depth.

- At the top of the plot, we have two conductive formations of mean resistivity 147.2Ω.m and 284 Ω.m, respectively. The contacts between these conductive formations are identified as faults detected at OS2 and OS5. The second formation, outcropping from station OS1 to OS2, is discordant to the third, and it is also marked by a collapse zone between stations OS2 and OS5.
- The third formation, with resistivity's values ranged between 374 Ω.m and 721.7 Ω.m (nearly 547.9 Ω.m mean resistivity), appears at 100 m and ends at 275 m depth below OS1. Its varying thickness diminishes toward the end of the profile. Indeed, this formation is jagged by many discontinuities (at stations OS2, OS4 and OS5) that can be interpreted as faults which mark collapse zones on the top of this formation; thus shaping it like stairs with four footsteps. The first step runs from OS1 to OS2, the second from OS2 to OS4, the third from OS4 to OS5 and the last from OS5 to the last station of the profile. Hence seemingly, the area suffered a collapse that affected the ground structures in Ossol area. This was imprinted to shallow near surface structures (**Figures 3.1-4** and **3.1-5**), so the top of the third structure is shaped like a graben as shown on the plot. Additionnally, a resistive intrusion of the underlying material seems to rise through a probable fracture affecting the third formation at station OS3, then forms a sill of 100 m

length and 25 m thick at about 150 m depth (the intrusive body is centred at OS3). The third terrain lays discordantly to the fourth.

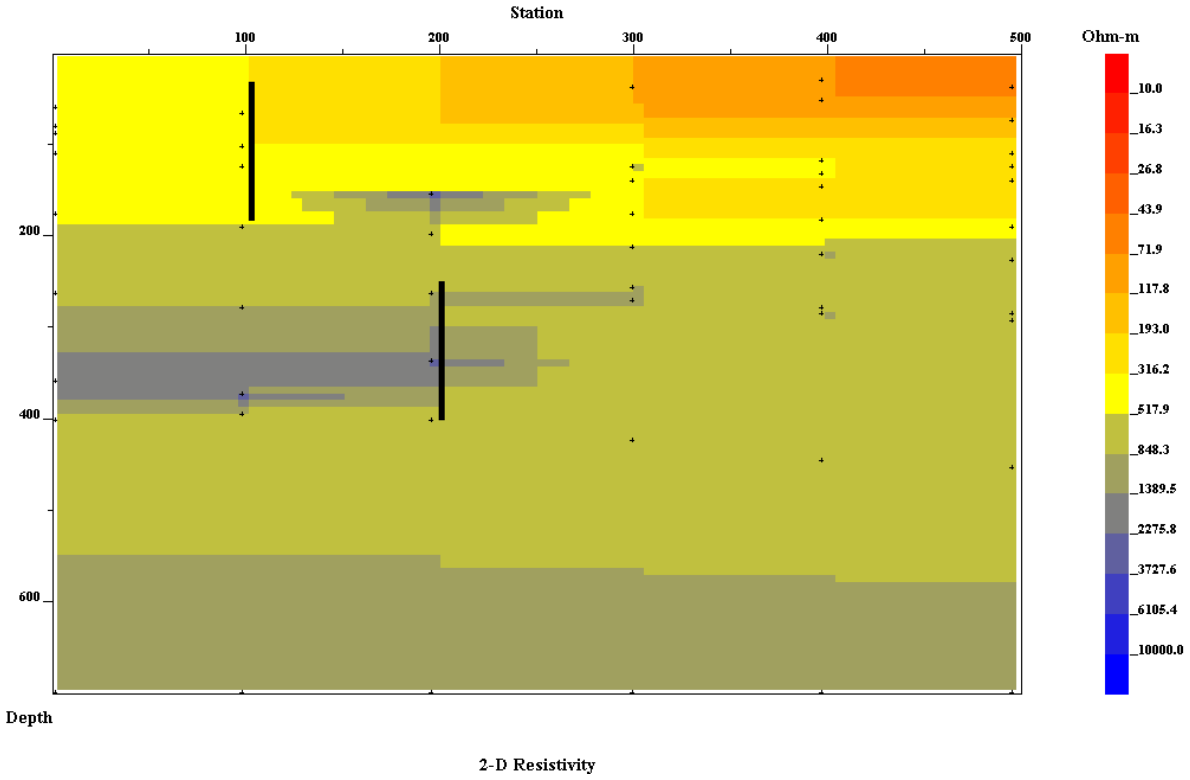

Figure 3.1-5 : Section from 0 to 650 m depth to emphasis on shallow structures.

- The fourth formation, characterized by a mean resistivity value of 1057 Ω.m (very resistant), is broadly encountered at 275 m from station OS1 to OS5. It is affected by discontinuities beneath stations OS3, OS4 and OS5. The one at OS3 and that below OS4 can be interpreted as faults while that under OS5 looks like a scarp because of its size. The roof of this fourth formation significantly forms a horst between stations OS3 (where it intrudes the overlying formation) and OS4. The geoelectrical section plot also reveals an intrusion of a more resistive material from OS1 to OS3 which resembles a fork or anything alike. The origin of this intrusive body is difficult to explain. The thickness of the fourth terrain is close to 1125 m (it extends from 275 m to 1400 m depth) and it seems to rest concordantly with the fifth terrain (with a mean resistivity's value of 3934.8 Ω.m) encountered at 1400 m depth and interpreted as the bedrock.

The geoelectrical section of profile 1 shows that the resistivity of ground formations in the Ossol village increases with depth.

3.1.3. Profile 2 (Beguele 1)

3.1.3.1. Phase pseudo section

Analysing the phase pseudo section (**Figure 3.1-6**) of profile 2 (Beguele1) leads to the differentiation of three main classes of phase anomalies, similarly to profile 1. The plot mainly exhibits a high phase anomaly value that dominates the section, with a mean value of 80°. This anomaly spans over the whole depth (in low frequencies). It is shallow around 316 Hz from BE1 to 150 m before BE2, rises to near surface (from 316 Hz to 10000 Hz) between BE3 and BE4, then collapses from BE4 to BE5 (very low frequencies range). Both middle and very low phase values anomalies overlain that high phase values anomaly from BE1 to BE3 and from BE4 to BE5. The very low phase anomaly is mainly located from BE1 to BE2, at near subsurface.

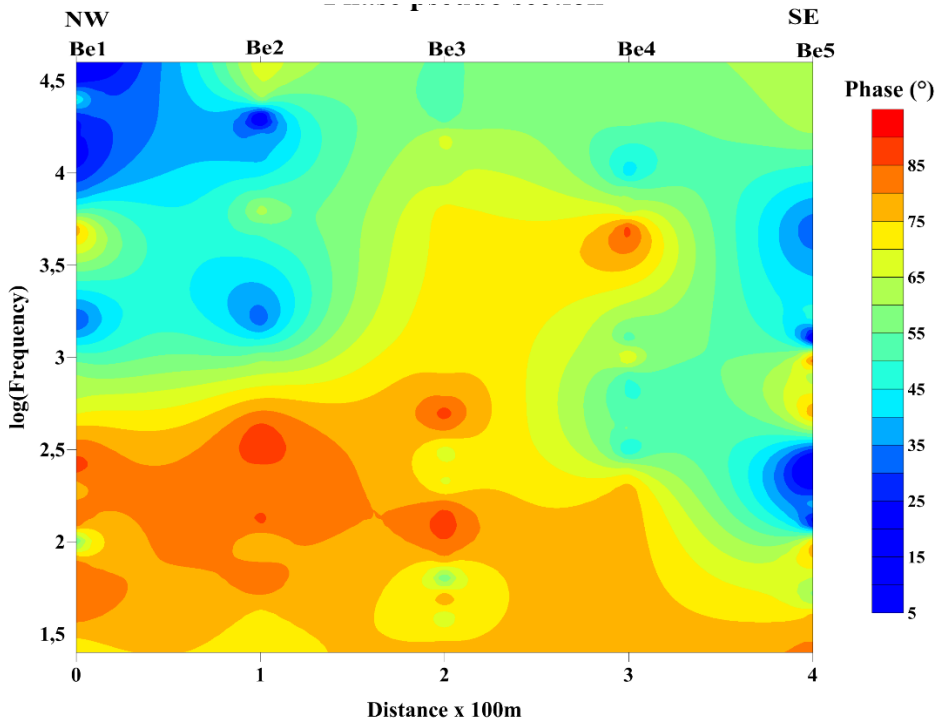

Figure 3.1-6 : Phase pseudo section of profile 2 (Beguele 1). The plot is dominated by a very high phase value anomaly characterising deep geology of the area. The mean phase value of this anomaly is 80°.

In addition to the above observations from the phase pseudo section of profile 2, it appears that the phase contour lines are very disturbed. They are vertical to subvertical around BE3 and BE4. This suggests than the area is dominated by two or three main lithological types and that the area is probably affected by a major discontinuity.

3.1.3.2. Apparent resistivity pseudo section

The apparent resistivity pseudo section (**Figure 3.1-7**) brings in additive information to the understanding of Beguele 1 geological setting. The apparent resistivity pseudo section from profile 2 (Beguele 1 village) reveals many outcomes but the prominent output is the partition of the subsurface into two main blocks. The first block spans from surface to middle depths (from

higher to nearly 3100 Hz). It corresponds to a group of conductive formations that seem to compose the Beguele 1 near subsurface. A shallower more conductive set is also observable within the above described block. This shallower conductive group is dipping NW-SE from station BE1 to station BE2.

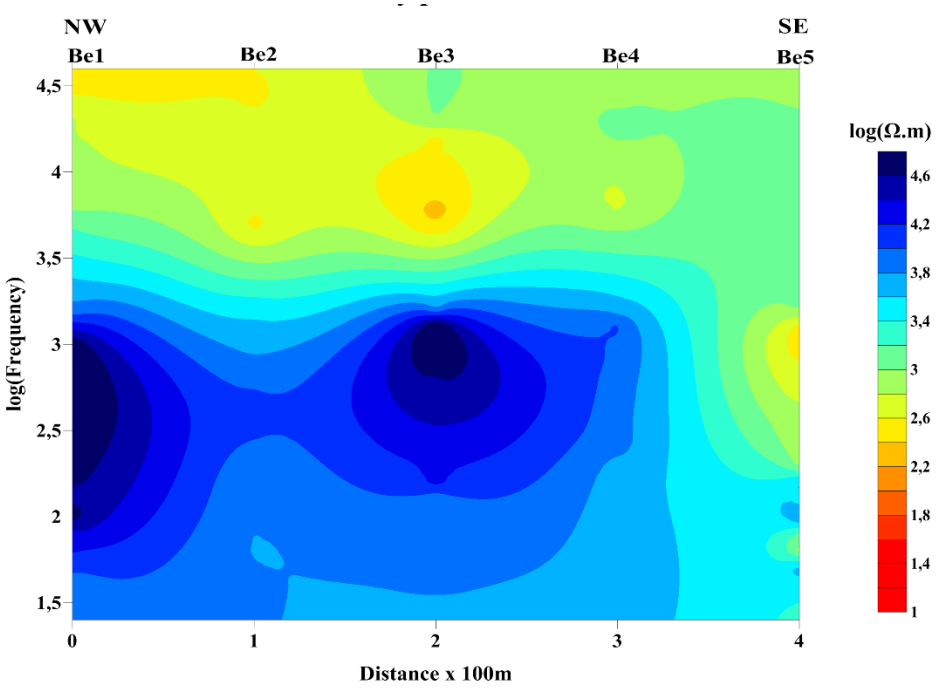

Figure 3.1-7 : Apparent resistivity pseudo section of profile 2 (Beguele 1). The plot is dominated by a very high resistivity value anomaly characterising the subsurface geology of the area.

The second block represents a set of very resistive formations. It dominates the subsurface from middle to very low frequencies (downward from middle depth). Vertically it occupies more than a half of the depth on the pseudo section, hence we can suggest that the first block is not very thick. The abrupt end beneath station BE4 shapes this resistivity anomaly like a rectangle while it is strangled at station BE2. The resistive and the conductive zones are separated by a thin transitional layer.

The high resistive anomalous zone ends below BE4 with vertical contour lines that suggest the presence of a major discontinuity. Further, the strangle affecting the iso-contour lines beneath BE2 also mark the presence of a discontinuity; probably vertical shear zones that could evidence vertical movements of subsurface blocks of formations. In addition to the discontinuities highlighted, the apparent resistivity contours are also irregular.

3.1.3.3. Geoelectrical section

The geoelectrical section of the profile 2 has been realised in order to image the subsurface of the Beguele 1 area up to 1500 m depth (**Figure 3.1-8**) but a focus was made for shallow subsurface imaging (**Figure 3.1-9**).

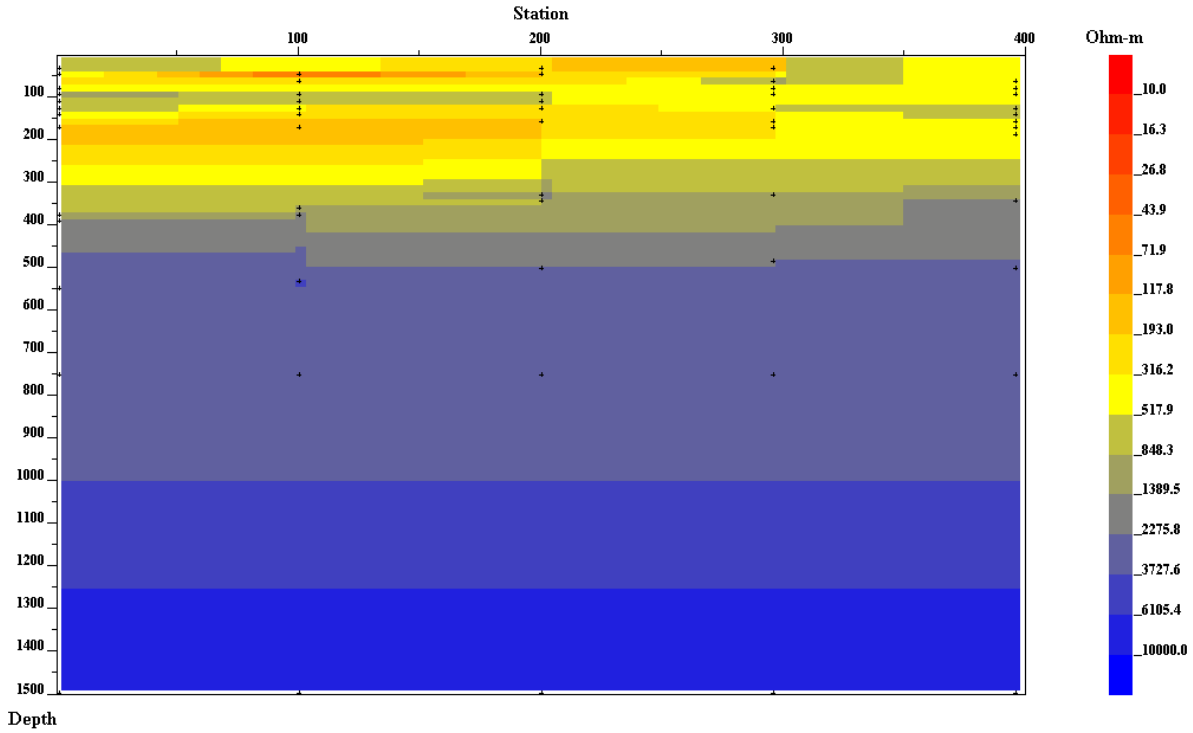

Figure 3.1-8 : Geoelectrical or 2-D resistivity section of profile 2 (Beguele 1) for 1500 m depth. The plot shows that the substratum (blue level) is shallow (encountered at 500 m depth).

The geoelectrical section of the Beguele 1 area suggests a four to five layered earth model. The section presents a four (04) layered earth model. From surface to depth we observe:

- The first terrain is characterised by resistivity values within the range [10.0-517.9] Ω.m, or a mean resistivity value of 264 Ω.m, with an average thickness of 300 m. A more conductive layer firstly above the 100 m depth level from BE2 to BE4 (300 m) and secondly between the 150 m and 250 m depth level. This conductive layer is not interpreted as a separate formation, but may rather correspond to an alteration zone within the first terrain. It is intruded in some parts by thin layers (or sills) and blocks of materials whose resistivity characteristics (especially value) correspond to those of the second terrain. Clearly the resistivity patterns observed on the plot show that this layer is not homogenous and it can be seen that the bottom of this layer is also affected by the underlying formation. The origin of underlying materials within this first terrain is not clearly explainable based on the profile 2 observation only.

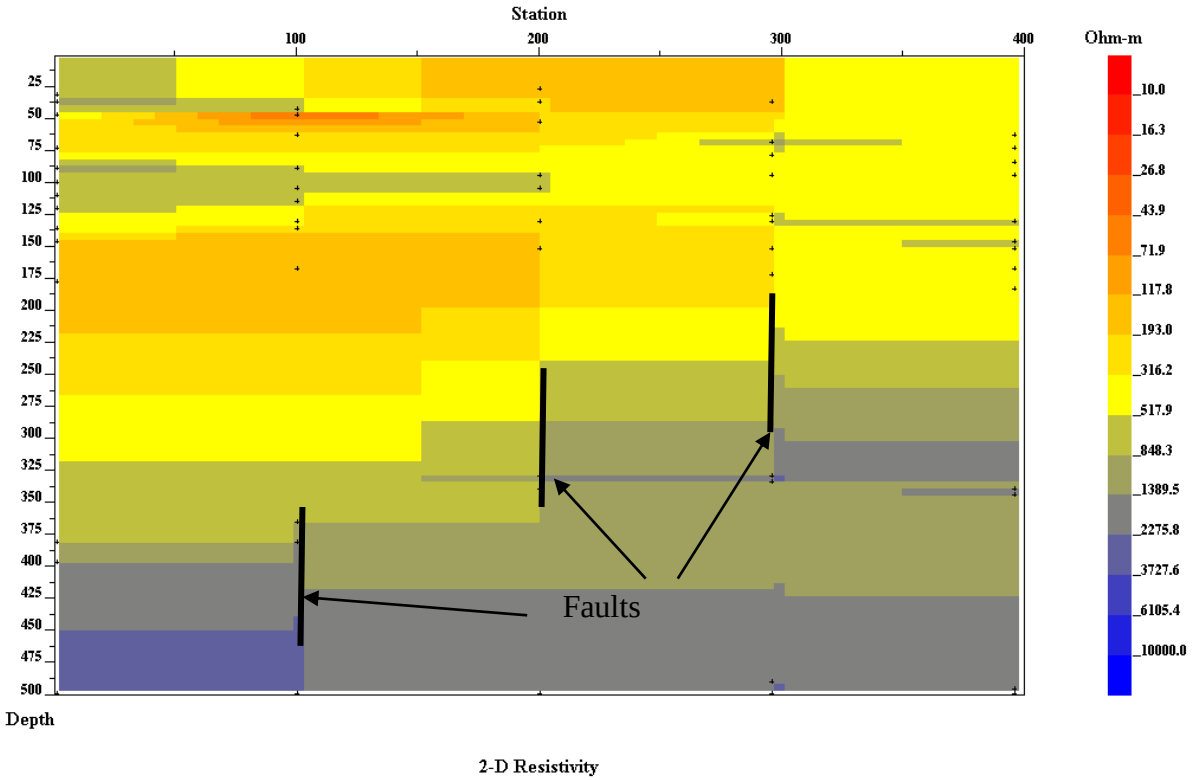

Figure 3.1-9 : Geoelectrical or 2-D resistivity section of profile 2 (Beguele 1) for 500 m depth. The upper terrain is very thick (averaging 300 m) while the second and the third terrains both form a thin sheet of 200 m, but display some discontinuities (between BE2 and BE3, at BE3 and BE4).

- The second terrain is encountered at 325 m depth (Figure 3.1-9), it has an approximate thickness of 50 m but it is thin from BE4 to BE5. The second formation is also conductive and it is characterised by a mean resistivity value of 953.7 Ω.m. Contrarily to the overburden, the second terrain seems homogenous. From Figure 3.1-6 b above, some discontinuities are observable at 50 m beyond BE2, at BE3 and BE4. These discontinuities can be interpreted as faults especially those located between stations BE2 and BE3 (with an upthrow of about 17 m) and BE3 (with an upthrow of 25 m); the discontinuity at BE4 can be interpreted as a scarp. Further, the aforesaid discontinuities shape the roof of this formation like a SE rising downstairs whose steps are at 50 m beyond BE2, at BE3 and BE4. The second formation seems therefore settled as a set of four (04) adjacent blocks; the first block is 150 m wide and starts from BE1, the second is narrow (50 m only), the third block is 100 m from BE3 to BE4 and the fourth, with the same dimension as the previous runs from BE4 to the end of the profile. This suggests a graben-like disposition of shallow surface structures beneath Beguele 1 area. The breaks in the second formation are relays from the third formation.
- The third formation is characterised by values of resistivity in the [1389.5-2275.8] Ω.m interval or a mean resistivity value of 1832.6 Ω.m. this layer is clearly observable on

Figure 3.1.9. We can see within it that it is very thin from BE1 to BE2, but thickens increasingly from BE2 to the end of the profile (where it has a thickness of more than 100 m). This formation is also jagged by discontinuities at BE2, BE3, and BE4. The discontinuity at BE3 can be interpreted as a fault but those at BE2 and BE4 can be interpreted as faults or scarps either. The third formation is also shaped like downstairs, in the same manner as the second formation above. It is additionally intruded from SE to NW by a resistive material of 25 m thick (but becomes tinny from BE4). This resistive intrusion can be interpreted as a probable sill; this material displays identical resistivity characteristics as the formation below.

- The fourth formation is encountered at 400 m depth, with a mean resistivity value of 3001.7 Ω.m. This formation doesn't exhibit irregular patterns of filling in materials like those above, i.e. this formation seems homogenous. The fourth terrain has an average thickness of 100 m but it thickens from 350 m to the end of the profile. Like the terrains above, the fourth layer is jagged by three (03) discontinuities located respectively at BE2, BE4 and 350 m (50 m beyond BE4). The discontinuities highlighted can be interpreted as faults. Some of these affect the overlying formations. The fourth formation seems to be affected by a collapse between BE2 and BE4. This collapse originates from the underlying layer which may correspond to the fifth formation.
- The fifth formation or layer is characterised by a mean resistivity greater than 3001.7Ω.m and it is encountered at around 500 m depth. This formation can be interpreted as the geoelectrical the basement of the area. However, this formation displays a first level running from 500 m to 1000 m depth; this upper level presents two discontinuities at BE2 and BE4 respectively which can be interpreted as faults. These faults are guides of the collapse noticed between the above mentioned stations, of this upper level of the basement. This upper level is rather interpreted as an oxidised or weathered level of the basement than as an individual layer or formation. From 1000 m to 1500 m and so on, we reach the proper basement of the Beguele 1 area.

The 2-D inverse model (or geoelectrical section) of the profile 2 shows that resistivity increases with depth. Further, outputs from the geoelectrical section are consistent with observations made on the apparent resistivity pseudo section (**Figure 3.1-7**). Indeed, the geoelectrical section also displays two main blocks. The first is represented by the first conductive terrain reported on the analysis of the geoelectrical section, while the second corresponds to the basement. These two blocks are separated by a thin (compared to the scale of the depth covered on the plot (**Figure 3.1-7**) level constituted by the second, the third and the

fourth terrains, in the same way as displayed on the corresponding apparent resistivity pseudo section of Beguele 1.

3.1.4. Profile 3 (Nkolafamba)

3.1.4.1. Phase pseudo section

The **Figure 3.1-10** below represents the phase pseudo section of profile 3. On this pseudo section plot, low phase anomalies are observed both at high and low frequencies. For low frequencies (less than 80 Hz), one has a dome shaped phase contours with a peak below NK1 affecting the domain beginning at NK1 and ending at NK3. Phase values range is 10° to 21°, with a minimum value (10°) recorded below NK2 for a frequency close to 60 Hz. The dome shaped anomaly is dissymmetric, its apex is centred at NK2, and the NW flank is very steep while the SE flank is gradational. The shapes of these isocontours suggest the presence of discontinuities at depth, the first dipping NW while the second is dipping SE.

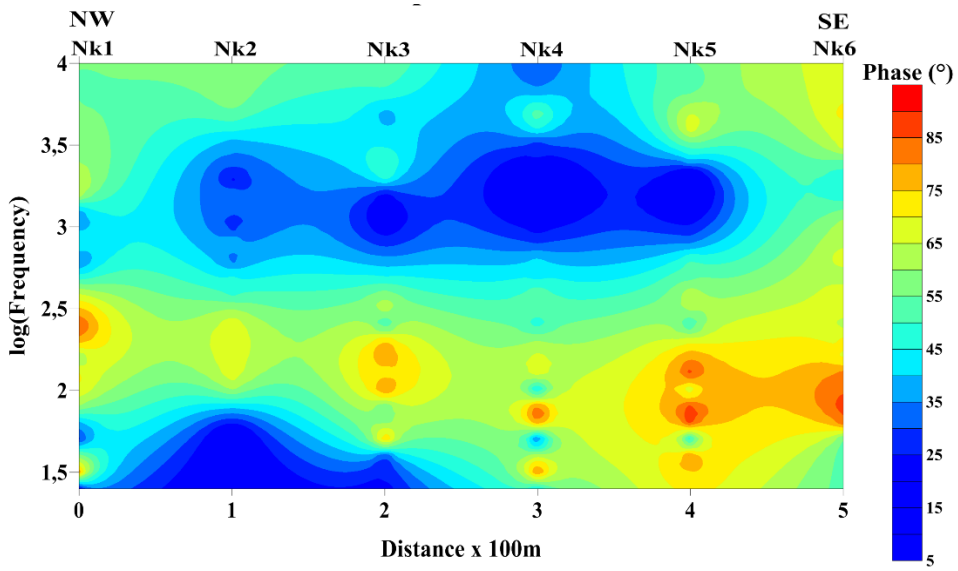

Figure 3.1-10 : Phase pseudo section of profile 3 (Nkolafamba). The plot exhibits two low phase anomalies (blue colour) separated by a high phase (reddish) anomaly channel.

For high frequencies, phase contours have a no ordinary shape (they look like a fish or a boat) that covers large part of the profile length. Meanwhile, a low phase anomalous zone is encountered from NK2 to beyond NK5 with a phase band values being 10° to 18° (it may reach 21°); the minimum phase values (average of 10°) are recorded between NK4 and NK5. Beside this major features observed, one can notice that isophase contour lines suggest a mixture of structures. Another noticeable element can be the vertical to subvertical isoresistivity contour lines centred at station NK4 that suggest a fault. Between these resistive structures one can observe a surrounding medium characterised by high phase values that suggests a conductive channel.

3.1.4.2. Apparent resistivity pseudo section

The apparent resistivity pseudo section of profile 3 (Nkolafamba) is given by the **Figure 3.1-11** below. The observation of the apparent resistivity plot enables to clearly outline three (03) main bands, from surface downward. The first band corresponds to conductive formations at near subsurface; the second band is a transition zone between the upper very conductive band and the lower resistive one. This transition zone is made up of intermediate conductive formations. The third and last band characterises very resistive formations that appear from 1200 Hz to lower frequencies (to deep levels).

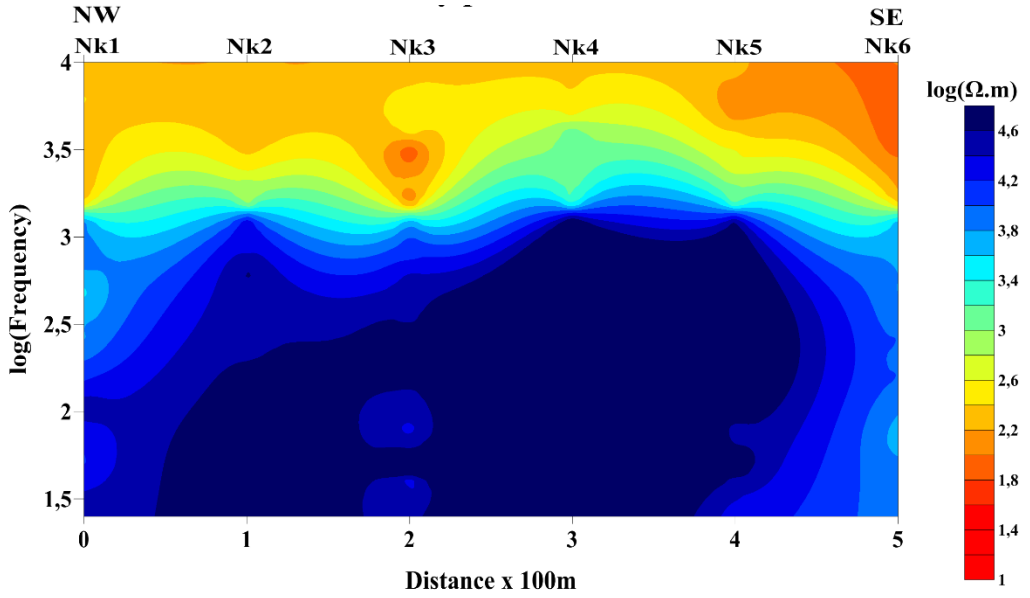

Figure 3.1-11 : Apparent resistivity pseudo section of profile 3 (Nkolafamba). On the plot the resistive materials dominate the subsurface. Insights of an uplift of ground formations is noticeable between stations NK3 and NK5

The above very resistive zone dominates the 2/3 of the plot, suggesting that the area is made of very resistive materials. This also suggests that the presence of a shallow basement in Nkolafamba and its vicinity. Within the resistive zone there is an oblique nucleus which seems to be responsible of the uplift observed between NK3 and NK5. This nucleus exhibits subvertical isocontour lines between NK5 and NK6, suggesting the presence of a major discontinuity. Moreover, there are oblique isocontour lines affecting the resistive zone that suggests a SW discontinuity dipping from NK2 to NK1. This discontinuity affects the deep basement formations. The curling of isocontours of the overburden formation are evidences of the folding processes that affected the shallow formations.

3.1.4.3. Geoelectrical section

In the same way as on profile 2 (**Figure 3.1-9**), the 2-D inverse electrical model or geoelectrical section of profile 3 has been realised to image the Nkolafamba subsurface. The

Figure 3.1-12 below presents the geoelectrical section of profile 3 (Nkolafamba). The observation of the geoelectrical section above shows following facts downwards:

- The first layer is a very conductive terrain which is characterised by a mean resistivity value of 94.45 Ω.m. This terrain has an average thickness of 100m. In addition, this formation is marked by a discontinuity at station NK4 which can be interpreted as a fracture or a fault. Another discontinuity seems to be present at station NK3, at it may be interpreted as a fracture. A careful look at station NK2 also suggests a discontinuity which however seems obvious. The discontinuities highlighted at NK2 and NK4 are probably relays of deformation affecting the second terrain below, and they obviously form a depressed area along profile from NK2 to NK4 (50 m beyond NK4).

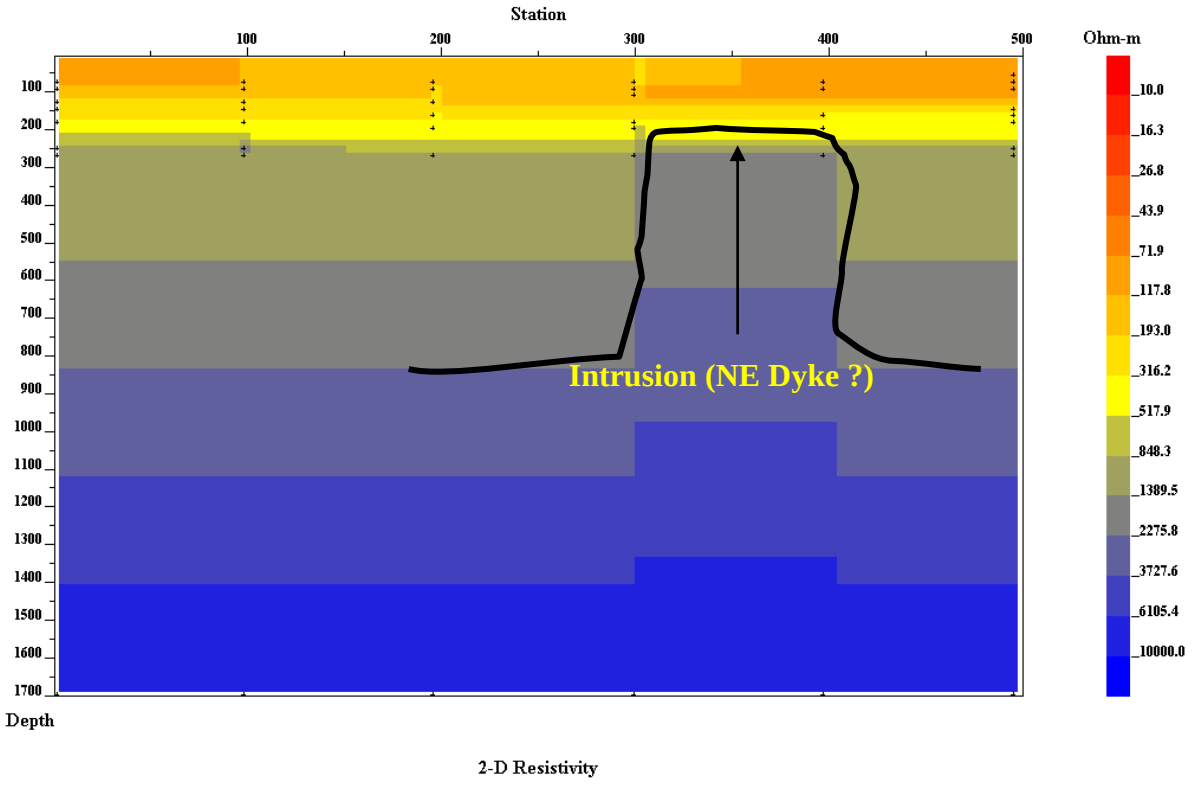

Figure 3.1-12 : Geoelectrical or 2-D resistivity section of profile 3 (Nkolafamba) for a total depth of 1500 m depth. The plot displays a channel between NK4 and NK5 through which the underlying resistive formations raise up

- The second perceptible layer on the plot has a mean resistivity value of 355.45 Ω.m. It is marked by a discontinuity interpreted as a fault beneath NK2. It has an appreciable thickness from NK1 to NK3 where it starts to diminish. This layer is characterized by a more resistive structure at the bottom, which thickens from the beginning to the end of the profile; it is marked by a slight intrusion of underlying material; scarps observed below stations NK3, and NK5 conFigure it like a stair with three foot-steps.

- The third zone encountered is a very thin quasi homogeneous structure at about 210m depth, with 683.1 Ω.m mean resistivity. It intrudes itself into the second structure at NK4 and its thickness is less than 50 m.
- At 250 m depth, the fourth formation highlighted is resistive; with a mean resistivity value of 1119 Ω.m. it has a mean thickness of 150 m, with a slight scarp beneath NK2. The major fact observable on this section related to this material is the 100 m wide passage way through which deep resistant material intrudes within it and form a concordant sill from station NK3 to NK6. The highly resistive character of this intrusion is probably due to the cooling of old melted magmatic materials that formed the basement.
- At 400 m depth under station NK1, one has the fifth structure, more resistant than that above (1832.6 Ω.m mean resistivity). This structure collapse slightly at NK2 and seems to be pushed inside the terrain above between stations NK4 and NK5, by the structure below it. The collapse observed at 400m below NK2 may not be interpreted as a fault.
- Structures encountered at 550 m depth seem to correspond to a transition zone between the overburden and the bedrock. These structures are resistive materials with resistivity values belonging to the interval [2275.8 - 6105.4] Ω.m. The hypothesis of the transition zone is supported by the identical shape observed on the structure that seems to be the basement.
- The top part of the basement is encountered at 1500 m depth with resistivity values comprised between 6105.4 Ω.m and 10,000 Ω.m. The noticeable feature is the uplift observed between stations NK4 and NK5. This uplift of the basement deforms structures above.

The geoelectrical section of profile 3 generally shows that resistivity increases with depth. In addition, it can also be seen that the basement in the Nkolafamba area is shallow. Besides, the uplift noticed between stations NK5 and NK5 can be interpreted as an intrusion, probably a dyke crossing the section. This results are in agreement with those obtained from the apparent resistivity pseudo section (**Figure 3.1-12**), although the geoelectrical section presented focuses only on the near subsurface.

3.1.5. Profile 4 (Beguele 2)

3.1.5.1. Phase pseudo section

The phase pseudo section of profile 4 (Beguele 2) is presented by the **Figure 3.1-13** below. The observation of the phase pseudo section enables to retrieve the following facts. At

frequencies lower than 1000 Hz (from middle depth downward), the plot exhibits a high value phase anomaly. This anomaly is characterised by a mean phase value of 80°. This anomaly covers the entire bottom of the plot. At frequencies greater than 10000 Hz a low phase anomaly value (mean phase value of 30°) occurs from BG3 to the end of the profile (BG6). This anomaly forms a basin-like structure between BG3 and BG5 where it forms a channel centred at BG4. The low phase and high phase anomalies are separated by a medium characterised by intermediate phase values with a mean value of 65°. This medium outcrops from BG1 to BG3.

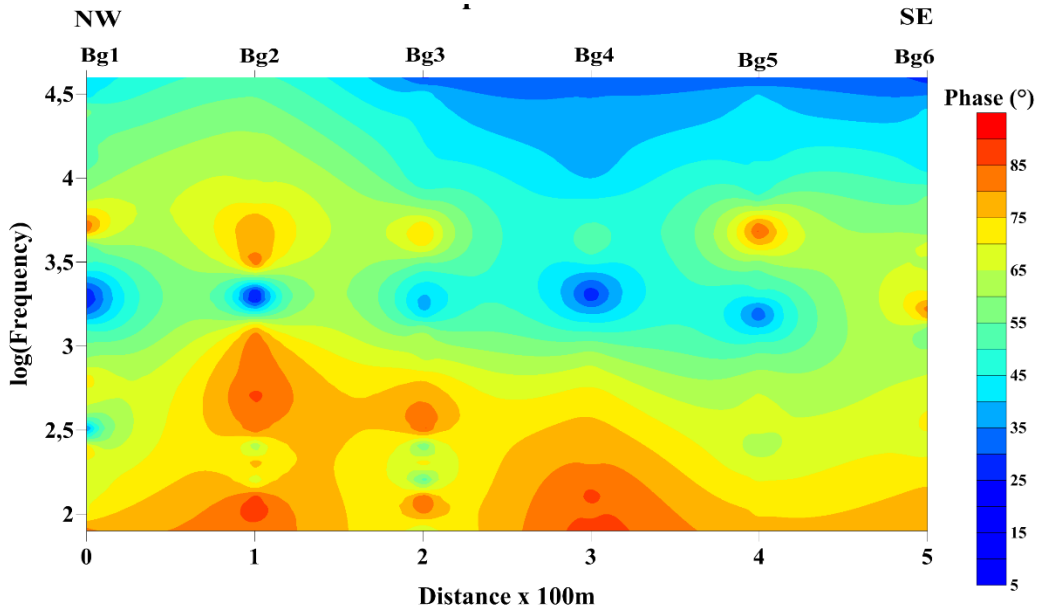

Figure 3.1-13 : Phase pseudo section of profile 4 (Beguele 2). The plot exhibits an intermediate phase anomaly that form a SE dipping channel from the beginning to the end of the profile.

Generally, the isocontour lines of phase are curled. This curling is more pronounced on the deep high phase anomaly but however affects the upper anomalies too. The above described curling can be interpreted as folding process that probably affected the formations in the Beguele 2 area. The isocontour lines are oblique between BG3 and BG4 at higher frequencies (near subsurface) and therein suggest the presence of a discontinuity, probably a SE dipping fault. Further the same pattern is observed between BG4 and BG5, suggesting a same type discontinuity there. This discontinuity can also be interpreted as a fault that affects the deepest structures of the area. In addition to these, there are oblique to subvertical isocontour lines from BG1 to BG2. This arrangement is also an imprint of a discontinuity that is probably interpreted as a fault that may also affects the deepest levels of the area.

In addition to all the above observed and interpreted, facts there is a circular or nearly elliptical intermediate anomaly that affects the subsurface from BG1 to BG3 at higher frequencies. This anomaly is probably an imprint of a conductive formation.

3.1.5.2. Apparent resistivity pseudo section

The **Figure 3.1-14** below presents the apparent resistivity pseudo section describing the 2-D resistivity variations along the profile 4 (Beguele 2). The apparent resistivity pseudo section from profile 4 (**Figure 3.1-14**) shows a very resistive formation that is encountered at depth between stations BG2 and BG6; it appears like an intrusion of more resistive materials, compared to the surrounding. This formation is embedded within a less resistive one that covers the whole area, while some very conductive formations appear from station BG1 to station BG2 and between stations BG4 and BG6 on surface; below stations BG1 and BG4 in depth.

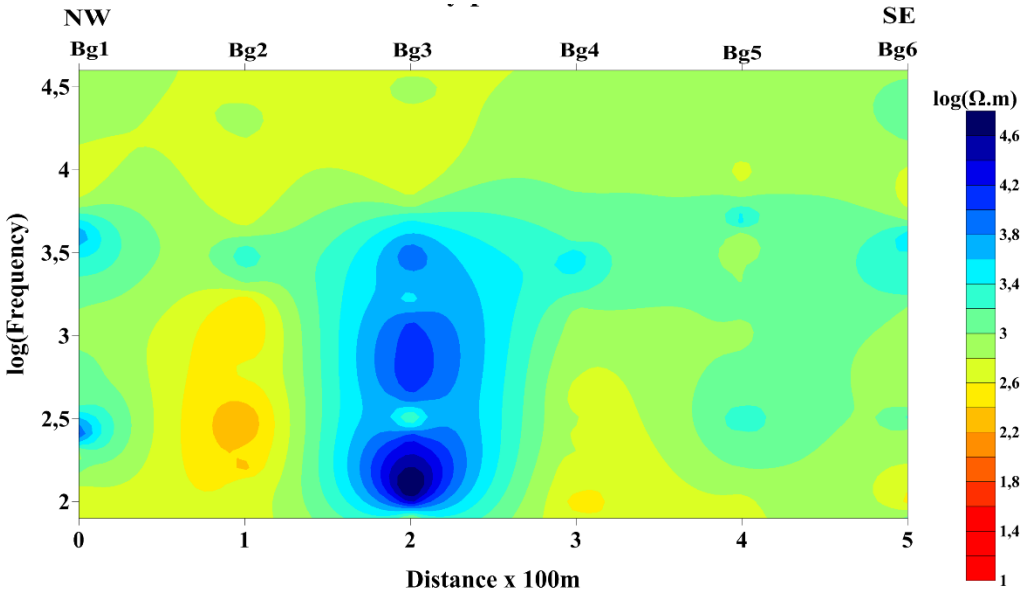

Figure 3.1-14 : Apparent resistivity pseudo section of profile 4 (Beguele 2)

The intermediate apparent resistivity values dominating the whole pseudo-section lead to assume the area is made up of mixture of both resistive and conductive formations. The phase pseudo-section mainly exhibits a depression or subsidence along the profile from BG1 to BG6. The irregular isocontour patterns on the pseudo sections suggest folding of formations therein.

3.1.5.3. Geoelectrical section

Figures 3.1- and **3.1-16** The 2-D inverse model or geoelectrical section of profile 4. The geoelectrical section focuses on the upper 1300 m with a detailed imaging of the uppermost 400m. The overview of the section (**Figure 3.1-15**) suggests a four-layered earth model.

- The first terrain characterised by a mean resistivity of 683.1 Ωm, occurs three times; on surface to 75 m, then from 325 m to 450 m depth and finally from 700 m to 750 m depth, below BG1. The portion appearing from 352 to 450 m depth thins from BG2 to the end of profile, as that appearing below seems to thicken from BG4 to BG6. This portion is jagged by discontinuities at BG2, BG3, BG4 and BG5 (**Figure 3.1-15**) which shape this

second level of the first terrain as a downstairs with five footsteps of 100 m each. The discontinuities highlighted can be interpreted as faults which also affect the formation above. The third portion is also featured by many discontinuities than can be interpreted as faults too; these also affect all the layers above. The superficial portion ends at BG4 by a fault-type contact with the second formation.

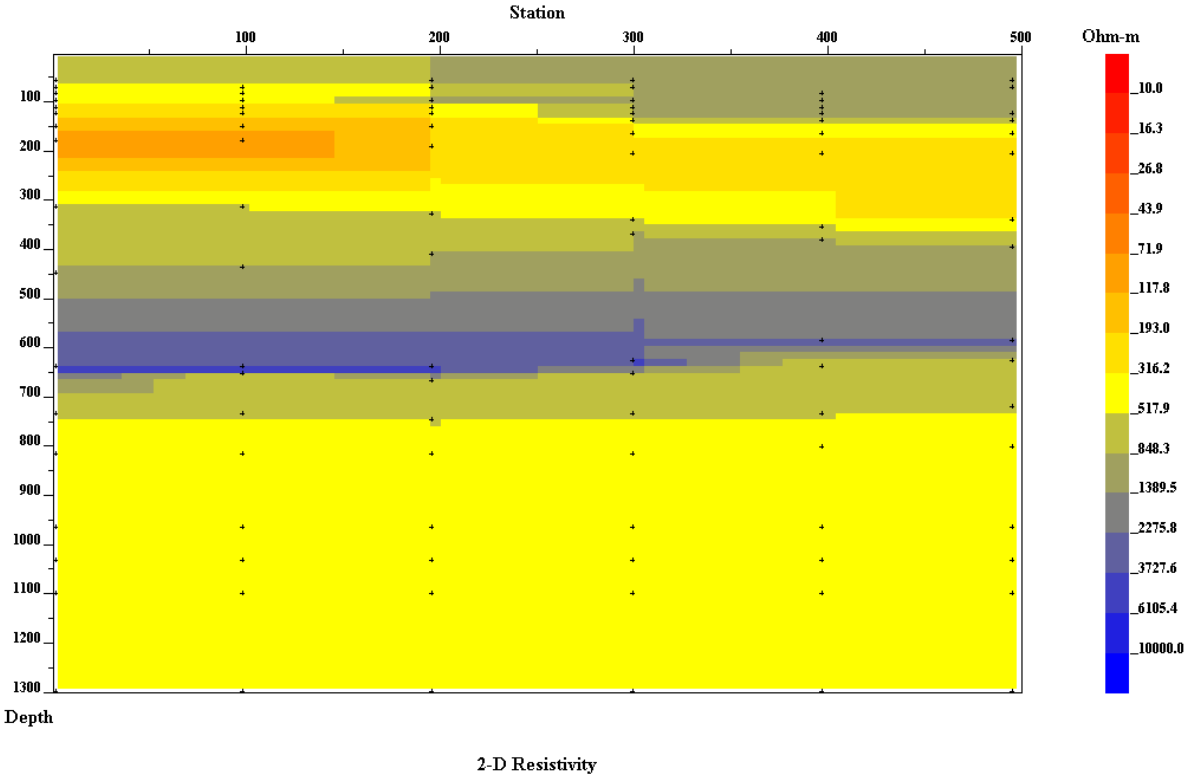

Figure 3.1-15 : Geoelectrical or 2-D resistivity section of profile 4 (Beguele) for a total depth of 1300 m depth. The plot displays a slightly SE dipping shallow channel running along the entire profile.

- The second terrain or formation is characterised by a mean resistivity value of 1119.3 Ωm. As said above, it seems separated on surface to the first formation by a fault-type contact at BG4. This superficial portion has an average thickness of 150 m and seems to embed a thin resistive layer. It also intrudes the first and the third formations from BG4 to BG3 (**Figure 3.1-15**) where it gently extrudes, suggesting a filled fracture at BG3 that affects the first formation. The second formation is also observable at 450 m depth below BG1. This second portion is characterised by a constant thickness of nearly 50 m from BG1 to BG4, then a slight thickening to nearly 75 m up to BG6. Some discontinuities interpretable as faults, are observed at BG3, BG4 and BG5. They shape this portion as downstairs till BG4, as a collapse is observed along the discontinuity at BG5. The observed discontinuities also affect the underlaying fourth formation; despite its high resistivity (mean value of 4190.6 Ωm), this fourth does not constitute the basement. The third occurrence of the second terrain is observed at 700 m depth below BG1. It has,

herein, a mean thickness of 50 m which nearly doubles to BG6 and displays some discontinuities too (many at the same stations) inferring a faulting of the whole near subsurface of Beguele 2.

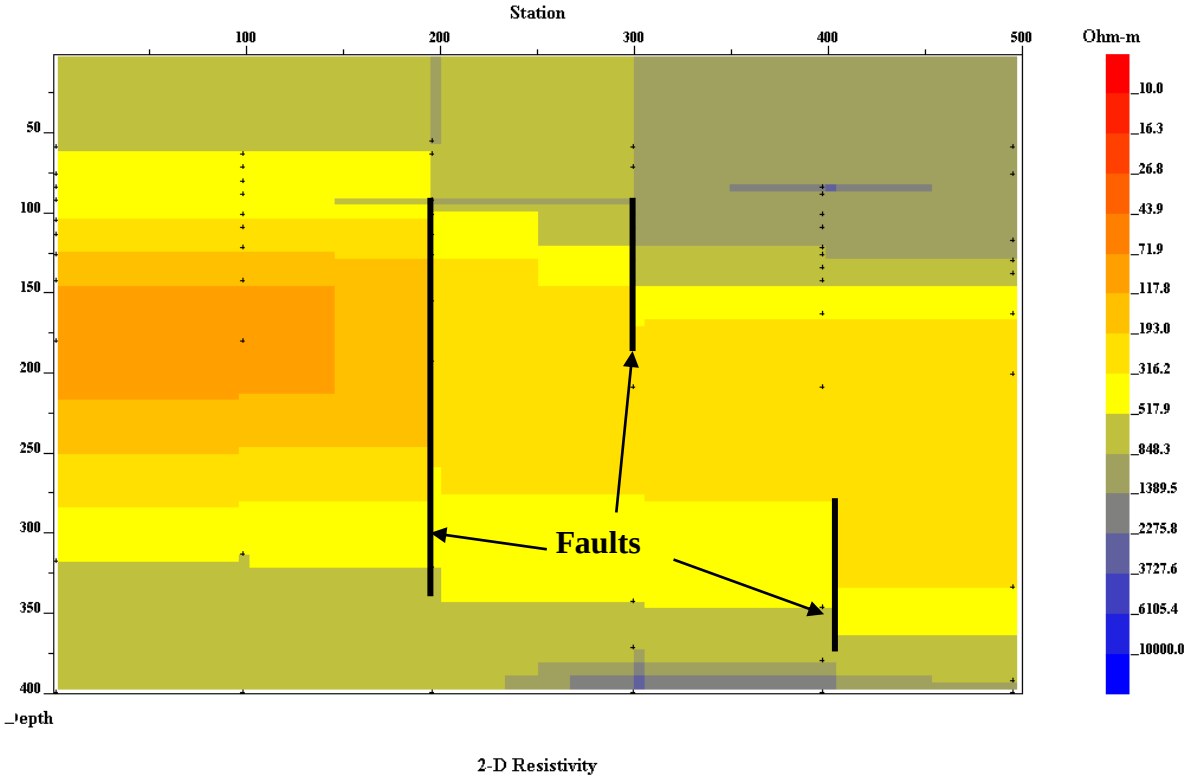

Figure 3.1-16 Geoelectrical or 2-D resistivity section of profile 4 (Beguele) for 600 m depth. The plot emphasises on features affecting the near subsurface.

- The very conductive third formation, firstly appears at nearly 75 m depth from BG1 to BG3. It has an average thickness of 300 m and a mean resistivity value of 417.2 Ωm. The roof of this formation is affected by discontinuities interpreted as faults at BG3 and 50 m beyond, and at BG4. These faults also appear at its bottom, on the contact with the fourth formation. The third formation herein forms a conductive channel with a resistive background constituted by the first and the second formations. This channel collapses along the highlighted faults from BG3 to the end of the profile; however, this collapse seems caused by deep processes. When considering the upper 400 m of the geoelectrical section (**Figure 3.1-16**), the domain occupied by the third formation looks like a graben. In addition, there is a more conductive thick layer (more than 100m) embedded in the third formation from BG1 to BG3, probably a weathered zone. This inner weathering spans concurrently through the whole formation in the entire profile. The third formation is reported again at 750 m depth below BG1.

The geoelectrical section of profile 4 shows that the area is not as resistive as seen on the previous profiles. Herein, formations alternate probably because of a folding process

accompanied or followed by faulting. Many faults affect all the formations at same locations, particularly at BG3, BG4 and BG5. The one highlighted at BG3 (**Figure 3.1-16**) is clearly evidenced on the apparent resistivity pseudo section.

3.1.6. Profile 5 (Kamba)

3.1.6.1. Phase pseudo section

The phase pseudo section of the profile 5 illustrated by the **Figure 3.1-17** below shows the dominance of low phase values (less than 30°), although some high phase circular anomalies are observed at Kb1, Kb2, Kb3 and Kb5. These high phase anomalies suggest local variations in the composition of the rocks or formations at these regions. The isophase contours suggest a concordant layering but their rough curling suggest that the area underwent intense ductile deformations. Particularly, the region between Kb and Kb6 portrays the existence of a nearly vertical breakup affecting the whole subsurface (probably a crustal feature).

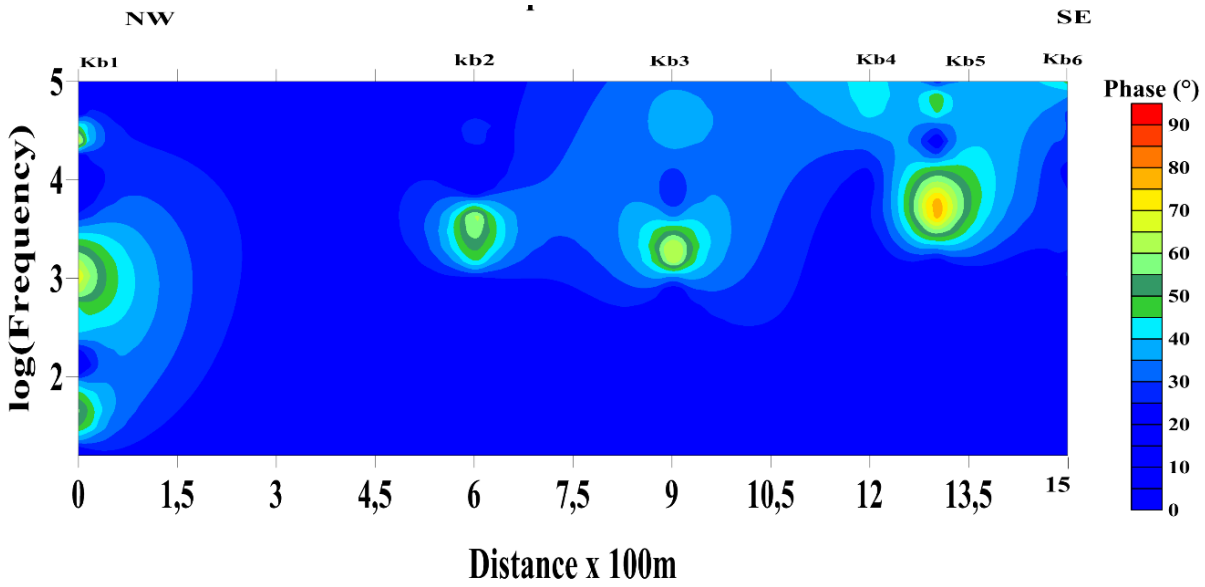

Figure 3.1-17 Phase pseudo section of profile 5 (Kamba).

3.1.6.2. Apparent resistivity pseudo section

The apparent resistivity pseudo section of the profile 5 (**Figure 3.1-18**) comforts the findings from the phase pseudo section above. It reveals three main types of formations observed top-down. On top (high frequencies), there are very conductive to conductive formations. The middle and lower frequencies areas are dominated by intermediate (in terms of resistivity values) formations which are entirely disrupted by the conductive formations above at Kb5.

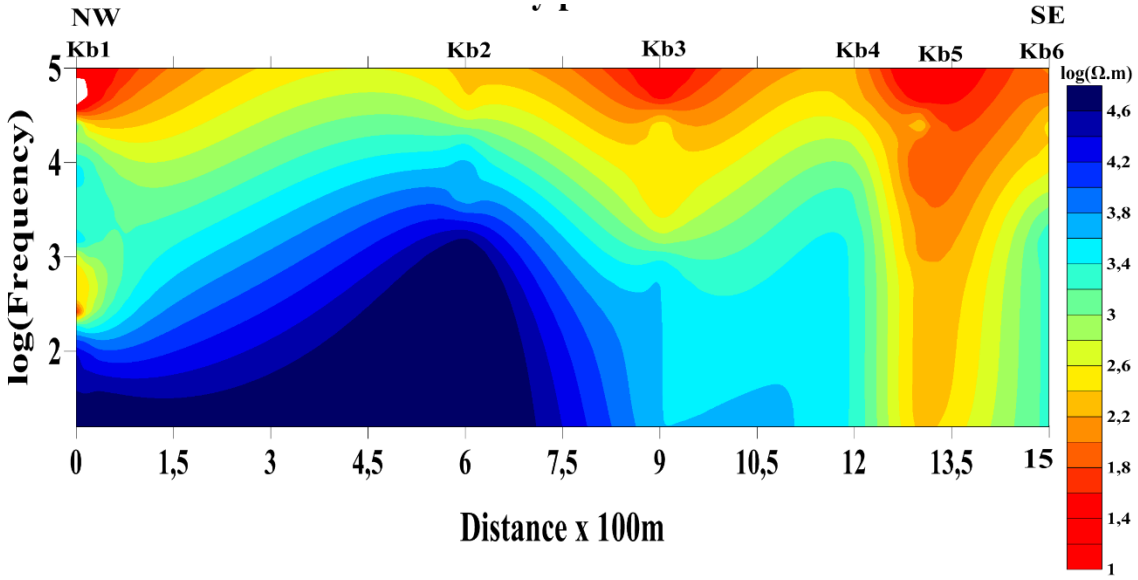

Figure 3.1-18 Apparent resistivity pseudo section of profile 5 (Kamba). The plot exhibits top-down three groups of formations (reddish, light-blue and blue, respectively) and a major electrical discontinuity at Kb5, probably an active fault

A strong anomaly characterising very resistive formations is observed from Kb1 to Kb3 where it ends by rudely. This strong resistive anomaly rises sharply from 100 Hz below Kb1 to nearly 10,000 Hz beneath Kb2, appearing like a dissymmetric dome whose summit is beneath Kb2, due to a probable uplift of the basement therein. The apparent resistivity isocontours patterns suggests an initial tabular layering followed by a strong folding process. They are oblique (with a nearly 45° slope observed on the resistive anomaly) from Kb1 to Kb2 and subvertical from 750 m to the end of the profile. The vertical to subvertical discontinuities are related to the major subvertical discontinuity centred at Kb5, filled by conductive materials, and interpreted as an active major fault that affect the whole subsurface (as it runs from the bottom to the top of the pseudo section).

3.1.6.3. Geoelectrical section

The geoelectrical section of the profile 5 (**Figure 3.1-19**), as that of the previous profile, focuses only on the uppermost part of the subsurface in Kamba. The geoelectrical section of profile 5 suggests that the subsurface therein is made up of four to five terrains. Downwards the followings are encountered:

- The first layer, very thin, is made up of formations characterised by a mean resistivity value of 617.6 Ωm.

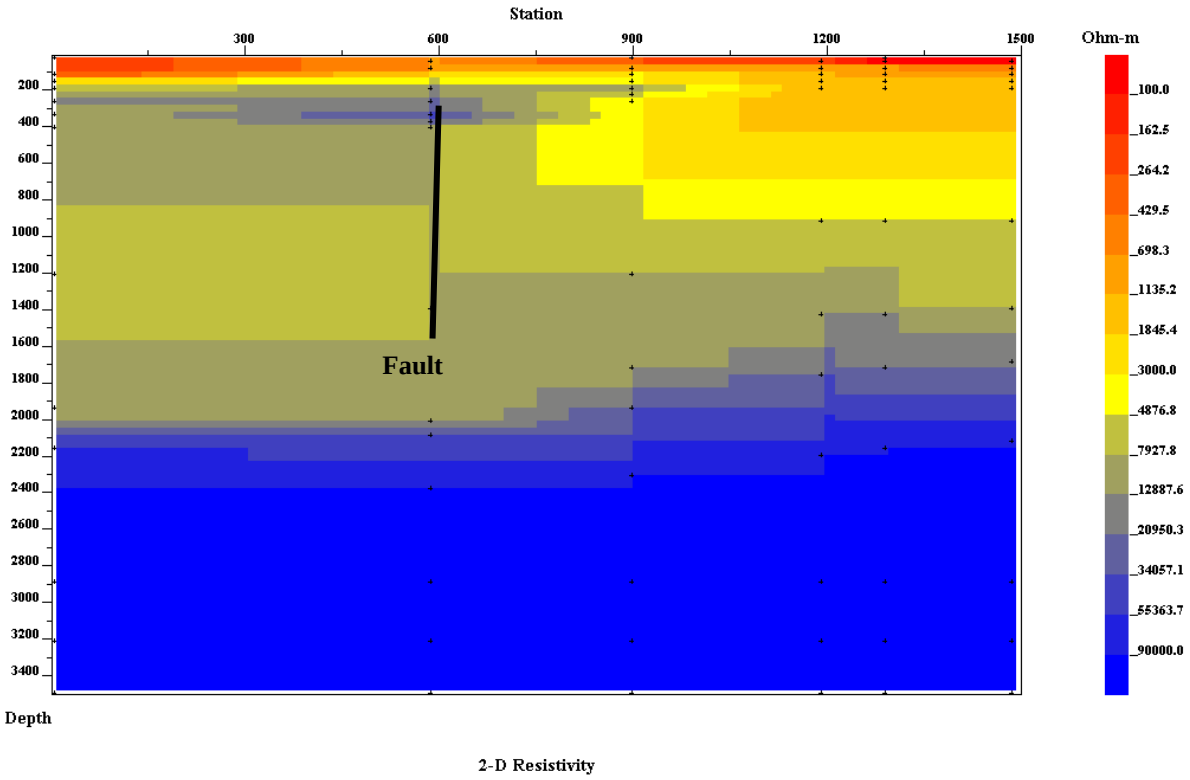

Figure 3.1-19 Geoelectrical or 2-D resistivity section of profile 5 (Kamba) for 3400 m depth.

- The second terrain is encountered near 175 m depth under Kb1. It is also very thin but thickens significantly to more than 400 m from Kb3 till the end of the profile. This second layer is characterised by formations with a mean resistivity value of 3006 Ωm. These formations are featured with many discontinuities from Kb1 to Kb2, and from Kb3 to Kb5 interpretable as faults. Faults from Kb1 to Kb2 shape this formation as a horse tail, while the section running from Kb3 to Kb5 corresponds to a collapse.
- The third layer appears near 200 m depth under Kb1. Like the previous, it is thinny from Kb1 to Kb2 where it starts thickening. The formations within are characterised by a mean resistivity value of 8882.2 Ωm. These formations are also affected by the discontinuities above interpreted as faults. The third terrain and those above form a dome whose slopes are from Kb1 to Kb2 and from Kb3 to Kb5.
- The fourth terrain is very resistant (resistivity greater than 9000 Ωm) and appears on the entire section. It is encountered at 275 m depth below Kb1 from where it is shallower, then suddenly collapses to nearly 1000 m from Kb3. This collapse occurs along a major discontinuity interpreted as a major fault affecting the area. This resistant layer seems to be responsible of the uplift or dome shaping of the terrains above.
- The fifth layer (the most resistive) corresponds to the basement. It displays a wondering uplift from Kb3 to Kb6, contrarily to the collapse observed with the formation above.

Summarily, the presence of many faults suggests that the area investigated through profile 5 is very weak (mainly on surface) and it is characterised by very resistive formations. The faults reported from station Kb3 toward the end of profile may be relays of a single major fault along which the highly resistive (more than 9000 Ωm) terrain broke apart and collapsed, leading to the subsidence of materials above. The geoelectrical section is in accordance with the observations from its related apparent resistivity pseudo section (**Figure 3.1-16**). The uplift of the basement remains an enigma to resolve in the future.

3.1.7. Profile 6 (Loum 2)

3.1.7.1. Phase pseudo section

The phase pseudo section of the profile 6 is displayed below (**Figure 3.1-20**). Its analysis enables to differentiate to main horizons downwards. The first horizon occurs at very high frequencies (20000 Hz). This shallow set corresponds to formations characterised by intermediate phase values ranging from 35° to 60°. Two half-circular high phase anomalies occur at Lm3 and Lm6, respectively. The first horizon is interrupted between Lm4 and Lm5 by materials constituting the second group of phase iso-values. The second group of phase isocontours occurs from near subsurface to very deep levels (frequencies less than 20000 Hz) characterised by low phase values ranged from 5° to 30°.

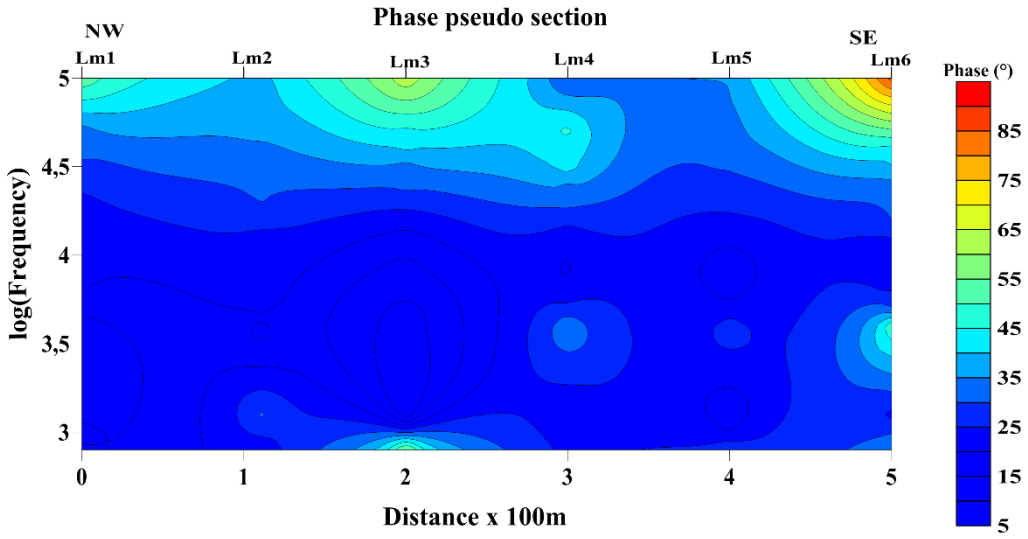

Figure 3.1-20 : Phase pseudo section of profile 6 (Loum 2).

This outcrops between Lm4 and Lm5 as reported above, and presents little circular intermediate anomalies below Lm4 and Lm5, respectively. The shape of isocontour lines is gently curled, suggesting that folding has affected the area however no ameliorated information is regained.

3.1.7.2. Apparent resistivity pseudo section

The apparent resistivity pseudo section of the profile 6 (**Figure 3.1-21**) enables to differentiate two main horizons. The first horizon corresponding to very conductive formations,

evolves from surface to near subsurface, between stations Lm1 and Lm2, and between Lm4 and Lm5. It reaches the middle depths Between Lm2 and Lm4, then sinks from Lm5 to Lm6.

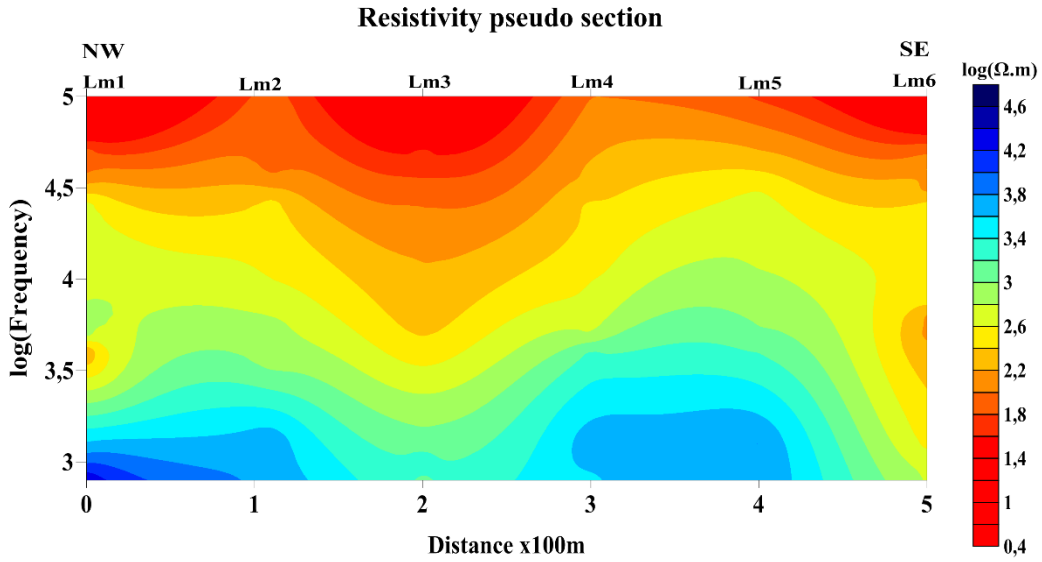

Figure 3.1-21 : Apparent resistivity pseudo section of profile 6 (Loum 2) evidencing ductile deformations in the area.

The second horizon characterising resistive formations, is encountered at frequencies less than 3162.3 Hz. It displays two highly resistive nuclei, from Lm1 to Lm2 and Lm4 to lm5, respectively. The first and second horizons are separated by a transition zone of intermediate conductive formations with abrupt slopes from Lm2 to Lm3 and from Lm4 to Lm3, while they are subvertical from Lm5 to Lm6 which are inferences of discontinuities centred at these stations.

Globally, the shape of the isocontours lines characterises folding in the area and the highlighted discontinuities suggest a subsidence or a basin between Lm2 and Lm3.

3.1.7.3. Geoelectrical section

The 2-D inverse model of the profile 6 is shown on figures 3.1.22 and 3.1.23 below. **Figure 3.1-22** and **Figure 3.1-23** provide respectively, the general and the detailed (for the upper 600 m) image of Loum 2 subsurface. This geoelectrical section (profile 6) suggests that the subsurface is made up of six (06) terrains (Figure 3.1.22) reported downward as follow:

- The first layer is a very conductive thin terrain (25 m mean thickness) characterised by a mean resistivity value of 43 Ωm and runs along the entire profile.

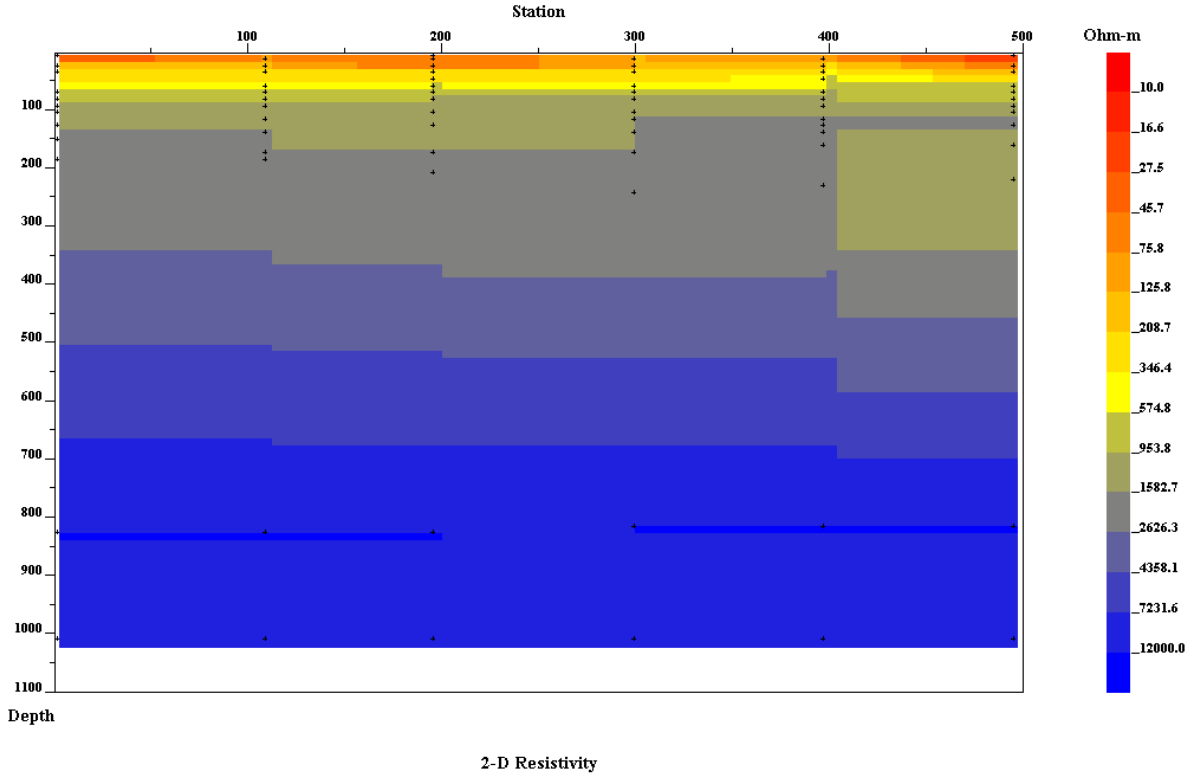

Figure 3.1-22 : Geoelectrical or 2-D resistivity section of profile 6 (Loum 2) for 1100 m depth.

- The second layer is also thin and conductive, includes formations characterised by a mean resistivity value of 340Ωm. With an average thickness of nearly 25 m, it is jagged by some discontinuities at Lm2, Lm3, at Lm5 and 350 m before Lm5, which can be interpreted either as faults or scarps (preferably faults). The plot shows that the limit with the first layer is rather gradational contrarily to what happens with the third layer.
- The third layer corresponds to formations with a mean resistivity value of 803Ωm. This layer is encountered around 75 m depth at station Lm1. Its thickness is relatively constant and close to 25 m. Two main discontinuities (probably faults) affect it at Lm3 and Lm5.
- The fourth terrain corresponds to formations characterised by a mean resistivity value of 1340Ωm. This layer occurs from 100 m to 175 m depth from Lm1 to Lm3; its thickness decreases slightly from Lm3 to Lm4 and increases between Lm4 and Lm6 (the layer therein runs from 100 m to 325 m depth). A thin concordant resistive intrusion is embedded within the fourth formation, from the Lm4 station to the end of the profile. Two discontinuities are noticeable at Lm3 and Lm5in the same way as shown by the above layer. This confirms the hypothesis of two faults that affect both the third and the fourth layers at Lm3 and Lm5, respectively (and affect the second upper layer too).
- The fifth layer is characterised by an average resistivity of 2236.3Ωm and an increasing thickness from Lm1 to Lm4 where it suddenly drops at a constant value of nearly 80 m.

This layer includes formations with same resistivity characteristics as the intrusion reported in the fourth layer above. The fifth layer is affected by two main discontinuities at Lm3 and Lm4 (**Figure 3.1-23**) interpretable as faults. Particularly, the fault at Lm4 has a significant upthrow (nearly 150 m) and its low compartment created a subsidence from Lm4 to Lm6 filled by overburden materials.

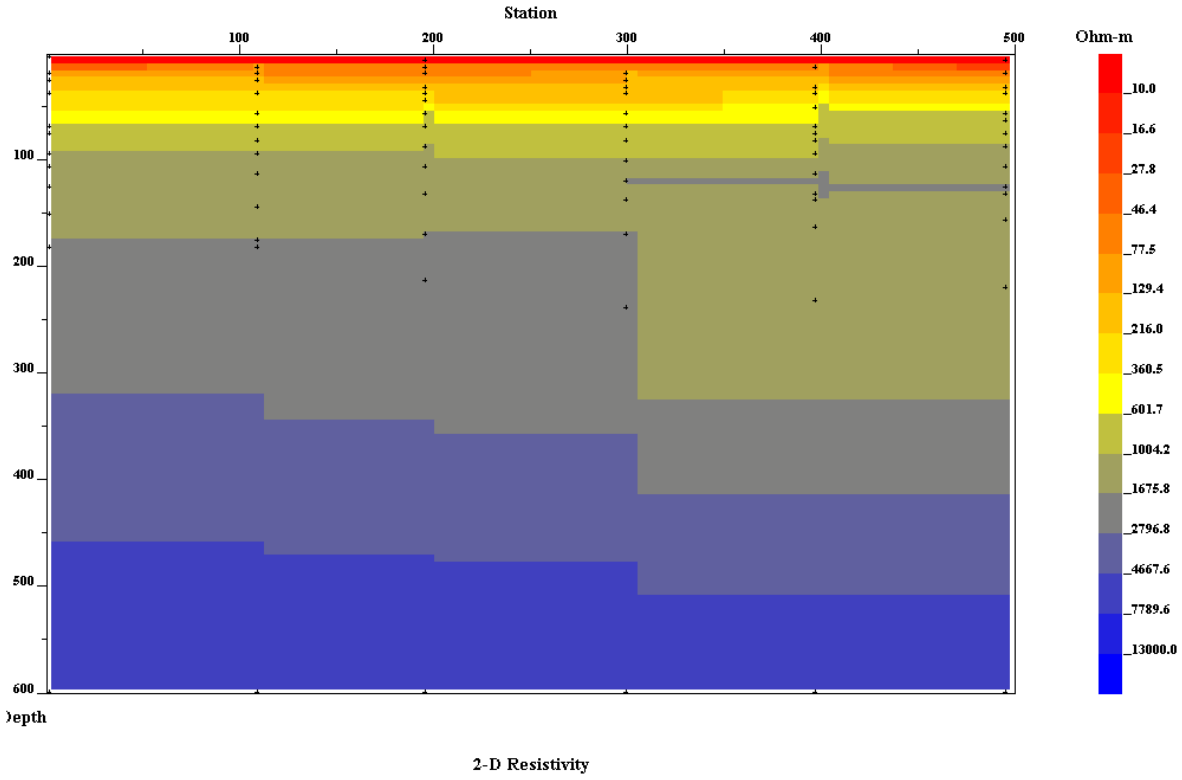

Figure 3.1-23 : Geoelectrical or 2-D resistivity section of profile 6 (Loum 2) for 600 m depth.

- The sixth layer corresponding to the basement is encountered at nearly 325 m depth under Lm1 and has resistivities greater 4249Ωm. Its first upper levels may correspond to a metamorphic areole due to the contact between the basement and the fifth layer. The basement displays discontinuities at Lm2, Lm3 and Lm4 which could correspond to faults shaping it like downstair steps along which it could have collapsed; thus featuring it like a graben. Seemingly, a deep faulting affected both the basement and formations above as specifically suggested by the faults evidenced at Lm2 and Lm4.

The apparent resistivity pseudo section of profile 6 highlights folds and discontinuities, the later being confirmed by its geoelectrical section and interpreted as faults. Moreover, these faults may correspond to weakness zones along which the subsurface broke up and subsided as a result of an intense tectonic activity. These faulting and folding are imprints of a multistage tectonic activities affecting the area.

3.1.8. Summary of AMT results

Summarily, the AMT surveyed area is made up of a mixture of both very resistive and conductive formations. The basement appears at 1400 m in profile 1; 825 m in profile 2; 550 m in profile 3 and deeper (more than 1400 m) in profile 4; on profile 5 it is encountered at 2,200 m and upraises to ~1,800 m and the end of the profile. In profile 6, the basement is shallower (~ 200 m) despite the important sink below station Lm4. That means, the basement rises up in some parts of the area while it collapses in other parts; uplift may be due to cooled intrusions beneath the basement. The pseudo-sections that show that the subsurface topography of the area is very rough, enable to interpret those subsidence and uplifts of the basement as grabens or basins. The roughness of this subsurface is also emphasised by the curling of isoresistivities on all the pseudo-sections; this suggests that the formations in the area have been folded.

According to the orientation of the AMT sounding profiles (nearly N135°), the folding processes may have been caused by a shortening a priori parallel to the direction of all the profiles. This shortening was caused probably by the collision between the CC and the NEFB. In addition, many faults, scarps and fractures have been highlighted in all the profiles; several faults have a significant throw (e.g. 150 m below station OS4 in profile1; 50 m and 100 m beneath BG2 and BG3, respectively in profile 4; 175 m below BE1 in profile 2). Further the pseudo section of apparent resistivity from profile 5 (Kamba) highlights a major discontinuity centred at station KB5 interpreted as an active fault (characterised by low resistivity values) that spans from surface to the bottom of the section. The conductive channel seen on profile 1 (**Figure 3.1-3**) is either an intrusion or the assent of an active faulting. Since, the general trend of profiles is N135°, faults and fractures highlighted are assumed to span broadly from SW-NE to WSW-ENE (but may also be E-W). The profiles being parallel and considering their offsets from each other along their azimuth, the study assumes these faults and fractures form a set of parallel or distributive faults corresponding to a main SW-NE lineament that may extend beyond the limits of the AMT-surveyed area, in the whole CC/NEFB transition zone. The curled apparent resistivity isocontours, faults and fractures from AMT survey suggest that brittle to brittle-ductile tectonics occurred in the area. Besides, the alternance of resistive and conductive structures in some geoelectrical sections (e.g. profile 4) evidences a flip of superficial materials possibly characterising the thrust of the Yaoundé nappes onto the CC in the area. The aeromagnetic data are used to deepen investigations in the remaining part of the study area..

3.2. AEROMAGNETIC DATA INTERPRETATION

Aeromagnetic data interpretation gives the possibility to investigate the part of the study area (the majority by far) uncovered by audiomagnetotellurics. Targeting a semi-regional scale study, analyses start with the TMI map reduced to the magnetic equator.

3.2.1. The total magnetic intensity reduced to the magnetic equator

The reduction to the magnetic equator (RTE) has the merit that it shifts magnetic anomalies directly above their causative sources in low latitudes areas. The RTE map in the study area (**Figure 3.2-1)** shows that the magnetic anomaly field ranges from -1113.34 nT to 1094.15 nT and portrays three main domains, southward from the left (Mbalmayo) to the lower right corner (Sangmelima) of the map.

- The first domain (A), is diagonally narrowed in the upper left corner and south-bounded by SW-NE line from Nkout to Akonolinga. This is characterised by a very high-intensity linear anomaly (valued from 15.5 nT to 1094.15 nT) in a fairly negative background. The observed anomalies correspond to high susceptibility possible mafic or basic to ultrabasic materials, or regional structures like faults or deep contacts affecting the basement of the Panafrican domain in the north of the study area.
- The second domain (B), forms a SW-NE channel of negative magnetic background (from – 63.5 nT to -16.5 nT) covering the central portion of the RTE map and south bounded by an imaginary line passing between Zoetele and Tekmo up to centre-east border of the map. Domain (B) is mainly characterised by the occurrence of small linear high intensity anomalies oriented SW-NE to WSW-ENE as we move northward beyond Zoetele. Additionally, these anomalies are sparse in the north (beyond NE-Zoetele) contrarily to the south (S-Akoeman) where they have highest intensities sometimes culminating at 83.7 nT. Also, domain (B) seems to be intersected by a WNW-ESE structure from N03º15’ (NE of Tekmo) to N03º30’ latitudes (Mbalmayo) which tends to orientate the features therein E-W to ESE-WNW (indigo line on **Figure 3.2-1**).

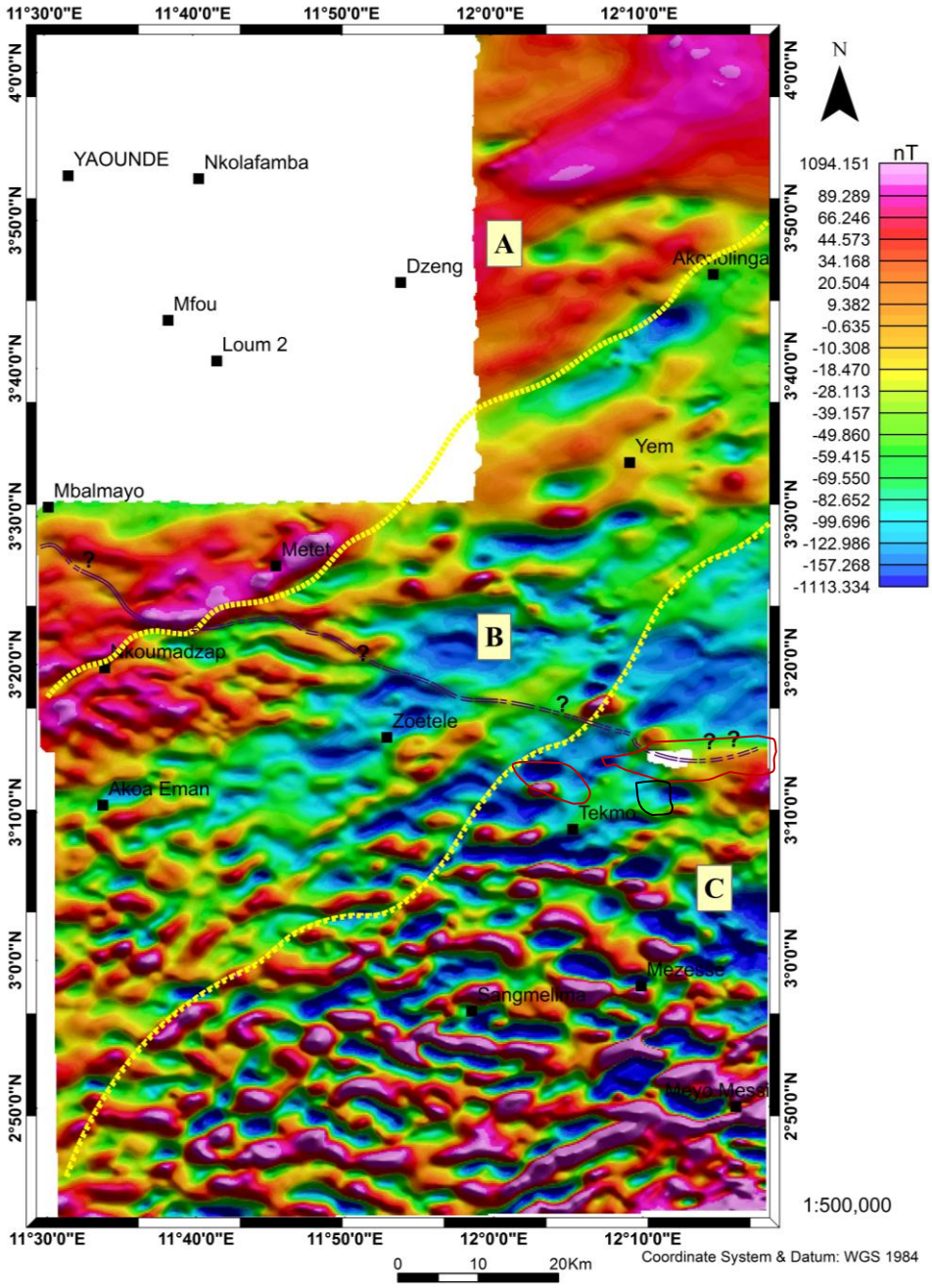

Figure 3.2-1 : The reduced to the magnetic equator (RTE) of the TMI map. The map is dominated in its centre by a NE channel (domain B) with some high intensity anomaly sources in the south.

- The third domain (C), in the southeast of the study area, experiences a dense occurrence of very high intensity anomaly's values in the Tekmo-Sangmelima area. The orientation, size and intensity of these anomalies contrast entirely with those previously described in the adjacent domain. its magnetic relief already show that formations therein are of a different nature, in comparison to doamins (A) and (B). Illustratively, anomalies in domain (C) have intensities around 910.7 nT with a nearly E-W to ESE-WNW general orientation resulting from a probable rotation to the west between Sangmelima and Tekmo (**Figure 3.2-1**). They suggest the presence of hypothetical presence of mafic to

ultramafic materials. Disruptions observed on these anomalies infer major fracturing mainly along the NE and the NW directions. The intensity of these anomalies suggests that their causatives sources may differ from those of other anomalies located in the southwest portion of the study area.

In general, the orientation of the main anomalies in the domain (A) and that of the channel forming domain (B) and the located anomalies gives a strong indication on the trends of lineaments which could affect the area's subsurface. Indeed, the observation of this whole set infers that the basement's control is carried out by SW-NE structures. The extend of domain (B) throughout the study area suggests that it is a unique weakness zones affecting both the NEFB and the CC domains. The anomalies herein observed are probable intrusions and/or discontinuities. The difference in the intensity shown by these anomalies (high intensities in the south portion of domain (B) compared to its north portion) suggests their emplacement occurred either at different periods or in different milieus, or even both. In the case of different periods, anomalies in the south of domain (B) are likely upwells of mafic to ultramafic materials or some ultrabasic like gabbros (hence their high intensity due to strong magnetisation effect) in the Ntem complex and anomalies in the north could be due to melted materials (basic materials) forming intrusions beneath the NEFB, thus suggesting that domains (A) and (B) form an early (probably Eburnean) NE-SW weakness zone which experienced reactivations (Panafrican and post-Panafrican). From the design of the anomalies in domain (C), their intensity and the background magnetic field, considering the spatial relation with domains (A) and (B), it seems evident that these features were put in place earlier, probably during the Liberian orogeny. The high intensity of anomalies therein may originate from magmatic TTG and supracrustal intrusions along with some greenstones belts relics in the Ntem complex.

Further, on the magnetic grids, features like fractures, faults and dykes can be observed although not clearly located. Dykes appears as narrow elongated magnetic heights while fractures and faults are detected through linear breaks in the magnetic background either positive or negative; therefore, it seems not possible, in certain circumstances, to discriminate faults from fractures. With the aim of highlighting magnetic lineaments, some geological structures interpreted as faults and/or fractures are observable on the RTE map (**Figure 3.2-1)** where they appear as throughs in the magnetic background. Despite their multiple directions, they already reveal the preponderance of the SW-NE, NW-SE, WSW-ENE and WNW-ESE to E-W directions, as well as the existence within the study area of a NE-SW sinistral system that affects both the CC and the NEFB, yet to be confirmed. However, the RTE map alone cannot entirely

help to map the lithology of an area. Therefore, application of advanced filtering techniques to the RTE field is necessary to complement the results.

3.2.2. 3D Analytic signal (AS) map

Some lithological units can be outline with the 3D analytic signal (AS) depending on their magnetization. The analytic signal map of the study area (**Figure 3.2-2)** globally presents north to south, a quiet domain extending south up to the north of Mbalmayo (domain I) and a gradually disturbed (spotted by some high-intensity AS anomalies - e.g. around Metet) domain to the south of the above boundary (domain II). Migmatites (gneisses) of the Yaounde series are particularly characterised by a quiet magnetic area in the north, while ectinites (micaschists) are characterised by a NE-SW to ENE-WSW trending magnetic area jagged by many high intensity anomalies (including intrusions) trending nearly ENE-WSW. The domain II forms a narrow E-W band (between Mbalmayo and Nkoumadzap) characterised by nearly E-W trending anomalies (foliation trace?) in a background weak field. This symptomatic characteristic of low-metamorphism materials suggests that local formations correspond to the Mbalmayo schist. The difference in the magnetic behaviour may expresses a difference in the composition and/or the origin of the formations encountered in these two domains. By equating both domain I and domain II to the Yaounde Group, obviously the southern area (domains III to V) would correspond to the Ntem complex.

In the area ascribed to the Ntem complex, three distinctive magnetic domains (domains III to V) have been outlined in regard to the density and orientation of anomalies. The domain III is a rough E-W band characterised by occurrence of relatively dense high-intensity AS anomalies, and E-W folding patterns (delimited by the Nkoumadzap-Akoeman-Zoetele triangle). It corresponds to the portion of the Ntem complex dominated by Tonalites (Soo granites). The second zone (domain IV) is easily identifiable through its highest anomalies on the map in the area south of Tekmo, in an area where charnokites have been mapped in the Ntem complex. Though they have high intensity, these anomalies are very dense and they are oriented SE-NW, to WNW-ESE (and even NE-SW) assuming a possible difference in the rock composition. The AS peaks are interpreted as supracrustal rocks or greenstones belts relics (**Figure 3.2-2**), as well as mafic to ultramafic intrusions that prove an effective hydrothermal activity within the area.

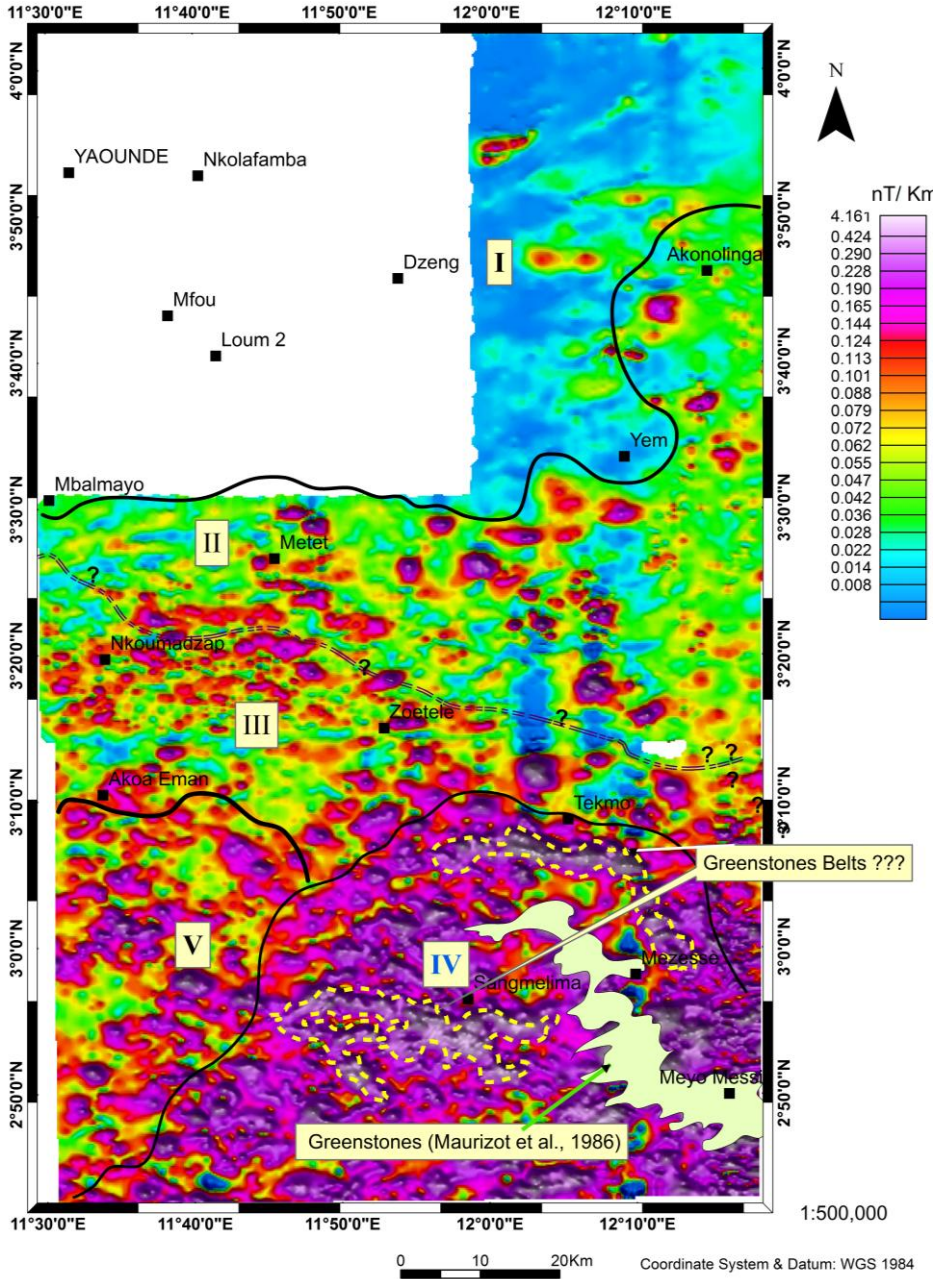

Figure 3.2-2 : The Analytic signal (AS) of the RTE field. The AS map herein delineates major lithological units (I to V) and greenstones belts. The broken black line illustrates the NEFB/CC limit.

The domain V seats east of domain IV and south of domain III, in the southwestern edge of the map. It, is characterised by dominating NW-SE anomalies. However, formations therein seem be close in composition to those of domain III, or they may be a different mix of all of hem, hence the noticeable diffenrence in the AS anomaly relief.

3.2.3. First vertical derivative (FVD) filtering

The first vertical derivative (FVD) filtering has the advantage of both, enhancing shallow sources while suppressing deeper ones, thus it enables to highlight linear structural features such as faults, fractures and dykes despite its ability to accentuate noise. The **Figure 3.2-3** below represents the FVD map of the Yaounde-Sangmelima area. According to gradient values, three

main group of anomaly gradients types are identified. The very low (down to -2.29 nT/km), the medium (amplitudes: -0.03 to 0.01 nT/km) and the steep positive (up to 1.40 nT/km) gradients.

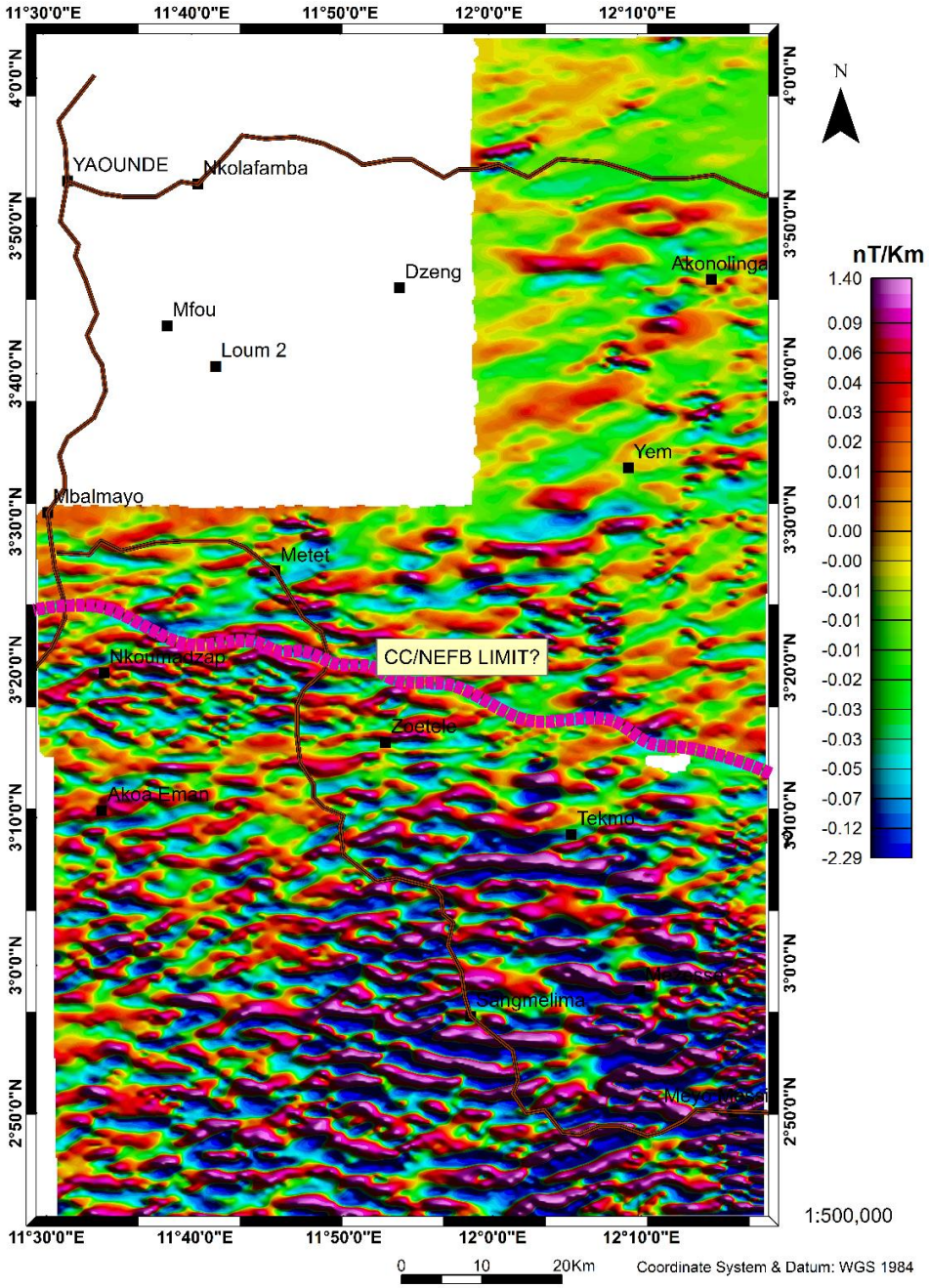

Figure 3.2-3 : FVD map of the Nkolafamba-Sangmelima area. The map evidences the difference in the nature and/or composition of the formations of the Ntem complex and the Panafrican, based on the the magnetic background field's intensity variations.

The density distribution of FVD gradients suggests that the area doesn't have the same magnetic character. This difference is probably caused by a difference in the rock composition emphasised by the difference in the way the geological units reacted to the stress/strain during the tectonic phases that affected the northern margin of the Congo craton. Two main magnetically disturbed zones are noticeable, a northern area which doesn't exhibit same anomaly

ranges nor shapes, size or distribution, in opposition to the southern area. The background magnetic relief (in green colour) accentuates the differentiation of the northern part from the southern one, thus assuming the existence of two adjacent blocks, the CC to the south and the NEFB to the north. Besides, the limit between those lithological units is depicted from the positions (E11º30'; N03º20') to (E12º15'; N03º15') by a curved line passing north of Nkoumadzap, below Metet and north Zoetele. This corresponds to a set of NE-SW, ENE-WSW and NW-SE anomalies forming a main E-W lineament interpretable as the local expression of the thrust-line between the NEFB and the Ntem complex. A ring complex surrounding Metet is observed (**Figure 3.2-3**), confirming observations made on the AS map the which probably outlines the micaschists from the Yaoundé series in the area.

Additionally, some structural information can be retrieved from the FVD map. This is particularly the case in the NE portion of the figure, where NE to ENE folds are observable. The size exhibited by long wavelength anomalies herein shows that these folds are gentle, and confirm the SE vergence of nappe thrusting onto the CC. Many lineaments interpreted as faults, fractures, dykes or outlines of intrusive bodies; or as contacts have been derived from the FVD filtering. These are probably deep or shallow structures affecting the basement of the study area. The main directions of the lineaments are NNE-SSW, NE-SW, ENE-WSW to E-W, WNW-ESE, NW-SE and N-S (very diffuse). To sum up, the FVD filtering provides good insights on the deformation history of the area because its outputs. Complementarily, a multiscale analysis is proposed to assess deep basement and regional tectonics.

3.2.4. Determination of regional structures

The regional lineaments are those affecting the deep basement. They are highlighted trough the multiscale analysis, a qualitative exercise supported by the calculation of the depth of the highlighted features.

3.2.4.1. The multiscale analysis of the magnetic anomaly map field

The multiscale analysis involved the detection of HGM peaks for the upward continued RTE field at the respective heights 1, 2, 3, 4 and 5 km. The superimposition of the peaks obtained at each height highlights deep seated features and solve their respective geometry by observing their orientation and the offset of their peaks for plunge, and for the strike.

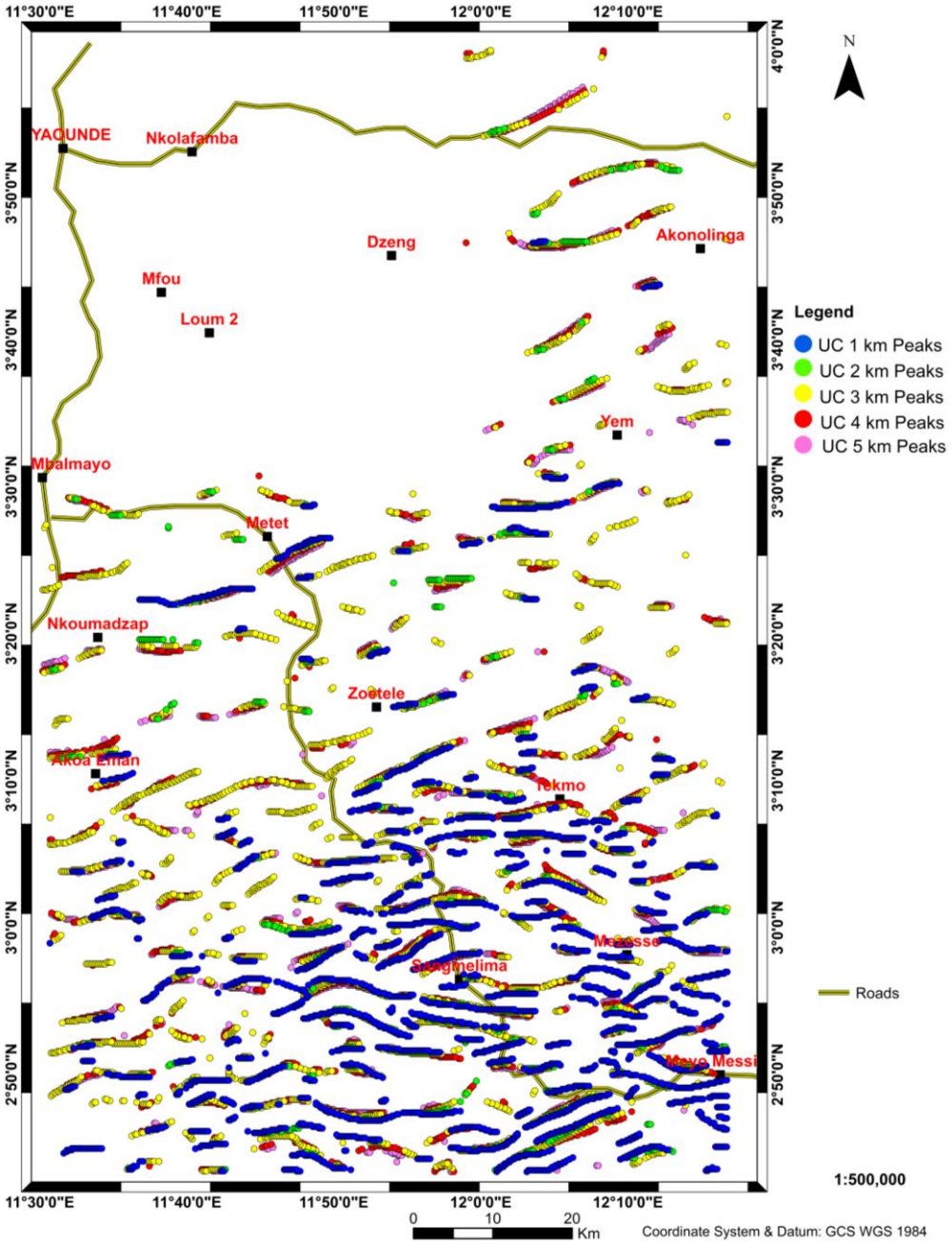

Figure 3.2-4 : Multiscale analysis map of the Nkolafamba-Sangmelima area. Lineaments are mainly vertical to subvertical or either dipping south or north.

The plot (**Figure 3.2-4**) discriminates very well the Panafrican and the CC domains in accordance with previous observations. The differentiation is made possible through the displayed difference in terms of density of the HGM peaks. Indeed, **Figure 3.2-4** shows that the lineaments are denser in the CC (south below Nkoumadzap) than in the Panafrican. In addition, peaks superposition shows that lineaments in the study area dip north or south (see **table 2**).

3.2.4.2. Interpretation of the lineaments from the multiscale analysis

a. Faults and fractures segregation

In this section, emphasizing on faults and fractures enabled to discriminate from dikes, contacts, etc. by underlaining the grey scaled RTE and FVD maps below peaks. Only coinciding features were interpreted as faults or fractures yielded **Figure 3.2-5** below.

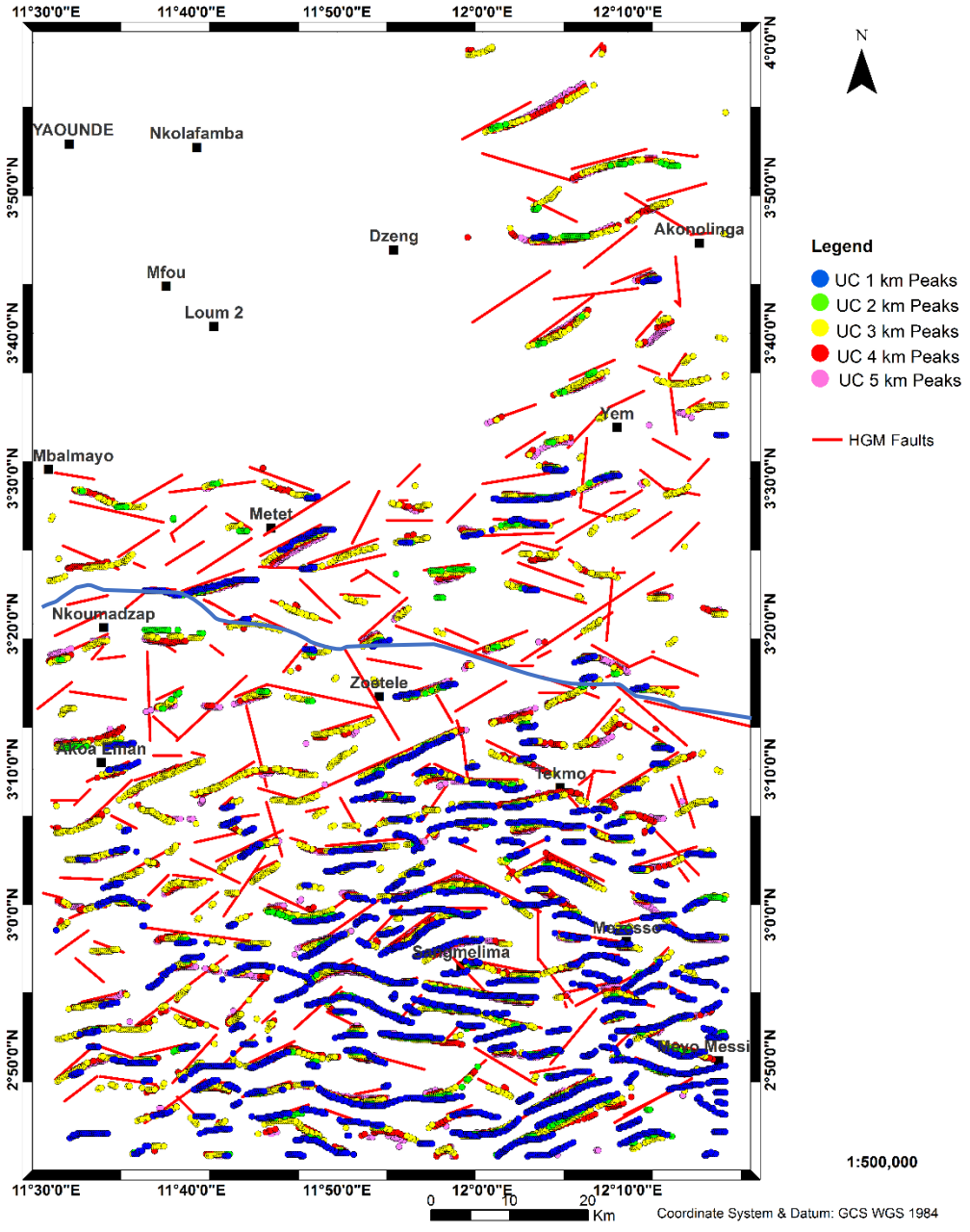

Figure 3.2-5 :Inferred major faults from the multiscale analysis map of the HGM. The superposition of peaks at various heights outlines the regional faults (red lines).

b. Characterisation of the interpreted faults

Characterising the faults means giving their attitudes (geometry) and determining their depth location. As for the geometry or attitude (**table 2**), the alignment of stacked peaks gives the strike and their offset indicates the plunge (coinciding peaks, mean a vertical dip). The table 2 below summarises the attitudes of the 31 interpreted faults extracted from **figure 3.2-5**. These faults are mainly vertical to subvertical and they form three main clusters, depending on their depth-location and extension.

Table 2 : Attitudes of the major lineaments in the Nkolafamba-Sangmelima area

Count	Fault's attitude		Depth class	Count	Fault's attitude		Depth class
	Strike	Dip or plunge			Strike	Dip or plunge	
1	SE-NW	North	Middle to deep	16	WSW-ENE	Vertical	Shallow
2	SE-NW	South	Middle to deep	17	WSW-ENE	Subvertical	Shallow
3	SE-NW	South	Shallow	18	WSW-ENE	North	Shallow to middle
4	SE-NW	Vertical	Shallow to deep	19	WSW-ENE	South	Shallow to deep
5	SE-NW	Subvertical	Shallow to middle	20	WSW-ENE	Vertical	Shallow to middle
6	SE-NW	Subvertical	Shallow	21	WSW-ENE	North	Shallow to deep
7	SE-NW	Vertical	Shallow to deep	22	WSW-ENE	North	Shallow to deep
8	SW-NE	N-Gradational	Shallow to deep	23	WSW-ENE	Subvertical	Shallow to middle
9	SW-NE	South	Shallow to deep	24	W-E	Vertical	Shallow to middle
10	SW-NE	Subvertical	Shallow to deep	25	W-E	Subvertical	Shallow to middle
11	SW-NE	Vertical	Shallow to middle	26	W-E	Subvertical	Shallow to middle
12	SW-NE	Subvertical	Shallow to middle	27	W-E	Subvertical	Shallow to middle
13	WSW-ENE	Subvertical	Shallow to middle	28	W-E	Subvertical	Shallow
14	WSW-ENE	Vertical	Shallow to deep	29	WNW-ESE	Vertical	Shallow to middle
15	WSW-ENE	Vertical	Shallow to deep	30	WNW-ESE	Vertical	Shallow to middle
16	WSW-ENE	Vertical	Shallow	31	WNW-ESE	Vertical	Shallow

Indeed, the distribution gives 2 deep-seated lineaments, 19 lineaments which are located in shallow/middle subsurface and extend to greater depths; while the last group comprises 10 lineaments with shallower (surface) expression and deep-extended. The along-strike distribution shows that the main orientations are WNW-ESE (3 counts), W-E (5 counts), NW-SE (7 counts), SW-NE (5 counts) and WSW-ENE (11 counts). Cumulatively, a dominant SW-NE to WSW-ENE cluster (16 counts i.e. 51.61%), followed by WNW-ESE to NW-SE cluster (10 counts, i.e. 32.25%) are highlighted in both the NEFB and the CC domains (separated by the blue line on **Figures 3.2-5**).

Depth-locations have been calculated using the Euler 3D algorithm, and solutions were superimposed on the map of the previously highlighted faults (**Figure 3.2-6**). To ensure fewer

but reliable solutions, calculations used a structural index of 0.35 and a depth tolerance of 5% with a 10 x 10 moving window.

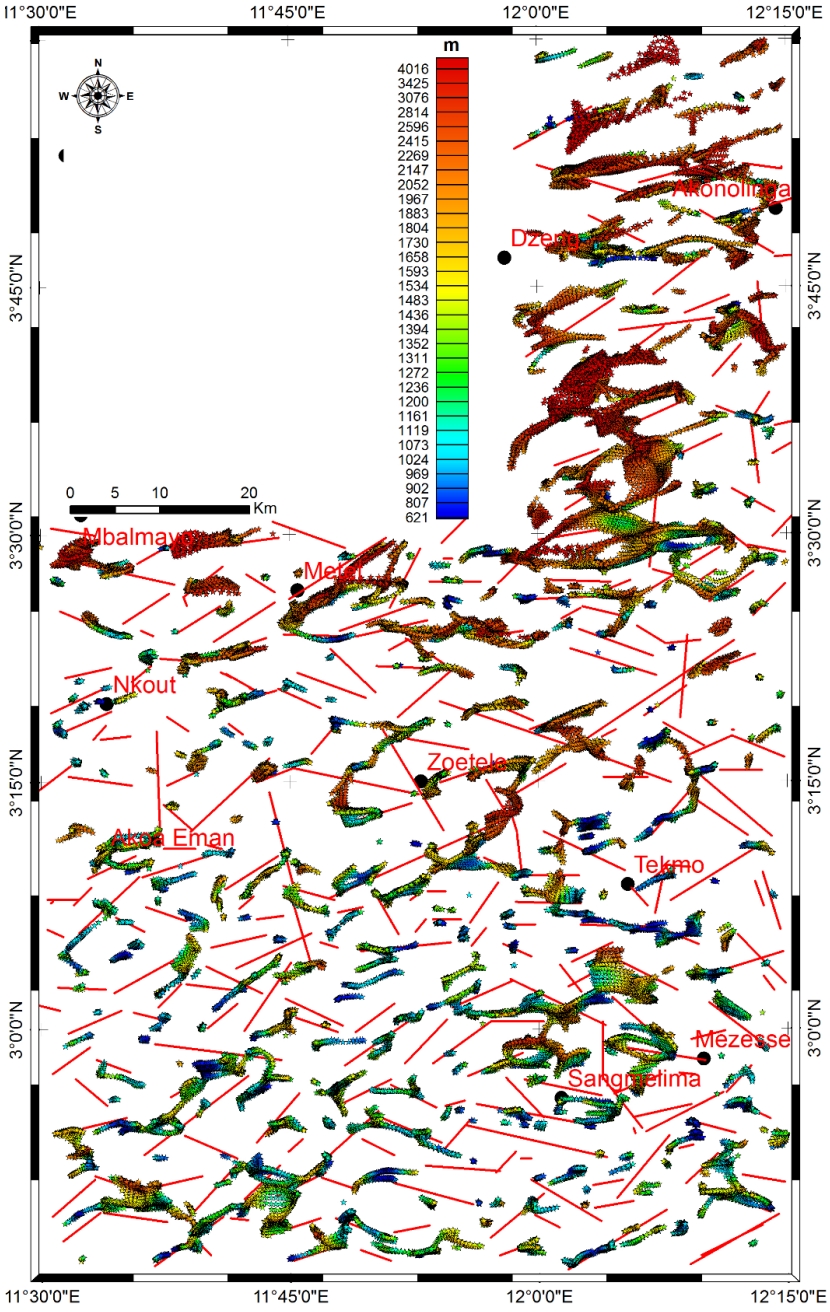

Figure 3.2-6 : Depth location of the regional faults in the Nkolafamba-Sangmelima. The good correlation between Euler solutions and the interpreted HGM fractures and faults is evidenced by the map.

Figure 3.2-6 validates the qualitative analyses of the previous paragraphs. Indeed, many Euler's solutions coincide with the interpreted faults from the multiscale study thus suggesting the validity of the present results. The depth ranges suggest three classes of faults: deep seated (depth > 2.1 km), intermediate (1.3 km < depth < 2.1 km) and shallow (depth < 1.3 km) faults; as seen with table 2.

Moreover, the observation of the Euler's solution map enables to outline the space location of the faults and complement the multiscale analysis. In general, it can be noted that the Euler's solutions divide the study area in three zones:

- The southern zone is the domain of shallower features (depth <1.3 km) despite the presence of some deep elements at the vicinity of Sangmelima and in the SW edge of the map, probably because of their sub crustal origin. The features have various trends possibly because of their rheology.
- The central domain located between ~N03º15' and N03º30', is ºfirstly characterised by the very low density of solutions, has the dominance of nearly E-W features and corresponds to the area of intermediate buried solutions (1.3 km < depth < 2.1 km).
- The northern domain (above latitude N03º30') is the region of deep seated features. These features follow the major NE-SW to ENE-WSW trend that characterises the Yaounde series.

The depth difference (increase) observed south to north is attributable to the subduction of the Congo Craton beneath the Panafrican belt and the intermediate depths recorded in the central domain as well as the dominance of the E-W trend are possibly explained by the presence of the Mbalmayo series and its stratigraphic position on top of the Panafrican belt in the area. As a matter of fact, the northern domain is interpreted as the Yaounde series; the high depths pertaining in that area might therefore be explained by the presence of a fractured subducted craton under the Yaounde Group.

3.2.5. Assessment of the regional magnetic foliation and deformation history

An attempt has been made to highlight the source behaviour by producing a map of source edges (**Figure 3.2.7**) which highlights both their plunge and strike. This approach examines the magnetic fabric of structures so as to assess the attitude of the regional foliation and infer the deformation regime. The difficulty to follow any particular magnetic foliation trace makes it uneasy to give clues on the foliation of structures encountered within the study area. This is particularly tributary to rejuvenation that occured in the region. In terms of line density, the magnetic foliation map can be slice up into three portion. The northern and the southern portions appear as areas with low to moderate line densities, probably because of their relative locations from the contact line between the NEFB and the CC. This is similar for the portion of CC directly in contact with the NEFB; which seems to have behaved differently to the post Panafrican stress that pertained at the northern margin of the CC.

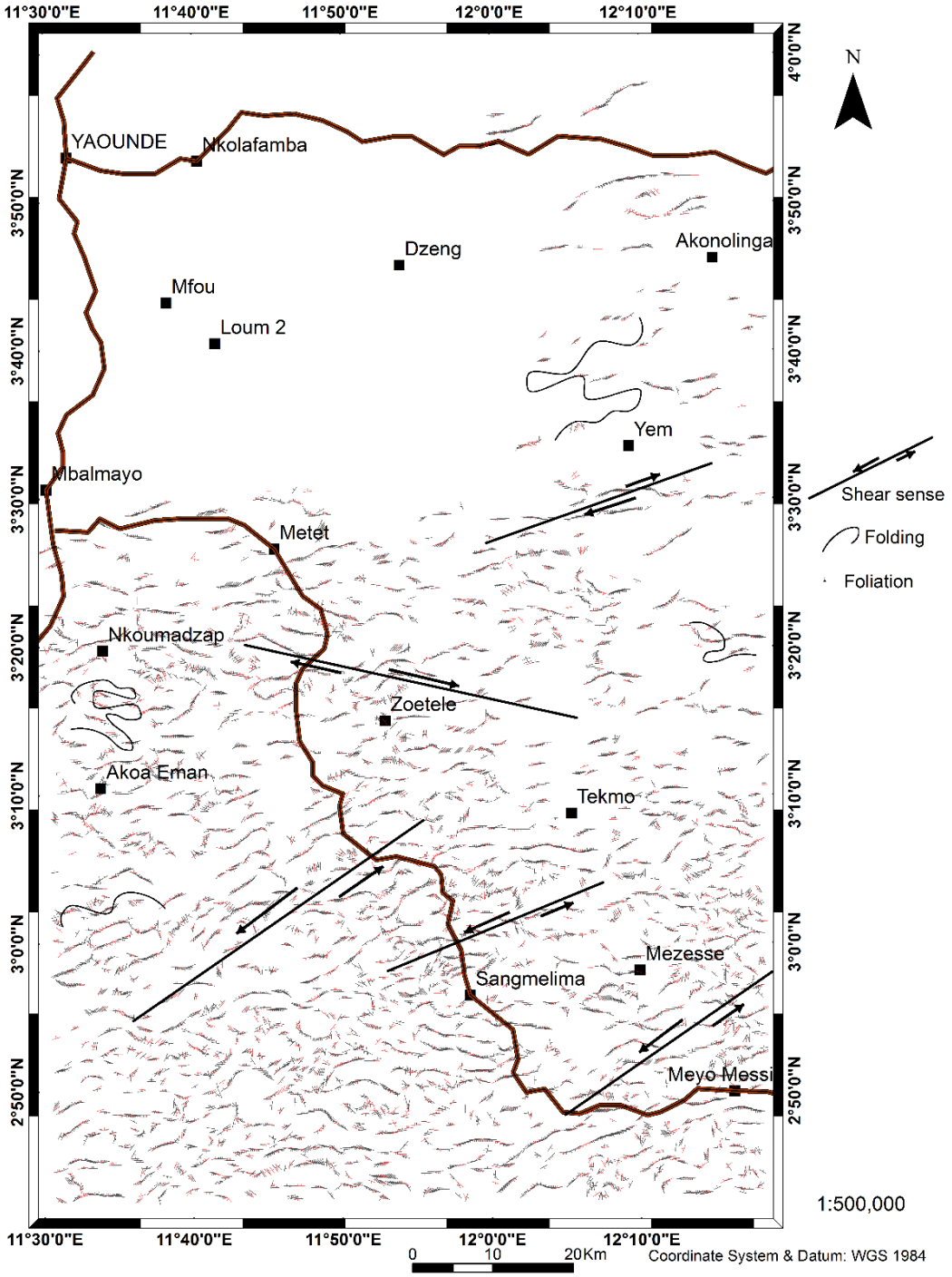

Figure 3.2-7 : Magnetic foliation. The magnetic foliation appears sparse in the north and dense in the south.

Considering the orientation of lines, the northern domain is characterised by two main directions, from the centre to the north of the map. In fact, in the region between Mbalmayo and Nkout (in terms of latitudes), the foliation is broadly E-W whereas it is nearly ENE-WSW in the northern part. The dip orientation varies alternatively from north to south. The ENE-WSW alignment in the north probably results from N-S to NW-SE compressions that affected the NEFB and triggered NE-SW to ENE-WSW extensions. The curling of the foliation characterises folding processes. Therefore, the two directions noticed correspond probably to the folding

trends hence it would be understandable that the area has been marked by an E-W and N-S folding episodes. This is particularly supported by the dipping attitudes which are south or north and sometimes east or west.

Additionally, many ruptures of the magnetic fabric are observed on **Figure 3.2-7**. These occur mainly along the NE, E-W and NW directions. These may correspond to shear trends related to shearing episodes which may have occurred along the SW-NE, the SE-NW and E-W directions but the timing of these events is fuzzy. The E-W shear zone has been identified south of Metet whereas the SW-NE shear zone is evidenced throughout the map, along a broad NE-SW. This shear patterns are consistent with the faults family previously highlighted. The map shows that this zone may have experienced many tectonic stages. This is witnessed by the curled patterns of the regional magnetic foliation which are probable imprints of folding (**Figure 3.2-7**). The various deformation stages can be assessed by observing the cutting relationships between These cross-cutting relationships suggest that the deformational history is an alternating occurrence of folding, faulting accompanied by shears supposedly triggered by compressional and/or extensional movements at different eras of the geologic history. The post-Panafrican events are particularly of interest as the central domain of the African Plate has been exposed to the stress regimes related to (1) the equatorial then the south Atlantic oceans opening, and (2) the ongoing rifting in East Africa leading to the individualisation of the Somalia Plate; questionning the existence of a fifth deformation stage. The qualitative interpretation of the aeromagnetic data has enabled to map various structures in the study area, including lineaneaments which testify that the area underwent brittle to brittle-ductile tectonics; and highlight rheological difference through which the Congo Craton/NEFB limit has been inferred. The geological modelling is hereafter made to refine its location.

3.2.6. Geological modelling: determination of the CC/NEFB limit

To propose an accurate location of the CC/NEFB limit, magnetic data were modelled along three N-S parallel profiles (P1 to P3) of nearly 52 km (**Figure 3.2-8**) from west to east.

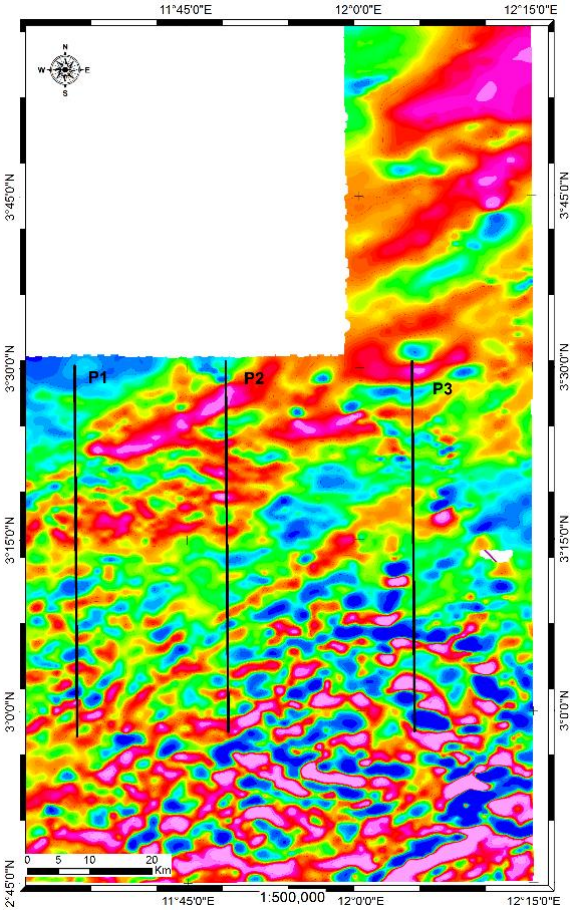

Figure 3.2-8 : Magnetic earth- modelling profiles. Profiles are labelled Line1, Line2, Line3.

3.2.6.1. Line 1:

Line 1 is the first and westernmost profile modelled to infer geology in the area surveyed with the magnetic method. Herein, the anomaly profile (**Figure 3.2-9a**) is smooth enough to allow straight analyses. Indeed, anomaly values vary from -192 nT to 45 nT. The profile's analysis assumes various discontinuities located respectively ca 3 km, 8.4 km, 22 km and 37 km. Some of these discontinuities are noticeable on the anomaly profile while other would correspond to hidden structures whose depth is not located yet. To produce a convenient geological model, the forward modelling strongly assumed that the anomaly profile results from various sources, including both suprabasement and intrabasement causes.

The modelling of Line 1 anomaly profile enabled to come out northward, with a model (**Figure 3.2-9b**) presenting four main faults, labelled from F1-1 to F1-4. The model was built assuming a uniform basement with a magnetic susceptibility (k) of 0.0015 cgs. The suprabasement effect corresponds to changes in the basement topography. These occur between

the faults F1-2 and F1-4. Therein an uplift of the basement is noticeable, coupled with a N-dipping intrabasement fault (F1-3) separating acidic granulites (k = 0.01977 cgs) from syenites overlying the basement between 20 and 38 km. This uplift smoothly affects the overlying formations between that same interval.

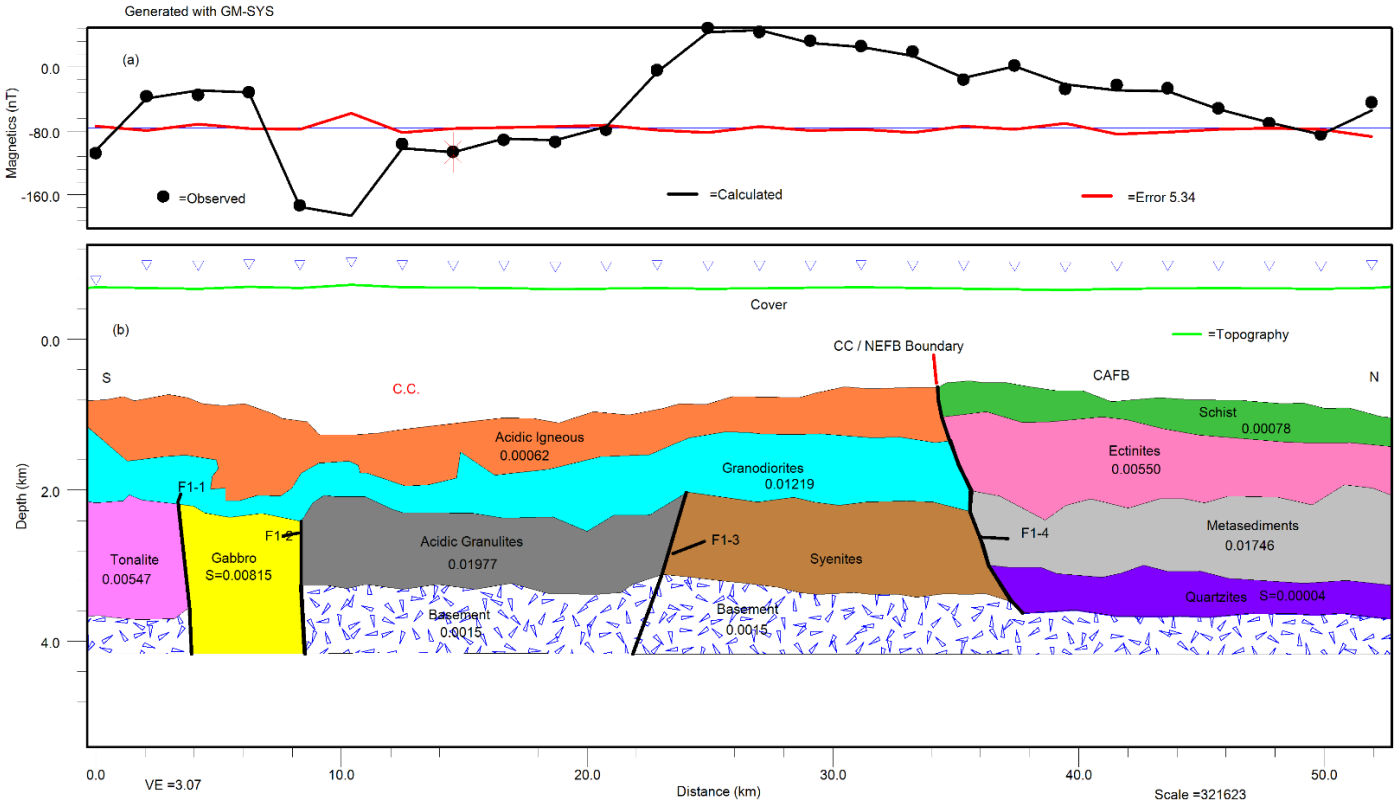

Figure 3.2-9 : Modelling along Line1. (a) Magnetic anomaly profile; (b) Geological section. The CC/NEFB limit is evidenced by the fault F1-4.

The intrabasement effect corresponds to the change basement lithology. Basement lithology variation is mainly observed between the faults F1-1 and F1-2, which bound an intrusive gabbro (k = 0.00815 cgs) encountered ca 2.3 km depth, with an approximate width of 4 km. This gabbro also occurs between tonalites (k= 0.00547 cgs). The previous described formations are topped upward by granodiorites (s= 0.01219 cgs) and acidic igneous formations (k = 0.00062 cgs) left of the F1-4 fault. Right of F1-4, the model yields upward above the basement, quartzites (k = 0.00004 cgs), metasediments (k= 0.01746 cgs), ectinites (k=0.00550 cgs) and schists (k=0.00078 cgs). The geological model (**Figure 3.2-9b**) shows that the basement is encountered at nearly 3.6 km depth from the origin of the profile to F1-1; at nearly 3.2 km from F1-2 to F1-4; then a progressive smooth subsidence from F1-4 to the end of the section. The F1-4 appears to be a north-dipping major discontinuity affecting the basement and separating an igneous complex to the left (south) from a metasedimentary complex to the right (north). By interpreting theat igneous complex as the CC, then the metasedimentary complex fit

with the southern part of the North equatorial fold belt (NEFB); therefore, the F1-4 illustrates the CC/NEFB limit (**Figure 3.2-9b**). The model realised with a satisfactory RMS error of 5.34%, shows no correlation between the subsurface geology and the topography.

3.2.6.2. Line 2:

The Line 2 particularity is its location at the middle of the area under consideration for magnetic prospecting. The anomaly profile (**Figure 3.2-10a**) values range between -192 nT and 35 nT. Its irregular profile's shape made it not obvious to identify anomaly sources, except for the portion spanning from 34 km till the end. Efficient modelling assumed that the observed anomaly profile pictures a combination of basement, normal faulting and faulted syncline effects involving the basement (Prieto, 1996). The geophysical modelling of the Line 2 anomaly profile (**Figure 3.2-10a**) has been realised with a significant RMS error of about 1.52 %, assuming a uniform crystalline basement of magnetic susceptibility (k) 0.0015 cgs. The basement effects mainly correspond to the change in the basement topography (suprabasement anomalies). The obtained section of Line 2 (**Figure 3.2-12b**) shows that the basement broadly dips northward. Indeed, it is encountered nearly at 3.5 km depth from the origin to 10 km (at F2-1) where it sinks to a nearly constant depth of 4 km up to F2-3; it sinks again therein to nearly 4.4 km depth till position 46 km (F2-10) where it is uplifted again to a constant depth of nearly 4 km. The basement is jagged by faults (F2-1, F2-2, F2-3 and F2-10) which affect partially or totally the overlying formations.

The formations on top the basement are affected by many faults like F2-1, F2-3 and F2-4 respectively separating different formations: migmatites (k=0.0039 cgs)/granite (k=0.03900 cgs), granulites (k=0.0706 cgs)-granite-gneisses (k=0.00858 cgs)/syenites (k=0.0268 cgs) and syenites/granulites-granite (k=0.00535 cgs). The faults F2-5 and F2-10 particularly, may correspond to limits of a basin or syncline extending northward in length from 33 km to 48 km. This is particularly supported by their respective geometry, as F2-5 dips north while F2-10 dips south, both being sub-vertical and normal. The faults F2-7, F2-8 and F2-9 apparently outline vertical movements affecting the schists (k=0.0021 cgs), ectinites (k=0.02366 cgs), migmatites (k = 0.0044 cgs), granulites, orthogneiss (k = -0.0578 cgs) and even the basement, in the aforesaid basin. This seems also to be the case for F2-1 and F2-2 regarding the granulites layer and the basement, nearly 10 km from the origin of the section.

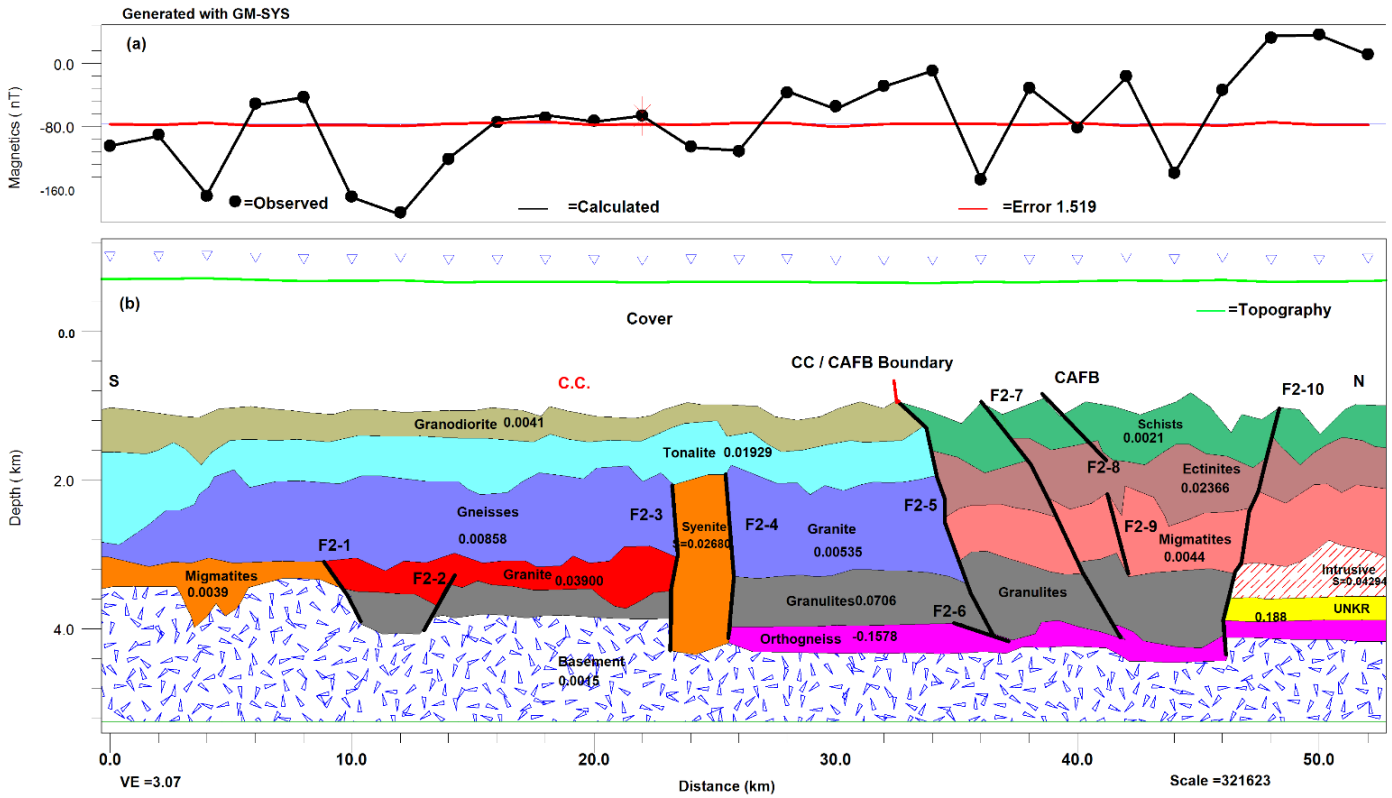

Figure 3.2-10 : Modelling along Line2. (a) Magnetic anomaly profile; (b) Geological section. The CC/NEFB limit is evidenced by the fault F2-5.

Further, from **Figure 3.2-10b**, two main blocks can be differentiated. One block is formed mainly by various igneous rocks and it is located to the left F2-5. This igneous complex seemingly corresponds to the CC formations. To the right of F2-5, the second block appears to be essentially made up of metamorphic rocks probably of sedimentary origin. This metasedimentary complex apparently corresponds to the NEFB formations. Therefore, F2-5 forms a sharp contact between the two above described blocks, making it interpretable locally as the CC/NEFB boundary. Moreover, the model shows that NEFB formations are affected by vertical movements imprints of compressions probably caused by pure compressions and/ or a collision. These are proofs of ductile to brittle-ductile tectonics in the area. The model does no correlate the subsurface geology with topography.

3.2.6.3. Line3:

The Line 3 is the easternmost modelled profile of the study. The anomaly profile (**Figure 3.2-11a**) looks more regular compared to the previous profiles. It is characterised by a peak value (100 nT) at the beginning of the line followed by a regional flat low of about -220 nT from 4km to 24 km where a new abrupt increase is observed. In the 24-32km interval, the profile displays a peak at 26.5 km and, alternative gradual decrease and increase till the end. This change shapes the anomaly profile like a valley between 32 and 44 km. The profile's patterns (**Figure 3.2-11a**) at 2 km and in the 24-32km interval, suggest the existence of discontinuities. In addition, the

regularity of the profile suggests two almost homogenous lithological blocks separated by a major discontinuity at 24 km; but, direct modelling and interpretation and remain not evident.

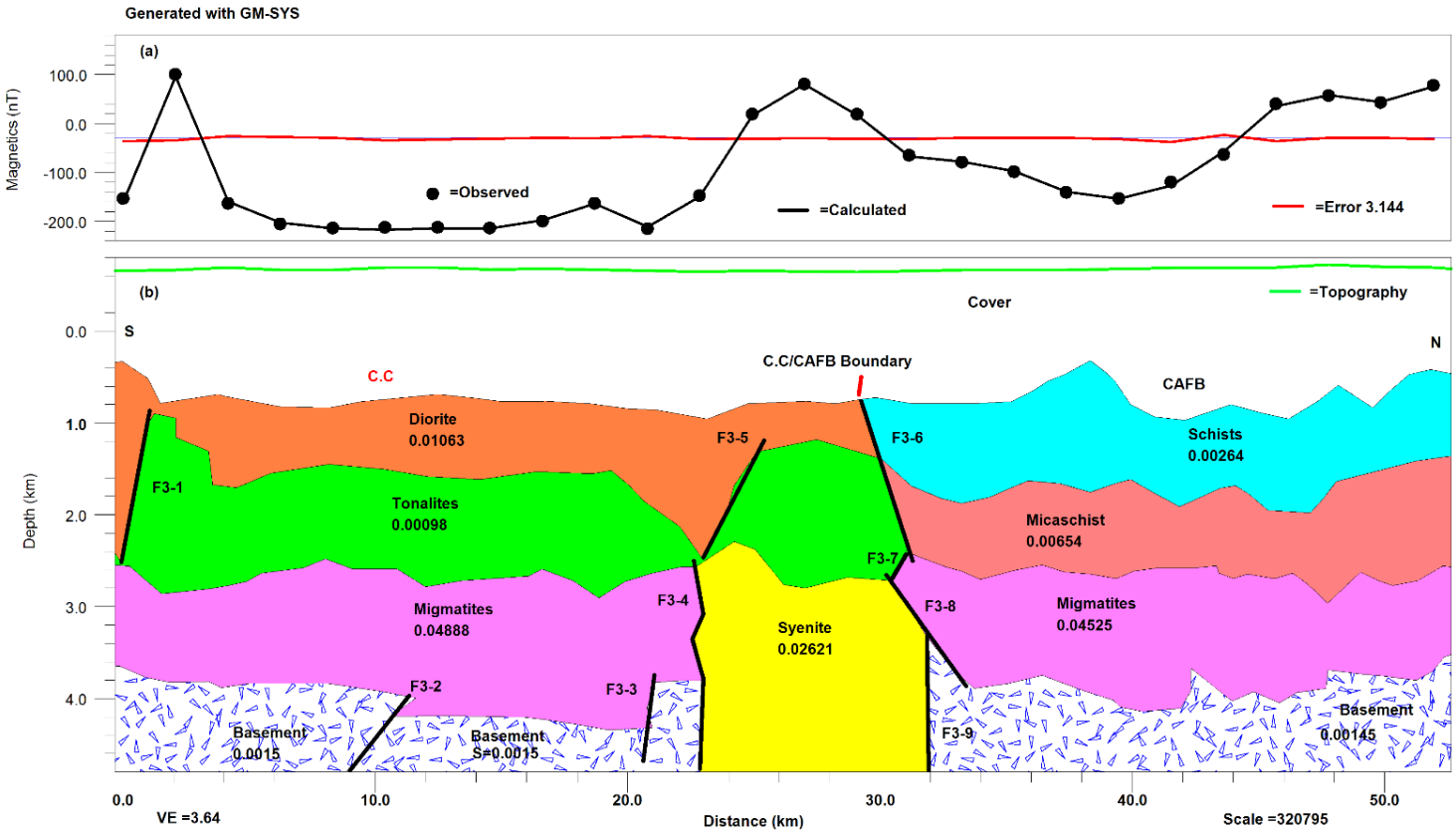

Figure 3.2-11 : Modelling along Line3. (a) Magnetic anomaly profile; (b) Geological section. The CC/NEFB limit is evidenced by the faults F3-6, F3-7, F3-8 and F3-9

The Line 3 model, with a RMS error of 3.14%; was built assuming that the anomaly sources involve both suprabasement and intrabasement variations and assuming a uniform basement with a magnetic susceptibility of 0.0015 cgs. The suprabasement effects are witnessed on **Figure 3.2-11b** along two manners. Progressively from 0 to 11 km, the basement occurs at approximately 3.6 km; it collapses to 4.2 km from 11 km to 21 km then raises again at 3.8 km up to 22.5 km; from 32 km to the end, it occurs above 4 km with a very rough topography. The main intrabasement variation modelled correspond to a body (k = 0.0261 cgs) affecting the basement. This body has been interpreted as a syenites intruding the basement and overlying migmatitic formations. The model outlines various discontinuities (9 discontinuities) labelled F3-1 to F3-9, which are somewhat hidden on the anomaly profile (**Figure 3.2-11a**). These discontinuities have been interpreted as faults or contacts. Particularly, F3-2 and F3-3 are related to a probable vertical movement that may have caused the collapse of the basement between 10 km and 21 km. Out of the interpreted faults, F3-4, F3-8 and F3-9 also play a very significant role. Indeed, the F3-4 and F3-9 faults are related to the intrusion of a body (interpreted as a syenite) through the basement, in one hand, whereas F3-4 and F3-8 are fault-contact structures

on another hand separating respectively, the migmatites I (k =0.04888 cgs)/syenites and syenites/migmatites II (k =0.04525 cgs). In addition, F3-7 and F3-6 also classify themselves as particular, within the modelled faults. This is emphasised by the fact that F3-6 probably outlines upward, left to right, gneiss (k = 0.00098 cgs) / micaschists (k = 0.00654 cgs) and diorite (k = 0.01063 cgs) / metasediments (k = 0.00264 cgs) contacts. Besides, F3-7 may constitute the gneiss/migmatites boundary. Also noticeable, the F3-1 fault which probably caused the peak in the anomaly profile observed at the beginning of Line 3 (**Figure 3.2-11a**).

The geological section of Line 3 (**Figure 3.2-11b**) advocates that the faults F3-6, F3-7, F3-8 and F3-9 are probable relays of a unique fault which separates two main units. The left unit (relative to the imaginary fault trace made by merging the aforementioned faults) globally has hypothetical high susceptibility magmatic and/or mafic formations, while the right unit encompasses probable low susceptibility detrital metasediments. Therefore, by equating the left magmatic unit to the Ntem complex (CC) and the right unit to NEFB formations, this fault would represent the CC/NEFB limit. Moreover, the zig-zag patterns of NEFB formations on the section suggests that N-S compressions (in the profile's direction) would have affected those formations.

3.2.6.4. Definition of the Ntem complex/North Equatorial Fold Belt southern limit

The NEFB has been distinguished from the Ntem complex trough the difference in the density of lineaments observed on qualitative interpretation maps (**Figures 3.2-2, 3.2-3, 3.2-5**). Indeed, the NEFB appears to be less fractured than the CC on magnetic maps. The boundary between those two area of unequal density of lineaments has been interpreted as the local CC/NEFB southern limit. Its location was defined through distance measurement from the north, along each profile (Line1, Line2 and Line3) as presented in **table 3** below.

Table 3 : Locations of the CC/NEFB southern limit. The distances are obtained from the north along profiles

Location of the CC/NEFB limit in km (west to east)			
Reference axis	Line1	Line2	Line3
Measured on map	19.24	17.87	21.42
From inversion	18.30	16.5	20.45
Difference .	0.94	1.37	0.97

In general, the three models (**Figures 3.2-9, 3.2-10** and **3.2-11**). are consistent with the existence of a low susceptibility block to the north, separated by a sharp discontinuity to a south-high susceptibility block. The high susceptibilities in the left are supposedly due to mafic terrains and low susceptibilities to detrital metasediments. This oulines an igneous complex interpreted as a portion of the CC (to the south) and a metamorphic complex equated to the NEFB (to the north), separated by sub-vertical faults probably representing the CC/NEFB limit. The location of that limit at each profile is directly measured on the geological sections and the values are

reported in **table 3**. These distances average the location of the CC/NEFB faulty southern limit around latitude N03º20' latitude (south of Mbalmayo), referred to as the Schists/Granites contact (Manguelle Dicoum et al., 1992).

3.2.7. Summary of the aeromagnetic findings

The analysis of Aeromagnetic data over the southern part of the study area (between latitude N03°30' and latitude N03°) evidenced various mafic to ultramafic deep sources (RTE and Analytic signal maps) characterised by high amplitude values. Key results are the differentiation of the Yaounde schists from the CC granitoids and the outlining of the CC/Panafrican thrust line as well. The magnetic intrusions and related lineaments beneath the Mbalmayo schists confirmed the subduction of the CC under the Panafrican belt. Various lineaments have been highlighted by the magnetic investigation. The main directions they follow are NE-SW to ENE-WSW, NW-SE to WNW-ESE and N-S. These may correspond to fracture, faults, dykes or geological contacts between major formations.

The multiple directions of faults and the folding patterns observed are evidences of a multistaged tectonic activity that affected the CC/NEFB transition zone in the ductile to brittle-ductile deformation conditions throughout Archaean, Paleo-, Meso- and Neoproterozoic periods. Further, the multiscale analysis of HGM peaks revealed that the basement of the northern part of the study area may be affected mostly by SW-NE to WSW-ENE faults, beneath the Yaounde series (micaschists and Mbalmayo schists) probably from the collapse of the basement; hence they probably shaped the basin in which the sediments that formed deposited ahead the Panafrican event. The SW-NE to WSW-ENE directions in the CC generally associated to the Panafrican orogeny in Central Africa may be related at least to the Eburnean event with Phanerozoic reactivations due to the Gondwana split and the Atlantic Ocean's formation in the Albian. The faults distribution and the regional magnetic foliation revealed NE, NW and N-S shear zones (NE and NW being dominant on a descending sorting, respectively). Also, many faults highlighted are arranged as en-echelon faults system. This tremendously enables to suggest that the Ntem complex experiences wrenches which are broadly oriented SW-NE to WSW-ENE, hence the study assumes that the faulting reactivation in the Congo Craton is in relation with the development of the Central Cameroon Shear Zone (CCSZ) and the ongoing NE collision between the African and Eurasian plates. However, the lineaments highlighted thanks to aeromagnetics need to be confirmed, and this proves to be challenging, because of the scarcity of ground controls on the southern zone. Moreover, to establish a direct link between the facts highlighted both the AMT and the magnetic results, an investigation involving Landsat-8 imagery over the entire study area has been made and the results are presented hereafter.

3.3. INTERPRETATION OF THE REMOTE SENSING DATA

In the recent years the use of satellite remote sensing to solve geological problems have gained notoriety. Indeed, it enables to outline lithology and geological structures (e.g. faults, fractures, contacts, etc). This second application will be discussed hereafter.

3.3.1. The Global view

The processing of Landsat-8 OLI images covering the study area has enable to map many lineaments. The **Figure 3.3-1** below corresponds to the map of remotely sensed lineaments above the entire area under study. This evidences a fuzzy distribution of those lineaments. However, a careful look shows that between Sangmelima (to the south) and Dzeng (to the north) the area is densely fractured. For Sangmelima belongs to the Ntem complex and Dzeng to the NEFB, the image highlights the intense tectonic activity that occurred at the northern margin of the CC. This activity (see **Figure 3.3-1**) is characterised by the multiplicity of the directions of the small lineaments (foliation trace) in general, and illustrated by the major lineaments (probable faults/fractures) which infer the structural control of the area along the NE-SW, NW-SE, N-S and E-W which would result from NW-SE to N-S, ENE-WSW, WNW-ESE, and NNE-SSW compressions. This suggests that the area underwent at least four deformation stages.

In details, **figure 3.3-1** exhibits a narrow transitional zone between Metet and Zoetele in such a way that above that three main zones can be outlined, north to south:

(i) The northern zone (zone A) extends from the northern edge of the map to nearly north of Mbalmayo. The zone is characterised by a high occurrence of lineaments turning progressively clockwise NW-SE to NNE-SSW as we go from west to east.

(ii) The central zone (Zone B), corresponds to a narrow band extending between zone A and the latitude passing through Nkout. This portion is characterised by a low density of lineaments and a noticeable highly fractured N-S break through between Metet and Zoetele. Zone A exhibits a lot of E-W trending lineaments probably the foliation trends as pertaining to the Mbalmayo schists that it can be equated to.

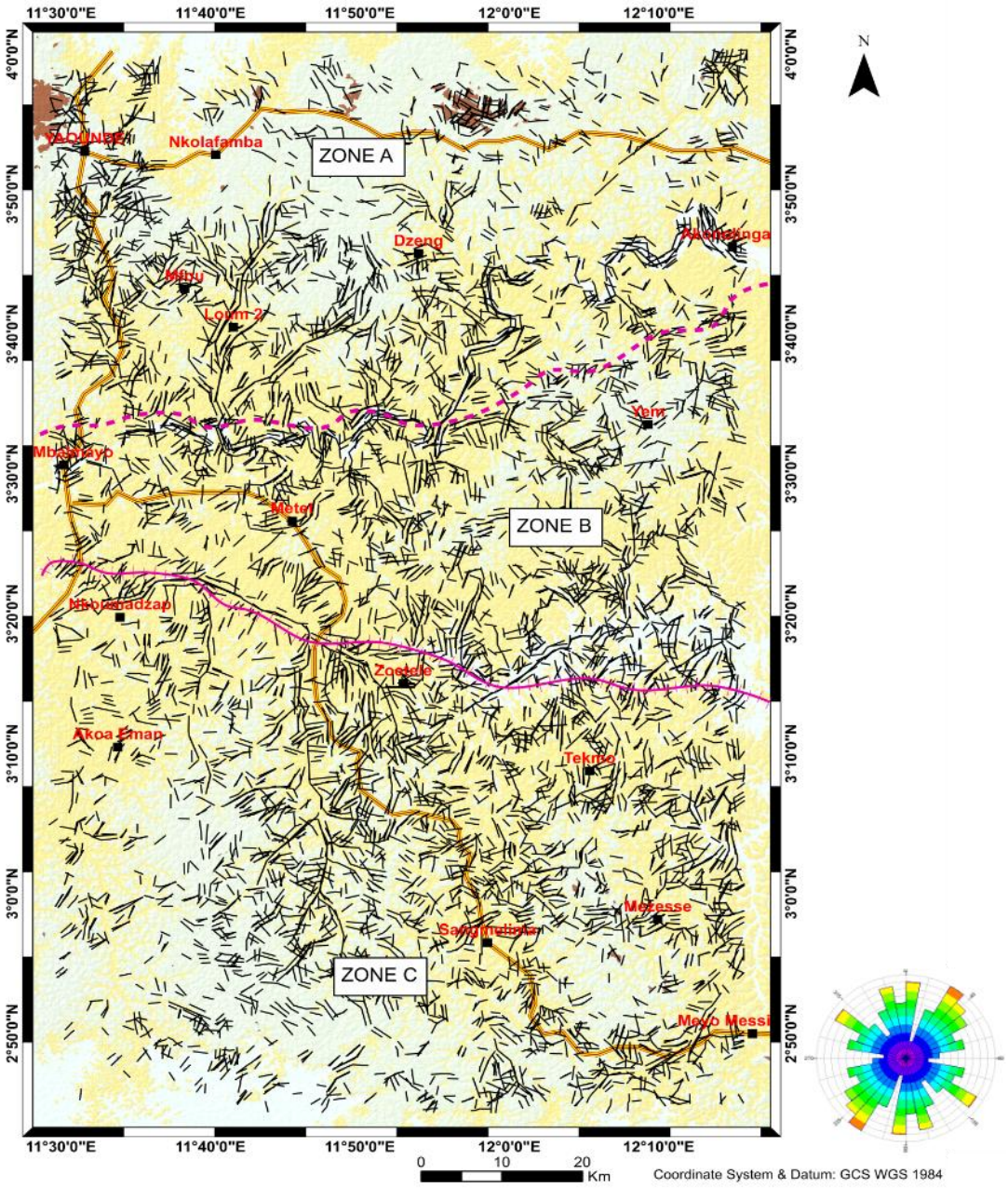

Figure 3.3-1 : Automatically extracted lineaments from Landsat 8

(iii) The southern zone (Zone C); it extends from the south-limit of zoneB to the south edge of the map. Compared to zone A, its lineaments' population is higher, probably because of the inability of its formations to undergo ductile tectonics, or maybe because they are older than the formations in Zones A and B. On that basis, this domain is interpretable as the CC domain. The diverse orientation of the foliation in this zone infers the existence herein of multiple formations.

3.3.2. Zonal analysis of interpreted Landsat faults and fractures

Clearly, the processing of Landsat 8 scenes shows that an important population of lineaments affects our area of interest. These lineaments reflect respectively foliation, folding and faulting; faults are the easiest interpretable structural features in the frame of this study. For

that purpose, a supervised classification of the outputs from **Figure 3.3-1** yielded interpreted lineaments, mostly faults and/or fractures that enable sound structural analyses.

Figure 3.3-2 : interpreted faults and fractures with respect to the zonal distribution.

The interpretation envolved (1) overlaying the previous image on the terrain model of the area; then (2) joining, when possible or reasonable, some segments to form more continuous lines. The interpreted lineaments as fractures or faults yielded a map that eases geological analyses, accordingly; following the aforesaid zonal repartition shown in **figure 3.3-2**.

3.3.2.1. The zone A

a. Quantitative analysis

The zone A covers an area limited by the northern edge of the map and a NE limit starting nearly south of Mbalmayo, and passing south of Mfou (**Figure 3.3-2**). This area is characterised by a high occurrence of lineaments corresponding to 26.75% of the total population of interpreted faults. Graphical statistics showing the distribution of lineaments considering the bearing (direction) attribute are summarised in **Figure 3.3-3** below.

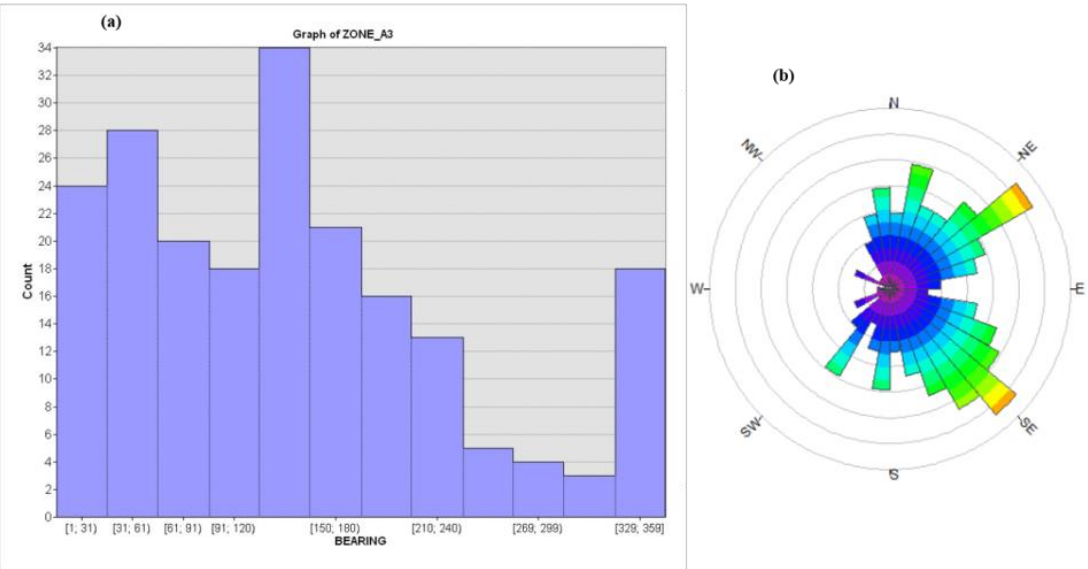

Figure 3.3-3: Graphical statistics in the Zone A; (a) Histogram (b) Rosacea of strikes.

The histogram (**Figure 3.3-3 a**) has been plotted assuming a bin amplitude of 30 degrees making a total of 12 bins; and the rosacea (**Figure 3.3-3 b**) assumed and aperture of 15º per petal. From the histogram of directions, the loosely dominant families would be N120-150º (34), N31-60º (28), N01-30º (24), N150-180º (21), N61-90º (20), N91-120º and N330-359º with 18 counts, respectively. The rosacea backs the histogram by strengthening the fact that the main directions of lineaments in zone A are NE-SW and NW-SE. A more detailed analysis by clustering the lineaments along the 8 main directions and integrating the length attribute as shown on **table 4** provided an attempt toward a more realistic description of the results illustrated by **figure 3.3-3**. Indeed, based on the decreasing number of lineaments, we have:

- The first family or group comprises lineaments oriented NE-SW. With a population of 42 lineaments (20.59% of the population in zone A), this family has a cumulative length of 229.39 km, an average length of lineaments equals to 5.46 km with a maximum and a minimum length of 14.04 km and 1.40 km, respectively.

- The second group comprises the N-S trending lineaments. They are 39, i.e. 19.12% of the total population of zone A. In terms of length, the shortest is 1.23 km and the longest is 13.63 km, while the average is 4.34 km and the cumulative length is 169.24 km.
- The third group encompasses lineaments oriented NW-SE. With 37 counts (18.14 % of the total population of zone A), this family has an average length of 4.75 km; its longest and shortest members are respectively 11.88 km and 1.24 km for a total length of 175.72 km.
- The fourth group comprises NNW-SSE lineaments. This family has 22 members (10.78 %), its less and most extended members are respectively 1.85 km and 21.73 km (the longest feature in zone A), for an average length of 5.50 km (and a total of 120.94 km).
- The ENE-WSW lineaments form the fifth group with 19 counts (9.31%), a total length of 109.11 km for an average of 5.74 km. The recorded extrema are 13.07 km and 2.16 km, respectively.
- The sixth group gathers the WNW-ESE and NNE-SSW families. They respectively have 18 (8.82 %) and 17 (8.33%) counts; their average lineaments lengths are 5.69 km and 5.71 km, respectively. Within this group, the NNE-SSW family particularly comes out with the maximum shortest length (2.40 km) of zone A.
- The last group corresponds to the E-W family. Less populated, this group particularly have a maximum and a minimum length of 15.55 km and 0.81 km for an average length of 6.32 km.

b. Qualitative analysis

The qualitative analysis of the lineaments consists in sorting the families of lineaments obtained by relevance. The classification is done by averaging the length obtained by subtracting the minimal and the maximal length from the cumulated sum of lengths in order to remove their influence in each cluster. The false average is then used to determine the influence of the group of lineaments i.e. groups are characterised as ***«major»***, ***«secondary»*** or ***«minor»;*** irrespective of their strike. These are coloured green, red and yellow, respectively in table 4. Therefore, on a decreasing order of importance, the classification yielded:

- The first class comprises the NNE-SSW, NNW-SSE, ENE-WSW and E-W families. These families have the highest false average lengths (5.44, 4.72, 5.34 and 5.30 km, respectively) compared to the false average (5.24 km) of the domain. Despite the false average criterion introduced, the NNW-SSE family is listed as it has the far most extended lineament in the domain (21.73 km). These criteria suggest that the faults and

fractures from these families are well extended in length. This enables to infer that these lineaments affect the deep subsurface and probably the basement of the northern zone of the study area; hence their classification as ***majors*** (or first order) lineaments.

- The second class gathers the NE-SW and WNW-ESE groups of lineaments. The respective average lengths in these families are 5.25 km and 5.21 km while the minimum lengths are between 1.40 km and 1.56 km, suggesting that these faults probably affect the area moderately; thus we propose them to be considered as secondary lineaments.
- The third class corresponding to ***minor*** or third order lineaments, includes the N-S and NW-SE families because of their lowest average length values.

Table 4 : Clustering of fractures in zone A along the 8 main geographical directions. The colours green, red and yellow denote the major, secondary and minor classes of lineaments, respectively

	N-S	NNE-SSW	NE-SW	ENE-WSW	E-W	WNW-ESE	NW-SE	NNW-SSE	Zone A
Counts	39	17	42	19	10	18	37	22	**204**
Sum	169.24	100.50	229.39	109.11	63.24	102.45	175.72	120.94	**1070.57**
Max	13.63	13.48	14.04	13.07	15.55	13.91	11.88	21.73	**21.73**
Min	1.23	2.40	1.40	2.16	0.81	1.56	1.24	1.85	**0.81**
Aver	4.34	5.91	5.46	5.74	6.32	5.69	4.75	5.50	**5.46**
%	19.12	8.33	20.59	9.31	4.90	8.82	18.14	10.78	**100.00**
False Av.	4.15	5.44	5.25	5.34	5.30	5.21	4.55	4.72	**5.24**

Summarily, 204 faults and /or fractures have been identified in zone A with lengths varying from 0.81 to 21.73 km, for a cumulated length of 1070.57 km. Though these fractures follow many directions, the major fractures are ENE-WSW to E-W. Their relationship with the intermediate and minor structures is not discussed. However, average length (5.46 km) indicates that they are globally lengthy thus, they should yield signatures that cannot be ignored or constrained to simple topographic variations. This suggests that they are deep structures affecting the basement, as it is somewhat the case in the NEFB.

3.3.2.2. The zone B

The zone B is outlined as shown on **Figure 3.3-2**. In comparison with zone A, this area is densely fractured but its features mostly occur in the west side of the domain i.e. from Mbalmayo to Metet.

a. Quantitative analysis

Zone B possesses nearly 22.34 % of the lineaments of the study area, making it a highly fractured zone, considering its surface area which forms a narrow portion between zone A and zone C. The histogram and the rosacea of the directions of the lineaments (**Figure 3.3-4 a & b**) do not evidently show the dominant directions in the area, despite the fact that the NE-SW and NW-SE tend to depart themselves from this observation.

Quantitatively from the histogram (**figure 3.3-4a**), the dominant directions are N02º-30º (30 counts), N31º-60º (28 counts), N91º-120º (23 counts), N120º-150º (27 counts) and N328º-358º (26 counts) representing respectively 15.38 %, 14.36%, 11.79%, 13.85% and 13.33% of the population of faults in zone B. For the histogram bin is wide (30º) causing overlaps of groups of directions, the clustering of faults along standard directions would permit a more reliable examination of these distribution.

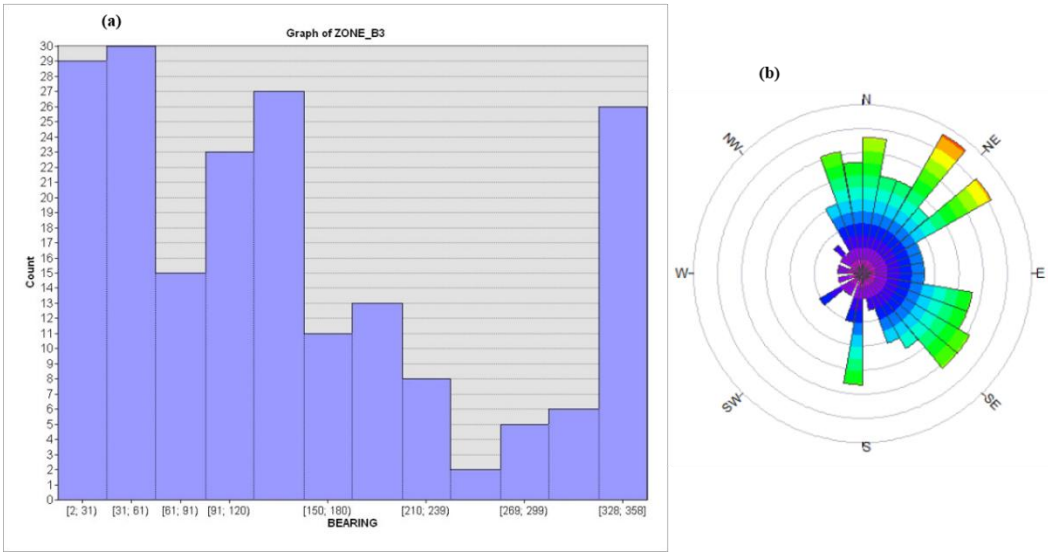

Figure 3.3-4: Graphical statistics in the Zone B; (a) Histogram (b) Rosacea strikes.

To come out with a sound geological significance, the lineaments of zone B have been clustered along the 8 main directions of a rosacea. From the clustering of the lineaments respective to their directions, one can distinguish with the decrease in the population (**table 5**):

- The first group is represented by N-S faults: with 23.59% of the total population, it has an average length of 4.02 km and the highest cumulative length (184.74), but records also the shortest lineament (0.96 km) of zone B.
- The NE-SW family constitutes the second group with 20.51 % of the total population of zone B and a cumulative length of 178.57 km; it shows up with a mean length of 4.46 km that makes it the third family with most extended lineaments.
- The NW-SE family, counted 3rd (17.44%) among the most populated group of lineaments, its mean lineament's length (3.94 km) infers its reduced significance despite the recorded cumulative length of 133.83 km.
- The fouth group comprises the E-W (9.74%), WNW-ESE (8.21%) and NNW-SSE (8.21%) families; these families have low cumulative lengths and the lowest average

length, in the exception of the WNW-ESE which have a mean length of 5.02 km (this family seems to have a geological relevance).

- The fifth group is represented by the NNE-SSW family. This family represents 7.18% of the total population and has the longest fracture (15.66 km), the highest average length (5.25 km) and the highest minimum length (2.25 km) of zone B, making it very important.
- The ENE-WSW family. This family is the less populated group of zone B (5.13 %) but possess an average length (3.72 km) of features that makes it interesting.

Table 5 : Clustering of fractures in zone B along the 8 main geographical directions. The colours green, red and yellow denote the major, secondary and minor classes of lineaments, respectively

	N-S	NNE-SSW	NE-SW	ENE-WSW	E-W	WNW-ESE	NW-SE	NNW-SSE	ZONE B
Counts	46	14	40	10	19	16	34	16	**195**
Sum	184.74	73.55	178.57	37.18	62.33	80.25	133.83	54.88	**805.32**
Max	13.14	15.66	15.39	6.15	14.78	12.13	9.10	5.54	**15.66**
Min	0.96	2.25	1.48	2.16	1.08	1.68	1.13	1.10	**0.96**
Aver	4.02	5.25	4.46	3.72	3.28	5.01	3.94	3.43	**4.14**
%	23.59	7.18	20.51	5.13	9.74	8.21	17.44	8.21	**100.00**
False Av.	3.88	4.72	4.18	3.89	2.64	4.54	3.78	3.29	**4.15**

b. Qualitative analysis

The qualitative analysis approach consisted in inferring the importance of families of faults based on the length attribute instead of the direction. This assumes that the high population along a direction does not make that direction necessarily more important. Removing the influence of the minimum and maximum length of each bin enabled the classification of families of faults in a ***major-secondary-minor*** scheme (table 5). This classification yields:

- The class of ***major*** lineaments: it embraces family directions NNE-SSW, NE-SW and WNW-ESE which possess highest *false mean* lengths (4.72, 4.18 and 4.54 km, respectively) in comparison with the domain's average (4.15 km). These families also contain almost all the longest lineaments of the zone B. Major lineaments are assumed to affect the middle-deep to the deep subsurface or basement. In this category, the NNE-SSW to NE-SW features are particularly interesting as they design a broad SW-NE channel in zone B, corresponding to a weakness zone beneath the schists.
- The ENE-WSW, NW-SE and N-S families whose respective false mean lengths are 3.89 km, 3.78 km and 3.88 km form the cluster of ***secondary*** lineaments.
- Finally, the lineaments of the NNW-SSE and E-W families will be considered as ***minor*** in regard to their lower false average lengths, 3.29 km and 2.64 km, respectively.

Summarily, the zone B is affected by lineaments of various lengths and directions. The lengths vary from 0.96 km to 15.66 km, with cumulative and average lengths of 805.32 km and 4.14 km, respectively. The classification of the NNE-SSW, SW-NE and ESE-WNW lineaments as major lineaments is consistent with the maps shown on **Figure 3.3-2** and **Figure 3.3-1** which conspicuously highlight that these directions form a NE channel within which lineaments of various directions occur (second and third order lineaments). This channel would affect the basement of the Mbalmayo series which lies transverse to its direction. The average length shows that faults in zone B are shorter compared to zone A (5.46 km) and zone C (4.42 km) but the density of faults and the scattering of their directions infer that these milieus are different.

3.3.2.3. The zone C

The zone C spans from the latitudes of Nkout and Zoetele to the bottom of the study area (**Figure 3.3-2**). This area is densely fractured and records the highest number (438) of faults in comparison with zones A and B.

a. Quantitative analysis

The quantitative analysis of the lineaments from zone C is based on the interpretation of the rose diagram and the histogram of the directions shown on **Figure 3.3-5.** Indeed, the rosacea

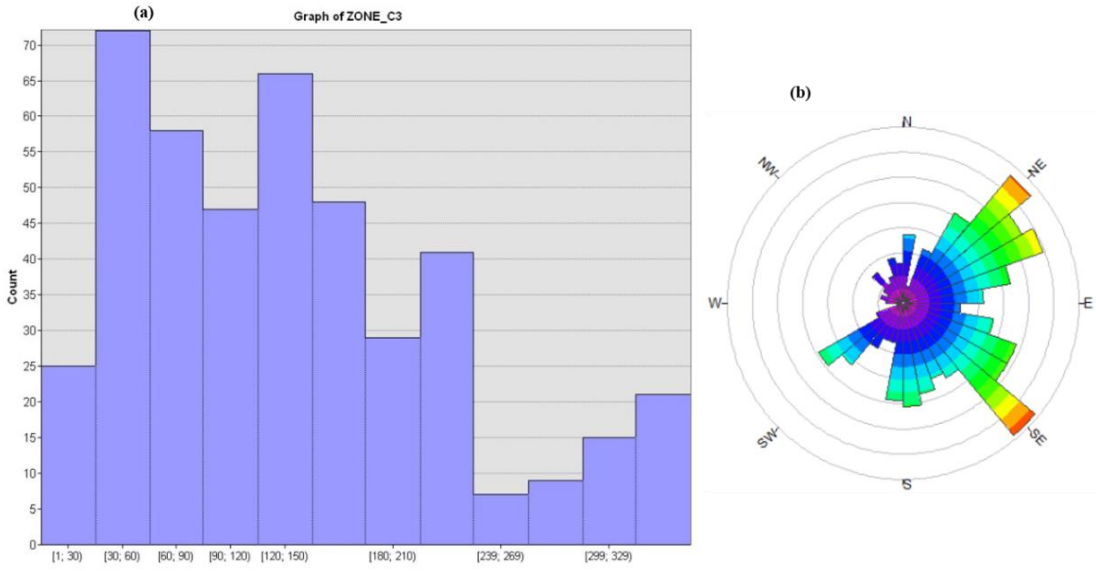

Figure 3.3-5 : Graphical statistics in the Zone C; (a) Histogram (b) Rosacea of strikes.

(**Figure 3.3-5b**) shows the predominance of NE-SW, NW-SE and N-S, alongside with various minor intermediate directions. The information from the rose diagram are complemented by the histogram of the directions of lineaments (**Figure 3.3-5a**), which brings more details and some figures. Indeed, the histogram's bins quantitatively distribute trends within 12 bins of 30º width. By relevance, the dominant direction fans are: N31º-60º (72 counts), N120º-150º (66 counts),

N61º-90º (59 counts), N150º-180º (47 counts), N91º-120º (46 counts) and N210º-239º (41 coounts). Alongside these dominant fans, the N180º-210º (29 counts), N01º-30º (25 counts) and N330º-359º (21 counts) are somewhat perceptible.

In addition to the frequency analyses above, the consideration of the length attribute and clustering of lineaments in zone C along the 8 main directions (table 6) yielded, by relevance:

- The NE-SW group of lineaments. Being the most represented in zone C with population percentage of 25.57% (112 counts), the length in this family varies between 0.56 km and 17.64 km (5.34 km average length) for a sum of 598.26 km. The predominance of this family is in accordance with analyses on other zones where it generally counts amongst the most populated families.
- The NW-SE family represents the second group (18.49 %) with 81 members. It is characterised by a mean length of 4.60 km, a cumulative length of 372.99 km distributed between features extended from 1.10 km and 14.64 km.
- The N-S family, with a total population of 75 (17.12% of total population), it represents the third group with faults lengths ranging between 0.70 km and 13.04 km making a sum of 272.85 km. Its mean length (3.64 km) is however the lowest of the south domain.
- The E-W family, represents the fourth group of lineaments with a population of 46 out of 438. This family has an average length of 3.95 km (the second lowest of the domain), with features extending from 1.20 km to 10.11 km for a cumulative sum of 181.65 km.
- The fifth group comprises the ENE-WSW and WNW-ESE families which make respectively 8.90 and 8.22 % of faults for respective cumulated length of 158.51 and 154.00 km. Their average lengths (4.06 and 4.28 km, respectively) show their elements are globally lengthy despite the lower ranking.
- The sixth group represents 6.85 % of the total population and corresponds to the NNW-SSE faults. The features in this family are particularly long (average length is 4.50 km) and the group records the longest measured fault of the domain (18.53 km); this may infer a sound geological relevance to the NNW-SSE family in zone C.
- The seventh group encompasses the NNE-SSW family which makes 4.34 % of the total population; its mean length (4.98 km) combined with its highest minimum length (1.90 km) of zone C assume its faults are amongst the longest. This infers that they are also significant, despite their small population compared to the other families.

Table 6 : Clustering of fractures in zone C along the 8 main geographical directions. The colours green, red and yellow denote the major, secondary and minor classes of lineaments, respectively

	N-S	NNE-SSW	NE-SW	ENE-WSW	E-W	WNW-ESE	NW-SE	NNW-SSE	ZONE C
Counts	75	19	112	39	46	36	81	30	**438**
Sum	272.85	94.72	598.26	158.51	181.65	154.00	372.99	135.12	**1968.01**
Max	13.04	12.38	17.64	16.64	10.11	15.62	14.54	18.53	**18.53**
Min	0.70	1.90	0.56	1.06	1.20	1.35	1.10	1.18	**0.56**
Aver	3.64	4.98	5.34	4.06	3.95	4.28	4.60	4.50	**4.42**
%	17.12	4.34	25.57	8.90	10.50	8.22	18.49	6.85	**100.00**
False Av.	3.45	4.23	5.18	3.61	3.70	3.80	4.41	3.84	**4.45**

b. Qualitative analysis

The qualitative analyses, following the principles established in the previous subsections enabled to assume the geological importance of the clustered families as colourly highlighted on **table 6**. The qualitative analysis revealed:

- The **major** or first order lineaments. These are families whose mean lengths are greater than the mean length of zone C (4.45 km) when influence of extreme features has been removed. This criterion favours the NE-SW and NW-SE families in zone C, according to their respective mean lengths (5.18 km and 4.41 km).
- The class of **secondary** lineaments includes the WNW-ESE, NNW-SSE and NNE-SSW families. Their respective false mean lengths (3.80 km, 3.84 km and 4.23 km) show they very important although they constitute the group of the less represented lineaments in the domain (lowest counts in table 6).
- Finally, the N-S, E-W and ENE-WSW form the **minor** or third order lineaments category albeit they are more populated than the families ranked as secondary lineaments. This is because they have the shortest lineaments false average albeit.

In brief, quantitatively, the zone C is affected by 438 lineaments whose cumulative length is 1968.01 km for a mean length of 4.42 km, assuming that globally theses lineaments have great linear extension. The azimuth distribution has revealed that the most represented features occur decreasingly, along the NW-SE, NE-SW, N-S, WNW-ESE, ENE-WSW and NNW-SSE directions; out ot which the NW-SE, NE-SW families revealed to corresponds to major lineaments while the WNW-ESE and NNW-SSE fall st secondary lineaments. The major lineaments are those who affect the deep subsurface and/or the basement and the proposed trends are consistend with the local geology.

3.3.3. Synthesis of the remote sensing survey

Globally, remote sensing made it possible to highlight various lineaments chiefly interpreted as faults or fractures (863). Theses lineaments make a cumulative length of 3843.90 km, a minimum of 0.56 km (in zone C) and a maximum of 21.73 km (in zone A) for an average length of 4.67 km. However, figures 3.3-1 and 3.3-2 show that those lineaments are irregularly distributed in the study area. Indeed, the study area has been subdivided into three zones, southward, zone B is the less populated, with only 22.34% % of the population of lineaments while zones A and C represent respectively 26.73% and 51.86%. Moreover, according to the mean length of the study area (4.67 km), the lineaments of zone A are longer (5.46 km) compared to those of the other zones (in zone B they are shortest, with 4.14 km mean length, while zone C exhibits 4.42 km average length). The geology of the study area could explain these differences.

Firstly, concerning the irregular distribution and density of the lineaments in the study, the differences percentages observed are linkable to the difference in lithology. Indeed, given some stress conditions, the rock materials react differently if their rheology differs. In line with that, the interpreted Landsat lineaments would portray an evolution from competent (zone A) to incompetent systems (zone C), north to south; these units being separated by a highly incompetent (zone B) environment. Therefore, these three zones would represent three different lithology groups. Particularly, the high density of fracturing in zone B is symptomatic to the fact that this zone is intermediary (transitional) and experienced a lot of stress, probably related to the compressions between zone A and zone C. Therefore, the study positions the zone C on the Congo Craton referred to as the Ntem Complex. In the same way, the zone A seems to be made up of very compact rocks, probably gneisses and micaschists. Then, high fracturing in zone B coupled with the small extend of fractures (mean length 4.14 km) suggests that the rocks therein are not very compact as those from other two zones – schists would be good soft rocks specimens here. The gneisses, micaschists and schists of the study area belong to the Yaounde group, hence zone A and zone B would belong to the NEFB. The limit between zone B and zone C would therefore represent the southern limit between the NEFB and the CC in the study area.

Apparently, the major lineaments from in the three outlined zones have different trends. Illustratively analyses revealed that in the zone A, they are NNW-SSE and NNE-SSW to ESE-WNW; in zone B, they are WNW-ESE and NNE-SSW to NE-SW, while they are NE-SW and NW-SE in zone C. Obviously, these zones have two by two, a common direction followed by these major lineaments; e.g. the common direction for zone A and zone B is NNE-SSW, whereas the NE-SW direction commonly appears in zone B and zone C. These major lineaments form

throughout the study area, a broad NE-SW network of en echelon faults which could constitute a pre-Panafrican major weakness zone affecting both the CC and the NEFB basement. This channel of faults would had formed during at least the Eburnean event at the northern margin of the CC, then the shallow features (corresponding to short faults) would reflect the syn- and post-panafrican events. The aforementioned channel of faults hence forms a NE strike-slips complex within which the displacements occur along WNW-ESE, NW-SE and WNW-ESE to NNW-SSE directions respectively in zone A, zone B and zone C. The variations in length and in directions displayed by the secondary and minor features may explain how this NE-SW channel turned from dextral to sinistral. In any case it is proposed that post-panafrican tectonics are responsible of the sinistral orientation observed. But, the existence the WNW-ESE to NNW-SSE major lineaments is a matter of debate.

The multiple of directions of the mapped major lineaments infer a polyphase deformation in the study area. Each stage of deformations is probably alternating compressions and extensions as suggested by the AMT and the aeromagnetic investigationsin previously sections.

3.4. DISCUSSION AND IMPLICATIONS

3.4.1. Discussions

3.4.1.1. Validity of the data, methodology and results

Poor data validity leads to inconsistent results. Basically, the consistency of AMT results lays on several factors: (1) the sensor (Stratagem EH4) uses a built-in algorithm based on the Bostick approach which permits to minimize the uncertainty on the resistivity value and allows the quality control of a good sounding by assuming that the apparent resistivity is inevitably positive. This quality control is assessed through the coherency among signals; herein, soundings with a good coherency have been recorded to obtain a good dataset to ensure reliable results. (2) Data were collected far away from human activity and infrastructure; and deep attention was paid to component impedances correlation and signals' correlation to reduce noise. Besides, either separately or concurrently, the aeromagnetic and the remote sensing methods are used worldwide in geological mapping, as shown by the literature (see chapter two). This entirely legitimates the use of these methods by this study. Whereas it is usual to combine methods over a same study area, the approach is somehow new as it juxtaposes two different methods on two different areas then, integrates a third one to bridge the obtained results.

3.4.1.2. Discussion of AMT results

The study area is north-bounded by latitude N04°, known as the mean geographical location of the CC/NEFB suture by previous geophysical studies (Tadjou et al., 2008; Ndougsa-Mbarga et al., 2010; Shandini et al., 2010; Basseka et al., 2011; references therein) expressed as an E-W major discontinuity. Hence the CC subducts from 50 to ~100 km beneath the NEFB, placing the study area in the transition zone between the NEFB and the CC. This is strengthened by resistivity models showing that the subsurface in the area is made up of mixtures of both Pan African (conductive) and CC (resistive) materials, in agreement with Meying et al. (2013) in a close area eastward (Ayos-Nguelemendouka). However, AMT analysis fails at detecting events coeval to the CC/NEFB limit (E-W faults) regarding the geoelectrical model defined by Tadjou et al. (2008), model in which the CC is a resistive block in the south and the NEFB is a conductive block to the north. The study has highlighted folding patterns within the Yaoundé-Nkolafamba subsurface. The folding system occurs along profiles strike i.e. they locally highlight NW-SE to N-S compressional movements of the crust's pieces. This result is consistent with some previous nearby AMT investigations (Ndougsa-Mbarga et al., 2010; Meying et al., 2013) which highlighted folding at the scale of the Yaoundé series. Amongst the major findings of the current study is the highlight of geoelectrical shallow discontinuities.

The AMT highlighted discontinuities have been interpreted as faults and fractures with directions spanning from SW-NE to WSW-ENE, in respect with the profiles azimuth (which is NW-SE). These faults may constitute shallow local expressions of the deep faults (along the same directions) evidenced both by Shandini et al. (2011) and Shandini and Tadjou (2012), using gravity method over a study area incorporating the current area (from nearly N02° to N05° latitudes and from E11° to 13° longitudes). The aforesaid NE-SW to ENE-WSW events form a NE trending structural lineament correlated to the NE secondary tectonic line highlighted by Meying et al. (2013) east of the study area, in the Abong-Mbang region, and linkable to the setup of the Central Cameroon Shear Zone (CCSZ) at a regional scale. The aforesaid NE tectonic lineament is assumed to be a strike-slip fault system. The statement is in agreement with early geoelectrical studies. Indeed, the MT study by Mbom-Abane (1997) proves the existence of E-W and NE-SW mainly oriented wrench fault sets: the first one extends as far as to the Abong-Mbang area, east of Ayos, and the second one runs parallel to the trend of the Trans-African strike-slips; the isoresistivity maps of the Akonolinga/Abong-Mbang area indicate E-W and NE-SW wrench faults (Njingti-Nfor et al., 2001).

In addition, the study images some uplifts and collapses of the basement in the Yaoundé-Nkolafamba area. Considering the highlighted faults that exhibit vertical to subvertical dips, we infer the subsurface topography as designed by grabens or basins and uplifts or horsts. Since sounding profiles are NW-SE oriented and according to their areal coverage, the basin and horst-likes subsurface structures are locally elongated in the SW-NE direction; in a broader way, gravity studies (Shandini et al., 2010, 2011; Basseka et al., 2011; Shandini and Tadjou, 2012) highlights same features in the same direction too and suggest they originate from the collapse of parts of the basement during the CC / NEFB collision. Also, a depth to surface conductive channel interpretable either as an intrusion or a signature of an active fault, has been highlighted. In the case of an intrusion, this result is in agreement at the local scale, with Basseka et al. (2011) who indicated the presence of granitic intrusions in the northern margin of the CC; in the case of faulting, this channel would infer horizontal movements corresponding to active wrenches or shears along the NE-SW direction, as seen by Basseka et al. (2011) despite the later did not interpret NE shears as an ongoing process. These NE shears would correspond to horizontal trans-current movements occurring in the Yaoundé series coeval to the CCSZ. While we suggest the NE tectonic lineament being correlated to the CCSZ represented nearby by the Sanaga Fault, the ongoing tectonic activity is consistent with the active seismicity along the Sanaga Fault (Ndougsa Mbarga et al., 2010).

3.4.1.3. Discussion of aeromagnetic results

The main faults orientations are WNW-ESE, W-E, NW-SE, SW-NE and WSW-ENE out of which two dominant clustered directions (SW-NE to WSW-ENE) and (WNW-ESE to NW-SE) have been outlined. These directions as well as the vertical to subvertical dips observed are consistent with those evidenced by several geophysical studies in the vicinities of the study area (Ndougsa-Mbarga et al., 2010, 2012; Basseka et al., 2011; Shandini et al., 2011; Feumoe et al., 2012; Akame et al., 2014, 2019; Assembe et al., 2016; Owona Angue et al., 2016). The calculated depth ranges locate these features in the brittle upper crust zone. This is in accordance with studies by Basseka et al. (2011) and Shandini et al. (2010, 2011) over a region that encompasses the study area. The current study emphasised a dominant WSW-ENE to SW-NE direction's fan which correlates well with the major direction outlined in the CC/NEFB transition zone and within the Ntem complex by several studies (e.g. Feumoe et al., 2012; Ndougsa-Mbarga et al., 2012; Akame et al., 2013, 2014; Assembe et al., 2016, 2019) south-east, north-east, north, east and within the investigated area.

The analyses show that the WSW-ENE to SW-NE family affects both the CC and the NEFB; this corresponds probably to pre-Neoproterozoic weakness zones which underwent

Neoproterozoic and post-Neoproterozoic reactivations and controlled deposition and metamorphism in the northern margin of the CC, in accordance with Nkoumbou et al. (2014). Specifically, the WSW-ENE fractures may correspond to a major sinistral strike-slip with conjugate sinistral WNW-ESE to NW-SE faults associated to E-W lateral wrenches due to NW-SE compressions, which affect both the CC and the NEFB domains, as shown by Ngako et al. (2003). The WSW-ENE strike-slips system hence corresponds to an extensional axis due to compressive movements (which are evidenced in geoelectrical sections) coeval to the setup of the Central Africa Rift System (Rolin, 1995) locally reprensented in Cameroon by the Centre Cameroon Shear Zone in a weakness zone set-up during the paleo- to meso-Proterozoic (Feybesse et al., 1998; Katumwehe et al., 2015). The results are particularly consistent with many geological and geophysical past or recent (Maurizot et al., 1986; Toteu et al., 1994; Tchameni, 1997; Tchameni et al., 2000; Shang et al., 2001, 2007; Lerouge et al., 2006; Olinga et al., 2010; Assembe et al., 2016, 2019; Yandjimain et al., 2017; Kankeu et al., 2017; Tchakounté Numbem et al., 2017) and on-going (Assembe et al., in preparation) studies carried out in southern Cameroon, as well as in other regions (e.g. Masterton et al., 2012; Fairhead et al., 2013; Heine et al., 2013; Kirkpatrick et al., 2013).

3.4.1.4. Cross-validation between audiomagnetotelluric, aeromagnetic and Landsat lineaments with faults and geological mapped faults

An internal cross-validation approach of the findings has been implemented by correlating methods two by two. In the northwest of the study area, it consists initially in comparing comparing AMT and Landsat 8 structures (**Figure 3.4-1**) then support these by field observations; Secondly, compare Landsat, magnetic and existing geological lineaments in the remaining sector (**Figure 3.4-2**).

a. Correlation of AMT faults with Landsat lineaments

Focusing on the northwestern portion of the study area, a map of lineaments both evidenced by the AMT and by remote sensing has been produced (**Figure 3.4-1**), in order to validate the results obtained in this sector. In addition to the enlightements from section 3.4.1.2, **figure 3.4-1** shows a strong correlation between the AMT and Landsat lineaments. The directions proposed by the AMT interpretation are due to the fact that structures are supposedly perpendicular to the traverses; but in the field, these directions are diverse as shown by the fractures observed on site in Loum 2 (Mfou), Nkolafamba, Nkometou, and Yaounde (see **table 5**) neighborhoods (Assembe et al., 2016). Both all AMT and Landsat lineaments may also have coincident directions (**Figure 3.4-1**); therefore, AMT and satellite lineaments totally correlate, hence the validation of the results in this study areas's portion.

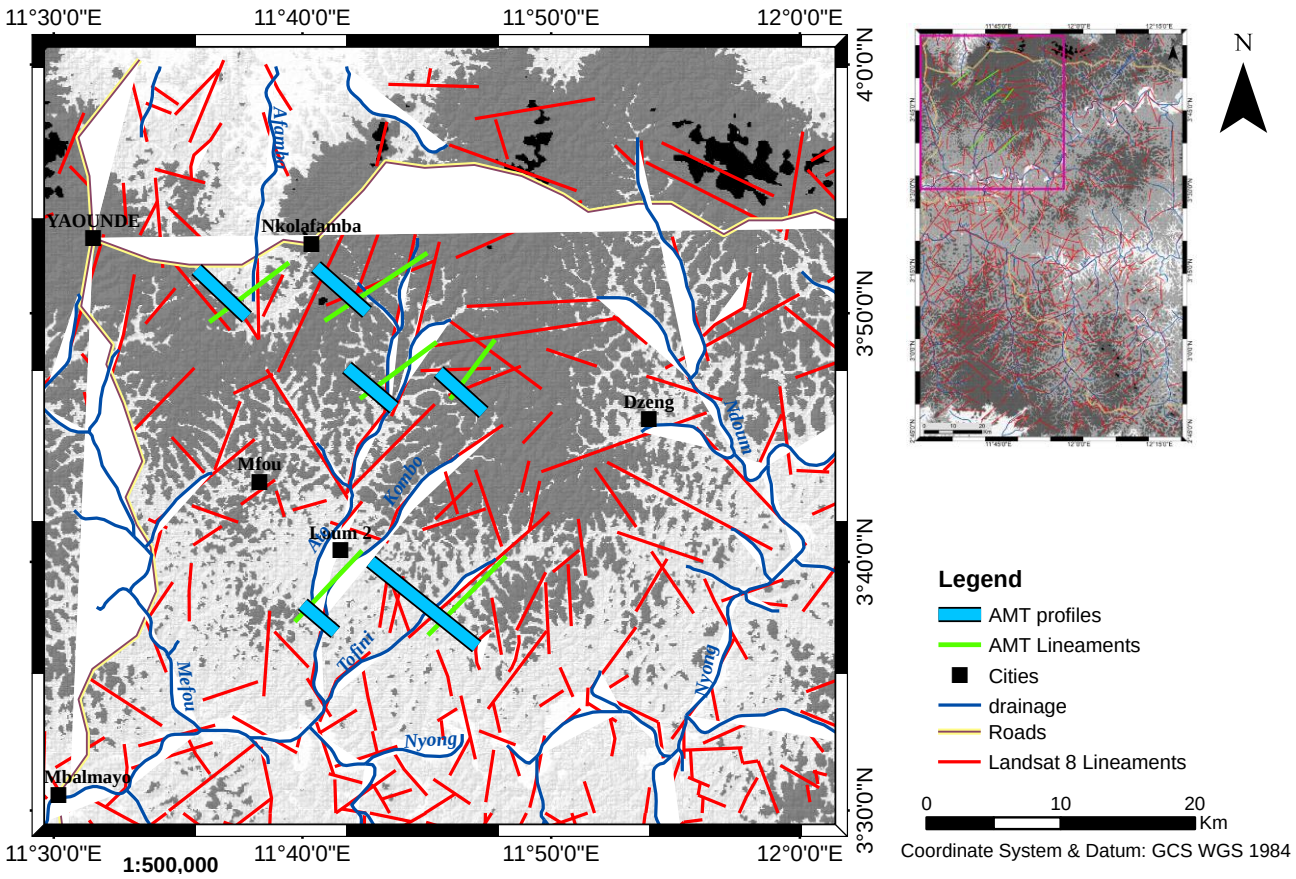

Figure 3.4-1 : Comparative map of AMT/CSAMT (green), OLI (red) lineaments with topography and drainage; the map shows the hydrography is structurally controlled.

b. Validation of aeromagnetic faults and Landsat 8 lineaments with existing faults

Due to the insufficiency of ground controls caused by the thick lateritic cover and the dense vegetation in the study area, the superimposition of magnetic onto Landsat-8 solutions helped to show the consistency of the lineaments detection in this study, as shown by the map in **Figure 3.4-2**. Therein, the almost perfect alignment of remotely sensed (red lines) and magnetic interpretation (black lines) lineaments within the portion covered simultaneously by both methods is evident. This proves the consistency of the approach used in one hand, and another, significantly validate the existence of the features highlighted by each method in the study area. Integrating the comments from the previous subsection (3.4.1.4a) cross-correlates and validate the AMT, magnetic and Landsat 8 faults. Extending this comparison to known geological structures in the region (Champetier de Ribes and Aubague, 1956; Maurizot et al., 1986) through the superimposition map of our results with previously mapped faults (**Figure 3.4-2**). **Figure 3.4-2** shows that faults from this study (black and red lines) correlate very well with faults from previously mapped by geological studies (green lines) in southern Cameroon (Champetier de Ribes and Aubague, 1956; Maurizot et al., 1986; Akame et al., 2014). The rosaceas (**Figure 3.4-**

3 (a) and **(b)**) show that the common dominant directions of the lineaments in the study area are NE-SW to ENE-WSW, NW-SE to WNW-ESE and N-S. These quantitatively correspond to

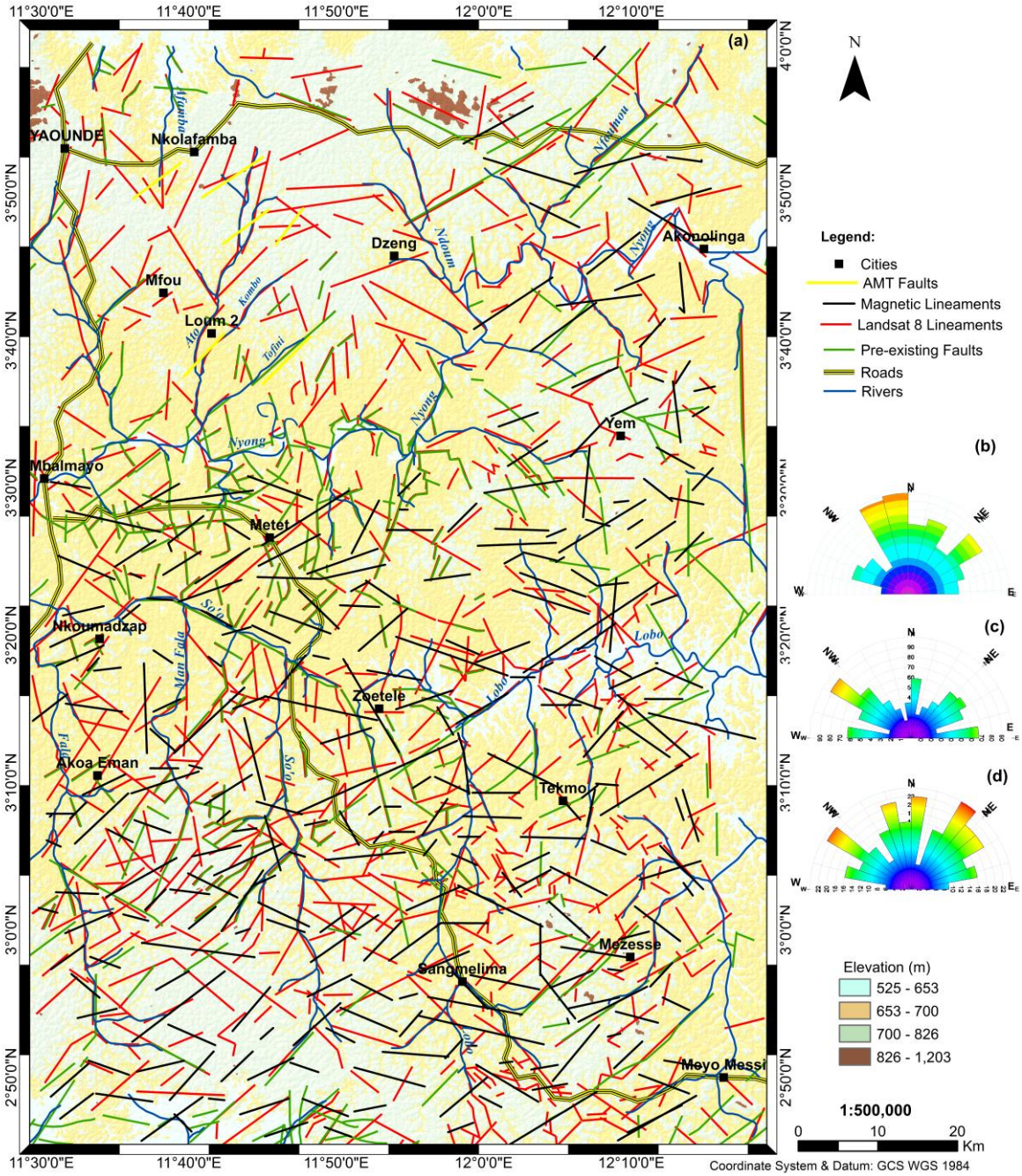

Figure 3.4-2 : Superposition of Landsat-8 (red), magnetic (black) and known (green) faults (Maurizot et al. 1986).

faults clusters N0-10 and N170, N30, N40-60, N70 and N110-140. However, the E-W direction (N80-100) is well represented in (b) and minor in (c). Similarly, the NNW-SSE direction clearly dominates in (c) whilst it seems minor in (b).

The above outlined directions from (b) and (c) are all present in the rosacea of the known lineaments (**Figure 3.4-2d**). Therein, the major trends by relevance are, NNW-SSE, N-S, NE-SW, NNE-SSW. The minor trends are ENE-WSW, WNW-ESE and E-W (poorly represented).

This proves the similar occurrence of the NNW-SSE, N-S, NNE-SSW, NW-SE, NE-SW, WNW-ESE, ENE-WSW and W-E directions. However, the NE-SW direction dominates with Landsat outputs (**Figure 3.4-3b**) contrarily to the major NNW-SSE to N-S trend shown by reference features (**Figure 3.4-3d**); maybe because of the difference in their populations. Nevertheless, the pertinent correlation amongst Landsat-8 and reference fractures validates the results.

3.4.1.5. Validation from field data

The findings from the AMT analysis are supported by some field observations from four sites where outcrops were accessible. The synthesis of the geometric parameters for 44 fractures and faults is given in table7. Among these fractures' families, the most interesting sets follow the NE-SW and ESE-WNW trends with vertical to subvertical dips. In agreement with the postulated vertical to subvertical dips from the current AMT investigation. Besides, many veins and families of fractures characterising the fourth deformation stage have been recorded. The NE-SW set correlates the faults highlighted by the AMT interpretation. The ESE-WNW family may represent faults nearly parallel to the AMT profiles. The folding and faulting underline the medium to high grade conditions experienced by the area that led to the amphibolite and the granulites facies characterized respectively, by amphibolite gneisses, and, biotite gneisses and biotite garnetiferous gneisses which are herein reported. The strength of tectonic forces occurred in the area has been recorded in the surrounding topography.

Table 7 : Attitudes of fault planes, veins and fractures recorded on the field

Structure ID	Strike and dip	Structure ID	Strike and dip	Structure ID	Strike and dip	Structure ID	Strike and dip
SITE : NKOLAFAMBA		SITE : NKOMETOU		SITE : NKOLBISSON (YAOUNDE)		SITE : LOUM 2 (MFOU)	
GEO1	N 178, 90	GEO16	WSW-ENE	GEO35	ESE-WNW	GEO29	SW-NE
GEO2	293, 75 SW	GEO17	WSW-ENE	GEO36	WSW-ENE	GEO30	SW-NE
GEO3	325, 76 SW	GEO18	SW-NE	GEO37	WSW-ENE	GEO31	E-W
GEO4	300, 70 SW	GEO19	SE-NW	GEO38	SW-NE	GEO32	WSW-ENE
GEO5	275, 90	GEO20	SE-NW	GEO39	SSE-NNW	GEO33	WSW-ENE
GEO6	209, 81 E	GEO21	ESE-WNW	GEO40	N-S	GEO34	N-S
GEO7	210, 90	GEO22	E-W	GEO41	E-W		
GEO8	263, 85 S	GEO23	N-S	GEO42	SE-NW		
GEO9	180, 90	GEO24	N-S	GEO43	ESE-WNW		
GEO10	345, 90	GEO25	SSW-NNE	GEO35	ESE-WNW		
GEO11	110, 69 SW	GEO26	E-W	GEO36	WSW-ENE		
GEO12	320, 90	GEO27	SW-NE	GEO37	WSW-ENE		
GEO13	206, 78 SE	GEO28	SSE-NNW				
GEO14	257, 85 S						
GEO15	185, 90						

The interpretation of AMT data suggests that profiles in Nkolafamba were settled on gneiss and eventually on quartzite. This fact is evidenced by the presence of gneiss formations outcrops (Photo 2c). These gneisses are of three types: clinopyroxene amphibolic gneiss, biotite

gneiss and garnetiferous biotite gneiss. The gneissic fabric presents a double boudinage (photo 2c) with E-W maximal stretch (B_1) and a N-S minimal stretch (B_2). In the Mfou area, field records confirmed that profiles were settled on migmatites (micaschists) and mica-quartzites (Photo 3); the migmatitic aspect being evidenced by the inclusion observed in the micaschist sample as shown on the photo below.

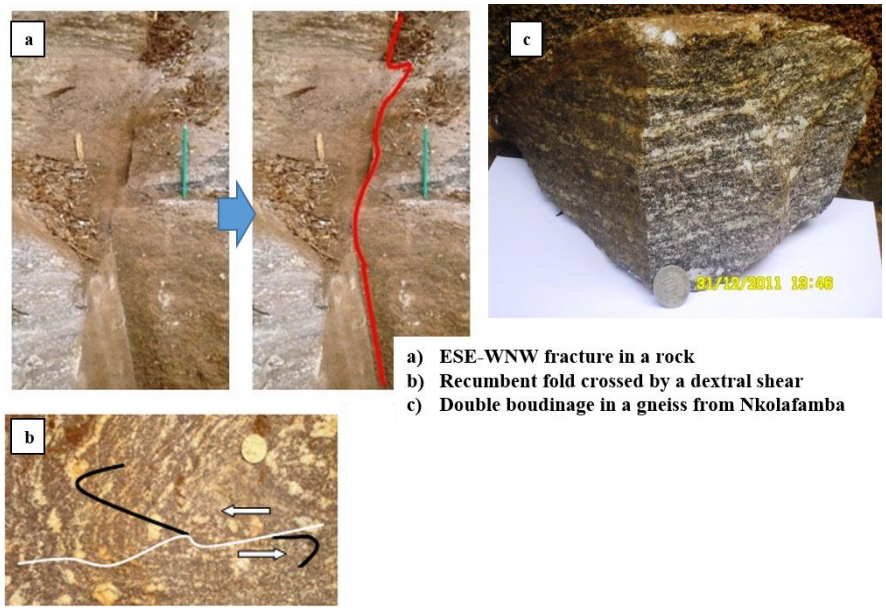

Photo 2 : Structural elements recorded in Nkolafamba (Assembe et al., 2016).

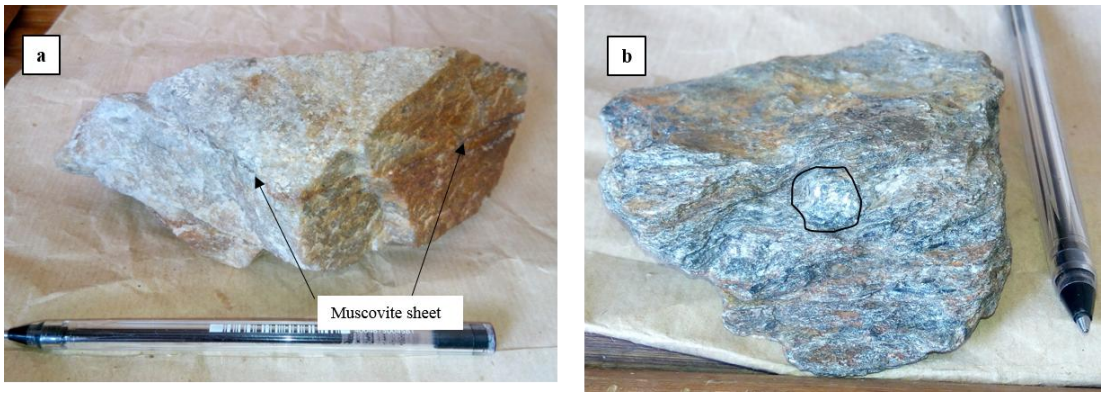

Photo 3 : Rock samples taken during field reconnaissance in Mfou. a) Quartzite with thin muscovite sheets; b) Micaschist sample with a rounded inclusion portrayed by the black circle.

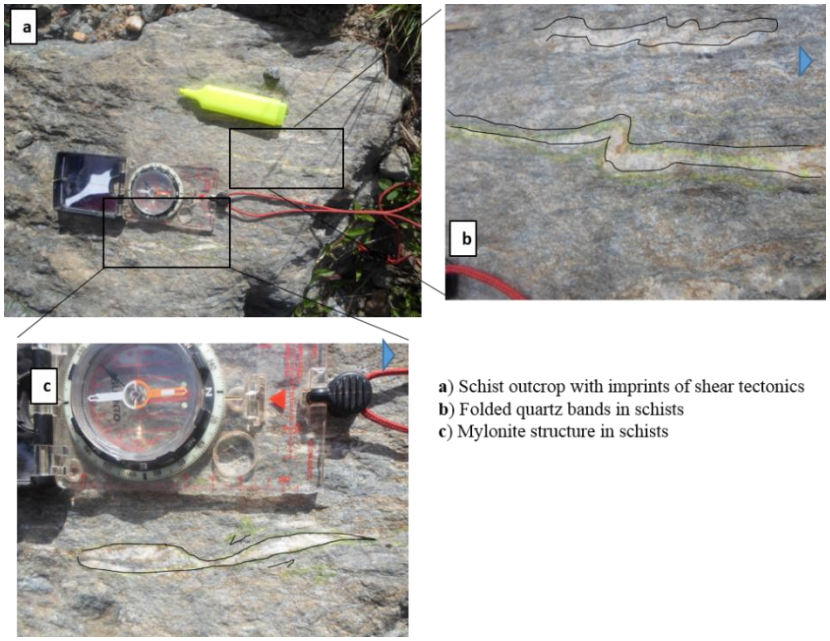

Photo 4 : Deformation elements evidenced from a schist outcrop in an abandoned quarry south of Mbalmayo.

The folding patterns, corresponding to another deformation stage, are also observed. These folds are cross-cut by many shears (Photo 2b). The double boudinage highlights extensive tectonics underlined by the NE-SW strike-slips as witnessed at the outcrop scale by shears (Photos 2 & 3) thus confirming that the area experienced many deformation stages.

3.4.2. Geologic and mining implications

3.4.2.1. Implication on the faulting kinematics

Many faults have been highlighted by the current study but a focus was not given to kinematic relationship. However, because of the difference, in nature, of the two highlighted geological sets (NEFB and CC), it is possible to portray a simple timing scheme. We base our point on the juvenile ages of NEFB formations compared to the Ntem complex. This enables to state that faulting in the Yaounde series are younger than in the Ntem complex (although some fractures and faults may be of same ages, especially those involved in the actual rifting). This is particularly in correlation with the structural control of the sedimentation in the Yaounde basin (Assembe et al., in preparation). Indeed, Assembe et al (2016) evidences various faults in the Yaounde series limiting some uplifts and sags supposedly related to extensional movements. The assumed active state of faults from the Yaounde series supports their post-collisional age.

As for the CC part, the faults correlate those from other recent geophysical studies (Shandini et al., 2010; Basseka et al., 2011; Feumoe et al., 2012; Ndougsa-Mbarga et al., 2012; Owona Angue et al., 2016). Basseka et al. (2011), Shandini et al. (2011) and Shandini and Tadjou (2012) interpreted some of the faults in the northern margin of the CC as basement collapse guides below the NEFB, confirming that faults in the CC may be older whilst they could

have been reactivated. With no references with ages and origins, considering the set-up of the Yaounde basin at the northern margin of the CC (Yonta Ngoune, 2010), it can be advanced that:

(i) The faulting history at the northern margin of the CC: oldest generation linked to the pre- and syn-Eburnean orogeny; the second generation probably related to extensional movements related to the evolvement of the Yaounde rift or basin; third generation related to the Neoproterozoic collision and reactivation during the breakup of Gondwana and the Atlantic Ocean's opening.

(ii) In the NEFB domain the faulting history is associated with the Neoproterozoic collision (West African Craton/Congo continent); and reactivations during the breakup of west Gondwana and the Atlantic Ocean's opening; then, probably the ongoing development rifting in East Africa (Fairhead et al., 2013; Heine et al., 2013; Pérez-Díaz and Eagles, 2014; Assembe et al., 2016, 2019; Akame et al., 2019; Assembe et al., in preparation).

Brittle structures in the study area are imprints of intense multistage tectonic activity characterised by alternating broad NW-SE and SW-NE compressions respectively implying SW-NE and NW-SE extensions. The extensions are witnessed by sinistral and dextral SW-NE to W-E and NW-SE to N-S shears movements (**Figure 3.2-7)** forming a major SW-NE sinistral strike-slips system affecting the area. The vertical-subvertical plunge of faults shows they controlled vertical (and horizontal) movements of the basement related to trans-transpressions in the African plate, the Ntem complex and the study area, decreasingly from regional to local scale. Thus, it seems opportune to state that the study area denotes a good continental strike-slips play. The following timing is proposed for the faulting activity in the area (Assembe et al., 2019).

1)- NE-SW faulting due to NW-SE compressions in the Paleo to Meso-Proterozoic;

2) then, the setup of N-S faults and the broad W-E fault (leading to the CC/NEFB limit), due to the detachment of the Adamawa block at the northern margin of the CC;

3) NW-SE faulting and post reactivation of NE-SW faults in response to syn- and post-Panafrican N-S to NE-SW compressions and NE-SW to ENE-WSW extensions.

The post-Panafrican events are particularly interesingt as the central domain of the African Plate has been exposed to the stress regimes related to the Atlantic Ocean opening and the actual individualisation of the Somalia Plate which questions neotectonics in the area (Assembe et al., in preparation).

3.4.2.2. Implication on the geodynamic context and evolution

The northern margin of the CC experienced many collisions and extensions related to the amalgamation from its nuclei, the formation of the Congo Continent (Sahara/CC suture, NE of the CC), the Neoproterozoic suture with the West African Craton and the breakup of Gondwana, respectively. These mainly correspond to two Precambrian deformation stages which are overprinted by Phanerozoic. The study highlightes a NE-SW strike-slip line probably associated to wrenches that affect both the NEFB and the CC; the orientations accommodate the CCSZ in the NEFB domain and the Precambriam orogenies in the CC (Assembe et al., 2016, 2019; Akame et al., 2019). The wrenches in the NEFB are normal events as mobile belts constitute weakness zones in the earth's crust (Kearey et al., 2009). Particularly, the WCARS and its local member, the CCSZ accommodate the intra-plate stress/strain regimes related to the actual deformation of the African plate (Ndougsa Mbarga et al., 2010; Weckmann, 2012; Heine et al., 2013; Kirkpatrick et al., 2013; Assembe et al., 2019).

The more questioning aspect concerns the wrenches highlighted within the Ntem complex. One possible answer could be the metacratonisation of the northern margin of the CC as described by Liégeois et al. (2013) and Abdelsalam et al. (2002) and supported by Goussi et al. (2017) who confirmed the metacratonisation of the Adamawa-Yade domain and the northern edge of the CC. But this shows the craton's margin was fit to panafrican deformation, not the mechanisms. This matter still requires the integration of diversified sources of data and limit our capabilities to propose a geodynamic model. However, further attempt to define a faulting history suggested extensional movements related to the setup of a basin in the northern margin of the CC, in accordance with Nkoumbou et al. (2014) and Tchakounté et al. (2017) who suggested that the Yaounde basin resulted from extensional processes at the north of the Congo Craton, which led to rifting, fragmentation and limited oceanisation in a Panafrican pre-collisional context. By assuming the Adamawa-Yade block equivalent to a micro-continent detached from the CC in the early Neoproterozoic. Recent studies (Nkoumbou et al., 2014; Tchakounté et al., 2017) validate geophysical interpretation of some faults beneath the NEFB as well as fragmentation and collapses of the underlying basement, probably the CC (Assembe et al., 2019 and 2016). This correlates results of Yonta Ngoune (2010), as well as the geodynamic evolution of the Ntem complex by Goussi et al. (2017).

3.4.2.3. Implications on mineral exploration

The current study highlighted many lineaments which show a good match with the drainage system. This correlation of the fractures with the drainage system open the way to groundwater flows and may infer high recharge capability of groundwater reservoirs in the study area as seen by Teikeu et al. (2016) who identified aquifers in the vicinity of Yaounde recharged by a network of faults and fractures affecting the Panafrican crystalline basement. This work generalises this result to the Yaounde-Sangmelima region (**Figure 3.4-4**).

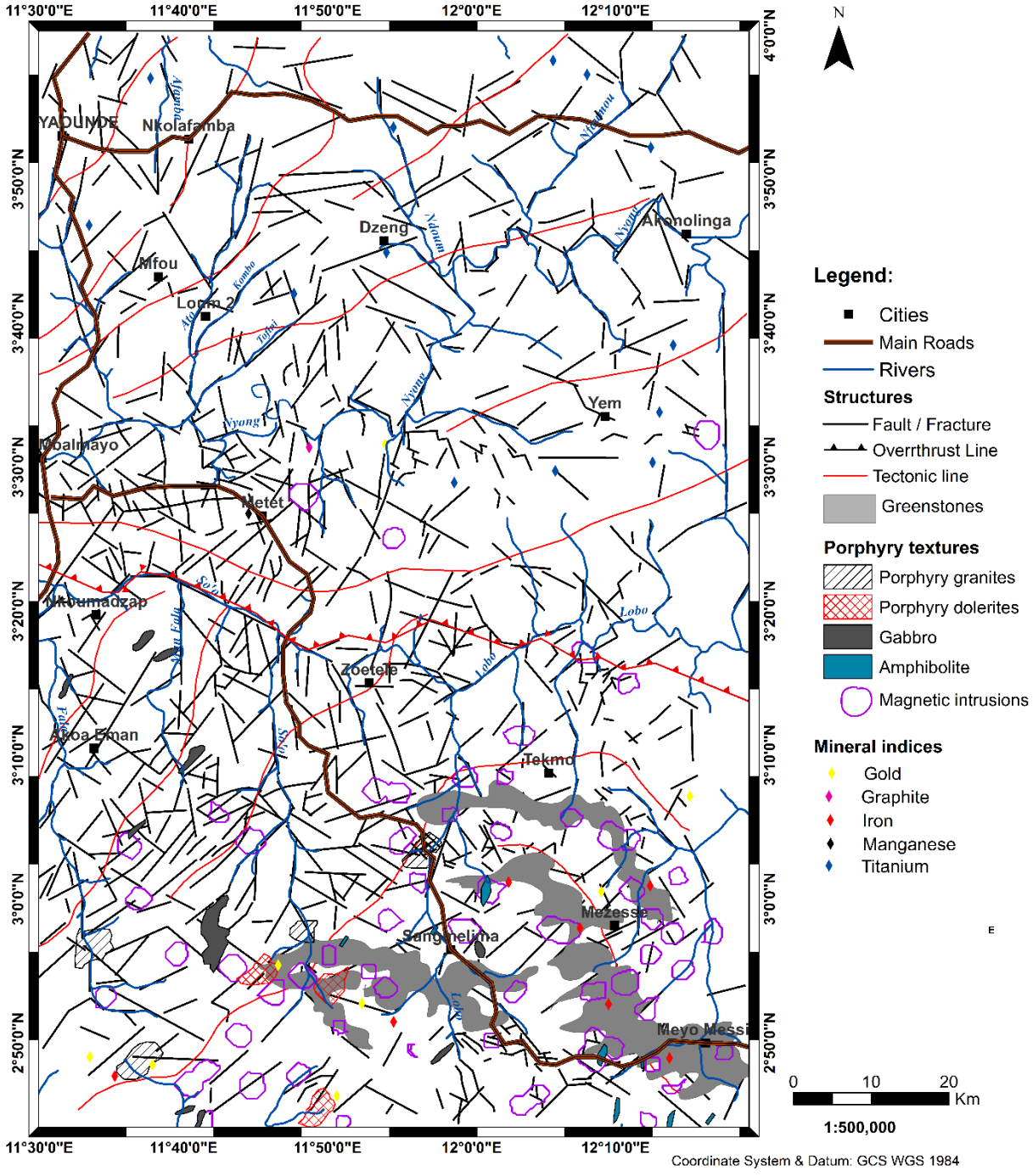

Figure 3.4-3 : Correlation between the drainage, faulting and mineral indices. The map reveals the proximity between faults and mapped intrusions and porphyry textures.

Besides, various strongly magnetic intrusions have been mapped, mostly in the Ntem complex, within the highlighted NE deformation channel affecting study area; their density prove hydrothermal processes in the Ntem complex (Assembe et al., 2020). These mafic to ultramafic intrusions are sometimes parallel, cut or squeezed by faults and fractures or lie at their junctions. Since these lineaments affect the basement, obviously they controlled fluid flows (water and magmatic melts) and later the distribution of anomalies. The ultramafic character associated to intrusions and the TTG natures (Shang et al., 2001, 2004a, 2010; Li et al., 2016) of Archaean terranes make them good to host economical mineralization (Faure, 2007; Mathieu, 2013). Indeed, the high magnetisation of the intrusions suggests that they are rich in oxide minerals generally associated to metals. Also, granodiorite TTG occur in the study area. Their Anorthosite-Mangerite-Charnokite-Granite type magma origin and, both the collisional and extensional intracratonic setting of the study area (Cawood and Hawkesworth, n.d.) could favour occurrence of IOCG, Ni and/or PGE deposits (Mathieu, 2013; Aye et al., 2017). Titanium, manganese, graphite and gold indices were recorded in the Yaounde Group (Champetier de Ribes and Aubague, 1956; Regnoult, 1986). Analyses locate these indices at the junction of fractures within schists and ectinites, along an E-W line, subparallel to the major second order shear zone and the CC/NEFB boundary. Manganese and graphite indices are located at the greenschist/garnetiferous micaschist contacts in Metet while gold and titanium are respectively in greenschist and garnetiferous micaschists. In the Ntem complex, iron and gold are the main minerals. Iron is closely linked to the greenstones belts SE of Sangmelima, where some advanced mineral exploration projects await to enter in the development stage (e.g. Nkout Iron project by Affero Mining). The outline of additional greenstones and the small gold mining artisanal workings carried out all around Sangmelima suggest that mineral exploration should be revamped in this region.

Conclusion

Investigating the NEFB/Congo Craton transition zone remains a great challenge for the geoscience community. The current study, by applying tensor-audiomagnetotellurics and aeromagnetics in two adjacent portions of the CC/NEFB transition zone has improved the geological map of southern Cameroon. The findings show both that the CC and the NEFB were affected by collisional and post-collisional deformations, related to the Gondwana breakup. Further, the highly deformed looks of the Ntem complex shows that the CC underwent various tectonic/tectono-thermal episodes; the resultant structures controlled the deposition of sediment in the Yaounde basin, influenced the Panafrican event in Central Africa and the Phanerozoic rifting that led to the Atlantic Ocean's opening and actual intra-plate stress accommodation.

GENERAL CONCLUSION AND PERSPECTIVES

1. Conclusions

Three geophysical techniques including the tensor AMT, aeromagnetic and remote sensing methods have been used to investigate nearly 12,000 km^2 in the Nkolafamba-Sangmelima area of southern Cameroon, a portion of the Central Africa Fold Belt and the Congo Craton transition zone.

1.1.Recall of the objectives and research methodology

The main research objectives are, scientific, economic and operational.

(1) The scientific objective was to contribute into the improvement of the of the geological evolution of the northern margin of the Congo Craton; the specific objective being to bring out evidences that may support the collisional model between the Panafrican belt and the Congo Craton in southern Cameroon, and ameliorate the geological information in the targeted area.
(2) The economic objective was to map new probable ore deposit features that would improve the mineral potential of the region.
(3) The operational objective was to come out with a new methodology that can enable the study of an area irregularly covered by different geophysical methods; particularly as the current study area primarily involves two adjacent zones covered by AMT and aeromagnetics.

The methodology conceived for the study consisted in respectively, firstly carrying a tensor AMT and field geology investigation (when possible) in some portions of the study area, secondly using aeromagnetics onto the uncovered portions, then overlapping the whole area by the remote sensing method (involving Landsat 8-OLI data). Cross-correlations amongst the methods, and, with existing information validate the results of the study. This methodology is proposed to overcome the scarcity of geophysical data.

1.2.Results and validations

1.2.1. Validation

The study enabled to confirm that the area has been affected by an intense tectonic activity that pertained throughout various tectonic deformation stages. Indeed:

- The interpretation of the AMT highlighted a network of hidden NE-SW strike-slip faults coeval to the CCSZ; geoelectrical sections shew graben-like topography due to basement collapses and uplifts with upward transport of deep resistive materials to

shallow depths, suggesting extensive or compressive tectonics in the Pan African Yaoundé series.

- The magnetic investigation revealed that the northern margin of the CC has been highly fractured as witnessed by the imaged vertical to subvertical faults that corroborate the vertical movements from the AMT study. These vertical to subvertical faults are mainly oriented NNW-SSE, N-S, NE-SW, NNE-SSW and E-W; and some of these form a major E-W fracture line corresponding to the CC/Panafrican southern limit located around latitude N03º20' in the area. Besides, the magnetic interpretation highlighted NE-SW and NW-SE compressions and extensions witnessed by dykes and other intrusive occurrences in some parts of the south zone suggesting that the TTGs of the Ntem complex experienced hydrothermal events.
- Both the AMT and aeromagnetic imaging highlighted folds that affected near subsurface formations both in the Panafrican and the CC domains; these folds are assumed to have been caused by the CC/Panafrican orogeny in the northern zone whereas they are assumed to be related to Archaean and/or Paleo to Mesoproterozoic orogeneses with some possible Panafrican overprints in the southern zone.
- The exploitation of Landsat 8 data highlighted many fractures which enabled to outline three differently fractured domains identified as Yaounde series, the Mbalmayo schists and the Ntem complex. This interpretation confirmed the NNW-SSE, N-S, NE-SW, NNE-SSW and E-W orientation of faulting in the whole study area but also suspects WNW-ESE sinistral movements at the northern margin of the CC.

1.2.2. Integration

The study revealed that both the NEFB and the CC are folded and affected by faults whose main directions are NNW-SSE, N-S, NE-SW, NNE-SSW (in the CC) and NE-SW to ENE-WSW and NNE-SSW (in the NEFB), though field data found the same trends represented in the CC. Folds highlighted in the NEFB testify for the CC/NEFB Neoproterozoic collision, whereas those in the CC may not, because of the difference in their respective ages. The folds in the CC are likely to be due to pre-Neoproterozoic orogeneses. The same conclusions abide for fractures (and/or faults). However, NNE-SSW to ENE-WSW fractures are related to pre-, syn, to post-PanAfrican events (transtensions and transpressions), reactivated with the ignition of the Gondwana split and alimented by the ongoing motion of the African plate toward Eurasia and the formation of the Somalia plate as well. The study defines a major NE trending weakness zone coeval to the CCSZ (linkable to the general NE-SW lineaments system consistent with the WCARS) that affects both the NEFB and the CC. The area is a major transpressive zone made

up of faults which control the vertical movements illustrated by basement collapses. Their setup is a typical example of intra-plate wrenches in a continental-continental convergence setting. The geophysical results are two by two cross-validated and they correlate both with field data and previous geosciences studies in the northern margin of the CC.

1.2.3. Summary on the structural analyses

The study revealed sets of subvertical to vertical lineaments that affected the subsurface of the study area. These structures testify that various compressional and extensional episodes affected both the study area and the entire northern margin of the CC (e.g. the CCSZ), as supported by the inferred basement uplifts and sags in Yaounde-Zoetele. Globally, the highlighted brittle features can be gathered within three (03) NE-SW, NNW-SSE and NW-SW lineaments families for an easier summary. Summarily, the structural analysis shows that (1) conspicuous NE-SW, NNW-SSE and NW-SW major lineaments (probably shear zones); and (2) tectonically related joints and/ or fault systems affect the area. The relative ages of these structures can be inferred from the cross-cutting relationships among them. Indeed, from the quick observation of the map (**Figure 0.1**), these relationships assume that the NE-SW trending shear zone was firstly emplaced, then was follow by, or was concurrent with the WNW-ESE trend. The dominant NE-SW shear movements seems to have been dextral (first order) though there have been several multi-directional episodes. This shear zone was then displaced by the NW-SE sinistral fault system (second order). The shear zones are elements of a regional shear zone characterising wrenches coeval to the CCSZ at the local scale, therefore they are assumed to be coeval to the WCARS at the regional scale. Thus, this fault system would illustrate a continental transpressive strike-slip system. An updated map of the region is given below (**Figure 0.1**).

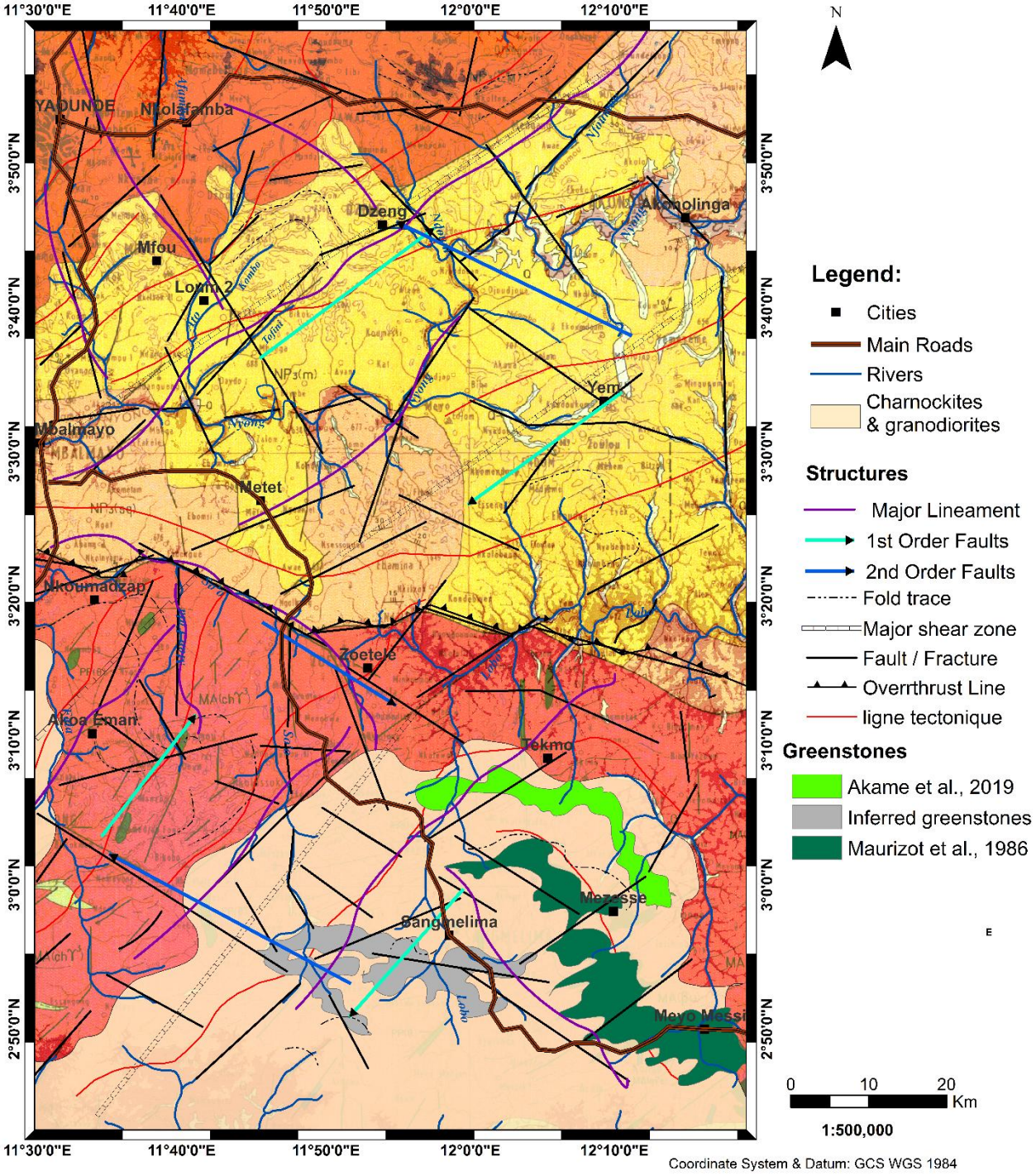

Figure 0-1 : Tectonic sketch of the Nkolafamba-Sangmelima area

2. Future trends

Despite the results from this study, explaining the geological evolution at the northern margin of the CC remains a great challenge. Therefore, additional work would help to define a better geodynamic model that emplaces the NEFB and the CC in the supercontinent-scale and outlines favourable environments for mineral resources. This needs local to regional scale integration of various geoscience data to both, produce enhanced models of the geological

history of Cameroon (and Central Africa); and improve the mineral resources valuation. So, researches ahead may consider data integration that brings together high resolution magnetic, gravity, magnetotelluric, remote sensing, drillhole and geochemical information. Particularly, future works may:

(i) Design and implement a joint inversion scheme of magnetic, gravity and magnetotelluric data.

(ii) Design an automated workflow for generating geologic models to constrain geophysical inversions.

(iii) Use high resolution multispectral remote sensing data to highlight mineral indices.

(iv) Improve the magnetic and gravity inversions by using radiogenic isotopes for both age constraints and petrogenetic understanding of the igneous rocks of the study area, with a focus on the ultramafic / intermediate rocks relationship.

(v) Investigate the regional geodynamic evolution by measuring the displacement and radon activity along the known and highlighted faults from the area; and assessing the thermal regime pertaining to the northen margin of the Congo Craton

If realised, these tasks will probably bring new perspectives to the geology of Central Africa in general, and Cameroon in particular.

REFERENCES

Abdelsalam, M.G., Liegeois, J., Stern, R.J., 2002. The Saharan Metacraton. *Journal of African Earth Sciences* **34**, 119–136.

Akame, J.M., Assembe, S.P., Zo'o Zame, P., Owona, S., Ndougsa-Mbarga, T., Azia, G.A., Mvondo-Ondoa, J., 2019. The Sangmelima granite-greenstone belts (South Cameroon): Integration of remote sensing and aeromagnetic data for structural interpretation. *The Egyptian Journal of Remote Sensing and Space Sciences* **22**, 37–47. https://doi.org/10.1016/j.ejrs.2018.11.005

Akame, J.M., Mvondo Ondoa, J., Olinga, J.B., Essono, J., Mbih, P.K., 2013. Utilisation des modèles numériques de terrain (MNT) SRTM pour la cartographie des linéaments structuraux : Application à l'Archéen de Mezesse à l'est de Sangmélima. *Geo-Eco-Trop.* **37**, 71–80.

Akame, J.M., Mvondo Ondoa, J., Teikeu Assatse, W., Owona, S., Olinga, J.B., 2014. Apport des images landsat-7 ETM+ a l'etude structurale du socle archeen de sangmelima (SUD CAMEROUN). *Revue Francaise de Photogrammetrie et de Teledetection* **206**, 15–26.

Anderson, E.D., Hitzman, M.W., Monecke, T., Bedrosian, P.A., Shah, A.K., Kelley, K.D., 2013. Geological analysis of aeromagnetic data from southwestern Alaska: Implications for exploration in the area of the Pebble Porphyry Cu-Au-Mo deposit. *Economic Geology* **108**, 421–436.

Archibald, N., Gow, P., Boschetti, F., 1999. Multiscale edge analysis of potential field data. *Exploration Geophysics* **30**, 38–44.

Assembe, S.P., Meying, A., Ndougsa-Mbarga, T., 2016. New structural facts from audio-magnetotelluric (AMT) data interpretation in the Yaoundé-Nkolafamba area (Centre Cameroon). *Journal of Indian. Geophysical. Union* **20**, 19–32.

Assembe, S.P., Ndougsa-Mbarga, T., Meying, A., Gouet, D.H., Ngoh, J.D., Mono, J.A., 2019. Contribution of Geophysics to the Understanding of the Geodynamic Activity at the Northern Margin of the Congo Craton : A Case Study from Aeromagnetic Data Interpretation Over the Metet-Zoetele Region (Southern Cameroon). *European Journal of Scientific Research* **152**, 286–303.

Assembe, S.P., Ndougsa-Mbarga, T., Enyegue A Nyam, F.M., Ngoumou, P.C., Meying, A., Gouet, D.H., Zanga Amougou, A., Ngoh, J.D., 2020. + − Evidence of Porphyry Deposits in the Ntem Complex: A Case Study from Structural and Hydrothermal Alteration Zones Mapping through Landsat-8 OLI, Aeromagnetic and Geological Data Integration in the Yaounde-Sangmelima Region (Southern Cameroon). *Advances in Remote Sensing* **9**, 53–84. https://doi.org/10.4236/ars.2020.92004

Aye, B.A., Sababa, E., Ndjigui, P., 2017. Geochemistry of S , Cu , Ni , Cr and Au-PGE in the garnet amphibolites from the Akom II area in the Archaean Congo Craton , Southern Cameroon. *Chemie Der Erde - Geochemistry* **77**, 81–93. https://doi.org/10.1016/j.chemer.2017.01.009

Bahr, K., 1988. Interpretadon of the magnetotelluric impedance tensor: regional induction and local telluric distortion. *Journal of Geophysics* **62**, 119–127.

Bailey, C., Groom, R.W., 1987. A decomposition of the magnetotelluric impedance tensor which is useful in the presence of channeling. *Geophysics* 154–156.

Baranov, V.., Naudy, H.., 1964. Numerical calculation of the formula of reduction to the

magnetic pole. *Geophysics* **29**, 67–79.

Basseka, C.A., Shandini, Y.N., Tadjou, J.M., 2011. Subsurface structural mapping using gravity data of the northern edge of the Congo craton , South Cameroon. *Geofizika* **28**, 229–245.

Bessoles, B., Lasserre, M., 1977. Le complexe de base du Cameroun. *Bull. Soc. Geol. France* **7**, 1085–1092.

Blakely, J., Simpson, R.W., 1986. Short Note Approximating edges of source bodies from magnetic or gravity anomalies. *Geophysics* **51**, 1494–1498.

Blakely, R.J., 1996. Potential theory in gravity and magnetic applications. Cambridge university press. https://doi.org/10.1017/CBO9780511549816

Boehl, J.E., Bostick, F.X., Smith, H.W., 1977. An application of the hilbert transform to the magnetotell uric method. Electrical Geophysics Research Laboratory.

Bostick, F.X.J., 1977. A simple almost exact method of MT analysis. Workshop on Electri-Cal Methods in Geothermal Exploration. Snowbird, Utah, 174–183.

Boyd, D.M., Isles, D.J., 2007. Geological Interpretation of Airborne Magnetic Surveys - 40 Years On. *In: Milkereit, B. (Ed.), Proceedings of Exploration 07: Fifth Decennial International Conference on Mineral Exploration*. 491–505.

Briggs, I.C., 1974. Machine contouring using minimum curvature. *Geophysics* **39**, 39–48. https://doi.org/10.1130/GSAT01607.1

Brodie, R.C., 2002. Airborne and magnetics. Geophysical and Remote Sensing Methods for Regolith Exploration, *CRCLEME Open File Report* **1**. 33–45.

Caby, R., Boesse, J.M., 2001. Pan-African nappe system in southwest Nigeria: The Ife- Ilesha schist belt. *Journal of African Earth Sciences* **23**, 211–225. https://doi.org/10.1130/GSAT01607.1

Cagniard, L., 1953. Basic theory of the magneto-telluric method of geophysical prospecting. 605–635.

Caldwell, T.G., Bibby, H.M., Brown, C., 2004. The magnetotelluric phase tensor. *Geophysical Journal International* **158**, 457–469. https://doi.org/10.1111/j.1365-246X.2004.02281.x

Campbell, W.C., 1997. Introduction to geomagnetic fields. Cambridge University Press. https://doi.org/10.1130/GSAT01607.1

Canfield, D.E., Poulton, S.W., Narbonne, G.M., 2007. Late-Neoproterozoic deep-ocean oxygenation and the rise of animal life. *Science* **315**, 92–95.

Cawood, P.A., Hawkesworth, C.J., n.d. Temporal relations between mineral deposits and global tectonic cycles : implications for prospectivity.

Cawood, Peter A., Kröner, A., Pisarevsky, S.A., 2006. Precambrian plate tectonics: Criteria and evidence. *GSA Today* **16**, 4–11.

Cawood, P.A., McCausland, P.J.A., Dunning, G.R., 2001. Opening Iapetus: constraints from the Laurentian margin in Newfoundland. *Geological Society of America Bulletin* **113**, 443–453.

Cawood, P.A., Nemchin, A.A., Strachan, R.A., Prave, T., Krabbendam, M., 2007. Sedimentary basin and detrital zircon record along East Laurentia and Baltica during the assembly and breakup of Rodinia. J*ournal of the Geological Society, London*, **164**, 257–275.

Cawood, P.A., Strachan, R.A., Pisarevsky, S.A., Gladkochub, D.P., Murphy, J.B., 2016. Linking collisional and accretionary orogens during Rodinia assembly and breakup: Implications for models of supercontinent cycles. *Earth and Planetary Science Letters* **449**, 118–126.

https://doi.org/10.1016/j.epsl.2016.05.049

Champetier de Ribes, G., Aubague, M., 1956. Carte geologique de reconnaissance a l'echelle 1/500000. Notice explicative sur la feuille Yaounde-Est, 40p.

Chatterjee, S., Scotese, C.R., 1999. The breakup of Gondwana and the evolution and biogeography of the Indian plate. *Pinsa* **65**, 397–425.

Chave, A.D., Jones, A.G., Mackie, R., Rodi, W., 2012. The Magnetotelluric Method. Cambridge University Press, Cambridge. https://doi.org/10.1017/CBO9781139020138

Clark, D.A., Emerson, D.W., 1991. Notes on rock magnetisation characteristics in applied geophysical studies. *Exploration Geophysics* **22**, 547–555.

Cocks, L.R.M., Torsvik, T.H., 2002. Earth geography from 500 to 400 million years ago: a faunal and palaeomagnetic review. *Journal of the Geological Society, London* **159**, 631–644.

Collignon, F., 1968. Gravimétrie de reconnaissance de la République Fédérale du Cameroun, Orstom. Paris.

Crippen, R.E., Blom, R.G., 2011. Unveiling the lithology of vegetated terrains in remotely sensed imagery. *Photogrammetric Engineering and Remote Sensing* **67**, 935–943.

Dalziel, I. W. D., 1997. Neoproterozoic–Palaeozoic geography and tectonics: Review, hypothesis and environmental speculation. *Geological Society of America Bulletin* **109**, 16–42. https://doi.org/10.1144/SP294.20

de Wit, M.J., Stankiewicz, J., Reeves, C., 2008. Restoring Pan-African-Brasiliano connections: more Gondwana control, less Trans-Atlantic corruption. *Geological Society, London, Special Publications* **294**, 399–412. https://doi.org/10.1144/SP294.20

Dirks, P.H.G.M., Bleinkinsop, T.G., Hielke, A.J., 2008. The geological evolution of Africa., *Encyclopedia of Life Support Systems*.

Dmitriev, V.I., Berdichevsky, M.N., 1979. The Fundamental Model of Magnetotelluric Sounding. *Proceedings of the IEEE*. 1034–1044.

Drury, S., 2001. Image Interpretation in Geology. Blackwell Science, 290p.

Ennih, N., Liégeois, J.P., 2008. The boundaries of the West African Craton, with a special reference to the basement of the Moroccan metacratonic Anti-Atlas belt. *Geological Society, London, Special Publications* **297**, 1–17.

Fairhead, J.D., 2009. The Mesozoic West and Central African Rift System : Qualitative Evaluation. Adapted from Oral Presentation at AAPG International Conference and Exhibition, 2008. Cape Town, 22p.

Fairhead, J.D., Cooper, G.R.J., Sander, S., 2017. Advances in Airborne Gravity and Magnetics. In: *Tschirhart, V., Thomas, M.D. (Eds.), Proceedings of Exploration 17: Sixth Decennial International Conference on Mineral Exploration*". 113–127.

Fairhead, J.D., Green, C.M., Masterton, S.M., Guiraud, R., 2013. The role that plate tectonics, inferred stress changes and stratigraphic unconformities have on the evolution of the West and Central African Rift System and the Atlantic continental margins. *Tectonophysics* **594**, 118–127. https://doi.org/10.1016/j.tecto.2013.03.021

Faure, S., 2007. Forecasting tools for mineral exploration in high grade metamorphic terrains : The Grenville parautochthonous belt, a high-potential zone.

Fernandez-Alonso, M., Tack, L., Tahon, A., De Waele, B., 2010. The Proterozoic history of the proto-Congo Craton of Central Africa.

Feumoe, A.N., Ndougsa-Mbarga, T., Manguelle-Dicoum, E., Fairhead, J.D., 2012. Delineation of tectonic lineaments using aeromagnetic data for the south-east Cameroon area. *Geofizika* **29**, 175–192.

Feumoe, S.A.N., 2014. Apport des filtrages et inversions 2D1/2 des anomalies aéromagnétiques dans la détermination des accidents tectoniques majeurs au Sud-est Cameroun. These Ddoctorat/PhD, Universite de Yaounde I, 143p.

Feybesse, J.L., Johan, V., Triboulet, C., Guerrot, C., Mayaga-Minkolo, F., Bouchot, V., Eko N'dong, J., 1998. The West Central African belt: a model of 2.5-2.0 Ma accretion and two-phase orogenic evolution. *Precambrian Research* **87**, 161–216.

Foley, S.F., Buhre, S., Jacob, D.E., 2003. Evolution of the archaean crust by delamination and shallow subduction. *Nature* **421**, 249–252.

Fumes, H., de Wit, M.J., Staudigel, H., Rosing, M., Muehlenbachs, K., 2007. A vestige of earth's oldest ophiolite. *Science* **315**, 1704–1707.

Gaina, C., Torsvik, T.H., Hinsbergen, D.J.J. Van, Medvedev, S., Werner, S.C., Labails, C., 2013. Tectonophysics The African Plate : A history of oceanic crust accretion and subduction since the Jurassic. *Tectonophysics* **604**, 4–25. https://doi.org/10.1016/j.tecto.2013.05.037

Garcia, X., Jones, A.G., 2002. Decomposition of three-dimensional magnetotelluric data. *Three-Dimensional Electromagnetics, Chapter 13*. 237–250.

Garcia, X., Jones, A.G., 2000. Advances in aspects of the application of magnetotellurics for mineral exploration. *2000 SEG Annual Meeting*. Society of Exploration Geophysicists.

Genik, G.J., 1992. Regional framework, structural and petroleum aspects of rift basins in Niger, Chad and the Central African Republic (C.A.R.). *Tectonophysics* **213**, 169-185.

Geometrics, 2000. Operation manual for Stratagem systems running IMAGEM, ver. 2.16. Geometrics Printing Press, San Jose, 16p.

Geosoft, n.d. Topics in Gridding.17p.

Goldstein, M.A., Strangway, D.W., 1975. Audio-frequency Magnetotellurics with a grounded electric dipole source. *Geophysics* **40**, 669–683. https://doi.org/10.1190/1.1440558

Goussi, J.F., Bisso, D., Abdelsalam, M.G., Atekwana, E.A., Katumwehe, A.B., Ekodeck, G.E., 2017. Geophysical imaging of metacratonizaton in the northern edge of the Congo craton in Cameroon. *Journal of African Earth Sciences* **129**, 94–107. https://doi.org/10.1016/j.jafrearsci.2016.12.010

Goussi Ngalamo, J.F., Sobh, M., Bisso, D., Abdelsalam, M.G., Atekwana, E., Ekodeck, G.E., 2018. Lithospheric structure beneath the Central Africa Orogenic Belt in Cameroon from the analysis of satellite gravity and passive seismic data. *Tectonophysics* **745**, 326–337. https://doi.org/10.1016/j.tecto.2018.08.015

Groom, R.W., Bailey, R.C., 1989. Decomposition of Magnetotelluric Impedance Tensors in the Presence of Local Three-Dimensional Galvanic Distortion. *Journal of Geophysical Research* **94**, 1913–1925.

Heine, C., Zoethout, J., Muller, R.D., 2013. Kinematics of the South Atlantic rift. Solid Earth.

Hinze, W.J., von Frese, R.R.B., Saad, A., 2013. Gravity and magnetic exploration: principles, practices and exploration. Cambridge University Press, 512p.

Houketchang Bouyo, M., 2018. Comment on "The Adamawa-Yadé domain, a piece of Archaean crust in the Neoproterozoic Central African Belt (Bafia area, Cameroon) by Tchakounté et al., 2017" (Precambrian Research 299, 210–229). *Precambrian Research* **305**, 504–507.

https://doi.org/10.1016/j.precamres.2017.12.002

Kankeu, B., Greiling, R.O., Paul, J., Ganno, S., Danguene, P.Y.E., Bassahak, J., Hell, J. V, 2017. Contrasting Pan-African structural styles at the NW margin of the Congo Shield in Cameroon. *Journal of African Earth Sciences* 1–20. https://doi.org/10.1016/j.jafrearsci.2017.06.002

Kato, Y., Nakamura, K., 2003. Origin and global tectonic significance of early Archean cherts from the Marble bar greenstone belt, Pilbara Craton, Western Australia. *Precambrian Research* **125**, 191–243.

Katumwehe, A.B., Abdelsalam, M.G., Atekwana, E.A., 2015. Tectonophysics The role of pre-existing Precambrian structures in rift evolution : The Albertine and Rhino grabens , Uganda. *Tectonophysics* 1–13. https://doi.org/10.1016/j.tecto.2015.01.022

Kearey, P., Klepeis, K.A., Vine, F.J., 2009. Global Tectonics, 3rd ed. Wiley-Blackwell.

Kirkpatrick, J.D., Bezerra, F.H.R., Shipton, K., Nascimento, A.F.D.O., Federal, U., Al, J.D.K.E., 2013. Scale-dependent influence of pre-existing basement shear zones on rift faulting : a case study from NE Brazil. *Journal of the Geological Society* **170**, 237–247. https://doi.org/10.1144/jgs2012-043.

Kröner, A., Stern, R.J., 2004. Pan-African orogeny., *Encyclopedia of Geology*. https://doi.org/10.2475/ajs.280.6.560

Lasserre, M., Soba, D., 1976. Age libérien des granodiorites et des gneiss à pyroxène du Cameroun méridional. Bulletin du Bureau de Recherches Geologiques et Minieres, France **section 2**, 17–32.

Ledo, J., Queralt, P., Marti, A., Jones, A.G., 2002. Two-dimensional interpretation of three-dimensional magnetotelluric data : an example of limitations and resolution. *Geophysical Journal International* **150**, 127–139.

Lerouge, C., Cocherie, A., Toteu, S.F., Penaye, J., Milési, J.P., Tchameni, R., Nsifa, E.N., Fanning, C.M., Deloule, E., 2006. Shrimp U–Pb zircon age evidence for Paleoproterozoic sedimentation and 2.05 Ga syntectonic plutonism in the Nyong Group, South-Western Cameroon: consequences for the Eburnean-Transamazonian belt of NE Brazil and Central Africa. *Journal of African Earth Sciences* **44**, 413–427.

Li, X.-H., Chen, Y., Li, J., Yang, C., Ling, X.-X., Tchouankoue, J.P., 2016. New isotopic constraints on age and origin of Mesoarchean charnockite, trondhjemite and amphibolite in the Ntem Complex of NW Congo Craton, southern Cameroon. *Precambrian Research*. https://doi.org/10.1016/j.precamres.2016.01.027

Li, Z.X., Bogdanova, S. V, Collins, A.S., De Waele, B., Ernst, R.E., Fitzsimons, I.C.W., Fuck, R.A., Gladkochub, D.P., Jacobs, J., Karlstrom, K.E., Lu, S., Natapov, L.M., Pease, V., Pisarevsky, S.A., Thrane, K., Vernikovsky, V., 2008. Assembly, configuration, and break-up history of Rodinia : A synthesis. *Precambrian Research* **160**, 179–210. https://doi.org/10.1016/j.precamres.2007.04.021

Liégeois, J., Abdelsalam, M.G., Ennih, N., Ouabadi, A., 2013. Metacraton : Nature , genesis and behavior. *Gondwana Research* **23**, 220–237. https://doi.org/10.1016/j.gr.2012.02.016

Liu, J.G., Mason, P.J., 2009. Essential Image Processing and GIS for Remote Sensing. Wiley-Blackwell, Oxford, 462p.

Liu, Z., Jiang, Y., Wang, G., Ni, C., Qing, L., Zhang, Q., 2015. Middle Neoproterozoic (~ 845 Ma) continental arc magmatism along the northwest side of the Jiangshan – Shaoxing suture , South China : Geochronology , geochemistry , petrogenesis and tect ... Middle

Neoproterozoic (~ 845 Ma) continental arc magmatism. *Precambrian Research* **268**, 212–226. https://doi.org/10.1016/j.precamres.2015.07.013

Lowrie, W., 2007. Fundamentals of Geophysics, 2nd ed. Cambridge University Press, New York. 393p

MacLeod, I.N., Jones, K., Dai, T.F., 1993. 3D Analitic signal in the interpretation of total magnetic field data at low magnetic latitudes. *Exploration Geophysics* **24**, 679–688.

Manguelle-Dicoum, E., 1988. Étude géophysique des structures superficielles et profondes de la région de Mbalmayo (Cameroun)., Thèse de Doctorat d'État ès Science, Universite de Yaounde, 202p .

Manguelle Dicoum, E., Bokosah, A.S., Kwende Mbanwi, T.E., 1992. Geophysical evidence for a major Precambrian schist-granite boundary in southern Cameroon. *Tectonophysics* **205**, 437–446.

Masterton, S.M., Fairhead, J.D., Mazur, S., Green, C.M., 2012. The influence of oceanic fracture zones on the segmentation and structural control of continental margins. *Extended Abstract EAGE Conference & Exhibition*. Copenhagen, 4p.

Mathieu, L., 2013. Exploration des gîtes magmatiques cuprifères dans Province de Grenville, Rappot 2012-03. Projet CONSOREM, 49p.

Maurizot, P., Abessolo, A., Feybesse, J., Johan, L., Lecomte, P., 1986. Etude et prospection minière du Sud-Ouest du Cameroun. Synthèse des travaux de 1978 à 1985, Rapport BRGM. Orleans, 274p.

Mbola-Ndzana, S.P., Mvondo-Ondoa, J., Owona, S., Sep-Nlongand, J.P., Olinga, J.B., Bilong, P., 2014. Evidence of the ~NE-SW extension in the Sa'a-Monatélé Region as in the Bafia and Yaounde groups within the Central Africa Fold belt (Cameroon): Implication for the Southern Cameroon Neoproterozoic extension. *Sciences, Technologies & Développement*, **15**, 1–15.

Mbom-Abane, S., 1997. Investigations géophysiques en bordure du craton du Congo (régiond'Abong Mbang/ Akonolinga, Cameroun) et implications structurales. Université de Yaoundé I, 180p.

Mcneice, G.W., Jones, A.G., 2001. Multisite , multifrequency tensor decomposition of magnetotelluric data. *Geophysics* **66**, 158–173.

McPhee, D.K., Bruce, A.C., Pellerin, L., 2006. Audiomagnetotelluric data and preliminary two-dimensional models from Spring, Dry Lake and Delamar Valleys, Nevada., U.S. Geological Survey, 44p.

McPhee, D.K., Chuchel, B.A., Pellerin, L., 2008. Audiomagnetotelluric data from Spring, Cave and Coyote Spring Valleys, Nevada, U.S. Geological Survey, 107p.

Meert, J.G., Libermann, B.S., 2007. The Neoproterozoic assembly of Gondwana and its relationship to the Ediacaran–Cambrian radiation. *Gondwana Research* **14**, 5–21. https://doi.org/10.1016/j.gr.2007.06.007

Meert, J.G., Libermann, B.S., 2004. A palaeomagnetic and palaeobiogeographical perspective on latest Neoproterozoic and early Cambrian tectonic events. Journal of the Geological Society 161, 477 – 487. *Journal of the Geological Society* **167**, 477–487.

Meert, J.G., Powell, C.M., 2001. Assembly and break-up of Rodinia : introduction to the special volume. *Precambrian Research* **110,** 1–8.

Meying, A., 2011. Investigations crustales profondes et superficielles par la méthode audio-

magnetotellurique (AMT) dans la région Ayos-Nguelemendouka (Cameroun). Universite de Yaoundé I, 139p.

Meying, A., Ndougsa-Mbarga, T., Gouet, D., Assembe, S.P., 2013. Near Surface Fractures Evidence from Audio-Magnetotelluric (AMT) Investigation in Ayos-Nguelemendouka Area (Eastern Cameroon). *International Journal of Geosciences* **4**, 480–493.

Meying, A., Ndougsa-Mbarga, T., Manguelle-Dicoum, E., 2009. Evidence of fractures from the image of the subsurface in the Akonolinga-Ayos area (Cameroon) by combining the Classical and the Bostick approaches in the interpretation of audio-magnetotelluric data. *Journal of Geology and Mining Research* **1**, 159–171.

Moulin, M., Aslanian, D., Unternehr, P., 2010. A new starting point for the South and Equatorial Atlantic Ocean. *Earth-Science Reviews*. https://doi.org/10.1016/j.earscirev.2009.08.001

Moyen, J., Hunen, J. Van, 2012. Short-term episodicity of Archaean plate tectonics. Geology 40, 451–454. https://doi.org/10.1130/G322894.1

Murphy, J B., Nance, R.D., 1991. Supercontinent model for the contrasting character of Late Proterozoic orogenic belts. *Geology* **19**, 469–472. https://doi.org/10.1130/0091-7613(1991)019<0469

Mvondo-Ondoa, J., Mvondo, H., Den Brok, B., 2009. Comment 'Pan-African tectonics in northwestern Cameroon : Implication for the history of western Gondwana. *Gondwana Research* **16**, 163–164. https://doi.org/10.1016/j.gr.2008.12.006

Mvondo, H., Den-Brok, S.W.J., Mvondo Ondoa, J., 2003. Evidence for symmetric extension and exhumation of the Yaoundé nappe (Pan-African fold Belt, Cameroon). *Journal of African Earth Sciences* **35**, 215–231. https://doi.org/10.1071/EG0325.Reid

Mvondo, H., Essono, J., Mvondo-Ondoa, J., Yene Atangana, J.Q., 2007a. Comment on "U-Pb dating of plutonic rocks involved in the nappe tectonic in southern Cameroon: Consequence for the Pan-African orogenic evolution of the central African fold belt" by Toteu et al. (Journal of African Earth Sciences 44 (2006) 479-493). *Journal of African Earth Sciences* **48**, 49–52. https://doi.org/10.1016/j.jafrearsci.2007.03.002

Mvondo, H., Owona, S., Mvondo-Ondoa, J., Essono, J., 2007c. Tectonic evolution of the Yaoundé segment of the Neoproterozoic Central African Orogenic Belt in southern Cameroon. *Canadian Journal of Earth Sciences* **44**, 433–444. https://doi.org/10.1139/e06-107

Mwaniki, M.W., Moeller, M.S., Schellmann, G., 2015. A comparison of Landsat 8 (OLI) and Landsat 7 (ETM +) in mapping geology and visualising lineaments : A case study of central region Kenya. *The International Archives of the Photogrammetry, Remote Sensing and Spatial Information Sciences* **XL–7**, 11–15. https://doi.org/10.5194/isprsarchives-XL-7-W3-897-2015

Nabighian, M.N., 1984. Toward a three-dimensional automatic interpretation of potential field data via generalized Hilbert transforms: fundamental relations. *Geophysics*. https://doi.org/10.1190/1.1441706

Nabighian, M.N., 1974. Additional comments on the analytic signal of two-dimensional magnetic bodies with polygonal cross-section. *Geophysics*. https://doi.org/10.1190/1.1440416

Nabighian, M.N., 1972. The analytic signal of two-dimensional magnetic bodies with polygonal cross- section: its properties and use for automated anomaly inter- pretation. *Geophysics* **37**, 507–517.

Nabighian, M.N., Grauch, V.J.S., Hansen, R.O., LaFehr, T.R., Li, Y., Peirce, J.W., Phillips, J.D., Ruder, M.E., 2005. The historical development of the magnetic method in exploration. *Geophysics* **70**, 33–61.

NASA, 2015. Fundamentals of Remote Sensing, 112p.

Ndougsa-Mbarga, T., Feumoe, A.N.S., Manguelle-Dicoum, E., Fairhead, J.D., 2012. Aeromagnetic Data Interpretation to Locate Buried Faults in South-. *Geophysica* **48**, 49–63.

Ndougsa-Mbarga, T., Meying, A., Bisso, D., Manguelle-Dicoum, E., 2010. Geological models derived from 1D and 2D audiomagnetotelluric (AMT) modeling using Bostick approach in the Messamena / Abong-Mbang area (East-Cameroon). *International Archive of Applied Sciences and Technology* **1**, 69–78.

Ndougsa Mbarga, T., Manguelle-Dicoum, E., Tabod, C.T., Mbom-Abane, S., 2003. Modelisation d'anomalies gravimétriques dans la région de Mengueme-Akonolinga (Cameroun). *Science, Technologie et Développement* **10**, 67–74.

Ndougsa Mbarga, T., Njilah, I.K., Nni, J., Nana, J., 2010. Note on the review of Earthquakes on Cameroon Territory., *Journal of Civil Protection, Ministry of Territorial Administration* **3**, 65–67.

Nedelec, A., Minyem, D., Barbey, P., 1993. High-P-High-T anatexis of Archaen tonalitic grey gneisses: The Eseka Migmatites, Cameroon. *Precambrian Research* **62**., 191–205.

Nedelec, A., Nsifa, E.N., Martin, H., 1990. Major and trace element geochemistry of the Archaean Ntem plutonic complex south Cameroon): petrogenesis and crustal evolution. *Precambrian Research* **47**, 35–50.

Nedelec, A., Nzenti, J.P., Barbey, P., 1986. Structural and metamorphic evolution of the Mbalmayo schists (Cameroon). Implications for the structure of the Pan-African mobile belt of central Africa , close to the Congo craton. *Comptes Rendus Academie Des Sciences* **303**.

Ngako, V., 1986. Evolution metamorphique et structurale de la bordure sud-ouest de la serie de Poli-segment camerounais de la chaine panafricaine. Universite de Rennes 1, 205p.

Ngako, V., Affaton, P., Njonfang, E., 2009. Reply (Pan-African tectonics in northwestern Cameroon : Implication for the history of western Gondwana). *Gondwana Research* **16**, 165–166. https://doi.org/10.1016/j.gr.2008.12.003

Ngako, V., Affaton, P., Njonfang, E., 2008. Pan-African tectonics in northwestern Cameroon : Implication for the history of western Gondwana. *Gondwana Research* **14**, 509–522. https://doi.org/10.1016/j.gr.2008.02.002

Ngako, V., Affaton, P., Nnange, J.M., Njanko, T., 2003. Pan-African tectonic evolution in central and southern Cameroon: Transpression and transtension during sinistral shear movements. *Journal of African Earth Sciences* **36**, 207–214. https://doi.org/10.1016/S0899-5362(03)00023-X

Ngako, V., Jegouzo, P., Nzenti, J.P., 1991. Le Cisaillement Centre Camerounais. Role structural et geodynamique dans l'orogenese panafricaine. *Comptes Rendus - Academie Des Sciences*, Serie II.

Ngako, V., Njonfang, E., 2018. Comment on "The Adamawa–Yade, a piece of Archaean crust in the Neoproterozoic Central African orogenic belt (Bafia area, Cameroon)" by Jacqueline Tchakounté et al. [Precambrian Research 299 (2017) 210–229]., *Precambrian Research*. https://doi.org/10.1016/j.precamres.2017.12.004

Ngako, V., Njonfang, E., 2011. Plates Amalgamation and Plate Destruction , the Western Gondwana History. *In: Dr. Closson, D. (Ed.), Tectonics* 3–36.

Ngako, V., Njonfang, E., Aka, F.T., Affaton, P., Nnange, J.M., 2006. The North-South Paleozoic to Quaternary trend of alkaline magmatism from Niger-Nigeria to Cameroon: Complex interaction between hotspots and Precambrian faults. *Journal of African Earth Sciences* **45**, 241–256. https://doi.org/10.1016/j.jafrearsci.2006.03.003

Ngnotue, T., Ganno, S., Nzenti, J.P., Schulz, B., Tchaptchet Tchato, D.I., Suh Cheo, E., 2012. Geochemistry and Geochronology of Peraluminous High-K Granitic Leucosomes of Yaound Series (Cameroon): Evidence for a Unique Pan-African Magmatism and Melting Event in North Equatorial Fold Belt. *International Journal of Geosciences* **03**, 525–548. https://doi.org/10.4236/ijg.2012.33055

Ngnotue, T., Nzenti, J.P., Barbey, P., Tchoua, F.M., 2000. The Ntui-Betamba high-grade gneisses: A northward extension of the Pan-African Yaounde gneisses in Cameroon. *Journal of African Earth Sciences* **31**, 369–381. https://doi.org/10.1016/S0899-5362(00)00094-4

Niblett, E.R., Sayn-Wittgenstein, C., 1960. Variation of electrical conductivity with depth by the magneto telluric method. *Geophyics* **25**, 998–1008.

Njingti-Nfor, Manguelle-Dicoum, E., Mbome-Abane, S., Tadjou, J.M., 2001. Major tectonic dislocations along the southern edge of Panafrican Mobile zone and the Congo Craton contact in southern region of Cameroon. *Proceedings of the Second International Conference on the Geology of Africa.* Assiut, Egypt, 799–811.

Njonfang, E., Ngako, V., Moreau, C., Affaton, P., Diot, H., 2008. Restraining bends in high temperature shear zones: The "Central Cameroon Shear Zone", Central Africa. *Journal of African Earth Sciences* **52**, 9–20. https://doi.org/10.1016/j.jafrearsci.2008.03.002

Nkoumbou, C., Barbey, P., Yonta-Ngouné, C., Paquette, J.L., Villiéras, F., 2014. Pre-collisional geodynamic context of the southern margin of the Pan-African fold belt in Cameroon. *Journal of African Earth Sciences* **99**, 245–260.

Nzenti, J.P., Barbey, P., Jegouzo, P., Moreau, C., 1984. Un nouvel exemple de ceinture granulitique dans une chaîne protérozoïque de collision: les migmatites de Yaoundé au Cameroun. *Comptes Rendus Academie Des Sciences de Paris* **299**, 1197–1199.

Nzenti, J.P., Barbey, P., Macaudière, J., Soba, D., 1988. Origin and evolution of the late Precambrian high, grade Yaoundé gneisses Cameroon. *Precambrian Research* **38**, 91–109.

Olinga, J.B., Mpesse, J.E., Minyem, D., Ngako, V., Ndougsa-Mbarga, T., Ekodeck, G.E., 2010. The Awaé – Ayos strike-slip shear zones (southern Cameroon): Geometry, kinematics and significance in the late Pan-African tectonics. *N. Jb. Geol. Paläont. Abh.* **257**, 1–11. https://doi.org/10.1127/0077-7749/2010/0042

Owona-Angue, M.L., Tabod, C.T., Nguiya, S., Kenfack, J.V., Tokam Kamga, A.P., 2013. Delineation of Lineaments in South Cameroon (Central Africa) Using Gravity Data. *Open Journal of Geology* **3**, 331–339. https://doi.org/http://dx.doi.org/10.4236/ojg.2013.35038

Owona Angue, M.L., Assembe, S.P., Njingti-Nfor, Ngoh, J.D., Ndougsa-Mbarga, T., Kue Petou, M.R., Bisso, D., 2016. Determination of the Structural Lineaments in the Kribi-Campo-Ma'an Area from a Multi-Scale Analysis of Gravity Data Using the HGM and Euler 3D Deconvolution Approaches. *International Journal of Geosciences* **7**, 1122–1143.

Owona Angue, M.L., Tabod, T.C., Nguiya, S., Kenfack, J.V., Tokam Kamga, A.P., 2013. Delineation of Lineaments in South Cameroon (Central Africa) Using Gravity Data. *Open Journal of Geology* **3**, 331–339. https://doi.org/http://dx.doi.org/10.4236/ojg.2013.35038

Palacky, G.J., 1988. Resistivity Characteristics of Geologic Targets. Geological Survey of Canada, 129p.

Parasnis, D.S., 1986. Principles of Applied Geophysics, 4th ed. Chapman and Hall, London, 412p.

Parker, R.L., 2011. New analytic solutions for the 2-D TE mode MT problem. *Geophysical Journal International* **186**, 980–986. https://doi.org/10.1111/j.1365-246X.2011.05091.x

Paterson Grant and Watson Ltd, 1976. Études aéromagnétiques sur certaines regions de la République Unie du Cameroun. Rapport d'interpretation. Toronto, 192p.

Paterson, N.R., Reeves, C. V, 1985. Applications of gravity and magnetic surveys : The state-of-the-art in 1985. *Geophysics* **50**, 2558–2594.

Peddie, N.W., 1983. International Geomagnetic Reference Field — Its evolution and the difference in total field intensity between new and old models for 1965–1980. *Geophysics* **48**, 1691–1696.

Penaye, J., Toteu, S.F., Van Schmus, W.R., Nzenti, J.P., 1993. U-Pb and Sm-Nd preliminary geochronologic data on the Yaounde Series, Cameroon: re-interpretation of the granulitic rocks as the suture of a collision in the "Centrafrican'' belt." *Comptes Rendus - Academie Des Sciences*, Serie II.

Penaye, J., Toteu, S.F., Van Schmus, W.R., Tchakounte, J., Ganwa, A., Minyem, D., Nsifa, E.N., 2004. The 2.1 Ga West Central African Belt in Cameroon : extension and evolution. *Journal of African Earth Sciences* **39**, 159–164. https://doi.org/10.1016/j.jafrearsci.2004.07.053

Pérez-Díaz, L., Eagles, G., 2014. Constraining South Atlantic growth with seafloor spreading data. *Tectonics* **33**, 1–26. https://doi.org/10.1002/2014TC003644

Piper, J.D.A., 2013. A planetary perspective on Earth evolution : Lid Tectonics before Plate Tectonics. *Tectonophysics* **589**, 44–56.

Piper, J.D.A., 2000. The Neoproterozoic Supercontinent: Rodinia or Palaeopangaea ? *Earth and Planetary Science Letters* **176**, 131–146. https://doi.org/10.1016/S0012-821X(99)00314-3

Pisarevsky, S.A., Wingate, M.T.D., Powell, C.M., Johnson, S., Evans, D.A.D., 2003. Models of Rodinia assembly and fragmentation. *Geological Society Special Publication*. https://doi.org/10.1144/GSL.SP.2003.206.01.04

Pouclet, A., Vidal, M., Doumnang, J.C., Vicat, J.P., Tchameni, R., 2006. Neoproterozoic crustal evolution in Southern Chad: Pan-African ocean basin closing, arc accretion and late- to post-orogenic granitic intrusion. *Journal of African Earth Sciences* **44**, 543–560. https://doi.org/10.1016/j.jafrearsci.2005.11.019

Prieto, C., 1996. Gravity/magnetic signatures of various geologic models-An exercise in pattern recognition. *IGC Footnotes on Interpretation* **4**.26p.

Reeves, C. V, 2005. Aeromagnetic Surveys-Principles, Practice & Interpretation. Geosoft, 245p.

Reeves, C. V, Korhonen, J. V, 2007. Magnetic anomalies for geology and resources. *In: Gubbins, D., Herrero-Bervera, E. (Eds.), Encyclopedia of Geomagnetism and Paleomagnetism* **XXVI**, 1054.

Reeves, C. V, Reford, S.W., Milligan, P.R., 1997. Airborne Geophysics : Old Methods , New Images. *In: Gubins, A.G. (Ed.), Proceedings of Exploration 97: Fourth Decennial International Conference on Mineral Exploration*. 13–30.

Regnoult, J.M., 1986. Synthèse géologique du Cameroun. Direction des Mines et de la Géologie du Cameroun, 119p.

Reid, A.B., Allsop, J.M., Granser, H., Millett, A.J., Somerton, I.W., 1990. Magnetic

interpretation in three dimensions using Euler deconvolution. *Geophysics* **55**, 80–91.

Rikitake, T., 1948. Notes on the Electromagnetic induction within the Earth. **XXIV**, 1–9.

Roberts, N.M.W., van Kranendonk, M.J., Parman, S., Clift, P.D., 2015. Continent formation through time. *Geological Society, London, Special Publications* **389**, 1–16. https://doi.org/http://dx.doi.org/10.1144/SP389.13

Roest, W.R., Verhoef, J., Pilkington, M., 1992. Magnetic interpretation using the 3-D analytic signal. *Geophysics* **57**, 116–125.

Rolin, P., 1995. La Zone de Décrochement Panafricain des Oubanguides en République Centrafricaine. *Comptes Rendu de l'Académie Des Sciences de Paris* **320**, 63–69.

Rolin, P., 1992. Nouvelles données tectoniques sur le socle précambrien de Centrafrique: implications géodynamiques. *Comptes Rendu de l'Académie Des Sciences de Paris* **315**, 467–470.

Rowell, A.J., Rees, M.N., Duebendorfer, E.M., Wallin, E.T., Van Schmus, W.R., Smith, E.I., 1993. An active Neoproterozoic margin: evidence from the Skelton Glacier area, Transantarctic Mountains. *Journal of the Geological Society, London.* https://doi.org/10.1144/gsjgs.150.4.0677

Schettino, A., Scotese, C.R., 2005. Apparent polar wander paths for the major continents (200 Ma to the present day): A palaeomagnetic reference frame for global plate tectonic reconstructions. *Geophysical Journal International* **163**, 727–759. https://doi.org/10.1111/j.1365-246X.2005.02638.x

Schowengerdt, R.A., 2007. Remote Sensing: Models and Methods for Image Processing, 3rd ed. Elsevier, Oxford, 558p.

Scotese, C.R., 2009. Late Proterozoic plate tectonics and palaeogeography: A tale of two supercontinent, Rodinia and Pannotia. *Geological Society, London, Special Publications* **326**, 67–83. https://doi.org/10.1144/SP326.4

Scotese, C.R., Boucot, A.J., Mckerrow, W.., 1999. Gondwanan palaeogeography and palaeoclimatology. *Journal of African Earth Sciences.* **99**–114.

Shandini, N.Y., Tadjou, J.M., 2012. Interpreting gravity anomalies in south Cameroon, central Africa. *Earth Sciences Research Journal* **16**, 5–9.

Shandini, N.Y., Tadjou, J.M., Basseka, C.A., 2011. Delineating deep basement faults in South Cameroon area. *World Applied Science Journal* **14**, 611–615.

Shandini, N.Y., Tadjou, J.M., Tabod, C.T., Fairhead, J.D., 2010. Gravity Data Interpretation in the Northern Edge of the Congo Craton , South-Cameroon. *Anuário Do Instituto de Geociências - UFRJ* **33**, 73–82.

Shang, C.K., Liégeois, J.P., Satir, M., Frisch, W., Nsifa, E.N., 2010. Late Archaean high-K granite geochronology of the northern metacratonic margin of the Archaean Congo craton, Southern Cameroon: Evidence for Pb-loss due to non-metamorphic causes. *Gondwana Research* **18**, 337–355. https://doi.org/10.1016/j.gr.2010.02.008

Shang, C.K., Sati, M., Nsifa, E.N., Liegeois, J.-P., Siebel, W., Taubald, H., 2007. Archaean high-K granitoids produced by remelting of earlier Tonalite-Trondhjemite-Granodiorite (TTG) in the Sangmelima region of the Ntem complex of the Congo craton , southern Cameroon. *International Journal of Earth Sciences (Geol Rundsch)* **96**, 817–841. https://doi.org/10.1007/s00531-006-0141-3

Shang, C.K., Satir, M., Siebel, W., Nsifa, E.N., Taubald, H., Liégeois, J.P., Tchoua, F.M., 2004a.

TTG magmatism in the Congo craton; a view from major and trace element geochemistry, Rb-Sr and Sm-Nd systematics: Case of the Sangmelima region, Ntem complex, southern Cameroon. *Journal of African Earth Sciences* **40**, 61–79. https://doi.org/10.1016/j.jafrearsci.2004.07.005

Shang, C.K., Satir, M., Siebel, W., Taubald, H., Nsifa, E.N., Westphal, M., Reitter, E., 2001. Genesis of K-rich granitoids in Sangmelima region, Ntem Complex (Congo Craton), Cameroon. *Terra Nostra* **5**, 60–63.

Shang, C.K., Siebel, W., Satir, M., Chen, F., Mvondo Ondoua, J., 2004b. Zircon Pb-Pb and U-Pb systematics of TTG rocks in the Congo craton: Constraints on crust formation, magmatism, and Pan-African lead loss. *Bulletin of Geosciences* **79**, 205–219. https://doi.org/10.1039/c2jm31907a

Simon, N., Ali Che, A., Mohamed, K.R., Sharir, K., 2016. Best Band Ratio Combinations for the Lithological Discrimination of the Dayang. *Sains Malaysiana* **45**, 659–667.

Simpson, F., Bahr, K., 2005. Practical magnetotellurics. https://doi.org/10.1017/CBO9780511614095

Sims, W.E., Bostick, F.X.J., Smith, H.W., 1971. The estimation of the magnetotelluric impedance tensor elements from measured data. *Geophysics* **36**, 938–942.

Spalletti, L.A., Limarino, C.O., Geuna, S., 2010. The Late Palaeozoic of Western Gondwana : New insights from South American records. *Geologica Acta* **8**, 341–347. https://doi.org/10.1344/105.000001576

Stewart, J.H., 2007. World Map showing surface and subsurface distribution, and lithologic character of Middle and Late Neoproterozoic Rocks., USGS Open-File Report. Menlo Park.

Strangway, D.W., Swift, C.M., Holmer, R.C., 1973. The application of Audio-frequency magnetotellurics (AMT) to mineral exploration. *Geophysics* **38**, 1159–1175. https://doi.org/10.1190/1.1440402

Tack, L., Wingate, M.T.D., De Waele, B., Meert, J., Belousova, E.A., Griffin, B., Tahon, A., Fernandez-Alonzo, M., 2008. The 1375 Ma "Kibaran Event" in Central Africa: prominent emplacement of bimodal magmatism under extensional regime. *Precambrian Research*. https://doi.org/10.1016/j.precamres.2010.02.022

Tadjou, J.M., Njingti-Nfor, Kamguia, J., Manguelle-Dicoum, E., 2008. Geophysical prospecting of the transition zone between the Congo Craton and the Panafrican belt in Cameroon. *Earth Science Research Journal* **12**, 169–180.

Tadjou, J.M., Nouayou, R., Kamguia, J., Kande, H.L., Manguelle-Dicoum, E., 2009. Gravity analysis of the boundary between the Congo craton and the Pan-African belt of Cameroon. *Austrian Journal of Earth Sciences* **102**, 71–79.

Takam, T., Makoto, A., Kokonyangi, J., Dunkley, Daniel, J., Nsifa, E.N., 2009. Paleoarchaean charnockite in the Ntem Complex, Congo Craton, Cameroon : insights from SHRIMP zircon U-Pb ages. *Journal of Mineralogical and Petrological Sciences* **104**, 1–11. https://doi.org/10.2465/jmps.080624

Tchakounté Numbem, J., Eglinger, A., Toteu, S.F., Zeh, A., Nkoumbou, C., Mvondo-Ondoa, J., Penaye, J., de Wit, M., Barbey, P., 2018a. Reply to comment by M. Bouyo on "The Adamawa–Yade domain, a piece of Archaean crust in the Neoproterozoic Central African Orogenic belt (Bafia area, Cameroon)", by Jacqueline Tchakounté et al., Precambrian Research 299 (2017) 210–229. *Precambrian Research* **305**, 514–515. https://doi.org/10.1016/j.precamres.2017.12.003

Tchakounté Numbem, J., Eglinger, A., Toteu, S.F., Zeh, A., Nkoumbou, C., Mvondo-Ondoa, J., Penaye, J., de Wit, M., Barbey, P., 2017. The Adamawa-Yadé domain, a piece of Archaean crust in the Neoproterozoic Central African Orogenic belt (Bafia area, Cameroon). *Precambrian Research* **299**, 210–229. https://doi.org/10.1016/j.precamres.2017.07.001

Tchakounté Numbem, J., Eglinger, A., Toteu, S.F., Zeh, A., Nkoumbou, C., Mvondo-Ondoa, J., Penaye, J., de Witt, M., Barbey, P., 2018b. Reply to comment by Ngako and Njonfang on "The Adamawa-Yade domain, a piece of Archaean crust in the Neoproterozoic Central African Orogenic belt (Bafia area, Cameroon)", by Jacqueline Tchakounté et al., Precambrian Research 299 (2017) 210-229. *Precambrian Research* **305**, 516–518. https://doi.org/10.1016/j.precamres.2017.12.035

Tchameni, R., 1997. Géochimie et géochronologie des formations de l'archéen du paléoprotérozoïque du Sud Cameroun groupe du Ntem, Craton du Congo. Thèse de Doctorat. Université d'Orléans, 227p.

Tchameni, R., Lerouge, C., Penaye, J., Cocherie, A., Milesi, J.P., Toteu, S.F., Nsifa, E.N., 2010. Mineralogical constraint for metamorphic conditions in a shear zone affecting the Archean Ngoulemakong tonalite, Congo craton (Southern Cameroon) and retentivity of U-Pb SHRIMP zircon dates. *Journal of African Earth Sciences* **58**, 67–80. https://doi.org/10.1016/j.jafrearsci.2010.01.009

Tchameni, R., Mezger, K., Nsifa, E.N., Pouclet, A., 2001. Crustal origin of Early Proterozoic syenites in the Congo Craton (Ntem Complex), South Cameroon. *Lithos* **57**, 23–42.

Tchameni, R., Mezger, K., Nsifa, E.N., Pouclet, A., 2000. Neoarchaean evolution in the Congo Craton: evidence from K-rich granitoids of the Ntem Complex, Southern Cameroon. *Journal of African Earth Sciences* **30**, 133–147.

Tchameni, R., Pouclet, A., Mezger, K., Nsifa, E.N., Vicat, J.., 2004. Monozircon and Sm–Nd whole rock ages from the Ebolowa greenstone belts: evidence for the terranes older than 2.9 Ga in the Ntem Complex (Congo Craton, South Cameroon). *Journal of the Cameroon Academy of Sciences* **4**, 213–224.

Teikeu, A.W., Njandjock, P., Tabod, C., Akame, J.M., Nshagali, G., 2016. Hydrogeological activity of lineaments in Yaounde Cameroon region using remote sensing and GIS techniques. *The Egyptian Journal of Remote Sensing and Space Sciences*. https://doi.org/10.1016/j.ejrs.2015.12.006

Telford, W.M., Geldart, L.P., Sherriff, R.E., Keys, D.A., 1990. Applied Geophysics. Cambridge University Press, Cambridge. https://doi.org/10.1130/0091-7613

Thompson, D.T., 1982. EULDEP : A New Technique for Making Computer-Assisted Depth Estimates from Magnetic Data. *Geophysics* **47**, 31–37.

Tikhonov, A.N., 1950. On determining electrical characteristics of the deep layers of the Earth's crust. *Doklady* **73**, 295–297. https://doi.org/10.1130/0091-7613

Toteu, S.F., Fouateu, R.Y., Penaye, J., Tchakounte, J., Mouangue, A.C.S., Van Schmus, W.R., Deloule, E., Stendal, H., 2006a. U-Pb dating of plutonic rocks involved in the nappe tectonic in southern Cameroon: consequence for the Pan-African orogenic evolution of the central African fold belt. *Journal of African Earth Sciences* **44**, 479–493. https://doi.org/10.1016/j.jafrearsci.2005.11.015

Toteu, S.F., Fouateu Yongue, R., Penaye, J., Seme Mouangue, A.C., Van Schmus, W.R., Tchakounte, J., Deloule, E., Stendal, H., 2007. Reply to the comment by Mvondo et al. on "U-Pb dating of plutonic rocks involved in the nappe tectonics in southern Cameroon: Consequence for the Pan-African orogenic evolution of the central African fold belt by

Toteu et al., 2006". *Journal of African Earth Sciences* **48**, 53–54. https://doi.org/10.1016/j.jafrearsci.2007.03.003

Toteu, S.F., Michard, A., Bertrand, J.M., Rocci, G., 1987. U/Pb dating of precambrian rocks from northern cameroon, orogenic evolution and chronology of the pan-african belt of Central Africa. *Precambrian Research* **37**, 71–87. https://doi.org/10.1016/0301-9268(87)90040-4

Toteu, S.F., Penaye, J., Deloule, E., Van Schmus, W.R., Tchameni, R., 2006b. Diachronous evolution of volcano-sedimentary basins north of the Congo craton: Insights from U-Pb ion microprobe dating of zircons from the Poli, Lom and Yaoundé Groups (Cameroon). *Journal of African Earth Sciences* **44**, 428–442. https://doi.org/10.1016/j.jafrearsci.2005.11.011

Toteu, S.F., Penaye, J., Djomani, Y.P., 2004. Geodynamic evolution of the Pan-African belt in central Africa with special reference to Cameroon. *Canadian Journal of Earth Sciences* **41**, 73–85. https://doi.org/10.1139/e03-079

Toteu, S.F., Van Schmus, W.R., Penaye, J., Michard, A., 2001. New U-Pb and Sm-Nd data from north-central Cameroon and its bearing on the pre-Pan African history of Central Africa. *Precambrian Research* **108**, 45–73. https://doi.org/10.1016/S0301-9268(00)00149-2

Toteu, S.F., van Schmus, W.R., Penaye, J., Nyobe, J.B., 1994. U-Pb and Sm-Nd evidence for Eburnian and Pan-African high-grade metamorphism in cratonic rocks of southern Cameroon. *Precambrian Research* **67**, 321–347.

US Geological Survey, 2016. Landsat 8 Data Users Handbook, LSDS-1574 Report V. 2.0, 95p.

van Hinsbergen, J.J., Buiter, S.J.H., Torsvik, T.H., Gaina, C., Webb, S.J., 2011. The formation and evolution of Africa from the Archaean to Present : Introduction. *Geological Society, London, Special Publication*s **357**, 1–8. https://doi.org/10.1144/SP357.1

van Schmus, W.R., Oliveira, E.P., da Silva Filho, A.F., Toteu, S.F., Penaye, J., Guimarães, I.P., 2008. Proterozoic links between the Borborema Province, NE Brazil, and the Central African Fold Belt. *Geological Society, London, Special Publications* **294**, 69–99. https://doi.org/10.1144/SP294.5

Vezinet, A., Moyen, J., Stevens, G., Nicoli, G., Laurent, O., Couzinié, S., Frei, D., 2018. A record of 0 . 5 Ga of evolution of the continental crust along the northern edge of the Kaapvaal Craton , South Africa : Consequences for the understanding of Archean geodynamic processes. *Precambrian Research* **305**, 310–326. https://doi.org/10.1016/j.precamres.2017.11.019

Vicat, J., Moloto-a-Kenguemba, G., 2001. Les granitoides de la couverture protérozoique de la bordure nord du craton du Congo (Sud-Est du Cameroun et Sud-Ouest de la République centrafricaine), témoins d ' une activité magmatique panafricaine. *Earth and Planetary Science* **332**, 235–242.

Vicat, J.P., Nsifa, E.N., Tchameni, R., Pouclet, A., 1998. La ceinture de roches vertes de Lolodorf-Ngomedzap (Sud-Cameroun) Petrologie, geochimie et cadre geodynamique. *In*: *Vicat, J., Bilong, P. (Eds.), Geosciences Au Cameroun* **1**, 325–337.

Vozoff, K., 1991. The Magnetotelluric method .*in Electromagnetic Methods in Applied Geophysics, Chapter 8.* Society of Exploration Geophysicists, Tulsa, 641–712. https://doi.org/doi.org/10.1190/1.9781560802686.ch8

Vozoff, K., 1990. Magnetotellurics: Principles and practice. Proceedings of the Indian Academy of Sciences - *Earth and Planetary Sciences* **99**, 441–471. https://doi.org/10.1007/BF02840313

Vozoff, K., 1972. The magnetotelluric methoc in the exploration of sedimentary basins. *Geophysics* **37**, 98–141.

Weaver, J.T., Agarwal, A.K., Lilley, F.E.M., 2000. Characterization of the magnetotelluric tensor in terms of its invariants.

Weaver, J.T., Agarwap, A.K., Lilley, F.E.M., 2006. The relationship between the magnetotelluric tensor invariants and the phase tensor of Caldwell, Bibby, and Brown. *Exploration Geophysics* **37**, 261–267.

Weckmann, U., 2012. Making and Breaking of a Continent: Following the Scent of Geodynamic Imprints on the African Continent Using Electromagnetics. *Surveys in Geophysics* **33**, 107–134. https://doi.org/10.1007/s10712-011-9147-x

Yandjimain, J., Ndougsa-Mbarga, T., Meying, A., Bikoro Bi-Alou, M., Ngoumou, P.C., Assembe, S.P., Ngoh, J.D., Owono Amougou, O.U.I., 2017. Combination of Tilt-Angle and Euler Deconvolution Approaches to Determine Structural Features from Aeromagnetic Data Modeling over Akonolinga-Loum Area. *International Journal of Geosciences* **8**, 925–947. https://doi.org/10.4236/ijg.2017.87053

Yonta Ngoune, C., 2010. Le contexte géologique des indices de talc de la région de Boumnyebel (Chaîne panafricaine d'Afrique Centrale, Cameroun). Universite de Yaounde 1 /Universite de Nancy. https://doi.org/10.1037/0735-7044.121.5.920

Zanga-Amougou, A., Layu, Y., Bikoro Bi-Alou, M., Manguelle-Dicoum, E., 2013. 2.5D Modeling of Crustal Structures along the Eastern Cameroon and Western Central African Republic Derived from Finite Element and Spectral Analysis Methods. *Geophysica* **49**, 75–97.

Zhang, P., Roberts, R.G., L. B. Pedersen, 1987. Magnetotelluric Magnetotelluric strike rules. *Geophysics* **52**, 267–278.

Zhao, G., Sun, M., Wilde, S.A., Li, S., Zhang, J., 2006. Some key issues in reconstructions of Proterozoic supercontinents. *Journal of Asian Earth Sciences.* https://doi.org/10.1016/j.jseaes.2004.06.010

Zhdanov, M.S., 2009. Geophysical electromagnetic theory. Methods in Geochemistry and Geophysics. Elsevier, 831p.

Zonge, K.L., Hughes, L.J., 1991. Controlled source audio-frequency magnetotellurics. *in Electromagnetic Methods in Applied Geophysics, Chapter 9*. Society of Exploration Geophysicists, Tulsa, 713–809. https://doi.org/doi.org/10.1190/1.9781560802686.ch9

APPENDICES

Appendix 1: coordinates of AMT sounding stations.

Station	Latitude	Longitude	Elevation (m)	Position (m)
		PROFILE 1 (OSSOL)		
OS1	03°50'45.40"	11°39'07.50"	701	0
OS2	03°50'43.00"	11°39'10.02"	708	100
OS3	03°50'40.90"	11°39'12.80"	702	200
OS4	03°50'39.10"	11°39'15.70"	693	300
OS5	03°50'36.64"	11°39'16.58"	691	400
OS6	03°50'34.41"	11°39'18.97"	684	500
		PROFILE 2 (BEGUELE 1-CARREFOUR)		
BE1	03°50'34.32"	11°39'49.50"	704	0
BE2	03°50'32.18"	11°39'51.79"	714	100
BE3	03°50'29.88"	11°39'54.10"	718	200
BE4	03°50'27.44"	11°39'56.32"	719	300
BE5	03°50'25.27"	11°39'58.68"	718	400
		PROFILE 3 (NKOLAFAMBA)		
NK1	03°51'06.80"	11°39'38.00"	685	0
NK2	03°51'04.14"	11°39'39.90"	678	100
NK3	03°51'01.00"	11°39'41.50"	684	200
NK4	03°50'57.10"	11°39'43.60"	691	300
NK5	03°50'56.20"	11°39'46.50"	683	400
NK6	03°50'54.70"	11°39'48.80"	684	500
		PROFILE 4 (BEGUELE 2)		
BG1	03°50'43.50"	11°40'05.50"	719	0
BG2	03°50'41.50	11°40'08.20"	718	100
BG3	03°50'38.80"	11°40'10.60"	702	200
BG4	03°50'34.80"	11°40'13.80"	700	300
BG5	03°50'33.00"	11°40'16.40"	720	400
BG6	03°50'31.70"	11°40'18.40"	717	500
		PROFILE 5 (KAMBA)		
KB1	03°40'44,3"	011°40'49,9"	668	0
KB2	03°40'32,6"	011°40'59,1"	661	600
KB3	03°40'32,6"	011°41'11,3"	664	900
KB4	03°40'20,3"	011°41'20,3"	680	1200
KB5	03°40'16,5"	011°41'24,1"	676	1300
KB6	03°40'12,6"	011°41’28,2"	666	1500
		PROFILE 6 (LOUM 2)		
LM1	03°40'44,3"	011°40'49,9"	668	0
LM2	03°40'32,6"	011°40'59,1"	661	600
LM3	03°40'32,6"	011°41'11,3"	664	900
LM4	03°40'20,3"	011°41'20,3"	680	1200
LM5	03°40'16,5"	011°41'24,1"	676	1300
LM6	03°40'12,6"	011°41’28,2"	666	1500

REPUBLIQUE DU CAMEROUN
Paix - Travail – Patrie
****
UNIVERSITE DE YAOUNDE I
****
CENTRE DE RECHERCHE ET DE FORMATION DOCTORALE EN SCIENCES, TECHNOLOGIES ET GEOSCIENCES
****
UNITE DE RECHERCHE ET DE FORMATION DOCTORALE PHYSIQUE ET APPLICATIONS
B.P. : 812 Yaoundé
E-mail : crfd_stg@uy1.uninet.cm

REPUBLIC OF CAMEROON
Peace - Work – Fatherland
****
THE UNIVERSITY OF YAOUNDE I
****
POSTGRADUATE SCHOOL OF SCIENCE, TECHNOLOGY AND GEOSCIENCES
****
RESEARCH AND POSTGRADUATE TRAINING UNIT FOR PHYSICS AND APPLICATIONS
Po Box : 812 Yaounde
E-mail : crfd_stg@uy1.uninet.cm

LABORATOIRE DE PHYSIQUE DE L'ENVIRONNEMENT TERRESTRE
LABORATORY OF THE EARTH ENVIRONMENT'S PHYSICS

EVIDENCES OF CRUSTAL STRUCTURES BASED ON GEOPHYSICAL DATA INTEGRATION IN THE NKOLAFAMBA- SANGMELIMA AREA (SOUTH CAMEROON)

A thesis defended for the award of the degree of Doctor of Philosophy (PhD) in Physics
Speciality: Geophysics and Geoexploration

By:

ASSEMBE Stéphane Patrick
MSc. Geophysics
Matricule: 00V145

Thesis Publicly defended on the 22 March 2021 before the Jury made up of:

President:	**NDJACKA Jean Marie Bienvenu**, *Professor, University of Yaounde I*
Rapporteur:	**NDOUGSA MBARGA**, *Professor, University of Yaounde I*
Members:	**NJANDJOCK NOUCK Phillipe**, *Professor, University of Yaounde I*
	NOUAYOU Robert, *Professor, University of Yaounde I*
	BEN-BOLIE Hubert Germain, *Professor, University of Yaounde I*
	MOUANGUE Ruben, *Associate Professor, University of Ngaoundere*

Academic year 2018/2019

DEDICATIONS

To my children, may this work inspire them in the future

To, my mothers

AND

In the loving memory of:

Assembe Ernest. Etienne, my father

Essoundou Jean. Hervé, my brother

Ebalé Christian. Brice, my nephew and friend

UNIVERSITÉ DE YAOUNDÉ I
THE UNIVERSITY OF YAOUNDE I

FACULTÉ DES SCIENCES
FACULTY OF SCIENCE

DÉPARTEMENT DE PHYSIQUE
DEPARTMENT OF PHYSICS

ATTESTATION DE CORRECTION DE LA THÈSE DE DOCTORAT/Ph.D

Nous, Professeur **Pr BEN-BOLIE Germain Hubert** et Professeur **NDJAKA Jean Marie Bienvenu**, respectivement Examinateur et Président du jury de la Thèse de Doctorat/Ph.D de Monsieur **ASSEMBE Stéphane Patrick**, Matricule **00V145**, préparée sous la direction du Professeur **NDOUGSA MBARGA Théophile,** intitulée : « **Evidences of crustal structures based on geophysical data integration in the Nkolafamba-Sangmelima area (South Cameroon)**», soutenue le **Lundi, 22 Mars 2021**, en vue de l'obtention du grade de Docteur/Ph.D en Physique, Spécialité **Physique de l'Environnement Terrestre,** Option **Geophysique et Geoexploration**, attestons que toutes les corrections demandées par le jury de soutenance ont été effectuées.

En foi de quoi, la présente attestation lui est délivrée pour servir et valoir ce que de droit.

Fait à Yaoundé le ..01 JUN 2021.....

Examinateur

Pr BEN-BOLIE Germain Hubert

Le Chef de Département de Physique

UNIVERSITE DE YAOUNDE I
FACULTE DES SCIENCES
Le Chef de Département
DEPARTEMENT DE PHYSIQUE

Pr NDJAKA Jean-Marie Bienvenu

Le Président du jury

Pr NDJAKA Jean-Marie Bienvenu

ACKNOWLEDGMENTS

I address thanks to Professor Théophile NDOUGSA MBARGA who initiated and supervised this work in the Geophysics & Geoexploration unit, Laboratory of Earth Environment Physics, University of Yaoundé I. Your availability despite your multiple occupations, your scientific rigor and devotion to work, your remarks and especially your advices as parent are the keystones to the completion of this project. Accept my timeless gratitude.

To Professor Luc Calvin. OWONO OWONO, Head of the Physics and Applications Research and Training Unit, Postgraduate School of Science, Technology and Geoscience at the University of Yaoundé I, who enabled the completion of this study. I am very thankful to you.

Credit to Professors TABOD Charles TABOD, Robert NOUAYOU, Philippe NJANDJOCK NOUCK, Marie Louise C. OWONO ANGUE who nurtured in me the essence of geophysics in the Geophysics & Geoexploration unit, Laboratory of Earth Environment Physics.

Professors Ute WECKMANN, Paul DIRKS and Colin REEVES provided interesting research materials and explanatory advises; Professors Germain H. BEN BOLIE and Bertrand BODO, endeavoured to overcome many obstructive difficulties towards the completion of this study; Professor Dieudonné BISSO and Mr. Christophe AVA offered the logistics for the Audiomagnetotelluric field campaign. Please receive my deep gratitude.

I extend my gratitude to the members of the Jury for all the precious time they will be sacrificing in order to examine this work; and to all the reviewers whose commitment will contribute into the improvement of this dissertation.

Special thanks to Professors Arsène MEYING, Jean L. NSOUANDELE and Jean G. TAMBA; and Doctors Francoise ENYEGUE A NYAM, Daniel GOUET, Paul NGOUMOU, Alain ZANGA, Marcelin BIKORO Bi ALOU, William TEIKEU ASSATSE, Olivier U. OWONO AMOUGOU, Serge POKAM KEGNI, Augustin D. PEPOGO MANVELE and Alain R. NZEUGA, for their indefectible support.

To Jean D. NGOH, Gaetan. ENEME, Fabrice EMBOLO and all the graduate researchers working alongside me, I appreciate your collaboration.

My endless thanks to my mothers Valentine NNOMO, Martine NGONO and Anne M. NGO NGUIMBOUS; to Serge ASSEMBE, Philemon ESSI, Charles ASSEMBE, Guy MEVELE, Stephanie S. ZE MEMANE, Veronique LAISIN, Pauline ELOMO, all my siblings, and my friends mainly Pierre C. NGA, Cyrille DJANG, Mr and Mrs ETOUNDI, for their timeless and indefectible supports throughout. My regrads to whosoever, unnamed, contributed in any manner to the completion of this program.

ABSTRACT

An integrated study combining the tensor audiomagnetotellurics (AMT), aeromagnetics, remote sensing and field geological data is used to better understand the structural geology in the Nkolafamba-Sangmelima region, a southern portion of the North Equatorial Fold (Panafrican) Belt -Congo Craton transition zone located between latitudes 02º45'N-04º00'N and longitudes 11º30'E-12º15'E. The lithology of the area comprises (i) the Yaounde Group (southern member of the Panafrican belt) represented by the Yaounde series (made up of migmatised gneisses, micaschists) and the Mbalmayo series; (ii) the Congo Craton, also referred to as the Ntem complex, which is made up of various granites and charnokites of the Tonalite-Trondheimite-Granodiorite suites. Three (or four) syn-, late to post-Panafrican deformation stages are identified in the NEFB whereas three stages supposedly related to pre-, syn to post Panafrican events affect the Congo Craton.

The AMT data have been collected along 6 profiles striking N135º. From data analyses, the phase and apparent resistivity pseudosections revealed or confirmed that folding and many discontinuities affected the Yaounde series, showing that the area underwent intense tectonics and that the subsurface is made up of a mixture of both Panafrican belt and Congo Craton formations. The discontinuities have been interpreted as faults and/or fractures on geoelectrical sections; active faults being related to the conductive discontinuities. The highlighted faults correlate many fractures and faults observed on outcrops from Yaounde, Nkolafamba and Loum 2. They form a network of parallel faults symptomatic of NE-SW strike-slips in the area initially assumed to be coeval to the Central Cameroon Shear Zone. Field data confirm the results and aeromagnetics is used to check the south and east continuity of this strike-slips system.

Aeromagnetics covers a contiguous area south and east of the AMT surveyed zone. The data deriving from a nationwide survey carried out in years 70s, have been provided as digital total magnetic intensity map at 1:50000 scale. The reduction to the magnetic equator highlighted a main NE-SW channel of strongly magnetised anomalies which presume the dominance of the NE-SW structural direction in the area. These anomalies are interpreted as lineaments, mafic to ultramafic or subcrustal intrusions affecting both the Yaounde Group and the Ntem complex. Analytic signal outlines magnetic domains sometimes matching known formations, potential mineral host including inferred greenstones belts relics. The difference in the anomalies (lineaments) density, due to difference in their nature of rocks, enabled to differentiate the Panafrican belt from the Ntem complex on the first vertical derivative map. Some lineaments are

interpreted either as faults or contacts, including the faults outlining the Congo Craton/Panafrican belt thrust limit. The dominant directions of lineaments are NE-SW to ENE-WSW, WNW-ESE to NW-SE and E-W. The multiscale edge analysis using the horizontal gradient magnitude isolates the major faults and contacts; these faults are vertical to sub-vertical and extend to depth located from 621 to 4000 m (or deeper) by the Euler 3D deconvolution method. The magnetic foliation map depicts folding subsequent to E-W, NNW-SSE and N-S compressions and various shear zones affecting the study area. The faults' geometry is consistent with both vertical movements (related to basement's collapses) and horizontal movements (wrenches) in both the Congo Craton and the Panafrican Belt. Vertical movements and the faults' geometry has been confirmed by geophysical 2.75 modelling which neatly locates the Congo craton/Panafrican belt between Latitudes 03º20'N and 03º15'N eastward. Magnetic study corroborates the existence of NE-SW strike-slips south of the AMT investigated area and is validated by remote sensing.

Remote sensing involves Landsat 8 OLI data over the entire study area; it is particularly efficient in lineaments detection, and serves as a validation tool. The remotely sensed lineaments interpreted as faults or contacts (total of 863) maintain the dominance of the NE-SW, NW-SE and N-S directions. However, an analysis based on length classified the NE-SW, NNW-SSE to WNW-ESE among the major lineaments, forming many shear zones and strike-slips. Remote sensing analysis validate the magnetic and the AMT faults, and establishes the continuity within the findings of the study which henceforth highlights a unique sinistral NE-SW shear zone affecting both the Panafrican belt and the Congo Craton as a result of pre-Neoproterozoic events followed by syn- and post-Neoproterozoic reactivations in a continent-continent convergence setting actually marked by WNW-ESE transpressions in the two units.

The study correlate and upgrade the number of greenstones relics and the faults mapped in the Yaounde region, thus, it improves the geological map of the southern Cameroon and the information on the Panafrican belt/Congo Craton transition with positive moods for mineral exploration. Also, the integration of geosciences methods and data reveals to be consistent in investigation areas with a non-uniform geophysical surveying coverage.

Keywords: Tensor audiomagnetotellurics; aeromagnetics; remote sensing; Panafrican belt; Congo Craton; faults; strike-slips

RESUMÉ

Afin de mieux appréhender la géologie structurale de la region de Nkolafamba-Sangmelima, située entre les latitudes 02º45N-04º00N et les longitudes 11º30E-12º15E dans la zone de transition entre la Chaine Panafricaine d'Afrique Centrale et le Craton du Congo, une approche combinant les données audio-magnétotelluriques tensorielles, aéromagnétiques, les images satellites et des données géologiques de terrain a été adoptée dans le cadre des présents travaux. La lithologie de la zone comprend (i) la série de Yaoundé représentée par les gneiss migmatisés, les micaschistes et les schistes de Mbalmayo ; (ii) le Craton du Congo, comprenant des granites divers et des charnockites de la série Tonalite-Trondheimite-Granodiorite. Trois (ou quatre) épisodes de déformation syn- à post-Pan-Africain sont identifiés dans la Chaine Panafricaine tandis qu'ils sont pré-, syn. à post-Pan-Africain dans le Craton Congo.

Les données AMT ont été collectés suivant six profiles de direction N135º (NO-SE). Les pseudos sections de phase et de résistivité apparente révèlent dans le sous-sol la zone d'étude, des plissements et de nombreuses discontinuités interprétées dans les sections géoélectriques comme des failles ou des fractures ; et un mélange des formations issues à la fois du Craton du Congo et du Panafricain. Certaines failles, de par leur faible conductivité, sont supposées actives. Les failles mise en exergue et confirmées par des observations de terrain à Nkolafamba, Yaounde et Loum 2, forment un réseau de failles parallèles suggérant l'existence dans la zone d'une ligne décrochements majeurs NE-SO corrélable au Cisaillement Centre Camerounais et donc Des données magnétiques aideraient à vérifier la continuité dans le reste de la zone cible.

La portion investiguée par la méthode aéromagnétique est dans le prolongement sud et est de la portion couverte par l'AMT. Les données utilisées, collectées lors d'une campagne nationale dans les années 70, nous ont été fournies sous forme de carte de champ total au 1/50000^{e} en version numérique. La réduction à l'équateur révèle un couloir NE-SO composé d'anomalies à fortes intensités, traduisant la prépondérance de la direction NE dans la zone d'étude. Ces anomalies majeures seraient liées à des linéaments ou à des apports mafiques à ultra mafiques ou sub-crustaux sous le Panafricain et le Craton du Congo. Le signal analytique définie des domaines magnétiques coïncidant parfois avec de sformations, des cibles minières connues et des reliques probables de roches vertes. L'individualisation respective du Craton du Congo et du Panafricain issue desdits domaines est renforcée par la première dérivée verticale, suivant la densité (liée à leurs natures distinctes), très élevée au sud, des linéaments identifiés. Certains des linéaments interprétés comme failles ou contacts marquent la ligne de chevauchement

Craton/Panafricain. De la multitude des directions observées, seuls les groupes NE-SO à ENE-OSO, ONO-ESE à NO-SE et NO-SE sont prépondérants. L'analyse multi-échelle impliquant le gradient horizontal souligne des failles majeures et des contacts subverticaux à verticaux dont les profondeurs selon la deconvolution d'Euler 3D se situent ente 621 et 4000 m. La foliation magnétique quant à elle relève des axes de compression E-O, N-S et NNO-SSE traduisant des plissements et des cisaillements. La géométrie des failles traduit des mouvements verticaux (effondrements du socle) et horizontaux (décrochements) que confirme la modélisation 2.75 qui par ailleurs affine la localisation de la limite Craton/Panafricain d'est en ouest entre 03º20'N et 03º15'N. Cette étude corrobore l'existence au sud d'un cisaillement NE-SO souligné en amont par l'AMT et validé par télédétection. Les failles dans le Craton seraient pré-Neoprotérozoiques mais connaissent des réactivations syn- à tardi- et post-Neoprotérozoiques. Ces failles réactivées sont donc contemporaines de la fracturation dans le Panafricain mise en évidence par l'AMT.

La télédetection par imagerie Landsat 8 dans l'ensemble de la zone d'étude, s'avere efficace dans la cartographie des linéaments et sert d'outils de validation aux autres methodes. Les linéaments interprétés comme des failles ou des contacts (863) suivent les directions majeures NE-SO, NO-SE et N-S. Selon la longueur, les failles d'orientations NE-SO, NNO-SSE à ONO-ESE sont des linéaments majeurs marquant des cisaillements et des décrochements. Dans l'ensemble, l'étude met en évidence un couloir de cisaillements NE-SO affectant à la fois le Craton du Congo et la Chaine Panafricaine, en réponse a une tectonique pré-panafricaine (dans le Craton du Congo d'abord) suivie de rajeunissements syn- et post-panafricain dans une convergence continent/continent et actuellement soulignée par des transpressions ONO-ESE dans les deux unités lithostructurales.

Le présent travail contribue donc par la cartographie de nouvelles failles et de reliques de ceintures roches vertes, à l'amélioration de la carte géologique du sud Cameroun et de la connaissance de la zone de transition Craton/Panafricain, ce qui devrait à coup sûr réorienter significativement l'exploration minière dans la zone. Par ailleurs, l'approche utilisée dans le cadre de ces travaux dans l'intégration de plusieurs méthodes et données géoscientifiques, se révèle efficace dans l'étude des zones impliquant une juxtaposition des méthodes géophysiques.

Mots clés : méthode audiomagnétotellurique tensorielle ; méthode aéromagnétique ; télédétection ; CPAC ; CC ; failles ; décrochements

TABLE OF CONTENTS

Table, figure and photo captions

List of tables

List of figures

List of photos

LIST OF SYMBOLS, ABBREVIATIONS AND ACRONYMS

$\vec{E}$: Electric field vector

mV/km: millivolt per kilometre

$\vec{H}$:Magnetic field vector

A/m: Ampere per metre

$\vec{j}$: Current density vector (A/m^2)

μ_o : Magnetic permeability of vacuum ($\mu_o=4\pi.10^{-7}$ U.S.I)

1-D: One dimension

2-D: Two dimensions

3-D: Three dimensions

A: Magnetic potential

f : Frequency

Hz: hertz

F_e :Total field

D: Declination

$\vec{D}$: Electric displacement field

$\vec{B}$: Magnetic induction

AFMAG: Audio-frequency magnetic

AMT: Audio-Magnetotelluric

NEFB: North Equatorial Fold Belt

BE: Beguele 1

BG: Beguele 2

CC: Congo Craton

CCSZ: Central Cameroonian Shear Zone

CSAMT: Controlled Source Audio-Magnetotelluric

DC: Direct current

E: East

ENE: East North-East

FVD: First Vertical Derivative

h : Penetration depth

km: kilometre

I: Inclination

Lm: Loum

k: magnetic susceptibility

KB: Kamba

M: Magnetic field intensity

Ma: Millions of years

MT.: Magnetotelluric

N: North

NE: North-East

NNE: North North-East

NK: NKol-Afamba

nT: nanoTesla

NW: North-West

NNW: North-North-West

OS: Ossol

PAB: Panafrican Belt

R: Earth Radius

s: second

S: South

SE: South-East

SSE: South-South-East

SW: South-West

SSW: South South-West

T: Period

TDEM: Time Domain Electromagnetic Methods

v: Velocity

W: West

WSW: West South-West

WNW: West North-West

$\mathbf{X_e}$: Horizontal north,

$\mathbf{Y_e}$: Horizontal east

γ: Unit of magnetic field intensity

δe: Skin depth

ε: Permittivity

μ: Magnetic permeability

ρ : Resistivity

ρ_a : Apparent Resistivity

Ω.m: Ohm metre

σ : Conductivity

S/m: Siemens per metre

Φ : Phase

°: Degree

ω: Electromagnetic wave pulsation

rad/s: radian per second

GENERAL INTRODUCTION

"Understanding the present to explain the past", there can be the fundamental objective of geosciences, but the reconstruction of the past environments and the associated processes, based on present-days' data is challenging because these data need to be first understood in their extant context before serving as evidences of past events or environments. In this quest, geology that primarily relied only on direct observations of landforms and outcrops is now getting a more valuable support from geophysics through indirect observations of the Earth's crust or shallow subsurface. Geophysical investigation of the crust involves at or near surface measurements to assess the space-variations of its physical properties. The multiplicity of physical parameters implies the existence of various survey methods. The contribution of geophysics to geosciences spans from lithological characterisation to structures delineation and mapping with direct applications in mineral exploration, civil engineering, geology and environment.

The current study applies various geophysical methods in order to investigate subsurface structures in the Nkolafamba-Sangmelima area. Its objective is to improve the understanding of geological history of the transition zone of Central Africa with particular attention on Cameroon. Within this frame, the specific objectives are: (1) to ameliorate the geological and mineral information on south Cameroon; and (2) to propose an approach that enables to investigate an area with a juxtaposition of geophysical methods. The study area is located in south Cameroon; it encompasses both the Mobile zone represented by the Yaounde series and Mbalmayo schists (Nedelec et al., 1986; Nzenti et al., 1984a, 1988) thrusting onto the northern edge of the Congo Craton referred to as the Ntem Complex (Maurizot et al., 1986; Nedelec et al., 1990). Globally, many studies have been achieved on the Mobile zone in Cameroon. These studies revealed an E-W deep tectonic accident marking the suturing line between the Congo Craton and the Central Africa Panafrican Belt at the latitude N04° and many NE oriented structures (Manguelle Dicoum et al., 1992; Mbom-Abane, 1997; Meying et al., 2009, 2013; Tadjou et al., 2009; Ndougsa-Mbarga et al., 2010) often supposed to be Neoproterozoic or Phanerozoic. Some of these structures form the Central Cameroon Shear Zone, whose nearby known member is the Sanaga Fault (Ngako et al., 2008). Despite the disputed models proposed to explain the geodynamic setting and evolution at the northern margin of the Congo Craton (e.g. Toteu et al., 2006, 2007; Mvondo et al., 2007a; Ngako and Njonfang, 2008, 2018; Ngako et al., 2009; Mvondo-Ondoa et al., 2009; Nkoumbou et al., 2014; Tchakounté Numbem et al., 2018a, 2017, 2018b; Houketchang Bouyo, 2018), a collision involving the Congo Craton and the NEFB is commonly agreed. Since these models are mainly based on geological inputs, contributions from geophysics may help

solving that dispute by proposing a unifying model. Moreover, convergent settings in general host various deposit types; based on the present known mineral potential of southern Cameroon, addressing the issue above would enable to upgrade its significance. This study involves an integration of field geological and geophysical data. Geophysical works consist in the application of tensor audiomagnetotellurics to investigate structures in a portion of the study area; check their continuity in the remain, using aeromagnetics (the study area has been divided into two adjacent portions) and further, apply remote sensing (Landsat 8 OLI) for validation purposes over the entire study area.

This dissertation is subdivided into three chapters:

Chapter one describes firstly, the global geodynamic evolution leading to the formation and dislocation of Gondwana; summarizes the geology of Cameroon, then presents the study area. The section reviews the deformations and tectonic processes that occurred in Africa until the South Atlantic Ocean's opening in the Cretaceous. Besides, focus is given to lithological constitution and structural features encountered through a literature review of past geoscience works carried on the Mobile zone in Cameroon, out of which the research questions and the awaiting goals of the study will be defined.

The second chapter presents the *instrumentum labores* of the study. Indeed, the fundamentals and key applications of the geophysical methods as well as remote sensing used in the current study are herein presented, emphasis being given to the audiomagnetotellurics and aeromagnetics. Besides, a description of the materials and the entire work methodology is presented herein.

The third chapter initially presents progressively, the audiomagnetotelluric, aeromagnetic and remote sensing results. Secondly, these results are summarised, cross-validated (validation in-between methods) and validated with field and existing geological data along with remote sensing analyses), then discussed. Some implications to the findings are also stated.

A general conclusion ends the dissertation by outlining the main objectives, the outputs and perspectives that swamp out of the study.

CHAPTER ONE: THE LITERATURE REVIEW

INTRODUCTION

"*Understanding the present to explain the past*", that is the mission to be fulfilled by this study in Central Africa with respect to southern Cameroon. Although geophysics has become very important in geological modelling, mastering of the geological setting of a studied area remains critical. Therefore, describing the study area's geology in the framework of a regional geodynamic setting would be a vital constraint to geophysical models. This first chapter aims at presenting the regional and local settings in regards of the recent geoscience literature, starting from the Precambrian evolution of the to induct readers with global tectonics.

1.1. GEODYNAMICS FROM PRECAMBRIAN TO THE PHANEROZOIC AGES

The Precambrian history is documented on all the actual continents though the events are not everywhere of the same ages. This matches two main eras, the Archaean and the Proterozoic.

1.1.1. The Archaean evolution (3800-2500 Ma)

1.1.1.1. The Archaean evolution: general facts

The Archaean in one sense, is the timeframe of first amalgamation processes of lithospheric fragments and terrains accretions (Scotese, 2009; Weckmann, 2012; Heine et al., 2013; Piper, 2013; Pérez-Díaz and Eagles, 2014) leading to the formation of major Precambrian plates and continents such as the Congo continent (Meert and Powell, 2001; Scotese 2009). Before the amalgamations, great terrain accretions led to the increase of the earth crust budget. The Archaean continental crust accretions occurred at various ages. The Pilbara Craton in Australia, formed at ca 3800 Ma, provides a good example of oldest Archaean terrains. The formation of continental crust nuclei and their subsequent accretion are the witnesses of many Archaean orogenies e.g. the Superior Province formed at ca 2740-2640 Ma, resulted from the accretion of many 3100 Ma to 2670 Ma continental blocks to form the largest Archaean cratons.

In the midst of theories on the mechanisms of the Archean tectonics, the first emerging ideology relates plate amalgamation origines to present-days'style subduction tectonics (e.g. Kato and Nakamura, 2003; Fumes et al., 2007; references therein) while the second ideology controversially favours plume-dominated and crustal delamination processes during vertical motions (Foley *et al.* 2003, references therein). However, recent studies (e.g. Moyen and Hunen, 2012; Roberts et al., 2015; Vezinet et al., 2018) confirm hypothetically short-lived subduction

processes to pertain on Archaean tectonics; i.e. arc magmatism dominantly contributed to the increase of the crust's budget. In addition, both schools agree on the existence of prior lithospheric blocks whose amalgamation formed continental landmasses after various tangential or vertical movements during several extension and compression episodes (e.g.Cawood et al., 2006b, 2016; de Wit et al., 2008), *as per* the Wilson cycle concept. Restricting the explanation of tectonics in these terms can be misguiding. The process implies alternative openings and closures of paleo-oceans along weakness zones between the landmasses where earth materials constantly rejuvenate and experience rifting.

1.1.1.2. The Archaean evolution of Central Africa

Africa Plate present-day look results only from recent tectonic activities as Archaean geodynamics essentially led to the formation between ca 3800-2550 Ma (Neoarchean to paleo Proterozoic), of the seven cratons which frame it. These continental nuclei are the Man shield, the Reguibat shield, the Sahara Metacraton, the Kaapvaal Craton, the Zimbabwe Craton, the Tanzania Craton and the Congo Craton (van Hinsbergen et al., 2011). Further some of these blocks merged to form three major cratons referred to as the West Africa, Central Africa (Congo-Tanzania) and Southern Africa (Zimbabwe-Kaapvaal) Cratons (Dirks et al., 2008).

The Congo-Tanzania Craton is a region of pre 2500 Ma continental crust located in Central Africa, which resulted from the amalgamation of the Tanzania and the Congo Cratons (van Hinsbergen et al., 2011). The Congo Craton particularly, is formed by many blocks which the Kasai block in NE Angola and S DR Congo; the Congo block in W-Uganda and NE-DR Congo and the Chaillu-Gabon block. The Chaillu-Gabon craton underlies SW-Equatorial Guinea, Gabon, Congo and S-Cameroon, where it is referred to as the Ntem Complex (e.g. Nedelec et al., 1990). Feybesse et al. (1998) describe this block as made up of ca 3190-3120 Ma (Mesoarchean) rocks affected by high-grade metamorphisms. These are post-associated by calk-alkaline tonalites and granites, felsic volcanics and ultrabasic rocks before the stabilisation of the block in Neoarchean, similarly to other major African cratons.

The available records infer many orogenic cycles and the setting of structures affecting the Earth's crusts; all these witnessed in many present-days continents. In Africa, a ca 2600-2500 Ma orogenic cycle (Neoarchean), the Liberian orogeny, reported by several authors (e.g. (Tchameni 1997; Shang *et al.* 2010; references therein), probably marks the transition to the Proterozoic in the Ntem Complex. In fine, the Archaean evolution mainly corresponds to continental crust's formation. Indeed, most of the continental crust budget balance was realised

through this period; this is particularly the case of the nuclei of the actual continents: the shields or Cratons. However, the amazing history was not yet to end with the Archaean.

1.1.2. The Proterozoic evolution

The Proterozoic, subdivided into three periods: The Paleoproterozoic (2600-1800 Ma), the Mesoproterozoic (1800-1000 Ma) and the Neoproterozoic (1000-540 Ma); is the most known Precambrian eon in the earth's geologic evolution saga. It provides a wide interval (ca 2060 Ma) of long and everlasting geodynamic and tectonic processes dominated by the making and demaking of supercontinents (de Wit et al., 2008; Weckmann, 2012; Fairhead et al., 2013a) leading to the actual continents.

1.1.2.1. The Paleo-Mesoproterozoic evolution

a. The pre-Neoproterozoic evolution: the global view

The evolution of supercontinents is the essential of the pre-Neoproterozoic history thanks to its link with the major accretionary events, continental crust augmentation and orogenic cycles. Herein, one psrticular supercontinent history requires some attention. In the late Mesoproterozoic, following the breakup of the Columbia Paleoproterozoic supercontinent (Scotese 2009), the Congo continent and the Rodinia supercontinent constituted the essential of the earth's landmasses. According to Scotese (2009), the Congo continent was constituted by the Congo-Sao Francisco Craton and the Sahara shield minus the West African Craton and the Hijaz island arcs (Sudan, Egypt and Arabia). Besides, in its final configuration, the Rodinia had two halves, the North Rodinia and South Rodinia (Rowell et al., 1993; Pisarevsky et al., 2003a; Zhao et al., 2006; Cawood et al., 2016a). North-Rodinia was constituted by East Gondwana, Cimmeria, Sibumasu and Kalahari/Mozambique (including East Arabia) Cratons; while. South-Rodinia comprised the Laurentia, Amazonia, Siberia, West Africa and Baltica Cratons (J Brendan Murphy and Nance, 1991; Meert and Powell, 2001; Schettino and Scotese, 2005; Cawood et al., 2007; Moulin et al., 2010; Heine et al., 2013; Pérez-Díaz and Eagles, 2014). The Grenville orogeny ended the formation of the Rodinia or *mother of all continents* at ca 1100 Ma (Piper, 2000; Schettino and Scotese, 2005; Li et al., 2008; Liu et al., 2015).

The paleoenvironment reconstruction by Scotese (2009) puts the Congo continent west from Rodinia, beyond the Pharusian/Mozambique paleo-ocean to the north, and the Adamastor (Panafrican) paleo-ocean to the south. This assumed the existence of a circum-Congo continuous subduction zone (The connection of the Mozambique Belt and the Pharusian–Adamastor subduction zones formed a continuous zone surrounding the Congo continent (Scotese et al., 1999) which played a major role in the geodynamic evolution of the Rodinia, by forcing its

convergence towards the Congo continent, so, causing the Panafrican thermo-tectonic event (Stewart, 2007). Scotese et al. (1999), Stewart (2007) and Scotese (2009); including references, provide comprehensive information about the supercontinents' evolution from Rodinia to modern continents.

The pre-Neoproterozoic evolution acknowledged many orogenies and riftings. Some of the resulting faults were probably related to the relaxation and earth's compensation after magmatic upwells. Examples of Paleo- to Mesoproterozoic orogenic systems are the Svecofennian system in Europe, the Trans-Hudson and the Grenville systems in North America and the Eburnean and the Kibaran systems in Africa.

b. Pre-Neoproterozoic activity in Africa

In Africa, the Eburnean and Kibaran orogeneses are the main orogenic cycles characterising the pre-Neoproterozoic period: The Eburnean occurring in the Paleoproterozoic (ca 2200-2000 Ma), met the growth and stabilisation of West Africa Craton (Ennih and Liégeois, 2008). Alongside, the Congo and Tanzania Cratons merged into Central Africa Craton along with passive margin development and orogeny at the west margin of the central and southern Africa cratons (Fernandez-Alonso et al., 2010).

The Kibaran event occurred in Mesoproterozoic, after the convergence of the Central Africa Craton to the north toward the southern Africa Craton between 1400 and 1000 Ma (Tack et al., 2008). Coeval formations have been reported in SE DR Congo, SW Nigeria and Cameroon (Ennih and Liégeois, 2008). The end of the Kibaran (ca 1000 Ma) corresponds to the final individualisation of the Congo continent and the development of a circum-Congo subduction zone that triggered the Congo continent / Rodinia collision.

1.1.2.2. The Neoproterozoic evolution

a. The global geodynamic evolution: The Pannotia supercontinent

The Neoproterozoic is characterised by the formation of the greater Gondwana supercontinent from 800 to 542 Ma (Cawood et al., 2001, 2007, 2016). The greater Gondwana or Pannotia (Dalziel, 1997) resulted from the suturing of continental blocks derived from Rodinia breakup. Scotese (2009) suggested that the collision of the Congo continental block with Rodinia triggered that breakup (**Figure 1.1-1**). The driving force of this process was generated by the circum-Congo subduction zone that forced the convergence of Rodinia onto the Congo continent. Fernandez-Alonso et al. (2010) assumed that the collision of the Central Africa (Congo) continent and the Kalahari Craton (Kibaran orogeny) is the premise in the Mesoproterozoic of the Rodinia/Congo continent's collision. As summarised in Scotese (2009), once the Congo continent collided and sutured with Rodinia (800-750 Ma), the former

continuous circum-Congo subduction zone divided by two. This led to the creation of the north (Hijaz-Mozambique) and the south (Pharusian-Adamastor) subduction zones at the rims of Congo. The differential plate tectonic stress created consequently tore Rodinia into two halves (N-Rodinia and S-Rodinia) and finally splited and dismembered it.

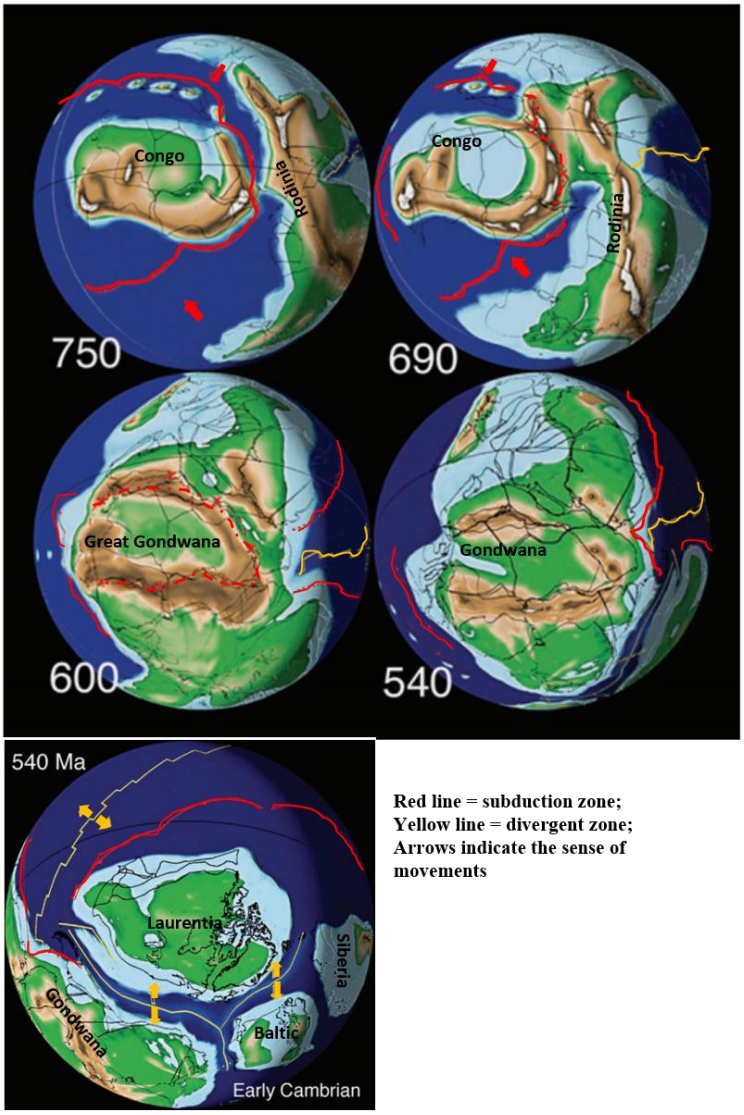

Figure 1.1-1 : Graphical summary of the Neoproterozoic evolution (Scotese, 2009)

The forces generated by the two formed subduction zones at the rims of Congo caused an anticlockwise of N-Rodinia toward the Hijaz-Mozambique subduction zone, leading to the formation of Mozambique belt as a consequence of progressive accretion of Hijaz arc shields north of the continent. Similarly, S-Rodinia rotated (**Figure 1.1-1**) clockwise, N-converging toward S-Congo. This caused the closure of the Adamastor Ocean and the formation of the Panthalassa rift (which later evolved into the Panthalassa Ocean). From this diachronous rotation of the Rodinia halves against Congo continent resulted the amalgamation of Pannotia at ca 600-540 Ma (Piper, 2000). This placed the Congo continent at the core of Pannotia (Cawood et al.,

2001, 2007; Scotese, 2009; and references therein). The final suturing of Pannotia around 540 Ma characterises the end of the Neoproterozoic era; but soon after its amalgamation, Pannotia broke-up into four main continents: Baltic, Gondwana, Laurentia and Siberia (Cocks and Torsvik, 2002, references therein) in the early Cambrian.

b. The Panafrican orogeny: definitions

The term 'Panafrican' initially, defined a system of orogenic belts mainly reported in Africa, Brazil and Eastern Antarctica that were formed during ca 540 Ma ago. The concept was then extended to describe tectonic, magmatic, and metamorphic activities the crust that was once part of Gondwana from Neoproterozoic to earliest Paleozoic age (Kröner and Stern, 2004), resulting in two main types of constructions. The first type consisted of predominantly Neoproterozoic supracrustal and magmatic assemblages, many of juvenile origin, with structural and metamorphic geneses that are similar to those in the Phanerozoic collision and accretion belts. The second type consisted of polydeformed high-grade metamorphic assemblages, exposing middle to lower crustal levels, whose origin, environment of formation and structural evolution are more difficult to reconstruct.

The Panafrican orogenic cycle corresponds to the Rodinia/Congo continent collision, then the breakup of Rodinia and the final amalgamation and suturing, from late Neoproterozoic to early Phanerozoic, of Pannotia or greater Gondwana (Spalletti et al., 2010; Piper, 2013).

c. The Panafrican system in Central Africa

The Panafrican system, sometimes referred to as North Equatorial Fold Belt (Nzenti et al., 1988, references therein) covers in Central Africa Cameroon, Chad and the Central African Republic; and the south western part of Nigeria known as the Ife–Ilesha schist belt (Caby and Boesse, 2001). According to Abdelsalam et al. (2002), the North Equatorial Fold Belt represents an E-W orogene that marks the suture between the Sahara Metacraton and the Congo Craton (CC). The Panafrican episode in Central Africa is represented by rejuvenated magmatic and metamorphic rocks (essentially migmatites and granites) originating from several Precambrian epochs (Ngako et al., 1991; Penaye et al., 1993).

Southwards in Cameroon, Ngako et al. (2008) described three main geotectonic units within the Panafrican concept:

- The Poli Group corresponding to an early Neoproterozoic back-arc basin formed between 830 and 665 Ma (Ngako, 1986; Toteu et al., 2006b), that includes: detrital and volcanoclastic deposits, metavolcanics (tholeitic basalts and calk-alkaline rhyolites), and pre-, syn- to late-tectonic calk-alkaline intrusions (diorites, granodiorites and granites) emplaced between 660 and 580 Ma (Toteu et al., 1987, 2001).

- The Adamawa domain including huge Panafrican batholiths and large scale Paleoproterozoic remnants that were metamorphosed during the Panafrican event (Toteu et al., 2001; Tchakounté Numbem et al., 2017).

- The Yaoundé Group comprising the Mbalmayo-Bengbis, the Ayos and the Yaoundé series (Nedelec et al., 1986; Mvondo et al., 2007c), is represented by a syntectonic basin and a Neoproterozoic belt.

1.1.3. The Phanerozoic evolution

1.1.3.1. The geological evolution of Gondwana

The Phanerozoic eon, also called "Cambrian explosion" by several authors (e.g. Meert and Libermann 2004, 2007; Canfield et al., 2007), is related to the development and diversification of life on Earth. Additionally, this corresponds to the period through which the final resurfacing processes of the planet took place yielding what we see nowadays. Indeed, the Panafrican events caused the split of Rodinia, then the amalgamation of Pannotia from late Neoproterozoic to early Phanerozoic followed by short after with ist break up into four major landmasses including the Gondwana in the early Cambrian (Spalletti et al., 2010; Piper, 2013).

The Gondwana comprises the West-Gondwana (South-America, Africa) and East-Gondwana (Australia, East-Antarctica, India). Despite its blurry absolute age, the suture between West and East Gondwana was defined along the East African Orogen (Meert and Lieberman 2008, references therein). Studies by Dirks et al. (2008) revealed that the Hercinian orogeny between 450-250 Ma at the NW and S margins of the African plate; and the ongoing Alpine orogeny caused by the subduction of Africa beneath the Eurasia plate.

1.1.3.2. The African rifts and shear zones: imprints of the post-Panafrican evolution

Collisional or divergent orogenic systems are both accompanied by the setting of brittle structures, generally shear zones and faults or joins characterising either compressional or extensional environments (Masterton et al., 2012). The well documented African rifts and shear zones are the East African (EARS), the West African (WARS) and the Central Africa Rift Systems (CARS). These features are mainly related to stress accommodation in the African plate during the Cretaceous-Albian evolution (Fairhead, 2009; Masterton et al., 2012; Fairhead et al., 2013a) characterised by the growth of the Atlantic Ocean and the individualisation of the Somalian plate. These rifts systems probably developed along earlier weakness zones between major shields that constitute the African plate. Illustratively, the CARS formed in pre-Panafrican extensional setting (Vicat and Moloto-a-Kenguemba, 2001). The development of these lineaments had enabled to consider the African plate as subdivided in sub-plates (NW-Africa, S-

Africa and E-Africa) which are allowed to move relative to each other, rather than a rigid plate; making it possible for intra-plate deformations to occur within Africa (Masterton et al., 2012).

Amongst the regional lineaments above mentioned, the WARS and the CARS are of great importance for this study. According to Fairhead (2009) and Fairhead et al. (2013), they form a unique system, the West Central Africa Rift System (WCARS) which constitutes the sub-plate boundary between NW Africa and S Africa. The WCARS runs from the Atlantic to the Indian oceans throughout the Central Africa, including Cameroon, hence its importance to this study. Additional details on African rift systems in de Wit et al. (2008).

1.2. PRESENTATION OF THE STUDY AREA AND RESEARCH QUESTION

1.2.1. Summary of Cameroon's geology

1.2.1.1. Lithology

Cameroon is constituted of a basement complex and superficial terrains.

a. The basement or basal complex

The basal complex is essentially made up of Precambrian magmatic and metamorphic rocks rejuvenated during the Panafrican orogeny (Penaye et al., 1993; Mvondo et al., 2007c; Olinga et al., 2010). It is composed of metamorphosed and granitised rocks that form the metamorphic complex (gneisses, quartzites, migmatites and charnockites), and platforms formations. Oldest basement units represent the Cameroonian part of the Congo Craton (CC) in the south (Regnoult, 1986).

b. The superficial terrains

Superficial terrains include volcanic formations and a sedimentary overburden. The sedimentary overburden is represented in the north and south respectively, by Cainozoic and Mesozoic rocks, and recent sedimentary layers like the lower Cretaceous sedimentary formations of the Benue trough, the Mamfé and Bida Gulfs (Genik, 1992). The sedimentary overburden lies on the Precambrian basement. The volcanic formations are represented by volcanic structures related to the Cameroon Volcanic Line. They include some cambro-ordovician (550-500 Ma) plutons and younger granites locally called hossérés (Nyoré, Gouna, Peské, etc.) which belong to the Adamaoua basement (Regnoult, 1986). The trachybasalts of Mount Cameroon prove the ongoing volcanism ignited in the late Eocene (Bessoles and Lasserre, 1977).

The Cameroon's territory is generally divided into three structural domains: the southern, the central and the northern domains (**Figure.1.2-1**). The southern domain corresponds to the CC or Ntem Complex. It is a set of formations which are assumed to have not been affected by the Panafrican thermo-tectonic event (Meying 2011, references therein). The central and northern domains correspond to the North Equatorial Fold Belt (NEFB), an E-W orogenic zone made up

of terrains which have been rejuvenated during the Panafrican episode, which extends to the east in Sudan (Ngako et al., 1991; Rolin, 1992, 1995) and to the west in NE-Brazil (van Schmus et al., 2008).

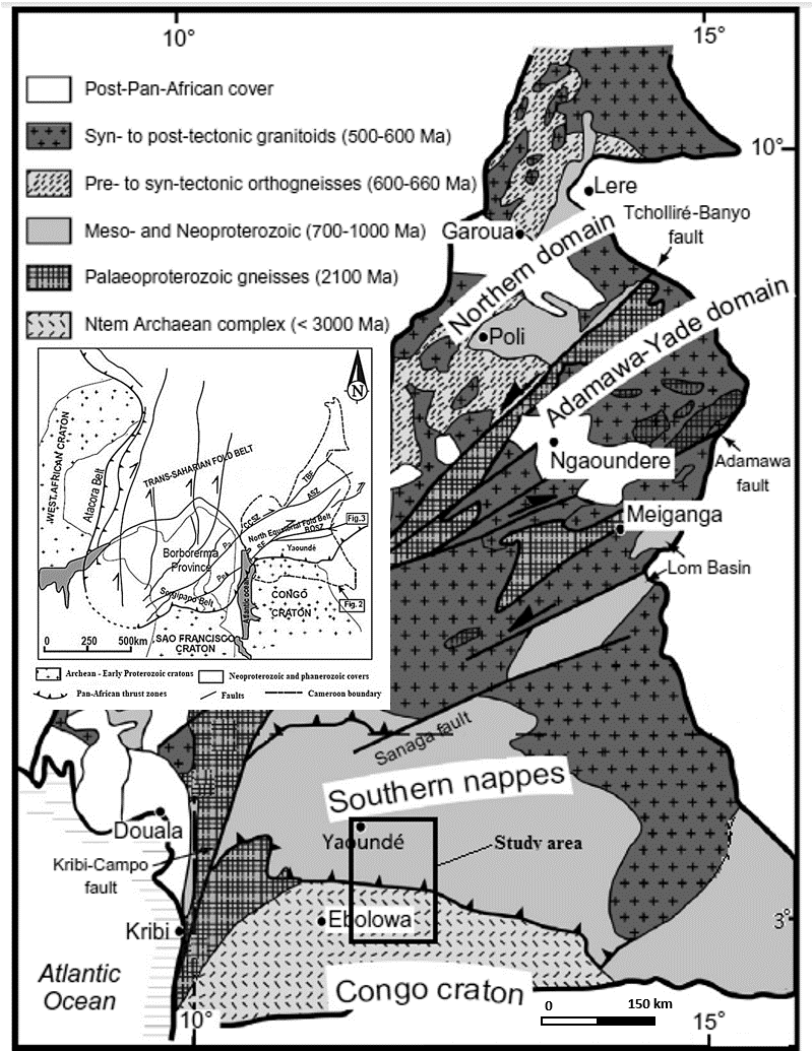

Figure 1.2-1 : Geological map of Cameroon (Toteu et al., 2001, modified)

1.2.1.2. Tectonic history

The tectonic history in the Mobile zone is more documented in the Panafrican chain than in the Craton which was hitherto assumed steady. At the regional scale, Mobile zones underwent at least three main deformation stages termed D1 to D2 which differ respectively in the north and the south of the Panafrican domain as revealed by Ngako et al. (2003) and Olinga et al. (2010). According to Ngako *et al.* (2006) and Olinga et al. (2010), the D1 stage is associated to a W and SW complex overthrust affecting the Eburnean bedrock in the north, while it occurs in the southern edge without any tangential deformation with an indefinite regional significance. The D2 stage occurs in the south with tangential tectonics marked by the setting up of the Yaoundé nappe oriented south towards the CC. Meanwhile, this stage in north is marked by N-S to E-W

en echelon or right folds and overfolds related to senestrial strike-slips which are transposed by a D3 stage marked by dextral strike-slips and shear movements along the Central Cameroon Shear Zone (Ngako et al., 1991, 2003; Njonfang et al., 2008; Olinga et al., 2010).

1.2.2. Presentation of the study area

1.2.2.1. Physiography

The study area stretches from the E11°30' to E12°15' longitudes; and, the N02°45' to N04°00' latitudes (**Figure 1 2-2**). This corresponds to an average area of 11,551 km^2. The study area spans over the Centre and the South Regions; and four (04) administrative divisions. The main localities are Yaoundé, Mbalmayo, Mfou, Nkolafamba, Metet, Sangmelima and Zoetele. There are many paved and unpaved roads that cross the entire area.

The area belongs to the south Cameroon plateau. Its global flat topography raises between 600 and 700 m with some peaks from 900 to 1000 m observed around Yaoundé where they form rounded hills stretching in the E-W direction. The climate is equatorial with four seasons (two dryers and two rainy). The temperature rate and annual average rainfall are 24°C and 1480 mm, respectively. The tropical vegetation is always green but presents a deterioration facies in the northern part of the study area while it is denser to the south.

The hydrographical system is dominated by the Nyong River (the main collector) which flows nearly NE-SW to ENE-WSW. Its main tributaries are Ato'o and So'o Rivers, respectively in the north and the south banks, fed up by many streams. In the south, the main river is Lobo, a tributary of Dja. The drainage is generally dendritic, but sometimes locally trellis or radial.

1.2.2.2. Geological context

The lithology of the study area is dominated by the North Equatorial Fold Belt (NEFB) and the Congo Craton (CC) formations, hereafter detailed, northwards (**Figure 1.2-2**).

a. Lithology

The NEFB in the study area is represented by the Yaounde and Mbalmayo series.

i). The Yaounde series

The Yaounde series (YS) forms the basal complex of the northern half of the study area. It is made up of old granitised and metamorphosed sediments in the high pressure granulite facies (Nkoumbou et al., 2014; references therein). Initially seen as the heart of the Panafrican thrust (Nedelec et al., 1986; Nzenti et al., 1988), its rock assemblage includes migmatites (dominant) mainly represented by garnetiferous and migmatised gneisses; and ectinites represented by gneisses associated to micaschists (Champetier de Ribes and Aubague, 1956). These formations are hereafter described.

- ***Gneisses associated with micaschists:***

- *Garnetiferous micaschists:*

They are foliated, made up of quartz, biotite, muscovite and garnets (commonly almandine), with few types of feldspar. They present some quartzite breaks containing muscovite and some garnets (Champetier de Ribes and Aubague, 1956).

- *Micaschist garnetiferous gneisses with two micas*

They contain more feldspars than those above. They are made up of oligoclases, biotite, muscovite, garnets and kyanite. They are fine grained with some biotite and muscovite rich quartzite breaks.

- ***Garnetiferous and migmatised gneisses***

- *Migmatised garnetiferous micaschists*

Their main pattern is the presence of coarse K-feldspars crystals inside micaschists and the development of pegmatite lenses.

- *Two micas embrechites or with biotite solely*

They are dominant, dense and banded. They are made up of: (1)- a framework composed of biotite, quartz and garnets soaked up with feldspars (microcline, oligoclase and albite) and kyanite; (2)- Drift lenses or veins made up of fine grained biotite, garnets and quartz grains elongated in the schistosity strike (Olinga et al., 2010; references therein). Beside the above described formations, there are many mica-quartzite formations that are encountered both in ectinites and migmatites. The economic minerals present are graphite and titanium iron oxides.

ii). The Mbalmayo series

The Mbalmayo series (MS) is the southernmost member of the YG (**Figure 1.2-2**). The MS lays discordant onto the CC and possibly corresponds to the sole of the Yaounde nappe which was exhumed after the collision and thrust of YG onto the CC (Toteu et al., 2004; Olinga et al., 2010). It outcrops as flattened domes without any vegetation in Mbalmayo and Metet. The MS formations are schists and quartz-sericite which slightly dip to the east and rest discordant to gneisses and embrechites; and some volcanic relics reported in Metet (Maurizot et al., 1986; Regnoult, 1986). Its mineralogy is mainly quartz, chlorite, tourmaline, zircon and iron oxides.

To sum up, the Yaounde domain corresponds to a vast anticlinorium where pelitic and volcanoclastic sediments were deposited, recrystallized and thrust onto the Congo Craton (Toteu et al., 2001; Olinga et al., 2010; Ngnotue et al., 2012a; Nkoumbou et al., 2014).

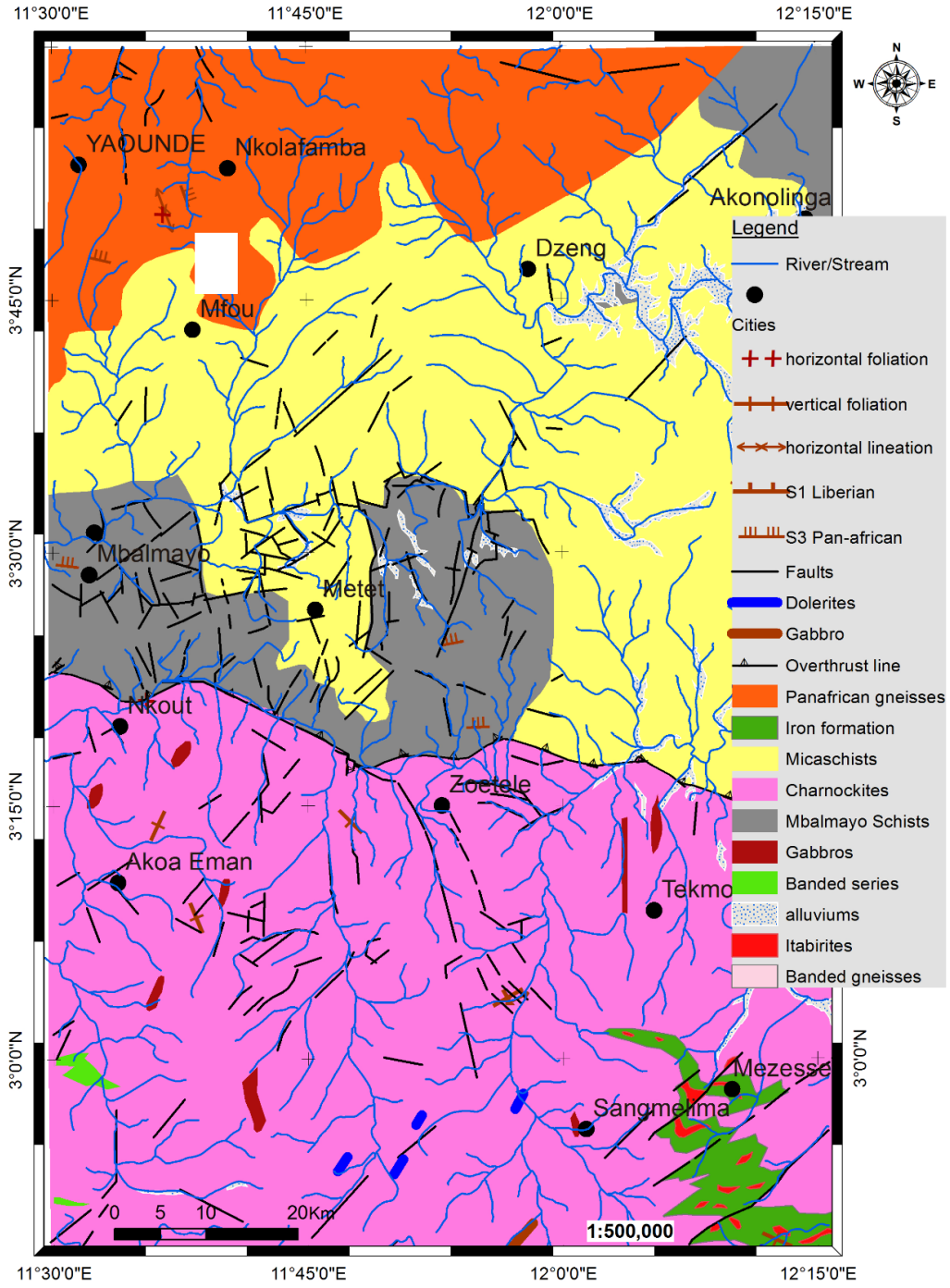

Figure 1.2-2 : Geological map of the study area (Maurizot, 1986 modified).

iii). The Congo Craton (CC)

The Congo Craton (CC) or Ntem complex seats in the southern part of the study area (**Figure 1.2-2**); its formations mainly result from a magmatic activity that ended in the Eburnean (Meso-Proterozoic). According to the geological studies, the main rock budget of the Ntem complex is formed by tonalite-tronghemite-granodiorite (TTG) and K-rich granitoids (Shang et al., 2007, 2010; Tchameni et al., 2010; references therein). Members of the TTG suite include charnockitic rocks, tonalites and granodiorites (Shang et al., 2004a). The tonalitic suite (early

known as Soo granites) essentially exposed to the north, is strongly mylonitized and retrogressed along the fault boundary with the NEFB, while granodioritic suite massifs form distinct bodies within the dominantly charnockitic southern zone (Nedelec et al., 1993; Shang et al., 2004a, 2004b; references therein). Charnockites crop out as xenoliths within TTG massifs and TTG-type veins also occurring charnockite massifs thus portraying relative chronology for these granitoids. Exposures of supracrustal rocks (banded iron formations, sillimanite-bearing paragneisses, garnet bearing amphibolites and pyroxenites) representing ca. 3100 Ma greenstone belts remnants are also present (Maurizot et al., 1986; Tchameni et al., 2004). Late- to post-tectonic granitoids and calc-alkaline to alkaline syenites which clearly postdate the major crust forming episode intrude the TTG (Nedelec et al., 1990; Tchameni et al., 2000, 2001; Shang et al., 2004a, 2007). Meanwhile, the magmatic activity contributing to the crust budget in the Ntem complex is witnessed by post-Archean doleritic dykes affected by Eburnean (2050 Ma) high-grade metamorphism (Toteu et al., 1994; Vicat and Moloto-a-Kenguemba, 2001).

b. Tectonics

The belonging of the study area to both the NEFB and the CC, imposes a description of tectonics as per domain.

i). Tectonics in the Panafrican domain

The evolution of the Yaounde basin and the its subsequent formations has been described by various models which are sometimes anatagonists; but globally, the deformations affecting the Panafrican domain in Cameroon are aged from the late Meso- to post Neoproterozoic. According to Ngako and Njonfang, (2011), that evolution started with a back-arc development which resulted in the opening of the Yaounde basin at the northern margin of the CC, which was later affected and shaped by that four events. The NEFB evolution involved (i) subduction and back-arc basin and range setting to the north of the CC (1000–640 Ma); (ii) collision leading to thickening, emplacement of early nappes (e.g. Yaounde and Bafia groups) and high-pressure granulite-facies metamorphism (640–630 Ma); (iii) protracted crustal shortening with migmatisation and exhumation of the southern metasediments (Yaounde granulites) in ca. 600 Ma; and (iv) conjugate wrench movements associated to delamination of the lithospheric mantle (585–570 Ma) leading to dextral shearing and widespread granitisation (CCSZ, Adamawa granitoids). Extensional tectonics at northern margin of the CC have been confirmed by many recent studies (e.g. Ngnotue et al., 2012; Nkoumbou et al., 2014; Tchakounté Numbem et al., 2017) despite their different implications on the evolution of the NEFB/CC transition zone.

The literature on the YS reveals that its position as a sheet on the northern edge of the CC resulted from sub-horizontal tangential deformations (Nzenti et al., 1988; Ngako et al., 2008a;

references therein). Detailed studies (Mvondo et al., 2003, 2007c; Olinga et al., 2010; Mbola-Ndzana et al., 2014) around Yaounde show that the textures of rocks correlate with four deformation stages. The D1 event preceding the calc-alkaline diorites mineralization is responsible of the nappe formation that led to the granulitic metamorphism of soft sediments. These nappes were reprinted during symmetrical extension D2 (that generated flat regional textures), probably associated to large scale foliation boudinages, gneissic domes formation, and intensive sub-superficial magmatic deposits. These formations were after upraised by unclassified D3 and D4 folding, defining a vertical constriction accompanied by an E-W to NW-SE major narrowing colinear to that of the D1 stage of thrust nappes piling. Olinga et al., (2010) summarised tectonics into alternative E-W to NW-SE contractions and N-S to NE-SW parallel orogenic stretches; all charactyerised by the thrusting of the Yaounde nappe onto the CC; and strike-slip shears in ductile to brittle-ductile conditions (characterized by N or S dipping penetrative foliation), an associated E-W to NW-SE stretching lineation and N-S to NE-SW folding due to the Trans-saharan collision.

ii). Tectonics in the Ntem Complex

The Ntem complex is mix-up of 3200-1800 Ma terrains evolving at the NW margin of the CC (Lasserre and Soba, 1976; Toteu et al., 1994) which recorded several tectonic events in the Archaean, the Paleoproterozoic and Neoproterozoic eras. The Archaean evolution mainly dominated by the Liberian orogeny (Lasserre and Soba, 1976) witnessed the development of greenstone belts and late diapiric intrusions of charnokitic (or not) TTG (Regnoult, 1986) and late anatexite K-granitoids (Tchameni, 1997). Structural events correspond to syn-metamorphic deformation D1-M1 characterised by E-W subvertical foliation and structures (Tchameni, 1997; Shang et al., 2001) associated with high to low-grade metamorphism (Takam et al., 2009).

The Eburnean orogeny mainly characterises the Paleo-Proterozoic of the CC (Toteu et al., 1994; Tchameni, 1997). This event corresponded to the emplacement of alkaline syenites and dolerites; and the prevalence of a D2-M2 deformation associated to a prograde metamorphism from amphibolite to granulite facies at ca. 2050 Ma (Tchameni et al., 2000, 2001). The deformations are characterised by the development of NNE-SSW lineaments (including dextral or sinistral shear zones) NW (**Figure 1.2-1**) of the Ntem complex (Lerouge et al., 2006; Shang et al., 2007; references therein) probably reactivated during the Panafrican episode. Penaye et al., (2004) linked the Eburnean corresponds to the Sao-Francisco-Congo collision. In opposition to the previous, the Neoproterozoic cycle is very diffuse in the Ntem complex albeit the records near the contact zone with the Yaounde Group (**Figure 1.2-2**). Some studies (Toteu et al., 1994;

Vicat et al., 1998) related it to the emplacement of dolerites at ca 1000 Ma, nepheline syenites around 570 Ma and a low grade metamorphism.

c. Synthesis of the geological evolution of the study area

Without timing investigations, Maurizot et al., (1986) highlighted N-S, NE-SW, E-W and NNW-SSE (**Figure 1.2-2**) lineaments corresponding to faults and strike-slips, in the Ntem complex. More recently, Akame et al., (2013) evidenced NE dolerite dykes; N-S to NNW-SSE and NNE-SSW sinistral shears affecting the granodiorites near Sangmelima. These features show that the Ntem complex is mostly affected by brittle tectonics. The Yaounde Group besides, underwent both ductile and brittle-ductile tectonics dominated by syn to post-Panafrican overprints. The major structural directions displayed are NE-SW to NNE-SSW, NW-SE to NNW-SSE, E-W to ESE-WNW and N-S. Among these, the NE-SW to NNE-SSW and E-W to ESE-WNW directions are related to strike-slips and wrench movements resulting from alternative compressions and orogenic stretches (Olinga et al., 2010; Mbola-Ndzana et al., 2014). Thus, the study area underwent a multistage tectonics activity causing the development of several structural features including foliation, faults and fractures which have been permanently overprinted or reactivated, from the Archaean to the Precambrian, as previously described. In regards with the global tectonics pertaining in the Mesozoic, changes in the African plate movements induced new stress/strain conditions. The accommodation to these led to the reactivation of many faults (Kirkpatrick et al., 2013; Katumwehe et al., 2015) and the development of the CARS, a member of the regional WCARS (Fairhead, 2009; Gaina et al., 2013; Heine et al., 2013). The NEFB accommodates well with the rift's development (see the CCSZ) contrarily to the CC which broke up again at ca. 140 Ma (Pérez-Díaz and Eagles, 2014).

1.2.2.3. Geophysical data

Inactive in early geoscience studies, geophysical investigations have significantly improved the geological information in Cameroon during the last two decades. Many of these studies concern the CC/NEFB transition zone which encompasses our study area.

a. Gravity studies

The gravity is the most ancient and widely used geophysical method for geological investigation in Cameroon. Analysis of heritage gravity data (Collignon, 1968) revealed an E-W zone characterised by strong anomaly gradients in the Akonolinga/Ayos/Nguelemendouka/Abong-Mbang area; interpreted around latitude N04 by Mbom-Abane, (1997) as a major E-W tectonic accident corresponding to the CC/NEFB limit; and in the Mengueme/Abong-Mbang area as an E-W normal fault (Ndougsa Mbarga et al., 2003). These was confirmed by Shandini et al., (2010, 2011) and Basseka et al., (2011) who

further highlighted NE-SW and NW-SE basement lineaments related to faulting at the northern edge of the CC as a consequence of a continent-continent collision (Shandini and Tadjou, 2012; Zanga-Amougou et al., 2013) involving the NEFB and the CC. Additional contributions (Owona Angue et al., 2013) highlighted N-S to NNE-SSW faults (Kribi Fault System) that limit the CC to the west in south-western Cameroon.

b. Magnetic studies

The initial studies involving magnetics realised in Cameroon used of airborne data collected in years 70s. The preliminary interpretation of the related maps over south Cameroon by Paterson Grant and Watson Ltd (1976) revealed minor magnetic anomalies attributed to metamorphic structures. The reinterpretation of some of these aeromagnetic maps by Feumoe et al. (2012) and Feumoe (2014) demonstrated the south extension of the Panafrican formations below latitude N03 and they highlighted WNW-ESE and ENE-WSW lineaments that affect both the CC and the Panafrican in the area. Additional studies in the same area (Ndougsa-Mbarga et al., 2012) imaged ENE-WSW and NE-SW buried Eburnean faults in the CC basement reactivated during the initiation of the CCSZ. Assembe et al. (in preparation) through a local study, correlate these results and associate faulting to collapse of basement below both the Mbalmayo series and the Sôo granites (Ntem complex) in the Yaounde-Sangmelima region.

c. Resistivity studies

The resistivity studies carried out for structural purposes involved mainly Magnetotellurics (MT). Indeed, MT revealed in the Akono outskirts, the NEFB's thrust line onto the CC corresponding to the Eseka-dja faults line (Manguelle-Dicoum, 1988) and a major E-W trending lineament corresponding to the CC/NEFB boundary and secondary ENE-WSW to NNW-SSE lineaments at Ayos, in the southern edge of the NEFB (Manguelle-Dicoum et al., 1992). Later, Tadjou et al., (2008) confirmed the interpretation of the E-W lineament as the CC/NEFB boundary and additionally inferred subsidence within the basement, associated with intrusions of low resistive materials beneath the NEFB domain in the Abong-Mbang/Akonolinga area, east from our study area. Recent applications of audiomagnetotellurics in the CC/NEFB transition zone confirmed the E-W CC/NEFB boundary and associated it to some faults, while theys related the NNW-SSE to ENE-WSW faults to post-collision tectonics (Meying et al., 2009, 2013; Ndougsa-Mbarga et al., 2010) including imprints of active extensional movements in the Yaounde series.

d. Remote sensing studies

A recent use of satellite remote sensing in the region by Akame et al. (2013, 2014) detailed many N-S to NNW-SSE and NNE-SSW fractures and faults that affected the Ntem Complex basement around Sangmelima (south Cameroon). The same technique was used by Teikeu et al. (2016) in the Yaoundé area to map N-S, NW–SE and NE–SW post-orogenic relaxation fractures in Panafrican basement of the Neoproterozoic Yaounde series to north, aligned with those in the Archaean domain to the south (Akame et al., 2013, 2014).

1.3. RESEARCH QUESTION AND INTERESTS

1.3.1. Research question and study objectives

1.3.1.1. Research question

Past and recent studies reveal a multi-staged evolution at the northern margin of the Congo Craton, including its flanking NEFB. Despite the various attempts to explain that evolution, divergences in the proposed explanatory geodynamic model (Penaye et al., 1993; Ngnotue et al., 2012, 2000; Mvondo et al., 2003, 2007a, 2007b, 2009; Pouclet et al., 2006; Toteu et al., 2006a, 2007; Ngako and Njonfang, 2008, 2011, 2018; Mbola-Ndzana et al., 2014; Nkoumbou et al., 2014; Tchakounté Numbem et al., 2017, 2018a, 2018b; Houketchang Bouyo, 2018) maintain the issue unsolved, especially in regards with the recent advances in defining the pre-Neoproterozoic setting at the northern margin of the CC and the global geodynamic evolution within which these models must fit, like the evolution of supercontinents (e.g. Murphy and Nance, 1991; Dalziel, 1997; Chatterjee and Scotese, 1999; Scotese et al., 1999; Piper, 2000, 2013; Pisarevsky et al., 2003b; Cawood et al., 2006, 2016; Scotese, 2009). Moreover, geophysics brought very worthy contributions by evidencing many structures (faults mainly) at various scale, but made few attempts toward geodynamic interpretion (Goussi et al., 2018) of these structures; keeping the debate pending. So, *using geophysics to produce a unifying model that would suitably explain the geodynamic evolution at the northern margin of the Congo Craton is the concern of this work.*

1.3.1.2. Objectives of the study

The current study aims at bringing more light into the understanding of the evolution of transition domain north of Congo Craton in Central Africa, with a reference on the Nkolafamba-Sangmelima region (southern Cameroon), by realising an updated geological map with a related improved mineral potential. Specifically, two objectives are targeted:

(1) The study supports the continent-continent collisional model; therefore, it will endeavour at seizing structural evidences that can validate that hypothesis.

(2) In the absence of geologic observations, geophysics is a good tool to solve geologic problems. But, access to data is the most complicated problem faced by geophysicists in less developed countries. Data, when available, may be from dirrent source, sparse and/or random. This study intends to propose an operational geophysical solution to handle this issue, particularly in the case of juxtaposition of geophysical data sources.

1.3.2. Research interests

From the main objectives above, some interests can exhale if expectations are fulfilled. Those interests are not scientific solely as the study might also influence the nation's wealth.

- The scientific interest comes out here on two aspects: (1) the amelioration of the structural and geodynamic evolution of the CC/NEFB transition zone; and (2) design of a new methodology in applying geophysics.
- At the economic level, by contributing to the amelioration of the geological map of this portion of southern Cameroon, this study can upgrade the mineral potential then increase the mineral exploration activity in this area by attracting more investors.
- The building constructions and groundwater exploitation are booming in some areas of the targeted region due to the increase of the population. This raises some social and environmental concerns (e.g. groundwater availability and pollution, soil stability, sinkholes monitoring, etc.) that the present study may help to mitigate.

Conclusion

The position of Cameroon in the West Central Africa is of great importance in regard to the geological evolution of both Africa and West Gondwana. Various-scales geoscience studies improved the geological information on the Cameroon territory in general and on its southern domain particularly. Geophysics on its own helped to map major structural features affecting the S-Cameroon region, among these are the Congo Craton/Panafrican limit and relays of the CCSZ. Despite the increasing number of geophysical studies carried over the Congo Craton/Panafrican transition zone, complete explanation of interplays between these two major litho-structural units (the CC and the NEFB) either at local or at regional scale remains limited. Also, linking the mapped structural features to the Precambrian supercontinents remain hazy (if not inexistent) till date, making it not possible for geophysics to the arbitrate on the debate about the geodynamic evolution of the Mobile Zone north of the CC. This study temptatively solve these issues by looming initially evidences to the CC/NEFB collision model then drawing sights of neotectonics in the actual global context.

CHAPTER TWO: MATERIALS AND METHODS

Introduction

Geophysics has become an important toolbox for earth sciences, in that it allows screening below the levels where no eye can reach for direct observations. It is the eye that brings the earth scientists beyond the limits they thought they would never go to perform their observations. However, efficient use of this toolbox requires a good understanding of how the tools within (methods and/or techniques) work. In other words, understanding the principles of each geophysical method is vital for their good application. Hence this chapter mainly aims at describing the methods to be used by the current study, starting from audiomagnetotellurics.

2.1. THE AUDIOMAGNETOTELLURIC METHOD

2.1.1. Basic concepts

The fundamental theory for electromagnetic (EM) fields behaviour has been established in the 19th century by James Maxwell through a system of four equations. Recently, Zhdanov, (2009) using the property of differential forms revealed that it is more suitable to consider electric and/or magnetic flux and work as major characteristics of the electromagnetic field, rather than the conventional vector representations. This other approach of Maxwell's equations spines electromagnetic geophysical experiments.

2.1.1.1. Maxwell's equations

Maxwell's equations below (Zhdanov, 2009) are mathematical formulation of laws describing EM fields behaviour, used to develop the electrical prospecting theory. These are:

$$\nabla \times \boldsymbol{H} = \boldsymbol{j} + \frac{\partial \boldsymbol{D}}{\partial t} \quad (1.a)$$

$$\nabla \times \boldsymbol{E} = -\frac{\partial \boldsymbol{B}}{\partial t} \quad (1.b)$$

$$\nabla \cdot \boldsymbol{B} = 0 \quad (1.c)$$

$$\nabla \cdot \boldsymbol{D} = \boldsymbol{q} \quad (1.d)$$

where $\boldsymbol{H}$, $\boldsymbol{B}$, $\boldsymbol{E}$ and $\mathbf{D}$ are respectively, the magnetic, the induction, the electric and the displacement fields vectors. j and q are the conduction current and the electrical charge densities, respectively.

The completeness of these equations comes with the so-called constitutive equations:

$$\boldsymbol{D} = \varepsilon \boldsymbol{E} \quad (2.a)$$

$$\boldsymbol{B = \mu H} \quad (2.b)$$

where, ε and μ are the permittivity and the magnetic permeability of the medium, respectively.

2.1.1.2. Electromagnetic field models

In electrical prospecting, two models for EM fields behaviour mainly used are the static and the quasi-stationary models. The first model governs Direct Current methods while the second is the frame of EM methods.

The quasi-stationary model is obtained by removing the term $\frac{\partial \boldsymbol{B}}{\partial \boldsymbol{t}}$ that is, neglecting effects of displacement current. The EM fields behaviour is then described by the diffusion equations:

$$\boldsymbol{\nabla^2 E - \mu\sigma E = 0} \quad (3.a)$$

$$\boldsymbol{\nabla^2 H - \mu\sigma H = 0} \quad (3.b)$$

where $\boldsymbol{\sigma}$ is the conductivity of the medium.

Equations (3.a & b) describe the propagation of EM fields into conductive media as *electromagnetic diffusion*. This supposes that in quasi-stationary regime, electromagnetic fields are independent of the dielectric properties of the medium (Zhdanov, 2009).

2.1.1.3. The monochromatic electromagnetic field

In the case of a monochromatic electromagnetic field, assuming that the time dependence is expressed by the term $\boldsymbol{e^{-\omega t}}$ in the equations above lead to complex expressions (Zhdanov, 2009).

$$\boldsymbol{\nabla^2 E + i\omega\mu\sigma E = 0} \quad (4.a)$$

$$\boldsymbol{\nabla^2 H + i\omega\mu\sigma H = 0} \quad (4.b)$$

Introducing the wave number k, equations (4.a & b) can be written in the form:

$$\boldsymbol{\nabla^2 E + k^2 E = 0} \quad (5.a)$$

$$\boldsymbol{\nabla^2 H + k^2 H = 0} \quad (5.b)$$

And then $\boldsymbol{k = (i\omega\mu\sigma)^{1/2} = (i)^{1/2}(\omega\mu\sigma)^{1/2}}$

To satisfy the condition Re(k)>0 and Im(K)<0, we will consider the positive square root of i: $\boldsymbol{(i)^{1/2} = e^{i\pi/4}}$ and according to the approximation $\boldsymbol{\mu \approx \mu_0}$ we obtain the expression of the wave number (equation 6):

$$\boldsymbol{k = e^{i\pi/4}(\omega\mu_0\sigma)^{1/2}} \quad (6)$$

Where $\boldsymbol{\mu_0}$ is the free-space magnetic permeability ($\boldsymbol{\mu_0 = 4\pi \cdot 10^{-7} \Omega \cdot s/m}$). Defining the parameter λ such as: $\frac{2\pi}{\lambda} = (\omega\mu_0\sigma)^{1/2}$ and recognizing that:$\boldsymbol{\omega = \frac{2\pi}{T}}$, where T is the period oscillation in seconds; and $\boldsymbol{\sigma = \frac{1}{\rho}}$, we deduce equation (7):

$$\boldsymbol{\lambda} = (\mathbf{10^7 \rho T})^{1/2}\text{m} \qquad (7)$$

λ is the wavelength and it is of extreme importance in electrical sounding as it permits to define the depth of penetration of the EM field into the earth, sometimes referred to as skin depth (δe).

$$\boldsymbol{\delta_e = \frac{\lambda}{2\pi} \approx 0.159(10^7 \rho T)^{1/2}}\ \text{m} \qquad (8)$$

2.1.2. The Audio-magnetotelluric (AMT) method

2.1.2.1. Overview

The premises of the EM methods have been laid by Rikitake (1948), but the development of the magnetotelluric (MT) method started first with Tikhonov (1950) and then by Cagniard (1953). The essence of the MT method is to observe the subsurface impedance over a spectrum of frequencies to determine conductivity (or resistivity) as function of depth, based on the recognition that the depth reached by a field depends on its attenuation (Telford et al., 1990). Further, a high-frequencies MT (or Audiomagnetotelluric (AMT)) application was developed (Niblett and Sayn-Wittgenstein, 1960; Vozoff, 1972; Strangway et al., 1973; Goldstein and Strangway, 1975) and applied to various fields such as geological surveys, mineral and petroleum explorations.

The MT/AMT method uses naturally occurring time-varying EM-fields generated by solar winds interaction with the magnetosphere or worldwide thunderstorms (spherics) to investigate the electrical conductivity of the Earth's structures (Vozoff, 1991; Garcia and Jones, 2000a). These time-varying magnetic fields induce electric fields within the Earth's. Thus, observations of the temporal and spatial variations of electric and magnetic fields at the Earth's surface contain information about the distribution of the electrical conductivity within the Earth. The conductivity, which depends on such things as rock composition and water content, may be related to geological structures, economic mineral, hydrocarbon and water-bearing formations. The typical range of the electrical conductivity of earth material varies widely from 10^{-5} to 10^{2} usi (Parasnis, 1986; Palacky, 1988; Telford et al., 1990).

2.1.2.2. Simplifying hypotheses

The development of the MT theory lies on the assumption of some hypotheses:

Firstly, the subsurface is assumed to be tabular. Then, the magnetotelluric wave is a plane wave propagating downwards along (O,z) and is polarized (**Figure 2.1.1**) so that electric field E and magnetic field H are directed along (O,x) and (O,y) axes, respectively, in the (O,x,y,z) Cartesian reference system.

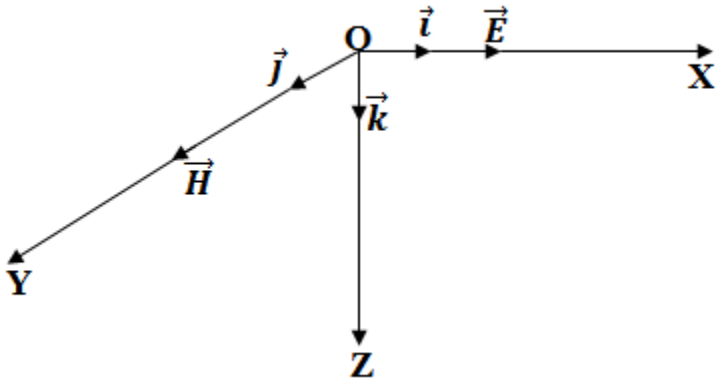

Figure 2.1-1 : Cartesian reference system in AMT/MT theory.

Secondly, displacement current effects are neglected. This supposes that electromagnetic fields are independent of the dielectric properties of the medium. Hence equations (5a), (5b) and (6) are valid.

Horizontal gradients of magnetic and telluric field vectors are insignificant compared to the vertical gradients, and that time variations are periodic (Niblett and Sayn-Wittgenstein, 1960; Dmitriev and Berdichevsky, 1979; Vozoff, 1990a; Chave et al., 2012) it results in following relations:

$$\frac{\partial}{\partial x} = \frac{\partial}{\partial y} = 0 \quad \text{and} \quad \frac{\partial}{\partial t} = -\frac{2\pi i}{T} \qquad (9)$$

Where variables are expressed in terms of Cartesian coordinates (x, y, z) and T is the period. These hypotheses suggest that the electrical conductivity is a function of depth only, and field variation sources are so that horizontal extension of phenomena at the surface are greater than their penetration depth.

2.1.2.3. The Tensor-Audiomagnetotelluric method

Modern AMT systems record variations of both the electric and magnetic fields in two orthogonal directions then calculate the subsurface impedance at a measurement site. The scalar subsurface impedance defined as:

$$Z_{ij} = \frac{E_i}{H_j} \qquad (10)$$

is easier to calculate but its weakness resides in its ability to vary with the direction of the source fields. A tensor formulation would better account for this variations (Bailey and Groom, 1987, n.d.; Bahr, 1988; Groom and Bailey, 1989; Vozoff, 1990a; Weaver et al., 2000). Indeed, the surface tensor impedance Z is complex, frequency-dependent, and, because of the presence of noise and the earth structures. The surface impedance tensor $\bar{\bar{\mathbf{Z}}}(\boldsymbol{\omega})$ should be thought helpfully as a two input, two output linear system where the inputs are the magnetic field components and the outputs are the electrical field components, as shown by equation (11) (Mcneice and Jones, 2001)

$$\bar{\mathbf{E}}(\boldsymbol{\omega}) = \bar{\bar{\mathbf{Z}}}(\boldsymbol{\omega}) \cdot \bar{\mathbf{H}}(\boldsymbol{\omega}) \text{ or } \begin{cases} \mathbf{E_x} = \mathbf{Z_{xx}H_x} + \mathbf{Z_{xy}H_y} \\ \mathbf{E_y} = \mathbf{Z_{yx}H_x} + \mathbf{Z_{yy}H_y} \end{cases} \qquad (11)$$

This tensor formulation is preferred over the scalar formulation because, when the source fields are nearly plane waves, the impedance elements $\boldsymbol{Z_{ij}}$ are time-invariant and permits a two- or three-dimensional (2-D or 3-D) study (Vozoff, 1990; Garcia and Jones, 2002; Ledo et al., 2002; Zhdanov, 2009). The surface impedance is usually expressed as apparent resistivity and impedance phase, calculated from the surface impedance components as (Zhdanov, 2009) (Geometrics, 2000):

$$\boldsymbol{\rho_{ij}} = \frac{\mathbf{1}}{\boldsymbol{\omega\mu_0}} \left|\mathbf{Z_{ij}}\right|^2 = \mathbf{0.2T}\left|\mathbf{Z_{ij}}\right|^2 \qquad (12.a)$$

$$\text{and } \boldsymbol{\emptyset_{ij}} = \mathbf{tan^{-1}}\left(\frac{\mathbf{Im(Z_{ij})}}{\mathbf{Re(Z_{ij})}}\right) \qquad (12.b)$$

The AMT method entails simultaneous measurements of electric and magnetic fields over the frequency range 10 Hz to 10 kHz. However, signals are generally weak in the frequency range 1 kHz to 5 kHz called the AMT dead band (Garcia and Jones, 2000) and data acquisition then requires a controlled source system or transmitter (Zonge and Hughes, 1991; Goldstein and Strangway, 1975; Vozoff, 1990). For valid interpretations, measurements site must be sufficiently distant from the transmitter to be located in the transmitter's far field, so as to enable the plane wave assumption (Zonge and Hughes, 1991; references therein).

2.1.3. AMT data acquisition and interpretation

2.1.3.1. Data acquisition

a. The equipment

The AMT data for our study have been collected with the Stratagem EH4 resistivity-meter made by EMI and Geometrics Inc (**figure 2.1-2**). This system uses a combination of natural and hybrid MT signals. Any available natural background signals are used in the entire frequency band while a transmitter is used to provide additional high-frequency signals in the

range of 1 kHz to 70 kHz where natural signals are weak. To optimise high/low frequency data collection, the operator can select the frequency bands and the number of time series "stacks" for data collection (Geometrics, 2000).

The EH4 transmitter, powered by a 12V DC battery, consists of a dual-loop antenna, transmitter's electronics, and a controller. It provides non-polarised source fields which allow for true tensor measurements of ground resistivity. This provides more accurate interpretation of true resistivity than conventional single-dipole transmitter source signals. The resolution depth is more than 1km but, in general, depth to which a target can be imaged depends on the earth's resistivity/conductivity at the survey site and the lowest frequency for which there are reliable data (Geometrics, 2000; McPhee et al., 2006, 2008).

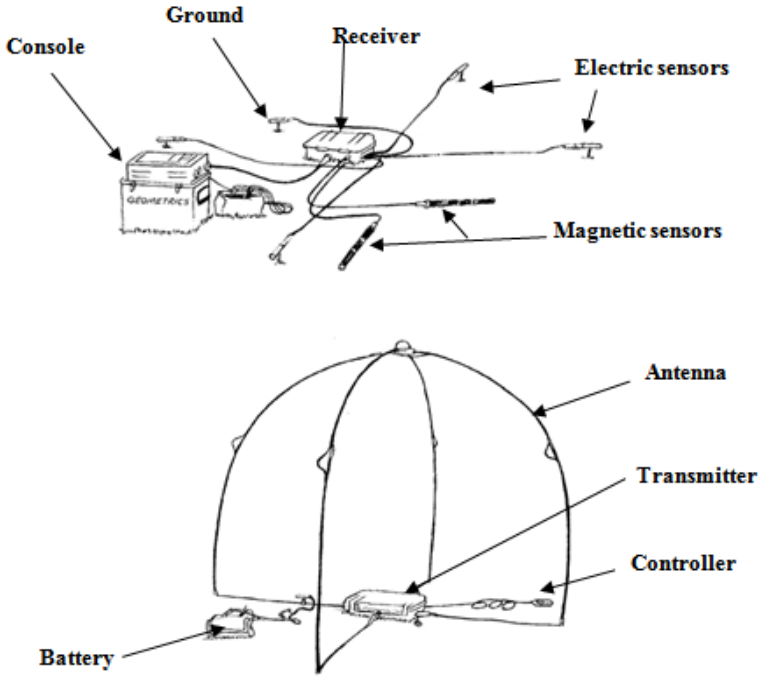

Figure 2.1-2 : Standard EH4 equipment layout (Geometrics, 2000).

Along with the EH4 system, standard field instruments were used. These are, a Garmin 60s GPS to record the stations location data; a compass; a water level to check the horizontality of coils; a 50 m tape to measure the length of dipoles.

b. Description of profiles

Generally, in geophysical surveys, profiles must be directed perpendicularly to the a priori geologic strike of a given area. The approximate orientation of profiles is N135, as the SW-NE strike supposedly controls the regional geology. AMT data were collected with a Stratagem EH4 kit during two field campaigns achieved progressively in August 2011 then August 2012 for a total of 35 stations and 6 profiles, two by two parallel. The first five profiles have an inter-station distance of 100m and a profile length of 500 m; each profile comprising six

stations (the second profile is 400 m length with five stations). Besides, profile 6 is 1500 m length with a mean stations spacing of 300 m.

The profile 1 to profile 4 forms a set of four profiles which were realised in the Nkolafamba subdivision while the second set (profiles 5 and 6) was realised in the Mfou subdivision, nearly 20 km away on bird's wing southeast from the first site. Except on profile 1 where x and y dipoles lengths are 50 m and 25 m, respectively, these lengths are equal (25 m) for the five remaining profiles.

c. Measurement sites

Generally, measurement sites were away from human activity (**photo 1**), in quiet places to avoid cultural noise revealed by signals distortion. Distortion of signals can be caused by the interaction between a near EM and the magnetotelluric fields. This happens when a measurement site is located near of power generation or consumption sites, noisy sources and mechanical activity sites. Noisy sources include power lines, electric fences, radio transmitters, pipelines with cathodic protection, proximity to large metal clumps, flowing water or wind vibration, etc.

Photo 1 : Recording of AMT data in a remote area (Profile 1).

The transmitter-antenna unit was sometimes set to improve signal strength. Geographical coordinates of the stations are given in the appendices. Data acquisition was done by recording several passes individually composed of one or more time-series segments in a particular band. Signals are processed into time series from electric and magnetic fields, which are converted into frequency domain measurements (spectral data) by Fast Fourier Transform.

2.1.3.2. Data processing

Tensor-AMT data recorded in the frequency domain are transformed into EM transfer functions from which apparent resistivity and phase tensors are estimated. The data are

processed within the stratagem EH4 using the Bostick transform (Sims et al., 1971; Boehl et al., 1977; Bostick, 1977) that links the apparent resistivity to the phase using the Hilbert transform.

a. Signals' correlation

Stratagem EH4 records the EM field through four channels representing electric and magnetic fields components. For electric and magnetic field are coupled, this must be the same for their components; thus, the signal response for transverse complementary components must be similar (**Figure 2.1-3**). This supposes that, the phase and amplitude of E_x should resemble those of H_y and so for E_y and H_x. The operator should be aware if, for example, at least one channel is constantly out of scale or doesn't correlate with the others.

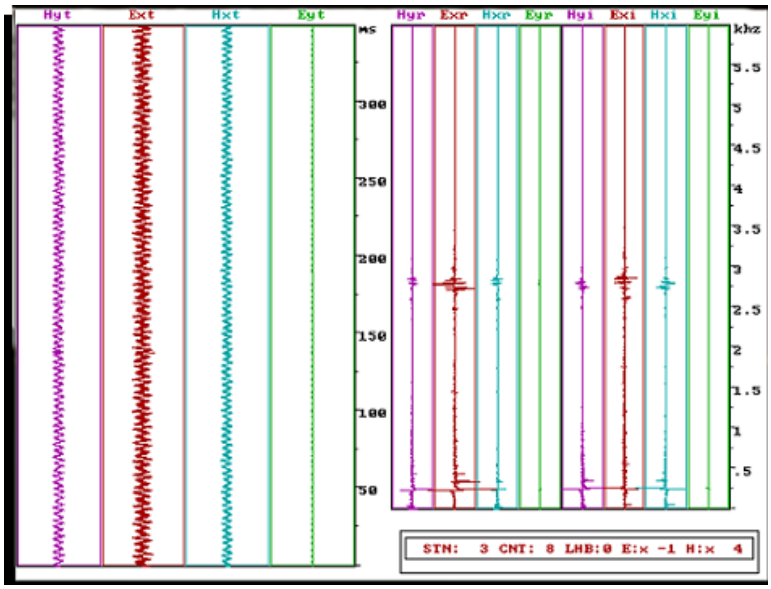

Figure 2.1-3 : Signal's correlation display (Ossol, station 3). Disturbances are observed in the same frequency ranges for all the signal components at the right of the display, meaning a good correlation of signals.

b. Impedance components' correlation

The correlation of impedance components ensures the validity of a sounding. When they correlate, we should observe a dip in the phase response when apparent resistivity increases with the period (or frequency decreases), and contrariwise for a period's decrease. This phenomenon is expected according to the relationship between impedance components:

$$\emptyset = \frac{\pi}{4}\left(1 - \frac{\partial(log\rho_a)}{\partial(logT)}\right) \qquad (13)$$

Slight departures from equation (13) are expected because of the normal low-level scatter in the data but when an important portion of the sounding curve fails to obey it, then cultural noise sources may have introduced a bias.

c. Data coherency

Typically, the correlation of EH4 data is expressed in terms of coherency (Geometrics, 2000). Since electric field values can be estimated from those of the magnetic field, the

coherency between predicted electric field values and those measured is the signal on noise ratio. In the Stratagem EH4 system, acceptable data are those for which the coherency is above 0.5.

2.1.3.3. Data interpretation.

Data interpretation consist in equating the resistivity imaging to a hypothetical subsurface geology of an area. The steps followed are (1) analysing resistivity and phase pseudo sections and (2) earth-modelling through geoelectrical sections; both after the dimensionality analysis.

a. Dimensionality analysis

Dimensionality refers to the subsurface geoelectrical structure or spatial distribution of the electrical resistivity, classified either as 1-D, 2-D or 3-D (Bailey and Groom, 1987; Zhang et al., 1987; Vozoff, 1991; Parker, 2011). In a 2-D earth, the conductivity is constant along one horizontal direction while changing both along the vertical and the other horizontal direction. The direction along which the conductivity is constant is known as the geo-electric strike (Vozoff, 1991; Chave et al., 2012). The Stratagem EH4 system performs simultaneous measurement of the EM field along two orthogonal directions which enable to decouple the impedance tensor components in to a TE and TM and to assume that the geoelectrical structure is at least 2-D (Geometrics, 2000; Simpson and Bahr, 2005; McPhee et al., 2006). Moreover, Groom and Bailey (1989) empirically established that dimensionality can be assessed by observing the behaviour of the resistivity curves in both TE and TM modes when plotted on the same graph. They found that when the ground structure is at least 2D, the TE and TM resistivity curves generally once coinciding depart from each other at low frequencies.

b. Apparent resistivity and phase pseudo sections

Pseudo-sections are contour plots with distance on the horizontal scale and frequency (log of) on the vertical. They picture how resistivity or phase varies with depth (lower frequency is equivalent to greater depth). The phase has the advantage of being non-sensitive to the effects of shallow subsurface anomalies, so it is particularly useful for the detection of deep structures (Caldwell et al., 2004; Weaver et al., 2006). Pseudo-sections enable to highlight lateral discontinuity zones which appear with strong horizontal resistivity gradient, thus contrasting with tabular zones where isoresistivity lines are horizontal (Vozoff, 1972). In this work pseudo-sections ploted with Surfer 13™.

c. Geoelectrical section

The geoelectrical section or 2-D resistivity is a model of the subsurface resistivity structure (Zhdanov, 2009), so as to give the hypothetical lithological arrangement beneath a

profile (Zhdanov, 2009; Chave et al., 2012; Meying et al., 2013).. The model assumes a tabular layering and that a resistivity contrast defines each layer.

2.1.3.4. Ancillary

The AMT data processing and interpretation were done with Imagem an EH4 built-in program which transforms the time-series into impedance data finally stored as apparent resistivity, phase, and as 2-D resistivity data. These processed data are visualised with plot2D, a program designed to view and print the 2D results produced by Imagem (Geometrics, 2000). However, for clarty pseudo sections are displayed with Surfer v.13 ™. Before any interpretation, the electrical structure has been assessed using ZondMT2D™.

2.2. THE MAGNETIC METHOD

The magnetic effect is far most the earliest physical parameter that seized the human though. Questioning the mutual attraction of lodestones has been traced back to the Greek philosopher Thales era, in the sixth century B.C. Additionally, the tendency of lodestones to align preferentially in certain directions, observed in early Christian era was apparently the first recognition that the earth is associated with a property that affects magnetic objects, thus opening the door to geomagnetic studies (Blakely, 1996). As geological applications of magnetics began as early as 1930, the World War II favoured the advent of aeromagnetics (Blakely, 1996).

2.2.1. The fundamentals

2.2.1.1. The geomagnetic field

a. The nature of the geomagnetic field

Historically, the Chinese invention of the compass is the main evidence of the earth's magnetic (or geomagnetic) field whose components were summarised by Campbell, (1997):

- The main field originates from the inner Earth and varies slowly. It results from convection currents in the outer core and the planet's rotation (dynamo effect). Considered as a dipolar field of about 50 000 nT, it contributes about 80-90 % of the geomagnetic field.
- The external field, smaller than the main field, is caused by spherics and all particles and radiations from the space and the sun (ionized flow in the upper atmosphere).
- The crustal field, also smaller than the main field, originates from ferromagnesian rocks and/or near-surface crustal heterogeneities seated where temperatures are sufficiently low, i.e., less than about 580◦C (Curie temperature of magnetite). This region is confined to the upper 20‑30 km of the crust. The crustal field is related to the distribution of

magnetic minerals within the crust, and the information this relation provides about exploration targets make the philosophy of magnetic exploration method.

The figure 2.2-1. gives two representations of the geomagnetic field and its components.

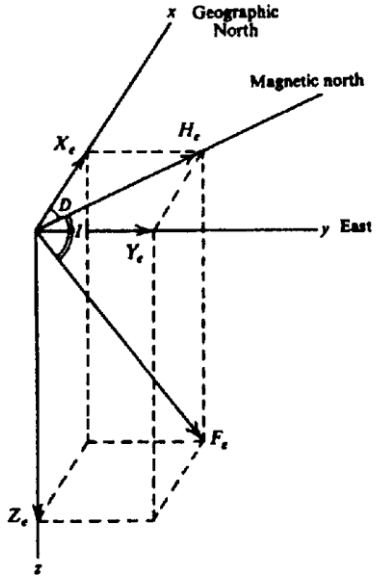

Figure 2.2-1 : Representation of the total magnetic field Fe.

The total magnetic field vector may be defined either (a) by its three orthogonal components (horizontal north $\mathbf{X_e}$, horizontal east $\mathbf{Y_e}$ and vertical $\mathbf{Z_e}$) or (b) by the scalar magnitude of the total field, $\mathbf{F_e}$ and two angles, the inclination from the horizontal, I and the declination from true (geographic) north, D. The second definition pertains to geophysics, since only the scalar magnitude Fe is generaly measured.

b. The International Geomagnetic Reference Field (IGRF)

The IGRF (Peddie, 1983) corresponds to the standardised value of the geomagnetic field at any point on the Earth's surface. It is published by the International Association of Geomagnetism and Aeronomy (IAGA) on a five-yearly basis, using a mathematical model which best fits all the actual observational data from geomagnetic observatories, satellites and other approved sources for a given epoch. The model is defined by a set of spherical harmonic coefficients to degree and order 13 (Campbell, 1997). The value of F_e worldwide at the epoch of the model (e.g. for 1995) and the annual rate of change in these coefficients for the following five years (e.g. 1995-2000) are computed, a software which permits the use of these coefficients to calculate IGRF values over any chosen survey area is available (Reeves, 2005). The values currently in use are based on the IGRF 2015 and its tentative extrapolation (prediction) to 2020. Eventually, a definitive model until 2020 will be adopted with an extrapolation to 2025, and so

on. The IGRF coefficients are published and freely availed by IAGA at http://www.iugg.org/IAGA/iaga_pages/pubs_prods/igrf.htm.

Magnetic field in SI units is defined in terms of the flow of electric current needed in a coil to generate that field. Thus, its units are volt-second per square metre or Weber/m2 or Tesla (T). Since the magnitude of the Earth's magnetic field is only about 5 x 10^{-5} T, the convenient SI unit of measurement in geophysics is the nanoTesla (nT = 10^{-9} T).

2.2.1.2. Magnetic properties of earth materials

a. Types of magnetisation

The inner earth magnetism originates from two main types of magnetisation, the induced or normal magnetisation and the remnant or permanent magnetisation.

- ***Induced magnetisation:***

Normal (or induced) magnetisation J_i is due to the induction of the Earth's magnetic field. When a magnetic material is placed in a magnetic field, the material becomes magnetised and the external magnetising field is reinforced by the magnetic field induced in the material itself. The direction and amplitude is proportional (the proportionality constant is the magnetic susceptibility) to the applied field (Reeves, 2005).

- ***Remnant magnetisation:***

Remnance is a type of permanent magnetisation J_r, which prevails in some rock types more than others, and contributes to the total magnetisation. When the external field is cancelled, the induced magnetisation disappears at once, but some materials retain a permanent or remnant magnetisation whose direction will be fixed within the specimen in the direction of the inducing field. Remnant magnetisation is complex and can be due to several causes including the thermo-remnant magnetisation, which happens when magnetic materials are cooled down to the Curie point (temperature above which magnetic properties theoretically vanish) in the presence of an external field (Hinze et al., 2013, references therein). Very old rocks shew that the remnant magnetisation vector can remain unchanged, regardless of any subsequent changes in the ambient field (see Clark and Emerson, (1991) for further reading on magnetisation).

Simply, it follows that any rock in situ may now be expected to have two magnetisations, one induced and one remnant. The induced component, J_i, is parallel to the Earth's present field, while the remnant component, J_r, may reasonably have any direction. As vector quantities, their sum is a vector giving the total magnetisation of the rock in situ. For simplifications, the Koenigsberger ratio, Q, defined by equation (14) is preferred in geophysicis.

$$\boldsymbol{Q = J_r / J_i} \qquad (14)$$

Very often, it is necessarily assumed that the value of Q is small, i.e. that all significant magnetisation in the rocks is induced and in the direction of the present day Earth's field.

b. The magnetic susceptibility

Clearly, all crustal rocks find themselves situated within the geomagnetic field. They are therefore likely to display induced magnetisation. The magnitude of the magnetisation they acquire, J_i, is proportional to the strength of the Earth's field, $\boldsymbol{F_e}$, in their vicinity. The constant of proportionality, k, is, by definition, the rock's magnetic susceptibility (Reeves, 2005; Lowrie, 2007):

$$\boldsymbol{J_i = kF_e} \qquad (15)$$

Magnetic susceptibility in SI units is a dimensionless ratio with values less than 1 for most rocks, as illustrated by the **figure 2.2-2** below from Clark and Emerson (1991).

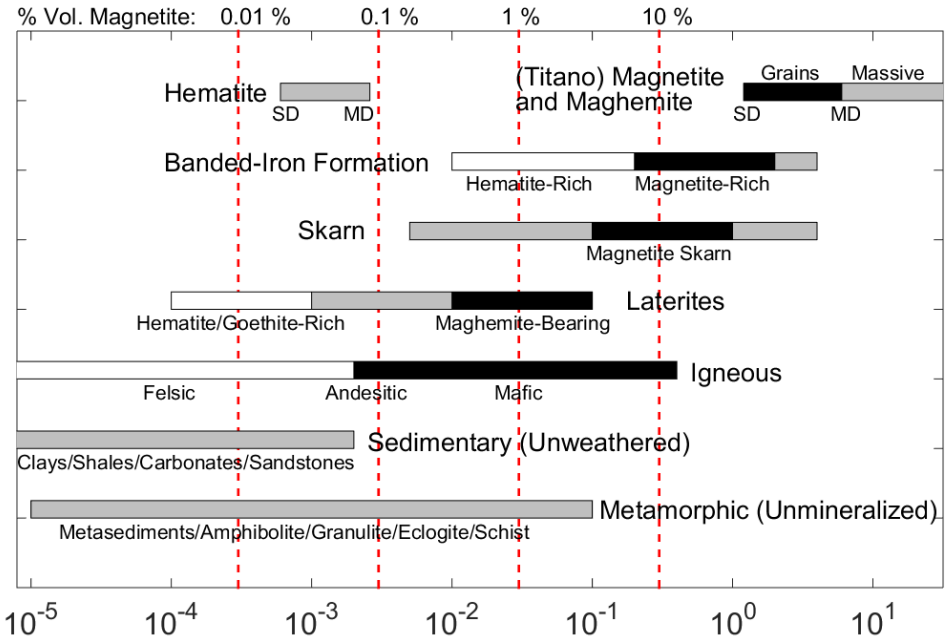

Figure 2.2-2 : Magnetic susceptibility scale for common minerals (Clark and Emerson, 1991).

c. The magnetic domains and minerals

- ***Magnetic domains or groups***

In general, solid materials are classified as diamagnetic, paramagnetic, ferromagnetic and anti-ferromagnetic. The first two types of magnetic property have been usually considered as insignificant in magnetic anomaly mapping; rocks having only these properties are often classed as ***non-magnetic***, since their magnetisation is orders of magnitude less than that of common sources of magnetic anomalies. Ferromagnetic materials, by contrast, contain magnetic "domains" which magnetise very easily, whereas anti-ferromagnetic materials have domains which cancel each other out to give zero magnetisation. Most magnetic materials of geological

significance are imperfectly anti-ferromagnetic, for which class the term ferrimagnetic is used. In fact, only a rather small number of minerals display significant magnetic properties are mixed oxides of iron, titanium, manganese plus one sulphide mineral, pyrrhotite (Reeves, 2005).

- ***Magnetic minerals***

The minerals that normally cause observable magnetic effects in mineral eexploration are (Redford, 2014 personal communication):

- Magnetite (Fe_3O_4): the most magnetic mineral, generally with neglectible remanence.
- Monoclinic Pyrrhotite (FeS): only the monoclinic form is magnetic and frequently has remnant magnetisation an order of magnitude greater than its induced magnetisation– the susceptibility of pyrrhotite is circa 1/10 that of magnetite.
- Hematite (Fe_2O_3): at times having strong remanence, it can show weak magnetic responses due to induced magnetisation.
- Ilmenite/Titanohematite ($Fe^{2+}TiO_3$/ $(Fe, Ti)_2O_3$): it can give weak but observable magnetic responses. Titanohematite is an intergrowth richer in hematite.
- Maghemite (Fe_2O_3): it is a weathering product of spinels containing ferrous oxides (usually magnetite or titano-magnetite) which can have strong magnetic responses.

2.2.2. Aeromagnetic surveying

2.2.2.1. The principles

The high-order terms in the energy density spectrum of the geomagnetic field are related to the magnetization of crustal rocks. Magnetic investigations then, can yield important data about geological structures. By analogy with gravity, a magnetic anomaly is defined as the local difference between the measured (and suitably corrected) magnetic field of the Earth and that which would be expected from the IGRF (Lowrie, 2007). This anomaly results from the contrast in magnetization when rocks with different magnetic properties are adjacent to each other; e.g. when a strongly magnetic basaltic dike intrudes a less magnetic host rock (Paterson and Reeves, 1985; Telford et al., 1990; Nabighian et al., 2005). The stray magnetic field surrounding the dike locally disturbs the geomagnetic field and can be measured with sensitive magnetometers. Equation (16) summarising these statements is part of the magnetic data reduction (Paterson and Reeves, 1985; Campbell, 1997; Nabighian et al., 2005; Reeves and Korhonen, 2007; Hinze et al., 2013) :

$$\mathbf{M} = \mathbf{F_e} - \mathbf{F_{IRGF}} \qquad (16)$$

Where $\mathbf{F_e}$, $\mathbf{F_{IGRF}}$ and $\mathbf{M}$ are respectively the total, the reference and the reduced magnetic fields.

2.2.2.2. Surveying procedures

In the airborne magnetic surveying, the procedures and stages are common to ground and marine magnetic surveying methods hereafter presented.

a. Data acquisition

Aeromagnetic meseaurements are usually made either through helicopter (bird) or plane (stinger). alsmost same patterns are required and the same equipment are used to collect data. Interested readers can nurture themselves on aeromagnetics, with the literature from Reeves et al. (1997), Reeves (2005); Boyd and Isles (2007), and Hinze et al. (2013). The aeromagnetic survey specifications are as follow:

- The traverse or survey line spacing is chosen regarding the desired resolution and size of the structures to image;
- The traverse trend is defined according to the known strike of geological structures in the area;
- The tie or cross line are perpendicular to traverse. Their spacing is 5 to 10 times the traverses' spacing;
- The flight height or survey elevation is either according to sea level or constantly above ground level (terrain clearance).

b. Data correction and reduction

The data correction stage involves some calculations to remove diurnal variations in the field due to the part of geomagnetic field that originates from ionosphere, position and altitude corrections (Brodie, 2002). Generally, these tasks are partly performed by the contractors (Hinze et al., 2013) who provide data as total magnetic field intensity (with raw data as well). Later, a reduced field strength's value (local field) is obtained by subtracting the IGRF from the total field measurements. This corresponds to the removal of the non-geologic or regional effects from the total field measurements to leave the magnetic anomaly (local geologic-residual information clearly visible for the interpreter) subsequently used for data analysis and interpretation through many filtering and transform operations.

2.2.2.3. Data processing and interpretation

Once reduced, data are presented as total magnetic intensity anomaly field map requiring several additional transforms and filtering depending on specific interpretations. However, initial care shall be given whereas the surveyed area's location is close to the poles or the equator. At low latitudes (the case of the current study), the reduction to the magnetic equator is the first data transformation applied. All the computer works done in Geosoft ® Oasis Montaj v.8.4.

a. Reduction to magnetic equator (RTE) and noise filtering

Generally, on a magnetic map, anomalies are shifted away from the location of their causative bodies, but application of the Reduction to the poles transform (Baranov and Naudy, 1964; Blakely, 1996) helps solving this matter by bringing back the anomaly at the apex of its source. In equatorial regions where inclination is less than 15°, the Reduction to the poles transform is generally unstable thus a similar operation, the Reduction to the magnetic equator (RTE) is applied instead (Hinze et al., 2013, references therein). The application of the RTE transform requires the knowledge of the inclination ***I*** (-6.2°**)** and declination ***D*** (-18.2°) of the geomagnetic field at the time of data acquisition (IGRF model of January 1970) -6.2°.

On magnetic anomaly grids, noise is often related to high frequency signals. Various noise suppression techniques exist (Blakely, 1996; Reeves, 2005) with different fortunes, but the upward continuation (described further in this paper) to a height of 125 m has been adopted for noise filtering. This distance (125 m) has been chosen so as to be comprised between half the flight height and the sixth of the lines spacing, to avoid subsequent reduced noise or Nyquist effects on signals (Drury, 2001; Hinze et al., 2013). Since data were collected along 750 m distant flight paths flown at 235 m height, the 125 m distance chosen is nearly the half of 235 and the sixth of 750. The resulting RTE map (**Figure 3.2-1)** while usable for regional appraisal of the area, also serves as input for further filtering and interpretations.

b. Analytic signal (Total gradient)

The analytic signal (AS) amplitude combines the horizontal and vertical gradients of a given field. Magnetic and gravity applications of the AS have been introduced by Nabighian (1972, 1974) to determine the depth and position of the anomaly source in the 2D case, since the form of the AS anomaly over causative bodies depends only on the locations of the bodies but not on their directions of magnetization. The technique has been improved with the Hilbert transform (Nabighian, 1984) then extended to 3D problems with gridded data (Roest et al., 1992) as formulated by equation (17):

$$\boldsymbol{A}(\boldsymbol{x},\boldsymbol{y},\boldsymbol{z}) = \frac{\partial \boldsymbol{M}}{\partial \boldsymbol{x}}\boldsymbol{i} + \frac{\partial \boldsymbol{M}}{\partial \boldsymbol{y}}\boldsymbol{j} + \frac{\partial \boldsymbol{M}}{\partial \boldsymbol{z}}\boldsymbol{k} \qquad (17)$$

where ***A (x, y, z)*** is the analytic signal vector; ***i, j, k*** are the unit vectors in the *x, y,* and *z*, directions, respectively; *M* being the anomaly field intensity.

With gridded data, the AS is used either as a mapping and depth-to source technique or as a way to learn about the nature of the causative magnetization (MacLeod et al., 1993; Reeves, 2005). Mapping applications have been clearly demonstrated by in recent mineral exploration plays, where the AS served as a geochemical tool for lithological units outlining (Geosoft, n.d.).

c. The First vertical derivative (FVD)

The application of first vertical derivative (FVD) is equivalent to observing the vertical gradient directly with a magnetic gradiometer. The FVD both enhances shallow sources while suppressing deeper ones and gives a better resolution of closely-spaced sources (Reeves, 2005). The FVD expressed by **equation (18)**, is filtering technique particularly useful in highlighting structural features like lineaments (Boyd and Isles, 2007; Feumoe et al., 2012; Fairhead et al., 2017), mostly the shallow ones.

$$\mathbf{FVD} = \frac{\partial \mathbf{M}}{\partial \mathbf{z}} \qquad (18)$$

where *M* is the magnetic field anomaly.

The FVD is generally much more responsive to local influences than to regional effects. Therefore, it tends to give sharper pictures than the total field intensity on maps.

d. Horizontal gradient

The horizontal gradient filtering (Blakely, 1996; references therein) is in many ways the simplest approach to estimate contact locations of the bodies (Anderson et al., 2013; Hinze et al., 2013; Feumoe, 2014), thanks to its low sensitivity to noise in the data because it only requires calculation of the two first-order horizontal derivatives of the field. If $\boldsymbol{M}$ is the magnetic field, then its horizontal gradient magnitude (HGM) is given by:

$$\boldsymbol{HGM}\,(\boldsymbol{x},\boldsymbol{y}) = \sqrt{\left(\frac{\partial \mathbf{M}}{\partial \mathbf{x}}\right)^{\mathbf{2}} + \left(\frac{\partial \mathbf{M}}{\partial \mathbf{y}}\right)^{\mathbf{2}}} \qquad (19)$$

$\frac{\partial \mathbf{M}}{\partial \mathbf{x}}$ and $\frac{\partial \mathbf{M}}{\partial \mathbf{y}}$ are horizontal gradients of the field *M* in the *x* and the *y* directions, respectively.

The HGM function gives a peak anomaly above magnetic contacts under the following assumptions (Feumoe, 2014): (1) the regional magnetic field is vertical, (2) the magnetizations are vertical, (3) the contacts are vertical, (4) the contacts are isolated, and (5) the sources are thick. Violations of the first four assumptions would shift peaks away from the contacts, while for the fifth it would produce secondary peaks parallel to contacts (Feumoe, 2014).

e. The upward continuation

Based on the Green's third identity, the upward continuation (UC) is an operation that enables to transform a potential field from a surface it was measured to a field that would had been measured to another surface farther from all sources (Blakely, 1996; Nabighian et al., 2005; Lowrie, 2007). The UC transform in the Fourier is given by:

$$\boldsymbol{UC} = \boldsymbol{M}\boldsymbol{e}^{-\Delta \boldsymbol{z}|\boldsymbol{k}|},\ \Delta \boldsymbol{z} > \mathbf{0} \qquad (20)$$

$\Delta \boldsymbol{z}$ is the distance used for the continuation in ground units and $|\boldsymbol{k}|$ is the wave number.

Clearly from **equation (20)**, the UC attenuates all wave numbers except $|\boldsymbol{k}| = \mathbf{0}$. The degree of attenuation increases with the continuation distance.

In practice, the UC acts as a low-pass filter by attenuating short wavelengths (or high frequencies) anomalies corresponding to shallow geological effects while accentuating high wavelength sources effects due to deep sources. Thus enabling to outline deep regional geological or basement structures (Blakely, 1996; Nabighian et al., 2005; Lowrie, 2007; Hinze et al., 2013; Fairhead et al., 2017). The combination of the upward continuation of magnetic field data at several heights and the detection of the peaks of their respective horizontal gradient magnitude grids (Blakely and Simpson, 1986) provides a pseudo 3D view of the geometry of deep magnetic sources. This approach known as the multiscale edge analysis (Archibald et al., 1999) has been applied in many studies (Basseka et al., 2011; Anderson et al., 2013; Owona-Angue et al., 2013).

f. The 3D Euler deconvolution method

Thompson (1982) proposed a 2D technique, the Euler deconvolution, to analyse magnetic profiles based on the Euler's homogeneity equation. The technique uses first-order x, y and z derivatives to determine location and depth for various targets, assuming an a priori information (at least the geometry) referred to as structural index (N). Reid et al. (1990) extended the technique to 3D data by applying the Euler operator to gridded data sets (see equation (21)):

$$\boldsymbol{N\,(B-M)} = \boldsymbol{(x-x_0)\frac{\partial M}{\partial x} + (y-y_0)\frac{\partial M}{\partial y} + (z-z_0)\frac{\partial M}{\partial z}} \qquad (21)$$

Where **B** is the regional field, (x0, y0, z0) is the position of the magnetic source producing the field M at (x, y, z). Theoretically, N=0 (practical values between 0.25 and 0.5 are preferred) for contacts and faults.

g. Geophysical inversion ($2^{3/4}$ modelling)

The modelling consists in designing and calculating the response of a theoretical geological model; then using the Marqardt algorithm to invert and linearize the solutions. The $2^{3/4}$ modelling particularity is that the source bodies are assigned fixed extensions across the profile. The modelling approach assumes that the anomalies are due to various sources (including both supra-basement and intrabasement responses) using local geology as model constraint (Prieto, 1996). The $2^{3/4}$ modelling is executed with GM-SYS ™ extension in Geosoft ® Oasis Montaj v.8.5.

2.2.2.4. The materials

a. Origin of data

The magnetic data used in this study were collected by the Survair Ltd in 1970s. The flight paths were flown N-S with a line spacing of 750 m a constant fly height of 235 m. The data were corrected and processed by Paterson, Watson and Grant Ltd, a consulting service that released data initially as 1: 50,000 total intensity contour maps to the Cameroonian government. The portion covered by this study has been availed in 2015 by the Directorate of Geology from the Ministry in charge of mines, in Cameroon.

b. Data preparation and materials

Dataset was provided as scanned-images of contour maps printed on paper. Once scanned-images of maps are acquired and viewed on the computer screen, then georeferenced. The georeferencing step is followed by the digitisation of data by capturing the x and y coordinates values along each flight line with the mouse's cursor. The total field value (z value) at each x, y location is entered and recorded in an output XYZ-file, leading to the compilation of a new digitally acquired survey database. The georeferencing and digitization tasks resulting into the new database were realised on Esri ® ArcGIS v.10.6. The final task in data preparation is gridding. Gridding is a contouring procedure herein done with a 250 x 250 m cell. The cell size (1/3 of the line spacing-750m) has been chosen to avoid aliasing effects (Reeves, 2005; Hinze et al., 2013). The gridding algorithm used was the minimum curvature (Briggs, 1974) implemented in Oasis montaj ™ platform.

2.3. THE REMOTE SENSING METHOD

Remote sensing is the process of detecting and monitoring the physical characteristics of an area by measuring its reflected and emitted radiation at a distance, using on-board airborne or space borne platforms (USGS, 2016). Remotely sensed imagery ensures rapid structural analyses by mapping regional or local lineaments and circular features (Liu and Mason, 2009).

2.3.1. Theoretical principles

2.3.1.1. Electromagnetic energy

The electromagnetic (EM) spectrum is the continuous range of electromagnetic radiation, extending from gamma rays (highest frequency and shortest wavelength) to radio waves (lowest frequency and longest wavelength) including visible light. The EM spectrum can be divided into seven different regions: gamma rays, X-rays, ultraviolet, visible light, infrared, microwaves and radio waves (**Figure 2.3-1)**. Remote sensing involves the measurement of energy in many parts of the EM spectrum (NASA, 2015).

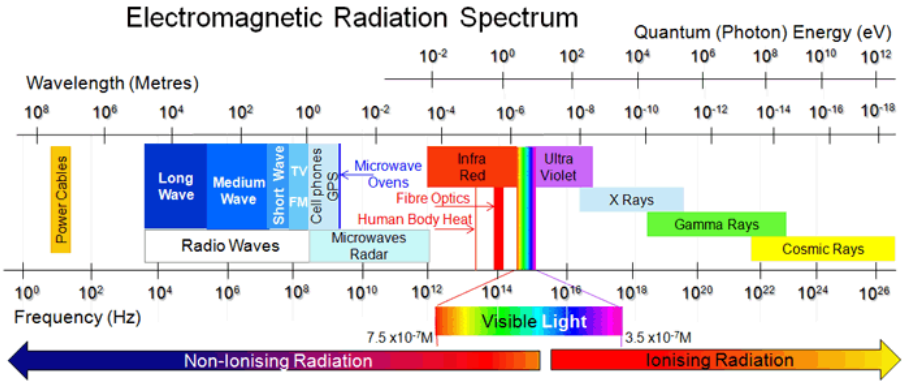

Figure 2.3-1 : EM spectrum

2.3.1.2. Reflection and absorption

The physical principle governing the remote sensing method is that when radiation from the Sun reaches the surface of the Earth, some of the energy at specific wavelengths is absorbed and the remaining is reflected by the surface materials. The only two exceptions (very rare in the natural world) to this situation are if the surface of a body is a perfect reflector or a true black body (Schowengerdt, 2007; Liu and Mason, 2009).

2.3.1.3. Reflectance-spectral signature-spectral band

Remote sensing involves the measurement of the EM radiations that is reflected back from the Earth's surface materials. Soil, water and vegetation exhibit different patterns of reflectance and absorption over different wavelengths. The reflectance of radiation from one type of surface material, such as soil, varies over the range of wavelengths in the EM spectrum. This is known as the spectral signature of the material, corresponding to its radiometrical response for a given set of wavelengths. Each surface feature, including minerals, vegetation, dry soil, water, and snow, has a unique spectral reflectance or signature. The measurement of the radiations takes place in spectral bands (or colours which are discrete intervals of the EM spectrum).

2.3.2. The remote sensing surveying

2.3.2.1. Satellite remote sensing principles

Satellites are equipped with sensors looking down to the earth which constantly observe the earth as they go round in predictable orbits. These sensors are designed to measure responses within particular spectral bands to enable the discrimination of the major Earth surface materials (see **Figure 2.3-2)**. The radiations are mainly recorded in the the visible and the infrared regions, corresponding to the wavelengths region extending from the visible and near-infrared (VNIR) to the short-wave infrared (SWIR).

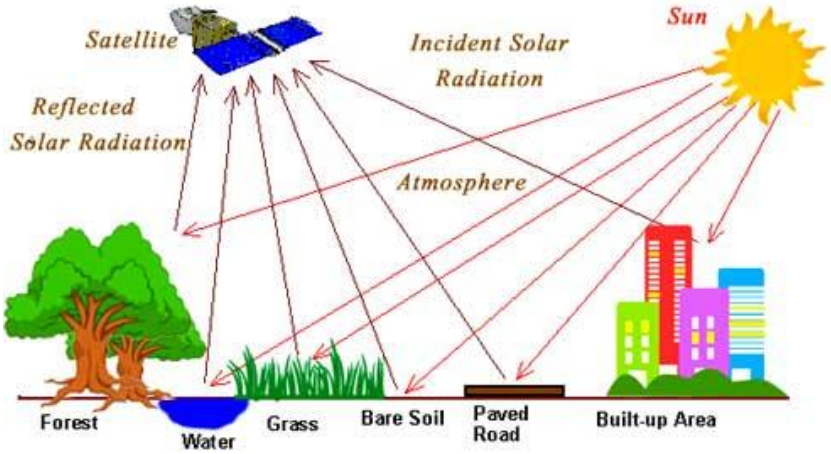

Figure 2.3-2 : Principle of satellite remote sensing (NASA, 2016)

2.3.2.2. Data description

The Remote sensing data of interest have been measured by the Operational Land Imager (OLI), a sensor on-board of the Landsat-8 satellite launched in February 2013 (http://earthexplorer.usgs.gov/). Landsat-8 (OLI) images scanned in nine bands categorised into multispectral (band 1 to 7), Panchromatic (band 8) and Cirrus (band 9). These spectral bands are presented in **table 1**. The approximate scene size is 185 km north-south by 180 km east-west. These data are freely available from the Global Land Cover Facility homepage (http://earthexplorer.usgs.gov/). USGS (2016) provides any interested reader with Landsat-8 products specifications.

Table 1 : Characteristics of a Landsat 8/ OLI data (USGS, 2016)

Band Number	Spectral range (µm)	Spectral band	Resolution
1	0.43 - 0.45	Coastal blue	30 m
2	0.45 – 0.51	Blue	30 m
3	0.53 – 0.59	Green	30 m
4	0.64 – 0.67	Red	30 m
5	0.85 – 0.88	NIR	30 m
6	1.57 – 1.65	SWIR-1	30 m
7	2.11 – 2.29	SWIR-2	30 m
8	0.50 – 0.68	Panchromatic	30 m
9	1.36 – 1.38	Cirrus	30 m

The data used in the current study have been recorded on the 12th January 2015. These are to two adjacent scenes whose respective path/row identifications are 185/057 and 185/058 (**Figure 2.3-3**). The Landsat-8 products used are standard L1T1 i.e. geometrically corrected data.

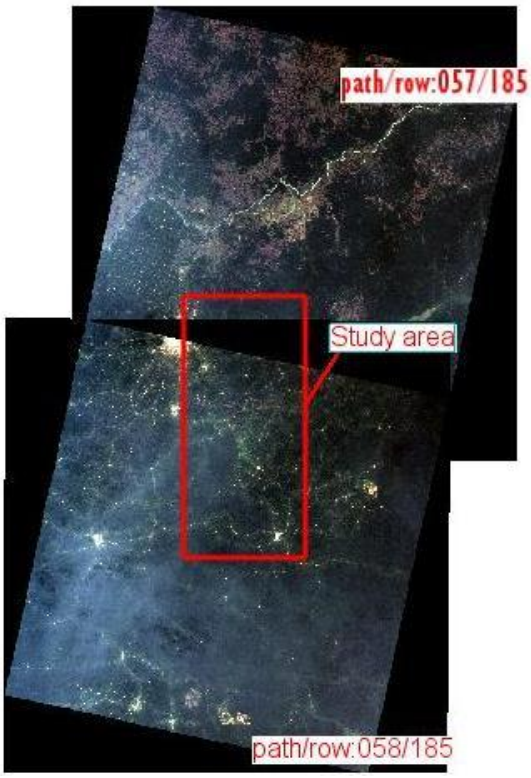

Figure 2.3-3 : True-colors Landsat 8 scenes used in this study.

2.3.2.3. Data processing and analyses

a. Data pre-processing

OLI data are level 1-T images, i.e. they are terrain-corrected (geometrical correction). However, these images necessitate additional pre-processing, starting with the radiometric calibration.

- ***The radiometric calibration:***

The radiometric calibration is a two-steps procedure which permits to transform digital numbers (DN) contained in one image into physical parameters i.e. radiance and reflectance, progressively for each band. The parameters values required for calculations are given in the metafile accompanying images:

Calculation of the radiance*:* The radiance is a measure of the energy radiated by an object. The operation (equation 21) corresponds to the transformation of digital number (DN) of each scene for a given band of wavelength λ to radiance at sensor L_λ, using the formula below:

$$L_\lambda = M_L * Q_{cal} + A_L \qquad (21)$$

With: L_λ = spectral radiance in $Wm^{-2}\ sr^{-1}\ \mu m^{-1}$; $\mathbf{Q_{cal}}$ = quantized calibrated pixel value in DN; M_λ and A_L = radiance multiplicative and additive scaling factors, respectively for the band.

***Calculation of the top of atmosphere (ToA) reflectance**:* The reflectance ρ is the measure of the ration of outgoing to incoming energy. The ToA is calculated using equation (22):

$$\boldsymbol{\rho_\lambda = [M_\rho * Q_{cal} + A_\rho]/sin\vartheta} \quad (22)$$

With: $\boldsymbol{\rho_\lambda}$ = ToA reflectance (unitless); $\mathbf{Q_{cal}}$ = quantized calibrated pixel value in DN; $\boldsymbol{M_\rho}$ and $\boldsymbol{A_\rho}$ = reflectance multiplicative and additive scaling factors, respectively for the band; $\boldsymbol{\vartheta}$ solar elevation angle. After the radiometric correction, the scenes are mosaicked then, spatially subset to the size of the study area before the next pre-processing step.

- ***Vegetation suppression:***

Vegetation suppression (Crippen and Bloom, 2011) removes the vegetation's spectral signature from multispectral and hyperspectral imagery, using information from red and near-infrared bands (**Figure 2.3-4**). This method helps to better interpret geologic and urban features in medium spatial resolution (as for Landsat-8) imagery.

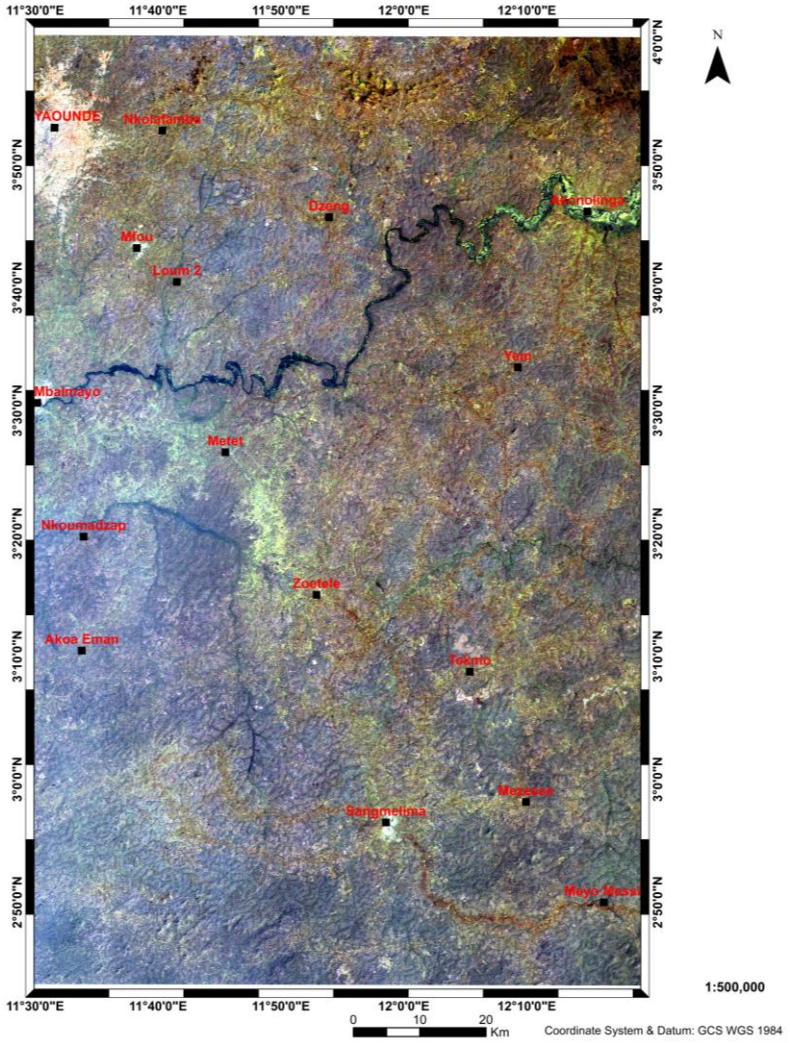

Figure 2.3-4 :Mosaicked image subset to the study area after the suppression of vegetation.

The algorithm models the amount of vegetation per pixel by calculating the relationship of each input band with vegetation, then decorrelating the vegetative component of the total signal on a pixel-by-pixel basis for each band. The result (**figure 2.3-4**) is useful for qualitative analysis, primarily for linear feature enhancement hidden by closed canopies.

b. Image enhancement: Principal components analysis (PCA)

The purpose of image enhancement is to highlight lithological features (Schowengerdt, 2007; Liu and Mason, 2009). The chosen image enhancement technique is the principal components analysis (PCA). This transform uses the variance to segregate noise components and to reduce the dimensionality of datasets, by finding a new set of orthogonal axes that have their origin at the data mean and that are rotated so that the data variance is maximized (Liu and Mason, 2009). The variance S_j^2 or second order momentum quantifies the spread of a distribution; it is given by the relation:

$$S_j^2 = \frac{1}{n}\sum_{i=1}^{n}\left(x_i^j - \overline{x^j}\right)^2 \qquad (23)$$

Where n is the number of bands, x_i^j is the jth vector of the ith band and $\overline{x^j}$ is the central mean of the j values which is defined as:

$$\overline{x^j} = \frac{1}{n}\sum_{i=1}^{n} x_i^j \qquad (24)$$

PCA seeks a linear combination of variables such that the maximum variance is extracted from the variables. It then removes this variance and seeks a second linear combination which explains the maximum proportion of the remaining variance, and so on till it produces orthogonal (uncorrelated) bands. The PCA is particularly useful because multispectral data bands are often highly correlated. The last PC bands appear noisy because they contain very little variance, much of which is due to noise in the original dataset (**figure 2.3-5)**. The preprocessing and image enhancement tasks have been realised with ENVI 5.3 ® software.

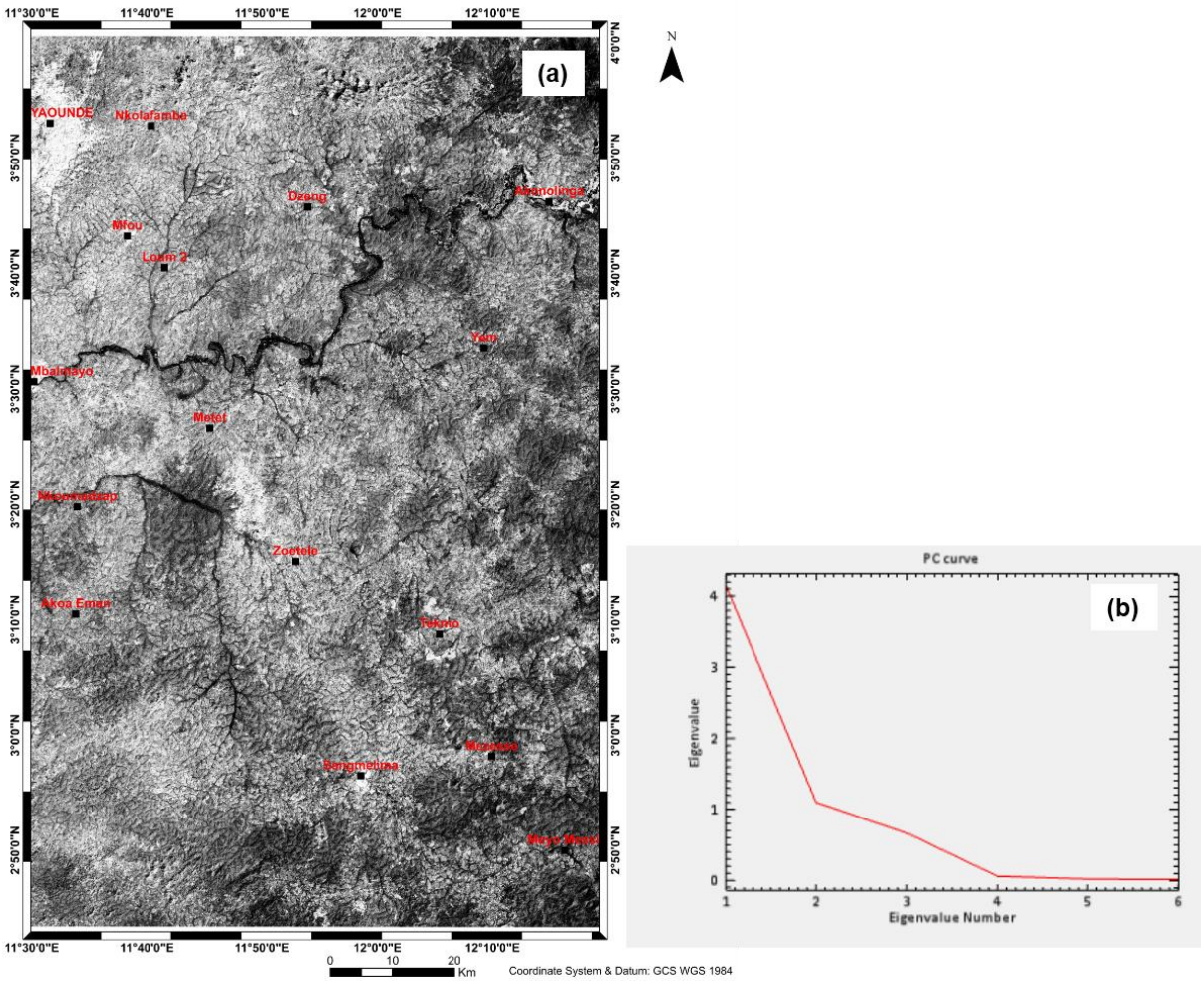

Figure 2.3-5 : Principal component analysis (PCA)from fig.2.3-4. (a) The PCA1 image over the study area; (b) PCA analysis graph showing that thePCA1 contains almost all the information from to the target area.

c. Lineament filtering and extraction

Filtering process involved the application of directional filter for lineaments detection. For the case, the Sobel filter have been applied to the greyscaled PCA1 image along four directions (N-S, NE-SW, E-W and SE-NW) using a 7 x 7 built-in window on ENVI 5.3 platform. The Sobel filter is an edge detector, particularly useful to delineate lithological contacts, faults, fractures or joints (Mwaniki et al., 2015; Teikeu et al., 2016; references therein).

The lineaments extraction involved a semi-supervised classification that consists in (1) merging the Sobel's filtered images into a unique image; (2) extracting lineaments automatically, using the LINE module in PCI ® Geomatica v.9.0 (**see Figure 3.3-1**); then, (3) removing manually the anthropic lineaments within the output after underlaining image from (1) by the digital elevation model generated from the SRTM data of the area; and applying the photo-geological approach to interpret structural lineaments based on visual continuity and hydrography. The tasks are performed with Esri® ArcGIS 10.6. (for map editing) and Rockworks 16 ™ (to compute lineaments statistics).

2.4. JUSTIFICATION OF THE STUDY APPROACH AND WORK METHODOLOGY

2.4.1. Justification of the approach

Geophysical investigation in least-developed countries like Cameroon remains very challenging. For scientists and researchers, the main challenge to overcome is the access to data because of the lack of geophysical equipment, and the lack of funding for data collection or data purchase. In this study, the coverage of the entire study area has been ruled by the data availability. In fact, because of the absence of funding, the AMT survey initially planned for the entire study area has been interrupted and thus restricted to the portion covering Yaounde-Nkolafamba-Mfou zone. Later access to aeromagnetic data enabled to cover the remaining space but the flight ban above Yaounde (the country's city-capital) made it impossible to have magnetic data in the AMT-surveyed zone. As a result, the space is divided into two adjacent sub study areas depending on the geophysical method. The northwestern area covered by the tensor-AMT survey while aeromagnetics prevails in the remaining domain. This led to a new approach in geophysical studies departing from usual superposition of methods over a same study area, as explicated in the next section.

2.4.2. Workflow methodology

The study is a juxtaposition of geophysical methods over the study area for regional structural study. It chiefly consisting in:

(a) Juxtaposing two differents methods (tensor-AMT and aeromagnetics) in two adjacent subsets areas, each serving to highlight structural features but the magnetic study additionnally aims verifying the south-continuity of structural features outlined by the tensor-AMT study, then possibly outline the lithology.

(b) Remote sensing the entire study area using Landsat-8 OLI data. The remote sensing herein mainly serves to correlate both AMT and magnetic outputs in order to (1) validate the spatial extension of the lineaments outlined all over the study area and (2) validate magnetic feature mapping.

(c) Cross-validating and integrating the three methods (two by two) by merging their outputs to form a unique study's final output.

(d) Validating the geophysical results from (c) with both existing geological results from previous studies and the geological information collected during field campaigns.

Conclusion

To fulfil the purposes of this thesis, researches were initially based on AMT and aeromagnetics. The insufficiency of ground controls and the coverage of the area by each of

these methods led to the integration of remote sensing to link them. The **figure 2.4-1** shows the coverage of the study area by each used geophysical prospecting method and the field geological investigation. Usually, studies rather involve the superposition of methods above the same area; departing from this approach, a new methodology capable of solving geological problems by juxtaposing geophysical methods is proposed. Since physical laws cannot entirely explain the Earth's behaviour as geologic complexities are above simple explanation, geophysical models always contain valuable information that can be extracted as errors using inadequate data are much less than those using no data at all.

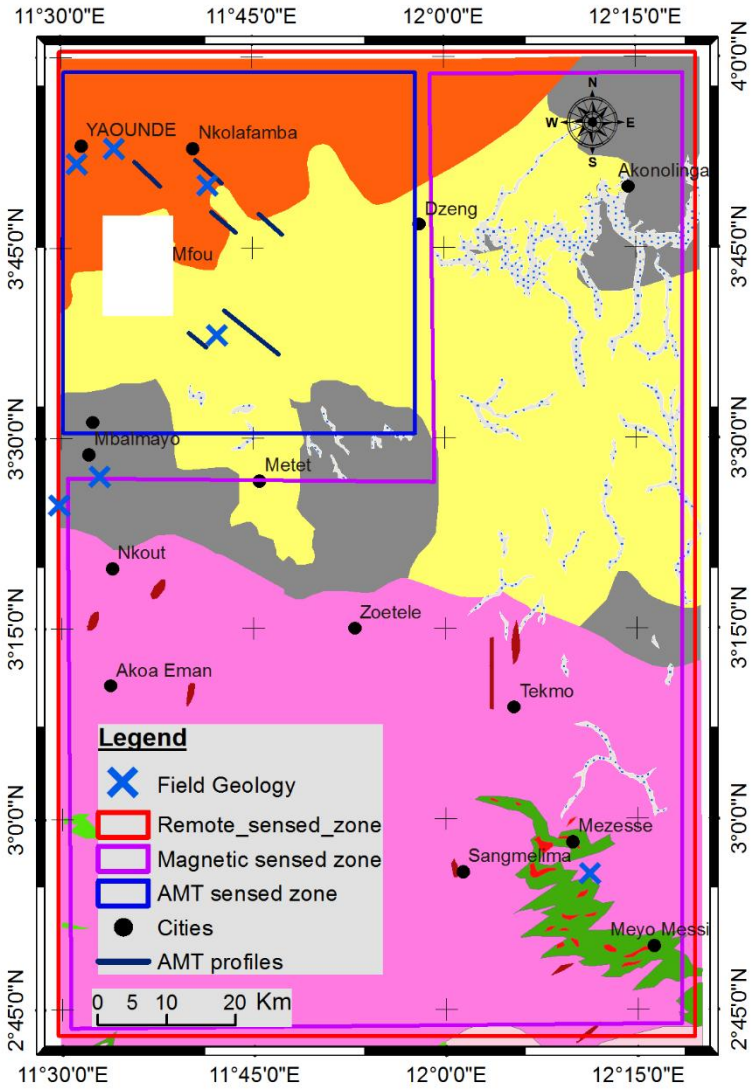

Figure 2.4-1 : Distribution of area coverage according to each method.

CHAPTER THREE: RESULTS AND DISCUSSIONS

Introduction

In geological investigation, the contribution of geophysics is merely at locating and determining the orientation of various structural elements and probable lithology. Inspite of being right or wrong, a geophysical model can also be irrelevant; hence the need of ground controls to constrain it. Alternatively, multiple geophysical techniques can be used as it follows.

3.1. AUDIOMAGNETOTELLURIC DATA INTERPRETATION

Though empirical means exist to assess the geoelectrical structure (Groom and Bailey, 1986) and despite the operational assumptions of the stratagem, a dimensional analysis has been carried out before any interpretation of AMT data.

3.1.1. Geoelectrical structure of resistivity anomalies

The dimensionality or geoelectrical structure of AMT data in the study area has been determined using ZondMT2D™ (**figure 3.1-1**). The dimensionality is evaluated by observing the behaviour of the impedance along a given profile. In general, the resistivity structure in the area is 2D; the 2D character is recognisable by the two petal flower shape observed at each sounding station (**Figure 3.1-1**).

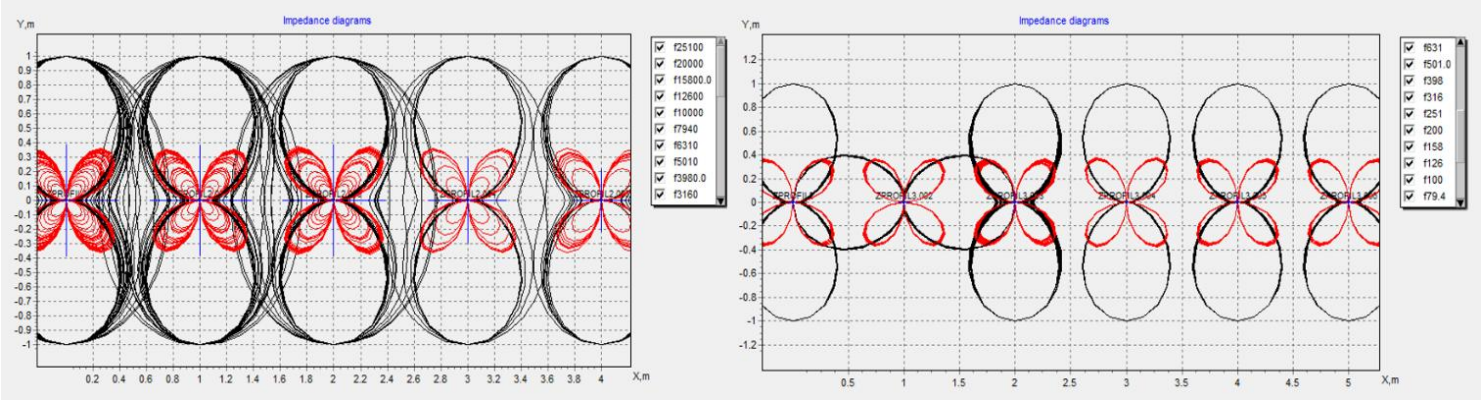

Figure 3.1-1 : Dimensionality analyses Nkolafamba data. The results presented for profile 2 (left) and profile 3 (right) show that the electrical structure is at least 2D.

The subcircles surrounding some flowers (**Figure 3.1.1 left**) show that the structure can be 2d or 3D, or either suffer some galvanic distortion. This is partly overcomed by the rotation of data within the Stratagem system, providing the best electrical strike of the impedance (Geometrics, 2000; McPhee et al., 2006). Based on that inferred two-dimensionality, AMT data interpretation is limited to the analysis of phase and apparent resistivity pseudo-sections, and geoelectrical sections.

3.1.2. Profile 1 (Ossol)

3.1.2.1. Phase pseudo section

The observation of the phase pseudo section plot (**Figure 3.1-2**) shows three (03) main features. The first is characterised by a mean phase value of 45°. It appears from surface to middle depth (frequencies greater than 1200 Hz) along the whole profile and at depth, below station OS5 and station OS6 (frequencies less than 80 Hz).

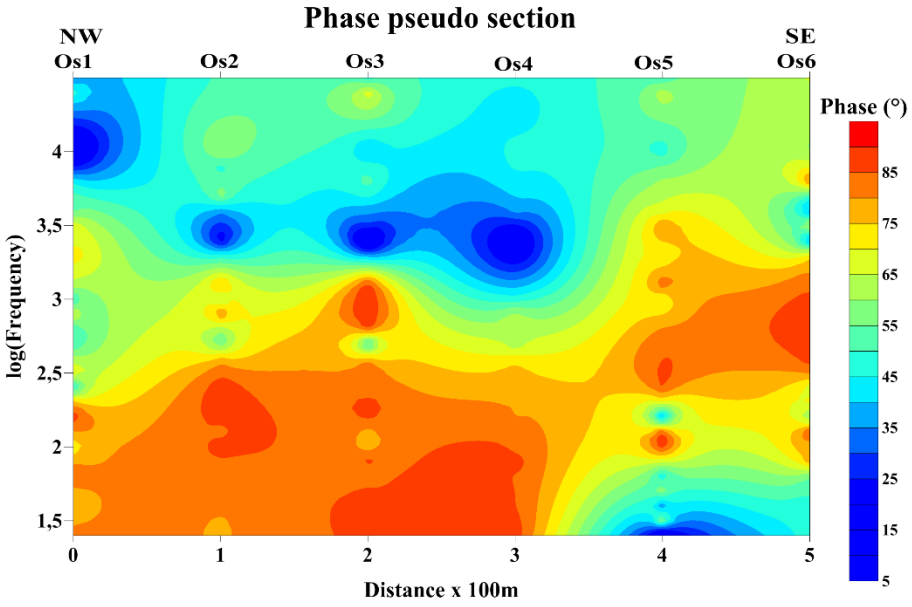

Figure 3.1-2: Phase pseudo section of profile 1 (Ossol). One of the most highlights is the high-phase values channel with a mean value of 85°.

The second feature is characterised by a mean phase value of 85°. It is displayed like an oblique channel along the whole section from the lower left to the middle (or the upper right in another view) right border. The third group of features is characterised by elliptical isophase anomalies at middle depth from OS2 to OS4, at near surface beneath OS1 and at depth under station OS5. These anomalies are characterised by a mean phase value of 14°. The phase pseudo-section (**Figure 3.1-2**) suggests a conductive shallow subsurface in the area. Some vertical to subvertical curve lines are also observed in various part of the pseudo section, particularly between 250 m and 350 m.

3.1.2.2. Apparent resistivity pseudo section

The apparent resistivity pseudo section (**Figure 3.1-3**) of profile 1 shows three concentric resistivity anomalies from depth to surface. These anomalies have a mean resistivity value of 193.0 Ω.m and they form a conductive channel located between stations OS3 and OS5, corresponding to a probable upwell or intrusion of conductive materials. The plot also portrays a conductive entire near surface and an anomalous resistant structure centred at OS3 and evolving

downwards. Another subcircular resistive anomaly is observed downward from mid-depth beneath stations OS5 and OS6.

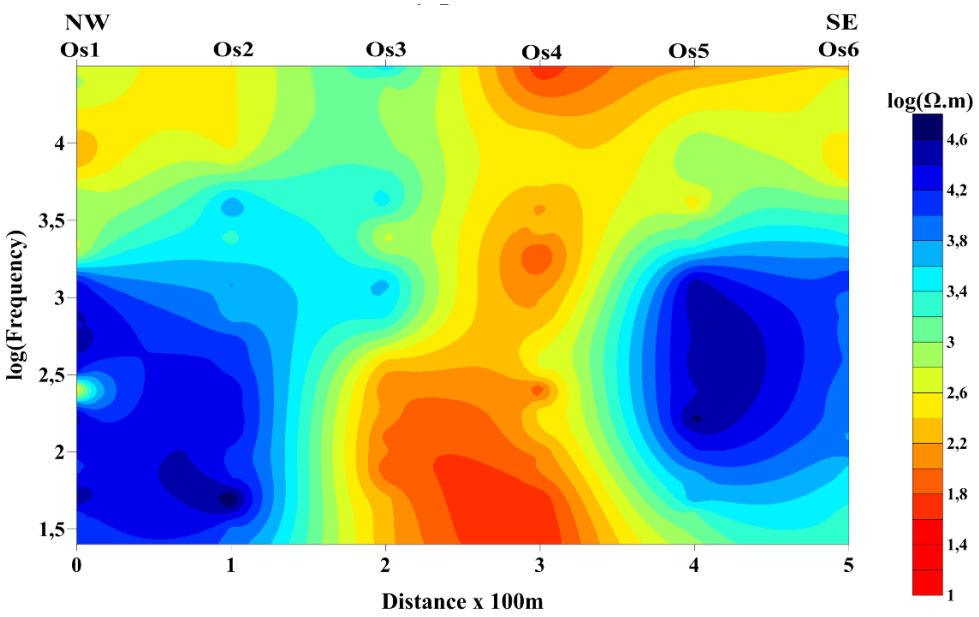

Figure 3.1-3 : Resistivity pseudo section of profile 1 (Ossol).A SW-NE conductive channel (reddish coloured) cross-cut the subsurface, probably a NE active fault.

The apparent resistivity pseudo section (Figure 3.1-3) of profile 1 (Ossol) shows irregular distribution and shapes of isoresistivity contours lines corresponding to variations of the resistivity. These variations along with the vertical to subvertical disposition of resistivity contour lines (beneath stations OS2 and OS5) may infer some geological discontinuities. The curling of these contours suggest that the area may have undergone a folding process. Discontinuities detected could be interpreted as faults or some geological major contacts. These facts (shapes of isoresistivity contour lines, curling, discontinuities, etc.) are inferrences of an intense tectonic activity in Ossol.

The pseudo-sections (**Figures 3.1-2** and 3.1-3) show irregularly shaped iso-contours shapes at all. They both exhibit dislocation patterns of blocks on one hand, and on another, they show that conductive formations are encountered both on surface and at depth.

3.1.2.3. Geoelectrical section

The analysis of the geoelectrical section (Figures 3.1.4 and 3.1.5) suggests that the Ossol subsurface lithology is broadly made up of five (05) formations. The following facts are noticeable, looking downwards:

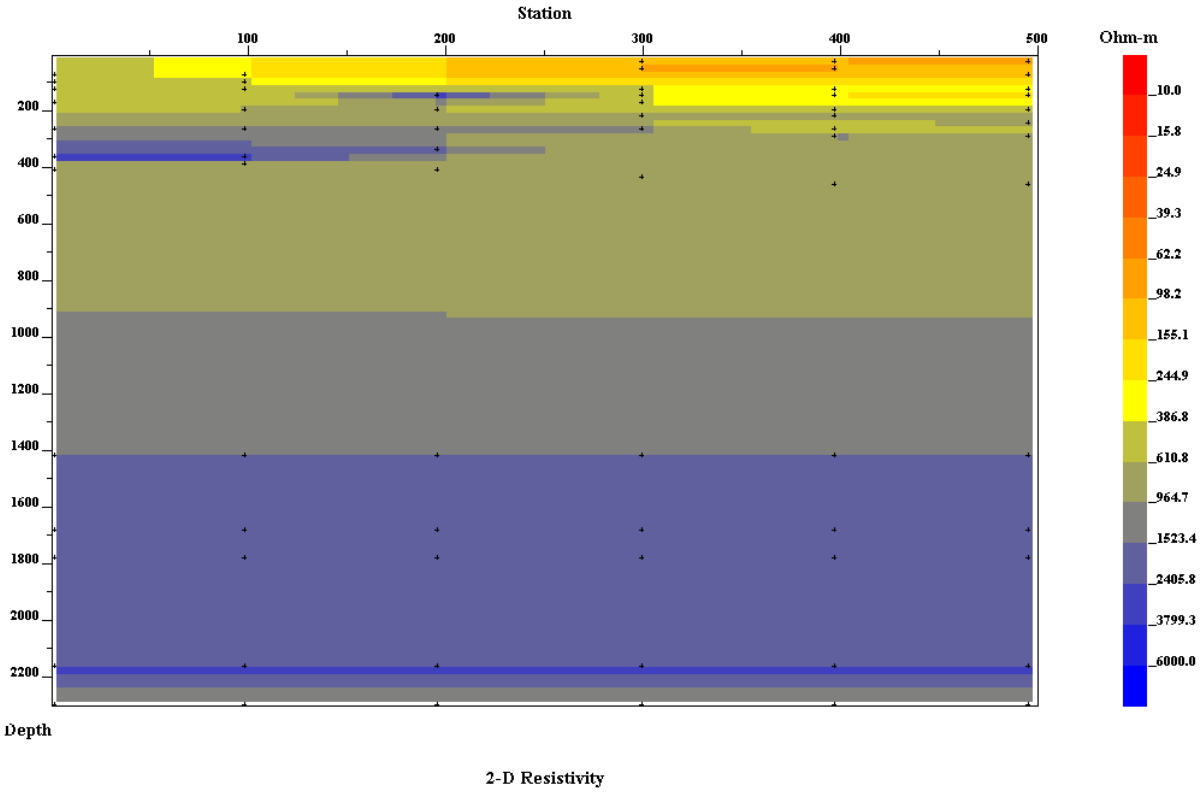

Figure 3.1-4 : Geoelectrical section of profile 1 (Ossol) from 0 to 2200 m depth.

- At the top of the plot, we have two conductive formations of mean resistivity 147.2Ω.m and 284 Ω.m, respectively. The contacts between these conductive formations are identified as faults detected at OS2 and OS5. The second formation, outcropping from station OS1 to OS2, is discordant to the third, and it is also marked by a collapse zone between stations OS2 and OS5.
- The third formation, with resistivity's values ranged between 374 Ω.m and 721.7 Ω.m (nearly 547.9 Ω.m mean resistivity), appears at 100 m and ends at 275 m depth below OS1. Its varying thickness diminishes toward the end of the profile. Indeed, this formation is jagged by many discontinuities (at stations OS2, OS4 and OS5) that can be interpreted as faults which mark collapse zones on the top of this formation; thus shaping it like stairs with four footsteps. The first step runs from OS1 to OS2, the second from OS2 to OS4, the third from OS4 to OS5 and the last from OS5 to the last station of the profile. Hence seemingly, the area suffered a collapse that affected the ground structures in Ossol area. This was imprinted to shallow near surface structures (**Figures 3.1-4** and **3.1-5**), so the top of the third structure is shaped like a graben as shown on the plot. Additionnally, a resistive intrusion of the underlying material seems to rise through a probable fracture affecting the third formation at station OS3, then forms a sill of 100 m

length and 25 m thick at about 150 m depth (the intrusive body is centred at OS3). The third terrain lays discordantly to the fourth.

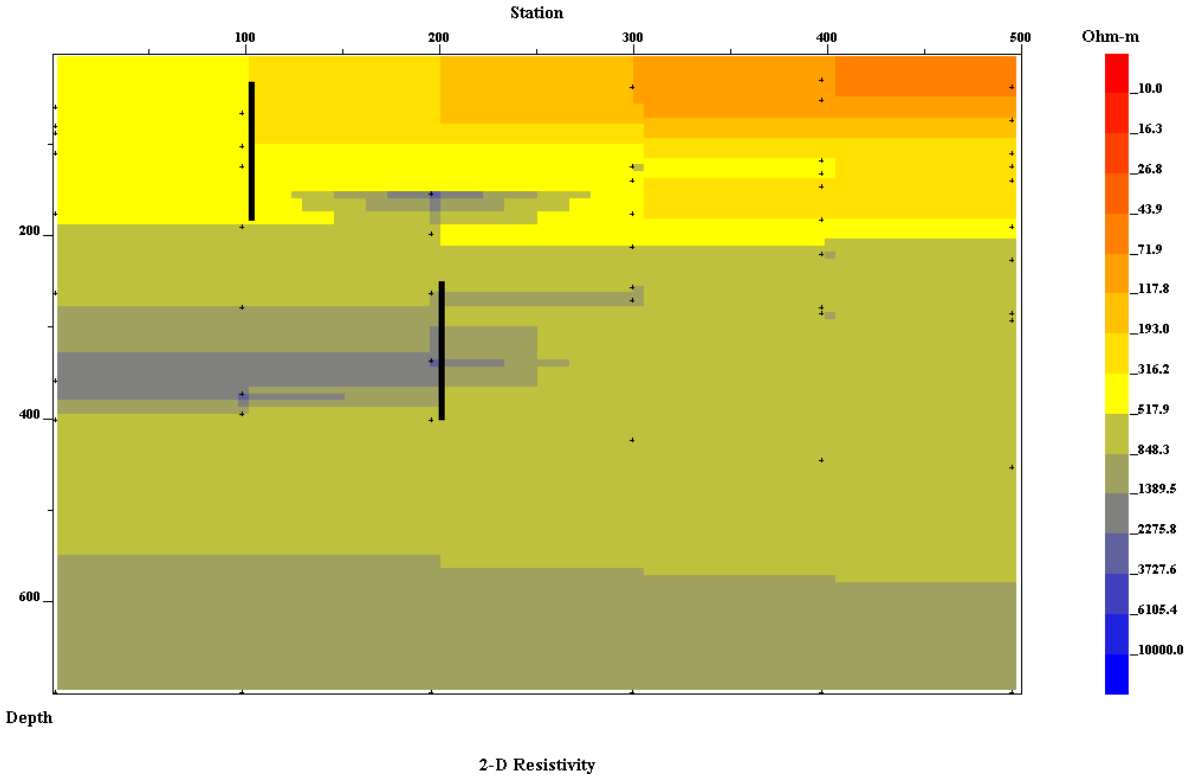

Figure 3.1-5 : Section from 0 to 650 m depth to emphasis on shallow structures.

- The fourth formation, characterized by a mean resistivity value of 1057 Ω.m (very resistant), is broadly encountered at 275 m from station OS1 to OS5. It is affected by discontinuities beneath stations OS3, OS4 and OS5. The one at OS3 and that below OS4 can be interpreted as faults while that under OS5 looks like a scarp because of its size. The roof of this fourth formation significantly forms a horst between stations OS3 (where it intrudes the overlying formation) and OS4. The geoelectrical section plot also reveals an intrusion of a more resistive material from OS1 to OS3 which resembles a fork or anything alike. The origin of this intrusive body is difficult to explain. The thickness of the fourth terrain is close to 1125 m (it extends from 275 m to 1400 m depth) and it seems to rest concordantly with the fifth terrain (with a mean resistivity's value of 3934.8 Ω.m) encountered at 1400 m depth and interpreted as the bedrock.

The geoelectrical section of profile 1 shows that the resistivity of ground formations in the Ossol village increases with depth.

3.1.3. Profile 2 (Beguele 1)

3.1.3.1. Phase pseudo section

Analysing the phase pseudo section (**Figure 3.1-6**) of profile 2 (Beguele1) leads to the differentiation of three main classes of phase anomalies, similarly to profile 1. The plot mainly exhibits a high phase anomaly value that dominates the section, with a mean value of 80°. This anomaly spans over the whole depth (in low frequencies). It is shallow around 316 Hz from BE1 to 150 m before BE2, rises to near surface (from 316 Hz to 10000 Hz) between BE3 and BE4, then collapses from BE4 to BE5 (very low frequencies range). Both middle and very low phase values anomalies overlain that high phase values anomaly from BE1 to BE3 and from BE4 to BE5. The very low phase anomaly is mainly located from BE1 to BE2, at near subsurface.

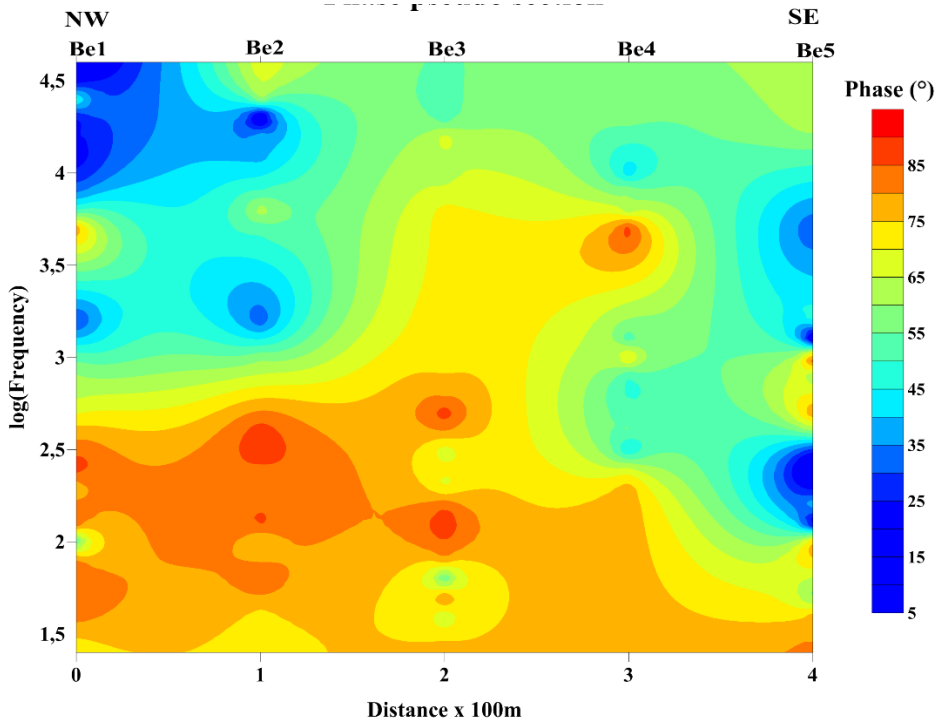

Figure 3.1-6 : Phase pseudo section of profile 2 (Beguele 1). The plot is dominated by a very high phase value anomaly characterising deep geology of the area. The mean phase value of this anomaly is 80°.

In addition to the above observations from the phase pseudo section of profile 2, it appears that the phase contour lines are very disturbed. They are vertical to subvertical around BE3 and BE4. This suggests than the area is dominated by two or three main lithological types and that the area is probably affected by a major discontinuity.

3.1.3.2. Apparent resistivity pseudo section

The apparent resistivity pseudo section (**Figure 3.1-7**) brings in additive information to the understanding of Beguele 1 geological setting. The apparent resistivity pseudo section from profile 2 (Beguele 1 village) reveals many outcomes but the prominent output is the partition of the subsurface into two main blocks. The first block spans from surface to middle depths (from

higher to nearly 3100 Hz). It corresponds to a group of conductive formations that seem to compose the Beguele 1 near subsurface. A shallower more conductive set is also observable within the above described block. This shallower conductive group is dipping NW-SE from station BE1 to station BE2.

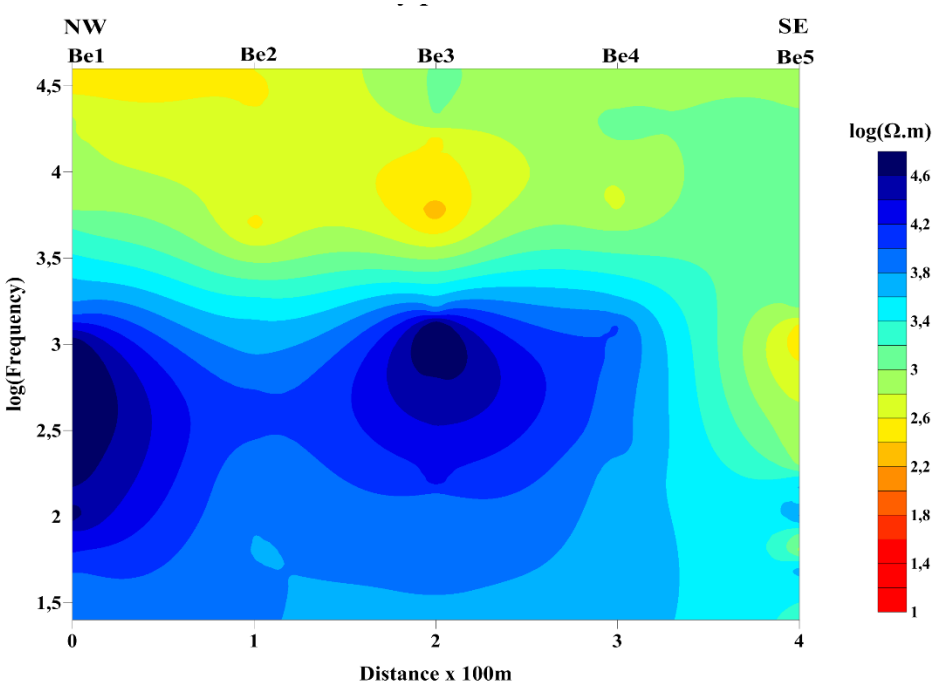

Figure 3.1-7 : Apparent resistivity pseudo section of profile 2 (Beguele 1). The plot is dominated by a very high resistivity value anomaly characterising the subsurface geology of the area.

The second block represents a set of very resistive formations. It dominates the subsurface from middle to very low frequencies (downward from middle depth). Vertically it occupies more than a half of the depth on the pseudo section, hence we can suggest that the first block is not very thick. The abrupt end beneath station BE4 shapes this resistivity anomaly like a rectangle while it is strangled at station BE2. The resistive and the conductive zones are separated by a thin transitional layer.

The high resistive anomalous zone ends below BE4 with vertical contour lines that suggest the presence of a major discontinuity. Further, the strangle affecting the iso-contour lines beneath BE2 also mark the presence of a discontinuity; probably vertical shear zones that could evidence vertical movements of subsurface blocks of formations. In addition to the discontinuities highlighted, the apparent resistivity contours are also irregular.

3.1.3.3. Geoelectrical section

The geoelectrical section of the profile 2 has been realised in order to image the subsurface of the Beguele 1 area up to 1500 m depth (**Figure 3.1-8**) but a focus was made for shallow subsurface imaging (**Figure 3.1-9**).

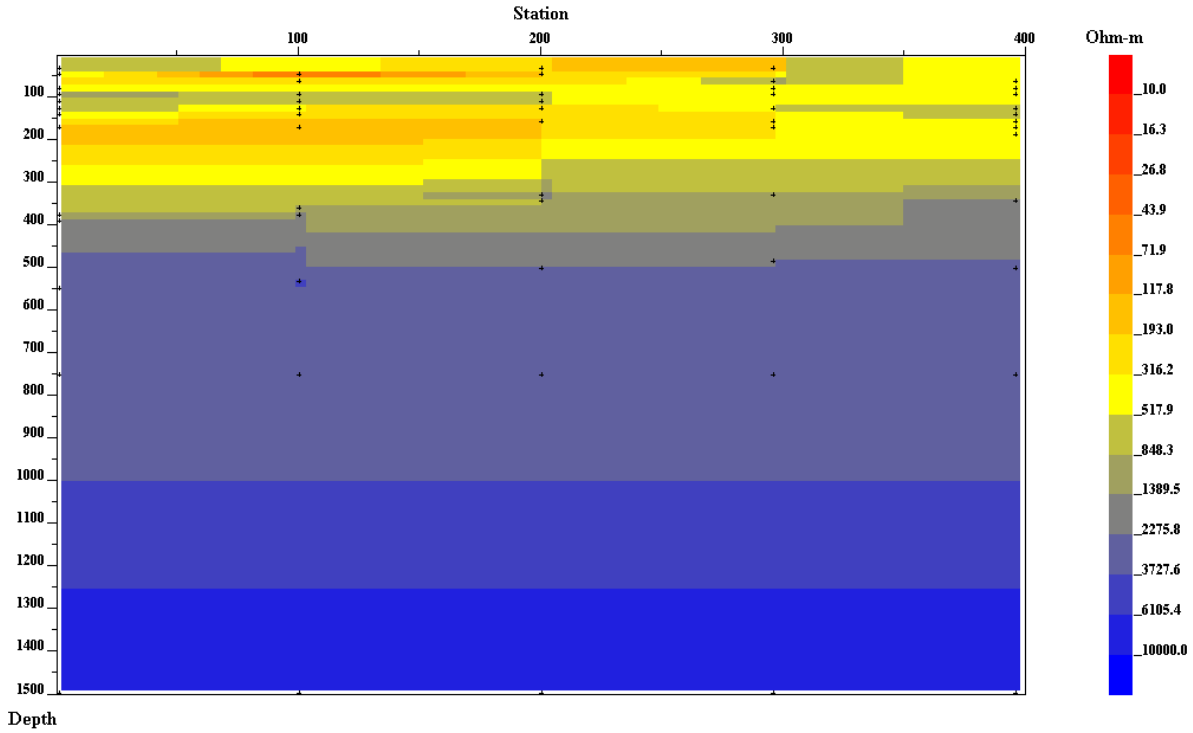

Figure 3.1-8 : Geoelectrical or 2-D resistivity section of profile 2 (Beguele 1) for 1500 m depth. The plot shows that the substratum (blue level) is shallow (encountered at 500 m depth).

The geoelectrical section of the Beguele 1 area suggests a four to five layered earth model. The section presents a four (04) layered earth model. From surface to depth we observe:

- The first terrain is characterised by resistivity values within the range [10.0-517.9] Ω.m, or a mean resistivity value of 264 Ω.m, with an average thickness of 300 m. A more conductive layer firstly above the 100 m depth level from BE2 to BE4 (300 m) and secondly between the 150 m and 250 m depth level. This conductive layer is not interpreted as a separate formation, but may rather correspond to an alteration zone within the first terrain. It is intruded in some parts by thin layers (or sills) and blocks of materials whose resistivity characteristics (especially value) correspond to those of the second terrain. Clearly the resistivity patterns observed on the plot show that this layer is not homogenous and it can be seen that the bottom of this layer is also affected by the underlying formation. The origin of underlying materials within this first terrain is not clearly explainable based on the profile 2 observation only.

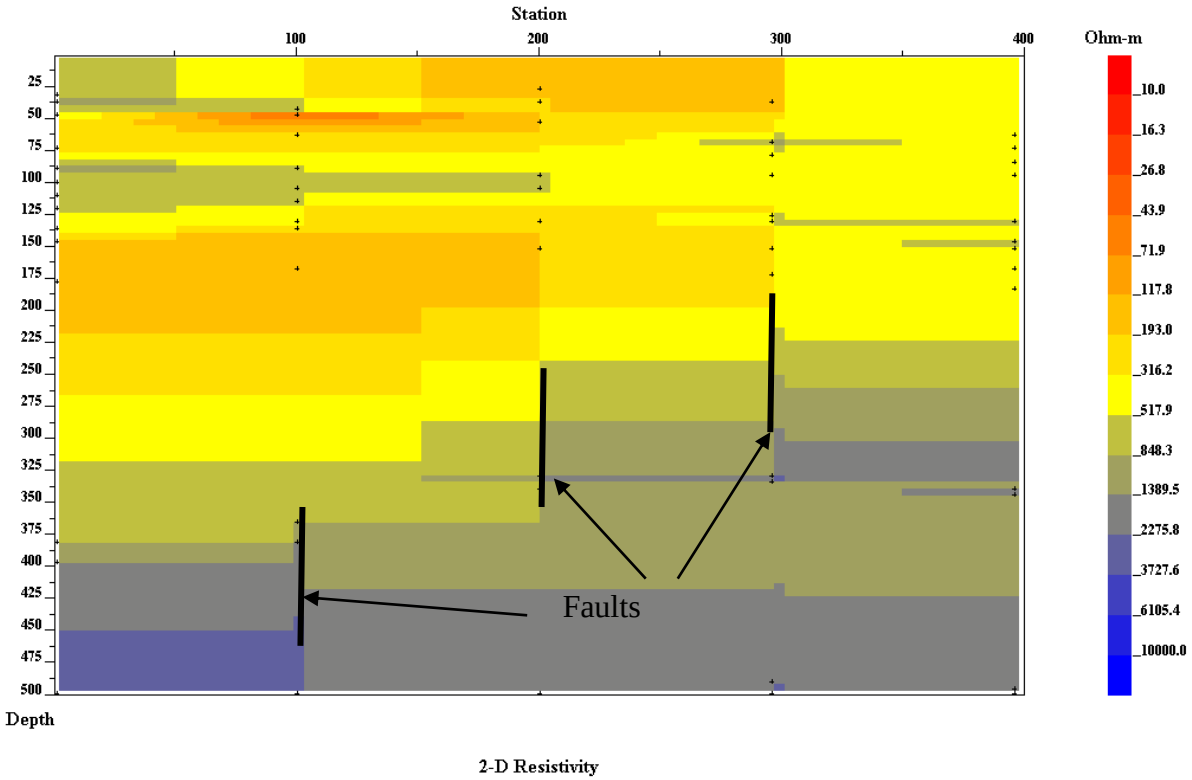

Figure 3.1-9 : Geoelectrical or 2-D resistivity section of profile 2 (Beguele 1) for 500 m depth. The upper terrain is very thick (averaging 300 m) while the second and the third terrains both form a thin sheet of 200 m, but display some discontinuities (between BE2 and BE3, at BE3 and BE4).

- The second terrain is encountered at 325 m depth (Figure 3.1-9), it has an approximate thickness of 50 m but it is thin from BE4 to BE5. The second formation is also conductive and it is characterised by a mean resistivity value of 953.7 Ω.m. Contrarily to the overburden, the second terrain seems homogenous. From Figure 3.1-6 b above, some discontinuities are observable at 50 m beyond BE2, at BE3 and BE4. These discontinuities can be interpreted as faults especially those located between stations BE2 and BE3 (with an upthrow of about 17 m) and BE3 (with an upthrow of 25 m); the discontinuity at BE4 can be interpreted as a scarp. Further, the aforesaid discontinuities shape the roof of this formation like a SE rising downstairs whose steps are at 50 m beyond BE2, at BE3 and BE4. The second formation seems therefore settled as a set of four (04) adjacent blocks; the first block is 150 m wide and starts from BE1, the second is narrow (50 m only), the third block is 100 m from BE3 to BE4 and the fourth, with the same dimension as the previous runs from BE4 to the end of the profile. This suggests a graben-like disposition of shallow surface structures beneath Beguele 1 area. The breaks in the second formation are relays from the third formation.
- The third formation is characterised by values of resistivity in the [1389.5-2275.8] Ω.m interval or a mean resistivity value of 1832.6 Ω.m. this layer is clearly observable on

Figure 3.1.9. We can see within it that it is very thin from BE1 to BE2, but thickens increasingly from BE2 to the end of the profile (where it has a thickness of more than 100 m). This formation is also jagged by discontinuities at BE2, BE3, and BE4. The discontinuity at BE3 can be interpreted as a fault but those at BE2 and BE4 can be interpreted as faults or scarps either. The third formation is also shaped like downstairs, in the same manner as the second formation above. It is additionally intruded from SE to NW by a resistive material of 25 m thick (but becomes tinny from BE4). This resistive intrusion can be interpreted as a probable sill; this material displays identical resistivity characteristics as the formation below.

- The fourth formation is encountered at 400 m depth, with a mean resistivity value of 3001.7 Ω.m. This formation doesn't exhibit irregular patterns of filling in materials like those above, i.e. this formation seems homogenous. The fourth terrain has an average thickness of 100 m but it thickens from 350 m to the end of the profile. Like the terrains above, the fourth layer is jagged by three (03) discontinuities located respectively at BE2, BE4 and 350 m (50 m beyond BE4). The discontinuities highlighted can be interpreted as faults. Some of these affect the overlying formations. The fourth formation seems to be affected by a collapse between BE2 and BE4. This collapse originates from the underlying layer which may correspond to the fifth formation.
- The fifth formation or layer is characterised by a mean resistivity greater than 3001.7Ω.m and it is encountered at around 500 m depth. This formation can be interpreted as the geoelectrical the basement of the area. However, this formation displays a first level running from 500 m to 1000 m depth; this upper level presents two discontinuities at BE2 and BE4 respectively which can be interpreted as faults. These faults are guides of the collapse noticed between the above mentioned stations, of this upper level of the basement. This upper level is rather interpreted as an oxidised or weathered level of the basement than as an individual layer or formation. From 1000 m to 1500 m and so on, we reach the proper basement of the Beguele 1 area.

The 2-D inverse model (or geoelectrical section) of the profile 2 shows that resistivity increases with depth. Further, outputs from the geoelectrical section are consistent with observations made on the apparent resistivity pseudo section (**Figure 3.1-7**). Indeed, the geoelectrical section also displays two main blocks. The first is represented by the first conductive terrain reported on the analysis of the geoelectrical section, while the second corresponds to the basement. These two blocks are separated by a thin (compared to the scale of the depth covered on the plot (**Figure 3.1-7**) level constituted by the second, the third and the

fourth terrains, in the same way as displayed on the corresponding apparent resistivity pseudo section of Beguele 1.

3.1.4. Profile 3 (Nkolafamba)

3.1.4.1. Phase pseudo section

The **Figure 3.1-10** below represents the phase pseudo section of profile 3. On this pseudo section plot, low phase anomalies are observed both at high and low frequencies. For low frequencies (less than 80 Hz), one has a dome shaped phase contours with a peak below NK1 affecting the domain beginning at NK1 and ending at NK3. Phase values range is 10° to 21°, with a minimum value (10°) recorded below NK2 for a frequency close to 60 Hz. The dome shaped anomaly is dissymmetric, its apex is centred at NK2, and the NW flank is very steep while the SE flank is gradational. The shapes of these isocontours suggest the presence of discontinuities at depth, the first dipping NW while the second is dipping SE.

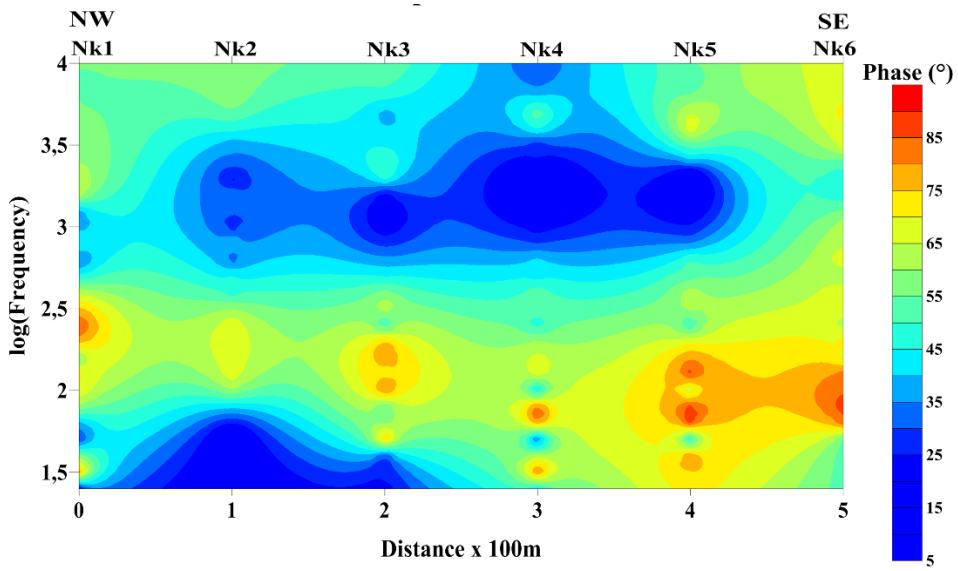

Figure 3.1-10 : Phase pseudo section of profile 3 (Nkolafamba). The plot exhibits two low phase anomalies (blue colour) separated by a high phase (reddish) anomaly channel.

For high frequencies, phase contours have a no ordinary shape (they look like a fish or a boat) that covers large part of the profile length. Meanwhile, a low phase anomalous zone is encountered from NK2 to beyond NK5 with a phase band values being 10° to 18° (it may reach 21°); the minimum phase values (average of 10°) are recorded between NK4 and NK5. Beside this major features observed, one can notice that isophase contour lines suggest a mixture of structures. Another noticeable element can be the vertical to subvertical isoresistivity contour lines centred at station NK4 that suggest a fault. Between these resistive structures one can observe a surrounding medium characterised by high phase values that suggests a conductive channel.

3.1.4.2. Apparent resistivity pseudo section

The apparent resistivity pseudo section of profile 3 (Nkolafamba) is given by the **Figure 3.1-11** below. The observation of the apparent resistivity plot enables to clearly outline three (03) main bands, from surface downward. The first band corresponds to conductive formations at near subsurface; the second band is a transition zone between the upper very conductive band and the lower resistive one. This transition zone is made up of intermediate conductive formations. The third and last band characterises very resistive formations that appear from 1200 Hz to lower frequencies (to deep levels).

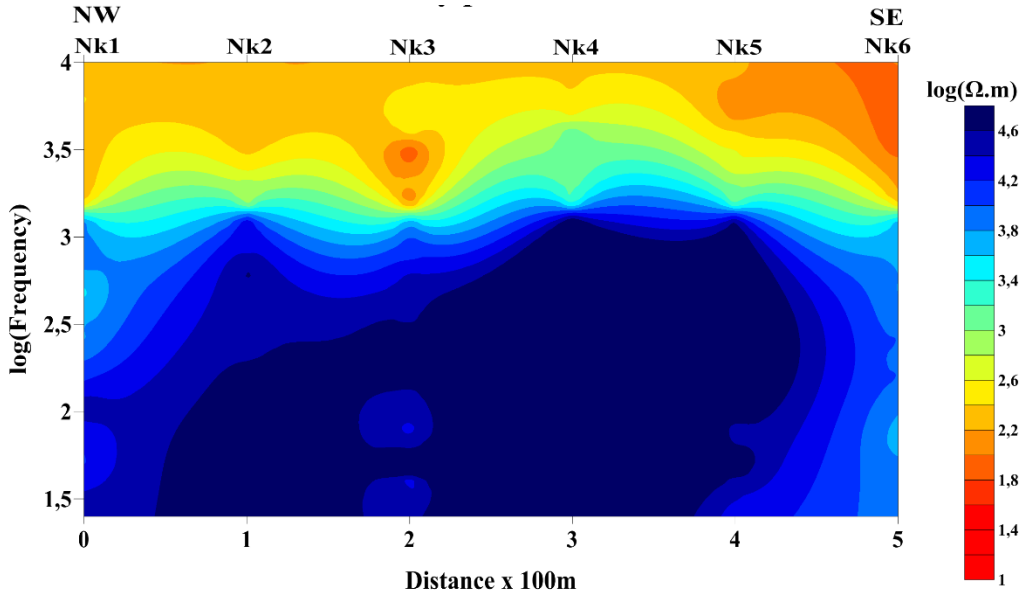

Figure 3.1-11 : Apparent resistivity pseudo section of profile 3 (Nkolafamba). On the plot the resistive materials dominate the subsurface. Insights of an uplift of ground formations is noticeable between stations NK3 and NK5

The above very resistive zone dominates the 2/3 of the plot, suggesting that the area is made of very resistive materials. This also suggests that the presence of a shallow basement in Nkolafamba and its vicinity. Within the resistive zone there is an oblique nucleus which seems to be responsible of the uplift observed between NK3 and NK5. This nucleus exhibits subvertical isocontour lines between NK5 and NK6, suggesting the presence of a major discontinuity. Moreover, there are oblique isocontour lines affecting the resistive zone that suggests a SW discontinuity dipping from NK2 to NK1. This discontinuity affects the deep basement formations. The curling of isocontours of the overburden formation are evidences of the folding processes that affected the shallow formations.

3.1.4.3. Geoelectrical section

In the same way as on profile 2 (**Figure 3.1-9**), the 2-D inverse electrical model or geoelectrical section of profile 3 has been realised to image the Nkolafamba subsurface. The

Figure 3.1-12 below presents the geoelectrical section of profile 3 (Nkolafamba). The observation of the geoelectrical section above shows following facts downwards:

- The first layer is a very conductive terrain which is characterised by a mean resistivity value of 94.45 Ω.m. This terrain has an average thickness of 100m. In addition, this formation is marked by a discontinuity at station NK4 which can be interpreted as a fracture or a fault. Another discontinuity seems to be present at station NK3, at it may be interpreted as a fracture. A careful look at station NK2 also suggests a discontinuity which however seems obvious. The discontinuities highlighted at NK2 and NK4 are probably relays of deformation affecting the second terrain below, and they obviously form a depressed area along profile from NK2 to NK4 (50 m beyond NK4).

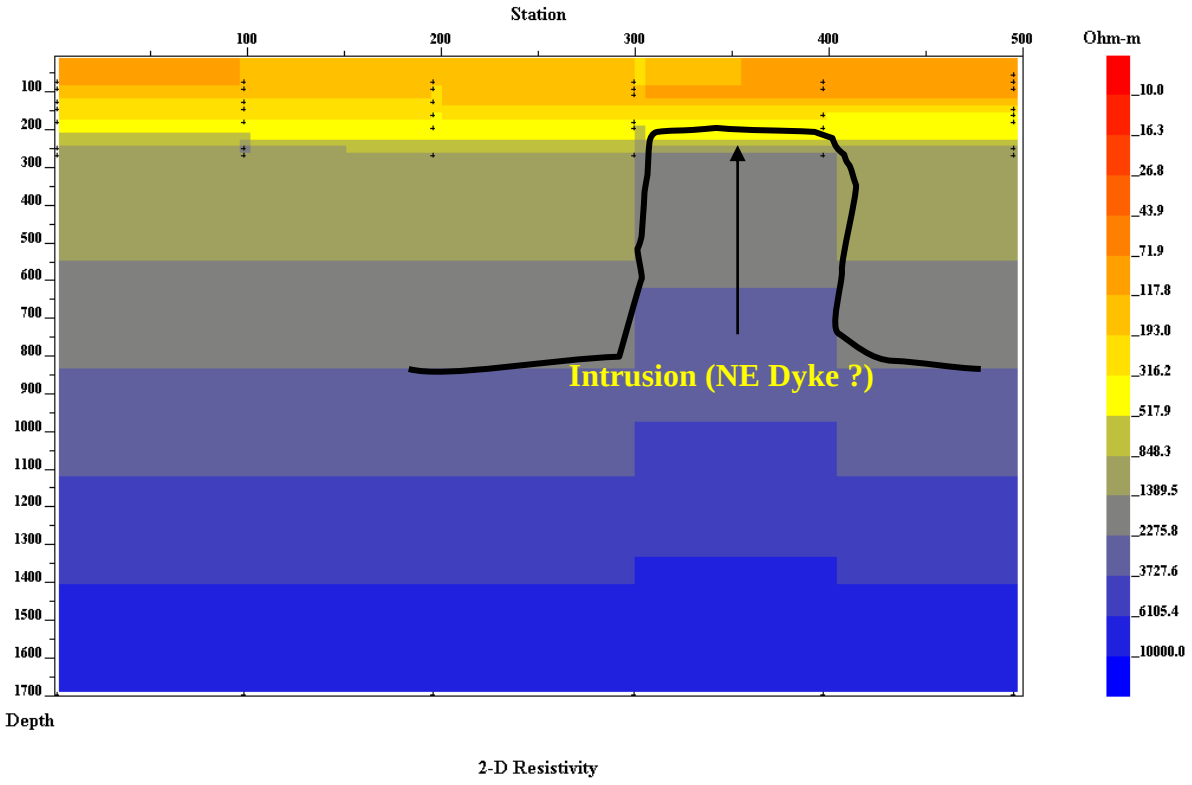

Figure 3.1-12 : Geoelectrical or 2-D resistivity section of profile 3 (Nkolafamba) for a total depth of 1500 m depth. The plot displays a channel between NK4 and NK5 through which the underlying resistive formations raise up

- The second perceptible layer on the plot has a mean resistivity value of 355.45 Ω.m. It is marked by a discontinuity interpreted as a fault beneath NK2. It has an appreciable thickness from NK1 to NK3 where it starts to diminish. This layer is characterized by a more resistive structure at the bottom, which thickens from the beginning to the end of the profile; it is marked by a slight intrusion of underlying material; scarps observed below stations NK3, and NK5 conFigure it like a stair with three foot-steps.

- The third zone encountered is a very thin quasi homogeneous structure at about 210m depth, with 683.1 Ω.m mean resistivity. It intrudes itself into the second structure at NK4 and its thickness is less than 50 m.
- At 250 m depth, the fourth formation highlighted is resistive; with a mean resistivity value of 1119 Ω.m. it has a mean thickness of 150 m, with a slight scarp beneath NK2. The major fact observable on this section related to this material is the 100 m wide passage way through which deep resistant material intrudes within it and form a concordant sill from station NK3 to NK6. The highly resistive character of this intrusion is probably due to the cooling of old melted magmatic materials that formed the basement.
- At 400 m depth under station NK1, one has the fifth structure, more resistant than that above (1832.6 Ω.m mean resistivity). This structure collapse slightly at NK2 and seems to be pushed inside the terrain above between stations NK4 and NK5, by the structure below it. The collapse observed at 400m below NK2 may not be interpreted as a fault.
- Structures encountered at 550 m depth seem to correspond to a transition zone between the overburden and the bedrock. These structures are resistive materials with resistivity values belonging to the interval [2275.8 - 6105.4] Ω.m. The hypothesis of the transition zone is supported by the identical shape observed on the structure that seems to be the basement.
- The top part of the basement is encountered at 1500 m depth with resistivity values comprised between 6105.4 Ω.m and 10,000 Ω.m. The noticeable feature is the uplift observed between stations NK4 and NK5. This uplift of the basement deforms structures above.

The geoelectrical section of profile 3 generally shows that resistivity increases with depth. In addition, it can also be seen that the basement in the Nkolafamba area is shallow. Besides, the uplift noticed between stations NK5 and NK5 can be interpreted as an intrusion, probably a dyke crossing the section. This results are in agreement with those obtained from the apparent resistivity pseudo section (**Figure 3.1-12**), although the geoelectrical section presented focuses only on the near subsurface.

3.1.5. Profile 4 (Beguele 2)

3.1.5.1. Phase pseudo section

The phase pseudo section of profile 4 (Beguele 2) is presented by the **Figure 3.1-13** below. The observation of the phase pseudo section enables to retrieve the following facts. At

frequencies lower than 1000 Hz (from middle depth downward), the plot exhibits a high value phase anomaly. This anomaly is characterised by a mean phase value of 80°. This anomaly covers the entire bottom of the plot. At frequencies greater than 10000 Hz a low phase anomaly value (mean phase value of 30°) occurs from BG3 to the end of the profile (BG6). This anomaly forms a basin-like structure between BG3 and BG5 where it forms a channel centred at BG4. The low phase and high phase anomalies are separated by a medium characterised by intermediate phase values with a mean value of 65°. This medium outcrops from BG1 to BG3.

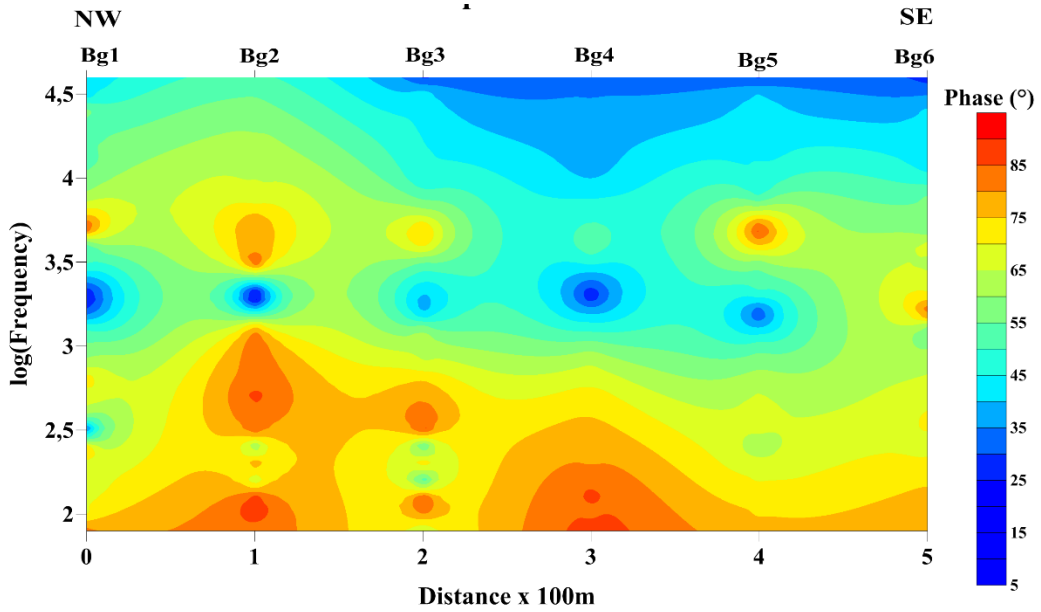

Figure 3.1-13 : Phase pseudo section of profile 4 (Beguele 2). The plot exhibits an intermediate phase anomaly that form a SE dipping channel from the beginning to the end of the profile.

Generally, the isocontour lines of phase are curled. This curling is more pronounced on the deep high phase anomaly but however affects the upper anomalies too. The above described curling can be interpreted as folding process that probably affected the formations in the Beguele 2 area. The isocontour lines are oblique between BG3 and BG4 at higher frequencies (near subsurface) and therein suggest the presence of a discontinuity, probably a SE dipping fault. Further the same pattern is observed between BG4 and BG5, suggesting a same type discontinuity there. This discontinuity can also be interpreted as a fault that affects the deepest structures of the area. In addition to these, there are oblique to subvertical isocontour lines from BG1 to BG2. This arrangement is also an imprint of a discontinuity that is probably interpreted as a fault that may also affects the deepest levels of the area.

In addition to all the above observed and interpreted, facts there is a circular or nearly elliptical intermediate anomaly that affects the subsurface from BG1 to BG3 at higher frequencies. This anomaly is probably an imprint of a conductive formation.

3.1.5.2. Apparent resistivity pseudo section

The **Figure 3.1-14** below presents the apparent resistivity pseudo section describing the 2-D resistivity variations along the profile 4 (Beguele 2). The apparent resistivity pseudo section from profile 4 (**Figure 3.1-14**) shows a very resistive formation that is encountered at depth between stations BG2 and BG6; it appears like an intrusion of more resistive materials, compared to the surrounding. This formation is embedded within a less resistive one that covers the whole area, while some very conductive formations appear from station BG1 to station BG2 and between stations BG4 and BG6 on surface; below stations BG1 and BG4 in depth.

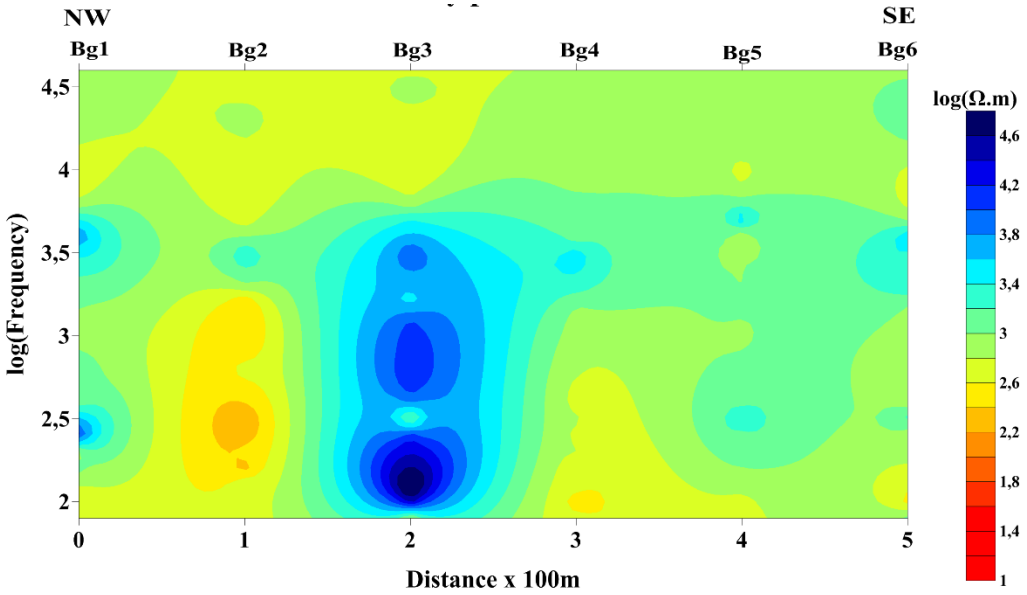

Figure 3.1-14 : Apparent resistivity pseudo section of profile 4 (Beguele 2)

The intermediate apparent resistivity values dominating the whole pseudo-section lead to assume the area is made up of mixture of both resistive and conductive formations. The phase pseudo-section mainly exhibits a depression or subsidence along the profile from BG1 to BG6. The irregular isocontour patterns on the pseudo sections suggest folding of formations therein.

3.1.5.3. Geoelectrical section

Figures 3.1- and **3.1-16** The 2-D inverse model or geoelectrical section of profile 4. The geoelectrical section focuses on the upper 1300 m with a detailed imaging of the uppermost 400m. The overview of the section (**Figure 3.1-15**) suggests a four-layered earth model.

- The first terrain characterised by a mean resistivity of 683.1 Ωm, occurs three times; on surface to 75 m, then from 325 m to 450 m depth and finally from 700 m to 750 m depth, below BG1. The portion appearing from 352 to 450 m depth thins from BG2 to the end of profile, as that appearing below seems to thicken from BG4 to BG6. This portion is jagged by discontinuities at BG2, BG3, BG4 and BG5 (**Figure 3.1-15**) which shape this

second level of the first terrain as a downstairs with five footsteps of 100 m each. The discontinuities highlighted can be interpreted as faults which also affect the formation above. The third portion is also featured by many discontinuities than can be interpreted as faults too; these also affect all the layers above. The superficial portion ends at BG4 by a fault-type contact with the second formation.

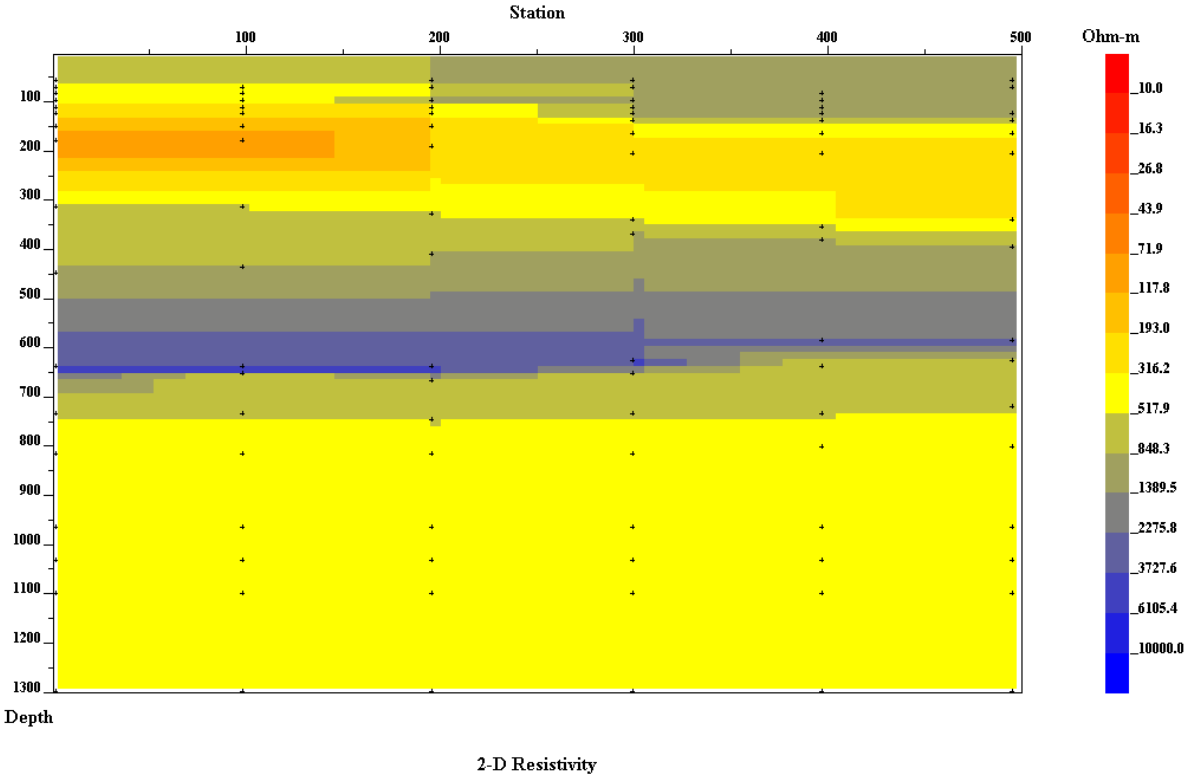

Figure 3.1-15 : Geoelectrical or 2-D resistivity section of profile 4 (Beguele) for a total depth of 1300 m depth. The plot displays a slightly SE dipping shallow channel running along the entire profile.

- The second terrain or formation is characterised by a mean resistivity value of 1119.3 Ωm. As said above, it seems separated on surface to the first formation by a fault-type contact at BG4. This superficial portion has an average thickness of 150 m and seems to embed a thin resistive layer. It also intrudes the first and the third formations from BG4 to BG3 (**Figure 3.1-15**) where it gently extrudes, suggesting a filled fracture at BG3 that affects the first formation. The second formation is also observable at 450 m depth below BG1. This second portion is characterised by a constant thickness of nearly 50 m from BG1 to BG4, then a slight thickening to nearly 75 m up to BG6. Some discontinuities interpretable as faults, are observed at BG3, BG4 and BG5. They shape this portion as downstairs till BG4, as a collapse is observed along the discontinuity at BG5. The observed discontinuities also affect the underlaying fourth formation; despite its high resistivity (mean value of 4190.6 Ωm), this fourth does not constitute the basement. The third occurrence of the second terrain is observed at 700 m depth below BG1. It has,

herein, a mean thickness of 50 m which nearly doubles to BG6 and displays some discontinuities too (many at the same stations) inferring a faulting of the whole near subsurface of Beguele 2.

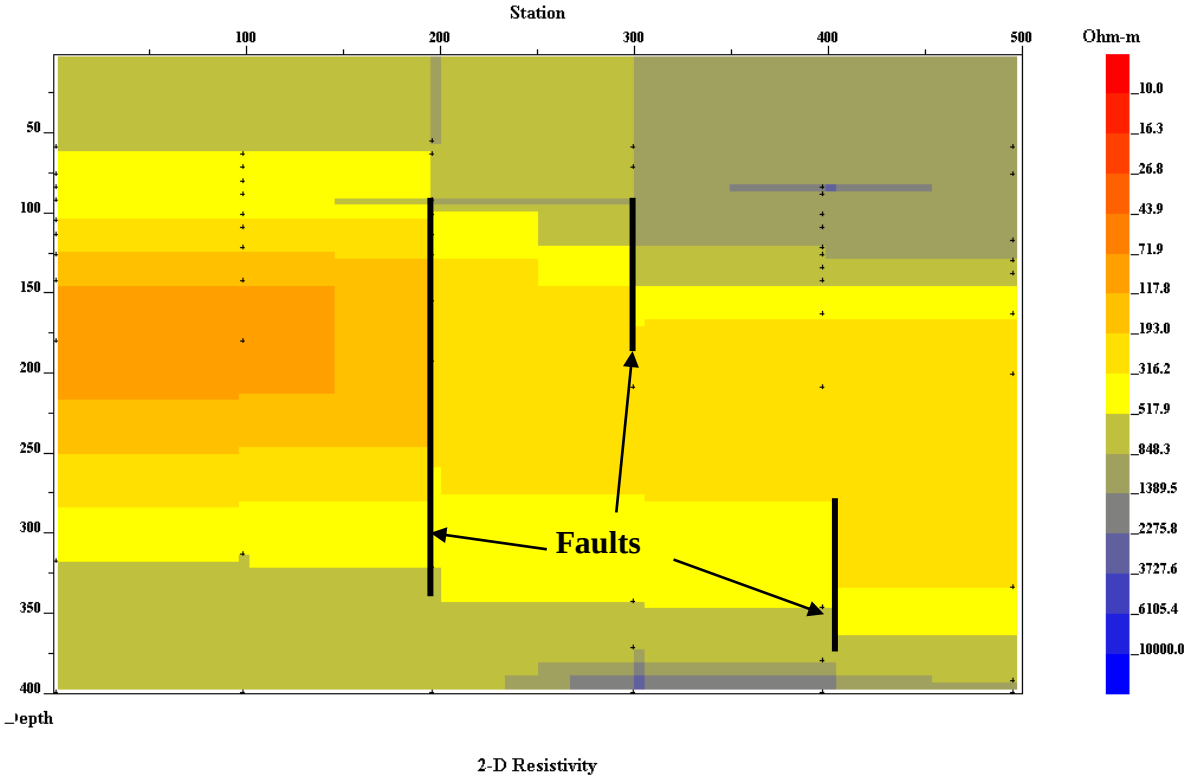

Figure 3.1-16 Geoelectrical or 2-D resistivity section of profile 4 (Beguele) for 600 m depth. The plot emphasises on features affecting the near subsurface.

- The very conductive third formation, firstly appears at nearly 75 m depth from BG1 to BG3. It has an average thickness of 300 m and a mean resistivity value of 417.2 Ωm. The roof of this formation is affected by discontinuities interpreted as faults at BG3 and 50 m beyond, and at BG4. These faults also appear at its bottom, on the contact with the fourth formation. The third formation herein forms a conductive channel with a resistive background constituted by the first and the second formations. This channel collapses along the highlighted faults from BG3 to the end of the profile; however, this collapse seems caused by deep processes. When considering the upper 400 m of the geoelectrical section (**Figure 3.1-16**), the domain occupied by the third formation looks like a graben. In addition, there is a more conductive thick layer (more than 100m) embedded in the third formation from BG1 to BG3, probably a weathered zone. This inner weathering spans concurrently through the whole formation in the entire profile. The third formation is reported again at 750 m depth below BG1.

The geoelectrical section of profile 4 shows that the area is not as resistive as seen on the previous profiles. Herein, formations alternate probably because of a folding process

accompanied or followed by faulting. Many faults affect all the formations at same locations, particularly at BG3, BG4 and BG5. The one highlighted at BG3 (**Figure 3.1-16**) is clearly evidenced on the apparent resistivity pseudo section.

3.1.6. Profile 5 (Kamba)

3.1.6.1. Phase pseudo section

The phase pseudo section of the profile 5 illustrated by the **Figure 3.1-17** below shows the dominance of low phase values (less than 30°), although some high phase circular anomalies are observed at Kb1, Kb2, Kb3 and Kb5. These high phase anomalies suggest local variations in the composition of the rocks or formations at these regions. The isophase contours suggest a concordant layering but their rough curling suggest that the area underwent intense ductile deformations. Particularly, the region between Kb and Kb6 portrays the existence of a nearly vertical breakup affecting the whole subsurface (probably a crustal feature).

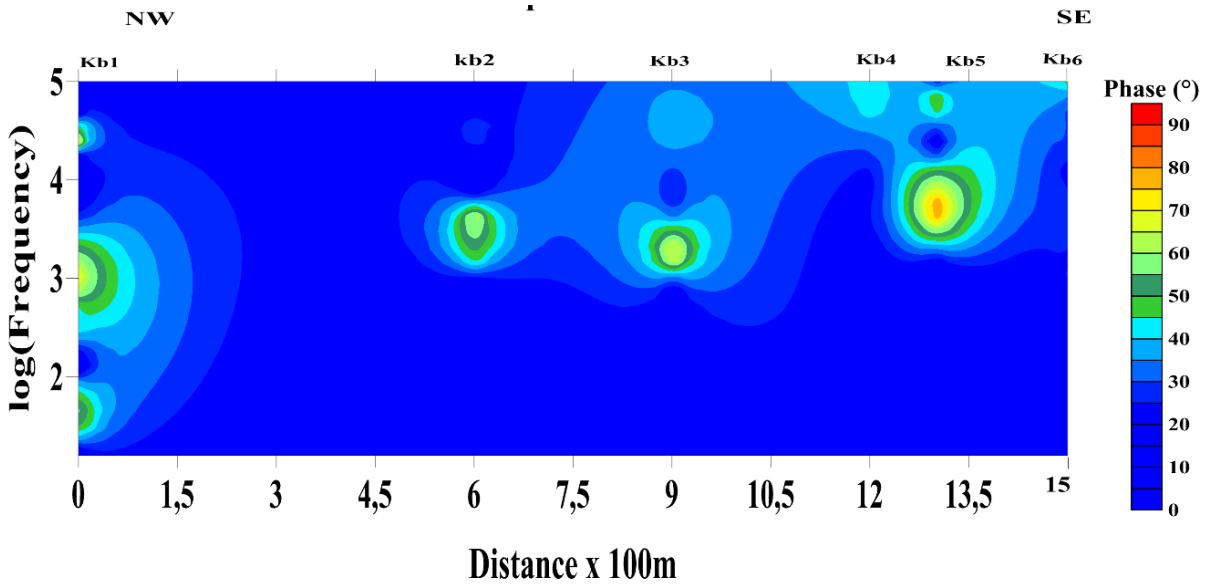

Figure 3.1-17 Phase pseudo section of profile 5 (Kamba).

3.1.6.2. Apparent resistivity pseudo section

The apparent resistivity pseudo section of the profile 5 (**Figure 3.1-18**) comforts the findings from the phase pseudo section above. It reveals three main types of formations observed top-down. On top (high frequencies), there are very conductive to conductive formations. The middle and lower frequencies areas are dominated by intermediate (in terms of resistivity values) formations which are entirely disrupted by the conductive formations above at Kb5.

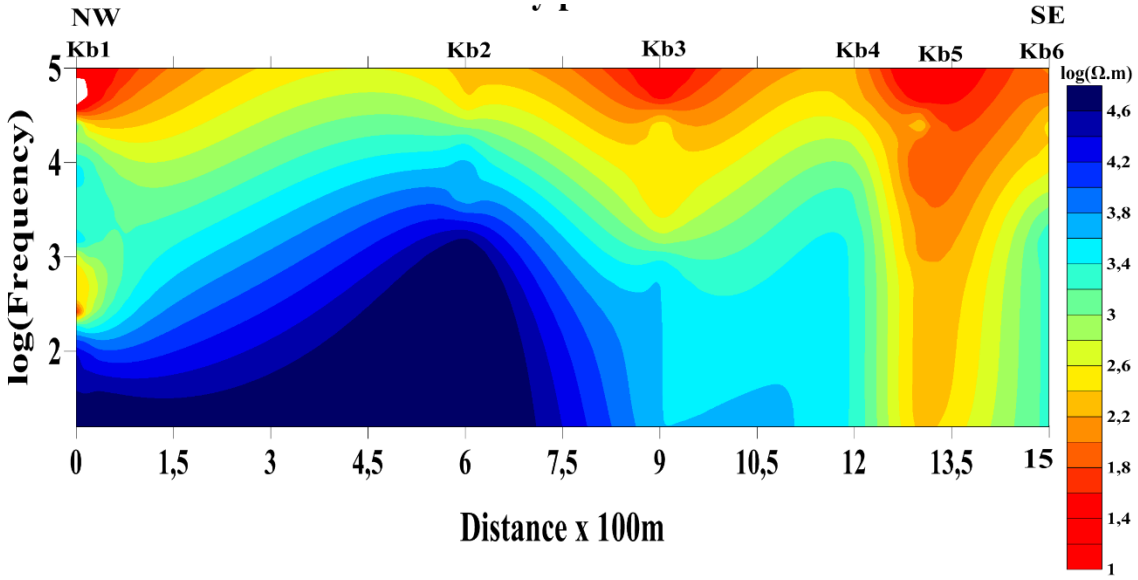

Figure 3.1-18 Apparent resistivity pseudo section of profile 5 (Kamba). The plot exhibits top-down three groups of formations (reddish, light-blue and blue, respectively) and a major electrical discontinuity at Kb5, probably an active fault

A strong anomaly characterising very resistive formations is observed from Kb1 to Kb3 where it ends by rudely. This strong resistive anomaly rises sharply from 100 Hz below Kb1 to nearly 10,000 Hz beneath Kb2, appearing like a dissymmetric dome whose summit is beneath Kb2, due to a probable uplift of the basement therein. The apparent resistivity isocontours patterns suggests an initial tabular layering followed by a strong folding process. They are oblique (with a nearly 45° slope observed on the resistive anomaly) from Kb1 to Kb2 and subvertical from 750 m to the end of the profile. The vertical to subvertical discontinuities are related to the major subvertical discontinuity centred at Kb5, filled by conductive materials, and interpreted as an active major fault that affect the whole subsurface (as it runs from the bottom to the top of the pseudo section).

3.1.6.3. Geoelectrical section

The geoelectrical section of the profile 5 (**Figure 3.1-19**), as that of the previous profile, focuses only on the uppermost part of the subsurface in Kamba. The geoelectrical section of profile 5 suggests that the subsurface therein is made up of four to five terrains. Downwards the followings are encountered:

- The first layer, very thin, is made up of formations characterised by a mean resistivity value of 617.6 Ωm.

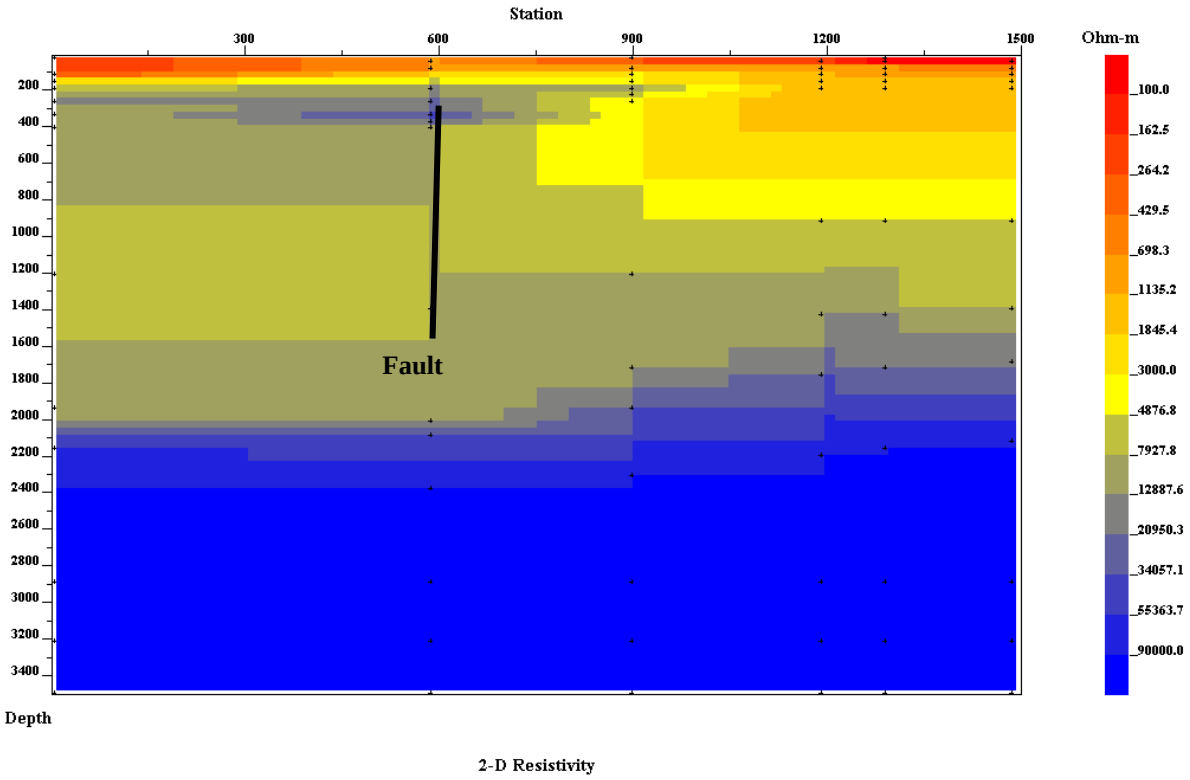

Figure 3.1-19 Geoelectrical or 2-D resistivity section of profile 5 (Kamba) for 3400 m depth.

- The second terrain is encountered near 175 m depth under Kb1. It is also very thin but thickens significantly to more than 400 m from Kb3 till the end of the profile. This second layer is characterised by formations with a mean resistivity value of 3006 Ωm. These formations are featured with many discontinuities from Kb1 to Kb2, and from Kb3 to Kb5 interpretable as faults. Faults from Kb1 to Kb2 shape this formation as a horse tail, while the section running from Kb3 to Kb5 corresponds to a collapse.
- The third layer appears near 200 m depth under Kb1. Like the previous, it is thinny from Kb1 to Kb2 where it starts thickening. The formations within are characterised by a mean resistivity value of 8882.2 Ωm. These formations are also affected by the discontinuities above interpreted as faults. The third terrain and those above form a dome whose slopes are from Kb1 to Kb2 and from Kb3 to Kb5.
- The fourth terrain is very resistant (resistivity greater than 9000 Ωm) and appears on the entire section. It is encountered at 275 m depth below Kb1 from where it is shallower, then suddenly collapses to nearly 1000 m from Kb3. This collapse occurs along a major discontinuity interpreted as a major fault affecting the area. This resistant layer seems to be responsible of the uplift or dome shaping of the terrains above.
- The fifth layer (the most resistive) corresponds to the basement. It displays a wondering uplift from Kb3 to Kb6, contrarily to the collapse observed with the formation above.

Summarily, the presence of many faults suggests that the area investigated through profile 5 is very weak (mainly on surface) and it is characterised by very resistive formations. The faults reported from station Kb3 toward the end of profile may be relays of a single major fault along which the highly resistive (more than 9000 Ωm) terrain broke apart and collapsed, leading to the subsidence of materials above. The geoelectrical section is in accordance with the observations from its related apparent resistivity pseudo section (**Figure 3.1-16**). The uplift of the basement remains an enigma to resolve in the future.

3.1.7. Profile 6 (Loum 2)

3.1.7.1. Phase pseudo section

The phase pseudo section of the profile 6 is displayed below (**Figure 3.1-20**). Its analysis enables to differentiate to main horizons downwards. The first horizon occurs at very high frequencies (20000 Hz). This shallow set corresponds to formations characterised by intermediate phase values ranging from 35° to 60°. Two half-circular high phase anomalies occur at Lm3 and Lm6, respectively. The first horizon is interrupted between Lm4 and Lm5 by materials constituting the second group of phase iso-values. The second group of phase isocontours occurs from near subsurface to very deep levels (frequencies less than 20000 Hz) characterised by low phase values ranged from 5° to 30°.

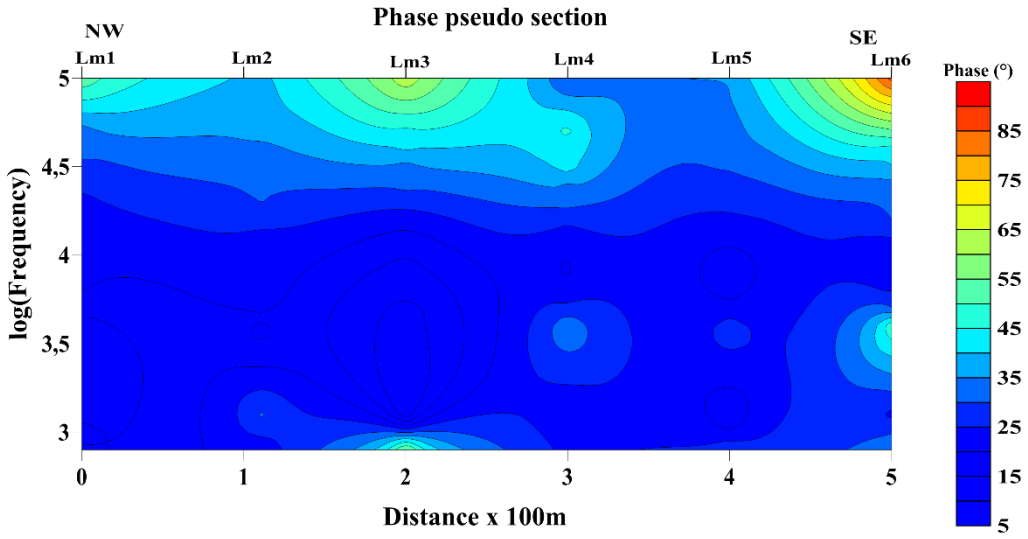

Figure 3.1-20 : Phase pseudo section of profile 6 (Loum 2).

This outcrops between Lm4 and Lm5 as reported above, and presents little circular intermediate anomalies below Lm4 and Lm5, respectively. The shape of isocontour lines is gently curled, suggesting that folding has affected the area however no ameliorated information is regained.

3.1.7.2. Apparent resistivity pseudo section

The apparent resistivity pseudo section of the profile 6 (**Figure 3.1-21**) enables to differentiate two main horizons. The first horizon corresponding to very conductive formations,

evolves from surface to near subsurface, between stations Lm1 and Lm2, and between Lm4 and Lm5. It reaches the middle depths Between Lm2 and Lm4, then sinks from Lm5 to Lm6.

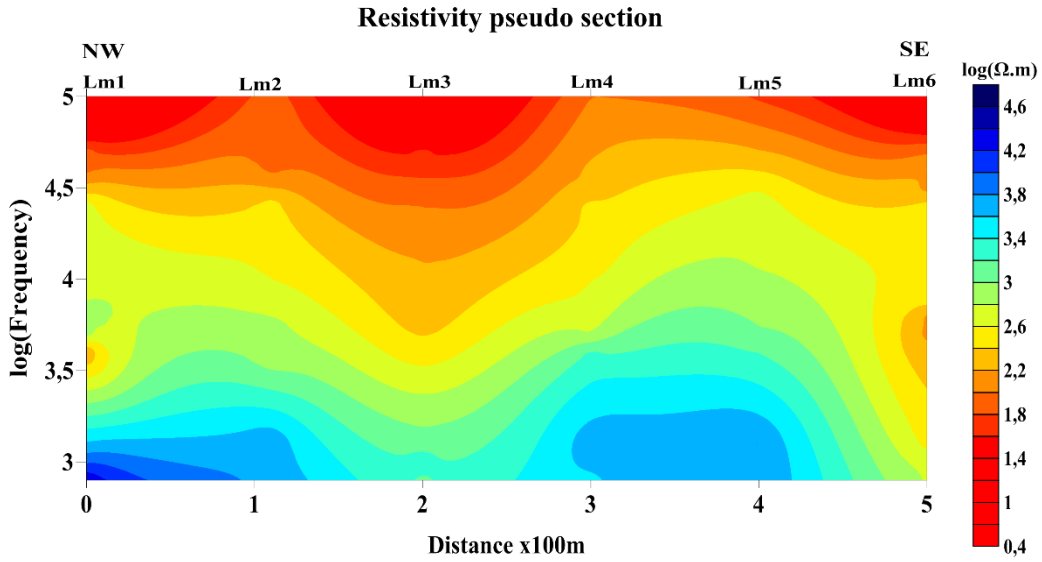

Figure 3.1-21 : Apparent resistivity pseudo section of profile 6 (Loum 2) evidencing ductile deformations in the area.

The second horizon characterising resistive formations, is encountered at frequencies less than 3162.3 Hz. It displays two highly resistive nuclei, from Lm1 to Lm2 and Lm4 to lm5, respectively. The first and second horizons are separated by a transition zone of intermediate conductive formations with abrupt slopes from Lm2 to Lm3 and from Lm4 to Lm3, while they are subvertical from Lm5 to Lm6 which are inferences of discontinuities centred at these stations.

Globally, the shape of the isocontours lines characterises folding in the area and the highlighted discontinuities suggest a subsidence or a basin between Lm2 and Lm3.

3.1.7.3. Geoelectrical section

The 2-D inverse model of the profile 6 is shown on figures 3.1.22 and 3.1.23 below. **Figure 3.1-22** and **Figure 3.1-23** provide respectively, the general and the detailed (for the upper 600 m) image of Loum 2 subsurface. This geoelectrical section (profile 6) suggests that the subsurface is made up of six (06) terrains (Figure 3.1.22) reported downward as follow:

- The first layer is a very conductive thin terrain (25 m mean thickness) characterised by a mean resistivity value of 43 Ωm and runs along the entire profile.

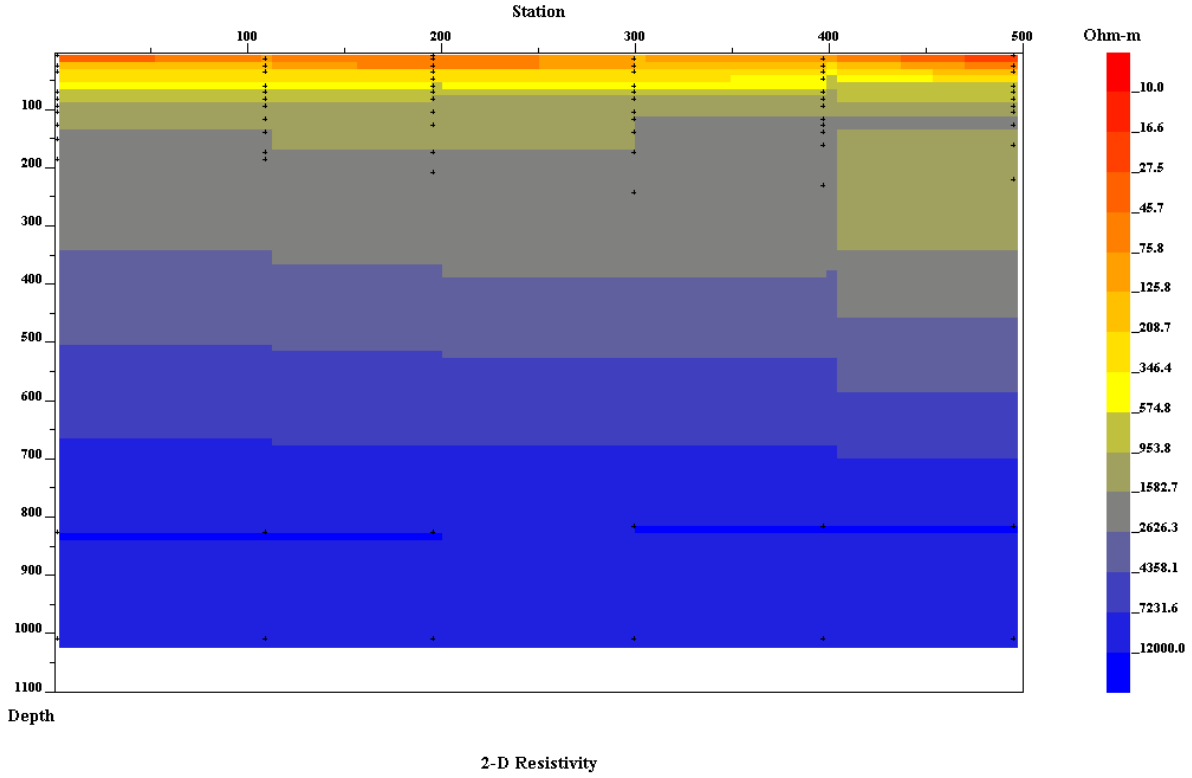

Figure 3.1-22 : Geoelectrical or 2-D resistivity section of profile 6 (Loum 2) for 1100 m depth.

- The second layer is also thin and conductive, includes formations characterised by a mean resistivity value of 340Ωm. With an average thickness of nearly 25 m, it is jagged by some discontinuities at Lm2, Lm3, at Lm5 and 350 m before Lm5, which can be interpreted either as faults or scarps (preferably faults). The plot shows that the limit with the first layer is rather gradational contrarily to what happens with the third layer.
- The third layer corresponds to formations with a mean resistivity value of 803Ωm. This layer is encountered around 75 m depth at station Lm1. Its thickness is relatively constant and close to 25 m. Two main discontinuities (probably faults) affect it at Lm3 and Lm5.
- The fourth terrain corresponds to formations characterised by a mean resistivity value of 1340Ωm. This layer occurs from 100 m to 175 m depth from Lm1 to Lm3; its thickness decreases slightly from Lm3 to Lm4 and increases between Lm4 and Lm6 (the layer therein runs from 100 m to 325 m depth). A thin concordant resistive intrusion is embedded within the fourth formation, from the Lm4 station to the end of the profile. Two discontinuities are noticeable at Lm3 and Lm5in the same way as shown by the above layer. This confirms the hypothesis of two faults that affect both the third and the fourth layers at Lm3 and Lm5, respectively (and affect the second upper layer too).
- The fifth layer is characterised by an average resistivity of 2236.3Ωm and an increasing thickness from Lm1 to Lm4 where it suddenly drops at a constant value of nearly 80 m.

This layer includes formations with same resistivity characteristics as the intrusion reported in the fourth layer above. The fifth layer is affected by two main discontinuities at Lm3 and Lm4 (**Figure 3.1-23**) interpretable as faults. Particularly, the fault at Lm4 has a significant upthrow (nearly 150 m) and its low compartment created a subsidence from Lm4 to Lm6 filled by overburden materials.

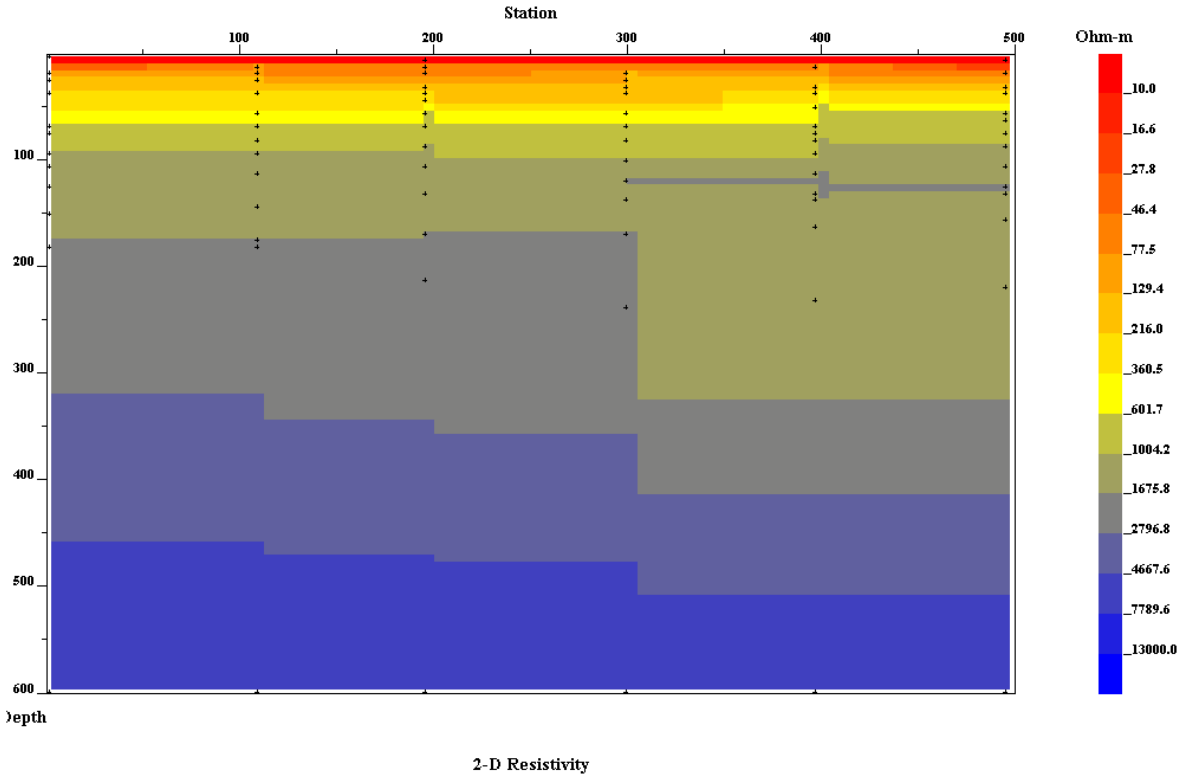

Figure 3.1-23 : Geoelectrical or 2-D resistivity section of profile 6 (Loum 2) for 600 m depth.

- The sixth layer corresponding to the basement is encountered at nearly 325 m depth under Lm1 and has resistivities greater 4249Ωm. Its first upper levels may correspond to a metamorphic areole due to the contact between the basement and the fifth layer. The basement displays discontinuities at Lm2, Lm3 and Lm4 which could correspond to faults shaping it like downstair steps along which it could have collapsed; thus featuring it like a graben. Seemingly, a deep faulting affected both the basement and formations above as specifically suggested by the faults evidenced at Lm2 and Lm4.

The apparent resistivity pseudo section of profile 6 highlights folds and discontinuities, the later being confirmed by its geoelectrical section and interpreted as faults. Moreover, these faults may correspond to weakness zones along which the subsurface broke up and subsided as a result of an intense tectonic activity. These faulting and folding are imprints of a multistage tectonic activities affecting the area.

3.1.8. Summary of AMT results

Summarily, the AMT surveyed area is made up of a mixture of both very resistive and conductive formations. The basement appears at 1400 m in profile 1; 825 m in profile 2; 550 m in profile 3 and deeper (more than 1400 m) in profile 4; on profile 5 it is encountered at 2,200 m and upraises to ~1,800 m and the end of the profile. In profile 6, the basement is shallower (~ 200 m) despite the important sink below station Lm4. That means, the basement rises up in some parts of the area while it collapses in other parts; uplift may be due to cooled intrusions beneath the basement. The pseudo-sections that show that the subsurface topography of the area is very rough, enable to interpret those subsidence and uplifts of the basement as grabens or basins. The roughness of this subsurface is also emphasised by the curling of isoresistivities on all the pseudo-sections; this suggests that the formations in the area have been folded.

According to the orientation of the AMT sounding profiles (nearly N135°), the folding processes may have been caused by a shortening a priori parallel to the direction of all the profiles. This shortening was caused probably by the collision between the CC and the NEFB. In addition, many faults, scarps and fractures have been highlighted in all the profiles; several faults have a significant throw (e.g. 150 m below station OS4 in profile1; 50 m and 100 m beneath BG2 and BG3, respectively in profile 4; 175 m below BE1 in profile 2). Further the pseudo section of apparent resistivity from profile 5 (Kamba) highlights a major discontinuity centred at station KB5 interpreted as an active fault (characterised by low resistivity values) that spans from surface to the bottom of the section. The conductive channel seen on profile 1 (**Figure 3.1-3**) is either an intrusion or the assent of an active faulting. Since, the general trend of profiles is N135°, faults and fractures highlighted are assumed to span broadly from SW-NE to WSW-ENE (but may also be E-W). The profiles being parallel and considering their offsets from each other along their azimuth, the study assumes these faults and fractures form a set of parallel or distributive faults corresponding to a main SW-NE lineament that may extend beyond the limits of the AMT-surveyed area, in the whole CC/NEFB transition zone. The curled apparent resistivity isocontours, faults and fractures from AMT survey suggest that brittle to brittle-ductile tectonics occurred in the area. Besides, the alternance of resistive and conductive structures in some geoelectrical sections (e.g. profile 4) evidences a flip of superficial materials possibly characterising the thrust of the Yaoundé nappes onto the CC in the area. The aeromagnetic data are used to deepen investigations in the remaining part of the study area..

3.2. AEROMAGNETIC DATA INTERPRETATION

Aeromagnetic data interpretation gives the possibility to investigate the part of the study area (the majority by far) uncovered by audiomagnetotellurics. Targeting a semi-regional scale study, analyses start with the TMI map reduced to the magnetic equator.

3.2.1. The total magnetic intensity reduced to the magnetic equator

The reduction to the magnetic equator (RTE) has the merit that it shifts magnetic anomalies directly above their causative sources in low latitudes areas. The RTE map in the study area (**Figure 3.2-1)** shows that the magnetic anomaly field ranges from -1113.34 nT to 1094.15 nT and portrays three main domains, southward from the left (Mbalmayo) to the lower right corner (Sangmelima) of the map.

- The first domain (A), is diagonally narrowed in the upper left corner and south-bounded by SW-NE line from Nkout to Akonolinga. This is characterised by a very high-intensity linear anomaly (valued from 15.5 nT to 1094.15 nT) in a fairly negative background. The observed anomalies correspond to high susceptibility possible mafic or basic to ultrabasic materials, or regional structures like faults or deep contacts affecting the basement of the Panafrican domain in the north of the study area.
- The second domain (B), forms a SW-NE channel of negative magnetic background (from – 63.5 nT to -16.5 nT) covering the central portion of the RTE map and south bounded by an imaginary line passing between Zoetele and Tekmo up to centre-east border of the map. Domain (B) is mainly characterised by the occurrence of small linear high intensity anomalies oriented SW-NE to WSW-ENE as we move northward beyond Zoetele. Additionally, these anomalies are sparse in the north (beyond NE-Zoetele) contrarily to the south (S-Akoeman) where they have highest intensities sometimes culminating at 83.7 nT. Also, domain (B) seems to be intersected by a WNW-ESE structure from N03º15’ (NE of Tekmo) to N03º30’ latitudes (Mbalmayo) which tends to orientate the features therein E-W to ESE-WNW (indigo line on **Figure 3.2-1**).

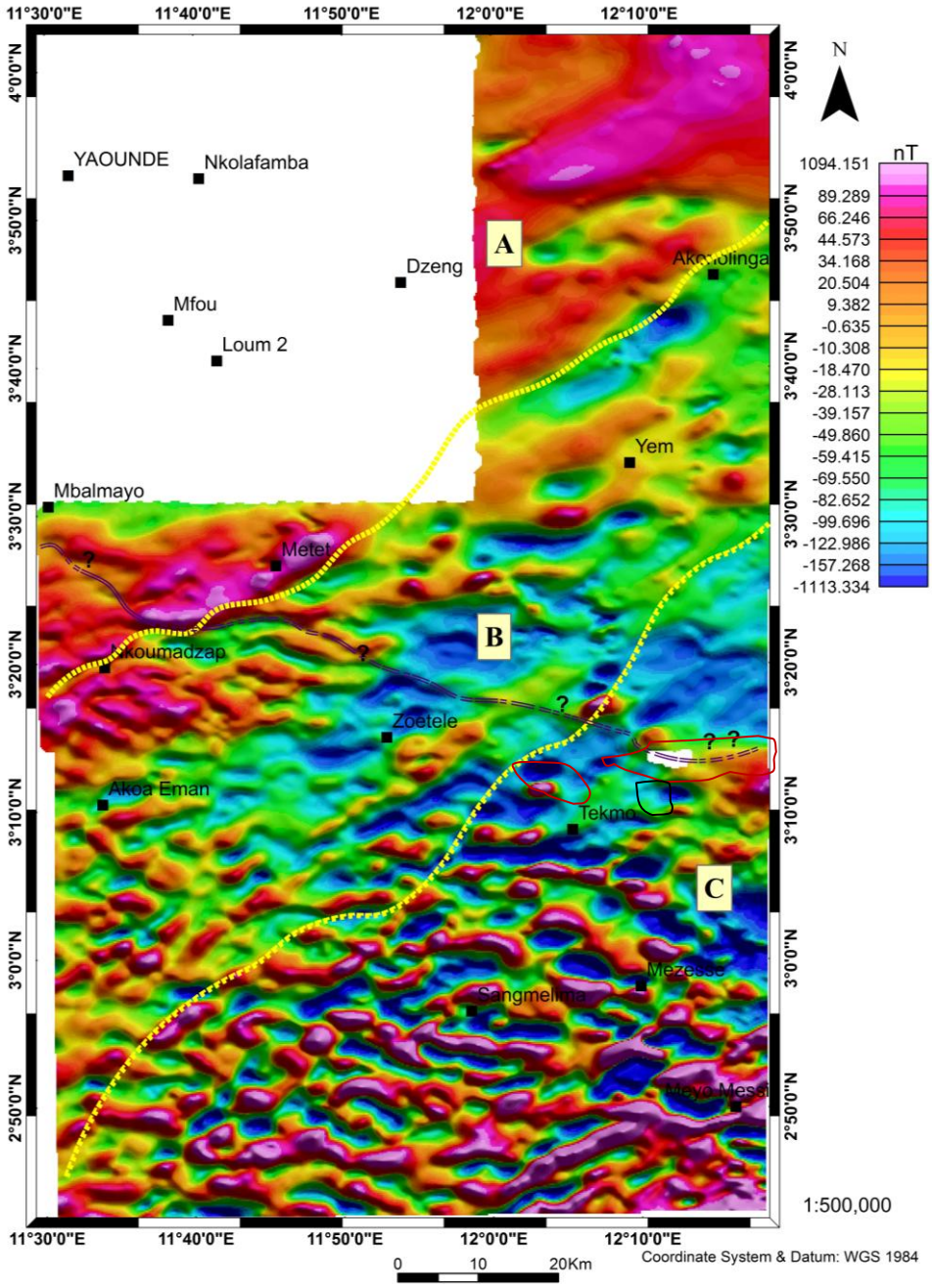

Figure 3.2-1 : The reduced to the magnetic equator (RTE) of the TMI map. The map is dominated in its centre by a NE channel (domain B) with some high intensity anomaly sources in the south.

- The third domain (C), in the southeast of the study area, experiences a dense occurrence of very high intensity anomaly's values in the Tekmo-Sangmelima area. The orientation, size and intensity of these anomalies contrast entirely with those previously described in the adjacent domain. its magnetic relief already show that formations therein are of a different nature, in comparison to doamins (A) and (B). Illustratively, anomalies in domain (C) have intensities around 910.7 nT with a nearly E-W to ESE-WNW general orientation resulting from a probable rotation to the west between Sangmelima and Tekmo (**Figure 3.2-1**). They suggest the presence of hypothetical presence of mafic to

ultramafic materials. Disruptions observed on these anomalies infer major fracturing mainly along the NE and the NW directions. The intensity of these anomalies suggests that their causatives sources may differ from those of other anomalies located in the southwest portion of the study area.

In general, the orientation of the main anomalies in the domain (A) and that of the channel forming domain (B) and the located anomalies gives a strong indication on the trends of lineaments which could affect the area's subsurface. Indeed, the observation of this whole set infers that the basement's control is carried out by SW-NE structures. The extend of domain (B) throughout the study area suggests that it is a unique weakness zones affecting both the NEFB and the CC domains. The anomalies herein observed are probable intrusions and/or discontinuities. The difference in the intensity shown by these anomalies (high intensities in the south portion of domain (B) compared to its north portion) suggests their emplacement occurred either at different periods or in different milieus, or even both. In the case of different periods, anomalies in the south of domain (B) are likely upwells of mafic to ultramafic materials or some ultrabasic like gabbros (hence their high intensity due to strong magnetisation effect) in the Ntem complex and anomalies in the north could be due to melted materials (basic materials) forming intrusions beneath the NEFB, thus suggesting that domains (A) and (B) form an early (probably Eburnean) NE-SW weakness zone which experienced reactivations (Panafrican and post-Panafrican). From the design of the anomalies in domain (C), their intensity and the background magnetic field, considering the spatial relation with domains (A) and (B), it seems evident that these features were put in place earlier, probably during the Liberian orogeny. The high intensity of anomalies therein may originate from magmatic TTG and supracrustal intrusions along with some greenstones belts relics in the Ntem complex.

Further, on the magnetic grids, features like fractures, faults and dykes can be observed although not clearly located. Dykes appears as narrow elongated magnetic heights while fractures and faults are detected through linear breaks in the magnetic background either positive or negative; therefore, it seems not possible, in certain circumstances, to discriminate faults from fractures. With the aim of highlighting magnetic lineaments, some geological structures interpreted as faults and/or fractures are observable on the RTE map (**Figure 3.2-1)** where they appear as throughs in the magnetic background. Despite their multiple directions, they already reveal the preponderance of the SW-NE, NW-SE, WSW-ENE and WNW-ESE to E-W directions, as well as the existence within the study area of a NE-SW sinistral system that affects both the CC and the NEFB, yet to be confirmed. However, the RTE map alone cannot entirely

help to map the lithology of an area. Therefore, application of advanced filtering techniques to the RTE field is necessary to complement the results.

3.2.2. 3D Analytic signal (AS) map

Some lithological units can be outline with the 3D analytic signal (AS) depending on their magnetization. The analytic signal map of the study area (**Figure 3.2-2)** globally presents north to south, a quiet domain extending south up to the north of Mbalmayo (domain I) and a gradually disturbed (spotted by some high-intensity AS anomalies - e.g. around Metet) domain to the south of the above boundary (domain II). Migmatites (gneisses) of the Yaounde series are particularly characterised by a quiet magnetic area in the north, while ectinites (micaschists) are characterised by a NE-SW to ENE-WSW trending magnetic area jagged by many high intensity anomalies (including intrusions) trending nearly ENE-WSW. The domain II forms a narrow E-W band (between Mbalmayo and Nkoumadzap) characterised by nearly E-W trending anomalies (foliation trace?) in a background weak field. This symptomatic characteristic of low-metamorphism materials suggests that local formations correspond to the Mbalmayo schist. The difference in the magnetic behaviour may expresses a difference in the composition and/or the origin of the formations encountered in these two domains. By equating both domain I and domain II to the Yaounde Group, obviously the southern area (domains III to V) would correspond to the Ntem complex.

In the area ascribed to the Ntem complex, three distinctive magnetic domains (domains III to V) have been outlined in regard to the density and orientation of anomalies. The domain III is a rough E-W band characterised by occurrence of relatively dense high-intensity AS anomalies, and E-W folding patterns (delimited by the Nkoumadzap-Akoeman-Zoetele triangle). It corresponds to the portion of the Ntem complex dominated by Tonalites (Soo granites). The second zone (domain IV) is easily identifiable through its highest anomalies on the map in the area south of Tekmo, in an area where charnokites have been mapped in the Ntem complex. Though they have high intensity, these anomalies are very dense and they are oriented SE-NW, to WNW-ESE (and even NE-SW) assuming a possible difference in the rock composition. The AS peaks are interpreted as supracrustal rocks or greenstones belts relics (**Figure 3.2-2**), as well as mafic to ultramafic intrusions that prove an effective hydrothermal activity within the area.

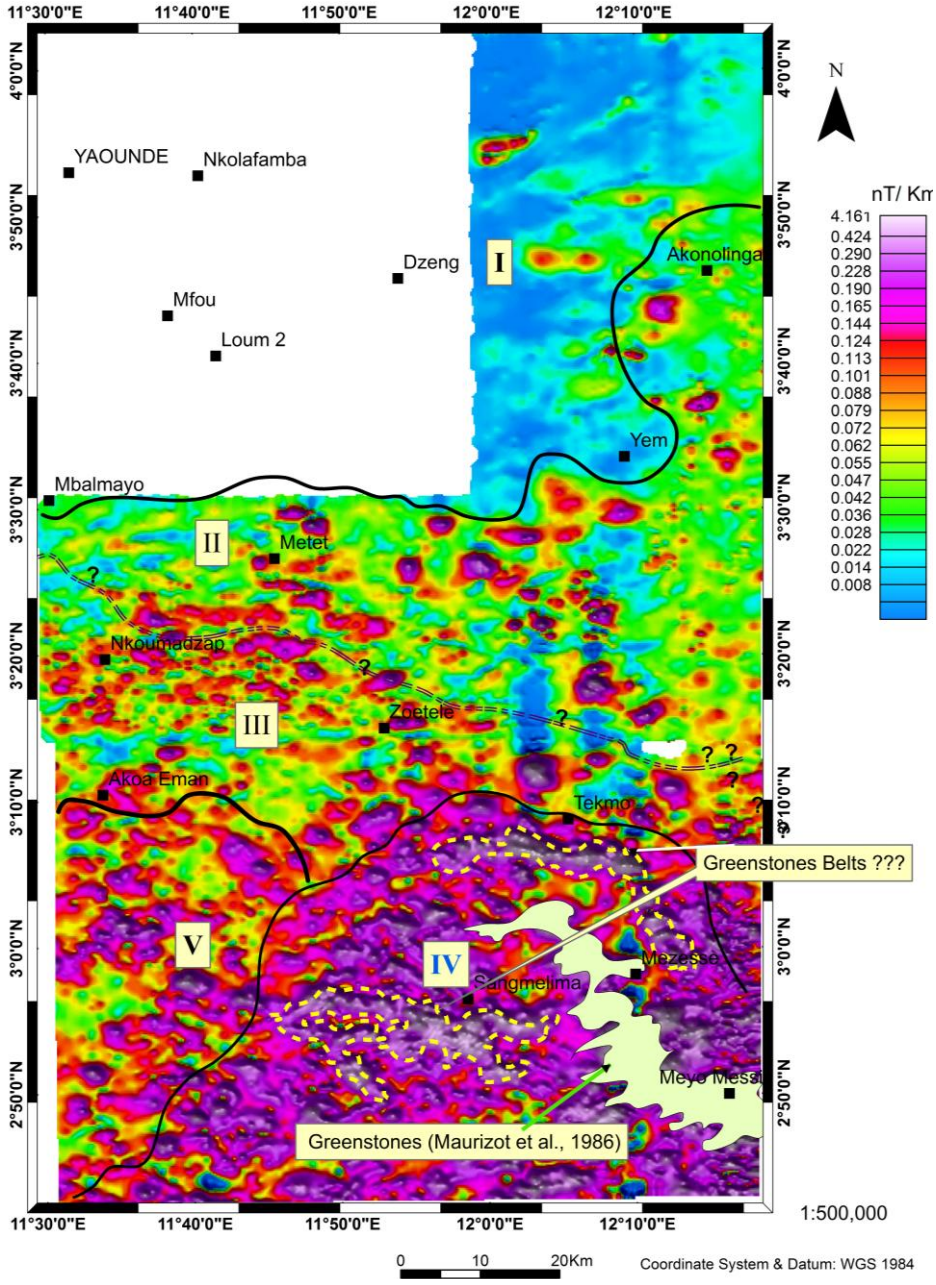

Figure 3.2-2 : The Analytic signal (AS) of the RTE field. The AS map herein delineates major lithological units (I to V) and greenstones belts. The broken black line illustrates the NEFB/CC limit.

The domain V seats east of domain IV and south of domain III, in the southwestern edge of the map. It, is characterised by dominating NW-SE anomalies. However, formations therein seem be close in composition to those of domain III, or they may be a different mix of all of hem, hence the noticeable diffenrence in the AS anomaly relief.

3.2.3. First vertical derivative (FVD) filtering

The first vertical derivative (FVD) filtering has the advantage of both, enhancing shallow sources while suppressing deeper ones, thus it enables to highlight linear structural features such as faults, fractures and dykes despite its ability to accentuate noise. The **Figure 3.2-3** below represents the FVD map of the Yaounde-Sangmelima area. According to gradient values, three

main group of anomaly gradients types are identified. The very low (down to -2.29 nT/km), the medium (amplitudes: -0.03 to 0.01 nT/km) and the steep positive (up to 1.40 nT/km) gradients.

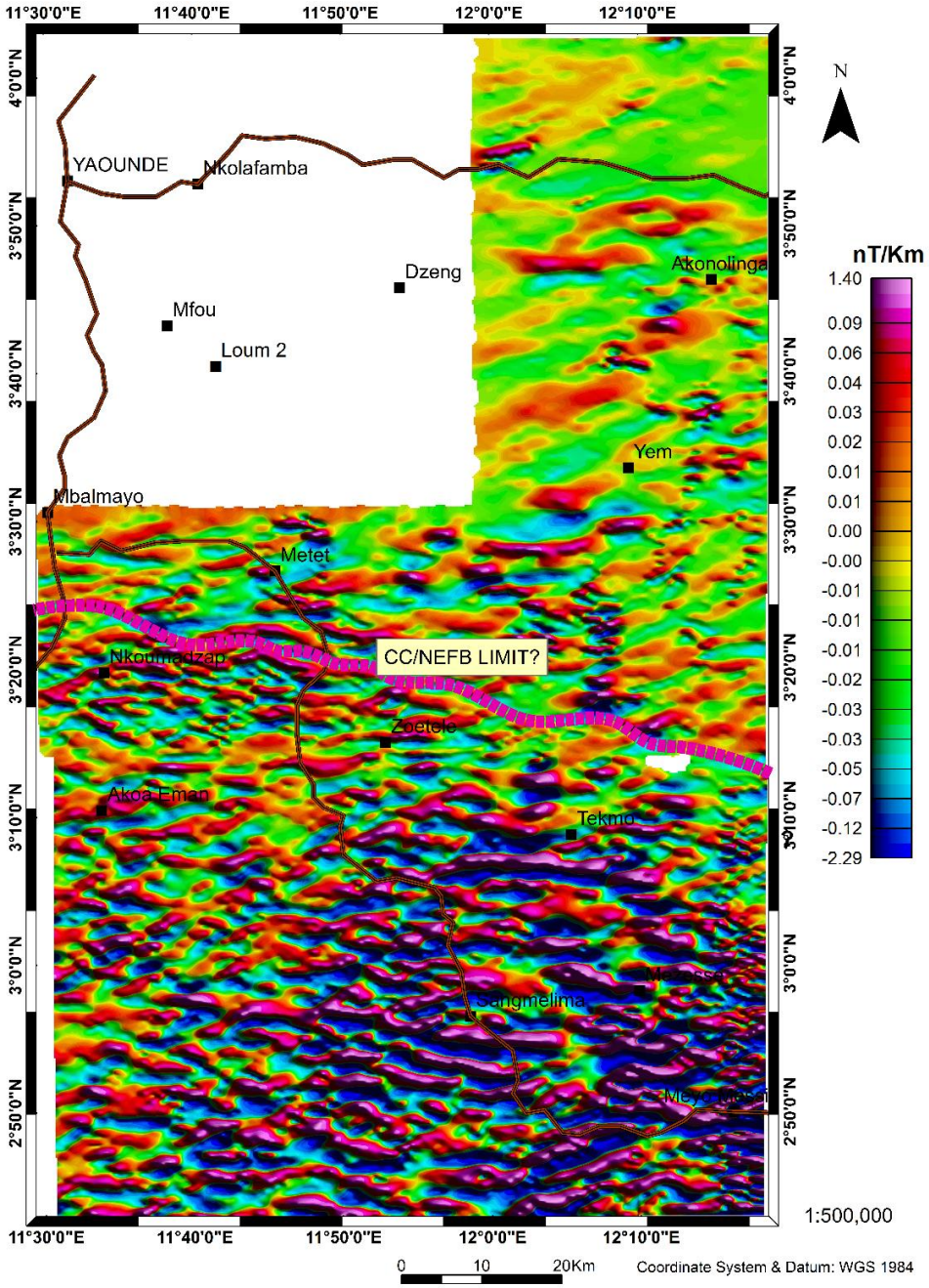

Figure 3.2-3 : FVD map of the Nkolafamba-Sangmelima area. The map evidences the difference in the nature and/or composition of the formations of the Ntem complex and the Panafrican, based on the the magnetic background field's intensity variations.

The density distribution of FVD gradients suggests that the area doesn't have the same magnetic character. This difference is probably caused by a difference in the rock composition emphasised by the difference in the way the geological units reacted to the stress/strain during the tectonic phases that affected the northern margin of the Congo craton. Two main magnetically disturbed zones are noticeable, a northern area which doesn't exhibit same anomaly

ranges nor shapes, size or distribution, in opposition to the southern area. The background magnetic relief (in green colour) accentuates the differentiation of the northern part from the southern one, thus assuming the existence of two adjacent blocks, the CC to the south and the NEFB to the north. Besides, the limit between those lithological units is depicted from the positions (E11º30'; N03º20') to (E12º15'; N03º15') by a curved line passing north of Nkoumadzap, below Metet and north Zoetele. This corresponds to a set of NE-SW, ENE-WSW and NW-SE anomalies forming a main E-W lineament interpretable as the local expression of the thrust-line between the NEFB and the Ntem complex. A ring complex surrounding Metet is observed (**Figure 3.2-3**), confirming observations made on the AS map the which probably outlines the micaschists from the Yaoundé series in the area.

Additionally, some structural information can be retrieved from the FVD map. This is particularly the case in the NE portion of the figure, where NE to ENE folds are observable. The size exhibited by long wavelength anomalies herein shows that these folds are gentle, and confirm the SE vergence of nappe thrusting onto the CC. Many lineaments interpreted as faults, fractures, dykes or outlines of intrusive bodies; or as contacts have been derived from the FVD filtering. These are probably deep or shallow structures affecting the basement of the study area. The main directions of the lineaments are NNE-SSW, NE-SW, ENE-WSW to E-W, WNW-ESE, NW-SE and N-S (very diffuse). To sum up, the FVD filtering provides good insights on the deformation history of the area because its outputs. Complementarily, a multiscale analysis is proposed to assess deep basement and regional tectonics.

3.2.4. Determination of regional structures

The regional lineaments are those affecting the deep basement. They are highlighted trough the multiscale analysis, a qualitative exercise supported by the calculation of the depth of the highlighted features.

3.2.4.1. The multiscale analysis of the magnetic anomaly map field

The multiscale analysis involved the detection of HGM peaks for the upward continued RTE field at the respective heights 1, 2, 3, 4 and 5 km. The superimposition of the peaks obtained at each height highlights deep seated features and solve their respective geometry by observing their orientation and the offset of their peaks for plunge, and for the strike.

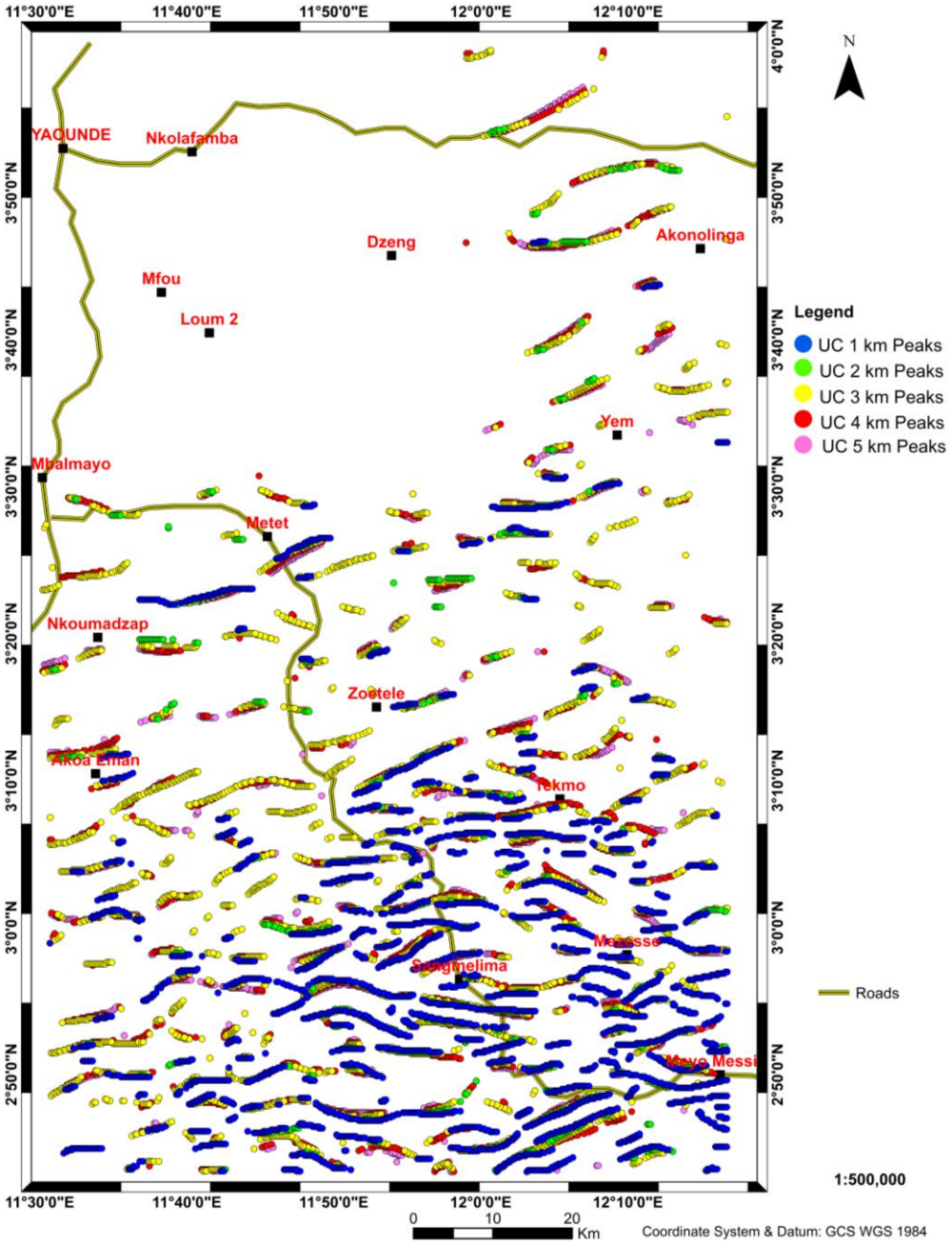

Figure 3.2-4 : Multiscale analysis map of the Nkolafamba-Sangmelima area. Lineaments are mainly vertical to subvertical or either dipping south or north.

The plot (**Figure 3.2-4**) discriminates very well the Panafrican and the CC domains in accordance with previous observations. The differentiation is made possible through the displayed difference in terms of density of the HGM peaks. Indeed, **Figure 3.2-4** shows that the lineaments are denser in the CC (south below Nkoumadzap) than in the Panafrican. In addition, peaks superposition shows that lineaments in the study area dip north or south (see **table 2**).

3.2.4.2. Interpretation of the lineaments from the multiscale analysis

a. Faults and fractures segregation

In this section, emphasizing on faults and fractures enabled to discriminate from dikes, contacts, etc. by underlaining the grey scaled RTE and FVD maps below peaks. Only coinciding features were interpreted as faults or fractures yielded **Figure 3.2-5** below.

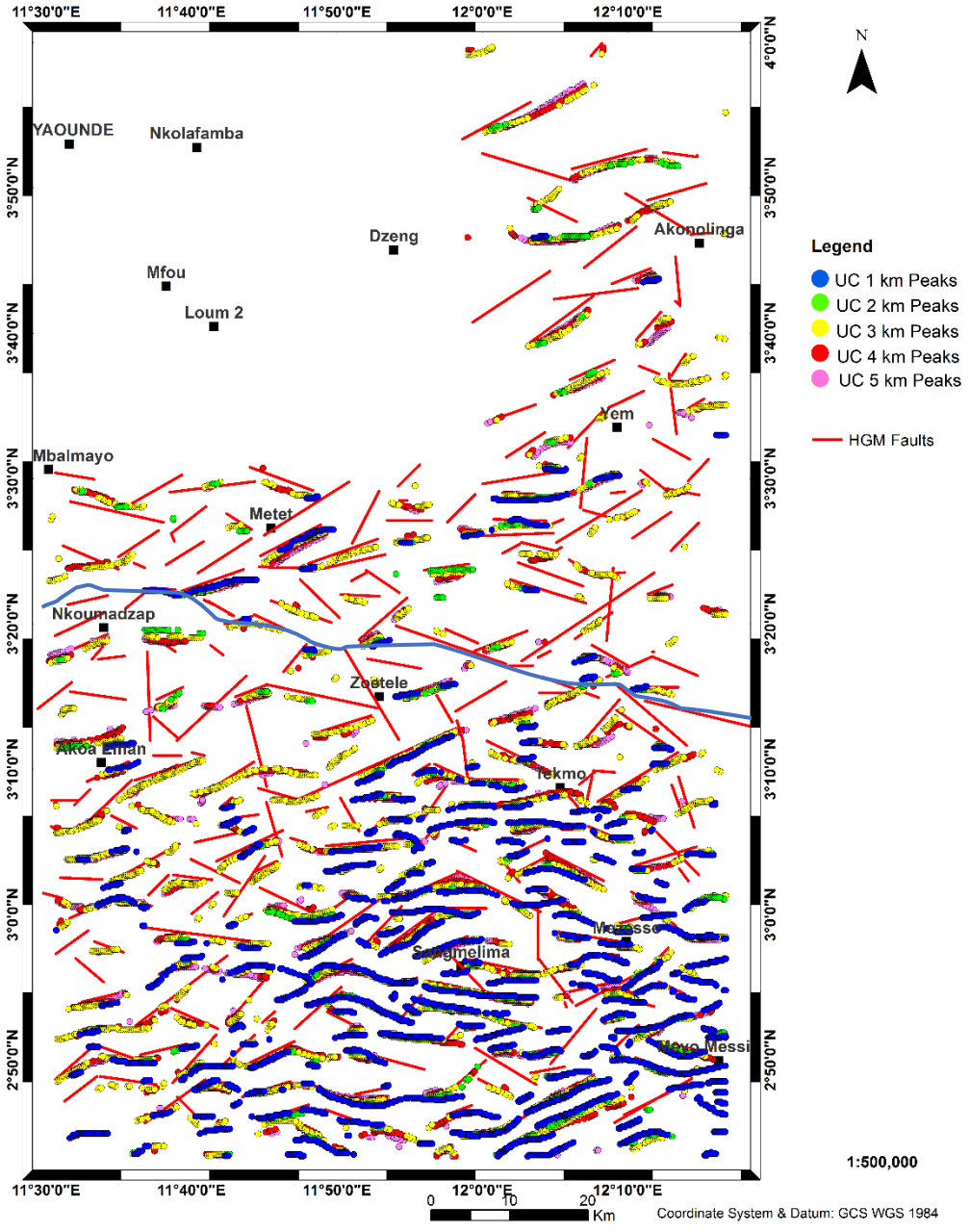

Figure 3.2-5 :Inferred major faults from the multiscale analysis map of the HGM. The superposition of peaks at various heights outlines the regional faults (red lines).

b. Characterisation of the interpreted faults

Characterising the faults means giving their attitudes (geometry) and determining their depth location. As for the geometry or attitude (**table 2**), the alignment of stacked peaks gives the strike and their offset indicates the plunge (coinciding peaks, mean a vertical dip). The table 2 below summarises the attitudes of the 31 interpreted faults extracted from **figure 3.2-5**. These faults are mainly vertical to subvertical and they form three main clusters, depending on their depth-location and extension.

Table 2 : Attitudes of the major lineaments in the Nkolafamba-Sangmelima area

Count	Fault's attitude		Depth class	Count	Fault's attitude		Depth class
	Strike	Dip or plunge			Strike	Dip or plunge	
1	SE-NW	North	Middle to deep	16	WSW-ENE	Vertical	Shallow
2	SE-NW	South	Middle to deep	17	WSW-ENE	Subvertical	Shallow
3	SE-NW	South	Shallow	18	WSW-ENE	North	Shallow to middle
4	SE-NW	Vertical	Shallow to deep	19	WSW-ENE	South	Shallow to deep
5	SE-NW	Subvertical	Shallow to middle	20	WSW-ENE	Vertical	Shallow to middle
6	SE-NW	Subvertical	Shallow	21	WSW-ENE	North	Shallow to deep
7	SE-NW	Vertical	Shallow to deep	22	WSW-ENE	North	Shallow to deep
8	SW-NE	N-Gradational	Shallow to deep	23	WSW-ENE	Subvertical	Shallow to middle
9	SW-NE	South	Shallow to deep	24	W-E	Vertical	Shallow to middle
10	SW-NE	Subvertical	Shallow to deep	25	W-E	Subvertical	Shallow to middle
11	SW-NE	Vertical	Shallow to middle	26	W-E	Subvertical	Shallow to middle
12	SW-NE	Subvertical	Shallow to middle	27	W-E	Subvertical	Shallow to middle
13	WSW-ENE	Subvertical	Shallow to middle	28	W-E	Subvertical	Shallow
14	WSW-ENE	Vertical	Shallow to deep	29	WNW-ESE	Vertical	Shallow to middle
15	WSW-ENE	Vertical	Shallow to deep	30	WNW-ESE	Vertical	Shallow to middle
16	WSW-ENE	Vertical	Shallow	31	WNW-ESE	Vertical	Shallow

Indeed, the distribution gives 2 deep-seated lineaments, 19 lineaments which are located in shallow/middle subsurface and extend to greater depths; while the last group comprises 10 lineaments with shallower (surface) expression and deep-extended. The along-strike distribution shows that the main orientations are WNW-ESE (3 counts), W-E (5 counts), NW-SE (7 counts), SW-NE (5 counts) and WSW-ENE (11 counts). Cumulatively, a dominant SW-NE to WSW-ENE cluster (16 counts i.e. 51.61%), followed by WNW-ESE to NW-SE cluster (10 counts, i.e. 32.25%) are highlighted in both the NEFB and the CC domains (separated by the blue line on **Figures 3.2-5**).

Depth-locations have been calculated using the Euler 3D algorithm, and solutions were superimposed on the map of the previously highlighted faults (**Figure 3.2-6**). To ensure fewer

but reliable solutions, calculations used a structural index of 0.35 and a depth tolerance of 5% with a 10 x 10 moving window.

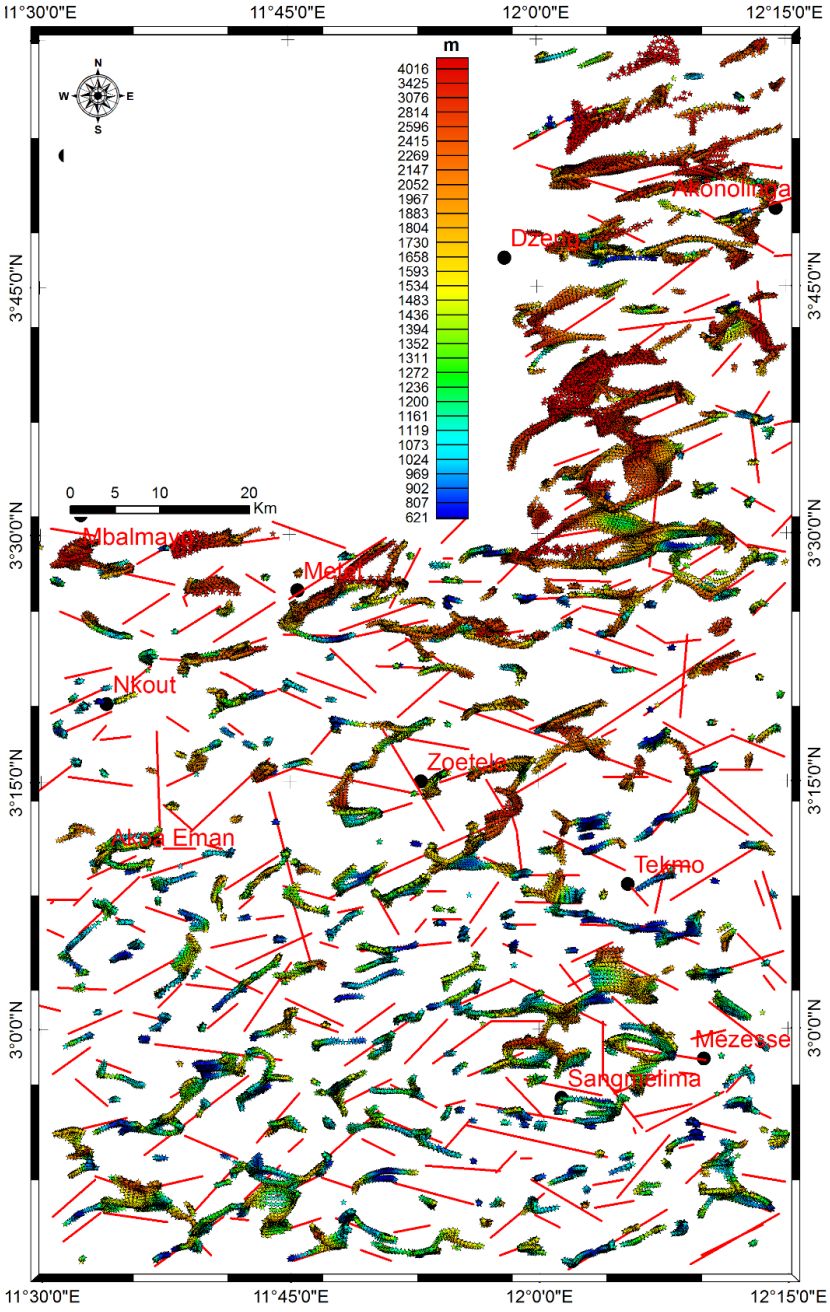

Figure 3.2-6 : Depth location of the regional faults in the Nkolafamba-Sangmelima. The good correlation between Euler solutions and the interpreted HGM fractures and faults is evidenced by the map.

Figure 3.2-6 validates the qualitative analyses of the previous paragraphs. Indeed, many Euler's solutions coincide with the interpreted faults from the multiscale study thus suggesting the validity of the present results. The depth ranges suggest three classes of faults: deep seated (depth > 2.1 km), intermediate (1.3 km < depth < 2.1 km) and shallow (depth < 1.3 km) faults; as seen with table 2.

Moreover, the observation of the Euler's solution map enables to outline the space location of the faults and complement the multiscale analysis. In general, it can be noted that the Euler's solutions divide the study area in three zones:

- The southern zone is the domain of shallower features (depth <1.3 km) despite the presence of some deep elements at the vicinity of Sangmelima and in the SW edge of the map, probably because of their sub crustal origin. The features have various trends possibly because of their rheology.
- The central domain located between ~N03º15' and N03º30', is ºfirstly characterised by the very low density of solutions, has the dominance of nearly E-W features and corresponds to the area of intermediate buried solutions (1.3 km < depth < 2.1 km).
- The northern domain (above latitude N03º30') is the region of deep seated features. These features follow the major NE-SW to ENE-WSW trend that characterises the Yaounde series.

The depth difference (increase) observed south to north is attributable to the subduction of the Congo Craton beneath the Panafrican belt and the intermediate depths recorded in the central domain as well as the dominance of the E-W trend are possibly explained by the presence of the Mbalmayo series and its stratigraphic position on top of the Panafrican belt in the area. As a matter of fact, the northern domain is interpreted as the Yaounde series; the high depths pertaining in that area might therefore be explained by the presence of a fractured subducted craton under the Yaounde Group.

3.2.5. Assessment of the regional magnetic foliation and deformation history

An attempt has been made to highlight the source behaviour by producing a map of source edges (**Figure 3.2.7**) which highlights both their plunge and strike. This approach examines the magnetic fabric of structures so as to assess the attitude of the regional foliation and infer the deformation regime. The difficulty to follow any particular magnetic foliation trace makes it uneasy to give clues on the foliation of structures encountered within the study area. This is particularly tributary to rejuvenation that occured in the region. In terms of line density, the magnetic foliation map can be slice up into three portion. The northern and the southern portions appear as areas with low to moderate line densities, probably because of their relative locations from the contact line between the NEFB and the CC. This is similar for the portion of CC directly in contact with the NEFB; which seems to have behaved differently to the post Panafrican stress that pertained at the northern margin of the CC.

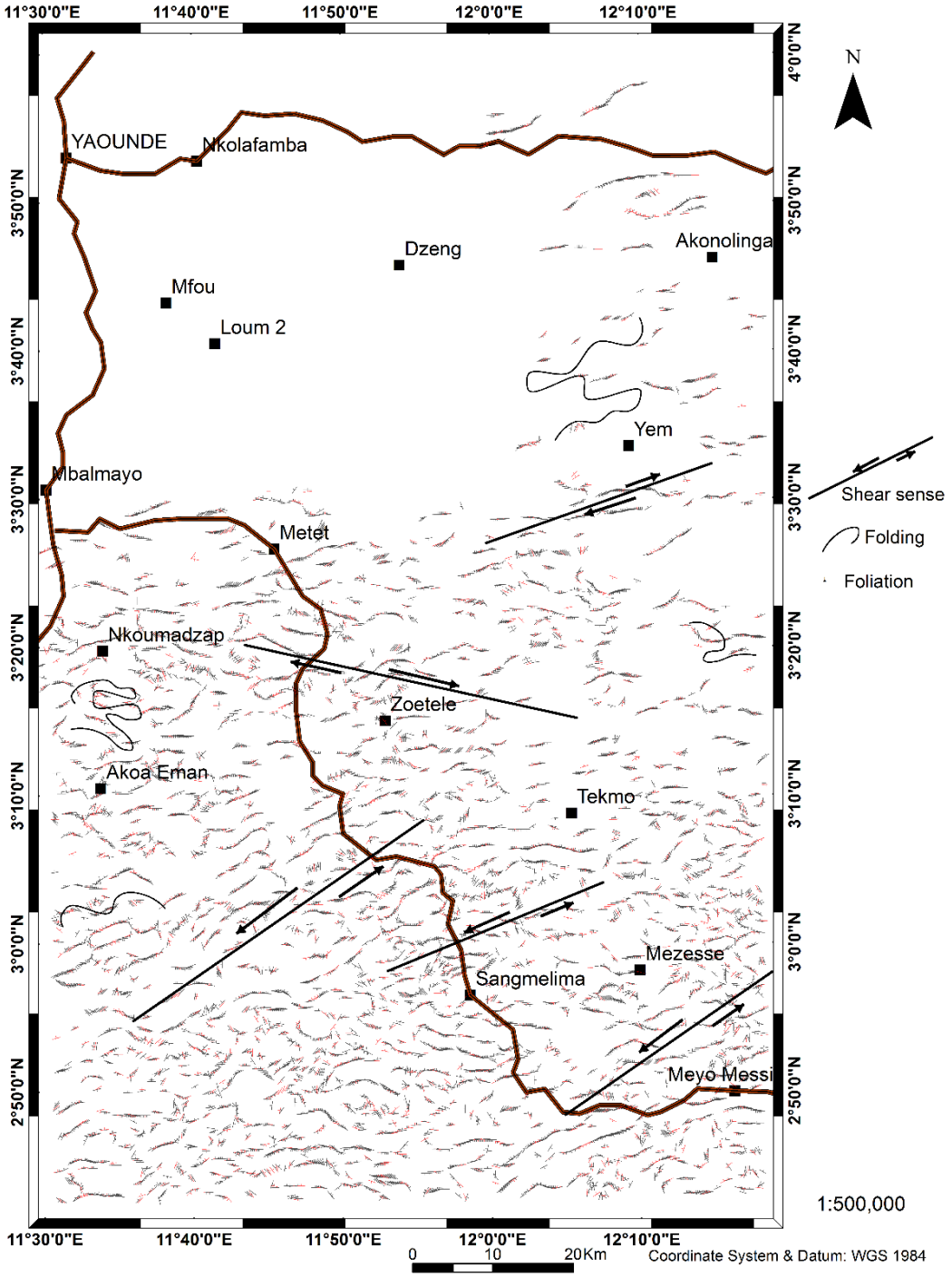

Figure 3.2-7 : Magnetic foliation. The magnetic foliation appears sparse in the north and dense in the south.

Considering the orientation of lines, the northern domain is characterised by two main directions, from the centre to the north of the map. In fact, in the region between Mbalmayo and Nkout (in terms of latitudes), the foliation is broadly E-W whereas it is nearly ENE-WSW in the northern part. The dip orientation varies alternatively from north to south. The ENE-WSW alignment in the north probably results from N-S to NW-SE compressions that affected the NEFB and triggered NE-SW to ENE-WSW extensions. The curling of the foliation characterises folding processes. Therefore, the two directions noticed correspond probably to the folding

trends hence it would be understandable that the area has been marked by an E-W and N-S folding episodes. This is particularly supported by the dipping attitudes which are south or north and sometimes east or west.

Additionally, many ruptures of the magnetic fabric are observed on **Figure 3.2-7**. These occur mainly along the NE, E-W and NW directions. These may correspond to shear trends related to shearing episodes which may have occurred along the SW-NE, the SE-NW and E-W directions but the timing of these events is fuzzy. The E-W shear zone has been identified south of Metet whereas the SW-NE shear zone is evidenced throughout the map, along a broad NE-SW. This shear patterns are consistent with the faults family previously highlighted. The map shows that this zone may have experienced many tectonic stages. This is witnessed by the curled patterns of the regional magnetic foliation which are probable imprints of folding (**Figure 3.2-7**). The various deformation stages can be assessed by observing the cutting relationships between These cross-cutting relationships suggest that the deformational history is an alternating occurrence of folding, faulting accompanied by shears supposedly triggered by compressional and/or extensional movements at different eras of the geologic history. The post-Panafrican events are particularly of interest as the central domain of the African Plate has been exposed to the stress regimes related to (1) the equatorial then the south Atlantic oceans opening, and (2) the ongoing rifting in East Africa leading to the individualisation of the Somalia Plate; questionning the existence of a fifth deformation stage. The qualitative interpretation of the aeromagnetic data has enabled to map various structures in the study area, including lineaneaments which testify that the area underwent brittle to brittle-ductile tectonics; and highlight rheological difference through which the Congo Craton/NEFB limit has been inferred. The geological modelling is hereafter made to refine its location.

3.2.6. Geological modelling: determination of the CC/NEFB limit

To propose an accurate location of the CC/NEFB limit, magnetic data were modelled along three N-S parallel profiles (P1 to P3) of nearly 52 km (**Figure 3.2-8**) from west to east.

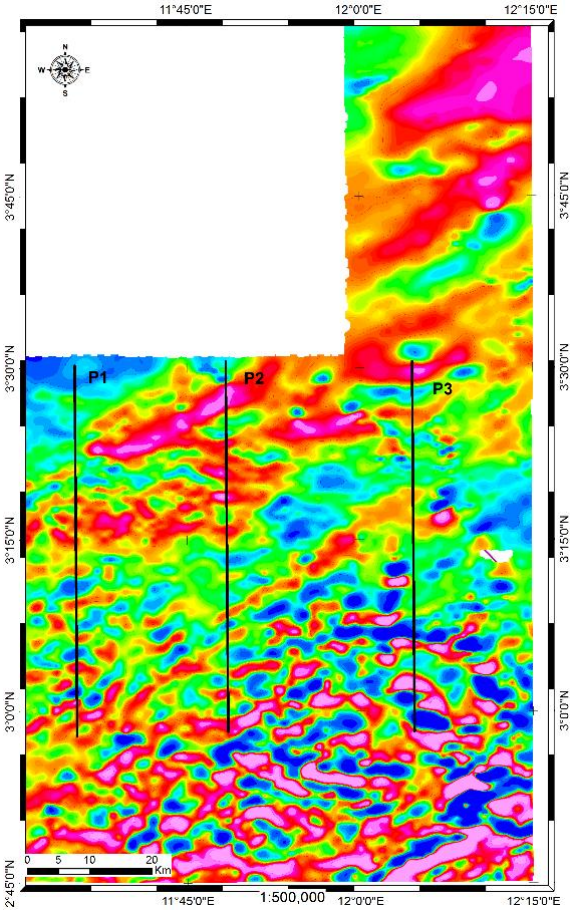

Figure 3.2-8 : Magnetic earth- modelling profiles. Profiles are labelled Line1, Line2, Line3.

3.2.6.1. Line 1:

Line 1 is the first and westernmost profile modelled to infer geology in the area surveyed with the magnetic method. Herein, the anomaly profile (**Figure 3.2-9a**) is smooth enough to allow straight analyses. Indeed, anomaly values vary from -192 nT to 45 nT. The profile's analysis assumes various discontinuities located respectively ca 3 km, 8.4 km, 22 km and 37 km. Some of these discontinuities are noticeable on the anomaly profile while other would correspond to hidden structures whose depth is not located yet. To produce a convenient geological model, the forward modelling strongly assumed that the anomaly profile results from various sources, including both suprabasement and intrabasement causes.

The modelling of Line 1 anomaly profile enabled to come out northward, with a model (**Figure 3.2-9b**) presenting four main faults, labelled from F1-1 to F1-4. The model was built assuming a uniform basement with a magnetic susceptibility (k) of 0.0015 cgs. The suprabasement effect corresponds to changes in the basement topography. These occur between

the faults F1-2 and F1-4. Therein an uplift of the basement is noticeable, coupled with a N-dipping intrabasement fault (F1-3) separating acidic granulites (k = 0.01977 cgs) from syenites overlying the basement between 20 and 38 km. This uplift smoothly affects the overlying formations between that same interval.

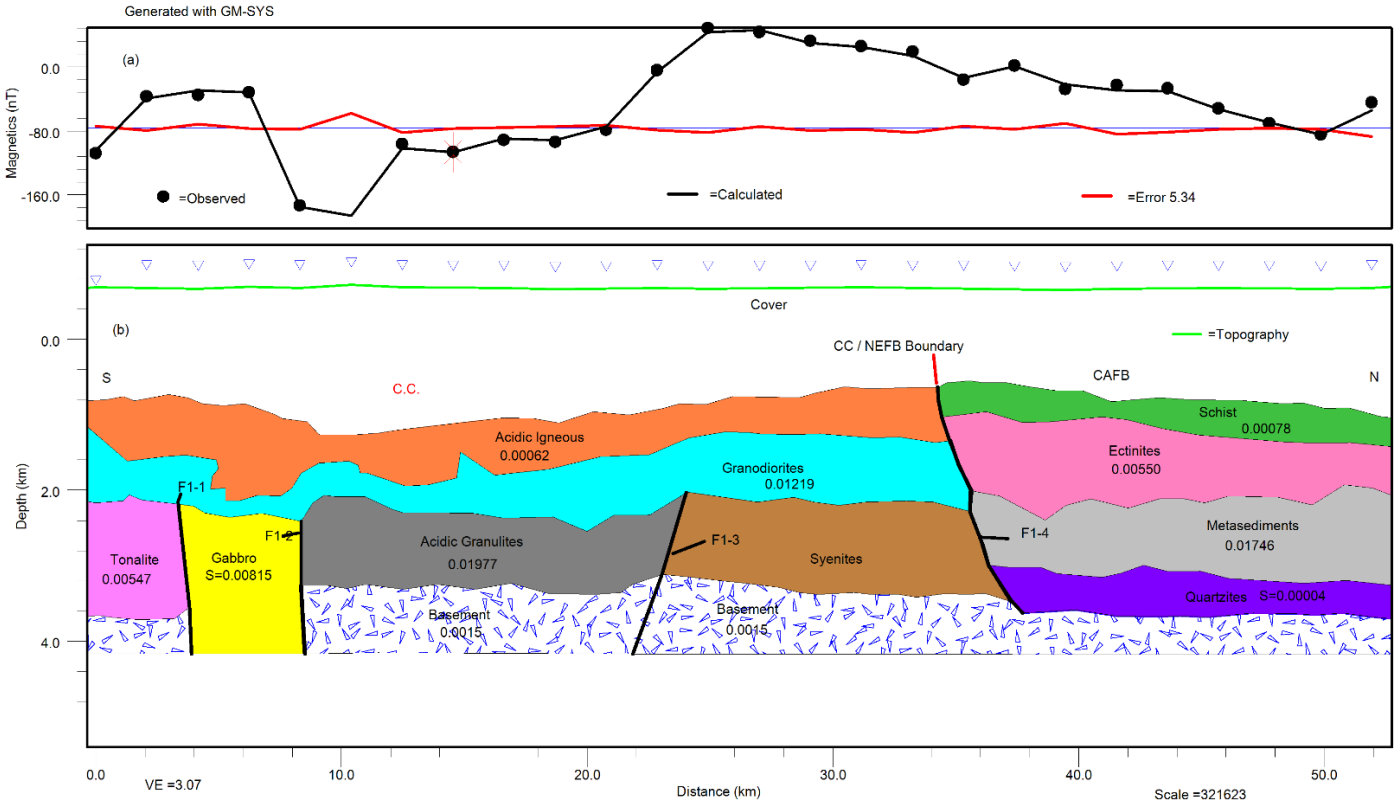

Figure 3.2-9 : Modelling along Line1. (a) Magnetic anomaly profile; (b) Geological section. The CC/NEFB limit is evidenced by the fault F1-4.

The intrabasement effect corresponds to the change basement lithology. Basement lithology variation is mainly observed between the faults F1-1 and F1-2, which bound an intrusive gabbro (k = 0.00815 cgs) encountered ca 2.3 km depth, with an approximate width of 4 km. This gabbro also occurs between tonalites (k= 0.00547 cgs). The previous described formations are topped upward by granodiorites (s= 0.01219 cgs) and acidic igneous formations (k = 0.00062 cgs) left of the F1-4 fault. Right of F1-4, the model yields upward above the basement, quartzites (k = 0.00004 cgs), metasediments (k= 0.01746 cgs), ectinites (k=0.00550 cgs) and schists (k=0.00078 cgs). The geological model (**Figure 3.2-9b**) shows that the basement is encountered at nearly 3.6 km depth from the origin of the profile to F1-1; at nearly 3.2 km from F1-2 to F1-4; then a progressive smooth subsidence from F1-4 to the end of the section. The F1-4 appears to be a north-dipping major discontinuity affecting the basement and separating an igneous complex to the left (south) from a metasedimentary complex to the right (north). By interpreting theat igneous complex as the CC, then the metasedimentary complex fit

with the southern part of the North equatorial fold belt (NEFB); therefore, the F1-4 illustrates the CC/NEFB limit (**Figure 3.2-9b**). The model realised with a satisfactory RMS error of 5.34%, shows no correlation between the subsurface geology and the topography.

3.2.6.2. Line 2:

The Line 2 particularity is its location at the middle of the area under consideration for magnetic prospecting. The anomaly profile (**Figure 3.2-10a**) values range between -192 nT and 35 nT. Its irregular profile's shape made it not obvious to identify anomaly sources, except for the portion spanning from 34 km till the end. Efficient modelling assumed that the observed anomaly profile pictures a combination of basement, normal faulting and faulted syncline effects involving the basement (Prieto, 1996). The geophysical modelling of the Line 2 anomaly profile (**Figure 3.2-10a**) has been realised with a significant RMS error of about 1.52 %, assuming a uniform crystalline basement of magnetic susceptibility (k) 0.0015 cgs. The basement effects mainly correspond to the change in the basement topography (suprabasement anomalies). The obtained section of Line 2 (**Figure 3.2-12b**) shows that the basement broadly dips northward. Indeed, it is encountered nearly at 3.5 km depth from the origin to 10 km (at F2-1) where it sinks to a nearly constant depth of 4 km up to F2-3; it sinks again therein to nearly 4.4 km depth till position 46 km (F2-10) where it is uplifted again to a constant depth of nearly 4 km. The basement is jagged by faults (F2-1, F2-2, F2-3 and F2-10) which affect partially or totally the overlying formations.

The formations on top the basement are affected by many faults like F2-1, F2-3 and F2-4 respectively separating different formations: migmatites (k=0.0039 cgs)/granite (k=0.03900 cgs), granulites (k=0.0706 cgs)-granite-gneisses (k=0.00858 cgs)/syenites (k=0.0268 cgs) and syenites/granulites-granite (k=0.00535 cgs). The faults F2-5 and F2-10 particularly, may correspond to limits of a basin or syncline extending northward in length from 33 km to 48 km. This is particularly supported by their respective geometry, as F2-5 dips north while F2-10 dips south, both being sub-vertical and normal. The faults F2-7, F2-8 and F2-9 apparently outline vertical movements affecting the schists (k=0.0021 cgs), ectinites (k=0.02366 cgs), migmatites (k = 0.0044 cgs), granulites, orthogneiss (k = -0.0578 cgs) and even the basement, in the aforesaid basin. This seems also to be the case for F2-1 and F2-2 regarding the granulites layer and the basement, nearly 10 km from the origin of the section.

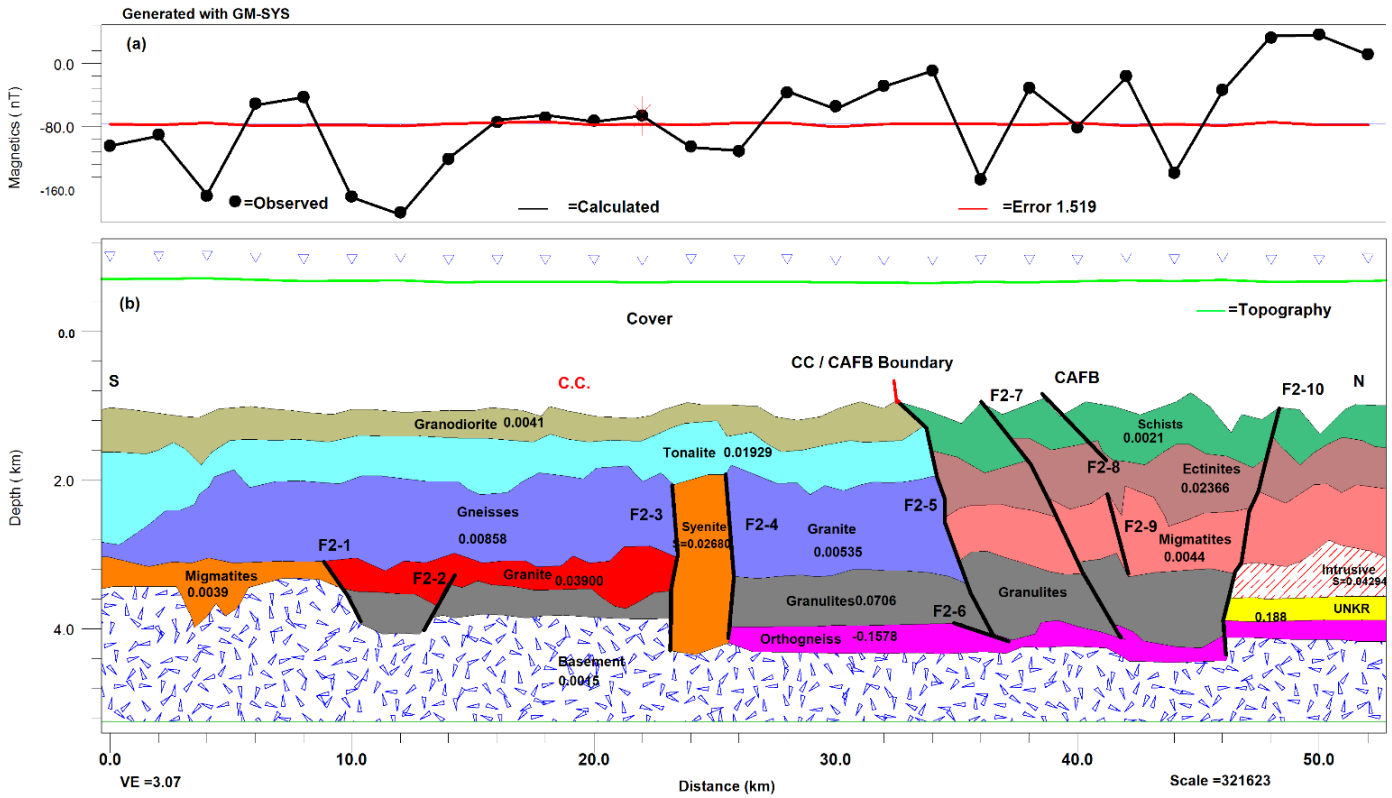

Figure 3.2-10 : Modelling along Line2. (a) Magnetic anomaly profile; (b) Geological section. The CC/NEFB limit is evidenced by the fault F2-5.

Further, from **Figure 3.2-10b**, two main blocks can be differentiated. One block is formed mainly by various igneous rocks and it is located to the left F2-5. This igneous complex seemingly corresponds to the CC formations. To the right of F2-5, the second block appears to be essentially made up of metamorphic rocks probably of sedimentary origin. This metasedimentary complex apparently corresponds to the NEFB formations. Therefore, F2-5 forms a sharp contact between the two above described blocks, making it interpretable locally as the CC/NEFB boundary. Moreover, the model shows that NEFB formations are affected by vertical movements imprints of compressions probably caused by pure compressions and/ or a collision. These are proofs of ductile to brittle-ductile tectonics in the area. The model does no correlate the subsurface geology with topography.

3.2.6.3. Line3:

The Line 3 is the easternmost modelled profile of the study. The anomaly profile (**Figure 3.2-11a**) looks more regular compared to the previous profiles. It is characterised by a peak value (100 nT) at the beginning of the line followed by a regional flat low of about -220 nT from 4km to 24 km where a new abrupt increase is observed. In the 24-32km interval, the profile displays a peak at 26.5 km and, alternative gradual decrease and increase till the end. This change shapes the anomaly profile like a valley between 32 and 44 km. The profile's patterns (**Figure 3.2-11a**) at 2 km and in the 24-32km interval, suggest the existence of discontinuities. In addition, the

regularity of the profile suggests two almost homogenous lithological blocks separated by a major discontinuity at 24 km; but, direct modelling and interpretation and remain not evident.

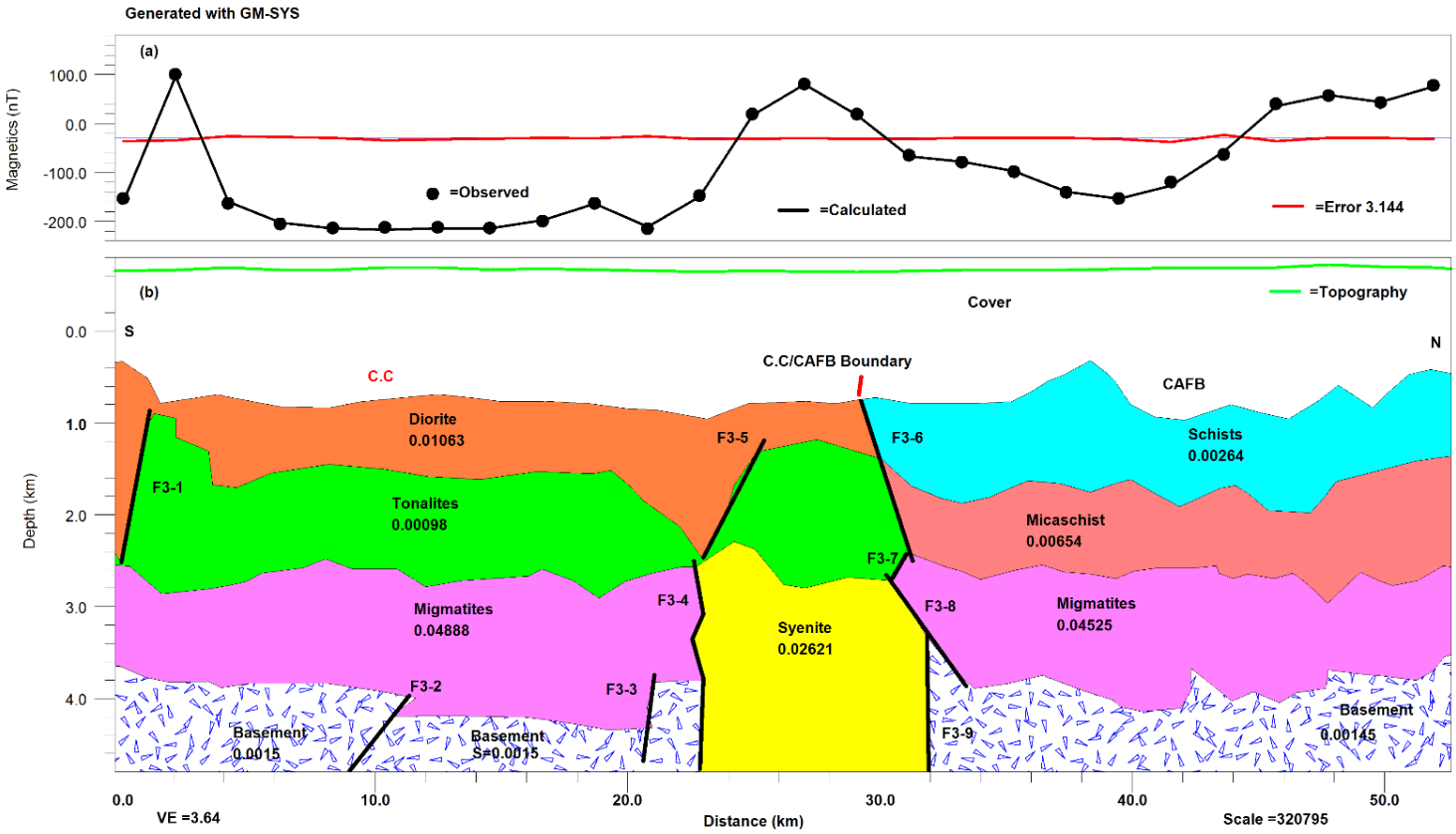

Figure 3.2-11 : Modelling along Line3. (a) Magnetic anomaly profile; (b) Geological section. The CC/NEFB limit is evidenced by the faults F3-6, F3-7, F3-8 and F3-9

The Line 3 model, with a RMS error of 3.14%; was built assuming that the anomaly sources involve both suprabasement and intrabasement variations and assuming a uniform basement with a magnetic susceptibility of 0.0015 cgs. The suprabasement effects are witnessed on **Figure 3.2-11b** along two manners. Progressively from 0 to 11 km, the basement occurs at approximately 3.6 km; it collapses to 4.2 km from 11 km to 21 km then raises again at 3.8 km up to 22.5 km; from 32 km to the end, it occurs above 4 km with a very rough topography. The main intrabasement variation modelled correspond to a body (k = 0.0261 cgs) affecting the basement. This body has been interpreted as a syenites intruding the basement and overlying migmatitic formations. The model outlines various discontinuities (9 discontinuities) labelled F3-1 to F3-9, which are somewhat hidden on the anomaly profile (**Figure 3.2-11a**). These discontinuities have been interpreted as faults or contacts. Particularly, F3-2 and F3-3 are related to a probable vertical movement that may have caused the collapse of the basement between 10 km and 21 km. Out of the interpreted faults, F3-4, F3-8 and F3-9 also play a very significant role. Indeed, the F3-4 and F3-9 faults are related to the intrusion of a body (interpreted as a syenite) through the basement, in one hand, whereas F3-4 and F3-8 are fault-contact structures

on another hand separating respectively, the migmatites I (k =0.04888 cgs)/syenites and syenites/migmatites II (k =0.04525 cgs). In addition, F3-7 and F3-6 also classify themselves as particular, within the modelled faults. This is emphasised by the fact that F3-6 probably outlines upward, left to right, gneiss (k = 0.00098 cgs) / micaschists (k = 0.00654 cgs) and diorite (k = 0.01063 cgs) / metasediments (k = 0.00264 cgs) contacts. Besides, F3-7 may constitute the gneiss/migmatites boundary. Also noticeable, the F3-1 fault which probably caused the peak in the anomaly profile observed at the beginning of Line 3 (**Figure 3.2-11a**).

The geological section of Line 3 (**Figure 3.2-11b**) advocates that the faults F3-6, F3-7, F3-8 and F3-9 are probable relays of a unique fault which separates two main units. The left unit (relative to the imaginary fault trace made by merging the aforementioned faults) globally has hypothetical high susceptibility magmatic and/or mafic formations, while the right unit encompasses probable low susceptibility detrital metasediments. Therefore, by equating the left magmatic unit to the Ntem complex (CC) and the right unit to NEFB formations, this fault would represent the CC/NEFB limit. Moreover, the zig-zag patterns of NEFB formations on the section suggests that N-S compressions (in the profile's direction) would have affected those formations.

3.2.6.4. Definition of the Ntem complex/North Equatorial Fold Belt southern limit

The NEFB has been distinguished from the Ntem complex trough the difference in the density of lineaments observed on qualitative interpretation maps (**Figures 3.2-2, 3.2-3, 3.2-5**). Indeed, the NEFB appears to be less fractured than the CC on magnetic maps. The boundary between those two area of unequal density of lineaments has been interpreted as the local CC/NEFB southern limit. Its location was defined through distance measurement from the north, along each profile (Line1, Line2 and Line3) as presented in **table 3** below.

Table 3 : Locations of the CC/NEFB southern limit. The distances are obtained from the north along profiles

Location of the CC/NEFB limit in km (west to east)			
Reference axis	Line1	Line2	Line3
Measured on map	19.24	17.87	21.42
From inversion	18.30	16.5	20.45
Difference .	0.94	1.37	0.97

In general, the three models (**Figures 3.2-9, 3.2-10** and **3.2-11**). are consistent with the existence of a low susceptibility block to the north, separated by a sharp discontinuity to a south-high susceptibility block. The high susceptibilities in the left are supposedly due to mafic terrains and low susceptibilities to detrital metasediments. This oulines an igneous complex interpreted as a portion of the CC (to the south) and a metamorphic complex equated to the NEFB (to the north), separated by sub-vertical faults probably representing the CC/NEFB limit. The location of that limit at each profile is directly measured on the geological sections and the values are

reported in **table 3**. These distances average the location of the CC/NEFB faulty southern limit around latitude N03º20' latitude (south of Mbalmayo), referred to as the Schists/Granites contact (Manguelle Dicoum et al., 1992).

3.2.7. Summary of the aeromagnetic findings

The analysis of Aeromagnetic data over the southern part of the study area (between latitude N03°30' and latitude N03°) evidenced various mafic to ultramafic deep sources (RTE and Analytic signal maps) characterised by high amplitude values. Key results are the differentiation of the Yaounde schists from the CC granitoids and the outlining of the CC/Panafrican thrust line as well. The magnetic intrusions and related lineaments beneath the Mbalmayo schists confirmed the subduction of the CC under the Panafrican belt. Various lineaments have been highlighted by the magnetic investigation. The main directions they follow are NE-SW to ENE-WSW, NW-SE to WNW-ESE and N-S. These may correspond to fracture, faults, dykes or geological contacts between major formations.

The multiple directions of faults and the folding patterns observed are evidences of a multistaged tectonic activity that affected the CC/NEFB transition zone in the ductile to brittle-ductile deformation conditions throughout Archaean, Paleo-, Meso- and Neoproterozoic periods. Further, the multiscale analysis of HGM peaks revealed that the basement of the northern part of the study area may be affected mostly by SW-NE to WSW-ENE faults, beneath the Yaounde series (micaschists and Mbalmayo schists) probably from the collapse of the basement; hence they probably shaped the basin in which the sediments that formed deposited ahead the Panafrican event. The SW-NE to WSW-ENE directions in the CC generally associated to the Panafrican orogeny in Central Africa may be related at least to the Eburnean event with Phanerozoic reactivations due to the Gondwana split and the Atlantic Ocean's formation in the Albian. The faults distribution and the regional magnetic foliation revealed NE, NW and N-S shear zones (NE and NW being dominant on a descending sorting, respectively). Also, many faults highlighted are arranged as en-echelon faults system. This tremendously enables to suggest that the Ntem complex experiences wrenches which are broadly oriented SW-NE to WSW-ENE, hence the study assumes that the faulting reactivation in the Congo Craton is in relation with the development of the Central Cameroon Shear Zone (CCSZ) and the ongoing NE collision between the African and Eurasian plates. However, the lineaments highlighted thanks to aeromagnetics need to be confirmed, and this proves to be challenging, because of the scarcity of ground controls on the southern zone. Moreover, to establish a direct link between the facts highlighted both the AMT and the magnetic results, an investigation involving Landsat-8 imagery over the entire study area has been made and the results are presented hereafter.

3.3. INTERPRETATION OF THE REMOTE SENSING DATA

In the recent years the use of satellite remote sensing to solve geological problems have gained notoriety. Indeed, it enables to outline lithology and geological structures (e.g. faults, fractures, contacts, etc). This second application will be discussed hereafter.

3.3.1. The Global view

The processing of Landsat-8 OLI images covering the study area has enable to map many lineaments. The **Figure 3.3-1** below corresponds to the map of remotely sensed lineaments above the entire area under study. This evidences a fuzzy distribution of those lineaments. However, a careful look shows that between Sangmelima (to the south) and Dzeng (to the north) the area is densely fractured. For Sangmelima belongs to the Ntem complex and Dzeng to the NEFB, the image highlights the intense tectonic activity that occurred at the northern margin of the CC. This activity (see **Figure 3.3-1**) is characterised by the multiplicity of the directions of the small lineaments (foliation trace) in general, and illustrated by the major lineaments (probable faults/fractures) which infer the structural control of the area along the NE-SW, NW-SE, N-S and E-W which would result from NW-SE to N-S, ENE-WSW, WNW-ESE, and NNE-SSW compressions. This suggests that the area underwent at least four deformation stages.

In details, **figure 3.3-1** exhibits a narrow transitional zone between Metet and Zoetele in such a way that above that three main zones can be outlined, north to south:

(i) The northern zone (zone A) extends from the northern edge of the map to nearly north of Mbalmayo. The zone is characterised by a high occurrence of lineaments turning progressively clockwise NW-SE to NNE-SSW as we go from west to east.

(ii) The central zone (Zone B), corresponds to a narrow band extending between zone A and the latitude passing through Nkout. This portion is characterised by a low density of lineaments and a noticeable highly fractured N-S break through between Metet and Zoetele. Zone A exhibits a lot of E-W trending lineaments probably the foliation trends as pertaining to the Mbalmayo schists that it can be equated to.

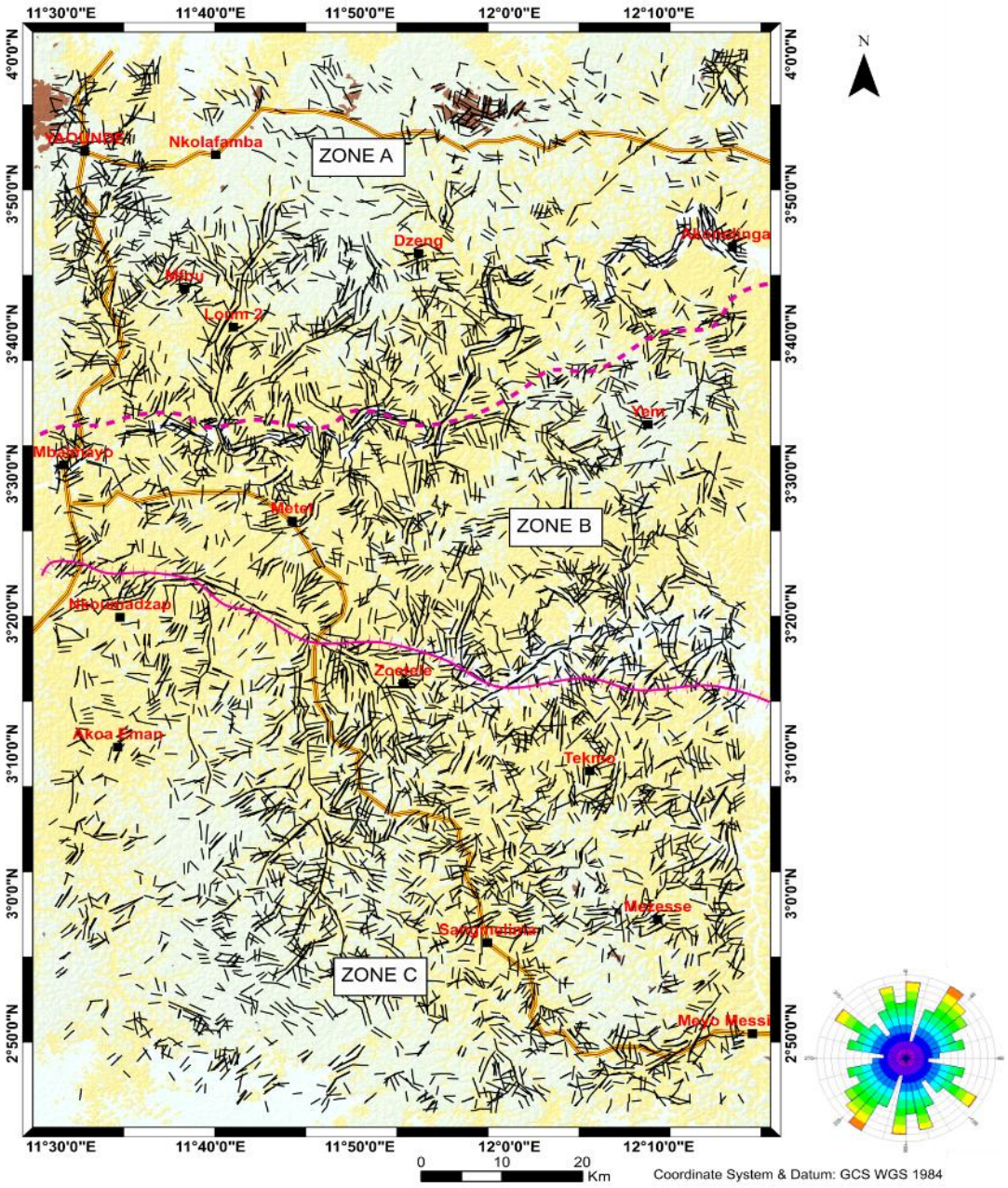

Figure 3.3-1 : Automatically extracted lineaments from Landsat 8

(iii) The southern zone (Zone C); it extends from the south-limit of zoneB to the south edge of the map. Compared to zone A, its lineaments' population is higher, probably because of the inability of its formations to undergo ductile tectonics, or maybe because they are older than the formations in Zones A and B. On that basis, this domain is interpretable as the CC domain. The diverse orientation of the foliation in this zone infers the existence herein of multiple formations.

3.3.2. Zonal analysis of interpreted Landsat faults and fractures

Clearly, the processing of Landsat 8 scenes shows that an important population of lineaments affects our area of interest. These lineaments reflect respectively foliation, folding and faulting; faults are the easiest interpretable structural features in the frame of this study. For

that purpose, a supervised classification of the outputs from **Figure 3.3-1** yielded interpreted lineaments, mostly faults and/or fractures that enable sound structural analyses.

Figure 3.3-2 : interpreted faults and fractures with respect to the zonal distribution.

The interpretation envolved (1) overlaying the previous image on the terrain model of the area; then (2) joining, when possible or reasonable, some segments to form more continuous lines. The interpreted lineaments as fractures or faults yielded a map that eases geological analyses, accordingly; following the aforesaid zonal repartition shown in **figure 3.3-2**.

3.3.2.1. The zone A

a. Quantitative analysis

The zone A covers an area limited by the northern edge of the map and a NE limit starting nearly south of Mbalmayo, and passing south of Mfou (**Figure 3.3-2**). This area is characterised by a high occurrence of lineaments corresponding to 26.75% of the total population of interpreted faults. Graphical statistics showing the distribution of lineaments considering the bearing (direction) attribute are summarised in **Figure 3.3-3** below.

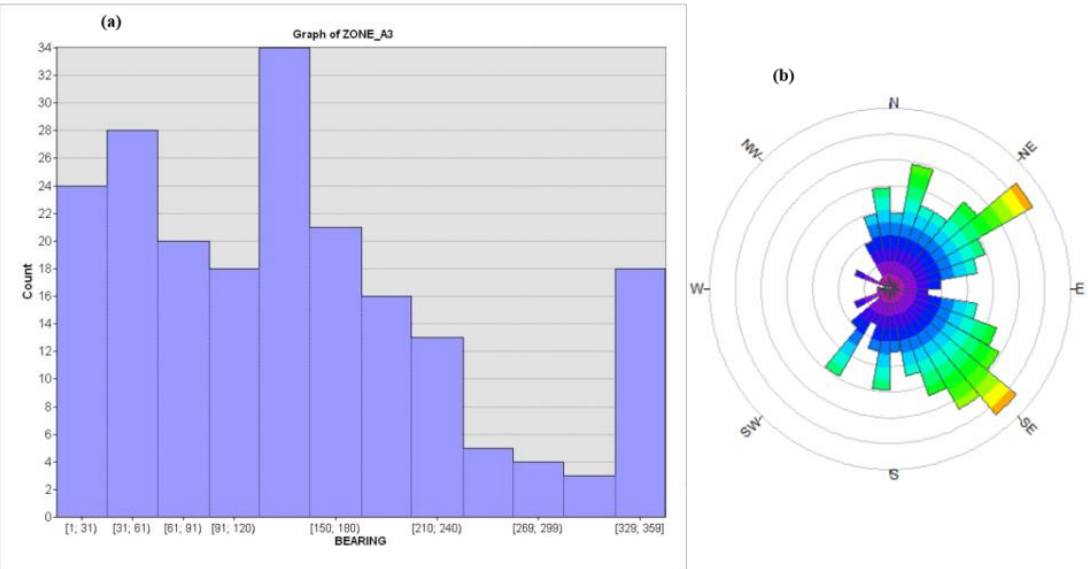

Figure 3.3-3: Graphical statistics in the Zone A; (a) Histogram (b) Rosacea of strikes.

The histogram (**Figure 3.3-3 a**) has been plotted assuming a bin amplitude of 30 degrees making a total of 12 bins; and the rosacea (**Figure 3.3-3 b**) assumed and aperture of 15º per petal. From the histogram of directions, the loosely dominant families would be N120-150º (34), N31-60º (28), N01-30º (24), N150-180º (21), N61-90º (20), N91-120º and N330-359º with 18 counts, respectively. The rosacea backs the histogram by strengthening the fact that the main directions of lineaments in zone A are NE-SW and NW-SE. A more detailed analysis by clustering the lineaments along the 8 main directions and integrating the length attribute as shown on **table 4** provided an attempt toward a more realistic description of the results illustrated by **figure 3.3-3**. Indeed, based on the decreasing number of lineaments, we have:

- The first family or group comprises lineaments oriented NE-SW. With a population of 42 lineaments (20.59% of the population in zone A), this family has a cumulative length of 229.39 km, an average length of lineaments equals to 5.46 km with a maximum and a minimum length of 14.04 km and 1.40 km, respectively.

- The second group comprises the N-S trending lineaments. They are 39, i.e. 19.12% of the total population of zone A. In terms of length, the shortest is 1.23 km and the longest is 13.63 km, while the average is 4.34 km and the cumulative length is 169.24 km.
- The third group encompasses lineaments oriented NW-SE. With 37 counts (18.14 % of the total population of zone A), this family has an average length of 4.75 km; its longest and shortest members are respectively 11.88 km and 1.24 km for a total length of 175.72 km.
- The fourth group comprises NNW-SSE lineaments. This family has 22 members (10.78 %), its less and most extended members are respectively 1.85 km and 21.73 km (the longest feature in zone A), for an average length of 5.50 km (and a total of 120.94 km).
- The ENE-WSW lineaments form the fifth group with 19 counts (9.31%), a total length of 109.11 km for an average of 5.74 km. The recorded extrema are 13.07 km and 2.16 km, respectively.
- The sixth group gathers the WNW-ESE and NNE-SSW families. They respectively have 18 (8.82 %) and 17 (8.33%) counts; their average lineaments lengths are 5.69 km and 5.71 km, respectively. Within this group, the NNE-SSW family particularly comes out with the maximum shortest length (2.40 km) of zone A.
- The last group corresponds to the E-W family. Less populated, this group particularly have a maximum and a minimum length of 15.55 km and 0.81 km for an average length of 6.32 km.

b. Qualitative analysis

The qualitative analysis of the lineaments consists in sorting the families of lineaments obtained by relevance. The classification is done by averaging the length obtained by subtracting the minimal and the maximal length from the cumulated sum of lengths in order to remove their influence in each cluster. The false average is then used to determine the influence of the group of lineaments i.e. groups are characterised as ***«major»***, ***«secondary»*** or ***«minor»;*** irrespective of their strike. These are coloured green, red and yellow, respectively in table 4. Therefore, on a decreasing order of importance, the classification yielded:

- The first class comprises the NNE-SSW, NNW-SSE, ENE-WSW and E-W families. These families have the highest false average lengths (5.44, 4.72, 5.34 and 5.30 km, respectively) compared to the false average (5.24 km) of the domain. Despite the false average criterion introduced, the NNW-SSE family is listed as it has the far most extended lineament in the domain (21.73 km). These criteria suggest that the faults and

fractures from these families are well extended in length. This enables to infer that these lineaments affect the deep subsurface and probably the basement of the northern zone of the study area; hence their classification as ***majors*** (or first order) lineaments.

- The second class gathers the NE-SW and WNW-ESE groups of lineaments. The respective average lengths in these families are 5.25 km and 5.21 km while the minimum lengths are between 1.40 km and 1.56 km, suggesting that these faults probably affect the area moderately; thus we propose them to be considered as secondary lineaments.
- The third class corresponding to ***minor*** or third order lineaments, includes the N-S and NW-SE families because of their lowest average length values.

Table 4 : Clustering of fractures in zone A along the 8 main geographical directions. The colours green, red and yellow denote the major, secondary and minor classes of lineaments, respectively

	N-S	NNE-SSW	NE-SW	ENE-WSW	E-W	WNW-ESE	NW-SE	NNW-SSE	Zone A
Counts	39	17	42	19	10	18	37	22	**204**
Sum	169.24	100.50	229.39	109.11	63.24	102.45	175.72	120.94	**1070.57**
Max	13.63	13.48	14.04	13.07	15.55	13.91	11.88	21.73	**21.73**
Min	1.23	2.40	1.40	2.16	0.81	1.56	1.24	1.85	**0.81**
Aver	4.34	5.91	5.46	5.74	6.32	5.69	4.75	5.50	**5.46**
%	19.12	8.33	20.59	9.31	4.90	8.82	18.14	10.78	**100.00**
False Av.	4.15	5.44	5.25	5.34	5.30	5.21	4.55	4.72	**5.24**

Summarily, 204 faults and /or fractures have been identified in zone A with lengths varying from 0.81 to 21.73 km, for a cumulated length of 1070.57 km. Though these fractures follow many directions, the major fractures are ENE-WSW to E-W. Their relationship with the intermediate and minor structures is not discussed. However, average length (5.46 km) indicates that they are globally lengthy thus, they should yield signatures that cannot be ignored or constrained to simple topographic variations. This suggests that they are deep structures affecting the basement, as it is somewhat the case in the NEFB.

3.3.2.2. The zone B

The zone B is outlined as shown on **Figure 3.3-2**. In comparison with zone A, this area is densely fractured but its features mostly occur in the west side of the domain i.e. from Mbalmayo to Metet.

a. Quantitative analysis

Zone B possesses nearly 22.34 % of the lineaments of the study area, making it a highly fractured zone, considering its surface area which forms a narrow portion between zone A and zone C. The histogram and the rosacea of the directions of the lineaments (**Figure 3.3-4 a & b**) do not evidently show the dominant directions in the area, despite the fact that the NE-SW and NW-SE tend to depart themselves from this observation.

Quantitatively from the histogram (**figure 3.3-4a**), the dominant directions are N02º-30º (30 counts), N31º-60º (28 counts), N91º-120º (23 counts), N120º-150º (27 counts) and N328º-358º (26 counts) representing respectively 15.38 %, 14.36%, 11.79%, 13.85% and 13.33% of the population of faults in zone B. For the histogram bin is wide (30º) causing overlaps of groups of directions, the clustering of faults along standard directions would permit a more reliable examination of these distribution.

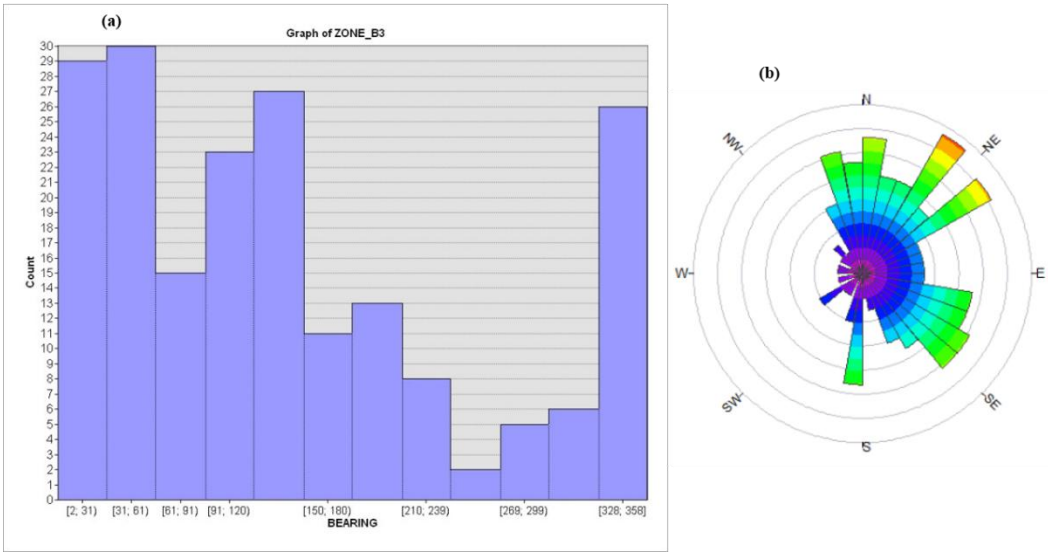

Figure 3.3-4: Graphical statistics in the Zone B; (a) Histogram (b) Rosacea strikes.

To come out with a sound geological significance, the lineaments of zone B have been clustered along the 8 main directions of a rosacea. From the clustering of the lineaments respective to their directions, one can distinguish with the decrease in the population (**table 5**):

- The first group is represented by N-S faults: with 23.59% of the total population, it has an average length of 4.02 km and the highest cumulative length (184.74), but records also the shortest lineament (0.96 km) of zone B.
- The NE-SW family constitutes the second group with 20.51 % of the total population of zone B and a cumulative length of 178.57 km; it shows up with a mean length of 4.46 km that makes it the third family with most extended lineaments.
- The NW-SE family, counted 3rd (17.44%) among the most populated group of lineaments, its mean lineament's length (3.94 km) infers its reduced significance despite the recorded cumulative length of 133.83 km.
- The fouth group comprises the E-W (9.74%), WNW-ESE (8.21%) and NNW-SSE (8.21%) families; these families have low cumulative lengths and the lowest average

length, in the exception of the WNW-ESE which have a mean length of 5.02 km (this family seems to have a geological relevance).

- The fifth group is represented by the NNE-SSW family. This family represents 7.18% of the total population and has the longest fracture (15.66 km), the highest average length (5.25 km) and the highest minimum length (2.25 km) of zone B, making it very important.
- The ENE-WSW family. This family is the less populated group of zone B (5.13 %) but possess an average length (3.72 km) of features that makes it interesting.

Table 5 : Clustering of fractures in zone B along the 8 main geographical directions. The colours green, red and yellow denote the major, secondary and minor classes of lineaments, respectively

	N-S	NNE-SSW	NE-SW	ENE-WSW	E-W	WNW-ESE	NW-SE	NNW-SSE	ZONE B
Counts	46	14	40	10	19	16	34	16	**195**
Sum	184.74	73.55	178.57	37.18	62.33	80.25	133.83	54.88	**805.32**
Max	13.14	15.66	15.39	6.15	14.78	12.13	9.10	5.54	**15.66**
Min	0.96	2.25	1.48	2.16	1.08	1.68	1.13	1.10	**0.96**
Aver	4.02	5.25	4.46	3.72	3.28	5.01	3.94	3.43	**4.14**
%	23.59	7.18	20.51	5.13	9.74	8.21	17.44	8.21	**100.00**
False Av.	3.88	4.72	4.18	3.89	2.64	4.54	3.78	3.29	**4.15**

b. Qualitative analysis

The qualitative analysis approach consisted in inferring the importance of families of faults based on the length attribute instead of the direction. This assumes that the high population along a direction does not make that direction necessarily more important. Removing the influence of the minimum and maximum length of each bin enabled the classification of families of faults in a ***major-secondary-minor*** scheme (table 5). This classification yields:

- The class of ***major*** lineaments: it embraces family directions NNE-SSW, NE-SW and WNW-ESE which possess highest *false mean* lengths (4.72, 4.18 and 4.54 km, respectively) in comparison with the domain's average (4.15 km). These families also contain almost all the longest lineaments of the zone B. Major lineaments are assumed to affect the middle-deep to the deep subsurface or basement. In this category, the NNE-SSW to NE-SW features are particularly interesting as they design a broad SW-NE channel in zone B, corresponding to a weakness zone beneath the schists.
- The ENE-WSW, NW-SE and N-S families whose respective false mean lengths are 3.89 km, 3.78 km and 3.88 km form the cluster of ***secondary*** lineaments.
- Finally, the lineaments of the NNW-SSE and E-W families will be considered as ***minor*** in regard to their lower false average lengths, 3.29 km and 2.64 km, respectively.

Summarily, the zone B is affected by lineaments of various lengths and directions. The lengths vary from 0.96 km to 15.66 km, with cumulative and average lengths of 805.32 km and 4.14 km, respectively. The classification of the NNE-SSW, SW-NE and ESE-WNW lineaments as major lineaments is consistent with the maps shown on **Figure 3.3-2** and **Figure 3.3-1** which conspicuously highlight that these directions form a NE channel within which lineaments of various directions occur (second and third order lineaments). This channel would affect the basement of the Mbalmayo series which lies transverse to its direction. The average length shows that faults in zone B are shorter compared to zone A (5.46 km) and zone C (4.42 km) but the density of faults and the scattering of their directions infer that these milieus are different.

3.3.2.3. The zone C

The zone C spans from the latitudes of Nkout and Zoetele to the bottom of the study area (**Figure 3.3-2**). This area is densely fractured and records the highest number (438) of faults in comparison with zones A and B.

a. Quantitative analysis

The quantitative analysis of the lineaments from zone C is based on the interpretation of the rose diagram and the histogram of the directions shown on **Figure 3.3-5.** Indeed, the rosacea

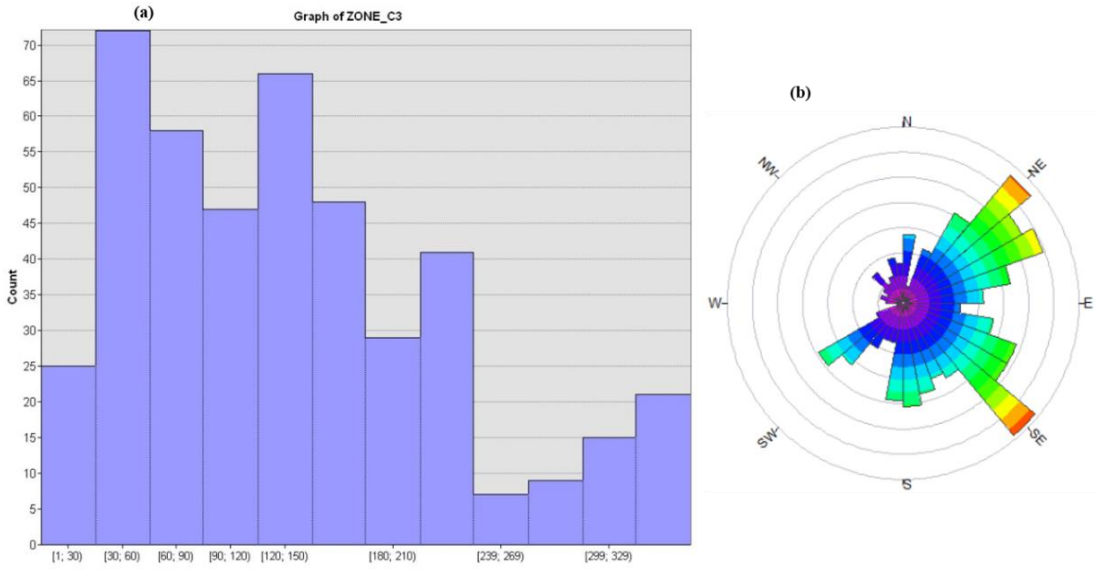

Figure 3.3-5 : Graphical statistics in the Zone C; (a) Histogram (b) Rosacea of strikes.

(**Figure 3.3-5b**) shows the predominance of NE-SW, NW-SE and N-S, alongside with various minor intermediate directions. The information from the rose diagram are complemented by the histogram of the directions of lineaments (**Figure 3.3-5a**), which brings more details and some figures. Indeed, the histogram's bins quantitatively distribute trends within 12 bins of 30º width. By relevance, the dominant direction fans are: N31º-60º (72 counts), N120º-150º (66 counts),

N61º-90º (59 counts), N150º-180º (47 counts), N91º-120º (46 counts) and N210º-239º (41 coounts). Alongside these dominant fans, the N180º-210º (29 counts), N01º-30º (25 counts) and N330º-359º (21 counts) are somewhat perceptible.

In addition to the frequency analyses above, the consideration of the length attribute and clustering of lineaments in zone C along the 8 main directions (table 6) yielded, by relevance:

- The NE-SW group of lineaments. Being the most represented in zone C with population percentage of 25.57% (112 counts), the length in this family varies between 0.56 km and 17.64 km (5.34 km average length) for a sum of 598.26 km. The predominance of this family is in accordance with analyses on other zones where it generally counts amongst the most populated families.
- The NW-SE family represents the second group (18.49 %) with 81 members. It is characterised by a mean length of 4.60 km, a cumulative length of 372.99 km distributed between features extended from 1.10 km and 14.64 km.
- The N-S family, with a total population of 75 (17.12% of total population), it represents the third group with faults lengths ranging between 0.70 km and 13.04 km making a sum of 272.85 km. Its mean length (3.64 km) is however the lowest of the south domain.
- The E-W family, represents the fourth group of lineaments with a population of 46 out of 438. This family has an average length of 3.95 km (the second lowest of the domain), with features extending from 1.20 km to 10.11 km for a cumulative sum of 181.65 km.
- The fifth group comprises the ENE-WSW and WNW-ESE families which make respectively 8.90 and 8.22 % of faults for respective cumulated length of 158.51 and 154.00 km. Their average lengths (4.06 and 4.28 km, respectively) show their elements are globally lengthy despite the lower ranking.
- The sixth group represents 6.85 % of the total population and corresponds to the NNW-SSE faults. The features in this family are particularly long (average length is 4.50 km) and the group records the longest measured fault of the domain (18.53 km); this may infer a sound geological relevance to the NNW-SSE family in zone C.
- The seventh group encompasses the NNE-SSW family which makes 4.34 % of the total population; its mean length (4.98 km) combined with its highest minimum length (1.90 km) of zone C assume its faults are amongst the longest. This infers that they are also significant, despite their small population compared to the other families.

Table 6 : Clustering of fractures in zone C along the 8 main geographical directions. The colours green, red and yellow denote the major, secondary and minor classes of lineaments, respectively

	N-S	NNE-SSW	NE-SW	ENE-WSW	E-W	WNW-ESE	NW-SE	NNW-SSE	ZONE C
Counts	75	19	112	39	46	36	81	30	**438**
Sum	272.85	94.72	598.26	158.51	181.65	154.00	372.99	135.12	**1968.01**
Max	13.04	12.38	17.64	16.64	10.11	15.62	14.54	18.53	**18.53**
Min	0.70	1.90	0.56	1.06	1.20	1.35	1.10	1.18	**0.56**
Aver	3.64	4.98	5.34	4.06	3.95	4.28	4.60	4.50	**4.42**
%	17.12	4.34	25.57	8.90	10.50	8.22	18.49	6.85	**100.00**
False Av.	3.45	4.23	5.18	3.61	3.70	3.80	4.41	3.84	**4.45**

b. Qualitative analysis

The qualitative analyses, following the principles established in the previous subsections enabled to assume the geological importance of the clustered families as colourly highlighted on **table 6**. The qualitative analysis revealed:

- The **major** or first order lineaments. These are families whose mean lengths are greater than the mean length of zone C (4.45 km) when influence of extreme features has been removed. This criterion favours the NE-SW and NW-SE families in zone C, according to their respective mean lengths (5.18 km and 4.41 km).
- The class of **secondary** lineaments includes the WNW-ESE, NNW-SSE and NNE-SSW families. Their respective false mean lengths (3.80 km, 3.84 km and 4.23 km) show they very important although they constitute the group of the less represented lineaments in the domain (lowest counts in table 6).
- Finally, the N-S, E-W and ENE-WSW form the **minor** or third order lineaments category albeit they are more populated than the families ranked as secondary lineaments. This is because they have the shortest lineaments false average albeit.

In brief, quantitatively, the zone C is affected by 438 lineaments whose cumulative length is 1968.01 km for a mean length of 4.42 km, assuming that globally theses lineaments have great linear extension. The azimuth distribution has revealed that the most represented features occur decreasingly, along the NW-SE, NE-SW, N-S, WNW-ESE, ENE-WSW and NNW-SSE directions; out ot which the NW-SE, NE-SW families revealed to corresponds to major lineaments while the WNW-ESE and NNW-SSE fall st secondary lineaments. The major lineaments are those who affect the deep subsurface and/or the basement and the proposed trends are consistend with the local geology.

3.3.3. Synthesis of the remote sensing survey

Globally, remote sensing made it possible to highlight various lineaments chiefly interpreted as faults or fractures (863). Theses lineaments make a cumulative length of 3843.90 km, a minimum of 0.56 km (in zone C) and a maximum of 21.73 km (in zone A) for an average length of 4.67 km. However, figures 3.3-1 and 3.3-2 show that those lineaments are irregularly distributed in the study area. Indeed, the study area has been subdivided into three zones, southward, zone B is the less populated, with only 22.34% % of the population of lineaments while zones A and C represent respectively 26.73% and 51.86%. Moreover, according to the mean length of the study area (4.67 km), the lineaments of zone A are longer (5.46 km) compared to those of the other zones (in zone B they are shortest, with 4.14 km mean length, while zone C exhibits 4.42 km average length). The geology of the study area could explain these differences.

Firstly, concerning the irregular distribution and density of the lineaments in the study, the differences percentages observed are linkable to the difference in lithology. Indeed, given some stress conditions, the rock materials react differently if their rheology differs. In line with that, the interpreted Landsat lineaments would portray an evolution from competent (zone A) to incompetent systems (zone C), north to south; these units being separated by a highly incompetent (zone B) environment. Therefore, these three zones would represent three different lithology groups. Particularly, the high density of fracturing in zone B is symptomatic to the fact that this zone is intermediary (transitional) and experienced a lot of stress, probably related to the compressions between zone A and zone C. Therefore, the study positions the zone C on the Congo Craton referred to as the Ntem Complex. In the same way, the zone A seems to be made up of very compact rocks, probably gneisses and micaschists. Then, high fracturing in zone B coupled with the small extend of fractures (mean length 4.14 km) suggests that the rocks therein are not very compact as those from other two zones – schists would be good soft rocks specimens here. The gneisses, micaschists and schists of the study area belong to the Yaounde group, hence zone A and zone B would belong to the NEFB. The limit between zone B and zone C would therefore represent the southern limit between the NEFB and the CC in the study area.

Apparently, the major lineaments from in the three outlined zones have different trends. Illustratively analyses revealed that in the zone A, they are NNW-SSE and NNE-SSW to ESE-WNW; in zone B, they are WNW-ESE and NNE-SSW to NE-SW, while they are NE-SW and NW-SE in zone C. Obviously, these zones have two by two, a common direction followed by these major lineaments; e.g. the common direction for zone A and zone B is NNE-SSW, whereas the NE-SW direction commonly appears in zone B and zone C. These major lineaments form

throughout the study area, a broad NE-SW network of en echelon faults which could constitute a pre-Panafrican major weakness zone affecting both the CC and the NEFB basement. This channel of faults would had formed during at least the Eburnean event at the northern margin of the CC, then the shallow features (corresponding to short faults) would reflect the syn- and post-panafrican events. The aforementioned channel of faults hence forms a NE strike-slips complex within which the displacements occur along WNW-ESE, NW-SE and WNW-ESE to NNW-SSE directions respectively in zone A, zone B and zone C. The variations in length and in directions displayed by the secondary and minor features may explain how this NE-SW channel turned from dextral to sinistral. In any case it is proposed that post-panafrican tectonics are responsible of the sinistral orientation observed. But, the existence the WNW-ESE to NNW-SSE major lineaments is a matter of debate.

The multiple of directions of the mapped major lineaments infer a polyphase deformation in the study area. Each stage of deformations is probably alternating compressions and extensions as suggested by the AMT and the aeromagnetic investigationsin previously sections.

3.4. DISCUSSION AND IMPLICATIONS

3.4.1. Discussions

3.4.1.1. Validity of the data, methodology and results

Poor data validity leads to inconsistent results. Basically, the consistency of AMT results lays on several factors: (1) the sensor (Stratagem EH4) uses a built-in algorithm based on the Bostick approach which permits to minimize the uncertainty on the resistivity value and allows the quality control of a good sounding by assuming that the apparent resistivity is inevitably positive. This quality control is assessed through the coherency among signals; herein, soundings with a good coherency have been recorded to obtain a good dataset to ensure reliable results. (2) Data were collected far away from human activity and infrastructure; and deep attention was paid to component impedances correlation and signals' correlation to reduce noise. Besides, either separately or concurrently, the aeromagnetic and the remote sensing methods are used worldwide in geological mapping, as shown by the literature (see chapter two). This entirely legitimates the use of these methods by this study. Whereas it is usual to combine methods over a same study area, the approach is somehow new as it juxtaposes two different methods on two different areas then, integrates a third one to bridge the obtained results.

3.4.1.2. Discussion of AMT results

The study area is north-bounded by latitude N04°, known as the mean geographical location of the CC/NEFB suture by previous geophysical studies (Tadjou et al., 2008; Ndougsa-Mbarga et al., 2010; Shandini et al., 2010; Basseka et al., 2011; references therein) expressed as an E-W major discontinuity. Hence the CC subducts from 50 to ~100 km beneath the NEFB, placing the study area in the transition zone between the NEFB and the CC. This is strengthened by resistivity models showing that the subsurface in the area is made up of mixtures of both Pan African (conductive) and CC (resistive) materials, in agreement with Meying et al. (2013) in a close area eastward (Ayos-Nguelemendouka). However, AMT analysis fails at detecting events coeval to the CC/NEFB limit (E-W faults) regarding the geoelectrical model defined by Tadjou et al. (2008), model in which the CC is a resistive block in the south and the NEFB is a conductive block to the north. The study has highlighted folding patterns within the Yaoundé-Nkolafamba subsurface. The folding system occurs along profiles strike i.e. they locally highlight NW-SE to N-S compressional movements of the crust's pieces. This result is consistent with some previous nearby AMT investigations (Ndougsa-Mbarga et al., 2010; Meying et al., 2013) which highlighted folding at the scale of the Yaoundé series. Amongst the major findings of the current study is the highlight of geoelectrical shallow discontinuities.

The AMT highlighted discontinuities have been interpreted as faults and fractures with directions spanning from SW-NE to WSW-ENE, in respect with the profiles azimuth (which is NW-SE). These faults may constitute shallow local expressions of the deep faults (along the same directions) evidenced both by Shandini et al. (2011) and Shandini and Tadjou (2012), using gravity method over a study area incorporating the current area (from nearly N02° to N05° latitudes and from E11° to 13° longitudes). The aforesaid NE-SW to ENE-WSW events form a NE trending structural lineament correlated to the NE secondary tectonic line highlighted by Meying et al. (2013) east of the study area, in the Abong-Mbang region, and linkable to the setup of the Central Cameroon Shear Zone (CCSZ) at a regional scale. The aforesaid NE tectonic lineament is assumed to be a strike-slip fault system. The statement is in agreement with early geoelectrical studies. Indeed, the MT study by Mbom-Abane (1997) proves the existence of E-W and NE-SW mainly oriented wrench fault sets: the first one extends as far as to the Abong-Mbang area, east of Ayos, and the second one runs parallel to the trend of the Trans-African strike-slips; the isoresistivity maps of the Akonolinga/Abong-Mbang area indicate E-W and NE-SW wrench faults (Njingti-Nfor et al., 2001).

In addition, the study images some uplifts and collapses of the basement in the Yaoundé-Nkolafamba area. Considering the highlighted faults that exhibit vertical to subvertical dips, we infer the subsurface topography as designed by grabens or basins and uplifts or horsts. Since sounding profiles are NW-SE oriented and according to their areal coverage, the basin and horst-likes subsurface structures are locally elongated in the SW-NE direction; in a broader way, gravity studies (Shandini et al., 2010, 2011; Basseka et al., 2011; Shandini and Tadjou, 2012) highlights same features in the same direction too and suggest they originate from the collapse of parts of the basement during the CC / NEFB collision. Also, a depth to surface conductive channel interpretable either as an intrusion or a signature of an active fault, has been highlighted. In the case of an intrusion, this result is in agreement at the local scale, with Basseka et al. (2011) who indicated the presence of granitic intrusions in the northern margin of the CC; in the case of faulting, this channel would infer horizontal movements corresponding to active wrenches or shears along the NE-SW direction, as seen by Basseka et al. (2011) despite the later did not interpret NE shears as an ongoing process. These NE shears would correspond to horizontal trans-current movements occurring in the Yaoundé series coeval to the CCSZ. While we suggest the NE tectonic lineament being correlated to the CCSZ represented nearby by the Sanaga Fault, the ongoing tectonic activity is consistent with the active seismicity along the Sanaga Fault (Ndougsa Mbarga et al., 2010).

3.4.1.3. Discussion of aeromagnetic results

The main faults orientations are WNW-ESE, W-E, NW-SE, SW-NE and WSW-ENE out of which two dominant clustered directions (SW-NE to WSW-ENE) and (WNW-ESE to NW-SE) have been outlined. These directions as well as the vertical to subvertical dips observed are consistent with those evidenced by several geophysical studies in the vicinities of the study area (Ndougsa-Mbarga et al., 2010, 2012; Basseka et al., 2011; Shandini et al., 2011; Feumoe et al., 2012; Akame et al., 2014, 2019; Assembe et al., 2016; Owona Angue et al., 2016). The calculated depth ranges locate these features in the brittle upper crust zone. This is in accordance with studies by Basseka et al. (2011) and Shandini et al. (2010, 2011) over a region that encompasses the study area. The current study emphasised a dominant WSW-ENE to SW-NE direction's fan which correlates well with the major direction outlined in the CC/NEFB transition zone and within the Ntem complex by several studies (e.g. Feumoe et al., 2012; Ndougsa-Mbarga et al., 2012; Akame et al., 2013, 2014; Assembe et al., 2016, 2019) south-east, north-east, north, east and within the investigated area.

The analyses show that the WSW-ENE to SW-NE family affects both the CC and the NEFB; this corresponds probably to pre-Neoproterozoic weakness zones which underwent

Neoproterozoic and post-Neoproterozoic reactivations and controlled deposition and metamorphism in the northern margin of the CC, in accordance with Nkoumbou et al. (2014). Specifically, the WSW-ENE fractures may correspond to a major sinistral strike-slip with conjugate sinistral WNW-ESE to NW-SE faults associated to E-W lateral wrenches due to NW-SE compressions, which affect both the CC and the NEFB domains, as shown by Ngako et al. (2003). The WSW-ENE strike-slips system hence corresponds to an extensional axis due to compressive movements (which are evidenced in geoelectrical sections) coeval to the setup of the Central Africa Rift System (Rolin, 1995) locally reprensented in Cameroon by the Centre Cameroon Shear Zone in a weakness zone set-up during the paleo- to meso-Proterozoic (Feybesse et al., 1998; Katumwehe et al., 2015). The results are particularly consistent with many geological and geophysical past or recent (Maurizot et al., 1986; Toteu et al., 1994; Tchameni, 1997; Tchameni et al., 2000; Shang et al., 2001, 2007; Lerouge et al., 2006; Olinga et al., 2010; Assembe et al., 2016, 2019; Yandjimain et al., 2017; Kankeu et al., 2017; Tchakounté Numbem et al., 2017) and on-going (Assembe et al., in preparation) studies carried out in southern Cameroon, as well as in other regions (e.g. Masterton et al., 2012; Fairhead et al., 2013; Heine et al., 2013; Kirkpatrick et al., 2013).

3.4.1.4. Cross-validation between audiomagnetotelluric, aeromagnetic and Landsat lineaments with faults and geological mapped faults

An internal cross-validation approach of the findings has been implemented by correlating methods two by two. In the northwest of the study area, it consists initially in comparing comparing AMT and Landsat 8 structures (**Figure 3.4-1**) then support these by field observations; Secondly, compare Landsat, magnetic and existing geological lineaments in the remaining sector (**Figure 3.4-2**).

a. Correlation of AMT faults with Landsat lineaments

Focusing on the northwestern portion of the study area, a map of lineaments both evidenced by the AMT and by remote sensing has been produced (**Figure 3.4-1**), in order to validate the results obtained in this sector. In addition to the enlightements from section 3.4.1.2, **figure 3.4-1** shows a strong correlation between the AMT and Landsat lineaments. The directions proposed by the AMT interpretation are due to the fact that structures are supposedly perpendicular to the traverses; but in the field, these directions are diverse as shown by the fractures observed on site in Loum 2 (Mfou), Nkolafamba, Nkometou, and Yaounde (see **table 5**) neighborhoods (Assembe et al., 2016). Both all AMT and Landsat lineaments may also have coincident directions (**Figure 3.4-1**); therefore, AMT and satellite lineaments totally correlate, hence the validation of the results in this study areas's portion.

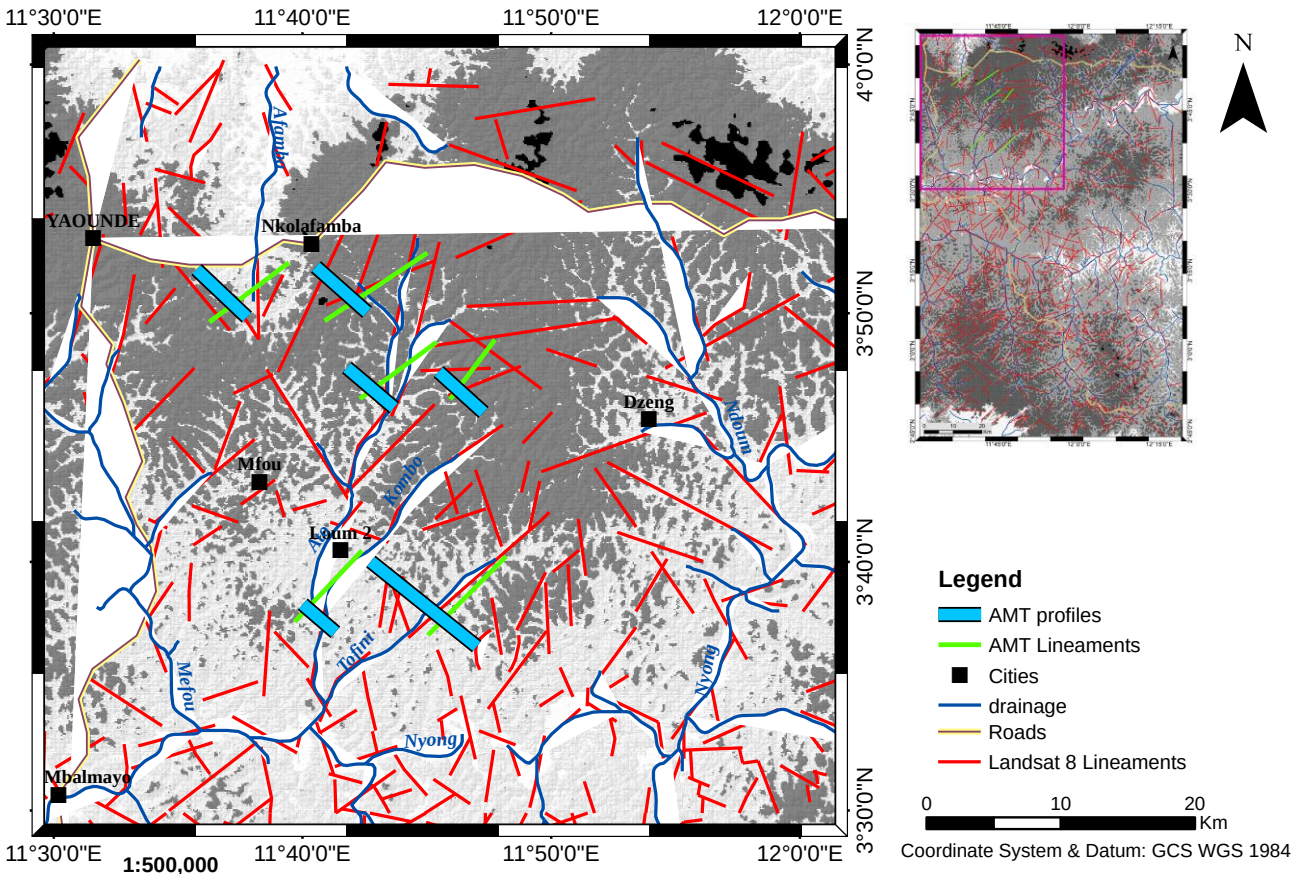

Figure 3.4-1 : Comparative map of AMT/CSAMT (green), OLI (red) lineaments with topography and drainage; the map shows the hydrography is structurally controlled.

b. Validation of aeromagnetic faults and Landsat 8 lineaments with existing faults

Due to the insufficiency of ground controls caused by the thick lateritic cover and the dense vegetation in the study area, the superimposition of magnetic onto Landsat-8 solutions helped to show the consistency of the lineaments detection in this study, as shown by the map in **Figure 3.4-2**. Therein, the almost perfect alignment of remotely sensed (red lines) and magnetic interpretation (black lines) lineaments within the portion covered simultaneously by both methods is evident. This proves the consistency of the approach used in one hand, and another, significantly validate the existence of the features highlighted by each method in the study area. Integrating the comments from the previous subsection (3.4.1.4a) cross-correlates and validate the AMT, magnetic and Landsat 8 faults. Extending this comparison to known geological structures in the region (Champetier de Ribes and Aubague, 1956; Maurizot et al., 1986) through the superimposition map of our results with previously mapped faults (**Figure 3.4-2**). **Figure 3.4-2** shows that faults from this study (black and red lines) correlate very well with faults from previously mapped by geological studies (green lines) in southern Cameroon (Champetier de Ribes and Aubague, 1956; Maurizot et al., 1986; Akame et al., 2014). The rosaceas (**Figure 3.4-**

3 (a) and **(b)**) show that the common dominant directions of the lineaments in the study area are NE-SW to ENE-WSW, NW-SE to WNW-ESE and N-S. These quantitatively correspond to

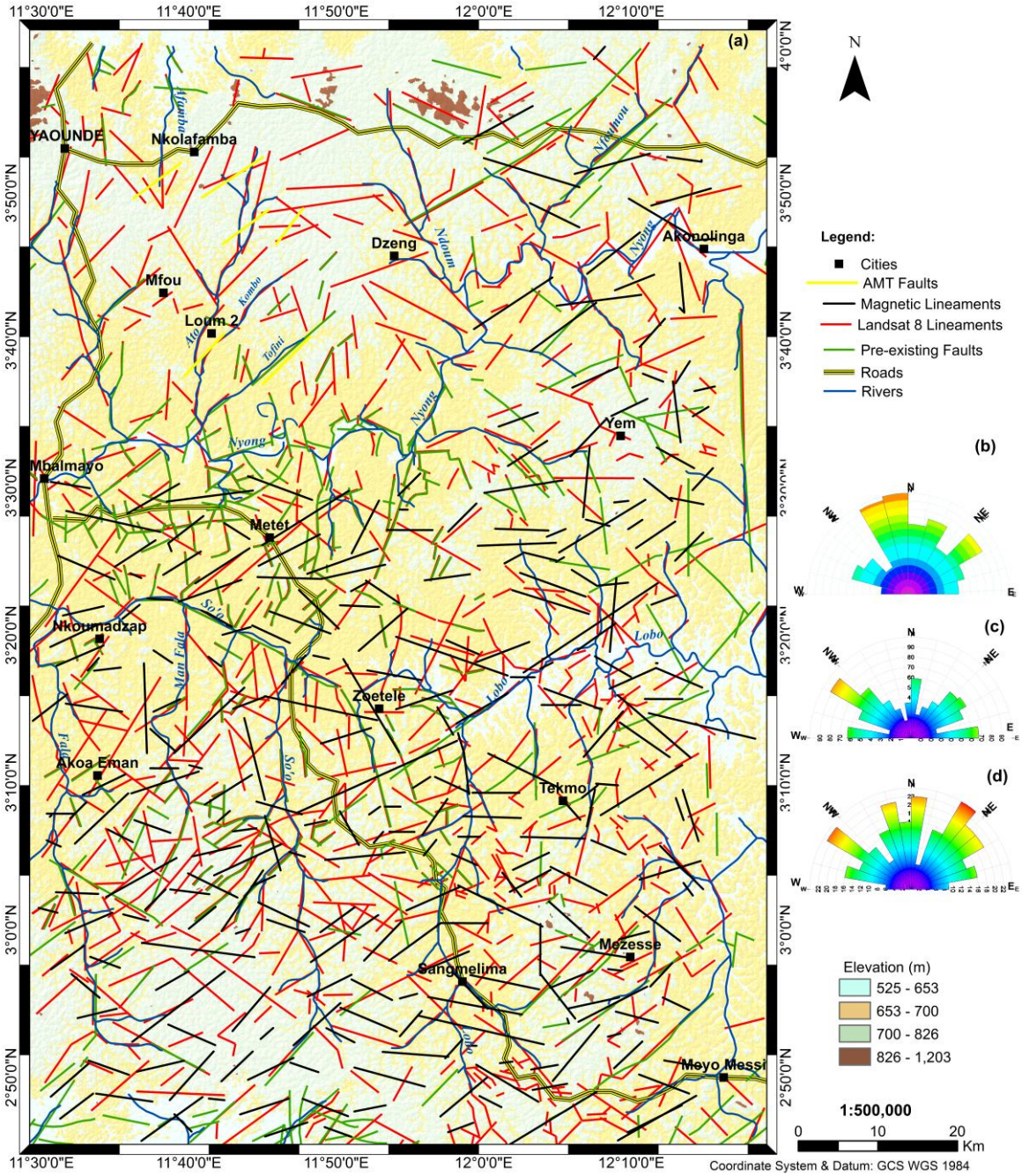

Figure 3.4-2 : Superposition of Landsat-8 (red), magnetic (black) and known (green) faults (Maurizot et al. 1986).

faults clusters N0-10 and N170, N30, N40-60, N70 and N110-140. However, the E-W direction (N80-100) is well represented in (b) and minor in (c). Similarly, the NNW-SSE direction clearly dominates in (c) whilst it seems minor in (b).

The above outlined directions from (b) and (c) are all present in the rosacea of the known lineaments (**Figure 3.4-2d**). Therein, the major trends by relevance are, NNW-SSE, N-S, NE-SW, NNE-SSW. The minor trends are ENE-WSW, WNW-ESE and E-W (poorly represented).

This proves the similar occurrence of the NNW-SSE, N-S, NNE-SSW, NW-SE, NE-SW, WNW-ESE, ENE-WSW and W-E directions. However, the NE-SW direction dominates with Landsat outputs (**Figure 3.4-3b**) contrarily to the major NNW-SSE to N-S trend shown by reference features (**Figure 3.4-3d**); maybe because of the difference in their populations. Nevertheless, the pertinent correlation amongst Landsat-8 and reference fractures validates the results.

3.4.1.5. Validation from field data

The findings from the AMT analysis are supported by some field observations from four sites where outcrops were accessible. The synthesis of the geometric parameters for 44 fractures and faults is given in table7. Among these fractures' families, the most interesting sets follow the NE-SW and ESE-WNW trends with vertical to subvertical dips. In agreement with the postulated vertical to subvertical dips from the current AMT investigation. Besides, many veins and families of fractures characterising the fourth deformation stage have been recorded. The NE-SW set correlates the faults highlighted by the AMT interpretation. The ESE-WNW family may represent faults nearly parallel to the AMT profiles. The folding and faulting underline the medium to high grade conditions experienced by the area that led to the amphibolite and the granulites facies characterized respectively, by amphibolite gneisses, and, biotite gneisses and biotite garnetiferous gneisses which are herein reported. The strength of tectonic forces occurred in the area has been recorded in the surrounding topography.

Table 7 : Attitudes of fault planes, veins and fractures recorded on the field

Structure ID	Strike and dip	Structure ID	Strike and dip	Structure ID	Strike and dip	Structure ID	Strike and dip
SITE : NKOLAFAMBA		SITE : NKOMETOU		SITE : NKOLBISSON (YAOUNDE)		SITE : LOUM 2 (MFOU)	
GEO1	N 178, 90	GEO16	WSW-ENE	GEO35	ESE-WNW	GEO29	SW-NE
GEO2	293, 75 SW	GEO17	WSW-ENE	GEO36	WSW-ENE	GEO30	SW-NE
GEO3	325, 76 SW	GEO18	SW-NE	GEO37	WSW-ENE	GEO31	E-W
GEO4	300, 70 SW	GEO19	SE-NW	GEO38	SW-NE	GEO32	WSW-ENE
GEO5	275, 90	GEO20	SE-NW	GEO39	SSE-NNW	GEO33	WSW-ENE
GEO6	209, 81 E	GEO21	ESE-WNW	GEO40	N-S	GEO34	N-S
GEO7	210, 90	GEO22	E-W	GEO41	E-W		
GEO8	263, 85 S	GEO23	N-S	GEO42	SE-NW		
GEO9	180, 90	GEO24	N-S	GEO43	ESE-WNW		
GEO10	345, 90	GEO25	SSW-NNE	GEO35	ESE-WNW		
GEO11	110, 69 SW	GEO26	E-W	GEO36	WSW-ENE		
GEO12	320, 90	GEO27	SW-NE	GEO37	WSW-ENE		
GEO13	206, 78 SE	GEO28	SSE-NNW				
GEO14	257, 85 S						
GEO15	185, 90						

The interpretation of AMT data suggests that profiles in Nkolafamba were settled on gneiss and eventually on quartzite. This fact is evidenced by the presence of gneiss formations outcrops (Photo 2c). These gneisses are of three types: clinopyroxene amphibolic gneiss, biotite

gneiss and garnetiferous biotite gneiss. The gneissic fabric presents a double boudinage (photo 2c) with E-W maximal stretch (B_1) and a N-S minimal stretch (B_2). In the Mfou area, field records confirmed that profiles were settled on migmatites (micaschists) and mica-quartzites (Photo 3); the migmatitic aspect being evidenced by the inclusion observed in the micaschist sample as shown on the photo below.

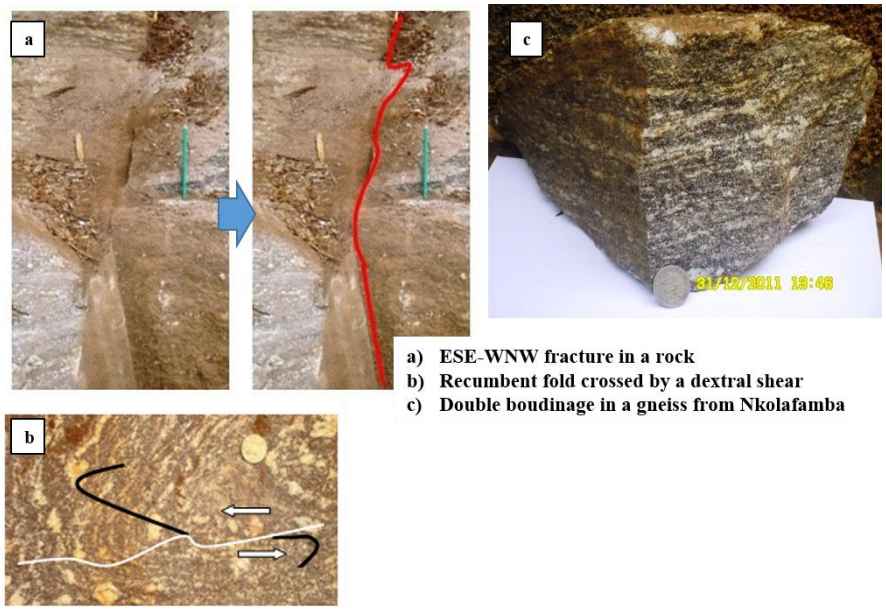

Photo 2 : Structural elements recorded in Nkolafamba (Assembe et al., 2016).

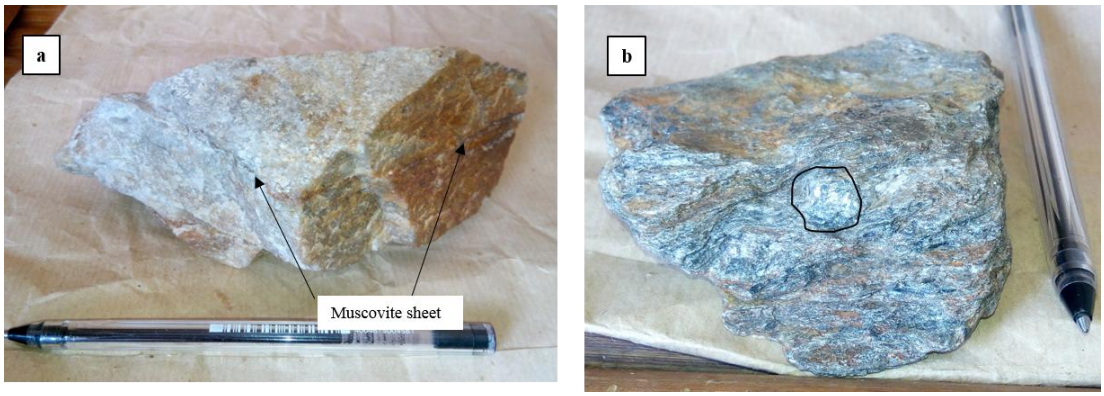

Photo 3 : Rock samples taken during field reconnaissance in Mfou. a) Quartzite with thin muscovite sheets; b) Micaschist sample with a rounded inclusion portrayed by the black circle.

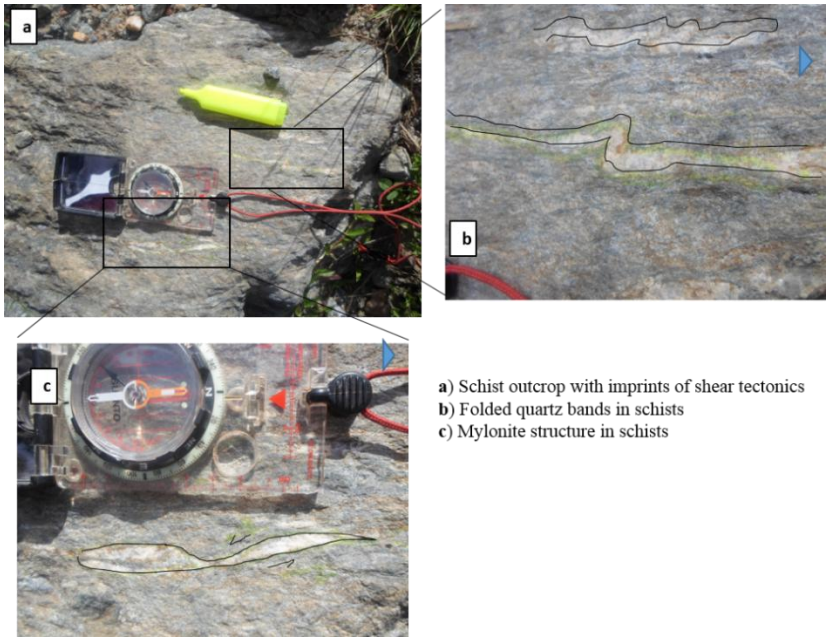

Photo 4 : Deformation elements evidenced from a schist outcrop in an abandoned quarry south of Mbalmayo.

The folding patterns, corresponding to another deformation stage, are also observed. These folds are cross-cut by many shears (Photo 2b). The double boudinage highlights extensive tectonics underlined by the NE-SW strike-slips as witnessed at the outcrop scale by shears (Photos 2 & 3) thus confirming that the area experienced many deformation stages.

3.4.2. Geologic and mining implications

3.4.2.1. Implication on the faulting kinematics

Many faults have been highlighted by the current study but a focus was not given to kinematic relationship. However, because of the difference, in nature, of the two highlighted geological sets (NEFB and CC), it is possible to portray a simple timing scheme. We base our point on the juvenile ages of NEFB formations compared to the Ntem complex. This enables to state that faulting in the Yaounde series are younger than in the Ntem complex (although some fractures and faults may be of same ages, especially those involved in the actual rifting). This is particularly in correlation with the structural control of the sedimentation in the Yaounde basin (Assembe et al., in preparation). Indeed, Assembe et al (2016) evidences various faults in the Yaounde series limiting some uplifts and sags supposedly related to extensional movements. The assumed active state of faults from the Yaounde series supports their post-collisional age.

As for the CC part, the faults correlate those from other recent geophysical studies (Shandini et al., 2010; Basseka et al., 2011; Feumoe et al., 2012; Ndougsa-Mbarga et al., 2012; Owona Angue et al., 2016). Basseka et al. (2011), Shandini et al. (2011) and Shandini and Tadjou (2012) interpreted some of the faults in the northern margin of the CC as basement collapse guides below the NEFB, confirming that faults in the CC may be older whilst they could

have been reactivated. With no references with ages and origins, considering the set-up of the Yaounde basin at the northern margin of the CC (Yonta Ngoune, 2010), it can be advanced that:

(i) The faulting history at the northern margin of the CC: oldest generation linked to the pre- and syn-Eburnean orogeny; the second generation probably related to extensional movements related to the evolvement of the Yaounde rift or basin; third generation related to the Neoproterozoic collision and reactivation during the breakup of Gondwana and the Atlantic Ocean's opening.

(ii) In the NEFB domain the faulting history is associated with the Neoproterozoic collision (West African Craton/Congo continent); and reactivations during the breakup of west Gondwana and the Atlantic Ocean's opening; then, probably the ongoing development rifting in East Africa (Fairhead et al., 2013; Heine et al., 2013; Pérez-Díaz and Eagles, 2014; Assembe et al., 2016, 2019; Akame et al., 2019; Assembe et al., in preparation).

Brittle structures in the study area are imprints of intense multistage tectonic activity characterised by alternating broad NW-SE and SW-NE compressions respectively implying SW-NE and NW-SE extensions. The extensions are witnessed by sinistral and dextral SW-NE to W-E and NW-SE to N-S shears movements (**Figure 3.2-7)** forming a major SW-NE sinistral strike-slips system affecting the area. The vertical-subvertical plunge of faults shows they controlled vertical (and horizontal) movements of the basement related to trans-transpressions in the African plate, the Ntem complex and the study area, decreasingly from regional to local scale. Thus, it seems opportune to state that the study area denotes a good continental strike-slips play. The following timing is proposed for the faulting activity in the area (Assembe et al., 2019).

1)- NE-SW faulting due to NW-SE compressions in the Paleo to Meso-Proterozoic;

2) then, the setup of N-S faults and the broad W-E fault (leading to the CC/NEFB limit), due to the detachment of the Adamawa block at the northern margin of the CC;

3) NW-SE faulting and post reactivation of NE-SW faults in response to syn- and post-Panafrican N-S to NE-SW compressions and NE-SW to ENE-WSW extensions.

The post-Panafrican events are particularly interesingt as the central domain of the African Plate has been exposed to the stress regimes related to the Atlantic Ocean opening and the actual individualisation of the Somalia Plate which questions neotectonics in the area (Assembe et al., in preparation).

3.4.2.2. Implication on the geodynamic context and evolution

The northern margin of the CC experienced many collisions and extensions related to the amalgamation from its nuclei, the formation of the Congo Continent (Sahara/CC suture, NE of the CC), the Neoproterozoic suture with the West African Craton and the breakup of Gondwana, respectively. These mainly correspond to two Precambrian deformation stages which are overprinted by Phanerozoic. The study highlightes a NE-SW strike-slip line probably associated to wrenches that affect both the NEFB and the CC; the orientations accommodate the CCSZ in the NEFB domain and the Precambriam orogenies in the CC (Assembe et al., 2016, 2019; Akame et al., 2019). The wrenches in the NEFB are normal events as mobile belts constitute weakness zones in the earth's crust (Kearey et al., 2009). Particularly, the WCARS and its local member, the CCSZ accommodate the intra-plate stress/strain regimes related to the actual deformation of the African plate (Ndougsa Mbarga et al., 2010; Weckmann, 2012; Heine et al., 2013; Kirkpatrick et al., 2013; Assembe et al., 2019).

The more questioning aspect concerns the wrenches highlighted within the Ntem complex. One possible answer could be the metacratonisation of the northern margin of the CC as described by Liégeois et al. (2013) and Abdelsalam et al. (2002) and supported by Goussi et al. (2017) who confirmed the metacratonisation of the Adamawa-Yade domain and the northern edge of the CC. But this shows the craton's margin was fit to panafrican deformation, not the mechanisms. This matter still requires the integration of diversified sources of data and limit our capabilities to propose a geodynamic model. However, further attempt to define a faulting history suggested extensional movements related to the setup of a basin in the northern margin of the CC, in accordance with Nkoumbou et al. (2014) and Tchakounté et al. (2017) who suggested that the Yaounde basin resulted from extensional processes at the north of the Congo Craton, which led to rifting, fragmentation and limited oceanisation in a Panafrican pre-collisional context. By assuming the Adamawa-Yade block equivalent to a micro-continent detached from the CC in the early Neoproterozoic. Recent studies (Nkoumbou et al., 2014; Tchakounté et al., 2017) validate geophysical interpretation of some faults beneath the NEFB as well as fragmentation and collapses of the underlying basement, probably the CC (Assembe et al., 2019 and 2016). This correlates results of Yonta Ngoune (2010), as well as the geodynamic evolution of the Ntem complex by Goussi et al. (2017).

3.4.2.3. Implications on mineral exploration

The current study highlighted many lineaments which show a good match with the drainage system. This correlation of the fractures with the drainage system open the way to groundwater flows and may infer high recharge capability of groundwater reservoirs in the study area as seen by Teikeu et al. (2016) who identified aquifers in the vicinity of Yaounde recharged by a network of faults and fractures affecting the Panafrican crystalline basement. This work generalises this result to the Yaounde-Sangmelima region (**Figure 3.4-4**).

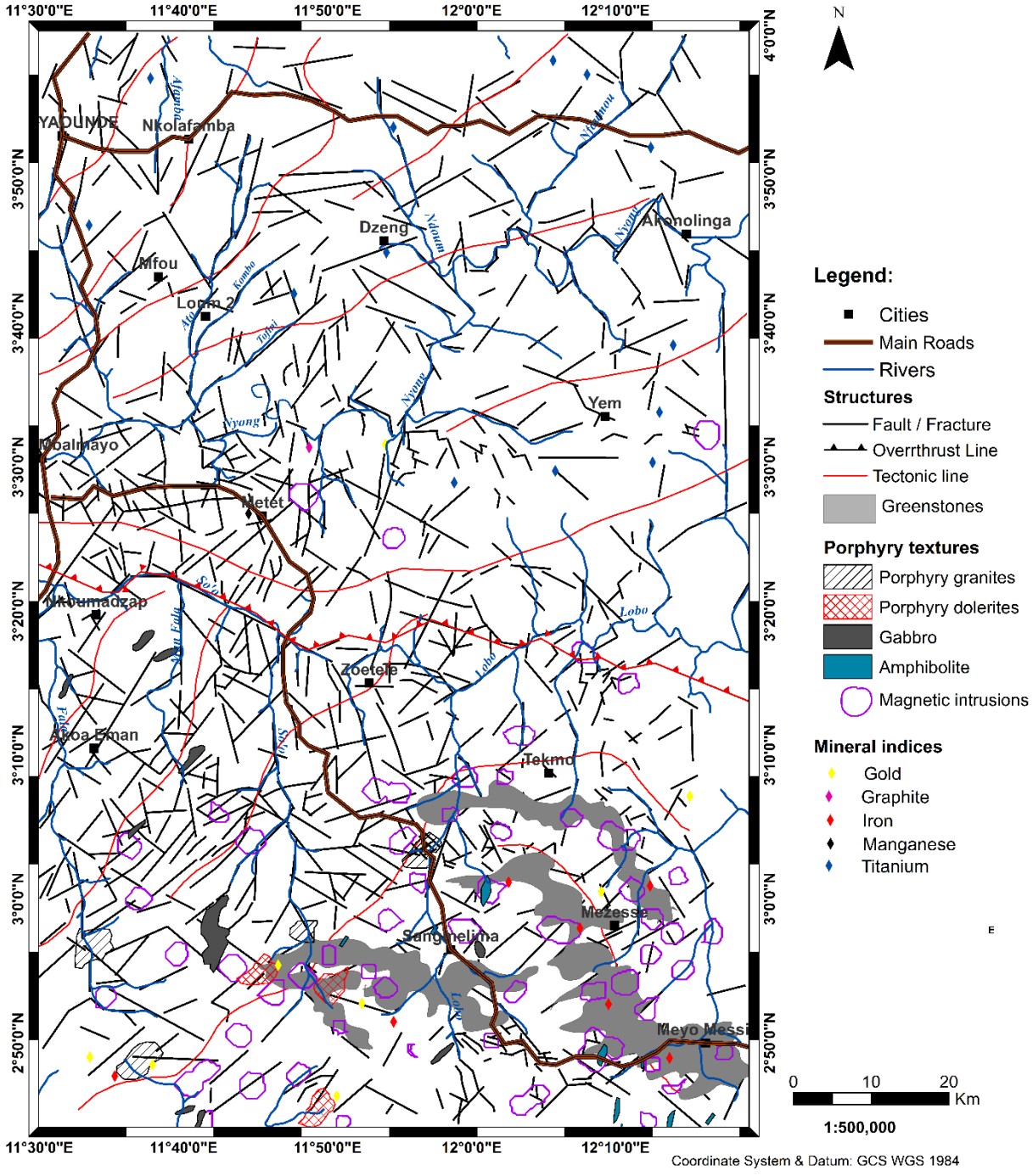

Figure 3.4-3 : Correlation between the drainage, faulting and mineral indices. The map reveals the proximity between faults and mapped intrusions and porphyry textures.

Besides, various strongly magnetic intrusions have been mapped, mostly in the Ntem complex, within the highlighted NE deformation channel affecting study area; their density prove hydrothermal processes in the Ntem complex (Assembe et al., 2020). These mafic to ultramafic intrusions are sometimes parallel, cut or squeezed by faults and fractures or lie at their junctions. Since these lineaments affect the basement, obviously they controlled fluid flows (water and magmatic melts) and later the distribution of anomalies. The ultramafic character associated to intrusions and the TTG natures (Shang et al., 2001, 2004a, 2010; Li et al., 2016) of Archaean terranes make them good to host economical mineralization (Faure, 2007; Mathieu, 2013). Indeed, the high magnetisation of the intrusions suggests that they are rich in oxide minerals generally associated to metals. Also, granodiorite TTG occur in the study area. Their Anorthosite-Mangerite-Charnokite-Granite type magma origin and, both the collisional and extensional intracratonic setting of the study area (Cawood and Hawkesworth, n.d.) could favour occurrence of IOCG, Ni and/or PGE deposits (Mathieu, 2013; Aye et al., 2017). Titanium, manganese, graphite and gold indices were recorded in the Yaounde Group (Champetier de Ribes and Aubague, 1956; Regnoult, 1986). Analyses locate these indices at the junction of fractures within schists and ectinites, along an E-W line, subparallel to the major second order shear zone and the CC/NEFB boundary. Manganese and graphite indices are located at the greenschist/garnetiferous micaschist contacts in Metet while gold and titanium are respectively in greenschist and garnetiferous micaschists. In the Ntem complex, iron and gold are the main minerals. Iron is closely linked to the greenstones belts SE of Sangmelima, where some advanced mineral exploration projects await to enter in the development stage (e.g. Nkout Iron project by Affero Mining). The outline of additional greenstones and the small gold mining artisanal workings carried out all around Sangmelima suggest that mineral exploration should be revamped in this region.

Conclusion

Investigating the NEFB/Congo Craton transition zone remains a great challenge for the geoscience community. The current study, by applying tensor-audiomagnetotellurics and aeromagnetics in two adjacent portions of the CC/NEFB transition zone has improved the geological map of southern Cameroon. The findings show both that the CC and the NEFB were affected by collisional and post-collisional deformations, related to the Gondwana breakup. Further, the highly deformed looks of the Ntem complex shows that the CC underwent various tectonic/tectono-thermal episodes; the resultant structures controlled the deposition of sediment in the Yaounde basin, influenced the Panafrican event in Central Africa and the Phanerozoic rifting that led to the Atlantic Ocean's opening and actual intra-plate stress accommodation.

GENERAL CONCLUSION AND PERSPECTIVES

1. Conclusions

Three geophysical techniques including the tensor AMT, aeromagnetic and remote sensing methods have been used to investigate nearly 12,000 km^2 in the Nkolafamba-Sangmelima area of southern Cameroon, a portion of the Central Africa Fold Belt and the Congo Craton transition zone.

1.1.Recall of the objectives and research methodology

The main research objectives are, scientific, economic and operational.

(1) The scientific objective was to contribute into the improvement of the of the geological evolution of the northern margin of the Congo Craton; the specific objective being to bring out evidences that may support the collisional model between the Panafrican belt and the Congo Craton in southern Cameroon, and ameliorate the geological information in the targeted area.
(2) The economic objective was to map new probable ore deposit features that would improve the mineral potential of the region.
(3) The operational objective was to come out with a new methodology that can enable the study of an area irregularly covered by different geophysical methods; particularly as the current study area primarily involves two adjacent zones covered by AMT and aeromagnetics.

The methodology conceived for the study consisted in respectively, firstly carrying a tensor AMT and field geology investigation (when possible) in some portions of the study area, secondly using aeromagnetics onto the uncovered portions, then overlapping the whole area by the remote sensing method (involving Landsat 8-OLI data). Cross-correlations amongst the methods, and, with existing information validate the results of the study. This methodology is proposed to overcome the scarcity of geophysical data.

1.2.Results and validations

1.2.1. Validation

The study enabled to confirm that the area has been affected by an intense tectonic activity that pertained throughout various tectonic deformation stages. Indeed:

- The interpretation of the AMT highlighted a network of hidden NE-SW strike-slip faults coeval to the CCSZ; geoelectrical sections shew graben-like topography due to basement collapses and uplifts with upward transport of deep resistive materials to

shallow depths, suggesting extensive or compressive tectonics in the Pan African Yaoundé series.

- The magnetic investigation revealed that the northern margin of the CC has been highly fractured as witnessed by the imaged vertical to subvertical faults that corroborate the vertical movements from the AMT study. These vertical to subvertical faults are mainly oriented NNW-SSE, N-S, NE-SW, NNE-SSW and E-W; and some of these form a major E-W fracture line corresponding to the CC/Panafrican southern limit located around latitude N03º20' in the area. Besides, the magnetic interpretation highlighted NE-SW and NW-SE compressions and extensions witnessed by dykes and other intrusive occurrences in some parts of the south zone suggesting that the TTGs of the Ntem complex experienced hydrothermal events.
- Both the AMT and aeromagnetic imaging highlighted folds that affected near subsurface formations both in the Panafrican and the CC domains; these folds are assumed to have been caused by the CC/Panafrican orogeny in the northern zone whereas they are assumed to be related to Archaean and/or Paleo to Mesoproterozoic orogeneses with some possible Panafrican overprints in the southern zone.
- The exploitation of Landsat 8 data highlighted many fractures which enabled to outline three differently fractured domains identified as Yaounde series, the Mbalmayo schists and the Ntem complex. This interpretation confirmed the NNW-SSE, N-S, NE-SW, NNE-SSW and E-W orientation of faulting in the whole study area but also suspects WNW-ESE sinistral movements at the northern margin of the CC.

1.2.2. Integration

The study revealed that both the NEFB and the CC are folded and affected by faults whose main directions are NNW-SSE, N-S, NE-SW, NNE-SSW (in the CC) and NE-SW to ENE-WSW and NNE-SSW (in the NEFB), though field data found the same trends represented in the CC. Folds highlighted in the NEFB testify for the CC/NEFB Neoproterozoic collision, whereas those in the CC may not, because of the difference in their respective ages. The folds in the CC are likely to be due to pre-Neoproterozoic orogeneses. The same conclusions abide for fractures (and/or faults). However, NNE-SSW to ENE-WSW fractures are related to pre-, syn, to post-PanAfrican events (transtensions and transpressions), reactivated with the ignition of the Gondwana split and alimented by the ongoing motion of the African plate toward Eurasia and the formation of the Somalia plate as well. The study defines a major NE trending weakness zone coeval to the CCSZ (linkable to the general NE-SW lineaments system consistent with the WCARS) that affects both the NEFB and the CC. The area is a major transpressive zone made

up of faults which control the vertical movements illustrated by basement collapses. Their setup is a typical example of intra-plate wrenches in a continental-continental convergence setting. The geophysical results are two by two cross-validated and they correlate both with field data and previous geosciences studies in the northern margin of the CC.

1.2.3. Summary on the structural analyses

The study revealed sets of subvertical to vertical lineaments that affected the subsurface of the study area. These structures testify that various compressional and extensional episodes affected both the study area and the entire northern margin of the CC (e.g. the CCSZ), as supported by the inferred basement uplifts and sags in Yaounde-Zoetele. Globally, the highlighted brittle features can be gathered within three (03) NE-SW, NNW-SSE and NW-SW lineaments families for an easier summary. Summarily, the structural analysis shows that (1) conspicuous NE-SW, NNW-SSE and NW-SW major lineaments (probably shear zones); and (2) tectonically related joints and/ or fault systems affect the area. The relative ages of these structures can be inferred from the cross-cutting relationships among them. Indeed, from the quick observation of the map (**Figure 0.1**), these relationships assume that the NE-SW trending shear zone was firstly emplaced, then was follow by, or was concurrent with the WNW-ESE trend. The dominant NE-SW shear movements seems to have been dextral (first order) though there have been several multi-directional episodes. This shear zone was then displaced by the NW-SE sinistral fault system (second order). The shear zones are elements of a regional shear zone characterising wrenches coeval to the CCSZ at the local scale, therefore they are assumed to be coeval to the WCARS at the regional scale. Thus, this fault system would illustrate a continental transpressive strike-slip system. An updated map of the region is given below (**Figure 0.1**).

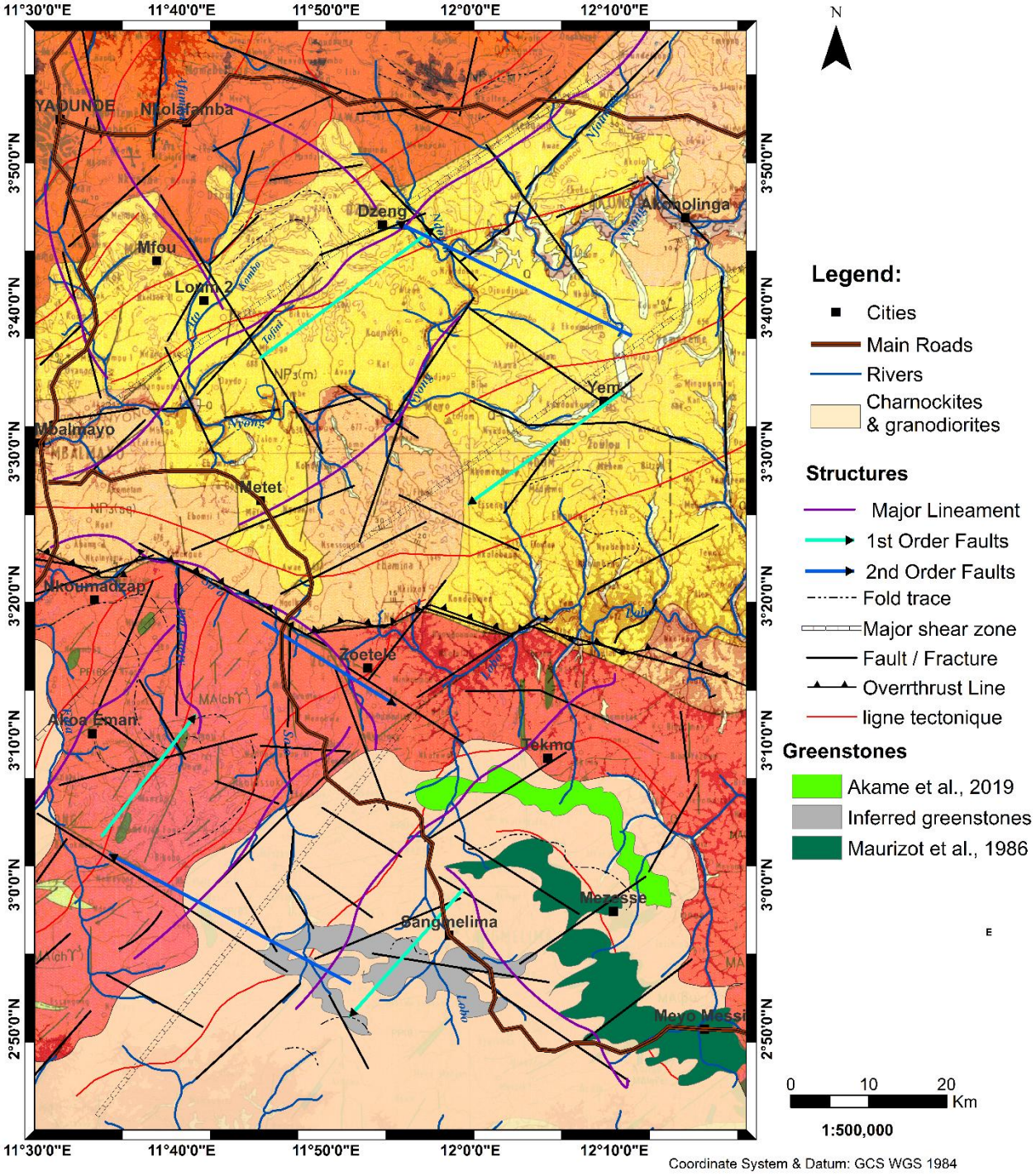

Figure 0-1 : Tectonic sketch of the Nkolafamba-Sangmelima area

2. Future trends

Despite the results from this study, explaining the geological evolution at the northern margin of the CC remains a great challenge. Therefore, additional work would help to define a better geodynamic model that emplaces the NEFB and the CC in the supercontinent-scale and outlines favourable environments for mineral resources. This needs local to regional scale integration of various geoscience data to both, produce enhanced models of the geological

history of Cameroon (and Central Africa); and improve the mineral resources valuation. So, researches ahead may consider data integration that brings together high resolution magnetic, gravity, magnetotelluric, remote sensing, drillhole and geochemical information. Particularly, future works may:

(i) Design and implement a joint inversion scheme of magnetic, gravity and magnetotelluric data.

(ii) Design an automated workflow for generating geologic models to constrain geophysical inversions.

(iii) Use high resolution multispectral remote sensing data to highlight mineral indices.

(iv) Improve the magnetic and gravity inversions by using radiogenic isotopes for both age constraints and petrogenetic understanding of the igneous rocks of the study area, with a focus on the ultramafic / intermediate rocks relationship.

(v) Investigate the regional geodynamic evolution by measuring the displacement and radon activity along the known and highlighted faults from the area; and assessing the thermal regime pertaining to the northen margin of the Congo Craton

If realised, these tasks will probably bring new perspectives to the geology of Central Africa in general, and Cameroon in particular.

REFERENCES

Abdelsalam, M.G., Liegeois, J., Stern, R.J., 2002. The Saharan Metacraton. *Journal of African Earth Sciences* **34**, 119–136.

Akame, J.M., Assembe, S.P., Zo'o Zame, P., Owona, S., Ndougsa-Mbarga, T., Azia, G.A., Mvondo-Ondoa, J., 2019. The Sangmelima granite-greenstone belts (South Cameroon): Integration of remote sensing and aeromagnetic data for structural interpretation. *The Egyptian Journal of Remote Sensing and Space Sciences* **22**, 37–47. https://doi.org/10.1016/j.ejrs.2018.11.005

Akame, J.M., Mvondo Ondoa, J., Olinga, J.B., Essono, J., Mbih, P.K., 2013. Utilisation des modèles numériques de terrain (MNT) SRTM pour la cartographie des linéaments structuraux : Application à l'Archéen de Mezesse à l'est de Sangmélima. *Geo-Eco-Trop.* **37**, 71–80.

Akame, J.M., Mvondo Ondoa, J., Teikeu Assatse, W., Owona, S., Olinga, J.B., 2014. Apport des images landsat-7 ETM+ a l'etude structurale du socle archeen de sangmelima (SUD CAMEROUN). *Revue Francaise de Photogrammetrie et de Teledetection* **206**, 15–26.

Anderson, E.D., Hitzman, M.W., Monecke, T., Bedrosian, P.A., Shah, A.K., Kelley, K.D., 2013. Geological analysis of aeromagnetic data from southwestern Alaska: Implications for exploration in the area of the Pebble Porphyry Cu-Au-Mo deposit. *Economic Geology* **108**, 421–436.

Archibald, N., Gow, P., Boschetti, F., 1999. Multiscale edge analysis of potential field data. *Exploration Geophysics* **30**, 38–44.

Assembe, S.P., Meying, A., Ndougsa-Mbarga, T., 2016. New structural facts from audio-magnetotelluric (AMT) data interpretation in the Yaoundé-Nkolafamba area (Centre Cameroon). *Journal of Indian. Geophysical. Union* **20**, 19–32.

Assembe, S.P., Ndougsa-Mbarga, T., Meying, A., Gouet, D.H., Ngoh, J.D., Mono, J.A., 2019. Contribution of Geophysics to the Understanding of the Geodynamic Activity at the Northern Margin of the Congo Craton : A Case Study from Aeromagnetic Data Interpretation Over the Metet-Zoetele Region (Southern Cameroon). *European Journal of Scientific Research* **152**, 286–303.

Assembe, S.P., Ndougsa-Mbarga, T., Enyegue A Nyam, F.M., Ngoumou, P.C., Meying, A., Gouet, D.H., Zanga Amougou, A., Ngoh, J.D., 2020. + − Evidence of Porphyry Deposits in the Ntem Complex: A Case Study from Structural and Hydrothermal Alteration Zones Mapping through Landsat-8 OLI, Aeromagnetic and Geological Data Integration in the Yaounde-Sangmelima Region (Southern Cameroon). *Advances in Remote Sensing* **9**, 53–84. https://doi.org/10.4236/ars.2020.92004

Aye, B.A., Sababa, E., Ndjigui, P., 2017. Geochemistry of S , Cu , Ni , Cr and Au-PGE in the garnet amphibolites from the Akom II area in the Archaean Congo Craton , Southern Cameroon. *Chemie Der Erde - Geochemistry* **77**, 81–93. https://doi.org/10.1016/j.chemer.2017.01.009

Bahr, K., 1988. Interpretadon of the magnetotelluric impedance tensor: regional induction and local telluric distortion. *Journal of Geophysics* **62**, 119–127.

Bailey, C., Groom, R.W., 1987. A decomposition of the magnetotelluric impedance tensor which is useful in the presence of channeling. *Geophysics* 154–156.

Baranov, V.., Naudy, H.., 1964. Numerical calculation of the formula of reduction to the

magnetic pole. *Geophysics* **29**, 67–79.

Basseka, C.A., Shandini, Y.N., Tadjou, J.M., 2011. Subsurface structural mapping using gravity data of the northern edge of the Congo craton , South Cameroon. *Geofizika* **28**, 229–245.

Bessoles, B., Lasserre, M., 1977. Le complexe de base du Cameroun. *Bull. Soc. Geol. France* **7**, 1085–1092.

Blakely, J., Simpson, R.W., 1986. Short Note Approximating edges of source bodies from magnetic or gravity anomalies. *Geophysics* **51**, 1494–1498.

Blakely, R.J., 1996. Potential theory in gravity and magnetic applications. Cambridge university press. https://doi.org/10.1017/CBO9780511549816

Boehl, J.E., Bostick, F.X., Smith, H.W., 1977. An application of the hilbert transform to the magnetotell uric method. Electrical Geophysics Research Laboratory.

Bostick, F.X.J., 1977. A simple almost exact method of MT analysis. Workshop on Electri-Cal Methods in Geothermal Exploration. Snowbird, Utah, 174–183.

Boyd, D.M., Isles, D.J., 2007. Geological Interpretation of Airborne Magnetic Surveys - 40 Years On. *In: Milkereit, B. (Ed.), Proceedings of Exploration 07: Fifth Decennial International Conference on Mineral Exploration*. 491–505.

Briggs, I.C., 1974. Machine contouring using minimum curvature. *Geophysics* **39**, 39–48. https://doi.org/10.1130/GSAT01607.1

Brodie, R.C., 2002. Airborne and magnetics. Geophysical and Remote Sensing Methods for Regolith Exploration, *CRCLEME Open File Report* **1**. 33–45.

Caby, R., Boesse, J.M., 2001. Pan-African nappe system in southwest Nigeria: The Ife- Ilesha schist belt. *Journal of African Earth Sciences* **23**, 211–225. https://doi.org/10.1130/GSAT01607.1

Cagniard, L., 1953. Basic theory of the magneto-telluric method of geophysical prospecting. 605–635.

Caldwell, T.G., Bibby, H.M., Brown, C., 2004. The magnetotelluric phase tensor. *Geophysical Journal International* **158**, 457–469. https://doi.org/10.1111/j.1365-246X.2004.02281.x

Campbell, W.C., 1997. Introduction to geomagnetic fields. Cambridge University Press. https://doi.org/10.1130/GSAT01607.1

Canfield, D.E., Poulton, S.W., Narbonne, G.M., 2007. Late-Neoproterozoic deep-ocean oxygenation and the rise of animal life. *Science* **315**, 92–95.

Cawood, P.A., Hawkesworth, C.J., n.d. Temporal relations between mineral deposits and global tectonic cycles : implications for prospectivity.

Cawood, Peter A., Kröner, A., Pisarevsky, S.A., 2006. Precambrian plate tectonics: Criteria and evidence. *GSA Today* **16**, 4–11.

Cawood, P.A., McCausland, P.J.A., Dunning, G.R., 2001. Opening Iapetus: constraints from the Laurentian margin in Newfoundland. *Geological Society of America Bulletin* **113**, 443–453.

Cawood, P.A., Nemchin, A.A., Strachan, R.A., Prave, T., Krabbendam, M., 2007. Sedimentary basin and detrital zircon record along East Laurentia and Baltica during the assembly and breakup of Rodinia. J*ournal of the Geological Society, London*, **164**, 257–275.

Cawood, P.A., Strachan, R.A., Pisarevsky, S.A., Gladkochub, D.P., Murphy, J.B., 2016. Linking collisional and accretionary orogens during Rodinia assembly and breakup: Implications for models of supercontinent cycles. *Earth and Planetary Science Letters* **449**, 118–126.

https://doi.org/10.1016/j.epsl.2016.05.049

Champetier de Ribes, G., Aubague, M., 1956. Carte geologique de reconnaissance a l'echelle 1/500000. Notice explicative sur la feuille Yaounde-Est, 40p.

Chatterjee, S., Scotese, C.R., 1999. The breakup of Gondwana and the evolution and biogeography of the Indian plate. *Pinsa* **65**, 397–425.

Chave, A.D., Jones, A.G., Mackie, R., Rodi, W., 2012. The Magnetotelluric Method. Cambridge University Press, Cambridge. https://doi.org/10.1017/CBO9781139020138

Clark, D.A., Emerson, D.W., 1991. Notes on rock magnetisation characteristics in applied geophysical studies. *Exploration Geophysics* **22**, 547–555.

Cocks, L.R.M., Torsvik, T.H., 2002. Earth geography from 500 to 400 million years ago: a faunal and palaeomagnetic review. *Journal of the Geological Society, London* **159**, 631–644.

Collignon, F., 1968. Gravimétrie de reconnaissance de la République Fédérale du Cameroun, Orstom. Paris.

Crippen, R.E., Blom, R.G., 2011. Unveiling the lithology of vegetated terrains in remotely sensed imagery. *Photogrammetric Engineering and Remote Sensing* **67**, 935–943.

Dalziel, I. W. D., 1997. Neoproterozoic–Palaeozoic geography and tectonics: Review, hypothesis and environmental speculation. *Geological Society of America Bulletin* **109**, 16–42. https://doi.org/10.1144/SP294.20

de Wit, M.J., Stankiewicz, J., Reeves, C., 2008. Restoring Pan-African-Brasiliano connections: more Gondwana control, less Trans-Atlantic corruption. *Geological Society, London, Special Publications* **294**, 399–412. https://doi.org/10.1144/SP294.20

Dirks, P.H.G.M., Bleinkinsop, T.G., Hielke, A.J., 2008. The geological evolution of Africa., *Encyclopedia of Life Support Systems*.

Dmitriev, V.I., Berdichevsky, M.N., 1979. The Fundamental Model of Magnetotelluric Sounding. *Proceedings of the IEEE*. 1034–1044.

Drury, S., 2001. Image Interpretation in Geology. Blackwell Science, 290p.

Ennih, N., Liégeois, J.P., 2008. The boundaries of the West African Craton, with a special reference to the basement of the Moroccan metacratonic Anti-Atlas belt. *Geological Society, London, Special Publications* **297**, 1–17.

Fairhead, J.D., 2009. The Mesozoic West and Central African Rift System : Qualitative Evaluation. Adapted from Oral Presentation at AAPG International Conference and Exhibition, 2008. Cape Town, 22p.

Fairhead, J.D., Cooper, G.R.J., Sander, S., 2017. Advances in Airborne Gravity and Magnetics. In: *Tschirhart, V., Thomas, M.D. (Eds.), Proceedings of Exploration 17: Sixth Decennial International Conference on Mineral Exploration*". 113–127.

Fairhead, J.D., Green, C.M., Masterton, S.M., Guiraud, R., 2013. The role that plate tectonics, inferred stress changes and stratigraphic unconformities have on the evolution of the West and Central African Rift System and the Atlantic continental margins. *Tectonophysics* **594**, 118–127. https://doi.org/10.1016/j.tecto.2013.03.021

Faure, S., 2007. Forecasting tools for mineral exploration in high grade metamorphic terrains : The Grenville parautochthonous belt, a high-potential zone.

Fernandez-Alonso, M., Tack, L., Tahon, A., De Waele, B., 2010. The Proterozoic history of the proto-Congo Craton of Central Africa.

Feumoe, A.N., Ndougsa-Mbarga, T., Manguelle-Dicoum, E., Fairhead, J.D., 2012. Delineation of tectonic lineaments using aeromagnetic data for the south-east Cameroon area. *Geofizika* **29**, 175–192.

Feumoe, S.A.N., 2014. Apport des filtrages et inversions 2D1/2 des anomalies aéromagnétiques dans la détermination des accidents tectoniques majeurs au Sud-est Cameroun. These Ddoctorat/PhD, Universite de Yaounde I, 143p.

Feybesse, J.L., Johan, V., Triboulet, C., Guerrot, C., Mayaga-Minkolo, F., Bouchot, V., Eko N'dong, J., 1998. The West Central African belt: a model of 2.5-2.0 Ma accretion and two-phase orogenic evolution. *Precambrian Research* **87**, 161–216.

Foley, S.F., Buhre, S., Jacob, D.E., 2003. Evolution of the archaean crust by delamination and shallow subduction. *Nature* **421**, 249–252.

Fumes, H., de Wit, M.J., Staudigel, H., Rosing, M., Muehlenbachs, K., 2007. A vestige of earth's oldest ophiolite. *Science* **315**, 1704–1707.

Gaina, C., Torsvik, T.H., Hinsbergen, D.J.J. Van, Medvedev, S., Werner, S.C., Labails, C., 2013. Tectonophysics The African Plate : A history of oceanic crust accretion and subduction since the Jurassic. *Tectonophysics* **604**, 4–25. https://doi.org/10.1016/j.tecto.2013.05.037

Garcia, X., Jones, A.G., 2002. Decomposition of three-dimensional magnetotelluric data. *Three-Dimensional Electromagnetics, Chapter 13*. 237–250.

Garcia, X., Jones, A.G., 2000. Advances in aspects of the application of magnetotellurics for mineral exploration. *2000 SEG Annual Meeting*. Society of Exploration Geophysicists.

Genik, G.J., 1992. Regional framework, structural and petroleum aspects of rift basins in Niger, Chad and the Central African Republic (C.A.R.). *Tectonophysics* **213**, 169-185.

Geometrics, 2000. Operation manual for Stratagem systems running IMAGEM, ver. 2.16. Geometrics Printing Press, San Jose, 16p.

Geosoft, n.d. Topics in Gridding.17p.

Goldstein, M.A., Strangway, D.W., 1975. Audio-frequency Magnetotellurics with a grounded electric dipole source. *Geophysics* **40**, 669–683. https://doi.org/10.1190/1.1440558

Goussi, J.F., Bisso, D., Abdelsalam, M.G., Atekwana, E.A., Katumwehe, A.B., Ekodeck, G.E., 2017. Geophysical imaging of metacratonizaton in the northern edge of the Congo craton in Cameroon. *Journal of African Earth Sciences* **129**, 94–107. https://doi.org/10.1016/j.jafrearsci.2016.12.010

Goussi Ngalamo, J.F., Sobh, M., Bisso, D., Abdelsalam, M.G., Atekwana, E., Ekodeck, G.E., 2018. Lithospheric structure beneath the Central Africa Orogenic Belt in Cameroon from the analysis of satellite gravity and passive seismic data. *Tectonophysics* **745**, 326–337. https://doi.org/10.1016/j.tecto.2018.08.015

Groom, R.W., Bailey, R.C., 1989. Decomposition of Magnetotelluric Impedance Tensors in the Presence of Local Three-Dimensional Galvanic Distortion. *Journal of Geophysical Research* **94**, 1913–1925.

Heine, C., Zoethout, J., Muller, R.D., 2013. Kinematics of the South Atlantic rift. Solid Earth.

Hinze, W.J., von Frese, R.R.B., Saad, A., 2013. Gravity and magnetic exploration: principles, practices and exploration. Cambridge University Press, 512p.

Houketchang Bouyo, M., 2018. Comment on "The Adamawa-Yadé domain, a piece of Archaean crust in the Neoproterozoic Central African Belt (Bafia area, Cameroon) by Tchakounté et al., 2017" (Precambrian Research 299, 210–229). *Precambrian Research* **305**, 504–507.

https://doi.org/10.1016/j.precamres.2017.12.002

Kankeu, B., Greiling, R.O., Paul, J., Ganno, S., Danguene, P.Y.E., Bassahak, J., Hell, J. V, 2017. Contrasting Pan-African structural styles at the NW margin of the Congo Shield in Cameroon. *Journal of African Earth Sciences* 1–20. https://doi.org/10.1016/j.jafrearsci.2017.06.002

Kato, Y., Nakamura, K., 2003. Origin and global tectonic significance of early Archean cherts from the Marble bar greenstone belt, Pilbara Craton, Western Australia. *Precambrian Research* **125**, 191–243.

Katumwehe, A.B., Abdelsalam, M.G., Atekwana, E.A., 2015. Tectonophysics The role of pre-existing Precambrian structures in rift evolution : The Albertine and Rhino grabens , Uganda. *Tectonophysics* 1–13. https://doi.org/10.1016/j.tecto.2015.01.022

Kearey, P., Klepeis, K.A., Vine, F.J., 2009. Global Tectonics, 3rd ed. Wiley-Blackwell.

Kirkpatrick, J.D., Bezerra, F.H.R., Shipton, K., Nascimento, A.F.D.O., Federal, U., Al, J.D.K.E., 2013. Scale-dependent influence of pre-existing basement shear zones on rift faulting : a case study from NE Brazil. *Journal of the Geological Society* **170**, 237–247. https://doi.org/10.1144/jgs2012-043.

Kröner, A., Stern, R.J., 2004. Pan-African orogeny., *Encyclopedia of Geology*. https://doi.org/10.2475/ajs.280.6.560

Lasserre, M., Soba, D., 1976. Age libérien des granodiorites et des gneiss à pyroxène du Cameroun méridional. Bulletin du Bureau de Recherches Geologiques et Minieres, France **section 2**, 17–32.

Ledo, J., Queralt, P., Marti, A., Jones, A.G., 2002. Two-dimensional interpretation of three-dimensional magnetotelluric data : an example of limitations and resolution. *Geophysical Journal International* **150**, 127–139.

Lerouge, C., Cocherie, A., Toteu, S.F., Penaye, J., Milési, J.P., Tchameni, R., Nsifa, E.N., Fanning, C.M., Deloule, E., 2006. Shrimp U–Pb zircon age evidence for Paleoproterozoic sedimentation and 2.05 Ga syntectonic plutonism in the Nyong Group, South-Western Cameroon: consequences for the Eburnean-Transamazonian belt of NE Brazil and Central Africa. *Journal of African Earth Sciences* **44**, 413–427.

Li, X.-H., Chen, Y., Li, J., Yang, C., Ling, X.-X., Tchouankoue, J.P., 2016. New isotopic constraints on age and origin of Mesoarchean charnockite, trondhjemite and amphibolite in the Ntem Complex of NW Congo Craton, southern Cameroon. *Precambrian Research*. https://doi.org/10.1016/j.precamres.2016.01.027

Li, Z.X., Bogdanova, S. V, Collins, A.S., De Waele, B., Ernst, R.E., Fitzsimons, I.C.W., Fuck, R.A., Gladkochub, D.P., Jacobs, J., Karlstrom, K.E., Lu, S., Natapov, L.M., Pease, V., Pisarevsky, S.A., Thrane, K., Vernikovsky, V., 2008. Assembly, configuration, and break-up history of Rodinia : A synthesis. *Precambrian Research* **160**, 179–210. https://doi.org/10.1016/j.precamres.2007.04.021

Liégeois, J., Abdelsalam, M.G., Ennih, N., Ouabadi, A., 2013. Metacraton : Nature , genesis and behavior. *Gondwana Research* **23**, 220–237. https://doi.org/10.1016/j.gr.2012.02.016

Liu, J.G., Mason, P.J., 2009. Essential Image Processing and GIS for Remote Sensing. Wiley-Blackwell, Oxford, 462p.

Liu, Z., Jiang, Y., Wang, G., Ni, C., Qing, L., Zhang, Q., 2015. Middle Neoproterozoic (~ 845 Ma) continental arc magmatism along the northwest side of the Jiangshan – Shaoxing suture , South China : Geochronology , geochemistry , petrogenesis and tect ... Middle

Neoproterozoic (~ 845 Ma) continental arc magmatism. *Precambrian Research* **268**, 212–226. https://doi.org/10.1016/j.precamres.2015.07.013

Lowrie, W., 2007. Fundamentals of Geophysics, 2nd ed. Cambridge University Press, New York. 393p

MacLeod, I.N., Jones, K., Dai, T.F., 1993. 3D Analitic signal in the interpretation of total magnetic field data at low magnetic latitudes. *Exploration Geophysics* **24**, 679–688.

Manguelle-Dicoum, E., 1988. Étude géophysique des structures superficielles et profondes de la région de Mbalmayo (Cameroun)., Thèse de Doctorat d'État ès Science, Universite de Yaounde, 202p .

Manguelle Dicoum, E., Bokosah, A.S., Kwende Mbanwi, T.E., 1992. Geophysical evidence for a major Precambrian schist-granite boundary in southern Cameroon. *Tectonophysics* **205**, 437–446.

Masterton, S.M., Fairhead, J.D., Mazur, S., Green, C.M., 2012. The influence of oceanic fracture zones on the segmentation and structural control of continental margins. *Extended Abstract EAGE Conference & Exhibition*. Copenhagen, 4p.

Mathieu, L., 2013. Exploration des gîtes magmatiques cuprifères dans Province de Grenville, Rappot 2012-03. Projet CONSOREM, 49p.

Maurizot, P., Abessolo, A., Feybesse, J., Johan, L., Lecomte, P., 1986. Etude et prospection minière du Sud-Ouest du Cameroun. Synthèse des travaux de 1978 à 1985, Rapport BRGM. Orleans, 274p.

Mbola-Ndzana, S.P., Mvondo-Ondoa, J., Owona, S., Sep-Nlongand, J.P., Olinga, J.B., Bilong, P., 2014. Evidence of the ~NE-SW extension in the Sa'a-Monatélé Region as in the Bafia and Yaounde groups within the Central Africa Fold belt (Cameroon): Implication for the Southern Cameroon Neoproterozoic extension. *Sciences, Technologies & Développement*, **15**, 1–15.

Mbom-Abane, S., 1997. Investigations géophysiques en bordure du craton du Congo (régiond'Abong Mbang/ Akonolinga, Cameroun) et implications structurales. Université de Yaoundé I, 180p.

Mcneice, G.W., Jones, A.G., 2001. Multisite , multifrequency tensor decomposition of magnetotelluric data. *Geophysics* **66**, 158–173.

McPhee, D.K., Bruce, A.C., Pellerin, L., 2006. Audiomagnetotelluric data and preliminary two-dimensional models from Spring, Dry Lake and Delamar Valleys, Nevada., U.S. Geological Survey, 44p.

McPhee, D.K., Chuchel, B.A., Pellerin, L., 2008. Audiomagnetotelluric data from Spring, Cave and Coyote Spring Valleys, Nevada, U.S. Geological Survey, 107p.

Meert, J.G., Libermann, B.S., 2007. The Neoproterozoic assembly of Gondwana and its relationship to the Ediacaran–Cambrian radiation. *Gondwana Research* **14**, 5–21. https://doi.org/10.1016/j.gr.2007.06.007

Meert, J.G., Libermann, B.S., 2004. A palaeomagnetic and palaeobiogeographical perspective on latest Neoproterozoic and early Cambrian tectonic events. Journal of the Geological Society 161, 477 – 487. *Journal of the Geological Society* **167**, 477–487.

Meert, J.G., Powell, C.M., 2001. Assembly and break-up of Rodinia : introduction to the special volume. *Precambrian Research* **110,** 1–8.

Meying, A., 2011. Investigations crustales profondes et superficielles par la méthode audio-

magnetotellurique (AMT) dans la région Ayos-Nguelemendouka (Cameroun). Universite de Yaoundé I, 139p.

Meying, A., Ndougsa-Mbarga, T., Gouet, D., Assembe, S.P., 2013. Near Surface Fractures Evidence from Audio-Magnetotelluric (AMT) Investigation in Ayos-Nguelemendouka Area (Eastern Cameroon). *International Journal of Geosciences* **4**, 480–493.

Meying, A., Ndougsa-Mbarga, T., Manguelle-Dicoum, E., 2009. Evidence of fractures from the image of the subsurface in the Akonolinga-Ayos area (Cameroon) by combining the Classical and the Bostick approaches in the interpretation of audio-magnetotelluric data. *Journal of Geology and Mining Research* **1**, 159–171.

Moulin, M., Aslanian, D., Unternehr, P., 2010. A new starting point for the South and Equatorial Atlantic Ocean. *Earth-Science Reviews*. https://doi.org/10.1016/j.earscirev.2009.08.001

Moyen, J., Hunen, J. Van, 2012. Short-term episodicity of Archaean plate tectonics. Geology 40, 451–454. https://doi.org/10.1130/G322894.1

Murphy, J B., Nance, R.D., 1991. Supercontinent model for the contrasting character of Late Proterozoic orogenic belts. *Geology* **19**, 469–472. https://doi.org/10.1130/0091-7613(1991)019<0469

Mvondo-Ondoa, J., Mvondo, H., Den Brok, B., 2009. Comment 'Pan-African tectonics in northwestern Cameroon : Implication for the history of western Gondwana. *Gondwana Research* **16**, 163–164. https://doi.org/10.1016/j.gr.2008.12.006

Mvondo, H., Den-Brok, S.W.J., Mvondo Ondoa, J., 2003. Evidence for symmetric extension and exhumation of the Yaoundé nappe (Pan-African fold Belt, Cameroon). *Journal of African Earth Sciences* **35**, 215–231. https://doi.org/10.1071/EG0325.Reid

Mvondo, H., Essono, J., Mvondo-Ondoa, J., Yene Atangana, J.Q., 2007a. Comment on "U-Pb dating of plutonic rocks involved in the nappe tectonic in southern Cameroon: Consequence for the Pan-African orogenic evolution of the central African fold belt" by Toteu et al. (Journal of African Earth Sciences 44 (2006) 479-493). *Journal of African Earth Sciences* **48**, 49–52. https://doi.org/10.1016/j.jafrearsci.2007.03.002

Mvondo, H., Owona, S., Mvondo-Ondoa, J., Essono, J., 2007c. Tectonic evolution of the Yaoundé segment of the Neoproterozoic Central African Orogenic Belt in southern Cameroon. *Canadian Journal of Earth Sciences* **44**, 433–444. https://doi.org/10.1139/e06-107

Mwaniki, M.W., Moeller, M.S., Schellmann, G., 2015. A comparison of Landsat 8 (OLI) and Landsat 7 (ETM +) in mapping geology and visualising lineaments : A case study of central region Kenya. *The International Archives of the Photogrammetry, Remote Sensing and Spatial Information Sciences* **XL–7**, 11–15. https://doi.org/10.5194/isprsarchives-XL-7-W3-897-2015

Nabighian, M.N., 1984. Toward a three-dimensional automatic interpretation of potential field data via generalized Hilbert transforms: fundamental relations. *Geophysics*. https://doi.org/10.1190/1.1441706

Nabighian, M.N., 1974. Additional comments on the analytic signal of two-dimensional magnetic bodies with polygonal cross-section. *Geophysics*. https://doi.org/10.1190/1.1440416

Nabighian, M.N., 1972. The analytic signal of two-dimensional magnetic bodies with polygonal cross- section: its properties and use for automated anomaly inter- pretation. *Geophysics* **37**, 507–517.

Nabighian, M.N., Grauch, V.J.S., Hansen, R.O., LaFehr, T.R., Li, Y., Peirce, J.W., Phillips, J.D., Ruder, M.E., 2005. The historical development of the magnetic method in exploration. *Geophysics* **70**, 33–61.

NASA, 2015. Fundamentals of Remote Sensing, 112p.

Ndougsa-Mbarga, T., Feumoe, A.N.S., Manguelle-Dicoum, E., Fairhead, J.D., 2012. Aeromagnetic Data Interpretation to Locate Buried Faults in South-. *Geophysica* **48**, 49–63.

Ndougsa-Mbarga, T., Meying, A., Bisso, D., Manguelle-Dicoum, E., 2010. Geological models derived from 1D and 2D audiomagnetotelluric (AMT) modeling using Bostick approach in the Messamena / Abong-Mbang area (East-Cameroon). *International Archive of Applied Sciences and Technology* **1**, 69–78.

Ndougsa Mbarga, T., Manguelle-Dicoum, E., Tabod, C.T., Mbom-Abane, S., 2003. Modelisation d'anomalies gravimétriques dans la région de Mengueme-Akonolinga (Cameroun). *Science, Technologie et Développement* **10**, 67–74.

Ndougsa Mbarga, T., Njilah, I.K., Nni, J., Nana, J., 2010. Note on the review of Earthquakes on Cameroon Territory., *Journal of Civil Protection, Ministry of Territorial Administration* **3**, 65–67.

Nedelec, A., Minyem, D., Barbey, P., 1993. High-P-High-T anatexis of Archaen tonalitic grey gneisses: The Eseka Migmatites, Cameroon. *Precambrian Research* **62**., 191–205.

Nedelec, A., Nsifa, E.N., Martin, H., 1990. Major and trace element geochemistry of the Archaean Ntem plutonic complex south Cameroon): petrogenesis and crustal evolution. *Precambrian Research* **47**, 35–50.

Nedelec, A., Nzenti, J.P., Barbey, P., 1986. Structural and metamorphic evolution of the Mbalmayo schists (Cameroon). Implications for the structure of the Pan-African mobile belt of central Africa , close to the Congo craton. *Comptes Rendus Academie Des Sciences* **303**.

Ngako, V., 1986. Evolution metamorphique et structurale de la bordure sud-ouest de la serie de Poli-segment camerounais de la chaine panafricaine. Universite de Rennes 1, 205p.

Ngako, V., Affaton, P., Njonfang, E., 2009. Reply (Pan-African tectonics in northwestern Cameroon : Implication for the history of western Gondwana). *Gondwana Research* **16**, 165–166. https://doi.org/10.1016/j.gr.2008.12.003

Ngako, V., Affaton, P., Njonfang, E., 2008. Pan-African tectonics in northwestern Cameroon : Implication for the history of western Gondwana. *Gondwana Research* **14**, 509–522. https://doi.org/10.1016/j.gr.2008.02.002

Ngako, V., Affaton, P., Nnange, J.M., Njanko, T., 2003. Pan-African tectonic evolution in central and southern Cameroon: Transpression and transtension during sinistral shear movements. *Journal of African Earth Sciences* **36**, 207–214. https://doi.org/10.1016/S0899-5362(03)00023-X

Ngako, V., Jegouzo, P., Nzenti, J.P., 1991. Le Cisaillement Centre Camerounais. Role structural et geodynamique dans l'orogenese panafricaine. *Comptes Rendus - Academie Des Sciences*, Serie II.

Ngako, V., Njonfang, E., 2018. Comment on "The Adamawa–Yade, a piece of Archaean crust in the Neoproterozoic Central African orogenic belt (Bafia area, Cameroon)" by Jacqueline Tchakounté et al. [Precambrian Research 299 (2017) 210–229]., *Precambrian Research*. https://doi.org/10.1016/j.precamres.2017.12.004

Ngako, V., Njonfang, E., 2011. Plates Amalgamation and Plate Destruction , the Western Gondwana History. *In: Dr. Closson, D. (Ed.), Tectonics* 3–36.

Ngako, V., Njonfang, E., Aka, F.T., Affaton, P., Nnange, J.M., 2006. The North-South Paleozoic to Quaternary trend of alkaline magmatism from Niger-Nigeria to Cameroon: Complex interaction between hotspots and Precambrian faults. *Journal of African Earth Sciences* **45**, 241–256. https://doi.org/10.1016/j.jafrearsci.2006.03.003

Ngnotue, T., Ganno, S., Nzenti, J.P., Schulz, B., Tchaptchet Tchato, D.I., Suh Cheo, E., 2012. Geochemistry and Geochronology of Peraluminous High-K Granitic Leucosomes of Yaound Series (Cameroon): Evidence for a Unique Pan-African Magmatism and Melting Event in North Equatorial Fold Belt. *International Journal of Geosciences* **03**, 525–548. https://doi.org/10.4236/ijg.2012.33055

Ngnotue, T., Nzenti, J.P., Barbey, P., Tchoua, F.M., 2000. The Ntui-Betamba high-grade gneisses: A northward extension of the Pan-African Yaounde gneisses in Cameroon. *Journal of African Earth Sciences* **31**, 369–381. https://doi.org/10.1016/S0899-5362(00)00094-4

Niblett, E.R., Sayn-Wittgenstein, C., 1960. Variation of electrical conductivity with depth by the magneto telluric method. *Geophyics* **25**, 998–1008.

Njingti-Nfor, Manguelle-Dicoum, E., Mbome-Abane, S., Tadjou, J.M., 2001. Major tectonic dislocations along the southern edge of Panafrican Mobile zone and the Congo Craton contact in southern region of Cameroon. *Proceedings of the Second International Conference on the Geology of Africa.* Assiut, Egypt, 799–811.

Njonfang, E., Ngako, V., Moreau, C., Affaton, P., Diot, H., 2008. Restraining bends in high temperature shear zones: The "Central Cameroon Shear Zone", Central Africa. *Journal of African Earth Sciences* **52**, 9–20. https://doi.org/10.1016/j.jafrearsci.2008.03.002

Nkoumbou, C., Barbey, P., Yonta-Ngouné, C., Paquette, J.L., Villiéras, F., 2014. Pre-collisional geodynamic context of the southern margin of the Pan-African fold belt in Cameroon. *Journal of African Earth Sciences* **99**, 245–260.

Nzenti, J.P., Barbey, P., Jegouzo, P., Moreau, C., 1984. Un nouvel exemple de ceinture granulitique dans une chaîne protérozoïque de collision: les migmatites de Yaoundé au Cameroun. *Comptes Rendus Academie Des Sciences de Paris* **299**, 1197–1199.

Nzenti, J.P., Barbey, P., Macaudière, J., Soba, D., 1988. Origin and evolution of the late Precambrian high, grade Yaoundé gneisses Cameroon. *Precambrian Research* **38**, 91–109.

Olinga, J.B., Mpesse, J.E., Minyem, D., Ngako, V., Ndougsa-Mbarga, T., Ekodeck, G.E., 2010. The Awaé – Ayos strike-slip shear zones (southern Cameroon): Geometry, kinematics and significance in the late Pan-African tectonics. *N. Jb. Geol. Paläont. Abh.* **257**, 1–11. https://doi.org/10.1127/0077-7749/2010/0042

Owona-Angue, M.L., Tabod, C.T., Nguiya, S., Kenfack, J.V., Tokam Kamga, A.P., 2013. Delineation of Lineaments in South Cameroon (Central Africa) Using Gravity Data. *Open Journal of Geology* **3**, 331–339. https://doi.org/http://dx.doi.org/10.4236/ojg.2013.35038

Owona Angue, M.L., Assembe, S.P., Njingti-Nfor, Ngoh, J.D., Ndougsa-Mbarga, T., Kue Petou, M.R., Bisso, D., 2016. Determination of the Structural Lineaments in the Kribi-Campo-Ma'an Area from a Multi-Scale Analysis of Gravity Data Using the HGM and Euler 3D Deconvolution Approaches. *International Journal of Geosciences* **7**, 1122–1143.

Owona Angue, M.L., Tabod, T.C., Nguiya, S., Kenfack, J.V., Tokam Kamga, A.P., 2013. Delineation of Lineaments in South Cameroon (Central Africa) Using Gravity Data. *Open Journal of Geology* **3**, 331–339. https://doi.org/http://dx.doi.org/10.4236/ojg.2013.35038

Palacky, G.J., 1988. Resistivity Characteristics of Geologic Targets. Geological Survey of Canada, 129p.

Parasnis, D.S., 1986. Principles of Applied Geophysics, 4th ed. Chapman and Hall, London, 412p.

Parker, R.L., 2011. New analytic solutions for the 2-D TE mode MT problem. *Geophysical Journal International* **186**, 980–986. https://doi.org/10.1111/j.1365-246X.2011.05091.x

Paterson Grant and Watson Ltd, 1976. Études aéromagnétiques sur certaines regions de la République Unie du Cameroun. Rapport d'interpretation. Toronto, 192p.

Paterson, N.R., Reeves, C. V, 1985. Applications of gravity and magnetic surveys : The state-of-the-art in 1985. *Geophysics* **50**, 2558–2594.

Peddie, N.W., 1983. International Geomagnetic Reference Field — Its evolution and the difference in total field intensity between new and old models for 1965–1980. *Geophysics* **48**, 1691–1696.

Penaye, J., Toteu, S.F., Van Schmus, W.R., Nzenti, J.P., 1993. U-Pb and Sm-Nd preliminary geochronologic data on the Yaounde Series, Cameroon: re-interpretation of the granulitic rocks as the suture of a collision in the "Centrafrican'' belt." *Comptes Rendus - Academie Des Sciences*, Serie II.

Penaye, J., Toteu, S.F., Van Schmus, W.R., Tchakounte, J., Ganwa, A., Minyem, D., Nsifa, E.N., 2004. The 2.1 Ga West Central African Belt in Cameroon : extension and evolution. *Journal of African Earth Sciences* **39**, 159–164. https://doi.org/10.1016/j.jafrearsci.2004.07.053

Pérez-Díaz, L., Eagles, G., 2014. Constraining South Atlantic growth with seafloor spreading data. *Tectonics* **33**, 1–26. https://doi.org/10.1002/2014TC003644

Piper, J.D.A., 2013. A planetary perspective on Earth evolution : Lid Tectonics before Plate Tectonics. *Tectonophysics* **589**, 44–56.

Piper, J.D.A., 2000. The Neoproterozoic Supercontinent: Rodinia or Palaeopangaea ? *Earth and Planetary Science Letters* **176**, 131–146. https://doi.org/10.1016/S0012-821X(99)00314-3

Pisarevsky, S.A., Wingate, M.T.D., Powell, C.M., Johnson, S., Evans, D.A.D., 2003. Models of Rodinia assembly and fragmentation. *Geological Society Special Publication*. https://doi.org/10.1144/GSL.SP.2003.206.01.04

Pouclet, A., Vidal, M., Doumnang, J.C., Vicat, J.P., Tchameni, R., 2006. Neoproterozoic crustal evolution in Southern Chad: Pan-African ocean basin closing, arc accretion and late- to post-orogenic granitic intrusion. *Journal of African Earth Sciences* **44**, 543–560. https://doi.org/10.1016/j.jafrearsci.2005.11.019

Prieto, C., 1996. Gravity/magnetic signatures of various geologic models-An exercise in pattern recognition. *IGC Footnotes on Interpretation* **4**.26p.

Reeves, C. V, 2005. Aeromagnetic Surveys-Principles, Practice & Interpretation. Geosoft, 245p.

Reeves, C. V, Korhonen, J. V, 2007. Magnetic anomalies for geology and resources. *In: Gubbins, D., Herrero-Bervera, E. (Eds.), Encyclopedia of Geomagnetism and Paleomagnetism* **XXVI**, 1054.

Reeves, C. V, Reford, S.W., Milligan, P.R., 1997. Airborne Geophysics : Old Methods , New Images. *In: Gubins, A.G. (Ed.), Proceedings of Exploration 97: Fourth Decennial International Conference on Mineral Exploration*. 13–30.

Regnoult, J.M., 1986. Synthèse géologique du Cameroun. Direction des Mines et de la Géologie du Cameroun, 119p.

Reid, A.B., Allsop, J.M., Granser, H., Millett, A.J., Somerton, I.W., 1990. Magnetic

interpretation in three dimensions using Euler deconvolution. *Geophysics* **55**, 80–91.

Rikitake, T., 1948. Notes on the Electromagnetic induction within the Earth. **XXIV**, 1–9.

Roberts, N.M.W., van Kranendonk, M.J., Parman, S., Clift, P.D., 2015. Continent formation through time. *Geological Society, London, Special Publications* **389**, 1–16. https://doi.org/http://dx.doi.org/10.1144/SP389.13

Roest, W.R., Verhoef, J., Pilkington, M., 1992. Magnetic interpretation using the 3-D analytic signal. *Geophysics* **57**, 116–125.

Rolin, P., 1995. La Zone de Décrochement Panafricain des Oubanguides en République Centrafricaine. *Comptes Rendu de l'Académie Des Sciences de Paris* **320**, 63–69.

Rolin, P., 1992. Nouvelles données tectoniques sur le socle précambrien de Centrafrique: implications géodynamiques. *Comptes Rendu de l'Académie Des Sciences de Paris* **315**, 467–470.

Rowell, A.J., Rees, M.N., Duebendorfer, E.M., Wallin, E.T., Van Schmus, W.R., Smith, E.I., 1993. An active Neoproterozoic margin: evidence from the Skelton Glacier area, Transantarctic Mountains. *Journal of the Geological Society, London.* https://doi.org/10.1144/gsjgs.150.4.0677

Schettino, A., Scotese, C.R., 2005. Apparent polar wander paths for the major continents (200 Ma to the present day): A palaeomagnetic reference frame for global plate tectonic reconstructions. *Geophysical Journal International* **163**, 727–759. https://doi.org/10.1111/j.1365-246X.2005.02638.x

Schowengerdt, R.A., 2007. Remote Sensing: Models and Methods for Image Processing, 3rd ed. Elsevier, Oxford, 558p.

Scotese, C.R., 2009. Late Proterozoic plate tectonics and palaeogeography: A tale of two supercontinent, Rodinia and Pannotia. *Geological Society, London, Special Publications* **326**, 67–83. https://doi.org/10.1144/SP326.4

Scotese, C.R., Boucot, A.J., Mckerrow, W.., 1999. Gondwanan palaeogeography and palaeoclimatology. *Journal of African Earth Sciences.* **99**–114.

Shandini, N.Y., Tadjou, J.M., 2012. Interpreting gravity anomalies in south Cameroon, central Africa. *Earth Sciences Research Journal* **16**, 5–9.

Shandini, N.Y., Tadjou, J.M., Basseka, C.A., 2011. Delineating deep basement faults in South Cameroon area. *World Applied Science Journal* **14**, 611–615.

Shandini, N.Y., Tadjou, J.M., Tabod, C.T., Fairhead, J.D., 2010. Gravity Data Interpretation in the Northern Edge of the Congo Craton , South-Cameroon. *Anuário Do Instituto de Geociências - UFRJ* **33**, 73–82.

Shang, C.K., Liégeois, J.P., Satir, M., Frisch, W., Nsifa, E.N., 2010. Late Archaean high-K granite geochronology of the northern metacratonic margin of the Archaean Congo craton, Southern Cameroon: Evidence for Pb-loss due to non-metamorphic causes. *Gondwana Research* **18**, 337–355. https://doi.org/10.1016/j.gr.2010.02.008

Shang, C.K., Sati, M., Nsifa, E.N., Liegeois, J.-P., Siebel, W., Taubald, H., 2007. Archaean high-K granitoids produced by remelting of earlier Tonalite-Trondhjemite-Granodiorite (TTG) in the Sangmelima region of the Ntem complex of the Congo craton , southern Cameroon. *International Journal of Earth Sciences (Geol Rundsch)* **96**, 817–841. https://doi.org/10.1007/s00531-006-0141-3

Shang, C.K., Satir, M., Siebel, W., Nsifa, E.N., Taubald, H., Liégeois, J.P., Tchoua, F.M., 2004a.

TTG magmatism in the Congo craton; a view from major and trace element geochemistry, Rb-Sr and Sm-Nd systematics: Case of the Sangmelima region, Ntem complex, southern Cameroon. *Journal of African Earth Sciences* **40**, 61–79. https://doi.org/10.1016/j.jafrearsci.2004.07.005

Shang, C.K., Satir, M., Siebel, W., Taubald, H., Nsifa, E.N., Westphal, M., Reitter, E., 2001. Genesis of K-rich granitoids in Sangmelima region, Ntem Complex (Congo Craton), Cameroon. *Terra Nostra* **5**, 60–63.

Shang, C.K., Siebel, W., Satir, M., Chen, F., Mvondo Ondoua, J., 2004b. Zircon Pb-Pb and U-Pb systematics of TTG rocks in the Congo craton: Constraints on crust formation, magmatism, and Pan-African lead loss. *Bulletin of Geosciences* **79**, 205–219. https://doi.org/10.1039/c2jm31907a

Simon, N., Ali Che, A., Mohamed, K.R., Sharir, K., 2016. Best Band Ratio Combinations for the Lithological Discrimination of the Dayang. *Sains Malaysiana* **45**, 659–667.

Simpson, F., Bahr, K., 2005. Practical magnetotellurics. https://doi.org/10.1017/CBO9780511614095

Sims, W.E., Bostick, F.X.J., Smith, H.W., 1971. The estimation of the magnetotelluric impedance tensor elements from measured data. *Geophysics* **36**, 938–942.

Spalletti, L.A., Limarino, C.O., Geuna, S., 2010. The Late Palaeozoic of Western Gondwana : New insights from South American records. *Geologica Acta* **8**, 341–347. https://doi.org/10.1344/105.000001576

Stewart, J.H., 2007. World Map showing surface and subsurface distribution, and lithologic character of Middle and Late Neoproterozoic Rocks., USGS Open-File Report. Menlo Park.

Strangway, D.W., Swift, C.M., Holmer, R.C., 1973. The application of Audio-frequency magnetotellurics (AMT) to mineral exploration. *Geophysics* **38**, 1159–1175. https://doi.org/10.1190/1.1440402

Tack, L., Wingate, M.T.D., De Waele, B., Meert, J., Belousova, E.A., Griffin, B., Tahon, A., Fernandez-Alonzo, M., 2008. The 1375 Ma "Kibaran Event" in Central Africa: prominent emplacement of bimodal magmatism under extensional regime. *Precambrian Research*. https://doi.org/10.1016/j.precamres.2010.02.022

Tadjou, J.M., Njingti-Nfor, Kamguia, J., Manguelle-Dicoum, E., 2008. Geophysical prospecting of the transition zone between the Congo Craton and the Panafrican belt in Cameroon. *Earth Science Research Journal* **12**, 169–180.

Tadjou, J.M., Nouayou, R., Kamguia, J., Kande, H.L., Manguelle-Dicoum, E., 2009. Gravity analysis of the boundary between the Congo craton and the Pan-African belt of Cameroon. *Austrian Journal of Earth Sciences* **102**, 71–79.

Takam, T., Makoto, A., Kokonyangi, J., Dunkley, Daniel, J., Nsifa, E.N., 2009. Paleoarchaean charnockite in the Ntem Complex, Congo Craton, Cameroon : insights from SHRIMP zircon U-Pb ages. *Journal of Mineralogical and Petrological Sciences* **104**, 1–11. https://doi.org/10.2465/jmps.080624

Tchakounté Numbem, J., Eglinger, A., Toteu, S.F., Zeh, A., Nkoumbou, C., Mvondo-Ondoa, J., Penaye, J., de Wit, M., Barbey, P., 2018a. Reply to comment by M. Bouyo on "The Adamawa–Yade domain, a piece of Archaean crust in the Neoproterozoic Central African Orogenic belt (Bafia area, Cameroon)", by Jacqueline Tchakounté et al., Precambrian Research 299 (2017) 210–229. *Precambrian Research* **305**, 514–515. https://doi.org/10.1016/j.precamres.2017.12.003

Tchakounté Numbem, J., Eglinger, A., Toteu, S.F., Zeh, A., Nkoumbou, C., Mvondo-Ondoa, J., Penaye, J., de Wit, M., Barbey, P., 2017. The Adamawa-Yadé domain, a piece of Archaean crust in the Neoproterozoic Central African Orogenic belt (Bafia area, Cameroon). *Precambrian Research* **299**, 210–229. https://doi.org/10.1016/j.precamres.2017.07.001

Tchakounté Numbem, J., Eglinger, A., Toteu, S.F., Zeh, A., Nkoumbou, C., Mvondo-Ondoa, J., Penaye, J., de Witt, M., Barbey, P., 2018b. Reply to comment by Ngako and Njonfang on "The Adamawa-Yade domain, a piece of Archaean crust in the Neoproterozoic Central African Orogenic belt (Bafia area, Cameroon)", by Jacqueline Tchakounté et al., Precambrian Research 299 (2017) 210-229. *Precambrian Research* **305**, 516–518. https://doi.org/10.1016/j.precamres.2017.12.035

Tchameni, R., 1997. Géochimie et géochronologie des formations de l'archéen du paléoprotérozoïque du Sud Cameroun groupe du Ntem, Craton du Congo. Thèse de Doctorat. Université d'Orléans, 227p.

Tchameni, R., Lerouge, C., Penaye, J., Cocherie, A., Milesi, J.P., Toteu, S.F., Nsifa, E.N., 2010. Mineralogical constraint for metamorphic conditions in a shear zone affecting the Archean Ngoulemakong tonalite, Congo craton (Southern Cameroon) and retentivity of U-Pb SHRIMP zircon dates. *Journal of African Earth Sciences* **58**, 67–80. https://doi.org/10.1016/j.jafrearsci.2010.01.009

Tchameni, R., Mezger, K., Nsifa, E.N., Pouclet, A., 2001. Crustal origin of Early Proterozoic syenites in the Congo Craton (Ntem Complex), South Cameroon. *Lithos* **57**, 23–42.

Tchameni, R., Mezger, K., Nsifa, E.N., Pouclet, A., 2000. Neoarchaean evolution in the Congo Craton: evidence from K-rich granitoids of the Ntem Complex, Southern Cameroon. *Journal of African Earth Sciences* **30**, 133–147.

Tchameni, R., Pouclet, A., Mezger, K., Nsifa, E.N., Vicat, J.., 2004. Monozircon and Sm–Nd whole rock ages from the Ebolowa greenstone belts: evidence for the terranes older than 2.9 Ga in the Ntem Complex (Congo Craton, South Cameroon). *Journal of the Cameroon Academy of Sciences* **4**, 213–224.

Teikeu, A.W., Njandjock, P., Tabod, C., Akame, J.M., Nshagali, G., 2016. Hydrogeological activity of lineaments in Yaounde Cameroon region using remote sensing and GIS techniques. *The Egyptian Journal of Remote Sensing and Space Sciences*. https://doi.org/10.1016/j.ejrs.2015.12.006

Telford, W.M., Geldart, L.P., Sherriff, R.E., Keys, D.A., 1990. Applied Geophysics. Cambridge University Press, Cambridge. https://doi.org/10.1130/0091-7613

Thompson, D.T., 1982. EULDEP : A New Technique for Making Computer-Assisted Depth Estimates from Magnetic Data. *Geophysics* **47**, 31–37.

Tikhonov, A.N., 1950. On determining electrical characteristics of the deep layers of the Earth's crust. *Doklady* **73**, 295–297. https://doi.org/10.1130/0091-7613

Toteu, S.F., Fouateu, R.Y., Penaye, J., Tchakounte, J., Mouangue, A.C.S., Van Schmus, W.R., Deloule, E., Stendal, H., 2006a. U-Pb dating of plutonic rocks involved in the nappe tectonic in southern Cameroon: consequence for the Pan-African orogenic evolution of the central African fold belt. *Journal of African Earth Sciences* **44**, 479–493. https://doi.org/10.1016/j.jafrearsci.2005.11.015

Toteu, S.F., Fouateu Yongue, R., Penaye, J., Seme Mouangue, A.C., Van Schmus, W.R., Tchakounte, J., Deloule, E., Stendal, H., 2007. Reply to the comment by Mvondo et al. on "U-Pb dating of plutonic rocks involved in the nappe tectonics in southern Cameroon: Consequence for the Pan-African orogenic evolution of the central African fold belt by

Toteu et al., 2006". *Journal of African Earth Sciences* **48**, 53–54. https://doi.org/10.1016/j.jafrearsci.2007.03.003

Toteu, S.F., Michard, A., Bertrand, J.M., Rocci, G., 1987. U/Pb dating of precambrian rocks from northern cameroon, orogenic evolution and chronology of the pan-african belt of Central Africa. *Precambrian Research* **37**, 71–87. https://doi.org/10.1016/0301-9268(87)90040-4

Toteu, S.F., Penaye, J., Deloule, E., Van Schmus, W.R., Tchameni, R., 2006b. Diachronous evolution of volcano-sedimentary basins north of the Congo craton: Insights from U-Pb ion microprobe dating of zircons from the Poli, Lom and Yaoundé Groups (Cameroon). *Journal of African Earth Sciences* **44**, 428–442. https://doi.org/10.1016/j.jafrearsci.2005.11.011

Toteu, S.F., Penaye, J., Djomani, Y.P., 2004. Geodynamic evolution of the Pan-African belt in central Africa with special reference to Cameroon. *Canadian Journal of Earth Sciences* **41**, 73–85. https://doi.org/10.1139/e03-079

Toteu, S.F., Van Schmus, W.R., Penaye, J., Michard, A., 2001. New U-Pb and Sm-Nd data from north-central Cameroon and its bearing on the pre-Pan African history of Central Africa. *Precambrian Research* **108**, 45–73. https://doi.org/10.1016/S0301-9268(00)00149-2

Toteu, S.F., van Schmus, W.R., Penaye, J., Nyobe, J.B., 1994. U-Pb and Sm-Nd evidence for Eburnian and Pan-African high-grade metamorphism in cratonic rocks of southern Cameroon. *Precambrian Research* **67**, 321–347.

US Geological Survey, 2016. Landsat 8 Data Users Handbook, LSDS-1574 Report V. 2.0, 95p.

van Hinsbergen, J.J., Buiter, S.J.H., Torsvik, T.H., Gaina, C., Webb, S.J., 2011. The formation and evolution of Africa from the Archaean to Present : Introduction. *Geological Society, London, Special Publication*s **357**, 1–8. https://doi.org/10.1144/SP357.1

van Schmus, W.R., Oliveira, E.P., da Silva Filho, A.F., Toteu, S.F., Penaye, J., Guimarães, I.P., 2008. Proterozoic links between the Borborema Province, NE Brazil, and the Central African Fold Belt. *Geological Society, London, Special Publications* **294**, 69–99. https://doi.org/10.1144/SP294.5

Vezinet, A., Moyen, J., Stevens, G., Nicoli, G., Laurent, O., Couzinié, S., Frei, D., 2018. A record of 0 . 5 Ga of evolution of the continental crust along the northern edge of the Kaapvaal Craton , South Africa : Consequences for the understanding of Archean geodynamic processes. *Precambrian Research* **305**, 310–326. https://doi.org/10.1016/j.precamres.2017.11.019

Vicat, J., Moloto-a-Kenguemba, G., 2001. Les granitoides de la couverture protérozoique de la bordure nord du craton du Congo (Sud-Est du Cameroun et Sud-Ouest de la République centrafricaine), témoins d ' une activité magmatique panafricaine. *Earth and Planetary Science* **332**, 235–242.

Vicat, J.P., Nsifa, E.N., Tchameni, R., Pouclet, A., 1998. La ceinture de roches vertes de Lolodorf-Ngomedzap (Sud-Cameroun) Petrologie, geochimie et cadre geodynamique. *In*: *Vicat, J., Bilong, P. (Eds.), Geosciences Au Cameroun* **1**, 325–337.

Vozoff, K., 1991. The Magnetotelluric method .*in Electromagnetic Methods in Applied Geophysics, Chapter 8.* Society of Exploration Geophysicists, Tulsa, 641–712. https://doi.org/doi.org/10.1190/1.9781560802686.ch8

Vozoff, K., 1990. Magnetotellurics: Principles and practice. Proceedings of the Indian Academy of Sciences - *Earth and Planetary Sciences* **99**, 441–471. https://doi.org/10.1007/BF02840313

Vozoff, K., 1972. The magnetotelluric methoc in the exploration of sedimentary basins. *Geophysics* **37**, 98–141.

Weaver, J.T., Agarwal, A.K., Lilley, F.E.M., 2000. Characterization of the magnetotelluric tensor in terms of its invariants.

Weaver, J.T., Agarwap, A.K., Lilley, F.E.M., 2006. The relationship between the magnetotelluric tensor invariants and the phase tensor of Caldwell, Bibby, and Brown. *Exploration Geophysics* **37**, 261–267.

Weckmann, U., 2012. Making and Breaking of a Continent: Following the Scent of Geodynamic Imprints on the African Continent Using Electromagnetics. *Surveys in Geophysics* **33**, 107–134. https://doi.org/10.1007/s10712-011-9147-x

Yandjimain, J., Ndougsa-Mbarga, T., Meying, A., Bikoro Bi-Alou, M., Ngoumou, P.C., Assembe, S.P., Ngoh, J.D., Owono Amougou, O.U.I., 2017. Combination of Tilt-Angle and Euler Deconvolution Approaches to Determine Structural Features from Aeromagnetic Data Modeling over Akonolinga-Loum Area. *International Journal of Geosciences* **8**, 925–947. https://doi.org/10.4236/ijg.2017.87053

Yonta Ngoune, C., 2010. Le contexte géologique des indices de talc de la région de Boumnyebel (Chaîne panafricaine d'Afrique Centrale, Cameroun). Universite de Yaounde 1 /Universite de Nancy. https://doi.org/10.1037/0735-7044.121.5.920

Zanga-Amougou, A., Layu, Y., Bikoro Bi-Alou, M., Manguelle-Dicoum, E., 2013. 2.5D Modeling of Crustal Structures along the Eastern Cameroon and Western Central African Republic Derived from Finite Element and Spectral Analysis Methods. *Geophysica* **49**, 75–97.

Zhang, P., Roberts, R.G., L. B. Pedersen, 1987. Magnetotelluric Magnetotelluric strike rules. *Geophysics* **52**, 267–278.

Zhao, G., Sun, M., Wilde, S.A., Li, S., Zhang, J., 2006. Some key issues in reconstructions of Proterozoic supercontinents. *Journal of Asian Earth Sciences.* https://doi.org/10.1016/j.jseaes.2004.06.010

Zhdanov, M.S., 2009. Geophysical electromagnetic theory. Methods in Geochemistry and Geophysics. Elsevier, 831p.

Zonge, K.L., Hughes, L.J., 1991. Controlled source audio-frequency magnetotellurics. *in Electromagnetic Methods in Applied Geophysics, Chapter 9*. Society of Exploration Geophysicists, Tulsa, 713–809. https://doi.org/doi.org/10.1190/1.9781560802686.ch9

APPENDICES

Appendix 1: coordinates of AMT sounding stations.

Station	Latitude	Longitude	Elevation (m)	Position (m)
		PROFILE 1 (OSSOL)		
OS1	03°50'45.40"	11°39'07.50"	701	0
OS2	03°50'43.00"	11°39'10.02"	708	100
OS3	03°50'40.90"	11°39'12.80"	702	200
OS4	03°50'39.10"	11°39'15.70"	693	300
OS5	03°50'36.64"	11°39'16.58"	691	400
OS6	03°50'34.41"	11°39'18.97"	684	500
		PROFILE 2 (BEGUELE 1-CARREFOUR)		
BE1	03°50'34.32"	11°39'49.50"	704	0
BE2	03°50'32.18"	11°39'51.79"	714	100
BE3	03°50'29.88"	11°39'54.10"	718	200
BE4	03°50'27.44"	11°39'56.32"	719	300
BE5	03°50'25.27"	11°39'58.68"	718	400
		PROFILE 3 (NKOLAFAMBA)		
NK1	03°51'06.80"	11°39'38.00"	685	0
NK2	03°51'04.14"	11°39'39.90"	678	100
NK3	03°51'01.00"	11°39'41.50"	684	200
NK4	03°50'57.10"	11°39'43.60"	691	300
NK5	03°50'56.20"	11°39'46.50"	683	400
NK6	03°50'54.70"	11°39'48.80"	684	500
		PROFILE 4 (BEGUELE 2)		
BG1	03°50'43.50"	11°40'05.50"	719	0
BG2	03°50'41.50	11°40'08.20"	718	100
BG3	03°50'38.80"	11°40'10.60"	702	200
BG4	03°50'34.80"	11°40'13.80"	700	300
BG5	03°50'33.00"	11°40'16.40"	720	400
BG6	03°50'31.70"	11°40'18.40"	717	500
		PROFILE 5 (KAMBA)		
KB1	03°40'44,3"	011°40'49,9"	668	0
KB2	03°40'32,6"	011°40'59,1"	661	600
KB3	03°40'32,6"	011°41'11,3"	664	900
KB4	03°40'20,3"	011°41'20,3"	680	1200
KB5	03°40'16,5"	011°41'24,1"	676	1300
KB6	03°40'12,6"	011°41’28,2"	666	1500
		PROFILE 6 (LOUM 2)		
LM1	03°40'44,3"	011°40'49,9"	668	0
LM2	03°40'32,6"	011°40'59,1"	661	600
LM3	03°40'32,6"	011°41'11,3"	664	900
LM4	03°40'20,3"	011°41'20,3"	680	1200
LM5	03°40'16,5"	011°41'24,1"	676	1300
LM6	03°40'12,6"	011°41’28,2"	666	1500

Appendix2: Publications related to the thesis

1. **Assembe, S.P**., Ndougsa-Mbarga, T., and Meying, A., 2016. New structural facts from audio-magnetotelluric (AMT) data interpretation in the Yaoundé-Nkolafamba area (Centre Cameroon). *Journal of Indian Geophysical Union*, **20** (1), 19-32.

2. Akame, J.M., **Assembe, S.P**., Zo'o Zame, P., Owona, S., Ndougsa-Mbarga, T., Azia, G.A., Mvondo-Ondoa, J., 2019. The Sangmelima granite-greenstone belts (South Cameroon): Integration of remote sensing and aeromagnetic data for structural interpretation. *The Egyptian Journal of Remote Sensing and Space Sciences* **22**, 37–47. https://doi.org/10.1016/j.ejrs.2018.11.005.

3. **Assembe, S.P.,** Ndougsa-Mbarga, T., Meying, A., Gouet, D.H., Ngoh, J.D., Mono, J.A., 2019. Contribution of Geophysics to the Understanding of the Geodynamic Activity at the Northern Margin of the Congo Craton : A Case Study from Aeromagnetic Data Interpretation Over the Metet-Zoetele Region (Southern Cameroon). *European Journal of Scientific Research* **152**, 286–303.

4. **Assembe, S.P.,** Ndougsa-Mbarga, T., Enyegue A Nyam, F.M., Ngoumou, P.C., Meying, A., Gouet, D.H., Zanga Amougou, A., Ngoh, J.D., 2020. + − Evidence of Porphyry Deposits in the Ntem Complex: A Case Study from Structural and Hydrothermal Alteration Zones Mapping through Landsat-8 OLI, Aeromagnetic and Geological Data Integration in the Yaounde-Sangmelima Region (Southern Cameroon). *Advances in Remote Sensing* **9**, 53–84. https://doi.org/10.4236/ars.2020.92004.

J. Ind. Geophys. Union (January 2016)
v.20, no.1, pp: 19-32

New structural facts from audio-magnetotelluric (AMT) data interpretation in the Yaoundé-Nkolafamba area (Centre Cameroon)

S. P. Assembe [1], T. Ndougsa-Mbarga *[1,2] and A. Meying [3]

[1] Postgraduate School of Sciences, Technologies & Geosciences, University of Yaoundé I, P.O. Box 8251, Yaoundé, Cameroon
[2]Department of Physics, Advanced Teachers' Training College, University of Yaoundé I, P.O. Box 47 Yaoundé, Cameroon
[3] School of Geology, Mining and Mineral Processing, University of Ngaoundéré, Cameroon
*Corresponding author: theopndougsa@gmail.com

ABSTRACT

Several geological models that explain the tectonic evolution of the Central Africa Pan-African Belt are discussed, each one having both outstanding results and unresolved questions. To improve the knowledge of the Pan-African domain in Cameroon, especially within the Yaoundé series, a geophysical investigation of shallow crustal structures was carried out in Nkolafamba, 26 km away from Yaoundé on the Yaoundé-Akonolinga highway, between the northing latitudes 03°45 and 04°, and easting longitudes 11°30 to 12° area during August 2011. The study combines field geological observations with twenty-three tensor Audio-magnetotelluric/Controlled source audio-magnetotelluric (AMT/CSAMT) experiments along four north 135° trending profiles, using a Geometric's Stratagem EH4 resistivitymeter. The 2D modelling of geophysical data exhibits: (1) That the formations encountered in the area are a mixture of both Pan-African and Congo Craton formations; (2) Many folding patterns and a set of strike-slip conductive faults and fractures that correlate the field observations. From the outcome of the study, we state that the study area belongs to the transition zone between the Congo Craton and the Pan-African belt. We propose that many of these faults form a southwest-northeast shallow tectonic line, seem to be related to the enhancement of the Centre Cameroon Shear Zone within the Yaoundé area. These facts demonstrate that the region has been affected by the collision between the Pan-African and the steady Congo Craton, followed by post Pan-African transpressional evolution characterized by dextral and sinistral strike-slips along the southwest-northeast trend. Therefore, we opine that the indentation tectonics model, earlier proposed through some geological studies, is more suitable in describing the geological evolution. It is also evident that geophysics played significant role in better understanding of the Yaoundé series' structural geology.

Keywords: Tensor audio-magnetotelluric experiment, Controlled source audio-magnetotelluric experiment, 2D modelling, tectonic line, Pan-African belt, Congo Craton, Yaoundé series.

INTRODUCTION

Structural geology divides South-Cameroon into two major sets: (**a**) The Congo Craton (CC)in the Southern part, represented by the Ntem complex, which has not been affected by the Pan-African thermo-tectonic event; (**b**) The central and northern parts that correspond to the Central African mobile zone, where the Pan-African orogeny occurs. This E-W orogenic zone, the Central Africa Pan-African Belt (CAPAB), is sited at the Northern edge of the CC and stretches from Cameroon to Sudan (Poidevin, 1985; Nzenti et al., 1988; Rolin, 1992 and 1995; Penaye et al., 1993).
The study area is located 26 km away from Yaoundé on the Yaoundé-Akonolinga highway, between north-latitudes 03°45 and 04°, and east-longitudes 11°30 to 12°. It belongs to the Yaoundé series, a unit of the Yaoundé Group, which is part of the CAPAB. The Yaoundé series is a Neoproterozoic feature located at the North of the CC, which stretches from west to east. It is made up of gneisses and migmatitic garnets coming from old granitised and metamorphosed sediments in the high pressure granulite facies. It constitutes the heart of the Pan-African thrust (Nzenti et al, 1984 and 1988; Nédelec et al, 1986). The Precambrian basement of the area, as that of the whole Yaoundé series (Figure 1), comprises two geological facies: gneisses associated with micaschists (ectinites), and migmatitic garnetiferous gneisses (migmatites).

The Neoproterozoic Yaoundé series has undergone structurally sub-horizontal tangential tectonics, which is the origin of its position as a sheet on the northern edge of the CC (Bessoles et Trompette, 1980; Nédelec et al 1986; Nzenti et al, 1988; Ngako et al., 2008) .Tectonics in the region can then be described as corresponding to alternative east-west to northwest-southeast contractions and to north-south to northeast-southwest parallel orogenic stretches. Olinga et al. (2010) state that the tectonics corresponds to: the thrusting of the Yaoundé nappe over the CC; and the strike-slip shearing in ductile to brittle-ductile conditions, characterized by penetrative foliation dipping north or south, an associated east-northeast-west-southwest

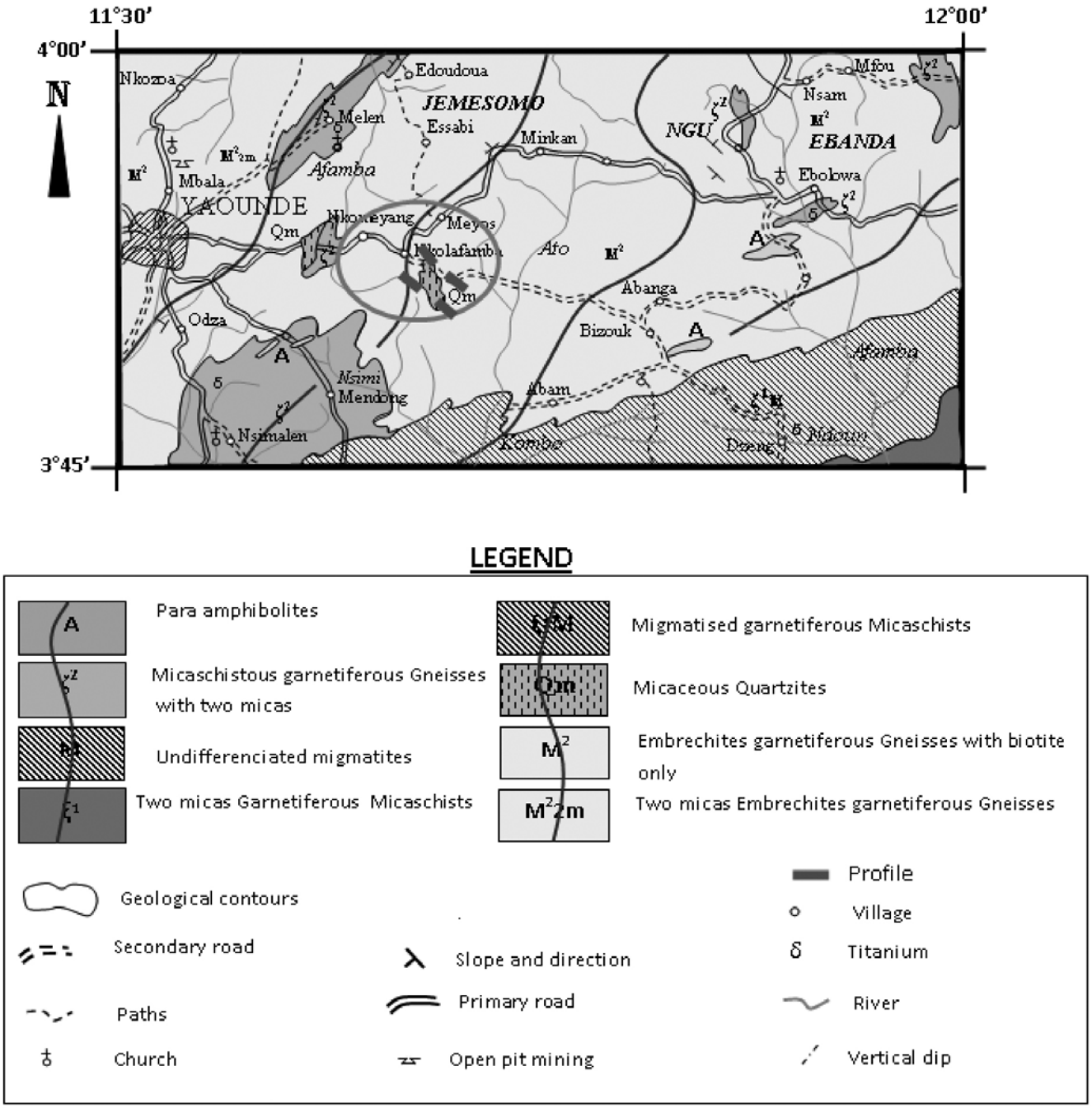

Figure 1. Geologic map of the study area (after Champetier de Ribes & Aubagues, 1956)

stretching lineation and north-south to northeast-southwest folding.

Geophysical inputs involving the CC/CAPAB transition zone are mainly from gravity studies. Early interpretations of gravity anomaly maps (Collignon, 1968) revealed E-W strong anomaly gradients in the Akonolinga/Ayos/Nguelemendouka/Abong-Mbang area, which were interpreted as an E-W tectonic activity along parallel 04°N (Mbom-Abane, 1997), while Ndougsa et al. (2003) suggest an E-W normal fault in the Mengueme/Abong-Mbang area. More recent studies by Shandini et al. (2010 & 2011) confirmed the CC/CAPAB boundary and highlighted NE-SW and NW-SE basement lineaments that Basseka et al. (2011) suggested to be related to faulting associated with the granitic rocks in the upper brittle crust. Hence, crustal faulting in the northern margin of the CC is assumed to be associated with deep-seated structures (Feumoe et al., 2012; Ndougsa et al., 2012; Shandini and Tadjou, 2012) related to the CC/CAPAB collision.

Magnetotellurics (MT) revealed the CAPAB's overthrust line onto the CC corresponding to the Eseka-Dja faults line (Manguelle-Dicoum et al., 1993) and a major E-W (N105°)

general trending lineament corresponding to the CC/CAPAB boundary and secondary ENE-WSW to NNW-SSE lineaments (Meying et al 2009) at Ayos, in the southern edge of the CAPAB. The E-W lineament corresponding to the CC/CAPAB boundary was confirmed by Tadjou et al. (2008), who additionally detailed about subsidence within the basement associated with intrusions of low resistive materials beneath the CAPAB domain in the Abong-Mbang/Akonolinga area, located east of our study area. Recent investigations in the CC/CAPAB transition zone using Audiomagnetotellurics confirmed that the E-W event associated with fault structures is related to the inferred tectonic boundary separating CC and CAPAB ,while NNW-SSE to ENE-WSW structures are related to post-collision tectonics occurring in the area (Meying et al., 2009; Ndougsa et al., 2011; Meying et al., 2013). It is important to state that the area under study has not been clearly subjected to AMT investigations. It is subjected to these geophysical investigations, in the recent past, as detailed above.

Studies of the CAPAB reveal that it collides with the CC. However, to date, in spite of its proximity with the CC/CAPAB limit, finer details of the Yaoundé series could not be obtained due to insufficiency of geophysical studies, to explicitly explain the tectonics. We have interpreted an AMT dataset and found evidences of CC/CAPAB collision in the Yaoundé-Nkolafamba area that belongs to the southern margin of the CAPAB. The results are correlated with geological observations made simultaneously in the area.

METHOD AND DATA ACQUISITION

Method

The Magnetotelluric (MT) method separately developed both by Thikonov (1950) and Cagniard (1953) is applied for geophysical and structural geology prospecting (Bostick, 1977**;** Vozoff, 1972 & 1990; Manguelle-Dicoum et al., 1992 & 1993**;** Meying et al., 2009 and references therein, Meying et al., 2013). It consists of simultaneous measurements of electric and magnetic natural fields at any point on the surface of the Earth, in order to deduce the resistivity of rocks of the homogeneous subsurface. For the real case, subsurface is inhomogeneous and apparent resistivity is determined using the Bostick law (1977) derived from the Cagniard's fundamental formula (Ndougsa et al., 2011).

Data Acquisition

In this work, the high frequency MT or Audio-magnetotelluric (AMT) method was used to image the subsurface structure of the Yaoundé/Nkol-Afamba area using a Geometrics' Stratagem EH4 AMT/CSAMT system. The data were acquired during six days of field work conducted during the first half of August 2011. The method has been chosen because of its reliability and its fast handling even in remote and hostile areas. We lately combined geophysical studies with some field geological levees to strengthen our statements.

The Geometrics Stratagem EH4 unit measures electrical resistivity with orthogonal electrical and magnetic field changes to depths ranging from few meters to more than 1 km in the frequency range of 10 Hz to 92 kHz. Data collected are processed to provide tensor impedance measurements, which allow full complex 2D structures interpretation (Geometrics, 2000). Nevertheless, natural signals are generally weak in the higher frequency range; hence the use of artificial signals (Vozoff, 1972; 1990 and 1991; Strangway et al., 1973; Goldstein and Strangway, 1975; Zonge and Hugues, 1991; Garcia and Jones, 2002; Zhdanov, 2009) produced by a transmitter to strengthen weak background field signals. The Geometrics Stratagem EH4 transmitter, when used, was assembled at least 300 m away from the receiver site to enable the plane wave assumption to be valid. AMT/CSAMT data were collected along four profiles; these profiles were parallel with a two by two recording pattern. They followed a NW-SE (N135°) direction based on the assumption that structural features in the Pan-African are generally E-W and/or NE-SW. The profiles were indexed from 1 to 4. The profile1, profile3 and profile 4 were 500 m in length and contained six sounding stations each, with a station-station spacing of 100 m. Profile 2 was 400 m in length with five stations at a constant separation distance of 100 m. Soundings data were acquired at each station with 25 m dipoles length both in the X and Y directions (however, dipoles length was 25 m in the Y direction and 50 m along the X direction in profile1). The X dipole was parallel to the profiles' trend. Data collected have been initially processed using the Bostick's transform, and then interpreted with Imagem software within the Stratagem EH4. We used Plot2D and Surfer 9.0 software, which provided the geoelectrical sections and pseudo sections, respectively for analyses. The frequencies ranged between 25.12 Hz to 39810 Hz, assuming a penetration depth from 8 m to 10000 m. The details presented below focus only on the upper 1000 m.

While collecting field geophysical data, some geological facts have been observed, according to outcrops available in the area. The formation is of gneissic type. The main structures that appear in are: a sub horizontal east-foliation; with an E-W maximal stretch and a N-S minimal stretch; folds, shears (Figure 2a) and fractures (Figure 2c) that include two major families, the first being NE-SW oriented and the second ESE-WSW. The double boudinage (Figure 2b) enables to highlight an extensive tectonics with a vertical maximal deformation. These structures are imprints of a multiphase deformation.

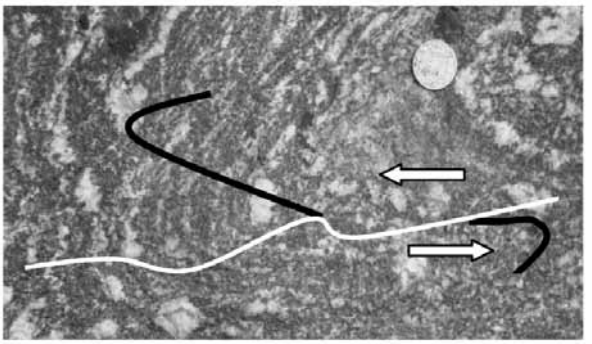

Figure 2a. Recumbent folds crossed by a dextral shear.

Figure 2b. Double boudinage

Figure 2c. ESE-WNW Fracture in the rock

RESULTS

Profile 1:

The pseudo-sections (Figure 3a & 3b) show irregularly shaped iso-contours. They exhibit dislocation patterns of blocks on one hand. They also show that conductive formations are encountered both on surface and at depth. The resistivity pseudo-section particularly presents three concentric anomalies, between OS2 and OS4, from depth to surface with a mean resistivity value of 193.0 Ω.m, forming a conductive channel. This channel may be an up well or intrusion of conductive materials. We also observe that entire near surface is conductive. However, an anomalous resistant structure centred at OS2 is found to continue downwards. The shape of isoresistivity contour

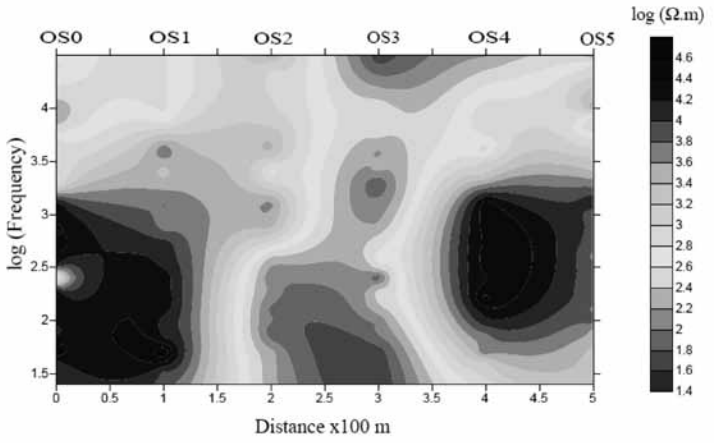

Figure 3a. Resistivity pseudo-section of profile 1

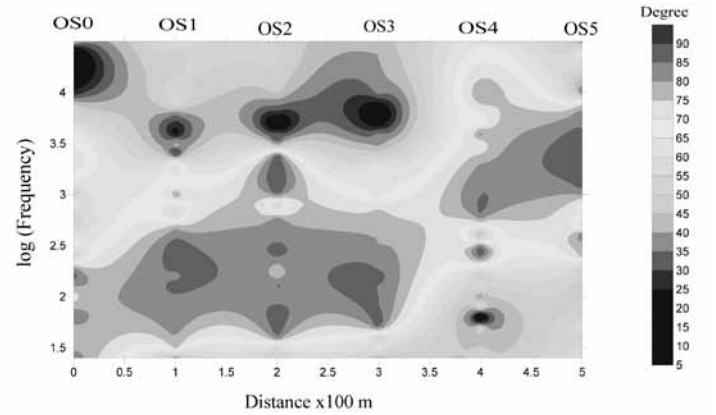

Figure 3b. Phase pseudo-section of profile 1

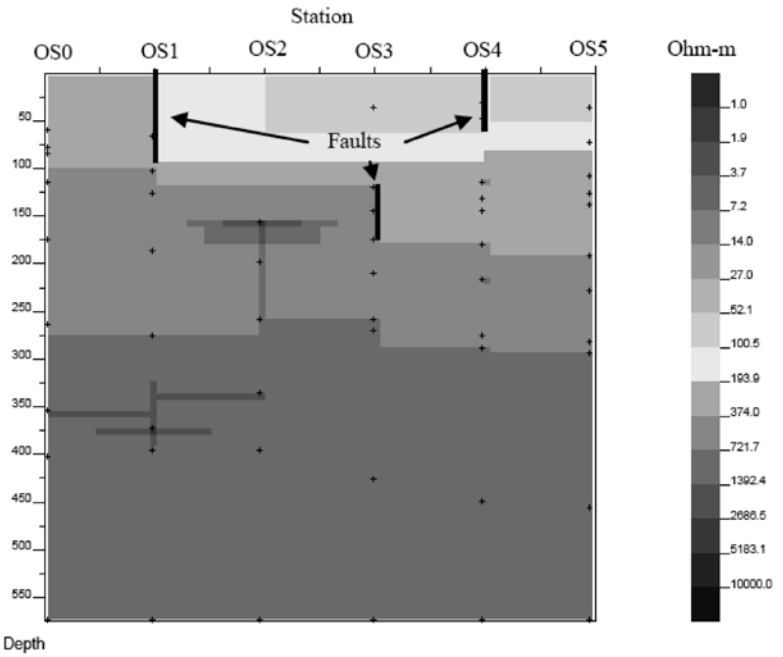

Figure 3c. Geoelectrical section of profile1. Depth in meters

lines suggests that the area might have undergone a folding process. Subvertical isoresistivity lines below OS1 and OS4 suggest the presence of discontinuities that are either faults or contacts.

The geoelectrical section plot (Figure 3c) confirms above observations. It shows two shallow conductive formations of mean resistivity 147.2 Ω.m and 284 Ω.m, respectively. The contacts between these formations are interpreted as faults at OS1 and OS4. The second formation outcrops from station OS0 to OS1. The third formation, with a mean resistivity of 547.9 Ω.m and a variable thickness, is jagged by faults at stations OS1, OS3 and OS4.It shapes like a graben. An intrusion of the underlying material at station OS2 forms a sill of 100 m wide and 25 m thick, near 150 m depth. The fourth formation, with a mean resistivity value of 1057 Ω.m, is marked by faults beneath stations OS2 and OS3. A resistive material embedded at OS0 that splits itself up to OS2, has a mean resistivity value of 3934.8 Ω.m (this fifth formation probably extends beyond 1 km depth and lays on a more resistive structure). This is not shown in the model.

Profile 2:

The apparent resistivity and phase pseudo-sections (Figure 4a & 4b respectively) exhibit a high anomalous zone (both resistivity and phase) from the beginning of the profile until almost the fourth station, where it forms vertical to subvertical contour lines characterizing a major discontinuity. The plot reveals a conductive basin-like feature between stations BE0 and BE1. The near-surface of the whole area seems to be conductive, and it suggests that the area probably experienced a tectonic activity.

The geoelectrical section (Figure 4c) exhibits a subsurface structure comprising some discontinuities, which may be faults or relief scarps. We observe, downward from the top, a conductive layer (mean resistivity 98.9 Ω.m around BE1, and 417.2 Ω.m in almost the whole area until 250 m depth). This formation is marked by many islets of resistive materials at stations BE0, BE2 and around station BE3. Another very thin formation is encountered at around 250 m depth. The fourth formation encountered has a mean thickness of 400 m with a mean resistivity value of 1119.2 Ω.m.It embeds a more resistive formation (1833.1 Ω.m), which seems to correspond to the fifth layer encountered at 725 m depth. The basement lays at 825 m depth with resistivity values ranging between 3728.1 Ω.m and 6105.8 Ω.m. A major discontinuity that seems to be a fault can be observed beneath station BE1, while others may be scarps.

Profile 3:

Analyses from pseudo-sections of profile 3 (Figure 5a & 5b respectively) exhibit two distinctive zones: a very resistive zone at depth (frequencies less than 1200Hz), contrasting with the conductive overburden (frequencies greater than 1200Hz), both separated by a narrow transition zone. Some anomalous isoresistivity values enclosed between stations NK2 and NK4 (with a paroxysmal uplift centred beneath station NK3) may correspond to an uplift of resistive materials in conductive structures. A discontinuity is also highlighted at middle depth below station NK1 and below NK4 by subvertical lines. The shape of isocontours of the overburden formation is an evidence of the folding processes that probably affected the shallow formations.
The geoelectrical section (Figure 5c) presents a first layer of mean resistivity 80.9 Ω.m with an average thickness of 100 m; the second layer has a mean resistivity of 355.5 Ωm; a third thin layer with a mean resistivity of 683.1 Ωm; the fourth layer with a mean resistivity of 1118.9 Ωm is very thick and marked by an intrusion of the underlying material between stations NK3 and NK4; the fifth formation has a mean resistivity of 1832.7 Ωm. It is deformed by the uplift of underlying formations, which have resistivity values ranging between 2275.8 and 10000 Ωm. This uplift can either be seen as an intrusion or channel of resistive materials from the basement. Some discontinuities interpreted as faults or discontinuities are highlighted below NK1 and NK4.

Profile 4:

Data from profile 4 (Figure 6a & 6b respectively) indicate presence of a prominent resistive formation at depth between stations BG1 and BG5; it appears like an intrusion of more resistive materials, compared to the surrounding. This formation is embedded within a less resistive formation covering the entire area, while some very conductive formations appear from station BG0 to station BG1 and between stations BG3 and BG5 on surface; below stations BG0 and BG3 they appear at deeper levels .The intermediate apparent resistivity values dominating the whole pseudo-section, have led us to conclude that the profile is set on an area made up of mixture of both resistive and conductive formations. The phase pseudo-section mainly exhibits a depression or subsidence along the profile from BG0 to BG5. The shape of isocontour lines on the pseudo-sections also show irregular patterns that suggest that formations have been folded.

The geoelectrical section from profile 4 (Figure 6c) outlines a near surface electrical lithology characterized by three main conductive formations. On the top of the plot, we have two formations with mean resistivity 683.4 Ωm and 1119.3 Ωm, respectively, with a fault type contact detected at station BG3; the third formation more conductive than the first two, with a mean resistivity value of 417.2 Ωm is encountered at 75 m depth below BG0.Its roof is jagged by many minor scarps ,which shape

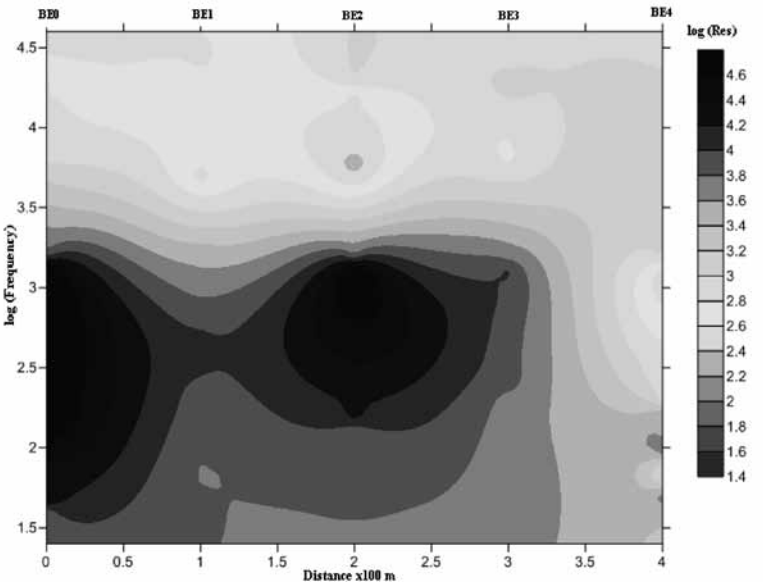

Figure 4a. pseudo-section of profile 2

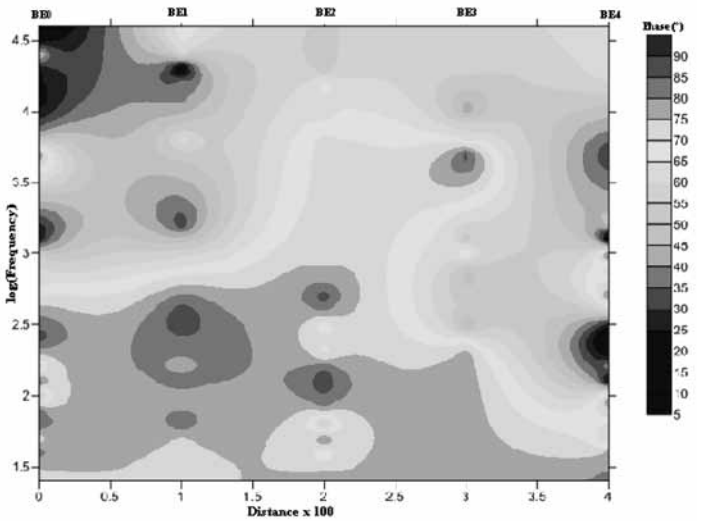

Figure 4b. Phase pseudo-section of profile 2

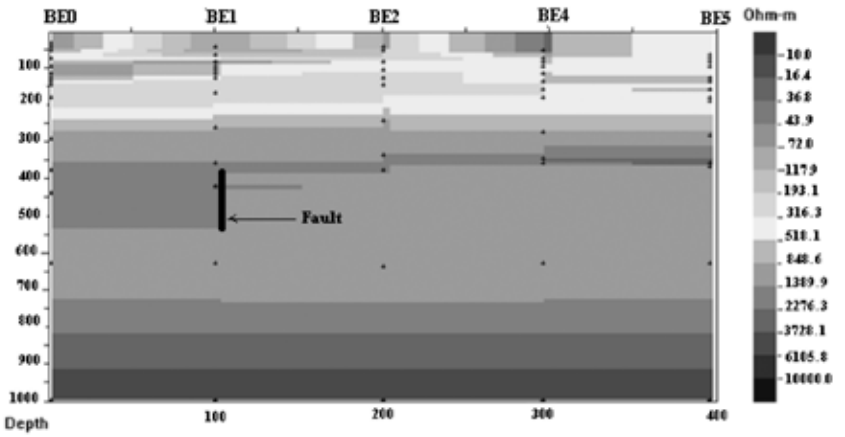

Figure 4c. Geoelectrical section of profile 2. Depth in meters.

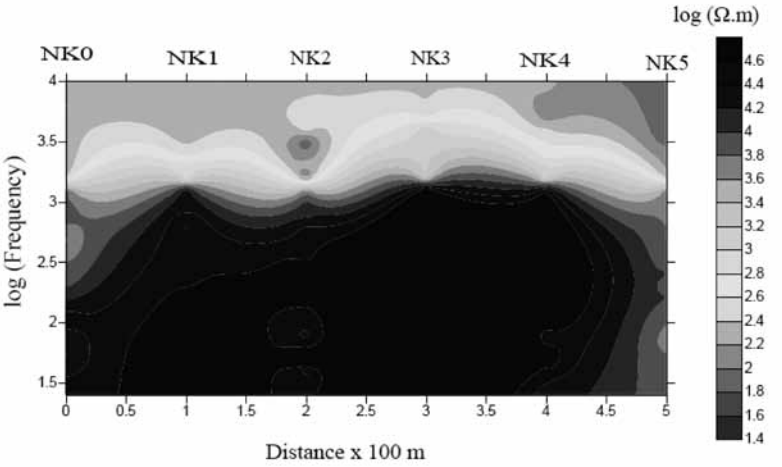

Figure 5a. Resistivity pseudo-section of profile 3

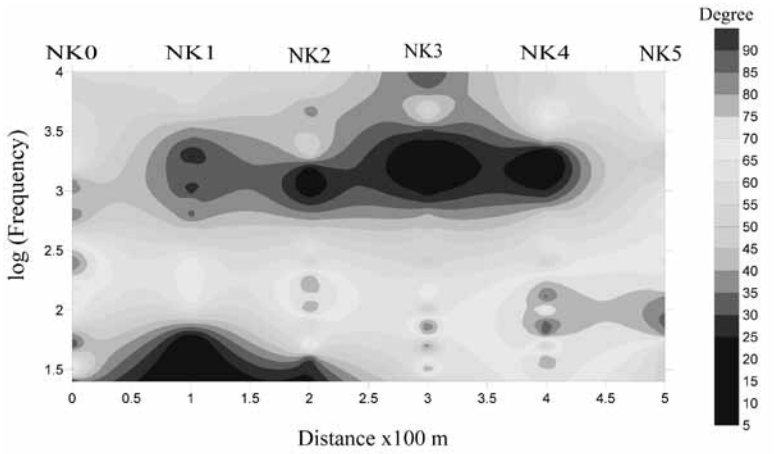

Figure 5b. Phase pseudo-section of profile 3

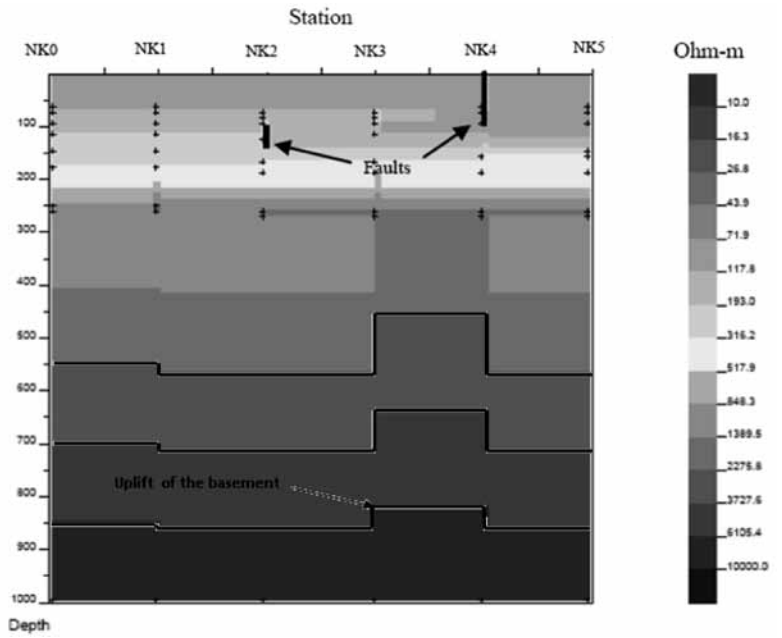

Figure 5c. Figure 5c. Geoelectrical section of profile 3. Depth in meters.

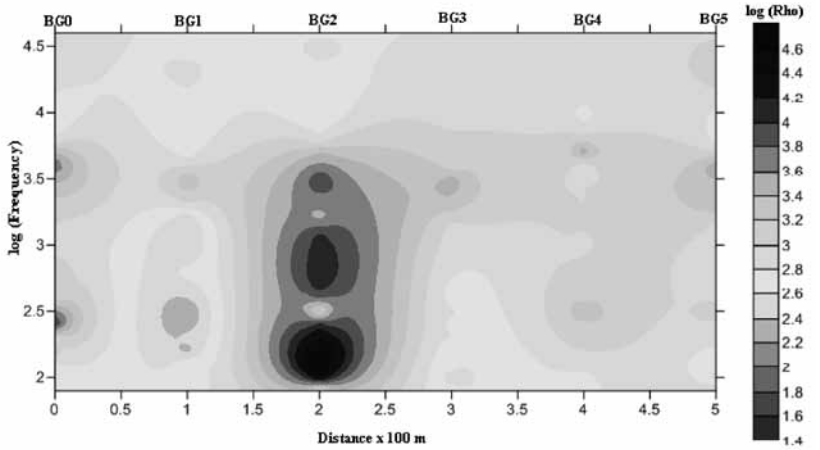

Figure 6a. Resistivity pseudo-section of profile 4

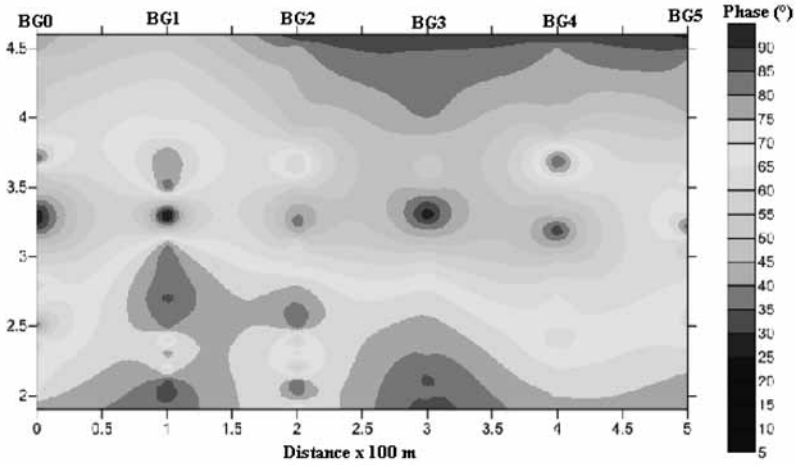

Figure 6b. Phase pseudo-section of profile 4

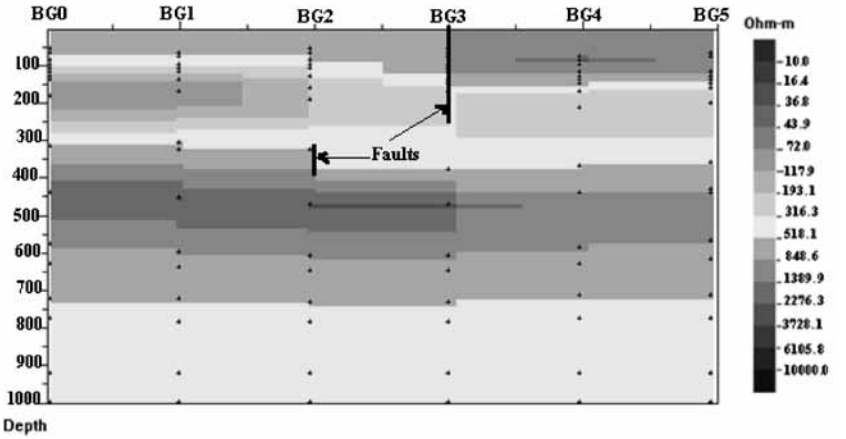

Figure 6c. Figure 6c. Geoelectrical section of profile 4. Depth in meters

it like downstairs from BG2 to BG5 while a fault type discontinuity is identified around 300 m depth under BG2; the first formation is encountered again at 300 m and extends up to 750 m depth enclosing the second formation (350 m to 600 m depth) within which a resistive structure (3002.2 Ωm mean resistivity) is embedded from BG0 to BG3 with a mean thickness of 100 m (from 400 m to 500 m depth). It appears from the geoelectrical section that there is a graben-like structure in near subsurface from BG2 to BG5, as shown in the phase pseudo-section.

DISCUSSION

AMT analyses

Analyses of results from the current study suggest that profiles 1, 2 and 4 are located on the same geological environment, where as profile 3 on a different environ. Soundings from profiles 1, 2 and 4 are made on fairly conductive areas, with a range of resistivity values that correspond to a weathered gneissic environment (Palacky, 1987). Profile 3 seems to be located on micaceous quartzites. It appears that the study area is composed of a mixture of both very resistive and conductive formations. The basement appears at 1400 m in profile 1, 825 m in profile 2, 550 m in profile 3 and deeper (more than 1400 m) in profile 4. This indicates that the basement rises up in some parts, while it collapses in other parts. This in turn might have induced thickening of overlying materials. The observed uplift of the basement may also be attributed to cooled intrusions beneath it. The subsidence and uplift of the basement probably attest the existence of a depressed structure (graben or basin), as evidenced by pseudo-sections. This shows a rugged subsurface structure of the area. The roughness of this subsurface structure is also emphasized by the shape of isocontour lines on all the pseudo-sections, hence suggesting that the formations in the area have been folded. The folding process is originated from a shortening,a priori, parallel to the direction of all the profiles (N135°). This shortening was caused probably by the collision between the CC and the CAPAB. In addition, many faults, scarps and fractures have been inferred in all the profiles. Some of the faults show significant throw (e.g. 150 m below station OS4 in profile1; 50 m and 100 m beneath BG2 and BG3 respectively in profile 4; 175 m below BE1 in profile 3).

As, the general trend of profiles is N135°, faults and fractures highlighted are generally SW-NE to WSW-ENE oriented through other faults with different trends (E-W direction probably). The conductive channel seen on profile 1 (figure 3a) could be either an intrusion or an active fault. The shape of apparent resistivity isocontours, faults and fractures detected by our study suggest that tectonics of the study area occurred in brittle to brittle-ductile conditions, as in the Yaoundé Group. Besides, the geoelectrical section of profile 4 shows that resistive formations alternate with conductive ones, suggesting a reversal phenomenon within superficial formations in the area. This reversal suggests operation of the folding and thrust processes of the Yaoundé series' nappes onto the CC. The investigated area is located near the latitude N04°, the CC/CAPAB limit identified by previous geophysical studies (Tadjou et al., 2008; Ndougsa et al., 2010; Basseka et al., 2011 and Shandini et al., 2012). It is considered as a major discontinuity oriented in E-W direction. This discontinuity limit is assumed to be a suture line between those aforesaid units below the CAPAB. The CC subducts approximately from 50 to 100 km beneath the CAPAB. Resistivity values show the signature of rock mixture from the Pan African (conductive) and the CC (resistive) materials. It is seated at the transition zone between the CC and the CAPAB, as suggested by Meying et al. (2013), over a closed eastward (Ayos-Nguelemendouka) area. The current geophysical analysis could not clearly detect events coeval to the CC/CAPAB limit (E-W faults), compared to the geoelectrical model defined by Tadjou et al. (2008). In Tadjou et al.(2008) model, the CC is a resistive block in the south and the CAPAB a conductive block to the north.

The study has highlighted folding patterns within the Yaoundé-Nkolafamba subsurface at shallower depth. The folding system occurs along profiles strike i.e. they are locally caused by NW-SE to N-S compressional movements of the crustal blocks. This result is consistent with those from previous AMT investigations (Ndougsa et al., 2011 and Meying et al., 2013), which highlighted folding at the scale of the Yaoundé series, but eastward of the present study. The present study shows significant geoelectrical shallow discontinuities. These shallower discontinuities oriented from SW-NE to WSW-ENE (perpendicular to the profiles which are directed NW-SE), are interpreted as faults and folds. These folds may constitute local signatures of deep faults (along the same broad directions). Such signatures were also noticed both by Basseka et al. (2011) and Shandini & Tadjou (2012), through a gravity study that encompassed the present sudy area (from nearly N02° to N05° latitudes and from E11° to 13° longitudes). The aforesaid NE-SW to ENE-WSW events form a NE trending structural lineament (Figure 7).This is coeval to the NE secondary tectonic line suggested by Meying et al. (2013).It is linked to the setup of the Centre Cameroon Shear Zone (CCSZ), at a regional scale. The NE tectonic lineament is assumed to be a strike-slip fault system. This is in agreement with earlier geoelectrical studies by Mbom Abane (1997). It proves the existence of E-W and NE-SW oriented wrench fault sets: (a) the first one extends as far as to the Abong-Mbang area, east of Ayos, and (b) the second one runs parallel to the trend of the Trans-African strike-slip. The finding supports the results from the isoresistivity map analyses , carried out by Njinti-Nfor et al. (2001), over an adjacent area (Akonolinga/Abong-Mbang). The study also brought out presence of, E-W and NE-SW trending wrench faults.

In addition, the study reveals the occurrences of uplifts and collapses of the basement in the Yaoundé-Nkolafamba area. Taking into consideration the importance of the highlighted faults and folds that exhibit vertical to subvertical dips, we infer that the subsurface topography

is probably controlled by grabens and horsts. According to the coverage of the profiles (oriented NW-SE), the basin and horst-like subsurface structures are elongated in the SW-NE direction. Gravity studies (Shandini at al., 2010; Basseka et al., 2011 and Shandini and Tadjou, 2012) highlighted presence of similarly trending features .It is further inferred that the basement collapse occurred during the CC and the CAPAB collision process. We also brought in to light qualitatively presence of a conductive channel from depth to surface on profile 1 pseudo-section, which can be either seen as an intrusion or a signature of an active faulting process. In the case of an intrusion, this result is in agreement at the local scale, with Basseka et al. (2012) who indicated the presence of granitic intrusions in the northern margin of the CC. If the faulting process is admitted, this channel correlated with horizontal movements linked to shearing processes along the NE-SW direction, as seen by Basseka et al. (2012). These NE shears correspond to horizontal trans-current movements occurring in the Yaoundé series coeval to the CCSZ. The NE tectonic lineament (Figure 7) is correlated to the CCSZ and inferred from the conductive channel as previously mentioned by some authors (Ndougsa et al., 2010; Bisso et al., 2004), who predicted the seismic activity generated on the Sanaga fault (SF) in 2005. The Yaoundé series investigated by AMT soundings over the Yaoundé-Nkolafamba area has provided evidence of collapses and uplifts of the basement. The study also helped in imaging near-subsurface folds and faults. The faults span from the SW-NE to WSW-ENE directions and have vertical to subvertical dips (i.e. they are nearly to normal faults).These faults, when considered together and correlated with geological observations, are linked to the NE shallow lineament (Figure 7) coeval to the setup of the CCSZ characterized by the Sanaga Fault, which is passing north of the study area. The results therefore are in agreement, at the local scale, with the previous geophysical studies. The folding and faulting processes bear witness to intense tectonic movement in the brittle to brittle-ductile conditions that have affected the area at shallow depths. These facts support presence of the multistage tectonic activities (including the CC/CAPAB collision) that occurred in the area, as well as in the whole CAPAB or the Mobile belt at the regional scale. The length of profiles (500 m) as well as the use of high frequencies may constitute a critical limitation to the current geophysical analysis. Inspite of this limitation, the study has detected new faults and clearly imaged folds affecting the near subsurface. These results are supported both at the local and the regional scale by previous geophysical studies , namely the gravity and farther located magnetotelluric (MT) studies.

Geological data integration

Geological data collected through direct observations during the field campaign coincides with results obtained from AMT analyses. The interpretation of AMT data suggests that profiles were laid on a terrain of gneissic and quartzite formations. This fact is supported by the presence of gneissic formations outcrops. These gneisses are of three types: clinopyroxene amphibolic gneiss, biotite gneiss and garnetiferous biotite gneiss. The gneissic fabric presents a double boudinage (Figure 2b) with E-W maximal stretch (B_1) and an N-S minimal stretch (B_2). The folding patterns, corresponding to another deformation stage, are also observed. These folds are cross-cut by many shears (Figure 2a). Besides, many veins and families of fractures characterising the fourth deformation stage have been recorded. Among these fractures' families, the most interesting sets follow the NE-SW and ESE-WNW trends with vertical to subvertical dips. The NE-SW set correlates the faults highlighted by the AMT interpretation (Figure 7). The ESE-WNW family may represent faults nearly parallel to the AMT profiles. The folding and faulting underline the presence of medium to high grade conditions experienced by the area .These conditions facilitated the amphibolite and the granulites facies formations, characterized respectively by amphibolic gneisses, and, biotite gneisses and biotite garnetiferous gneisses, which are herein reported. The strength of tectonic forces occurred in the area has been recorded in the surrounding topography. Indeed, the study area topography is very rough with too many undulations .Even rivers like the Afamba and Ato kept those imprints as they flow in the NE direction. The double boudinage helped to bring to light role of an extensive tectonic activity that resulted in the NE-SW tectonic line suggested by the AMT study. The NE-SW line may constitute strike slip system, owing to the shears observed (Figure 2a). At the outcrop scale, the Yaoundé-Nkolafamba area experienced many deformation stages, as reported on the entire PanAfrican belt in southern Cameroon.

In agreement with geological studies, the faulting system proposed correlates at a local scale, with the SW-NE faults within the Yaoundé domain (significant to the Awaé-Ayos strike-slip shear zones in the late Pan-African tectonics)- (Olinga et al., 2010). At the regional scale, the fault system seems to be correlative with the Centre Cameroon Shear Zone, whose local segment is the Sanaga Fault. The strain field that affected the area is on the scale of that of Central African Fold Belt (Olinga et al., 2010) and consistent with the northeast-southwest Trans-Saharan collision system proposed by Mvondo et al. (2007 & 2009). Further, the NE-SW tectonic line proposed by this study

is within the Yaoundé series, imprint of a remarkable extension due to dextral wrenches still occurring in the African plate as witnessed by earthquakes, which struck the Yaoundé region in March, 2005 (Ndougsa et al., 2010). This extension is the modern outcome of the breakup of Gondwana and probably a consequence of the currently occurring NE movements of the African plate towards the Eurasian plate. The NE-SW tectonic line is then correlative to the general NE-SW trending lineaments system running W-E from the Gulf of Guinea to the Aden Gulf (Genik, 1992; Mvondo et al., 2007 & 2009; Olinga et al., 2010).

CONCLUSIONS

The AMT imaging has enabled to highlight folds that affected near subsurface formations. They are assumed to be caused by the Congo Craton/Panafrican collision.

Some geoelectric sections show graben-like topography due to the basement collapses and upward transport of resistive materials to shallow depth, forming basement uplifts.

The analyses have outlined a family of hidden strike-slip normal faults, which form a shallow structural line oriented NE-SW. This faulting network suggests extensive tectonic movement in the Pan African Yaoundé series, and correlates with the Centre Cameroon Shear Zone, while linked to the general NE-SW trending lineaments system running west-east from the Gulf of Guinea to the Aden Gulf.

The fault system, the uplifting of the basement and folding support the intense multistage tectonic activity, including the CC/CAPAB collision that occurs in the Yaoundé-Nkolafamba area, at the regional scale. The seismic activity recorded in Yaoundé in 2005 suggests ongoing tectonic activity. The CC and the CAPAB continue to collide, as part of continent-continent convergence activity.

ACKNOWLEDGEMENTS

The authors respectfully thank Mr Ava Christophe, Country Manager of Harvest Mining Corporation for the logistical support provided to facilitate the AMT survey. Thanks are due to the anonymous reviewer and Editor of JIGU for valuable remarks that enabled to improve the quality of this paper.

REFERENCES

Basseka, C. A., Shandini, Y. and Tadjou, J.M., 2011. Subsurface structural mapping using gravity data of the northern edge of the Congo craton, South Cameroon, Geofizika, v.28, pp: 229-245.

Bessoles, B. & Trompette, M., 1980. Géologie de l'Afrique. La chaîne Pan-Africaine « Zone Mobile » d'Afrique Centrale (partie sud) et zone mobile soudanaise, Mémoires du Bureau de Recherches Géologiques et Minières,Orléans, v.19, pp: 396.

Bisso D., Manguelle-Dicoum E., Ndougsa-Mbarga T., Tabod C. T., Njandjock N. P., Njingti N., Tadjou J. M. and Essono J., 2004.Geophysical Determination of the Sanaga Fault using Audio-magnetotelluric soundings in the Ebebda region, Cameroon, Segmite International, v.1, no.1, pp: 31-34

Bostick, F. X., 1977. A Simple Almost Exact Method of MT Analysis, Workshop on Electrical Methods in Geothermal Exploration, US Geological Survey, Contract No.14080001-8, pp:174-183.

Cagniard, L., 1953. Basic Theory of the Magneto Telluric Method of Geophysical Prospecting, Geophysics, v.18, no.3, pp: 605-635.

Champetier De Ribes, G. and Aubague, M., 1956. Notice explicative sur la feuille Yaoundé-Est (1/500 000), Bulletin Direction des Mines et de la Géologie, Yaoundé, Cameroun, pp: 35.

Feumoe Siyapdje, A.N., Ndougsa Mbarga, T., Manguelle-Dicoum, E. and Fairhead, J. D., 2012. Delineation of tectonic lineaments using aeromagnetic data for the south-east Cameroon area. Geofizika. v.29, pp: 175-192.

Garcia, X. and Jones, A.G., 2002. Atmospheric sources for audio-magnetotelluric (AMT) sounding, Geophysics, v.67, no.2, pp: 448-458.

Genik, G. J., 1992. Regional framework, structural and petroleum aspects of rift basins in Niger, Chad and the Central African Republic (C.A.R.), Tectonophysics, v.213, pp:169-185.

Geometrics, 2000. Operation manual for Stratagem systems running IMAGEM, ver. 2.16, Geometrics Printing Press, San Jose, California, pp: 16.

Goldstein, M.A. and Strangway, D. W., 1975. Audio-frequency magnetotellurics with a grounded electric dipole source, Geophysics, v.40, no.4, pp: 669-683.

Manguelle-Dicoum, E., Nouayou, R., Bokossah, A. S. and Kwende-Mbanwi T. E., 1993. Audio-magnetotelluric Soundings on the Basement-Sedimentary Transition Zone around the Eastern Margin of the Douala Basin in Cameroun, Journal of African Earth Sciences, v.17, no.4, pp: 487-496.

Manguelle-Dicoum, E., Bokossah, A.S., and Kwende-Mbanwi, T.E., 1992. Geophysical evidence for a major Precambrian schist-granite boundary in Southern Cameroon, Tectonophysics, v.205, pp: 437-446.

Mbome Abane, S., 1997. Investigations géophysiques en bordure du Craton du Congo et implications structurales. Thèse de Doctorat es sciences, Université de Yaoundé 1., pp: 180.

Meying, A., Ndougsa-Mbarga, T., and Manguelle-Dicoum, E., 2009. Evidence of fractures from the image of the subsurface in the Akonolinga-Ayos area (Cameroon) by combining the Classical and the Bostick approaches in the interpretation of

The Egyptian Journal of Remote Sensing and Space Sciences 22 (2019) 37–47

HOSTED BY

Contents lists available at ScienceDirect

The Egyptian Journal of Remote Sensing and Space Sciences

journal homepage: www.sciencedirect.com

Research Paper

The Sangmelima granite-greenstone belts (South Cameroon): Integration of remote sensing and aeromagnetic data for structural interpretation

Akame Joseph Martial [a,e,f,*], Assembe Stéphane Pactrick [b], Zo'o Zame Philemon [a], Owona Sébatien [d], Ndougsa Mbarga Théophile [c,e], Azia Giles Abuara [e], Mvondo Ondoa Joseph [a]

[a] Department of Earth Sciences, Faculty of Science, University of Yaoundé I, PO Box 812, Yaoundé, Cameroon
[b] Department of Physics, Faculty of Science, University of Yaoundé I, PO Box 812, Yaoundé, Cameroon
[c] Department of Physics, Advanced Teacher's Training College University of Yaoundé I, PO Box 47 Yaoundé, Cameroon
[d] Department of Earth Sciences, Faculty of Science, University of Douala, P.O. Box. 24157, Cameroon
[e] Department of Geology in the Ministry of Mines Industry & Technological Development of Cameroon, Cameroon
[f] Laboratoire G-Time (Géochimie: Tracage isotopique, minéralogique et élémentaire) Université Libre de Bruxelles 50, Av. F.D. Roosevelt CP 160/02 B-1050 Brussels, Belgium

ARTICLE INFO

Article history:
Received 8 January 2017
Revised 22 November 2018
Accepted 29 November 2018
Available online 13 December 2018

Keywords:
Remote sensing
Aeromagnetic
Lineament
Structural
Archeaen
Sangmelima
Cameroon

ABSTRACT

The integration of geology, geophysics and remote sensing data was used to map the Sangmelima granite-greenstone belt terrain located in the South Cameroon. The region was not easily accessible, because of dense vegetation and thick lateritic overburden. Aeromagnetic data were help in mapping new possible small greenstone belts and structural features in this area. Many of the identified lineaments are interpreted to represent fracture/fault zones, some of strike-slip faults. The NE–SW, NW–SE, N–S and E–W are the main revealed from remote sensing processing; while the NE–SW, E–W to ESE–WNW, NW–SE and N–S are the dominant structural trends revealed from aeromagnetic data. We distinguish three deformation events within the Sangmelima area: D_1 is recorded by a sub-vertical penetrative S_1 foliation bearing steeply plunging stretching lineations. D_2 overprints D_1 structures with tight-to-isoclinal folds with associated foliation, N160°–175°E and N05°–25°E ductile shear zones, indicating ENE–WSW shortening. The D_3 strike slip shearing is likely the result of the Eburnean deformation phase. The mafic dykes are striking NE–SW, N–S and NW–SE, and field evidence and airborne magnetic data suggest that some of them intrude preexisting structures. Many faults/fractures might have originated during previous deformation phases and they were only reactivated during the pan-African events.

1. Introduction

The Sangmelima Archean granite greenstone belt were studied to better understand the evolution of geological structures and their bearing on mineral potential. The Sangmelima region is located in the wet tropical forest on Archean flattened bedrock whose altitude ranges between 600 and 900 m, with a thick weathered overburden, vegetation, and isolated granitic domes (Akame et al., 2014). The integration of airborne geophysics, remote sensing data, and field observations was used to aid geological mapping and ground structural. The efficiency of these integration was demonstrated in Precambrian terrains in Australia, West Africa, and Canada (Betts et al., 2003; Direen et al., 2005; Peschler et al., 2006; Aitken et Betts, 2009; Stewart and Betts, 2010; Metelka, 2011; Pilkington and Keating, 2009). The data integration approach provided efficient results in a recent study involving the Dalema region in West-Senegal (Moussa and Tahar, 2013), or Wadi Allaqi area, South Eastern Desert of Egypt (Eldosouky et al., 2017). The field observations and measures as well as laboratory data were used to constrain and validate the results.

The study also involved investigation of the Ntem Archean Complex that is part of the Congo Craton in South-Cameroon, and occurring in the Sangmelima region (Fig. 1). The Complex was reported to be less understood compared to its Brazilian geologic equivalent, the Sao Francisco Craton as well as the West and the South African cratons (Metelka, 2011; Block et al., 2012; Dabo

Peer review under responsibility of National Authority for Remote Sensing and Space Sciences.

* Corresponding author at: Laboratoire G-Time (Géochimie: Tracage isotopique, minéralogique et élémentaire) Université Libre de Bruxelles 50, Av. F.D. Roosevelt CP 160/02 B-1050 Brussels Belgium

E-mail addresses: akamejosephmartial@gmail.com, akamejosephmartial@yahoo.fr (A. Joseph Martial).

https://doi.org/10.1016/j.ejrs.2018.11.005
1110-9823/

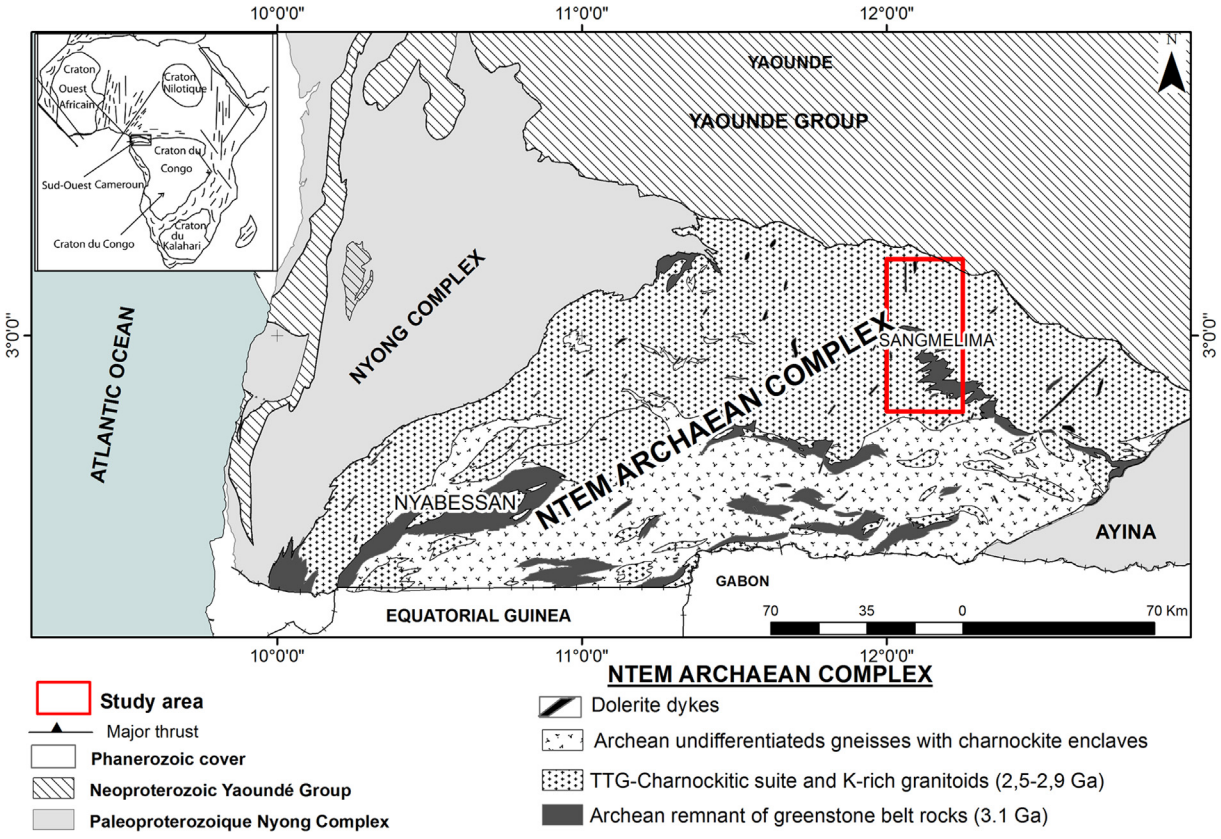

Fig. 1. Simplified geological map of the south-west Cameroon and location of the study area (Maurizot et al., 1986).

and Aïfa, 2013; Teixeira et al., 2017, and references therein). The results of the study highlighted various tectonic structures: fractures, faults, folds, and foliation related to Archean and Precambrian (Eburnean) tectono-magmatic events.

2. Geological setting

The Ntem Complex represents the north-western part of the Congo Craton in Central Africa(Lasserre and Soba, 1976; Maurizot et al., 1986; Caen-Vachette et al., 1988; Tchameni et al., 2000), comprising the Paleoproterozoic Nyong Unit to the north-west and the Archean Ntem Unit to southeast (Fig. 1). It is limited to the north by a major thrust that marks the contact with the Pan-Africanorogenic belt (Yaounde group). The Nyong Unit consists mainly of metasedimentary and metavolcanic rocks as wellas some syn- to late-tectonic intrusive rocks (Toteu et al., 1994). The Ntem Unit includes an Intrusive Series and a Banded Series BandedSeries as well as minor amount of supracrustal rocks (Maurizot et al., 1986; Shang et al., 2004a; Pouclet et al., 2007; Tchameni et al., 2004). The Intrusive Series is essentially exposed in the northern part of the Ntem Complex and is strongly mylonitized and retrogressed along the thrust boundary with the Pan-African Yaounde Group (Takam et al., 2009). It is dominated by a magmatic charnockitic suite and a TTG suite. The Banded Series outcrops over the southern part of the Ntem Complex and is dominated by strongly deformed granitic gneisses. Charnockitic enclaves are found within the gneisses of the Banded Series. Supracrustal rocks include banded iron formations (BIF) and sillimanite-bearing paragneisses occurring as xenoliths in the TTG; they are thought to be the remnants of greenstone belts (Suh et al., 2008; Chombong and Suh, 2013). K-rich granitoid rock sand dolerite dikes intrude the TTG and greenstone belts (Toteu et al., 1994; Tchameni et al., 2000; Shang et al., 2010).

Petro-structural studies suggest two major episodes of deformation in this geological domain. (*1*) The first deformation episode is characterized by vertical foliation, stretching and vertical lineation and isoclinal folds. These structural elements are correlated with successive emplacements of the mid-Archaean granitoids (Shang et al., 2004b), considered to be diapiric by Shang (2001) and Tchameni (1997). (*2*) The second major deformational event is marked by the development of sinistral shear planes of N0°–N45°E and of partial melting of TTG and of the supracrustal country rocks with the generation of various granites. This event is described as post-Archaean and postcharnockitic migmatization by Nsifa and Riou (1990) but is now thought to be late Archaean: 2666 Ma (e.g. Tchameni et al., 2000) and 2721 Ma (e.g. Shang et al., 2007).

3. Methodology

3.1. Processing of remote sensing data

The satellite imageries used were: (1) the 213–906 Landsat 7 ETM+ scene of March 18th, 2001 (Path 185 and Row 058); and (2) SRTM (Shuttle Radar Topography Mission) 90 m (Path: p184/SRTM_ff03_p184r058). The Landsat image was first orthorectified (rectification of the raw image distortion) then directly imported as a georeferenced on a GIS platform.

To enable the detection of lineaments, ETM+ channels 4, 5, and 7 have been chosen because of their spectral and spatial characteris-

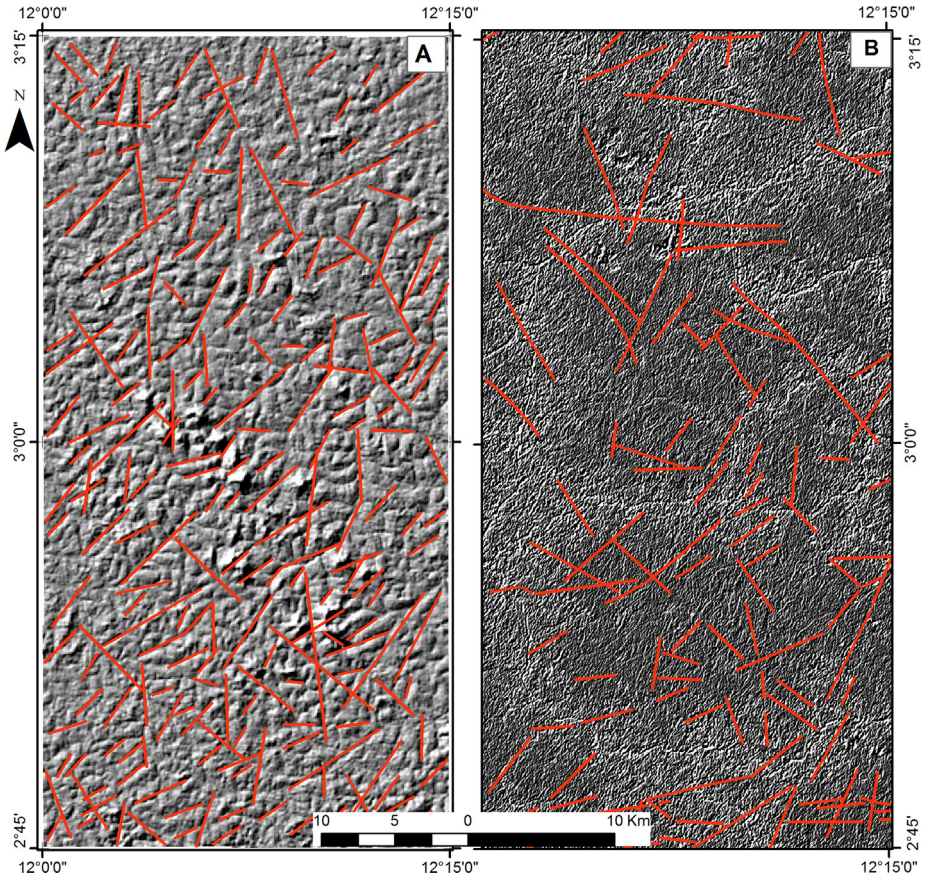

Fig. 2. Images from remote sensing of the study area with the main lineaments identified: (A) A shaded relief of the STRM; (B) A window of the gradient filter (Yésou et al., 1993).

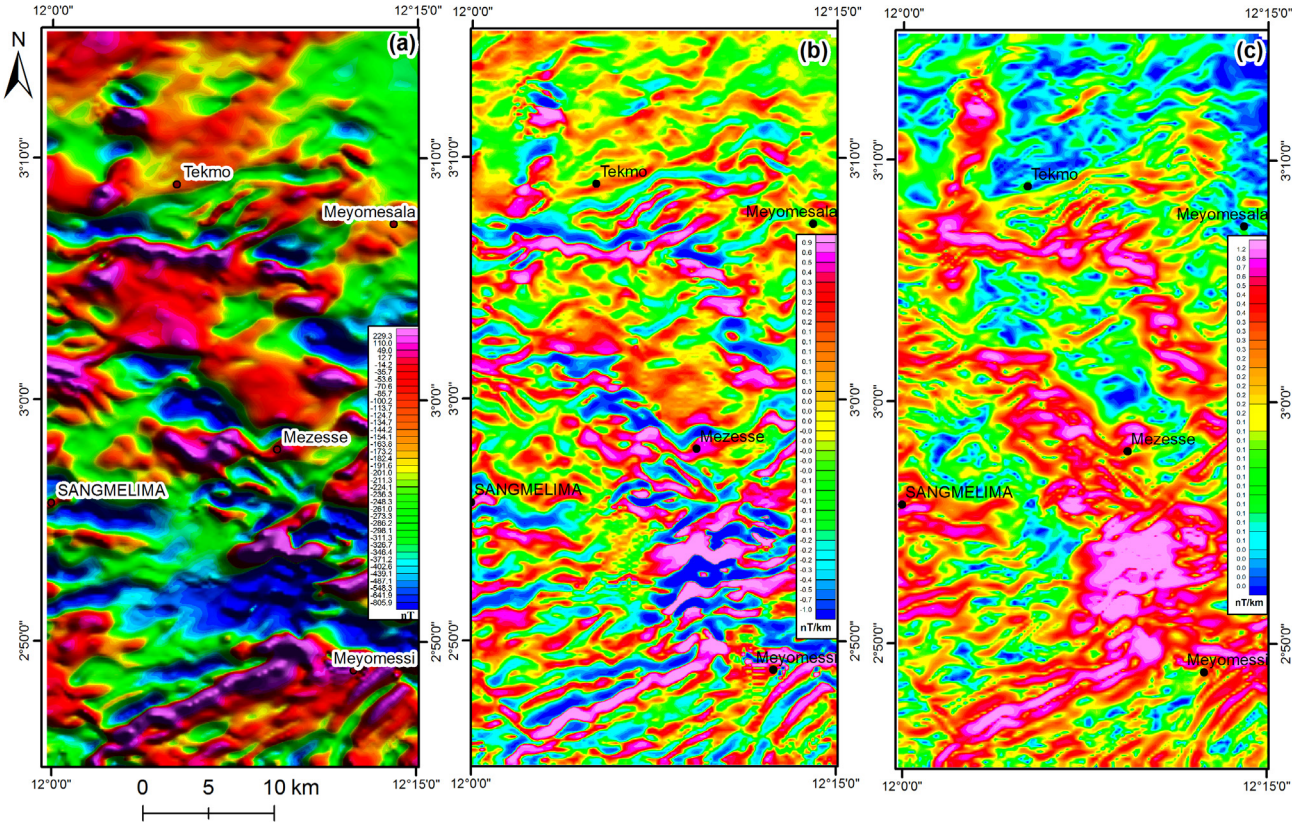

Fig. 3. **(a)** Total magnetic intensity reduced to the equator of the Sangmelima. **(b)** First vertical derivative of the total magnetic intensity reduced to the equator. **(c)** First horizontal derivative of the total magnetic intensity reduced to the equator.

tics (30 m). The principal components analysis (PCA) of pre-processed channels produced new channels for which only the first component could deliver efficient results. Linear structures were most visible on the first principal component (PCA1) than on a multispectral image. The discontinuities were enhanced through the application of both the Sobel filter on a 7×7 window along the N00°, N45° and N315° directions, and the gradient filtering from Yésou *et al.* (1993) to ETM + 5, ETM + 7, ETM + 5/ETM + 4 and PCA1 channels. The study focused on structural lineaments (Fig. 2).

Maps of the shaded relief, of the slope gradient and of the slope orientations were particularly helpful to highlight breaks-in-slope, ideal to detect tectonic features, such as faults characterized by a linear topographic step. Therefore, major lineaments/fractures probably faults, topographic differences are

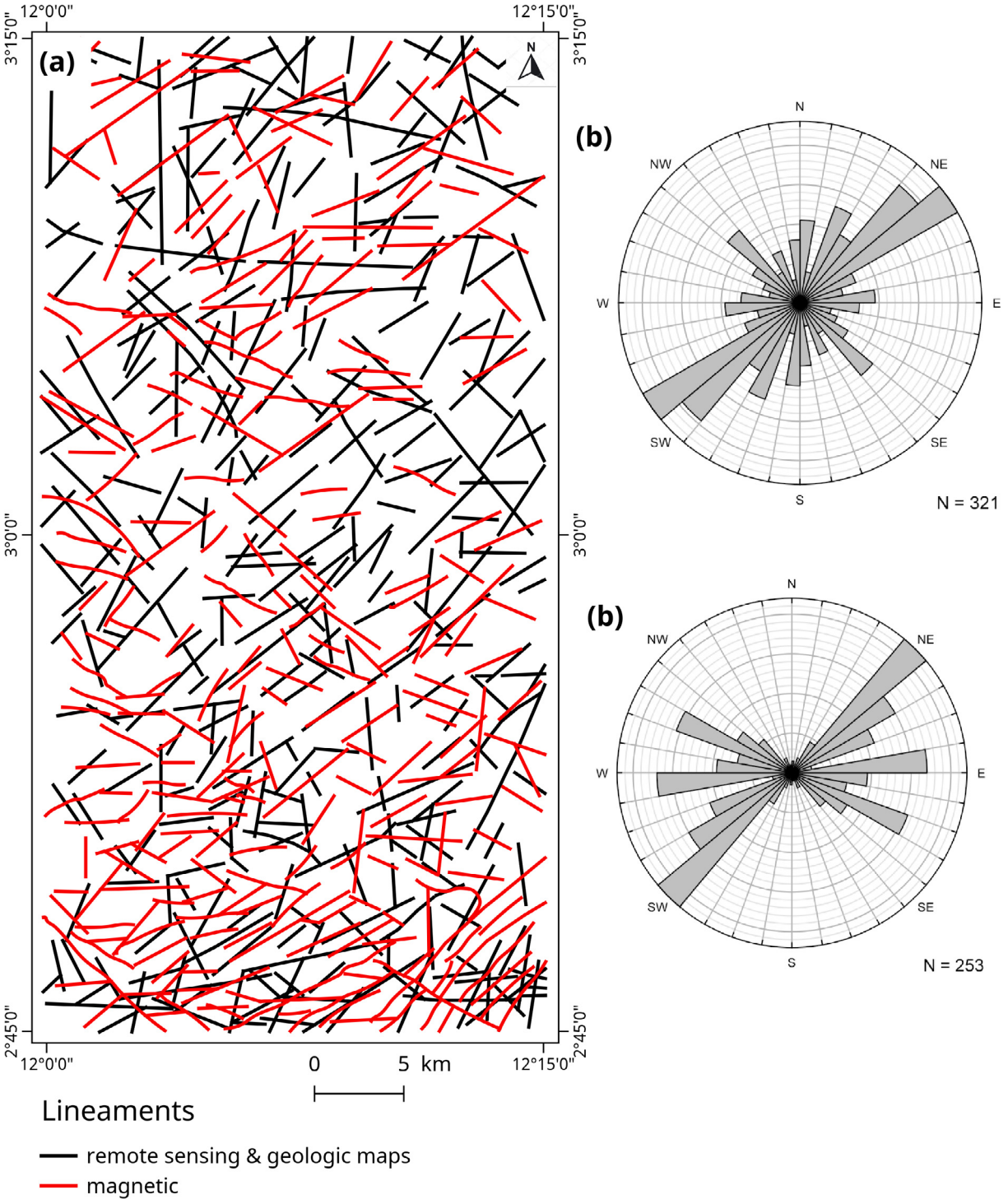

Fig. 4. Lineaments extraction and analysis. (a) Lineaments of Sangmelima revealed from remote sensing, aeromagnetic and geologic data; (b) and (c) rose diagrams show the distribution of the remote sensing and magnetic lineaments.

easily seen on Shuttle Radar Topography Mission; since these features cover large areas (Fig. 2). The lineaments were manually extracted by photo-interpretation and classified using the ArcGis 10. Both the natural and cultural artefacts (roads, power lines, farms and forest boundaries) were removed from the interpreted lineaments. The frequencies of the remote sensed lineaments were analysed to highlight their main directions for comparison with field observations.

3.2. Aeromagnetic data set and processing

The digital aeromagnetic dataset used in this study was a compilation of various digitalised contour maps of wide regional aeromagnetic surveys. The data was collected under taken under a cooperative agreement between the government of Canada and that of the Federal Republic of Cameroon (Patterson and Watson Ltd, 1976). The aeromagnetic survey was flown in the year 1970, with a line spacing of between 750 m and a mean flight height of 235 ± 20 m (Sheet: NA-33-XIII-1 and NA-33-XIX-13. 1971). The data was manually contoured to generate magnetic intensity maps at a scale of 1:50 000 Magnetic intensity values were extracted with ArcGIS. Magnetic data was processed and filtered with Geosoft Oasis Montaj software version 8.2. The residual total field was obtained by subtracting the International Geomagnetic Reference Field (IGRF). Reduction to Equator (RTE) transform was applied to the Total Magnetic Intensity (TMI) grid using an inclination of −18.59°and declination of −6.22° (Milligan and Gunn, 1997). To enhance the magnetic linear features associated with the Precambrian structures, frequency filtering operators were applied on the RTE to create the first vertical derivative image, analytic signal, and Tilt angle maps (Fig. 3). The resulted images were mainly interpreted individually using the ArcGIS.

4. Results

4.1. Remote sensing lineaments

A total of 321 lineaments were identified from the remote sensing data (Fig. 4a). The maximum linear length detected was 12189 m, while the minimum length was 508 m (average 3289 m). Both data sets are characterized by a heterogeneous spatial distribution of the lineaments. In the southern part of the study area an apparent higher lineament density is observed in both data sets. The rose diagram showing their orientations (Fig. 4b) indicates two major trends: NE–SW (035−065°) and NW–SE (120−140°). The N–S and E–W systems are less significant and can be identified throughout the whole domain. In the southern domain, the E–W lineaments do not seem to cross-cut the NE–SW fractures network, but rather to articulate towards them. The N–S network is sharply secant compared to the previous one.

4.2. Interpretation of aeromagnetic data

The total magnetic field map showed heterogeneous variations of the magnetic amplitude which span from −805.9 to 229.3 nT. The prominent variation in magnetic intensity was located at the centre of the map while the other anomalies were set within a NE trending zone. The main zone extended along the NW to SE direction and it corresponds to the greenstone belts and associated granitoids (Fig. 3a). The first vertical derivation (FVD) displays several dominant trends NE–SW and WNW–ESE to NW–SE, the belts zone was outline by NW strike lines boths (Fig. 3b). In the southestern area (Meyomessi) tight folded structures in supracrustal rock are clearly seen on color shaded relief image of FVD (Fig. 3b). The faults/fractures were traced easily along of linear

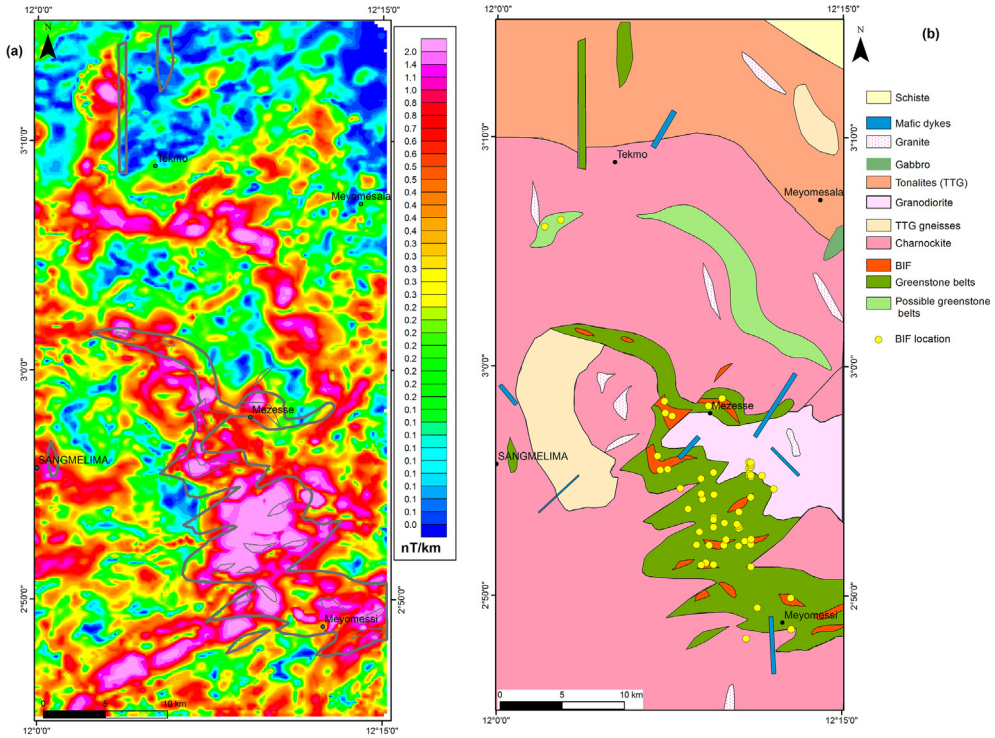

Fig. 5. (a) Greenstone belt and associated iron formation superimpose on the Analytical Signal map. (b). Lithological map, potential target for new green rock belts and iron formation.

features which are related to the trend of faults in the horizontal derivatives map (Fig. 3c). The frequency analysis of the lineaments directions showed a high frequency of NE–SW and E–W to ESE–WNW lineaments followed by the dominance of the NW–SE direction (Fig. 4a–c). The frequencies of N–S lineaments were lower (Fig. 4a–c). The south eastern region exhibited long lineaments trending NE–SW but, in general, lineament of magnetic map where shorter than lineaments extracted from remote sensing data. The maximum linear length detected was 10635 m, while the minimum length was 1045 m. These tectonic structures are comparable with those structures stated in remote sensing data.

The analytical signal can be useful in locating edges of remanently magnetized bodies in areas of low magnetic latitude. The interpretations of the analytical signal map make it possible to identify geophysical anomalies similar to the signature of small known greenstone belts. The method consists in superimposing the known greenstone belts shapefiles on the analytical signal to identify the corresponding anomalies (Fig. 5a). Subsequently, similar anomalies were identified in areas where there is no recent and detailed mapping. As an example, the banded iron formation of Mezesse shows high magnetic amplitudes (Fig. 5a). A total of 57 outcrops of Banded Iron Formation (BIF) were located, so two possible small belts or greenstone belts extensions were interpreted (Fig. 5b).

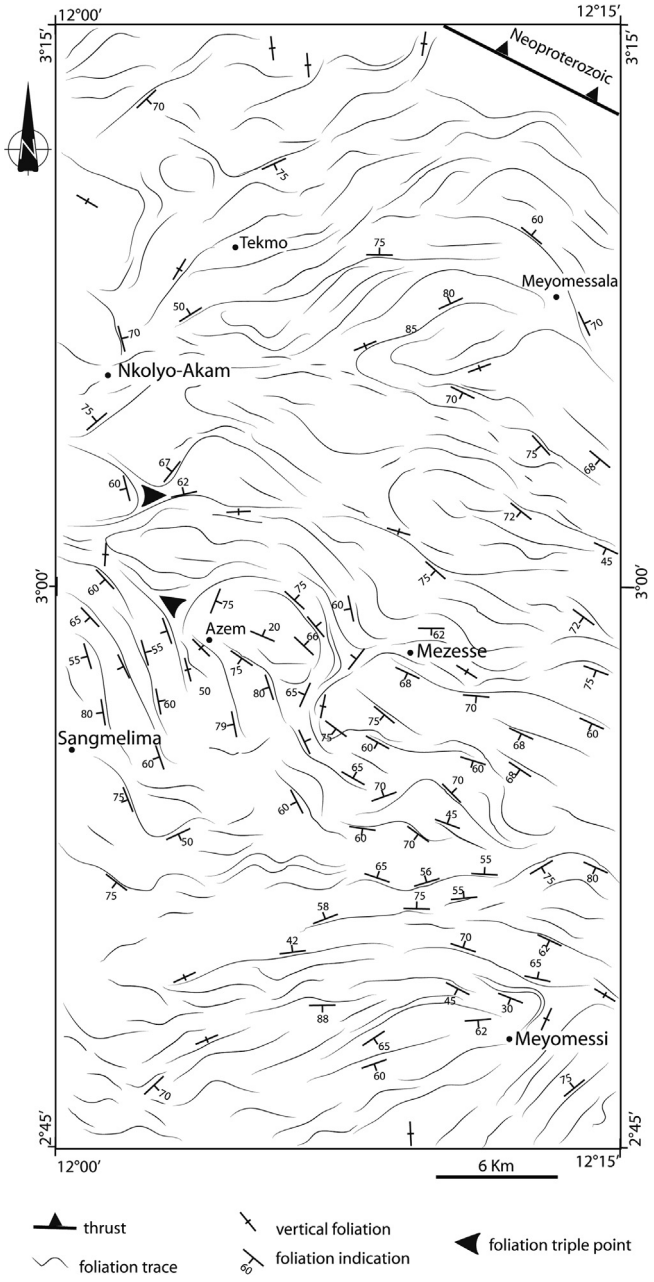

Fig. 6. Associated foliation data and interpreted foliation trajectories in the study area.

4.3. Structural analysis

The main structural features are:

The *metamorphic foliation* (S_1) is a regional structure affected by many folding episodes. Foliation trajectories have been partly drawn from the interpretation of aeromagnetic map in this study (Fig. 6). Foliation trajectories highlight several heterogeneities in the strain pattern. They appear locally folded and tend to define underline domes structures (Fig. 6). But, no conclusive evidence as to domes and basin geometries were observed. S_1 is oriented NW–SE to NNW–SSE or N–S and sometimes E–W; it dips 30° to 70° west (Figs. 6 and 7). Vertical foliations are observed all over the study area. The S_1 planes displayed stretching or mineral *linéations* (L_1), maked by ferromagnesian minerals (biotite, orthopyroxene) and elongation of clasts (quartz, feldspath). Centimetre to metre-scale shear bands are observed in association with the granulitic foliation, but they bear a very variable sense of shear, with both strike-slip components.

Shear zones are frequent in the Sangmelima area. In plane view, N160°−175°E and N05°−25°E striking ductile shear bands (C_2) show components of dextral and sinistral strike slip, respectively (Fig. 8a). They are compatible with a N85°E strike of shortening. Locally, a normal sense of shear is observed but in general no shear bands are recorded. The C_2 shears zones are generally associated with the development of mylonitic foliation and F_2 synmetamorphic folds that display oblique axes (Fig. 8a).

Brittle shear zones C_3 are observed at all scales throughout the belt (Fig. 4 and Fig. 8b and c). At the regional scale, the N40°–N60° structures are clearly outlined by aerial photographs. Locally, C_3 shears are N40°–N60°, N20°−30°, N70°–N80°oriented sinistral strike-slips and associated with some conjugated dextral shear bands (Fig. 9c and d). N20°–N30° and N40–N60° oriented shear bands (C_3) are the most common structures. They indicate sinistral movements. The geometrical of C_3 shear zone of the D_3 deformation compatible with a Riedel system in a wide NE–SW channel setting affected by sinistral movements (Fig. 9c). Therefore, NNE–SSW and ENE–WSW sinistral shear zones correspond to the R and P, respectively. R' is represented by NNW–SSE dextral shear zones.

Abundant faults and fractures were found throughout the study area (Fig. 8d). They display variable strikes from N040−070°E to N120−160°E with sub-vertical dip and low pitch striations oscillating between 10 and 40° (Fig. 10). Faults show occasionally an antagonist movement, being either sinistral or dextral along a similar direction and may correspond to C_3 NNE–SSW and NE–SW sinistral shear bands reactivations, with dextral movements. The intensity of the dextral shear is lower than the sinistral one. The Fig. 10 present the statistical analysis of shear bands using the right-dihedra method (Angelier and Mechler, 1979). The orientation of the deformation's maximal main stress (6_1) is 03°N187, the intermediary (6_2) and the minimal (6_3) stresses are oriented 87°N017 and 01°N087.2, respectively. The reconstitution of these stress axes suggests that the strike-slip component may dominate

at the scale of the study area (R = 0.50, Fig. 10). This horizontal shortening correlates the N–S sinistral transpression that caused the C_3 synthetic sinistral ENE–WSW, NNE–SSW and C_3 antithetic dextral NNW–SSE strike-slips of a main NE–SW shear zone (Fig. 9a).

5. Discussion

Geological structures and lineaments were delineated from satellite imagery and aeromagnetic studies. The regional litho-structural architecture of Sangmelima region was updated based on the use of remote sensing data. Lithological boundaries recognized from image interpretations were supported by available geological maps and field observation datasets. A geodynamic model was built which incorporated the integrated approach, fault-system geometry, and the relative structural kinetics. The NE–SW, NW–SE, N–S and E–W are the main revealed from remote sensing processing; while the NE–SW, E–W to ESE–WNW, NW–SE and N–S are the dominant structural trends revealed from aeromagnetic data (Fig. 4). The structural grain is defined by S_1 regional foliation, F_2 folds, shear zones, brittle bands and Fault/fractures. D_1 is recorded by a sub-vertical penetrative S_1 foliation bearing stee-

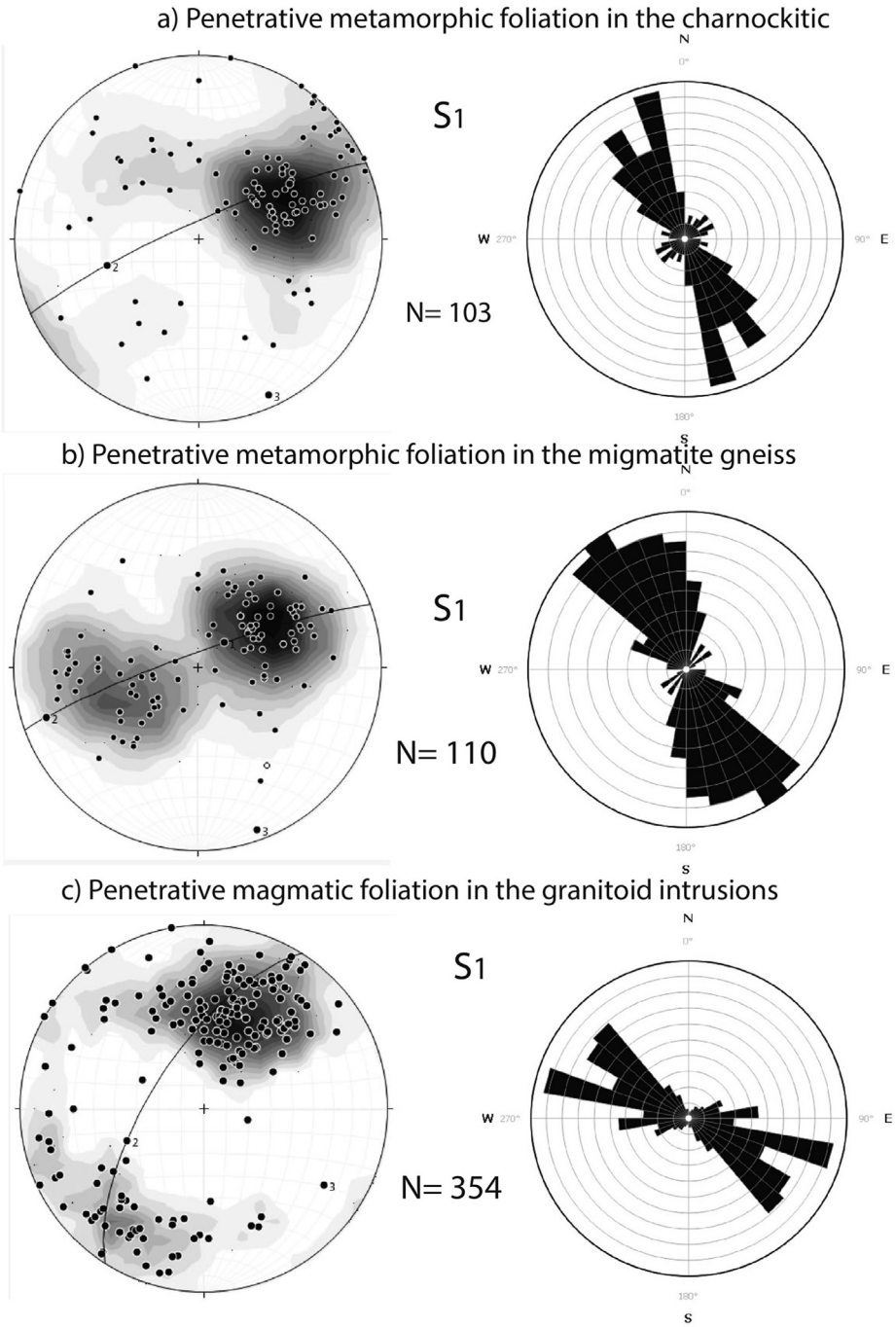

Fig. 7. Equal area lower hemisphere stereoplots showing distribution of foliation poles. Rose diagrams show the distribution of the foliation strikes in the study area.

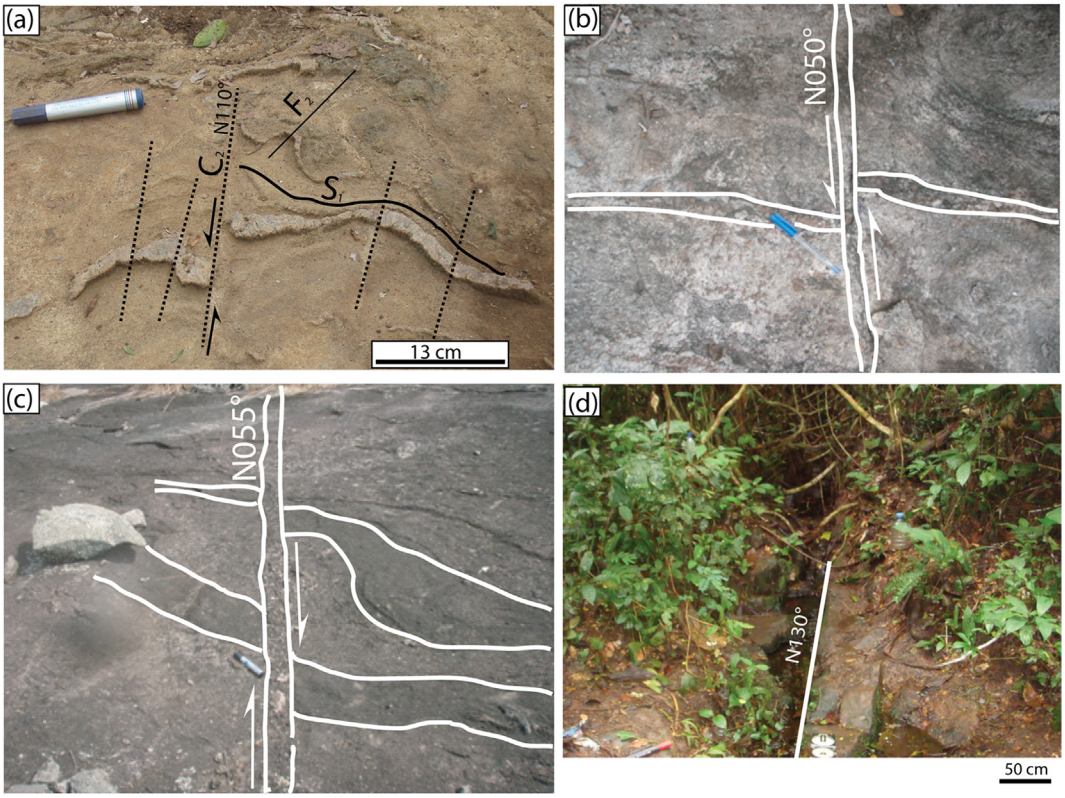

Fig. 8. Field photographs of representative structures**. (a)** Relations between penetrative metamorphic foliation S_1, subvertical NNW-trending shear zone C_2 and F_2 folds in charnockites. **(b)** and **(c)** C_3 Shear zones NE–SW antagonists to motion. (d) Fracture network.

ply plunging stretching lineations (L_1). Kinematics associated with the D_1 events is difficult to assess. However, the distribution of greenstone belts in the lower part of Fig. 5b is characterized by a linear pattern clearly reflects horizontal shortening, similar to other Archean cratons such as North China Craton (Kusky et al., 2016 and references therein), Slave craton of Canada (Card, 1990; Gapais et al., 2005; Bleeker and Hall, 2007; Helmstaedt, 2009; Gerya, 2014 and references therein; Mvondo et al., 2017) and Barberton Greenstone Belt of South Africa (Furnes et al., 2013 and references). D_2 overprints D_1 structures with tight-to-isoclinal folds with associated foliation, N160°−175°E and N05°−25°E ductile shear zones, indicating ENE–WSW shortening. Therefore, we suggest that D1 and D2 should be grouped in a single progressive deformation even. On the other hand, deformation–metamorph ism relationships indicate that all ductile structures, from earliest S_1 foliation to mylonitic foliations in C_2 shear zones, are coeval with migmatisation.

A well-constrained overprinting relationship was observed between the D_2-D_3 shear zones both in the field and in remote sensing/aeromagnetic data. In the Sangmelima belt, many small scales shear zones C_3 cross-cut S_1 foliation and F_2 folds. Most of these shear zones show sinistral displacements and are interpreted to have formed in response to a later phase of deformation that we identify as D_3. Therefore D_3 is attributed to late strike slip shearing affected the Ntem Complex. At the regional scale, satellite, magnetic images and fields observation show at least two syn-D_3 shear zone generations. The first one is oriented N035−65°E lineaments and the kinematic interpretation of brittle shear measured in the area suggest that the tectonic lineaments are controlled by a system of strike-slip faults, more precisely by a system of Riedel shear fractures (Fig. 9 and Fig. 11). This Riedel model show that the principal horizontal stress ($\sigma 1$) is oriented at N–S, and the minimum horizontal stress ($\sigma 3$) is oriented at N085°. N00° E < T < N10°E where T is the direction of tensional fractures. Many of them are intruded by mafic dykes in the study area (Fig. 5b). P and P', have orientations of ∼60−65° and ∼110°, whit an with an extension direction E in E–S. These three directions were also identified by Maurizot et al. (1986) at a regional scale. R and R', which are sets of synthetic and antithetic shear fractures, are oriented at N20−25° and 150°−155°, respectively.

The second is oriented N–S and cross-cuts earlier N045°E shears and the D_3 thrusts within the Nyong Complex (e.g Maurizot et al., 1986; Feybesse et al., 1987; Owona et al., 2011, 2012). This lineament system extends to the southwest of study area, through the Kribi peneplain to the Atlantic coast.

The D_3 strike slip shearing is likely the result of the Eburnean deformation phase (Fig. 11). Our D_3 therefore corresponds to D_2 of Maurizot et al. (1986), Feybesse et al. (1998), Owona et al. (2011). The mafic dykes are striking NE–SW, N–S and NWSE, and field evidence and airborne magnetic data suggest that some of them intrude preexisting structures. The faults/fractures are clearly visible in remote sensing/geophysical data from the Sangmelima belt (Figs. 4 and 11) and we attribute them to the D_4 deformation event. Nevertheless, some of these faults/fractures might have originated during previous deformation phases and they were only reactivated during the D_4.

6. Conclusion

This paper presents the results of a integration of remote sensing, aeromagnetic and field data for mapping structural

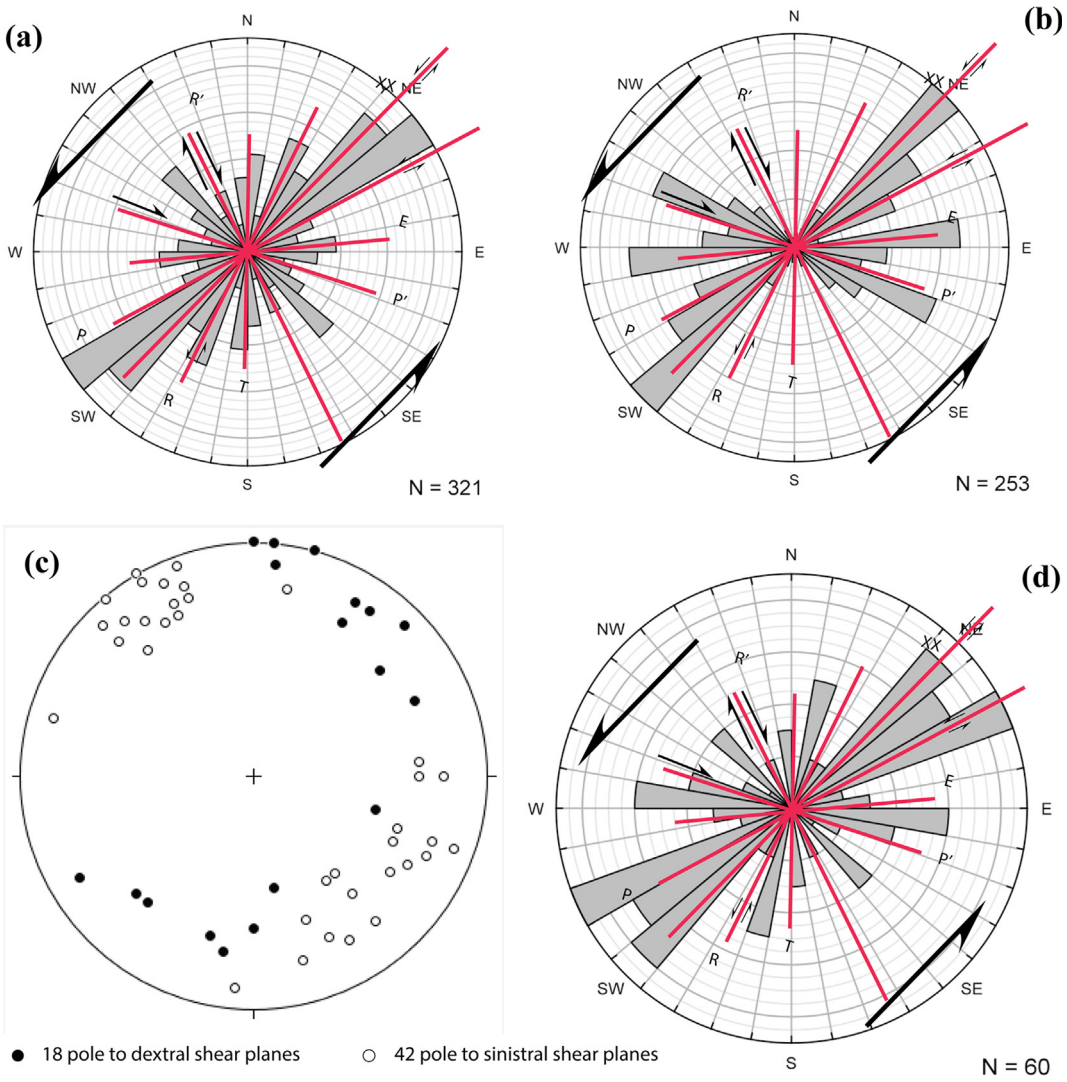

Fig. 9. Schematic Riedel model using a sinistral simple shear associated with rose diagrams.

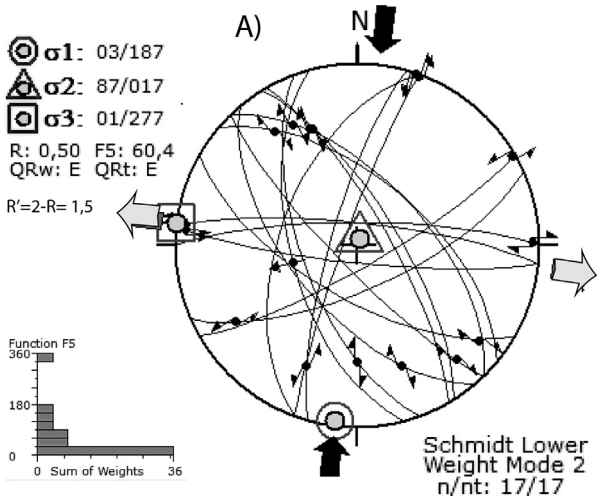

Fig. 10. Stereograms(Equal area, lower hemisphere) showing the fault shear population measured for this study and calculated principal axes for all shear bands (axes 1, 2, and 3).

features and update lithological map in Sangmelima area, South Cameroon. Analytical signal, vertical and horizontal derivatives of total field magnetic also helped in mapping new possible greenstone belts and structural features. Many of the identified lineaments are interpreted to represent fracture/fault zones, some of strike-slip faults. We distinguish three deformation events within the Sangmelima area: D_1 is recorded by a sub-vertical penetrative S_1 foliation bearing steeply plunging stretching lineations. No conclusive evidence as to domes and basin geometries were observed. D_2 overprints D_1 structures with tight-to-isoclinal folds with associated foliation, N160°–175°E and N05°–25°E ductile shear zones, indicating ENE–WSW shortening. According to field data and structural analysis, we suggest that D_1 and D_2 should be grouped in a single progressive deformation even. The D_3 strike slip shearing is likely the result of the Eburnean deformation phase. The mafic dykes are striking NE–SW, N–S and NWSE, and field evidence and airborne magnetic data suggest that some of them intrude preexisting structures. Many faults/fractures might have originated during previous deformation phases and they were only reactivated during the pan-African events.

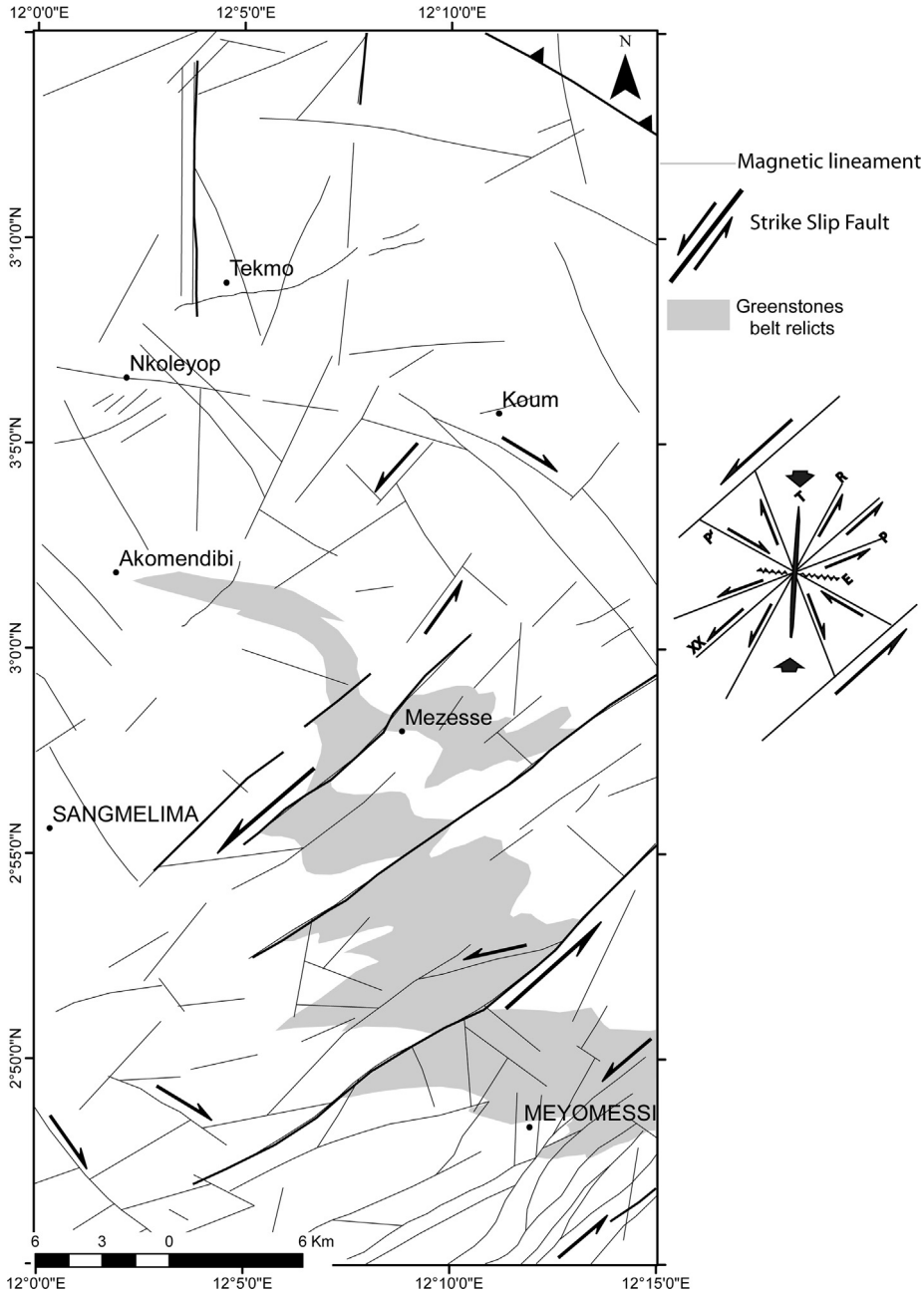

Fig. 11. Tectonic map of the Sangmelima and fractures associated with the Riedel model, showing the relationship between the orientation of the main compressional strain axis and the direction of shearing.

Conflict of interest

None.

Acknowledgements

We thank the anonymous reviewer for kindly contacting us for any data need.

Appendix A. Supplementary data

Supplementary data to this article can be found online at https://doi.org/10.1016/j.ejrs.2018.11.005. These data include Google maps of the most important areas described in this article.

References

Aitken, A.R.A., Betts, P.G., 2009. Constraints on the Proterozoic supercontinent cycle from the structural evolution of the south-central Musgrave Province, central Australia. Precambrian Res. 168, 284–300.

Akame, J.M., Mvondo Ondoa, J., William, Assatse Teikeu, Owona, S., Olinga, J. B., Ottou, E., Messi, J., Ntomba, S.M., 2014. Apport des images Landsat-7 ETM+ a l'étude structurale du socle archéen de Sangmélima (Sud Cameroun). Revue Française de Photogrammétrie et de Télédétection 206, 15–26.

Angelier, J., Mechler, P., 1979. Sur une méthode graphique de recherche des contraintes principales également utilisable en tectonique et en sismologie: La méthode des dièdres droits. Bull. Soc. Geol. Fr. 7, 597–608.

Betts, P.G., Valenta, R.K., Finlay, J., 2003. Evolution of the Mount Woods inlier, northern Gawler Craton, Southern Australia: an integrated structural and aeromagnetic analysis. Tectonophysics 366, 83–111.

Bleeker, W., Hall, B., 2007. The Slave Craton: Geology and metallogenic evolution. In: Goodfellow, W.D. (Ed.), Mineral Deposits of Canada: A Synthesis of Major

Deposit-Types, District Metallogeny, The Evolution of Geological Provinces, and Exploration Methods. Geological 731 Association of Canada, Mineral Deposits Division. Special Publication, pp. 849–879.

Block, S., Moyen, J.F., Zeh, A., Poujold, M., Jaguin, J., Paquette, J.L., 2012. The Murchison Greenstone Belt, South Africa: accreted slivers with contrasting metamorphic conditions. Precambrian Res. 2012. https://doi.org/10.1016/j.precamres.2012.03.005.

Caen-Vachette, M., Vialette, Y., Bassot, J.P., Vidal, P., 1988. Apport de la géochronologie à la connaissance de la géologie gabonaise. Chron. Rech. Min. 491, 35–54.

Card, K.D., 1990. A review of the Superior Province of the Canadian Shield, a product of Archean accretion. Precambrian Res. 48, 99–156.

Chombong, N.N., Suh, C.E., 2013. 2883 Ma commencement of BIF deposition at thenorthern edge of Congo craton, southern Cameroon: new zircon SHRIMP dataconstraint from metavolcanics. Episodes 36, 47–57.

Dabo, Moussa, Aïfa, Tahar, 2013. **A**rchitecture tectonique des formations paleoproterozoïques de la Dalema (Senegal Oriental): apport des lineaments d'images landsat-7 etm+/srtm et aeromagnetique. J. Sci. 13 (1).

Direen, N.G., Cadd, A.G., Lyons, P., Teasdale, J.P., 2005. Architecture of Proterozoic shear zones in the Christie Domain, western Gawler Craton, Australia: geophysical appraisal of a poorly exposed orogenic terrane. Precambrian Res. 142, 28–44.

Eldosouky, A.M., Abdelkareem, M., Sayed, O., Elkhatee, S.O., 2017. Integration of remote sensing and aeromagnetic data for mapping structural features and hydrothermal alteration zones in Wadi Allaqi area, South Eastern Desert of Egypt. J. Afr. Earth Sci. 130, 28–37. https://doi.org/10.1016/j.jafrearsci.2017.03.006.

Feybesse, J.L., Johan, V., Maurizot, P., Abessolo, A., 1987. Evolution tectonométamorphique libérienne et éburnéenne de la de la partie NW du craton zaïrois (SW Cameroun). In: Matheis, J., Schandelmeier, G. (Eds.), Current Research in African Earth Sciences. Balkema, Rotterdam, pp. 9–12.

Feybesse, J.L., Johan, V., Triboulet, C., Guerrot, C., Mayaga-Minkolo, F., Bouchot, V., Eko N'dong, J., 1998. The West Central African belt: a model of 2.5-2.0 Ma accretion and two-phase orogenic evolution. Precamb. Res. 87, 161–216.

Furnes, H., de Wit, M.J., Robins, B., 2013. A review of new interpretations of the tectonostratigraphy, geochemistry and evolution of the Onverwacht Suite, Barberton Greenstone Belt, South Africa. Gondwana Res. 23, 403–428.

Gapais, D., Potrel, A., Machado, N., 2005. Kinematics of long-lasting Paleoproterozoic transpression within the Thompson Nickel Belt, Manitoba, Canada. Tectonics 24. https://doi.org/10.1029/2004TC001700.

Gerya, T., 2014. Precambrian geodynamics: concepts and models. Gondwana Res. 24, 442–463.

Helmstaedt, H., 2009. Crust-mantle coupling revisited: The Archean Slave craton, NWT, Canada. Lithos 112 (S2), 1055–1068.

Kusky, T.M., Polat, A., Windley, B.F., Burke, K.C., Dewey, J.F., Kidd, W.S.F., Maruyama, S., Wang, J.P., Hao, D., Wang, Z.S., Wang, C., Dong, F., Li, X.W., Peng, H.T., 2016. Insights into the tectonic evolution of the North China Craton through comparative tectonic analysis: a record of outward growth of Precambrian continents. Earth-Sci. Rev. 162, 387–432.

Lasserre, M., Soba, D., 1976. Age liberien des granodiorites et des gneiss à pyroxènes du Cameroun Meridional. Bull. BRGM 2 (4), 17–32.

Maurizot, P., Feybesse, J.K., Johan, Lecomte, P., 1985. Etude et prospection minière du Sud-Ouest Cameroun, synthèse des travaux de 1978 à 1985. Rapport du Bureau de Recherche géologique et minière 85, 274. CMR066.

Václav Metelka, 2011. Application des méthodes de géophysique et de télédétection à l'analyse du régolithe et de la géologie du Burkina Faso, Afrique de l'Ouest. (Thèse de doctorat). l'Université Toulouse III - Paul Sabatier, 230P. tel-00670786, version 1 - 17 Feb 2012.

Milligan, P.R., Gunn, P.J., 1997. Enhancement and presentation of airborne geophysical data. AGSO J. Aust. Geol. Geophys. 17, 63–75.

Mvondo, H., Lentz, D., Bardoux, M., 2017. Crustal shortening and thickening in Neoarchean granite-greenstone belts: a case study from the link between the ~2.7 Ga Elu and Hope Bay belts, northeast Slave craton, Canada. J. Struct. Geol. 2017. https://doi.org/10.1016/ j.jsg.2017.10.004.

Nsifa, E.N., Riou, R., 1990. Post Archean migmatization in the charnockitic series of the Ntem complex, Congo craton, Southern Cameroon. 15th colloquium on African Geology. Publications Occasionnelle, CIFEG, pp. 33–36.

Owona, S., Mvondo Ondoa, J., Ratschbacher, L., Mbola Ndzana, S.P., Tchoua, M.F., Ekodeck, G.E., 2011. The geometry of the Archean, Paleo- and Neoproterozoic tectonics in the Southwest Cameroon. Compte. Rendus de Geosci. 343, 312–322.

Owona, S., Ndzana Mbola, S.P., Mvondo Ondoa, J., Nsangou Ngapna, Moussa, Nkabsaah, C., Ratschbacher, L., Ekodeck, G.E., 2012. Geological control of geomorphologic units in the Southwest (SW) Cameroon (Central Africa). J. Geol. Mining Res. 4 (7), 152–167.

Paterson, G., Watson Ltd., 1976. Etudes aeromagnetiques sur certaines Régions de la République Unie du Cameroun. ACDI, Toronto, Canada. 190.

Peschler, A.P., Benn, K., Roest, W.R., 2006. Gold-bearing fault zones related to Late Archean orogenic folding of upper and middle crust in the Abitibi granite-greenstone belt, Ontario. Precambrian Res. 151, 143–159.

Pilkington, M., Keating, P.B., 2009. The utility of potential field enhancements for remote predictive mapping. Can. J. Remote Sens. 35 (Suppl. 1), S1–S11.

Pouclet, A., Tchameni, R., Mezger, K., Vidal, M., Nsifa, N.E., Penaye, P., 2007. Archaeancrustal accretion at the northern border of the Congo Craton (South Cameroon). The charnockite-TTG link. Bull. Soc. Geol. Fr. 178, 3–14.

Shang, C.K., 2001 Unpublished Ph.D. Thesis. In: Geology, Geochemistry and Geochronology of Archaean Rocks from the Sangmelima Region, Ntem complex, NW Congo craton, South Cameroon. University of Tubingen, Germany, p. 313.

Shang C.K, Liégeois J.P, Satir M, Frisch W, Nsifa E.N., 2010. Late Archaean high-K granite geochronology of the northern metacratonic margin of the Archaean Congo craton, Southern Cameroon: Evidence for Pb-loss due to non-metamorphic causes. (article In press) Gondwana Research xxx (2010) xxx–xxx.

Shang, C., Satir, M., Siebel, W., Nsifa, E.N., Taubald, H., Liegeois, J.P., Tchoua, F.M., 2004a. TTG magmatism in the Congo Craton; a view of major and trace element geochemistry, Rb-Sr and Sm-Nd systematics: case of the Sangmelima region, Ntem Complex, Southern Cameroon. J. Afr. Earth Sci. 40, 61–79.

Shang, C.K., Wolfgang, S., Muharrem, S., Funken, C., Mvondo Ondoa, J., 2004b. Zircon Pb-Pb and U-Pb systematics of TTG rocks in the Congo Craton: Constraints on crust formation, magmatism, and Pan-African lead loss. Bull. Geosci. 79 (4), 205–219.

Shang, C.K., Satir, M., Nsifa, E.N., Liegeois, J.P., Siebel, W., Taubald, H., 2007. Archean high-K granitoids produced by remelting of earlier Tonalite-Trondhjemite-Graondiorite (TTG) in the Sangmelima region of the Ntem complex of the Congo craton, Southern Cameroon. Int. J. Earth Sci. (Geol Rundsch) 96, 817–841.

Stewart, J.R., Betts, P.G., 2010. Late Paleo-Mesoproterozoic plate margin deformation in the southern Gawler Craton: insights from structural and aeromagnetic analysis. Precambrian Res. 177, 55–72.

Suh, C.E., Cabral, A.R., Shemang, E.M., Mbinkar, L., Mboudou, G.G.M., 2008. Two contrasting iron deposits in the Precambrian mineral belt of Cameroon, West Africa. Explor. Min. Geol. 17, 197–207.

Takam, T., Arima, M., Kokonyangi, J., Dunkley, D.J., Nsifa, E.N., 2009. Paleoarcheancharnockite in the Ntem Comples, Congo Craton, Cameroon: in sights fromSHRIMP zircon U-Pb ages. J. Mineral. Petrol. Sci. 104, 1–11.

Tchameni, R., 1997. Géochimie et géochronologie des formations de l'archéen et du paléoprotozoïque du Sud-Cameroun (groupe du Ntem Thèse non publiée de l. Université d'Orléans, Craton du Congo), p. 335p.

Tchameni, R., Mezger, K., Nsifa, E.N., Pouclet, A., 2000. Neoarchean evolution in the Congo Craton: evidence from. K rich granitoids of the Ntem complex, Southern Cameroon. J. Earth Sci. 30 (1), 113–147.

Tchameni, R., Pouclet, A., Mezger, K., Nsifa, E.N., Vicat, J.P., 2004. Monozircon and Sm-Nd whole rock ages from the Ebolowa greenstone belts: evidence for the terranes older than 2.9 Ga in the Ntem Complex (Congo craton, South Cameroon). J. Cameroon Acad. Sci. 4, 213–224.

Teixeira, W., Oliveira, E.P., Marques, L.S., 2017. Nature and evolution of the archean crust of the São Francisco Craton. Regional Geol. Rev. https://doi.org/10.1007/978-3-319-01715-0_3.

Toteu, S.M., Van Schmus, W.R., Penaye, J., Nyobe, J.B., 1994. U-Pb and Sm–Nd evidence for Eburnean and Pan-African high grade metamorphism in cratonic rocks of southern Cameroon. Precambrian Res. 67, 321–347.

European Journal of Scientific Research
ISSN 1450-216X / 1450-202X Vol. 152 No 3 April, 2019, pp. 286-303
http://www. europeanjournalofscientificresearch.com

Contribution of Geophysics to the Understanding of the Geodynamic Activity at the Northern Margin of the Congo Craton: A Case Study from Aeromagnetic Data Interpretation Over the Metet-Zoetele Region (Southern Cameroon)

Assembe Stéphane Patrick
Corresponding Author, Postgraduate School of Science Technology and Geosciences
University of Yaounde 1 PO Box 812 Yaounde, Cameroon
Faculty of Science, University of Bamenda, PO Box 39 Bambili, Cameroon
E-mail: assembest@yahoo.fr

Ndougsa Mbarga Théophile
Postgraduate School of Science Technology and Geosciences
University of Yaounde 1 PO Box 812 Yaounde, Cameroon
Higher Teacher Training College, University of Yaounde 1
PO Box 47 Yaounde, Cameroon
E-mail: tndougsa@yahoo.fr

Meying Arsene
School of Geology and Mining Engineering, University of Ngaoundere
PO Box 115 Meiganga, Cameroon

Gouet Daniel Hervé
Faculty of Mining and Petroleum Industries
University of Maroua, PO Box Kaele, Cameroon

Ngoh Jean Daniel
Postgraduate School of Science Technology and Geosciences
University of Yaounde 1 PO Box 812 Yaounde, Cameroon

Mono Jean Aime
Basical Science Department, Advanced Technical Teacher Training School
University of Douala, Cameroon

Abstract

The qualitative and quantitative geophysical investigations involving image enhancement, multiscale edge analysis, Euler's deconvolution and 23/4 D inverse modelling are applied to aeromagnetic data over the Metet-Zoetele area (southern Cameroon), a portion of the Congo Craton (CC)/North Equatorial Fold Belt (NEFB) transition zone. The study investigates the geodynamic evolution of the northern margin of the CC through the detection of lineaments. The geology of the area is made up of the NEFB and the CC both affected by multi-stage tectonics summarised in to alternating compressions and extensions. The analyses highlight a broad NE-SW high amplitudes channel which presumes the dominance of a NE structural direction in the area. The study

differentiated the CC from NEFB by outlining a subvertical boundary at N03º20'; WNW-ESE, W-E, NW-SE, SW-NE and WSW-ENE vertical to sub-vertical lineaments defining shear zones affecting both the CC and the NEFB. These lineaments are interpreted as pre-Neoproterozoic events which experienced syn- to -late and post-Neoproterozoic reactivations. The post-Neoproterozoic events are coeval to, or postdate the Central Cameroon Shear Zone. Therefore, the WSW-ENE to SW-NE fractures form dextral strike-slips corresponding to wrenches related to a SW-NE shear zone overprinted by sinistral NW-SE to WNW-ESE displacements inferring neo-tectonic activity in the CC/NEFB transition zone as a consequence of the on-going movements that affect the African Plate.

Keywords: Aeromagnetic data; Congo Craton; strike-slips; wrenches; neo-tectonic activity

Introduction

Understanding the geological evolution of the transition zone between the North Equatorial Fold Belt (NEFB) in Central Africa and the Congo Craton (CC) remains a great challenge for geoscience researchers despite the recent advances. For example, the geodynamic setting remains discussed although some unifying points exist (Toteu *et al* 2006; Mvondo *et al* 2007; 2009; Ngako and Njonfang 2011; Ngnotue *et al* 2012). One of the major limitations comes from the limited aerial extend of the studied areas from which inferences are made on the regional scale and the limited use of geophysical methods, e.g. airborne magnetic surveying.

Aeromagnetics within few decades, has gained a strong reputation in mapping buried structures and lithology irrespective of the terrain conditions and availability of outcrops (Paterson and Reeves 1985; Nabighian *et al* 2005; Boyd and Isles 2007; Fairhead *et al* 2017), as it is the case for the study area where the vegetation is thick and outcrops scarce. The method has permitted to update the geology of some areas of the Cameroon (Feumoe *et al* 2012; Ndougsa-Mbarga *et al* 2012; Yandjimain *et al* 2017), involving either the NEFB and/or the CC setting. Most of these studies used traditional derivative-based filters (edge detectors) which have proven their efficiency in mapping lineaments, though they are limited to qualitative analyses and accentuate noise [13]. Some edge detectors like the tilt-angle method additionally evaluate the depth-to-the-source but it is limited to shallow subsurface sources; this depth limitation is mitigated by the Euler deconvolution method (Reid *et al* 1990) which provides full location of the source. The need to get maximum geological information from magnetic data has seen the emergence of more robust interpretation approaches involving the combination of edge detectors and depth-to-basement calculations. In order to get updated insights on the geology of the NEFB/CC transition zone, we apply both modern edge detection filters, depth-to basement and inverse modelling methods to aeromagnetic data collected in the Metet-Zoetele region (Southern Cameroon) in a region whose lithology is dominated by Neoproterozoic and Archaean terrains.

Geological Setting

Neoproterozoic Formations and Related Tectonics

The Neoproterozoic terrains in Cameroon corresponds belong to the NEFB herein represented north to south respectively, by the Yaounde and Mbalmayo series (figure 1). *(i)* The Yaounde series is mainly represented by foliated garnetiferous micaschists, high pressure granulitic metasediments made up of quartz, biotite, muscovite and garnets, with various feldspars (Toteu *et al* 2004; Nkoumbou *et al* 2014; references therein). *(ii)* The Mbalmayo Series, made up of schists and quartz-sericite formations with

some volcanic relics, is the southernmost member of the NEFB laying discordantly onto the CC (Toteu *et al*. 2006, *references therein*).

Figure 1: Local geology map (Maurizot *et al* 1986; Ngako and Njongfang 2011, modified)

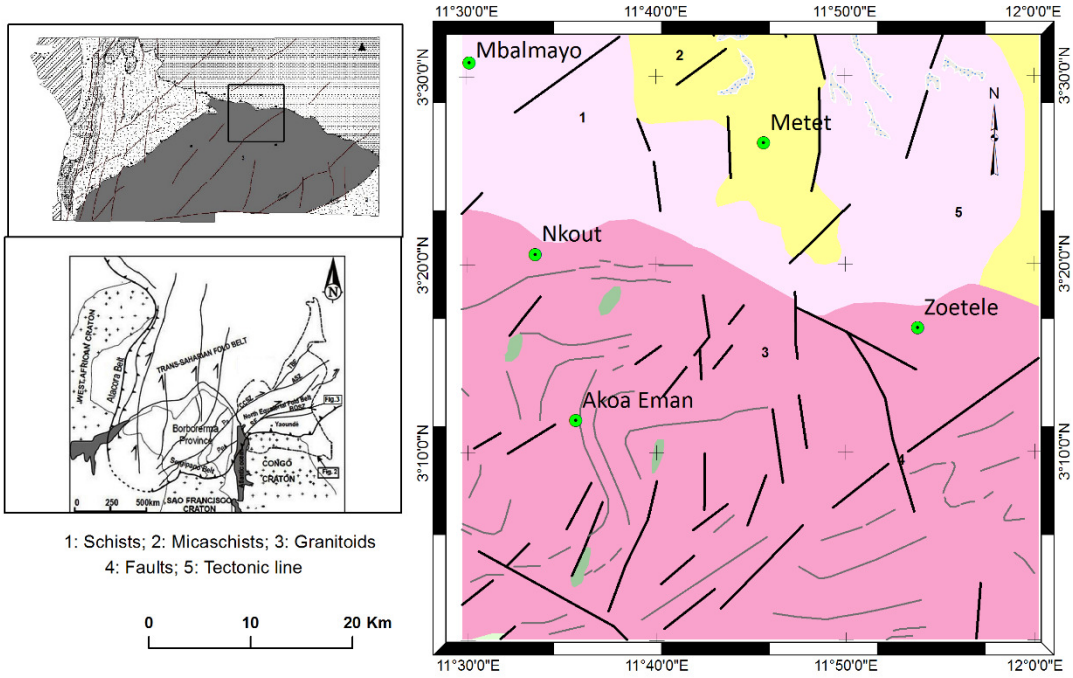

Tectonics in the Yaounde Group corresponds to four deformation stages D1 to D4 exhibited by outcropping metamorphic rocks surrounding Yaounde (Toteu *et al* 2004; 2006; Mvondo *et al* 2007; Mvondo Ondoa *et al* 2009). The D1 event, prior to the calc-alkaline diorites mineralization, is responsible of the nappe formation that led to the granulites facies metamorphism of soft sediments. A great reprint of these nappes during symmetrical extend D2 is probably associated to large scale foliation boudinage and (or) gneissic domes formation along with intensive sub-superficial magmatic deposits. This reprint generated flat regional textures. These formations have been upraised again by unclassified D3 and D4 folding, defining a vertical constriction which occurred with an E-W to NW-SE major narrowing, in the same trend as that of the D1 stage of thrust nappes piling (Olinga *et al* 2010; Mbola-Ndzana *et al* 2014; and references).

The Archaean (Congo Craton) Group and Related Tectonics

The Archaean group referred to as the Ntem complex in Cameroon (Shang *et al* 2007, and references), corresponds to Archaean to Mesoproterozoic terrains dominating the southern part of the study area (figure 1). The Ntem complex is mainly formed by Tonalite-Tronghemite-Granodiorite (TTG) and K-rich granitoids [23]. The tonalites (Soo granites), essentially exposed to the north, is strongly mylonitized and retrogressed along the fault boundary with the NEFB, while granodiorite massifs form distinct bodies within the dominantly charnockitic southern zone (Shang *et al* 2010). Late- to post-tectonic granitoids and syenites with calc-alkaline to alkaline affinity intrude the TTG and clearly postdate the major crust forming episode. This magmatic activity in the Ntem unit ends with post-Archean doleritic dykes affected by Eburnean high-grade metamorphism (Tchameni *et al* 2001, 2010; Shang *et al* 2010).

According to Takam *et al* (2009), the tectonic events in the CC start in the Archaean by the Liberian orogeny related to the development of greenstone belts and late diapiric intrusions of

charnockitic TTG plus late anatexite K-granitoids which was accompanied by high to low-grade metamorphism, associated to a D1-M1 syn-metamorphic deformation characterised by E-W sub-vertical foliation and structures. The Paleo-Proterozoic evolution is dominated by the Eburnean orogeny, a collision between the Sao-Francisco and the Congo Cratons identified by alkaline syenites and dolerites, with a prevalent D2-M2 deformation associated to a prograde metamorphism from amphibolite to granulite facies. Many studies (Toteu *et al* 1994; Akame *et al* 2013; Loose and Schenk 2018) suggest that the deformations witnessed the development of NNE-SSW lineaments (including dextral or sinistral shear zones) NW of the CC which were reactivated during a very diffuse Panafrican episode marked by dolerites (~1000 Ma) and nepheline syenites (~570 Ma) intrusions along with a low grade metamorphism.

Material and Methods

Materials and Data Preparation

The study used the only available data covering the area, acquired under the Cameroon/Canada cooperation. This data has been collected in 1970s with a 0.5 nT sensitive magnetometer, along N-S flight lines with a line spacing of 750 m for a constant fly height of 235 m, monitored by a radar altimeter at ±20 m accuracy. The data were processed by Paterson, Grant and Watson Ltd and delivered as 1/50,000 scaled total intensity contour maps availed to us in a pdf format by the Ministry of Mines (Cameroon). These maps have been georeferenced and digitised using ArcGIS 10.4.1 software. Then, the resulting database was further gridded using a squared 250 m cell to produce the total magnetic field intensity (TMI) anomaly map. The cell size was chosen in accordance with Reeves (2005) and (Hinze *et al* 2013) to avoid noisy cross-track ringing effects. For inversion and geological modelling, three 52 km length S-N parallel profiles have been digitised on the filtered RTE map. Interpolation, processing/filtering and modelling (with GMSYS) were done in Oasis Montaj 8.4 platform.

Methods

The Reduction to the Magnetic Equator, Noise Filtering and RTE Image Enhancement

The reduction to magnetic equator (RTE) transform is applied to the TMI anomaly data. It is an equivalence to the reduction to the poles, which enables to shift the magnetic anomalies above their causative sources in low latitudes areas (Reeves 2005; Hinze *et al* 2013). The operation was conducted considering average values of the inclination -6.2° and declination -18.2° of the geomagnetic magnetic reference field model pertaining when the data were collected, i.e. January 1970 (figure 2).

The RTE map was upward continued to 125 m (comprised between half the flight height -235 m- and the sixth of the lines spacing - 750 m) to suppress noise, often related to high frequency signals in grids (Nabighian *et al* 2005; Reeves 2005; Hinze *et al* 2013). The colour shaded image of RTE draped on a shaded relief image of the digital elevation (figure 3) yielded an enhanced image which favoured the direct detection of regional structures (lineaments) of crustal origin.

The Multiscale Edge Detection

The multiscale analysis (Archibald *et al* 1999) is a processing technique involving the combination of the upward continuation of magnetic field data at several heights and the detection the peaks (Blakely and Simpson, 1986) of their respective horizontal gradient magnitude grids. This modern approach enables to infer the 3D geometry of deep structures. Its main constitutive filters are hereafter described:

The Upward Continuation (UC) Filter

The UC transforms a potential field from a surface it was measured to a field that would had be measured to another surface farther from all sources. It is a low-pass filter which enables to outline deep regional geological sources and basement structural patterns (Reeves *et al* 1997).

The Horizontal Gradient Magnitude (HGM) Filter

The HGM filter uses the two first-order horizontal derivatives of the field to estimate contact locations of bodies at depths; its biggest advantage is its low sensitivity to noise in the data [13,32]. The multiscale analysis map over Metet-Zoetele is obtained overlaying the HGM peaks UC field at respectively, 1, 2, 3 and 4 km.

The 3D Euler Deconvolution Method

The 3D Euler deconvolution (Reid *et al.* 1990, *references therein*) method, applied to gridded data, is based on Euler's homogeneous functions and uses first-order x, y and z derivatives to determine location and depth targets, assuming an a priori information (known as structural index, N, theoretically 0 for contact and fault structures). Applications to field data have enabled to solve geological problems in Cameroon and other settings worldwide (Owona-Angue *et al* 2016; Yandjimain *et al* 2018; references therein). We applied the 3D Euler method using a 9 x9 window, a depth tolerance of 5 % and a structural index (SI) of 0.5 to avoid noisy solutions.

Geophysical Inversion ($2^{3/4}$ Modelling)

The modelling consists in designing and calculating the response of a theoretical model using the GMSYS program on Oasis montaj 8.5. Local known geology is used to constraint models as and we use assumed that both various supra-basement and intrabasement sources caused the observed anomalies; the final models were chosen for RMS error less than 7 % (Prieto 1996).

Results and Discussion

Results

Analysis of Reduced to the Magnetic Equator (RTE) Map

The signal on the RTE map (figure 2) spans from -676 nT to 276 nT, with two clearly outlined main areas. The first area is a small portion located south of Zoetele with a very low magnetic background (down to -676 nT) jagged by nearly E-W very high intensity elongated anomalies corresponding to very high susceptibility materials, probably related to basic to ultramafic intruded rocks, or greenstones relics within charnockites (e.g. dolerites, gabbros or granites) of the CC. The second area forms a NE-SW channel of very high intensity anomalies (peaking at 276 nT) between Abang and Zoetele; with three main blocks of probable old mafic/ultramafic or basic materials intruding the tonalities, as seen at Nkout, Zoetele, and around Metet; and underlying or intruding the Mbalmayo schists west of Metet. By assuming its south continuation between Abang and Nkout, we infer that those materials intruded the Paleoproterozoic crust before the formation of the Yaounde basin. Meanwhile, the anomaly in the east of Metet may be related to garnetiferous micaschists of the Yaounde series.

Figure 2: The reduced to the magnetic equator (RTE) of the TMI map. Evidenced prominent NE high anomaly channel in the centre of the map; yellow lines modelling profiles

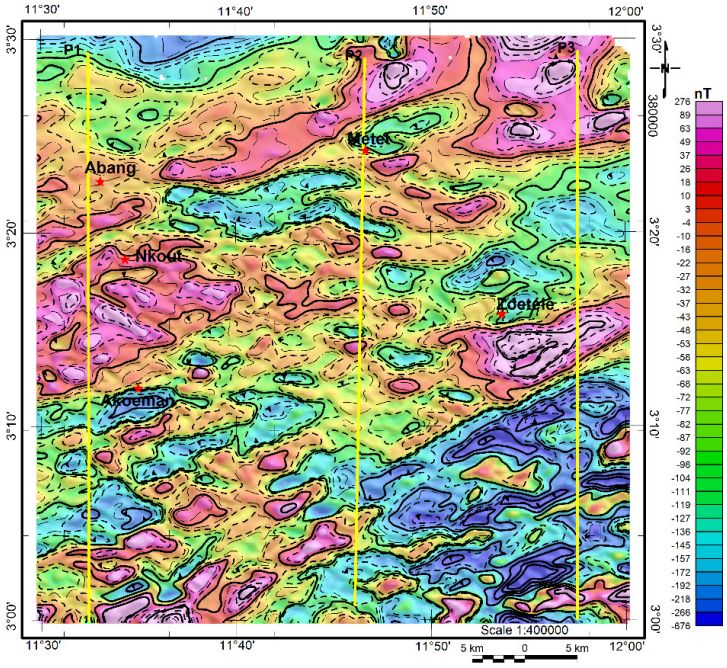

The broad SW-NE orientation of the central domain is a strong indication on the major deformation trend which could have affected the study area's subsurface. Indeed, at first sight, it can be inferred that the basement is controlled by a SW-NE architecture. On Figure 2, the throws and the highs are stretched along the WNW-ESE to NW-SE, E-W or ENE-WSW to NE-SW extensional directions as a consequence of ENE-WSW to NW-SE, N-S and WNW-ESE to NE-SW possible compressions that affected the area. So, the Nkout and Zoetele anomalies seem to have form a unique block tore by relative E-W to ENE-WSW shear movements. This axis is linked to regional ENE-WSW to NE-SW trans-tensions, probably accompanied by the upwells of basic or mafic materials in both the CC and the NEFB as depicted by high susceptibility anomaly blobs within the SW-NE outlined channel.

Analyses of Structures in the Metet-Zoetele Area

The faulting in the Metet-Zoetele area

Lineaments in the Metet-Zoetele area are highlighted by the combined analysis of the RTE enhanced image (figure 3) and the multiscale HGM map (figure 4).

Figure 3: Enhanced RTE image with highlighted faults. The two grey arrows give the direction of the trans-tensional (shear) movements which forcibly corresponds to sinistral strike-slips

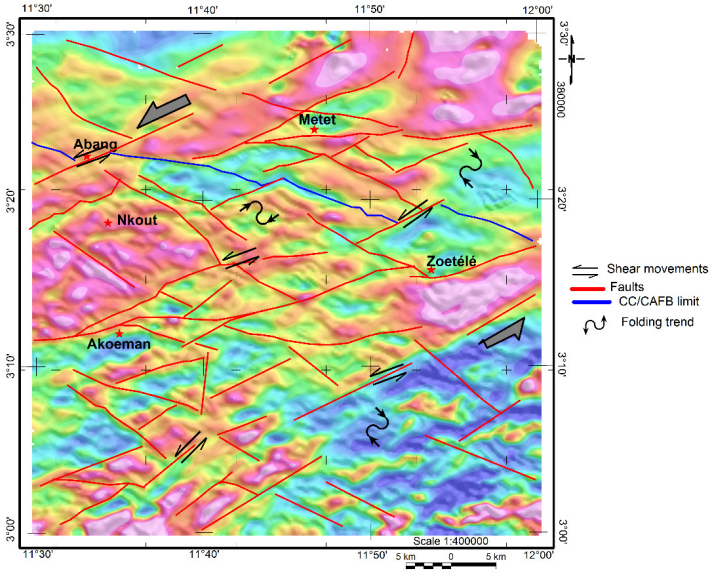

As HGM lineaments (figure 4) are interpretable as faults, fractures, dykes, or simply contacts, a fractures-segregation technique has been done by superimposing the faults from Figure 3 onto the HGM lineaments map (figure 4). On the resulting image (figure 5), only HGM lineaments superimposed by highlighted faults (in red) are interpreted as faults or fractures hereafter. The faults and fractures (Figures 3, and 5) are mainly SW-NE, ENE-WSW, and W-E to NW-SE and WNW-ESE oriented.

Figure 4: Multiscale analysis map of the Metet-Zoetele area. The Lineaments highlighted are mainly vertical to sub-vertical. Dipping either south or north

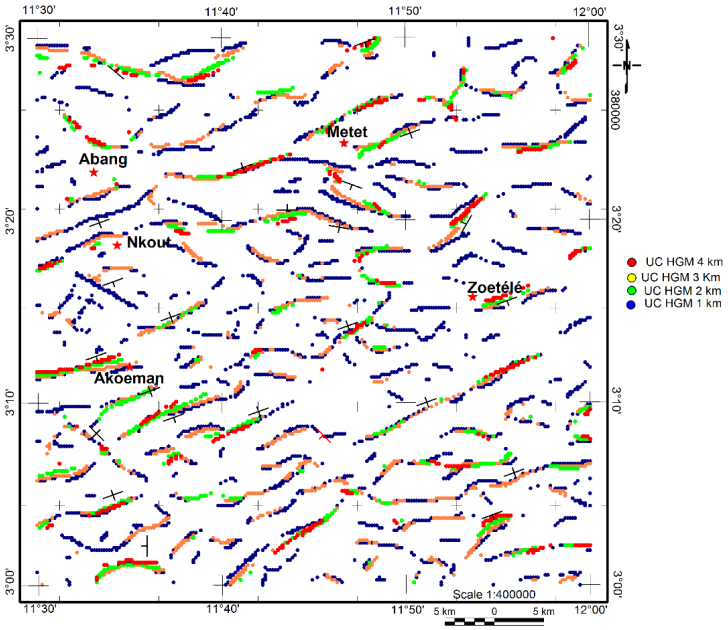

Figure 5: Segregation of faults out of HGM lineaments. Red lines represent early defined faults and the blue line depicts the CC/CAFB limit

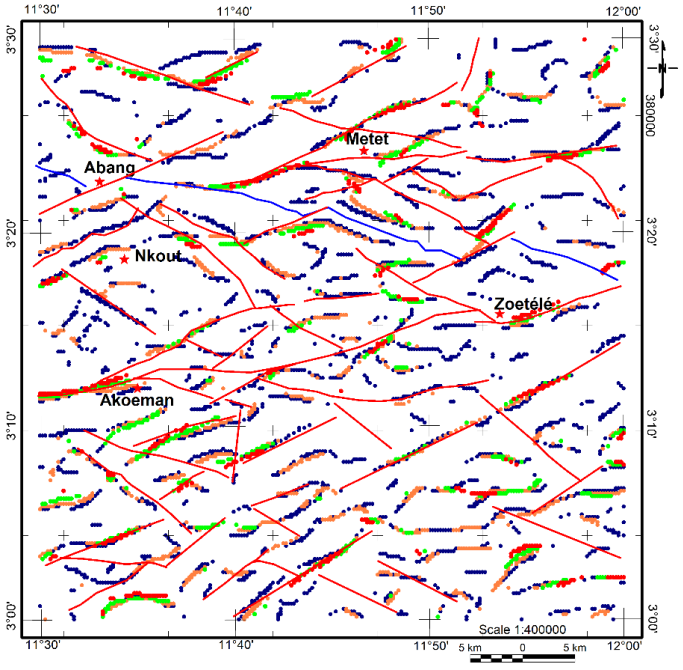

These faults probably guided E-W and NE-SW to NW-SE movements that triggered some compressions herein responsible of the NE-SW and NW-SE folding that occurred in the area. The cross-cutting relationships between those structures show that they either belong to various deformation stages or they are syn- emplaced. Anyhow, the two modes are obvious in regards with the geological history pertaining onto the region. Illustratively in Figure 3, the emplacement of the SW-NE anomaly stretched from Abang to Metet was probably controlled by an early NE-SW structure (Eburnean?), then intersected by a E-W to WNW-ESE (Pan-African?) structure itself post-cut by a NW-SE fault (due to NE-SW sinistral shears) near Abang. The northern area is less fractured, probably the NEFB, in opposition to a southern area, probably the CC (figures 3 and 5). The highlighted nearly E-W set of faults separating those two areas may define the CC/NEFB southernmost limit (blue line on figure 3); hence, NE-SW faults are sinistral strike-slips affecting both the CC and the NEFB.

Attitudes and Depth Range Classification of Faults

The directions and qualitative plunge attitude of lineaments are inferred from Figures 3 and 4 and presented in Table 1. The plunge is assessed by the offset between shallowest (blue) and the deepest (red) peaks. Globally, the lineaments in the area (figure 4) dip north or south and are vertical to sub-vertical. Also, the depth range of fractures has been assessed, depending on their depth perception (presence of peaks levels), yielding three classes (table 1); shallow to the deep (peaks from all levels), middle to deep (peaks from 3 km and 4km only) and deep (4 km peaks).

Table 1: Faults attitudes and depth ranges

Count	Fault's attitude		Depth class	Count	Fault's attitude		Depth class
	Strike	Dip or plunge			Strike	Dip or plunge	
1	SE-NW	North	Middle to deep	16	WSW-ENE	Vertical	Shallow
2	SE-NW	South	Middle to deep	17	WSW-ENE	Subvertical	Shallow
3	SE-NW	South	Shallow	18	WSW-ENE	North	Shallow to middle

Count	Fault's attitude		Depth class	Count	Fault's attitude		Depth class
	Strike	Dip or plunge			Strike	Dip or plunge	
4	SE-NW	Vertical	Shallow to deep	19	WSW-ENE	South	Shallow to deep
5	SE-NW	Subvertical	Shallow to middle	20	WSW-ENE	Vertical	Shallow to middle
6	SE-NW	Subvertical	Shallow	21	WSW-ENE	North	Shallow to deep
7	SE-NW	Vertical	Shallow to deep	22	WSW-ENE	North	Shallow to deep
8	SW-NE	N-Gradational	Shallow to deep	23	WSW-ENE	Subvertical	Shallow to middle
9	SW-NE	South	Shallow to deep	24	W-E	Vertical	Shallow to middle
10	SW-NE	Subvertical	Shallow to deep	25	W-E	Subvertical	Shallow to middle
11	SW-NE	Vertical	Shallow to middle	26	W-E	Subvertical	Shallow to middle
12	SW-NE	Subvertical	Shallow to middle	27	W-E	Subvertical	Shallow to middle
13	WSW-ENE	Subvertical	Shallow to middle	28	W-E	Subvertical	Shallow
14	WSW-ENE	Vertical	Shallow to deep	29	WNW-ESE	Vertical	Shallow to middle
15	WSW-ENE	Vertical	Shallow to deep	30	WNW-ESE	Vertical	Shallow to middle
16	WSW-ENE	Vertical	Shallow	31	WNW-ESE	Vertical	Shallow

The table1 yielded a total of vertical to sub-vertical 31 faults. The main orientations are WNW-ESE (3 counts), W-E (5 counts), NW-SE (7 counts), SW-NE (5 counts) and WSW-ENE (11 counts). Cumulatively, the dominant SW-NE to WSW-ENE cluster (16 counts i.e. 51.61%), followed by the WNW-ESE to NW-SE cluster (10 counts, i.e. 32.25%) are both highlighted in the NEFB and the CC domains, in accordance with previous analyses.

Depth-to-Sources Estimation

The 3D Euler deconvolution provided depth estimates of faults and fractures in the Metet-Zoetele area. The solutions (faults and fractures) are clustered on four depth ranges, from shallow to deep subsurface at [0; 1 km [, [1; 2 km [, [2; 3 km [and more than 3 km intervals, respectively (figure 6). Many solutions match the WNW-ESE, W-E, NW-SE, SW-NE and WSW-ENE directions already highlighted in this study.

Figure 6: Euler 3D solutions underlain by the lineaments map. Depth estimation uses a 9 x 9 window, a depth tolerance of 5% and a structural index of 0.5 for contacts and steep-dipping faults. Solutions correlate with RTE enhanced and HGM faults

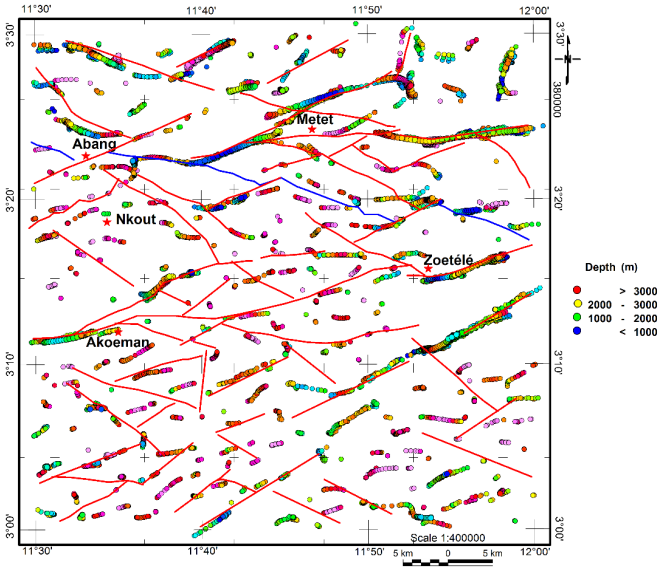

Geological Models

Three profiles (figure 2) were considered for inversion, assuming (1) a uniform basement of magnetic susceptibility $\boldsymbol{k}$ =0.0015. $\boldsymbol{k}$ values in cgs can translated in SI if divided by 4π.

Profile 1

The shape of anomaly profile (figure 7a) suggests the existence of some evident discontinuities interpreted as faults (F1-1 to F1-4) respectively at 3 km, 8.4 km, 22 km and 37 km along profile (figure 7b). The supra-basement effects correspond to a basement's uplift (between F1-2 and F1-4), coupled with an intrabasement N-dipping fracture (F1-3) which separates acidic granulites ($\boldsymbol{k}$ = 0.01977) from syenites overlying the basement between 20 and 38 km. The assumed intrabasement effects are mainly observed between the faults F1-1 and F1-2, which bound a probable gabbro ($\boldsymbol{k}$ = 0.00815) intrusion located at ~2.3 km depth, with ~4 km width, between granulites and tonalites ($\boldsymbol{k}$= 0.00547). Those formations are topped by granodiorites ($\boldsymbol{k}$= 0.01219) and acidic igneous formations ($\boldsymbol{k}$ = 0.00062) left of the F1-4 fault. Right of F1-4, the model yields upward above the basement, quartzites ($\boldsymbol{k}$ = 0.00004), metasediments ($\boldsymbol{k}$= 0.01746), ectinites ($\boldsymbol{k}$=0.00550) and schists ($\boldsymbol{k}$=0.00078).

Figure 7: Modelling along profile 1 (a) Magnetic anomaly profile; (b) Combined geophysical model and geological section. The CC/NEFB limit is represented by the fault F1-4; susceptibility values are in cgs, a division by 4π yields SI values

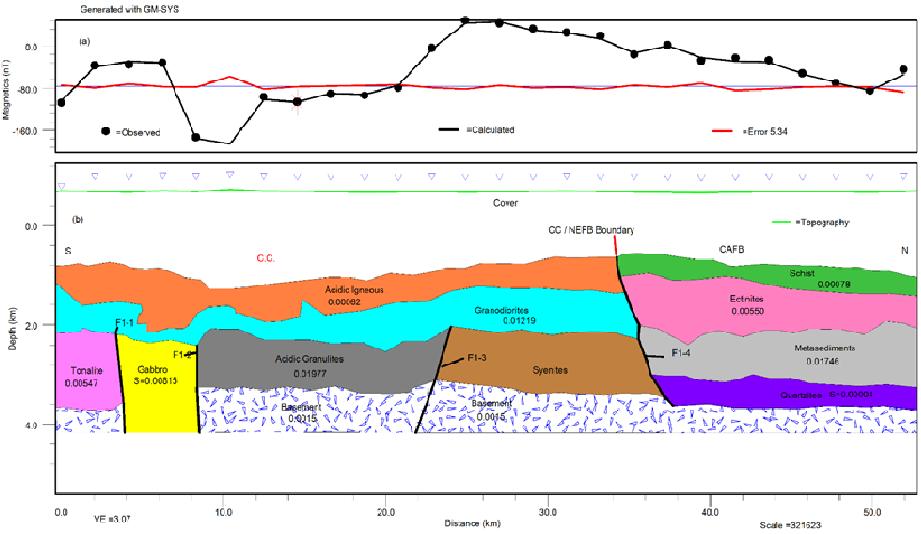

The inversion was performed with a RMS of 5.34%. The geological model (figure 7b) locates the basement nearly at 3.6 km depth from the origin of the profile to F1-1; at 3.2 km from F1-2 to F1-4; then a progressive smooth subsidence from F1-4 to the end of the section. The F1-4 appears to be a north-dipping major discontinuity affecting the basement and separating an igneous complex to the left (south), from a metasedimentary complex to the right (north).

Profile 2

On profile 2, the irregular shape of the curve (figure 8a) testifies the complex geology of the area. The geophysical modelling (figure 8b) assumes only supra-basement effects. The basement is encountered nearly at 3.5 km depth from the origin to 10 km (at F2-1) where it sinks to a nearly constant depth of 4 km up to F2-3; it sinks again therein to nearly 4.4 km depth till position 46 km (F2-10) where it raises again to a constant depth of 4 km. The basement is jagged by faults (F2-1, F2-2, F2-3 and F2-10) which affect partially or totally the overlying formations.

Figure 8: Modelling along profile 2. (a) Magnetic anomaly profile; (b) Combined geophysical model and geological section. The CC/NEFB limit is represented by the fault F2-5 susceptibility values are in cgs, a division by 4π yields SI values

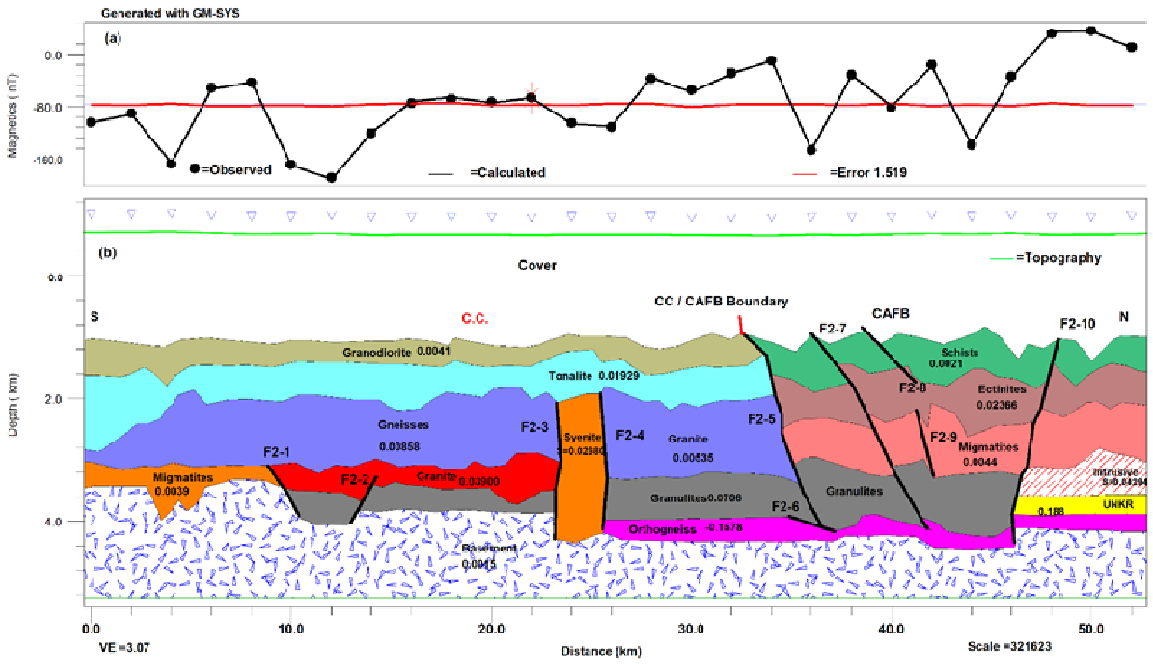

The accepted geological model (RMS error of 1.519 %) shows top-basement formations affected by many faults e.g. F2-1, F2-3 and F2-4 which separate different lithologies: migmatites (***k***=0.0039)/granite (***k***=0.03900), granulites (***k***=0.0706)-granite-gneisses (***k***=0.00858)/syenites (***k***=0.0268) and syenites/granulites-granite (***k***=0.00535). The F2-5 and F2-10 faults seem to limit a basin or syncline stretched in length from 33 km to 48 km; this is supported by their respective geometry, as F2-5 dips north while F2-10 dips south. The faults F2-7, F2-8 and F2-9 seem to outline vertical movements that affect the schists (***k***=0.0021), ectinites (***k***=0.02366), migmatites (***k*** = 0.0044), granulites, orthogneisses (***k*** = -0.0578) and even the basement, in the aforesaid basin. This seems also to be the case for F2-1 and F2-2 regarding the granulites layer and the basement, ~10 km from the origin of the section. Finally, an igneous complex and a metasedimentary complex separated by F2-5 summarises the section (Figure 8b).

Profile 3

The anomaly profile (Figure 9a) starts with a peak (100 nT) attributable to the F3-1 fault (Figure 9b), followed by a general flat low of -220 nT from 4km to 24 km where a new abrupt increase is observed. In the 24-32 km interval the profile peaks at 26.5 km and, then decreases and increases alternatively till the end, shaping the anomaly profile like a valley between 32 and 44 km. The patterns (Figure 9a) at 2 km and in the 24-32km interval, infer discontinuities. Globally, the profile suggests that the subsurface lithology is made up of 2 blocks separated by a major discontinuity at 24 km. The modelling (figure 9b) revealed supra-basement effects witnessed by a collapse of the basement from 11 km to 21 km and from 32 km to the end. The main intrabasement anomaly is interpreted as a syenites intrusion (***k*** = 0.0261).

Figure 9: Modelling along profile 3. (a) Magnetic anomaly profile; (b) Combined geophysical model and geological section. The CC/NEFB limit is represented by the faults F3-6, F3-7, F3-8 and F3-9; susceptibility values are in cgs, a division by 4π yields SI values

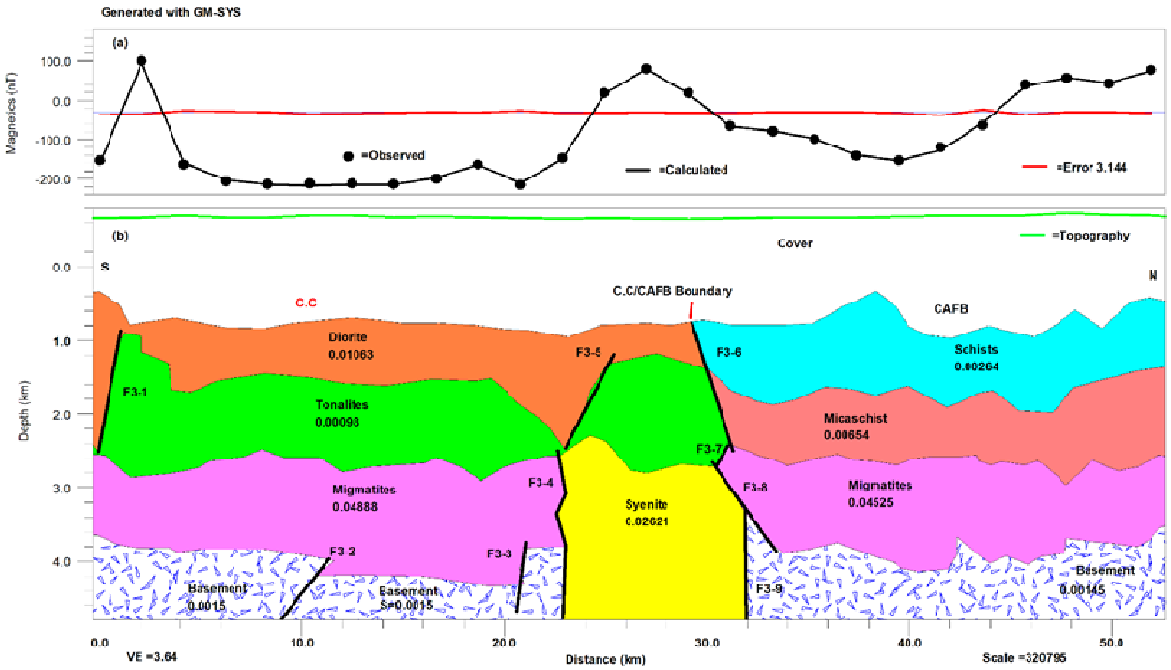

The geological model (obtained for a RMS error of 3.144%) outlines various probable faults, F3-1 to F3-9, which are somewhat hidden on the anomaly profile. Particularly, F3-2 and F3-3 are related to probable vertical movements that may have caused a basement collapse between 10 km and 21 km. Accordingly, F3-4 and F3-9 are related to the modelled intrusion in the basement, in one hand, whereas F3-4 and F3-8 are faulted-contacts separating respectively, the migmatites I (k =0.04888)/syenites and syenites/migmatites II (k =0.04525). In addition, F3-7 and F3-6 seem particular, as F3-6 outlines upward, left to right, gneiss (k = 0.00098)/micaschists (k = 0.00654) and diorite (k = 0.01063)/metasediments (k = 0.00264) contacts; and F3-7 may constitute the gneiss/migmatites boundary. Assuming that F3-6, F3-7, F3-8 and F3-9 faults are relays of a unique fault, they separate a left (south) unit of high susceptibility formations probably of magmatic and origin, to a right (north) group of low susceptibility materials assimilated to detrital metasediments. Also, the zig-zag displayed by NEFB layers infer some probable N-S compressional movements.

Summarily, the three models are consistent with the existence of a low susceptibility block to the north, separated by a sharp discontinuity to a south-high susceptibility block. The high susceptibilities in the left are supposedly due to mafic terrains and low susceptibilities to detrital metasediments. Thus, the study delineates an igneous (equated to the CC) and a metasedimentary (equated to the NEFB) complexes separated by sub-vertical faults, probably the CC/NEFB limit.

Discussion

Validation of the Mapping Methodology

The mapping methodology involved the combined analysis of the multiscale HGM and the Euler 3D methods to detect and locate faults and fractures. The efficiency of these techniques have been proven by various studies including those involving the southern Cameroon context (e.g. Basseka *et al* 2011; Shandini *et al* 2010; Owona Angue *et al* 2016; Yandjimain *et al* 2017). Further, the choice of a depth

tolerance of 5 % and a structural index of 0.5 to recover Euler's solutions enabled to avoid spurious solution and to provide good depth estimates, in accordance with Hinze *et al* (2013). Besides, interpretation of enhanced image of magnetic images are good in locating structures with regional significance (Paterson and Reeves 1985; Reeves 2005). Thus, combining these methods strengthens the validity of the results presented in this paper.

Validation of Highlighted Fractures and Correlation with Previous Studies

The study has revealed the presence of many faults based on qualitative (figures 3 and 4) and quantitative (figure 6) interpretations. The classification of these faults as per the descriptive depth ranges (table 1) matches with the quantitative Euler's depth ranges (figure 6). In regard with the absence of supportive field data, an additional cross-validation between Euler's solutions, RTE enhanced and HGM highlighted faults is done by superimposing those outputs on a same diagram (figure 6) which shows a good fit in between these different results.

The faults orientations are globally WNW-ESE, W-E, NW-SE, SW-NE and WSW-ENE with two dominant outlined clusters (SW-NE to WSW-ENE) and (WNW-ESE to NW-SE). These directions, as well as the vertical to sub-vertical dips observed, are consistent with other geophysical studies in the vicinities of the study area (Shandini *et al* 2010; Basseka *et al* 2011; Ndougsa-Mbarga *et al* 2012; Akame *et al* 2013, 2018; Bikoro-Bi-Alou *et al* 2014; Assembe *et al* 2016; Owona-Angue *et al* 2016). The calculated depth ranges locate these features in the brittle upper crust zone as shown by Basseka *et al* (2011) and Shandini *et al* (2011) over a region that includes the study area. This study emphasised on a dominant WSW-ENE to SW-NE direction's fan which correlates well with the major directions outlined in the CC/NEFB transition zone and within the Ntem complex by previous studies and by Assembe *et al* (*in preparation*), respectively to the east, south-east, the north and within the investigated area. This direction probably corresponds to pre-Neoproterozoic weakness zones which underwent Neoproterozoic and post-Neoproterozoic reactivations, and controlled deposition and metamorphism in the northern margin of the CC as noticed by Nkombou *et al* (2014) in accordance with Katumwehe *et al* (2015).

Clearly, it appears that both in the CC and NEFB domains, WSW-ENE to SW-NE fractures form a major strike-slip line overprinted by sinistral WNW-ESE to NW-SE faults associated to E-W lateral wrenches potentially due to WNW-ESE to NW-SE shears, in accordance with Ngako *et al* (2004). The WSW-ENE strike-slips system hence corresponds to an extensional axis (coeval to the setup of the Central Africa Rift System whose local member is the Centre Cameroon Shear Zone-CCSZ) in a weakness zone set-up during the paleo- to meso-Proterozoic (Ngako *et al* 2004; Mbola Ndzana *et al* 2014). These results are consistent with many geological studies carried out in southern Cameroon (Toteu *et al* 1994; Ngako *et al* 2008; Olinga *et al* 2010; Tchameni *et al* 2010; Mbola-Ndzana *et al* 2014), as well as at the regional scale (Binks and Fairhead 1992; Fairhead *et al* 2013; Kirkpatrick *et al* 2013; Katumwehe *et al* 2015). We assume that the WNW-ESE to NW-SE shears responsible to the E-W wrenches result from the on-going dynamics of the Africa-Eurasia convergence and the rifting in east Africa.

On the Ntem Complex/North Equatorial Fold Belt Limit

The differentiation of the NEFB from the Ntem complex, based on the difference in fracturing density observed on produced maps (figures 3, 4 and 5) of Metet-Zoetele, was linked to the difference in rheology of the in situ materials. That interpretation is supported by the inversion results (figures 7, 8 and 9) which globally define a magmatic complex to south and a metasedimentary complex to the north, and provide a clear location of the CC/NEFB limit on each profile. The location of that limit, measured from the north edge of the map, along each profile is compared to inversion output in table 2.

Table 2: Locations of the CC/NEFB southern limit. The distances are obtained from the north along profiles

Location of the CC/NEFB limit in km (west to east)			
	P1	**P2**	**P3**
Measured on map	19.24	17.87	21.42
From inversion	18.3	16.5	20.45
Stdev.		1.59	

These distances set the average location of the CC/NEFB southern limit at the UTM N370000 (or N03º20') latitude, initially located in the area at N03º30' (Shandini *et al* 2010; Basseka *et al* 2011). Additionally, the models (figures 7, 8 and 9) infer a high susceptibility material beneath the NEFB and a unique basement underlying the Metet-Zoetele area that may reflect the subduction of the Congo Craton under the Yaounde group as evidenced by other studies (Shandini *et al* 2010; Shandini and Tadjou 2012; Meying *et al* 2013; Assembe *et al* 2016). Although the high susceptibility materials beneath the NEFB at the vicinity of the CC/NEFB limit correlate the high density formations outlined and interpreted as a CC/NEFB suture in the area (Tadjou *et al* 2009; Shandini *et al* 2010; Basseka *et al* 2017), the current study suggests that this shall be reviewed in regard to recent studies on the CC northern margin (e.g. Goussi Ngalamo *et al* 2017, 2018). The faults intersecting the CC/NEFB limit (Figure 3) are imprints of the dislocations in the northern margin of the CC (Njingti-Nfor *et al* 2017a.,b). Despite the study correlates past studies, some outstanding points remain; such as the absence of N-S and NNE-SSW fractures reported by other studies. This issue, along with a more detailed quest on the tectonic evolution of the Congo Craton-Panafrican transition zone are still investigated by the authors.

Conclusions

The paper presents an interpretation of aeromagnetic data over a portion of the Congo Craton/Pan-African transition zone in southern Cameroon, in order to improve the understanding of the geological evolution in the northern margin of the Congo Craton. Various fractures have been highlighted mainly along the WNW-ESE, W-E, NW-SE, SW-NE and WSW-ENE directions both in the Congo Craton and the Pan-African domains. The WSW-ENE fractures correspond to a dextral extensional paleo structural network reactivated by NW-SE compressions, coeval to the Central Cameroon Shear Zone, further overprinted by a sinistral WNW-ESE to NW-SE displacement as a response to the on-going general NE convergence of Africa towards Eurasia and the rifting in east Africa. This suggests the existence of on-going wrenches both in the Ntem complex (CC) and the Pan-African (NEFB) system. Additionally, the inverse modelling of the magnetic data corroborates compressions between the CC and the NEFB, clearly defines the southern NEFB/CC limit as a sharp fault-contact line located at latitude N03º20'; and validates the existence of craton materials beneath NEFB. However, further investigations are on-going by the authors towards a consistent geodynamic model northern margin of the Congo Craton that integrates pending tectonics in the African Plate.

Acknowledgement

The authors are thankful to Professor Colin Reeves for his critical remarks and advises; and the anonymous reviewers who will endeavour themselves into the improvement of the quality of this paper through their welcomed critics and remarks.

References

[1] Toteu S F, Schmus W R V and Penaye J 2006a The Precambrian of Central Africa: Summary and perspectives *J. African Earth Sci.* **44**

[2] Mvondo H, Essono J, Mvondo Ondoa J and Yene Atangana J Q 2007 Comment on "U-Pb dating of plutonic rocks involved in the nappe tectonic in southern Cameroon: Consequence for the Pan-African orogenic evolution of the central African fold belt" by Toteu et al. (Journal of African Earth Sciences 44 (2006) 479-493) *J. African Earth Sci.* **48** 49–52

[3] Mvondo Ondoa J, Mvondo H and Den Brok B 2009 Pan-African tectonics in northwestern Cameroon : Implication for the history of western Gondwana *Gondwana Res.* **16** 163–4

[4] Ngako V and Njonfang E 2011 Plates Amalgamation and Plate Destruction , the Western Gondwana History *Tectonics*

[5] Ngnotue T, Ganno S, Nzenti J P, Schulz B, Tchaptchet Tchato D I and Suh Cheo E 2012 Geochemistry and Geochronology of Peraluminous High-K Granitic Leucosomes of Yaound Series (Cameroon): Evidence for a Unique Pan-African Magmatism and Melting Event in North Equatorial Fold Belt *Int. J. Geosci.* **03** 525–48

[6] Paterson N R and Reeves C V 1985 Applications of gravity and magnetic surveys : The state-of-the-art in 1985 *Geophysics* **50** 2558–94

[7] Nabighian M N, Ander M E, Grauch V J S, Hansen R O, LaFehr T R, Li Y, Pearson W C, Peirce J W, Phillips J D and Ruder M E 2005 Historical development of the gravity method in exploration *Geophysics* **70** 63–89

[8] Boyd D M and Isles D J 2007 Geological Interpretation of Airborne Magnetic Surveys - 40 Years On *Proceedings of Exploration 07: Fifth Decennial International Conference on Mineral Exploration* ed B Milkereit pp 491–505

[9] Feumoe A N, Ndougsa-Mbarga T, Manguelle-Dicoum E and Fairhead J D 2012 Delineation of tectonic lineaments using aeromagnetic data for the south-east Cameroon area *Geofizika* **29**

[10] Ndougsa-Mbarga T, Feumoe A N S, Manguelle-Dicoum E and Fairhead J D 2012 Aeromagnetic Data Interpretation to Locate Buried Faults in South- *Geophysica* **48** 49–63

[11] Yandjimain J, Ndougsa-mbarga T, Meying A, Bi-alou M B, Ngoumou P C, Assembe S P, Ngoh J D and Owono-amougou O U I 2017 Combination of Tilt-Angle and Euler Deconvolution Approaches to Determine Structural Features from Aeromagnetic Data Modeling over Akonolinga-Loum Area *Int. J. Geosci.* **8** 925–47

[12] Yandjimain J, Ndougsa-Mbarga T, Bikoro Bi-alou M and Meying A 2018 Aeromagnetic Data Modeling for Geological and Structural Mappings over the DJADOM-ETA Area, in the Southeastern Cameroon *Int. J. Geosci.* **9** 354–70

[13] Blakely R J 1996 *Potential Theory in Gravity and Magnetic* (Cambridge university press)

[14] Reid A B, Allsop J M, Granser H, Millet A J and Somerton I W 1990 Magnetic interpretation in three dimensions using Euler deconvolution **55**

[15] Nkoumbou C, Barbey P, Yonta-Ngouné C, Paquette J L and Villiéras F 2014 Pre-collisional geodynamic context of the southern margin of the Pan-African fold belt in Cameroon *J. African Earth Sci.* **99** 245–60

[16] Toteu S F, Fouateu R Y, Penaye J, Tchakounte J, Mouangue A C S, Van Schmus W R, Deloule E and Stendal H 2006b U-Pb dating of plutonic rocks involved in the nappe tectonic in southern Cameroon: consequence for the Pan-African orogenic evolution of the central African fold belt *J. African Earth Sci.* **44** 479–93

[17] Toteu S F, Penaye J and Djomani Y P 2004 Geodynamic evolution of the Pan-African belt in central Africa with special reference to Cameroon *Can. J. Earth Sci.* **41** 73–85

[18] Toteu S F, Penaye J, Deloule E, Van Schmus W R and Tchameni R 2006 Diachronous evolution of volcano-sedimentary basins north of the Congo craton: Insights from U-Pb ion

microprobe dating of zircons from the Poli, Lom and Yaoundé Groups (Cameroon) *J. African Earth Sci.* **44** 428–42

[19] Mvondo H, Owona S, Ondoa J M and Essono J 2007 Tectonic evolution of the Yaoundé segment of the Neoproterozoic Central African Orogenic Belt in southern Cameroon *Can. J. Earth Sci.* **44** 433–44

[20] Olinga J B, Mpesse J E, Minyem D, Ngako V, Ndougsa-Mbarga T and Ekodeck G E 2010 The Awaé – Ayos strike-slip shear zones (southern Cameroon): Geometry, kinematics and significance in the late Pan-African tectonics *N. Jb. Geol. Paläont. Abh.* **257** 1–11

[21] Mbola-Ndzana S P, Mvondo-Ondoa J, Owona S, Sep-Nlongand J P, Olinga J B and Bilong P 2014 Evidence of the ~NE-SW extension in the Sa'a-Monatélé Region as in the Bafia and Yaounde groups within the Central Africa Fold belt (Cameroon): Implication for the Southern Cameroon Neoproterozoic extension *Sci. Technol. Développement, Technol. Développement* **16** 1–15

[22] Shang C K, Muharrem S, Nsifa Nkonguin E, Liegeois J-P, Siebel W and Taubald H 2007 Archaean high-K granitoids produced by remelting of earlier Tonalite – Trondhjemite – Granodiorite (TTG) in the Sangmelima region of the Ntem complex of the Congo craton, southern Cameroon *Int J Earth Sci (Geol Rundsch)* **96** 817–41

[23] Tchameni R, Lerouge C, Penaye J, Cocherie A, Milesi J P, Toteu S F and Nsifa N E 2010 Mineralogical constraint for metamorphic conditions in a shear zone affecting the Archean Ngoulemakong tonalite, Congo craton (Southern Cameroon) and retentivity of U-Pb SHRIMP zircon dates *J. African Earth Sci.* **58** 67–80

[24] Shang C K, Liégeois J P, Satir M, Frisch W and Nsifa E N 2010 Late Archaean high-K granite geochronology of the northern metacratonic margin of the Archaean Congo craton , Southern Cameroon : Evidence for Pb-loss due to non-metamorphic causes *Gondwana Res.* **18** 337–55

[25] Tchameni R, Mezger K, Nsifa N E and Pouclet A 2001 Crustal origin of Early Proterozoic syenites in the Congo Craton (Ntem Complex), South Cameroon *Lithos* **57** 23–42

[26] Vicat J and Moloto-a-kenguemba G 2013 Les granitoides de la couverture protérozoique de la bordure nord du craton du Congo (Sud-Est du Cameroun et Sud-Ouest de la République centrafricaine), témoins d'une activité magmatique panafricaine

[27] Takam T, Makoto A, Kokonyangi J, Dunkley, Daniel J and Nsifa Nkonguin E 2009 Paleoarchaean charnockite in the Ntem Complex, Congo Craton, Cameroon : insights from SHRIMP zircon U-Pb ages *J. Mineral. Petrol. Sci.* **104** 1–11

[28] Toteu S F, van Schmus W R, Penaye J and Nyobe J B 1994 U-Pb and Sm-Nd evidence for Eburnian and Pan-African high-grade metamorphism in cratonic rocks of southern Cameroon. *Precambrian Res.* **67** 321–47

[29] Akame J M, Mvondo Ondoa J, Olinga J B, Essono J and Kemeng M P 2013 Utilisation des modèles numériques de terrain (MNT) SRTM pour la cartographie des linéaments structuraux : Application à l'Archéen de Mezesse à l'est de Sangmélima *Geo-Eco-Trop.* **37** 71–80

[30] Loose D and Schenk V 2018 2.09 Ga old eclogites in the Eburnian-Transamazonian orogen of southern Cameroon : Significance for Palaeoproterozoic plate tectonics *Precambrian Res.* **304** 1–11

[31] Reeves C 2005 *Aeromagnetic Surveys-Principles, Practice & Interpretation* (Geosoft)

[32] Hinze W J, von Frese R R B and Saad A 2013 *Gravity and magnetic exploration: principles, practices and exploration* (Cambridge university press)

[33] Archibald N, Gow P and Boschetti F 1999 Multiscale edge analysis of potential field data *Explor. Geophys.* **30** 38–44

[34] Blakely J and Simpson R W 1986 Short Note Approximating edges of source bodies from magnetic or gravity anomalies **51** 1494–8

[35] Reeves C V, Reford S W and Milligan P R 1997 Airborne Geophysics : Old Methods , New Images *Proceedings of Exploration 97: Fourth Decennial International Conference on Mineral Exploration* ed A G Gubins pp 13–30

[36] Owona-Angue M L, Assembe S P, Njingti-Nfor, Ngoh J D, Ndougsa-Mbarga T, Kue Petou M R and Bisso D 2016 Determination of the Structural Lineaments in the Kribi-Campo-Ma ' an Area from a Multi-Scale Analysis of Gravity Data Using the HGM and Euler 3D Deconvolution Approaches *Int. J. Geosci.* **7** 1122–43

[37] Fernandez-Alonso M, Tack L, Tahon A and De Waele B 2010 The Proterozoic history of the proto-Congo Craton of Central Africa

[38] Prieto C 1996 Gravity/magnetic signatures of various geologic models-An exercise in pattern recognition *IGC Footnotes Interpret.* **4**

[39] Akame J M, Assembe S P, Zo'o Zame P, Owona S, Ndougsa-Mbarga T, Azia G A and Mvondo-Ondoa J 2018 The Sangmelima granite-greenstone belts (South Cameroon): Integration of remote sensing and aeromagnetic data for structural interpretation *Egypt. J. Remote Sens. Sp. Sci.*

[40] Assembe S P, Meying A and Ndougsa-Mbarga T 2016 New structural facts from audio-magnetotelluric (AMT) data interpretation in the Yaoundé-Nkolafamba area (Centre Cameroon) *J. Ind. Geophys. Union* **20** 19–32

[41] Basseka C A, Shandini Y and Tadjou J M 2011 Subsurface structural mapping using gravity data of the northern edge of the Congo craton , South Cameroon *Geofizika* **28** 229–45

[42] Bikoro-Bi-Alou M, Ndougsa-Mbarga T and Tabod T C 2014 Quantitative Interpretation of Magnetic Anomalies in Ebolowa-Djoum area (Southern Cameroon) *Geophysica* **50** 11–25

[43] Shandini Y N, Tadjou J M, Tabod C T and Fairhead J D 2010 Gravity Data Interpretation in the Northern Edge of the Congo Craton , South-Cameroon *Anuário do Inst. Geociências - UFRJ* **33** 73–82

[44] Katumwehe A B, Abdelsalam M G and Atekwana E A 2015 Tectonophysics The role of pre-existing Precambrian structures in rift evolution : The Albertine and Rhino grabens , Uganda *Tectonophysics* 1–13

[45] Ngako V, Affaton P and Njonfang E 2008 Pan-African tectonics in northwestern Cameroon : Implication for the history of western Gondwana *Gondwana Res.* **14** 509–22

[46] Binks R M and Fairhead J D 1992 A plate tectonic setting for Mesozoic rifts of West and Central Africa *Tectonophysics* **213** 141–51

[47] Fairhead J D, Green C M, Masterton S M and Guiraud R 2013 Tectonophysics The role that plate tectonics , inferred stress changes and stratigraphic unconformities have on the evolution of the West and Central African Rift System and the Atlantic continental margins *Tectonophysics* **594** 118–27

[48] Kirkpatrick J D, Bezerra F H R, Shipton K, Nascimento A F D O, Federal U and Al J D K E 2013 Scale-dependent influence of pre-existing basement shear zones on rift faulting : a case study from NE Brazil *J. Geol. Soc. London.* **170** 237–47

[49] Basseka C A, Eyike Yomba A, Kenfack J V, Njiteu Tchoukeu D C, Som Mbang M C and Shandini Njankouo Y 2017 Magnetic Anomaly Interpretation of the Northern Congo Craton Boundary : Results from Depth Estimation and 2.5D Modeling *J. Geosci. Environ. Prot.* **5** 90–101.

[50] Shandini Y and Tadjou J M 2012 Interpreting gravity anomalies in south Cameroon, central Africa *Earth Sci. Res. J.* **16** 5–9

[51] Goussi Ngalamo J F, Bisso D, Abdelsalam M G, Atekwana E A, Katumwehe A B and Ekodeck G E 2017 Geophysical imaging of metacratonizaton in the northern edge of the Congo craton in Cameroon *J. African Earth Sci.*

[52] Goussi Ngalamo J F, Sobh M, Bisso D, Abdelsalam M G, Atekwana E and Ekodeck G E 2018 Lithospheric structure beneath the Central Africa Orogenic Belt in Cameroon from the analysis of satellite gravity and passive seismic data *Tectonophysics* **745** 326–37

[53] Njingti-Nfor, Owona-Angue M L, Kue Petou M R, Bisso D and Lando Tsakou J A 2017 Application of Coefficient of Anisotropy to the Geophysical Prospecting of Campo — Ma ' an Area of the Ntem Complex in Cameroon *Open J. Geol.* **2017** 1801–18

[54] Njingti-Nfor, Owona Angue M L, Petou Kue M R, Bisso D and Piameu Kwagag J 2017 Magnetotelluric Investigation of the Geo-Tectonic Stability of Campo-Ma ' an Area in South Cameroon *Int. J. Geosci.* 1427–41**.**

Scientific Research Publishing

Advances in Remote Sensing, 2020, 9, 53-84
https://www.scirp.org/journal/ars
ISSN Online: 2169-2688
ISSN Print: 2169-267X

+−Evidence of Porphyry Deposits in the Ntem Complex: A Case Study from Structural and Hydrothermal Alteration Zones Mapping through Landsat-8 OLI, Aeromagnetic and Geological Data Integration in the Yaounde-Sangmelima Region (Southern Cameroon)

Stephane Patrick Assembe[1,2*], Theophile Ndougsa Mbarga[3*], Françoise Enyegue A. Nyam[4], Paul Claude Ngoumou[5], Arsene Meying[5], Daniel Herve Gouet[6], Alain Zanga[7], Jean Daniel Ngoh[1]

[1]Postgraduate School of Technology, Science and Geoscience, University of Yaounde 1, Yaounde, Cameroon
[2]Department of Physics, Faculty of Science, University of Bamenda, Bambili, Cameroon
[3]Department of Physics, Higher Teachers Training College, University of Yaounde 1, Yaounde, Cameroon
[4]Department of Physics, Faculty of Science, University of Yaounde 1, Yaounde, Cameroon
[5]School of Geology and Mining Engineering, University of Ngaoundere, Meiganga, Cameroon
[6]Faculty of Mining and Petroleum Industries, University of Maroua, Kaele, Cameroon
[7]Department of Physics, Faculty of Science, University of Douala, Douala, Cameroon
Email: *assembest@yahoo.fr, *tndougsa@yahoo.fr

How to cite this paper: Assembe, S.P., Mbarga, T.N., Nyam, F.E.A., Ngoumou, P.C., Meying, A., Gouet, D.H., Zanga, A. and Ngoh, J.D. (2020) +−Evidence of Porphyry Deposits in the Ntem Complex: A Case Study from Structural and Hydrothermal Alteration Zones Mapping through Landsat-8 OLI, Aeromagnetic and Geological Data Integration in the Yaounde-Sangmelima Region (Southern Cameroon). *Advances in Remote Sensing*, **9**, 53-84.
https://doi.org/10.4236/ars.2020.92004

Received: January 26, 2020
Accepted: June 5, 2020
Published: June 8, 2020

Abstract

A semi-regional study was carried out in the Yaounde-Sangmelima area, a densely vegetated tropical region of southern Cameroon located in the Central Africa Fold Belt (CAFB)/Congo Craton (CC) transition zone. Towards structural lineaments and predictive hydrothermal porphyry deposits mapping, an integrated analysis of Landsat-8 OLI data, aeromagnetic, geological and mineral indices maps was performed. The Remote sensing using False colour composite images involving bands combinations and Crosta method (features oriented principal components analysis) enabled the mapping of the gneisses and schists domains without a clear differentiation between the Yaounde and Mbalmayo schists; despite the reflectance anomalies evidenced NW of Akonolinga, hydrothermal alterations in the study area failed to be detected. Besides, aeromagnetics depicted a moderately fractured northern zone (the CAFB) contrasting with a high densely fractured zone (the CC,

known as Ntem complex). The Ntem complex displays signatures of a meta-igneous, an intrusive complex, greenstone relics south of Sangmelima and hydrothermal activity. Indeed, CET porphyry analysis tool detected many porphyry centres. In general, the study revealed many lineaments including contacts, fractures faults zones and strike-slips. The major aeromagnetics structures are SW-NE to WSW-ENE and WNW-ESE to NW-SE while those from Landsat-8 are NE-SW, WNW-ESE, NW-SE, WSW-ENE and NW-ESE to NNW-SSE. Together, these structures depict trans-compressions or trans-tensions corresponding to a broad NE-SW strike-slips channel that affect both the CAFB and the Ntem Complex, and they control the intrusions thus confirming a pervasive hydrothermal activity within the Ntem Complex. The proximity or coincidence of these porphyry centres with some mapped Iron-Gold affiliated mineral indices and porphyry granites indicate the possible occurrence of many hydrothermal ore deposits. These results show the high probability for the Ntem complex to host porphyry deposits so they may serve to boost mineral exploration in the Yaounde-Sangmelima region and in the entire southern Cameroon as well.

Keywords

Porphyry Centres, Hydrothermal Ore Deposits, Ntem Complex, Remote sensing, Aeromagnetics, Southern Cameroon

1. Introduction

Hydrothermalism alters rocks and provokes various types of mineralization occurring in general as polymetallic deposits (e.g. (IOCG; porphyry Cu-Au) +/− Ag, U, Mo, Pb, REE, Zn, etc). Most common hydrothermal deposits styles are intrusion related, epithermal, skarns and porphyry [1] [2] [3]. In general, porphyry deposits are hosted in Archaean to Proterozoic terrains in a convergent setting [2] [4] [5] [6]. The CAFB/CC transition zone in southern Cameroon, at the northern margin of the Congo craton (CC), in regards to its geological history, becomes good candidate host of these deposit types. Therefore, a detailed geoscience work needs to be done in this region, to assess this potential and subsequently revamp mineral exploration industry.

Remote sensing (RS) and aeromagnetics are solutions to geoscientific studies in wide and inaccessible regions. in geological RS, surface alteration controls better the reflectance of geologic materials so, high discrimination capabilities of lithology are found in the visible near infrared-VNIR and Shortwave infrared (SWIR) regions *i.e.* 0.7 to 3.0 μm interval [7] [8]. Various pre-processing and processing technique/enhancement workflows exist and are intuitively used to meet desired goals. However, the most common approaches involve whether alone or in combination, bands combination, band rationing, data dimensional reduction and image filtering (e.g. see, [8] [9] for detailed discussions). RS has become a standard tool in geological studies by highlighting faults/fractures in

structural studies [10] [11] [12] [13] [14] and in mapping lithology and/or hydrothermal alteration zones related to mineral ore deposits [15]-[20] in different geological contexts across continents. Some recent pioneer studies involving Landsat suites data have been done in Cameroon to address structural [21] hydrological [22] or lithology and mineral exploration [23] [24] [25] issues.

Aeromagnetics is a premium tool in geological and mineral exploration studies for its high capabilities in mapping structures and lithology irrespective of the terrain conditions and availability of outcrops at any scale [26] [27]. Various filtering and processing techniques have been developed for qualitative, quantitative or both, interpretation. Qualitative interpretation involves mostly the use of edge detection filters for lineaments detection and even specific features like porphyry and kimberlite bodies [27] [28] [29] [30]. Quantitative interpretation involves depth-to-basement (e.g. Euler deconvolution approaches by [31] [32]) and modelling methods which solve either or both the nature, location, shape and susceptibility of the source (e.g. see [33]). Significant contributions from aeromagnetics to update the geology of the CC/CAFB transition zone are being made by many workers [34] [35] [36], but most of these lack field evidences. In geophysics, the adjunction of at least two methods gives more consistent results; thus, we combine the strong mapping capabilities of aeromagnetics, RS so as to yield more accurate and credible results while investigating the Yaounde-Sangmelima region. The consistency of this approach has been proven by several workers (e.g. [14] [25] [37] [38]) who combined Landsat, aeromagnetic and geological data to map both hydrothermal targets, lithology and lineaments as well, in various geological contexts.

2. Geological Setting

The Yaounde-Sangmelima area is located in southern Cameroon, a region entirely dominated by the tropical dense forest with thick lateritic soil at the northern margin of the CC. The main lithological units are, southward, the CAFB and the Ntem complex (**Figure 1(a)**). according to [39] [40] [41], the Ntem complex comprises various Archaean to Paleoproterozoic rocks. Archaean formations are mainly tonalites [42] [43] [44]; calc-alkaline to alkaline granitoids and granodiorites in dominantly occurring charnockites, as well as greenstones relics [40] [45] [46] [47]. Moreover, [40] and [48] identified dolerite dykes, syenites, metabasites and gneisses as in the Nyong series as Paleoproterozoic. The CAFB regroups Neoproterozoic terranes overlying a Paleoproterozoic basement. According to [43] [49] [50] [51] (and references therein), the Neoproterozoic assemblages are: 1) dominantly garnetiferous gneisses and micaschists, amphibolites and some quartzites that form the granulitic Yaounde series; and 2) low-grade schists and quartz-sericite rocks associated with volcanic relics forming the Mbalmayo series discordant to the Ntem complex (**Figure 1(b)**).

The tectonic activity at the northern margin of the CC takes into consideration the difference in its lithological arrangement. Indeed, according to some

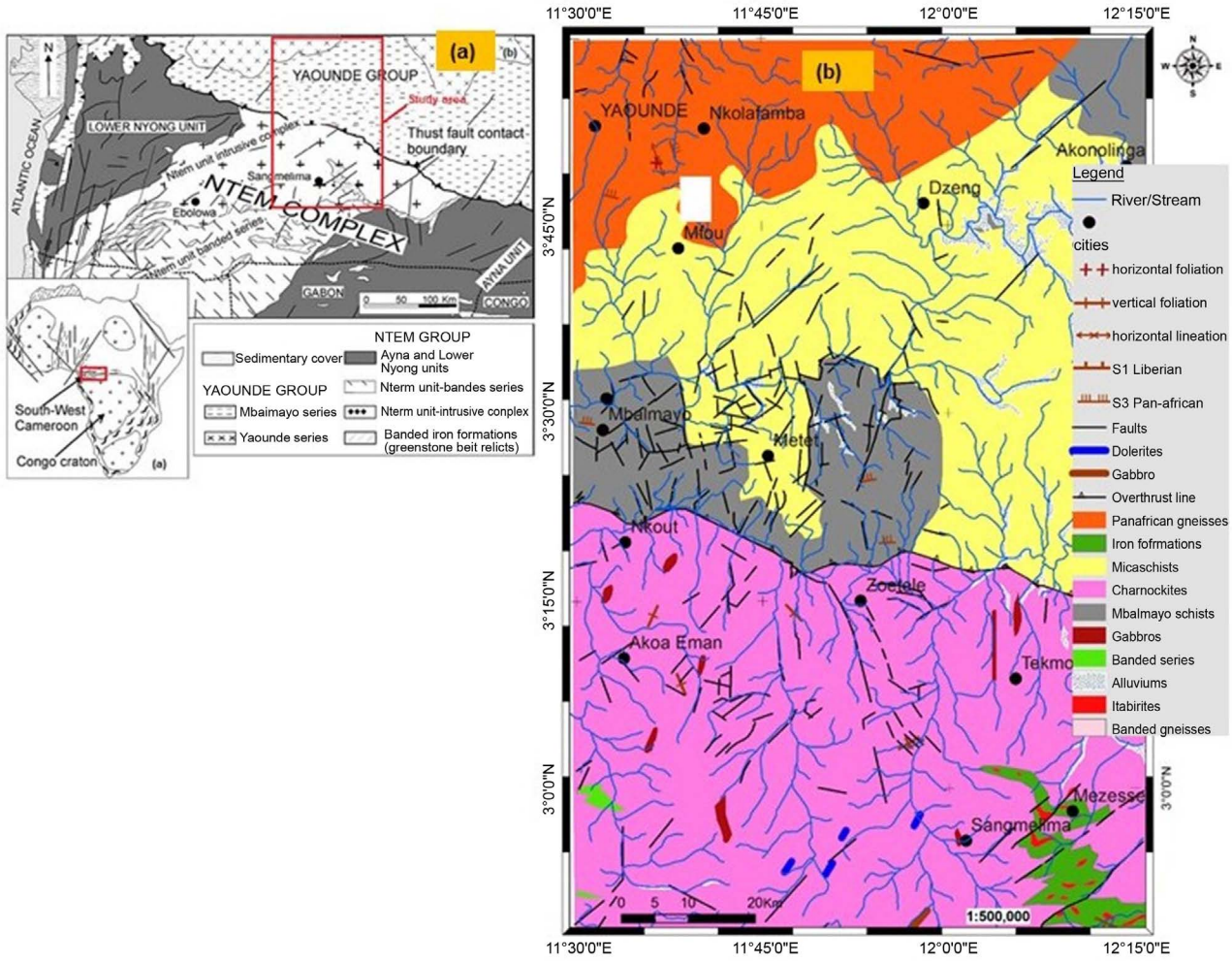

Figure 1. Local geological map of the Yaounde-Sangmelima after [42] [43].

workers the Ntem complex seems to have been first influenced by the Liberian orogeny marked by various folds and brittle structures [52] with an Archaean magmatism [45] [53]. The second main event in the Ntem complex is the Eburnean orogeny marking the Sao-Francisco Craton/Congo Craton collision [54] [55] during which NE–SW, E–W to ESE–WNW, NW–SE and N–S main lineaments formed and the crust rejuvenated at the NW edge of the CC [56] [57] [58] [59]. Obviously, this seems to be the more documented event affecting the cratonic part of the study area.

The CAFB besides is clearly affected by Panafrican and post-Panafrican tectonics. Previous studies identified four Panafrican deformation stages (e.g. [60] [61] [62]). In the Yaounde group, [63] summarised it into the thrusting of the CAFB nappes onto the followed by ENE-WSW strike-slips. These tectonics caused by overall dextral transpressions due to alternating E-W to NW–SE contractions and N-S to NE–SW orogenic-parallel extensions [62] generated N or S penetrative foliation associated with ENE-WSW stretching lineation and a N-S to NE-SW folding. However, this evolution is still debated (see e.g., [50] [64] [65] [66]), regarding the collisional system, the location and direction and the

geodynamic history of the Yaounde domain. Despite some relevant interpretations of the faults/fractures that they discovered (see e.g. [67] [68]), most geophysical studies fail to reconcile the aforesaid matters as they don't propose structural history of the northern margin of the CC based at least on these mapped features. Also, insufficient geophysical works towards predictive mapping of the ore minerals potentialities in the CAFB/CC transition zone have been done. This paper brings contributions to resolve the two above outstanding points through an integrated analysis of remote sensing, aeromagnetic and geological data over the Yaounde-Sangmelima region.

3. Data and Methods

3.1. Geological Datasets

The geological information used for this study comes from the official maps of the Republic of Cameroon that cover the Yaounde-Sangmelima area. To obtain a digital geological database, these maps were initially georeferenced, then warped in Google map for geographical rectification; then lithological, structural and mineral indices information was extracted through ArcGIS desktop 10.6.

3.2. Remote Sensing Method

3.2.1. Data Description and Preparation

The satellite data used are SRTM and Landsat 8 Operational Land Imager (OLI). SRTM are topographic data that model the elevation of a given surface relative to the sea level. They are availed as 1 × 1 degree scenes at a 30 m spatial resolution. OLI is a multispectral sensor on board of the Landsat 8 satellite whose bands characteristics are summarised in Table 1.

These are standard geometrically corrected (L1T1) images projected on the corresponding UTM zone freely available from the Global Land Cover Facility portal (*http://earthexplorer.usgs.gov/*). The current study uses two adjacent scenes whose respective path/row identifications are 185/057 and 185/058, recorded on the 12th January 2015 at approximately 09h 45 min. The two OLI scenes underwent a 3-steps preparation pre-processing stage consisting in:

Table 1. Landsat 8 OLI images characteristics [68].

Band Number	Spectral range (μm)	Spectral band	Resolution
1	0.43 - 0.45	Coastal blue	30 m
2	0.45 - 0.51	Blue	30 m
3	0.53 - 0.59	Green	30 m
4	0.64 - 0.67	Red	30 m
5	0.85 - 0.88	NIR	30 m
6	1.57 - 1.65	SWIR-1	30 m
7	2.11 - 2.29	SWIR-2	30 m
8	0.50 - 0.68	Panchromatic	30 m
9	1.36 - 1.38	Cirrus	30 m

1) The radiometric calibration for atmospheric correction to remove the influence of the atmosphere and haze, and conversion of digital numbers of each individual scene into surface reflectance which is physically meaningful for earth objects investigation. The operation was realised using the Quick atmospheric correction (QUAC®) which determines atmospheric correction parameters directly from the observed pixel spectra in a scene, without ancillary information.

2) Vegetation suppression by removing the signal related to the canopy on each individual scene in order to produce a multispectral image that mimics the surface reflectance without vegetation.

3) the mosaicking of the pre-processed scenes, then spatially subsetting the mosaicked image to the study area and reducing its spectral dimension by removing the coastal band (band 1) which is not useful in geology.

3.2.2. Multispectral Images Processing Methods

Colour composition. Colour composition is an image enhancement technique which consists in combining natural or hybrid bands (e.g. band ratios, eigenvectors, etc.). When using natural bands, the appropriate bands combinations were determined using the optimum index factor (OIF) initially designed by [69] statistically determines the most appropriate combinations represented by the highest OIF ranking as presented in **Table 2**.

These combinations were used to map the lithology of the Yaounde-Sangmelima area, by undelaying the SRTM map to identify changes in texture (**Figure 2(a)**).

Principal components (PC) analysis. The PC transform segregates noise components, decorrelates and reduces the dimensionality of data sets. The dimensionality reduction removes the redundancy in the dataset, yielding uncorrelated hybrids bands (PC bands) which concentrate maximum information from the multispectral data. [70] developed a feature-oriented PC (FPCS) approaches to focus on specific goals (minerals). The principle consists in the calculation of PCs from a specific group of bands containing information on the sought feature then select the most informative FPC band. The FPCS were calculated in the bands (2, 3, 4, 5) for iron oxides and hydroxides detection; and in the bands (4, 5, 6, 7) for clays (OH). The resulting FPCS are presented in **Table 3**.

Lineaments extraction. To map lineaments, the greyscaled standard PC1 image is high-pass filtered using a 3 × 3 window to reduce noise and enhance

Table 2. OIF ranking showing the highest five statistically convenient FCC images.

OIF Highest ranking			
Band 7	Band 6	Band 2	0.51
Band 7	Band 6	Band 3	0.47
Band 7	Band 5	Band 2	0.44
Band 6	Band 5	Band 2	0.42
Band 6	Band 3	Band 2	0.38

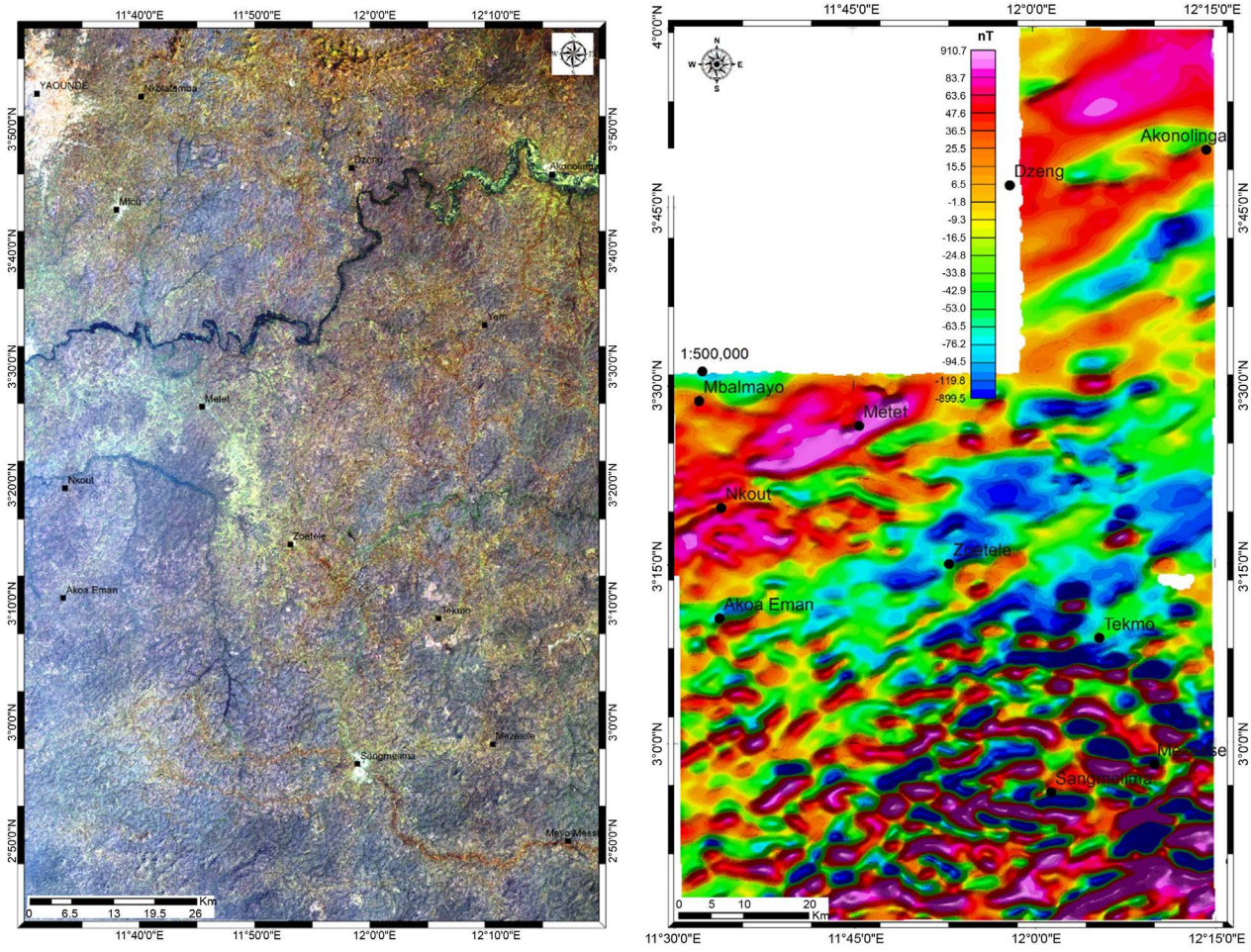

Figure 2. (a) Natural colour composite (RGB432) with the vegetation suppressed. The image mimics the soil surface reflectance. (b) Magnetic anomaly field reduced to the equator. The map has a NE anomaly passing through Metet depicting a discontinuity affecting both the CAFB and the Ntem Complex.

Table 3. Feature-oriented PCs for respectively clays (PCOH) and iron (PCFe) oxides/hydroxide minerals.

(a)

	PCOH			
	Band 2	Band 5	Band 6	Band 7
PCOH1	0.246	0.412	0.578	0.660
PCOH2	0.887	0.259	−0.174	−0.339
PCOH3	0.389	−0.826	−0.042	0.407
PCOH4	−0.036	0.285	−0.796	0.532

(b)

	PCFe			
	Band 2	Band 3	Band 4	Band 5
PCFe1	0.521	0.471	0.501	0.506
PCFe 2	0.763	−0.067	−0.086	−0.638
PCFe 3	0.382	−0.456	−0.555	0.581
PCFe 4	−0.026	−0.752	0.658	0.022

edges. The filtering is performed on Envi 5.3 platform. The features extraction involved a semi-supervised classification that consists in 1) automatically detect lineaments from the high-pass filtered image of PC1 using the Canny edge filter within the LINE module in PCI-Geomatica 9.0 software. Later, 2) the image of the computer extracted features is underlain by the digital elevation model generated from the SRTM data above the area, to manually extract the lineaments using the photo-geological approach.

3.3. The Magnetic Method

3.3.1. Data Description and Preparation

The study utilises aeromagnetic data collected in January 1970 during a nationwide campaign held in Cameroon. The flight paths flown at a nominal altitude of 235 m, were spaced at 750 m and oriented S-N. major equipment consisted in a radar altimeter of 20 m precision. The field data were processed by Paterson Ltd and availed as total field maps at 1/50,000 scale. The total magnetic intensity (TMI) anomaly field was obtained by removing the geomagnetic field that pertained in 1970; assuming a mean declination of −18.2˚ and a mean inclination of −6.2˚, Reduction-to-the magnetic equator (RTE) transform was applied to the anomaly field to shift anomalies on top of their sources [29]. The resultant RTE map (**Figure 2(b)**) served as input for further analyses.

3.3.2. Magnetic Data Processing and Interpretation

Analytic signal method. The analytic signal (AS) is formed through the combination of horizontal and vertical gradients of a potential field [29]. Introduced by [71] to solve the depth and position of the anomaly sources in the 2D case, [72] extended the method to solve 3D problems on gridded data. The AS is used either as a mapping and depth-to source technique and as a way to learn about the nature of the causative magnetization [30].

The horizontal gradient method. The horizontal gradient method (HGM) is in many ways the simplest approach to estimate contact locations of the bodies at depth and it is advantageously less sensitive to the noise in the data because it only requires calculations of the two first-order horizontal derivatives of the field [29]. The HGM function gives a peak anomaly above magnetic sources which will be interpreted as lineaments [30] [73]; HGM peaks can be evaluated at different the upward continued heights, leading to a multiscale analysis [74]. The multiscale HGM is commonly has been used in lineaments mapping by several workers using magnetic or gravity data in structural investigations [27] [75] [76] [77].

CET Porphyry analysis. The CET Porphyry analysis tool was developed by the Centre for Exploration Targeting (CET), an Australian research group addressing mineral exploration industry problems. Developed by [78], this tool relies on the fact that an ideal porphyry hydrothermal mineralisation typically appears as a circular central intrusion surrounded by concentric circular alteration zones. The detection process involves sequentially applying: 1) the circular feature transform which uses a radial symmetry transform algorithm to detect cir-

cular shaped (elevated or depressed) features by identifying where image gradients converge or diverge respectively. 2) Performing central peak detection; and then visualising the feature boundaries using the amplitude contrast transform and the boundary tracing using a spline energy function that specifies porphyry boundaries.

The preparation and processing of Landsat 8 data was done in Envi 5.3 and lineament were automatically extracted with PCI-Geomatica v9.0; all the magnetic data preparation and processing was done in Oasis montaj 8.4. Maps were finalised and edited with ArcGIS 10.6 and Rockworks 16 served to draw lineaments rosaceas.

The work methodology consisted in detecting key lithology, zone of hydrothermal activity and lineaments from remote sensing and aeromagnetics, separately; then making a fusion and cross-validation of the results between the two methods at a first stage, and the final outputs are validated by the available geological data to yield the more plausible map of structural lineaments and porphyry deposits in the study area. This methodology is summarised by the flowchart (**Figure 3**).

4. Results

4.1. Lithology Mapping

4.1.1. Colour Composite Images Analyses

The true colour composition (**Figure 2(a)**) makes it difficult to outline specific

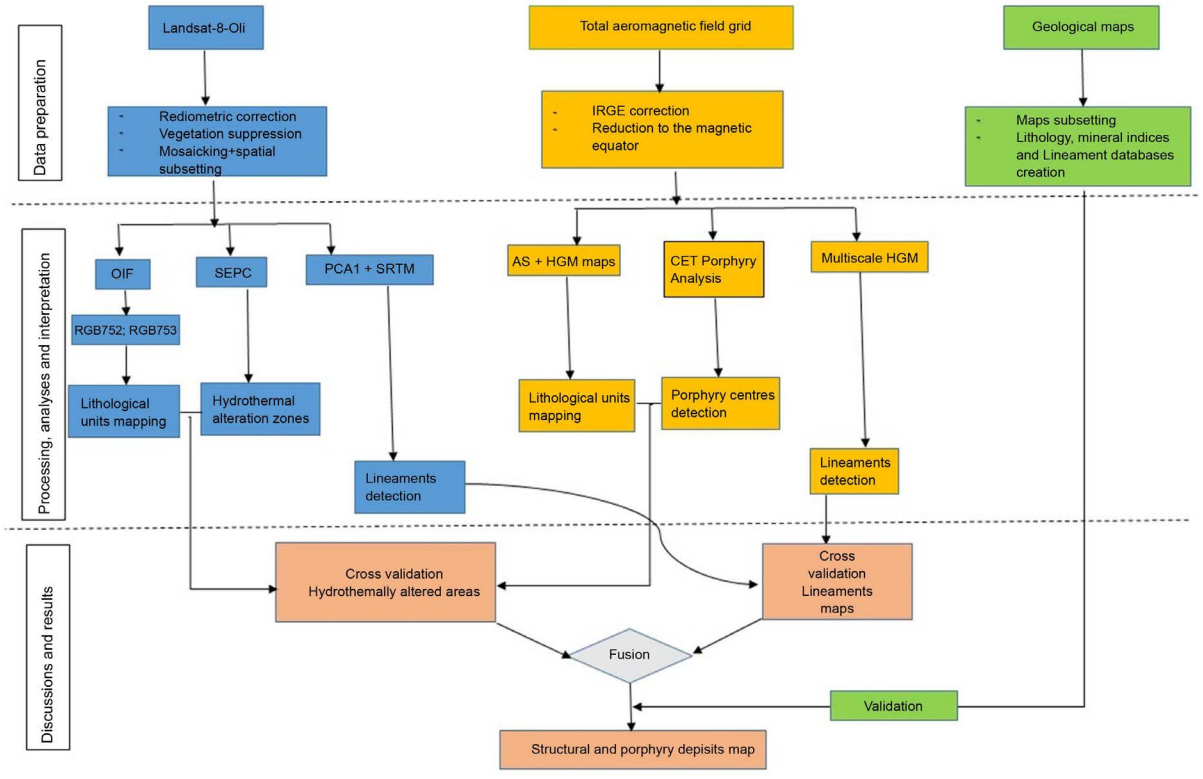

Figure 3. Flow chart summarising the methodology of work.

lithology. The overall coloration is marked by dark tones showing that the lithology is made up of only metamorphic crystalline rocks. The FCC involving the bands 752; 753 in the RGB order (Figure 4) outline well the gneiss formations in the northern part of the study area as a yellow (Figure 4(a)) or a reddish (Figure 4(b)). These colours are due to high absorption of probably iron oxides, micas, feldspars and amphibole minerals in the SWIR bands. These minerals are dominant in gneisses. The gneiss rocks have a south boundary formed by a broad NE-SW line passing south of Yaounde and west of Akonolinga which seems to correspond to the gneiss/schists formations boundary in the Neoproterozoic domain.

The FCC maps (Figure 4) show south and east of gneisses as a mix of dark, dark reddish and dark blue tones with some greyish patchworks. The dark shades of blue may be characteristic to the presence of minerals such as calcite, muscovite, dark minerals, fine grains of pyrite and graphite. Reddish tones may be caused by the presence of ferric oxides, chlorite and amphiboles while the greyish tones throughout the entire map result from the reflection in all the

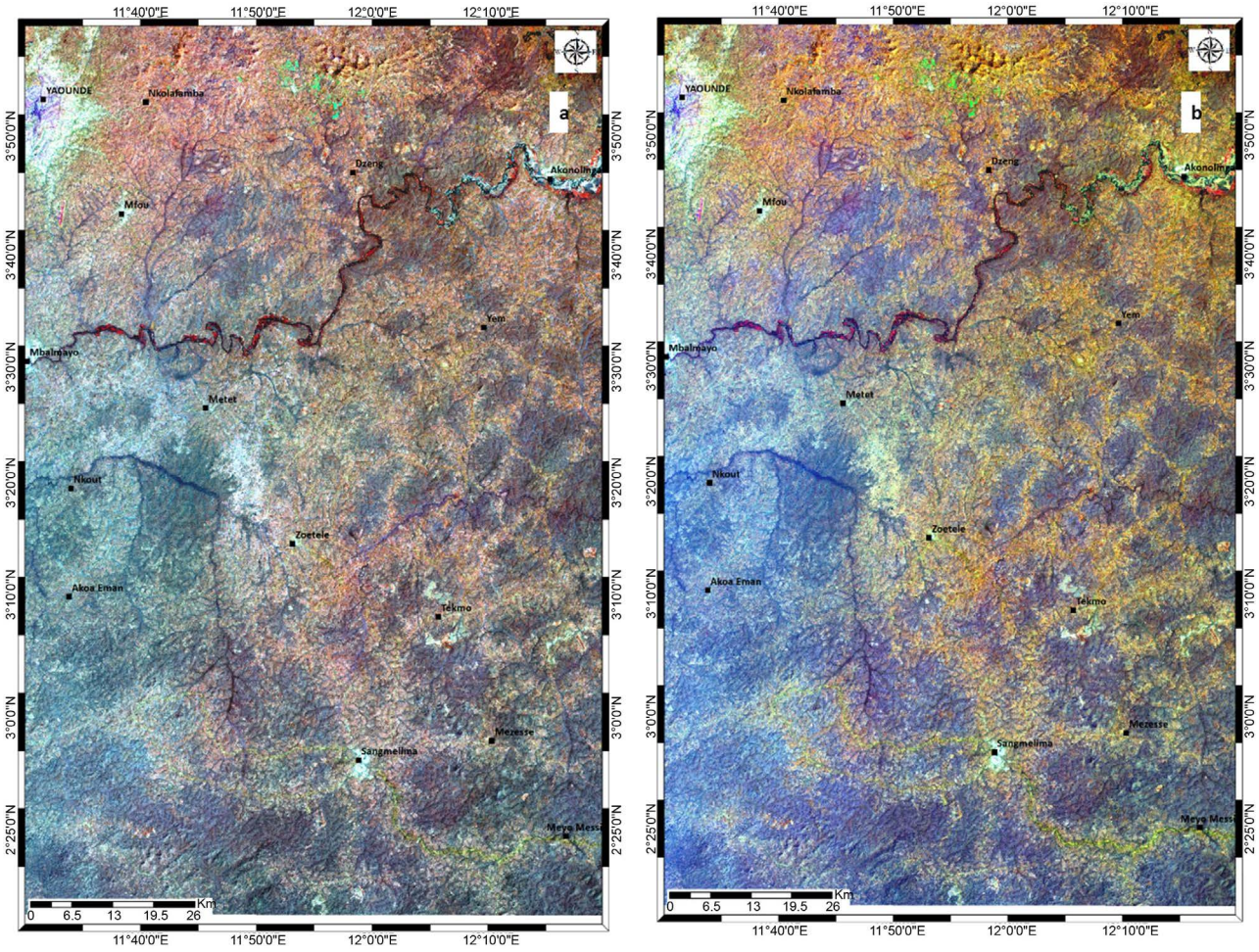

Figure 4. False colour composites (a) RGB752; (b) RGB753. The two images clearly outline the Panafrican gneisses (reddish) and schists (dark red) in the north of the study area.

bands characterising quartz-rich minerals (quartzites). The candidate rocks here are quartz-muscovite schists, pyritic or graphitic schists and quartz-schists. In the schists region, the boundaries between the varieties of schists are diffuse because they are mixed. Thus, they probably form the same schists belt.

South of Nkout (Figure 4), discrimination of the Ntem complex rocks is not obvious. However, the Akoaeman zone, exhibits dark blue tones with patchwork of pale blue to cyan and pale greenish which probably correspond to tonalites. In the Sangmelima zone, the tones are pink to reddish due to high SWIR and medium to low reflectance in bands 5 and 2 or 3 of amphiboles, feldspars, micas, pyroxenes and olivine minerals. This suggests the existence of an igneous or meta-igneous complex, probably the granites/granodiorites and other mafic to ultramafic or subcrustal materials herein. These rocks are better evidenced by magnetic data.

4.1.2. Aeromagnetic Qualitative Analyses

Magnetic data (Figure 5) differentiate Panafrican terranes to the north from CC rocks to the south. The Panafrican domain appears as a quiet magnetic background (low HGM and AS values, Figure 4) with some anomaly peaks around

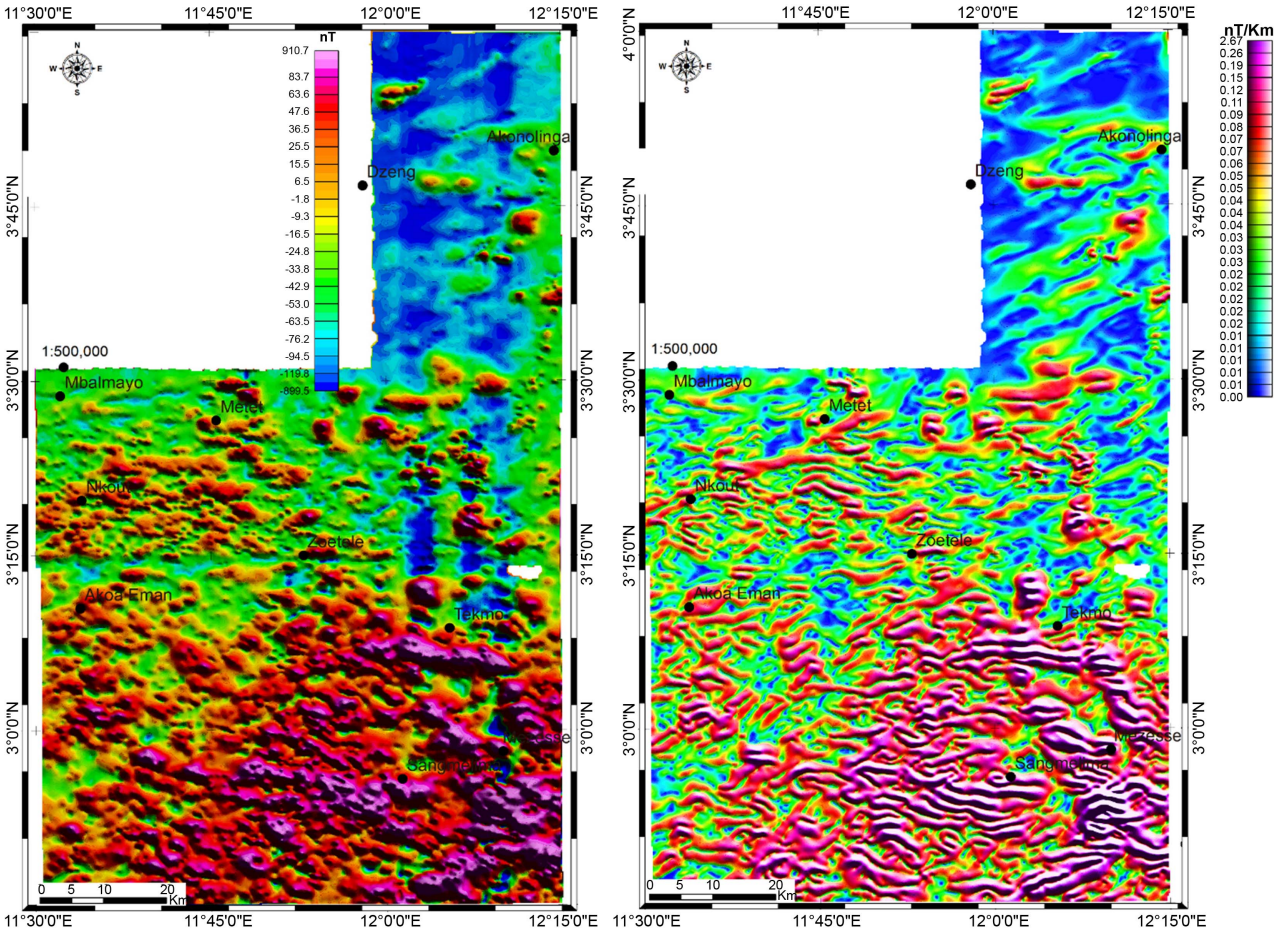

Figure 5. (a) Analytic signal and (b) Horizontal gradient magnitude maps.

Akonolinga, around Metet, probably due to intrusions or deep faults or fractures affecting the Paleoproterozoic basement of the CAFB. Southward from Nkout, an area of HGM intermediate anomalies represents the Ntem complex TTGs, gneisses and other granitoids. The AS and HGM anomaly peaks surrounding Sangmelima (**Figure 5**) possibly charnockites and many other mafic to ultramafic or subcrustal contributions into the local rock budget recognised as greenstones belt relics. The TTG/Charnockites boundary is sub-circular east to north, and NE-SW, west of Sangmelima.

The refinement from the AS map reveals a sparse occurrence of intrusions in the CAFB (except at, and, east of Metet) whereas the Ntem complex has more intrusions (**Figure 5(b)**). The high number of sub-circular anomaly peaks interpreted as various age intrusions is a possible imprint of a hydrothermal activity which was high in charnockites, moderate in the TTG and low in the CAFB. Particularly, we interpret this poor occurrence of intrusions in the schists/TTG boundary as an evidence of a discrete influence of the Panafrican event on the CC.

4.2. Lineaments Detection and Interpretation

Quantitatively, the remotely sensed data analysis (**Figure 6(a)**) enabled to highlight more (863) lineaments than the aeromagnetics. These lineaments make a cumulative length of 3843.90 km, for a minimum length of 0.56 km, a maximum length of 21.73 km and a corresponding average length of 4.67 km. Qualitatively, the major lineaments in the CAFB follow the WNW-ESE to NNW-SSE and NNE-SSW directions in gneisses; and the WNW-ESE and NNE-SSW to NE-SW, directions in schists. In the Ntem complex, the major lineaments are oriented NE-SW and NW-SE. These lineaments describe locally, contacts, faults, folds, dextral (e.g. Yaounde-Mfou area) or sinistral (e.g. Zoetele-Sangmelima) shear zones or strike-slips.

The aeromagnetic data analysis over the Yaounde-Sangmelima area evidenced various lineaments (**Figure 6(b)**). The main directions they follow are NE-SW to ENE-WSW, NW-SE to WNW-ESE and N-S. These probably correspond to folding traces, fracture, faults, dykes or geological contacts between major formations. The continuation of these lineaments clearly shows that some of them are faults affecting both the CAFB and the Ntem complex.

Together, remote sensing and magnetic lineaments (**Figure 9**) highlight the dominance of the NE-SW, NW-SE and N-S directions with some local variations (WNW-ESE, ENE-WSW, NNW-SSE and NNE-SSW). Putting aside all the secondary and minor lineaments, the major lineaments form throughout the whole Yaounde-Sangmelima region a broad NE-SW network of faults that affect the deep basement of both the Ntem complex and the Yaounde Group. Thus it would had formed before the emplacement of the Yaounde Group that it affected through post emplacement reactivations. These NE-SW lineaments intersect or are intersected by N-S and WNW-ESE to NW-SE lineaments which make

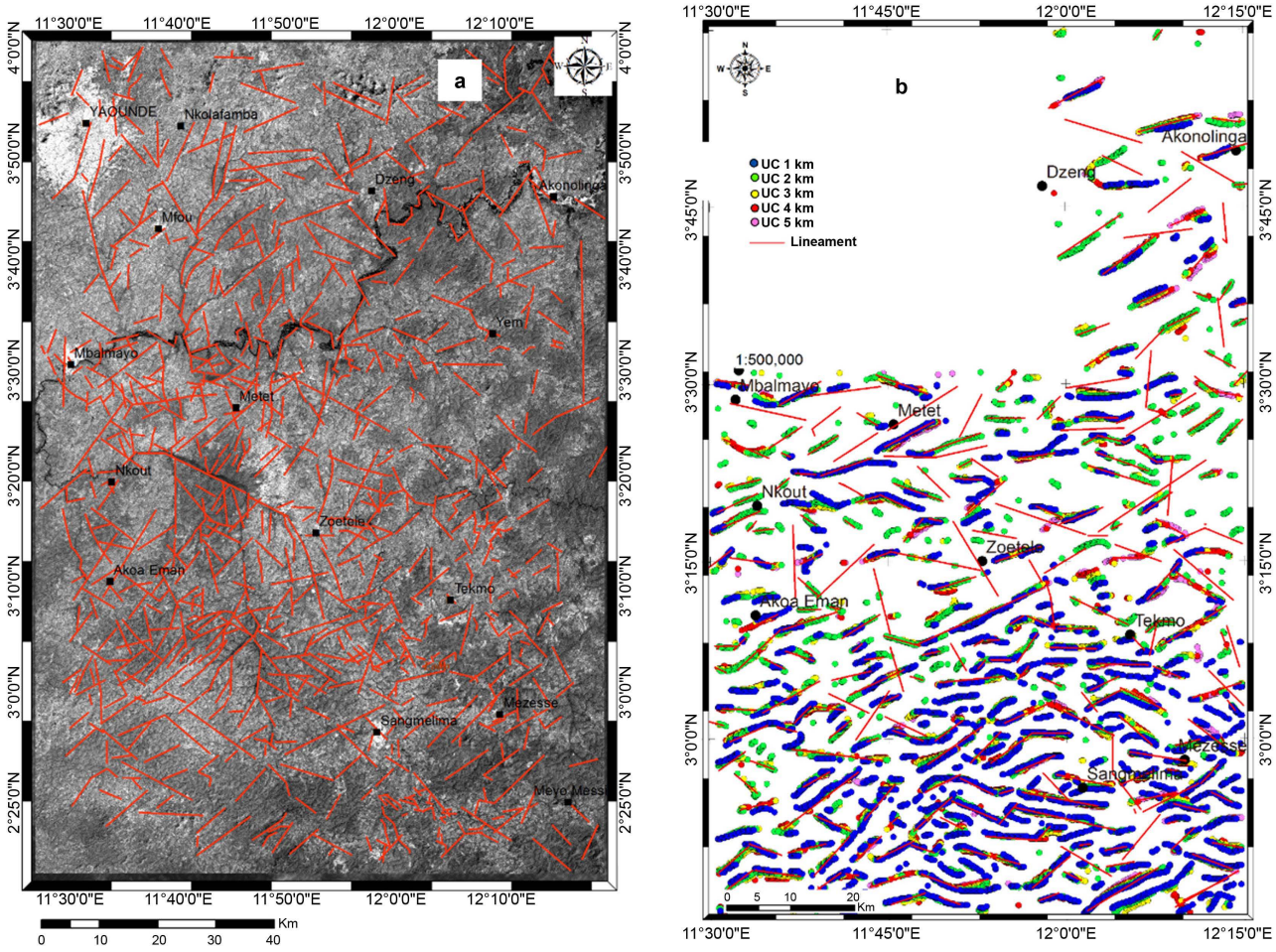

Figure 6. (a) Landsat 8 sensed lineaments; (b) Magnetic lineaments from HGM.

it interpretable as a major sinistral shear concupiscent to transpressional movements both the Ntem complex and the Yaounde Group. Moreover, there is a family of major WNW-ESE and E-W lineaments that form an E-W band between Mbalmayo and Tekmo that can be interpreted as the CAFB/CC southern limit, a faulty contact that represents the thrust line of the CAFB/CC along which visible WNW-ESE to NW-SE strike-slips of shear movements seems to have occurred.

In the CAFB, the subparallel lineaments are relatively widely spaced, as a result of a gentle folding of gneisses and schists probably resulting from a less intense compression in the southern part of the CAFB. The folds and faults as well as other fractures and shear zones (e.g. the area is affected to the north by NE-SW dextral strike-slips-see **Figure 6** and **Figure 9**) observed, suggest that the deformation conditions were ductile to brittle-ductile and the variability in their directions is an imprint of a multi staged and intense tectonics. Indeed, these lineaments in the CAFB result from the Gondwana amalgamation (Neoproterozoic) and breakup (Atlantic Ocean formation), and to the actual Somali Plate individualisation (East African Rift spreading) and the Africa/Eurasia Plates con-

vergence tectonics.

In the Ntem complex, some lineaments are assumed to be Archaean, while other are may be related to:

1) The Eburnean event in Paleoproterozoic causing the development (or reactivation of pre-existing faults) of the SW-NE to WSW-ENE and WNW-ESE to NW-SE faults affecting both the Ntem complex and the Paleoproterozoic basement of the future Yaounde Group. These appeared as a response to pertaining compressional and extensional movements. This would lead to the development of strike-slips that would constitute the paleo senestrial SW-NE shear zone as revealed by this study in the Yaounde-Sangmelima area.

2) The rifting at the northern edge of the Congo Craton caused by the detachment of the Adamawa-Yade block that led to the development of the Yaounde basin. During that rifting the faults above may have acted as a transform faults system where the SW-NE to WSW-ENE faults are in the spreading direction. The WNW-ESE to NW-SE faults and fractures would line up with the rift axis and later become the southern CAFB/Congo Craton limit depicted by the set of WNW-ESE faults that form an E-W lineament around latitudes N03˚20' and N03˚17'.

It is then evident that all the brittle structures outlined in the study area are either newly created or reactivated, depending on the stress and strain regimes upon the northern margin of the CC from Archaean to Cainozoic.

4.3. Hydrothermal Alteration Zones Mapping

4.3.1. Feature Oriented PCs

The application of the Crosta technique for the detection of clays and iron oxides anomalies led to **Table 3**. Clays are traced by the behaviour of the hydroxyl (OH) group in the Clay band (SWIR region) where it has a high reflectance in the SWIR 1 and a strong absorption in SWIR2. Scrutinising the loading of each band for the four FPCs obtained for the OH (**Table 3(a)**), for PCOH4 band 6 contributes at −0.796 and band 7 loading is 0.532, in line with the above comments. By inverting PCOH4, clayey zones will be observable as pale grey to white pixels in the southern part on the PCOH4 grey-scaled image (**Figure 7(a)**). In the north, alluvia in the Nyong River appear bright white in Akonolinga, whereas an anomalous clayey zone is visible west of Akonoloinga.

Regarding the detection of iron-rich minerals, in **Table 3(b)**, PCFe4 is characterised by a high loading from band 4 (0.658) related to a high reflectance and a very low contribution from band 2 (−0.026) corresponding to a very strong absorption. This is characteristic to the presence of iron-rich minerals which generally have a very high reflectance in the red band and a strong absorption in the blue band. Therefore, iron oxide targets will appear as greyish to dark pixels on the grey-scaled image. But the PCFe4 is influenced by the high loading from band 3 (green) due to the dense canopy in the area what makes them almost no detectable (**Figure 7(b)**).

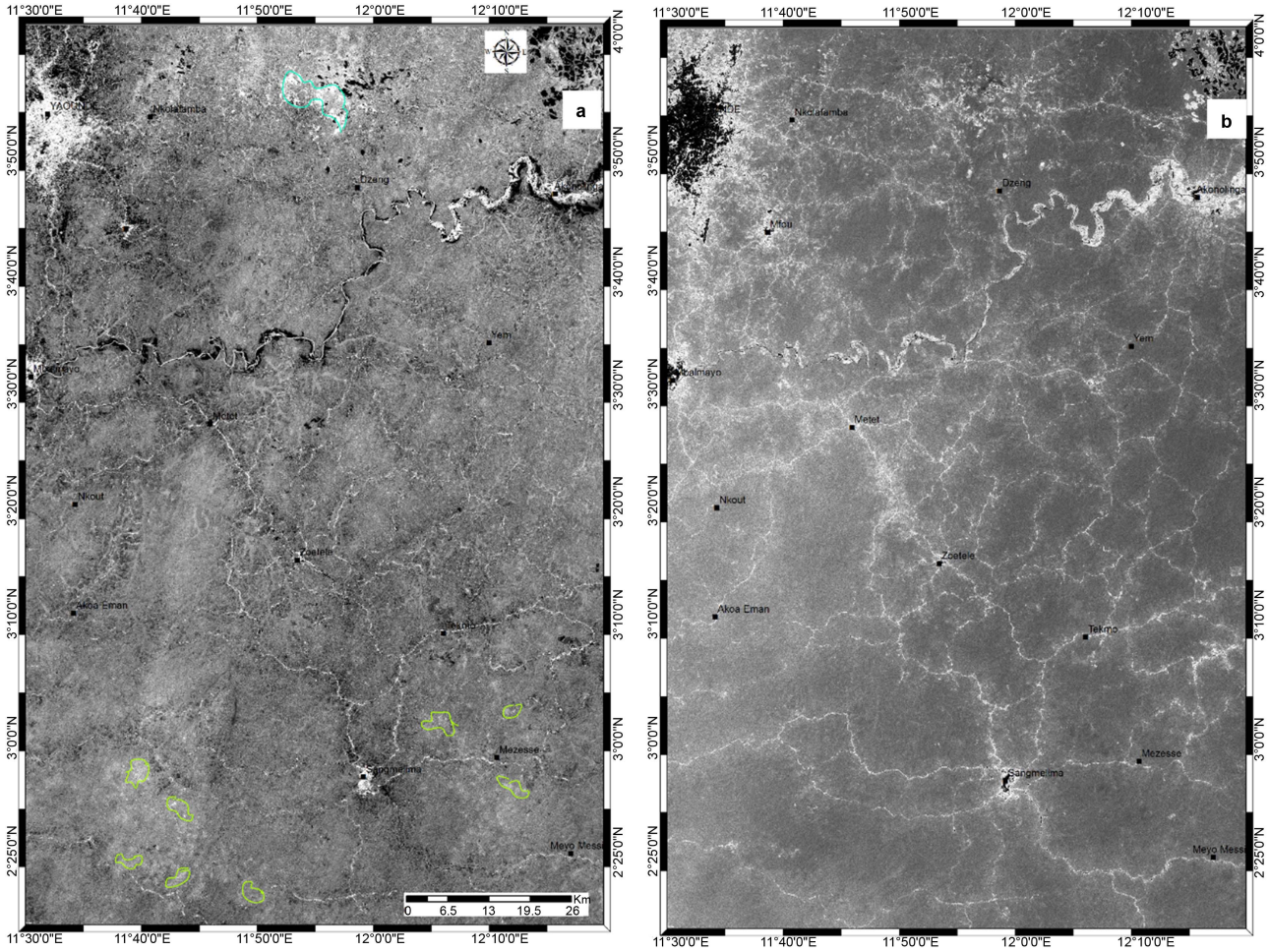

Figure 7. FPCS maps of the study area. (a) FPCOH1 and (b) FPCFe2 highlighting respectively, clays and iron oxides.

4.3.2. Porphyry Centre Detection from Magnetic Data

The application of the CET-porphyry detection tool on magnetic data led to the mapping of a total of 66 centres porphyry centres which correspond to intrusive bodies that occur in the study area (**Figure 8**). The straight visible point is that 61 of these centres are located in the Ntem complex and the remaining 5 centres (*i.e.* 7.58% of the gross total) are located in the Yaounde Group of the CAFB. Of the porphyry centres mapped in the CAFB domain, 3 centres are found in schists, in the vicinity of the schists/TTG boundary while the 2 other centres are located at this boundary. As a result, we interpret this very low occurrence of porphyry centres as an evidence of the absence of magmatic activity within the Yaounde Group in general, suggesting that no hydrothermal alteration of the Neoproterozoic rocks of the Yaounde and Mbalmayo series.

Contrasting with the CAFB domain, the Ntem complex records.92.42% of the porphyry centres of the study area (**Figure 8**) but their variable distribution depends on the change in the nature or composition of its main rocks formations. Indeed, the results enable to distinguish an area of less dense occurrence of porphyry centres (21 centres) from an area of more densely populated (40) porphyry centres which corresponds to what is hitherto regarded as an intrusive

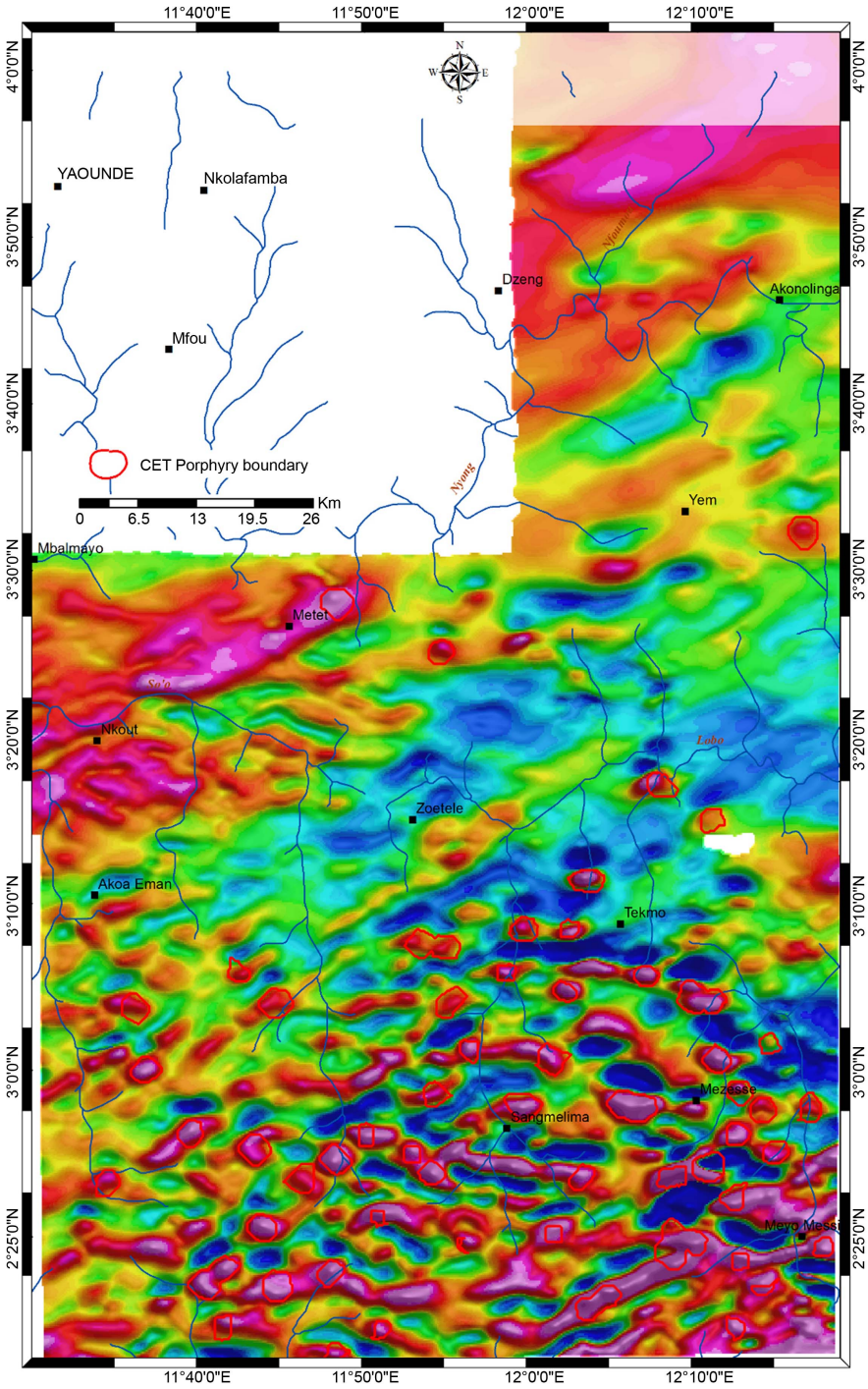

Figure 8. Porphyry domains overlain on the RTE map.

complex, in regards with its dramatically high porphyry centres percentage (60.60% of the gross total). This intrusive complex merely corresponds to the charnockites, whereas the less densely populated area seemingly matches the intrusive TTG of the Ntem complex. This location of intrusive bodies within the TTG and charnockites complex shows that the Panafrican orogeny did not affect or slightly affected the Ntem complex. It can also show that no magmatic events

occurred in the Ntem complex in relation with the Panafrican event but they are rather pre-Panafrican and possibly not tectono-metamorphic.

5. Discussion

5.1. On Lithology Mapping

The lithology mapping from remote sensing confirmed the metamorphic character of the basement lithology as they are generally visible in dark shades in the true colour composition. The reflectance signatures in the north of the study area (**Figure 4(a)**; **Figure 4(b)**) has been interpreted as corresponding to a mixture of garnet, biotite, amphibole, quartz, kyanite, feldspar and chalcopyrite. These minerals are constituents of Panafrican gneisses of the Yaounde Group [42] [79] and various age gneisses worldwide. Besides, mix of dark reddish, dark blue, dark greenish and greyish tones in metamorphic rocks in general indicate the presence of muscovite, calcite, feldspars (orthoclase and albite), garnets, chlorite, quartz along with accessories minerals such as iron oxides, tourmaline or zircon [42] [44] [80] This has been globally interpreted as schists (quartz-muscovite schists, quartz-schists and muscovite schists) and quartzites in accordance with [42] [43] [65]. Moreover, the study was incapable of differentiating the Mbalmayo schists from the schists of the Yaounde series based on the spectral reflectance. This unquestioned differentiation to date, was recognised by pioneer studies (e.g. [43]) on the southern member unit of the CAFB which consider the Yaounde Group as made up of two distinct series: 1) the Yaounde series (gneisses + micaschists) and 2) the Mbalmayo schists. One probable reason of the inability of this study to clearly distinguish the schists of the Yaounde series from the Mbalmayo schists is that they may belong to the same unit, hence differences between them would account for simple variations observed in a same schists belt. Till date, only works by [44] are supportive of this point of view so, more geochemical studies in the schists formations of the Yaounde Group need to be carried out for clarifications.

The discrimination in between the Ntem complex rocks was not evident from the RS analysis (**Figure 2(a)**; **Figure 3(a)**; **Figure 4(b)**). In fact, their close mineralogical content provides them with almost the same signature, possibly because the rocks of the Ntem Complex derive from the same igneous protolith [47] [53]. Thus the igneous nature of these rocks favoured their mapping and differentiation through aeromagnetics. Indeed, the complementary use of aeromagnetic data permitted to segregate Tonalites TTG from an intrusive complex of granodiorites and granites centred on Sangmelima as well as greenstone relics documented from previous works (e.g. [43] and references therein). Moreover, from the HGM and the AS maps (**Figure 5**) and integrating the available geological information in the area [43], the study inferred, other greenstone relics south of Sangmelima in the intrusive complex. The same approach was used by [81] to highlight new greenstone relics northeast of those of the geological map. Highlighting another greenstone relic is a contribution in updating the reference geological map of southern Cameroon and it increases the mineral interest in the

Ntem Complex.

5.2. Structural Mapping and Geodynamic Evolution at the Northern Margin of the Congo Craton

The study highlights in the Yaounde-Sangmelima region, many fractures and faults that affect both the Ntem Complex and the CAFB. The directions of the major structures are mainly SW-NE, WNW-ESE, NW-SE, SSW-NNE, WSW-ENE and N-S. The remote sensing results are consistent with magnetic results (**Figure 9**). These structures and directions are consistent with previous studies [25] [35] [82] [83] [84] [85] in the area and at the vicinities. Indeed, these works have highlighted many faults or fractures interpreted as tectonic accidents affecting the CC, the basement of the CAFB domain without providing a real explanation on the faulting history or kinematics to help understanding geodynamics at the northern margin of the CC.

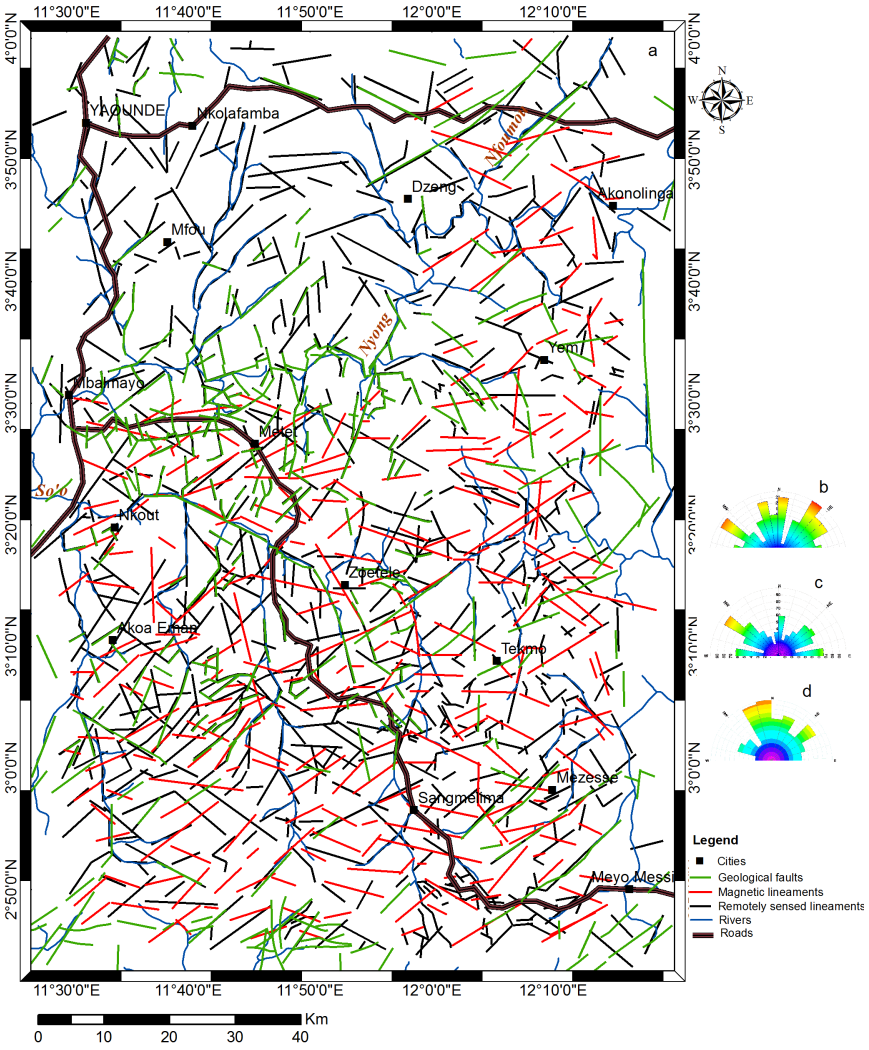

Figure 9. Lineaments map of the study area showing the correlation between previous geological (green lines), the magnetic (red lines) and the remotely sensed (black lines) lineaments. Respective rose diagrams (b, c, d).

This study proposes that the NE-SW to WSW-ENE major faults/fractures affecting both the Ntem complex and the CAFB are within a single paleo shear zone which have controlled deformations at the northern margin of the Congo Craton from the Archaean to the Precambrian and further in the Cenozoic. This confirms the idea recently suggested by [86] and correlates the shear zones highlighted by [82] in the Sangmelima area that we suggest it belongs to the network from this paper. The sinistral shear movements in the Ntem Complex are pre-Panafrican as suggested by the orientation of the greenstone relics (**Figure 1**). The weakening of the Ntem complex crust in response to resurgence of various tectonothermal events [53] [87] may have led to the setting of the NE-SW lineaments during the Eburnean orogeny and the maturation of the ESE-WNW to E-W faults affecting the paleo Proterozoic basement, that would later form a rift at the northern margin of the CC.

Rifting at the northern margin of the CC has been recognised by [65] and [86]. Therefore, the NE-SW to WSW-ENE fractures and faults affecting both the Ntem complex and the Paleoproterozoic basement of the CAFB to the north, would be the structures guiding the spreading direction of the Yaounde basin. Rifting and limited oceanisation was related with the late Paleoproterozoic to early Neoproterozoic detachment of the Adamawa-Yade block from the CC before the Panafrican orogeny [88]. So, the collapse of the basement evidenced by [85] [89] [90] under the Yaounde group are imprints of these extensional processes at the northern and southern margins of the Congo continent due to the circum-Congo subduction zone depicted by [91] in his reconstruction of the Rodinia supercontinent at ca 1000 Ma. Hence, the stress from the northern branch of the circum-Congo subduction zone would cause the opening of the Paleoproterozoic reworked crust at a weakened cratonic zone north of the CC, the metacratonised Ntem Complex [92], to form the Yaounde basin. The ESE-WNW to E-W faults south of Mbalmayo and north of Tekmo define a main E-W lineament corresponding to the southern CAFB/CC boundary (thrust line). The vertical to subvertical geometry of this faults [43] [66] [79] may have been acquired when they development during the rifting and probably remained unchanged thus inherited from the aforesaid rifting. In this case, that would justify the absence of Panafrican schists relics on top of the Ntem Complex (even at the vicinity of the CAFB/CC south boundary) as pointed by [42] [79]. Also, this geometry preservation raises the question on the involvement of the CC during the Panafrican orogeny at its northern margin.

Despite the need of more structural and petrophysical data at the vicinities of the CAFB/CC south limit, this study considers the mentioned faults geometry to back up the assumption that the Ntem Complex and its foreland constituted a passive margin [61], hence the diffuse effects of the Panafrican tectonics onto the Ntem Complex reported by some geological works [79]. [49] observed mylonites in the TTGs south of Mbalmayo along the CAFB/CC boundary that we interpret as imprints of ESE-WNW transpressive movements along the Mbalmayo schists

/CC contact line in response to late to post-Panafrican tectonics (Trans-Saharan orogeny) proving the importance of this tectonic feature. This importance as well as the geodynamic response of the CC and the Central Africa Rift System must be investigated by future works in regards with the ongoing stress related to the East African rifting and the NNE-SSW to NE-SW convergence of Africa towards Eurasia. Whatever, the multiplicity of the directions of the mapped faults shows how difficult it is to reconstruct the tectonic history of the northern margin of the CC.

The use of magnetic data permitted to highlights some intrusions mainly located in granitoids of the Ntem Complex (**Figure 7**) whereas almost no evidence of igneous activity is highlighted north in the CAFB domain. This spatial close relation of these intrusive bodies with granitoids presumed at the regional scale that there is no real Panafrican influence on the Ntem Complex rocks. [41] supposed that the Panafrican was not hot enough *i.e.* that the collision was weak at the margin of the Ntem Complex hence generating LP-LT metamorphic conditions which could only lead to the formation of low grade schists at the CAFB/CC boundary in Neoproterozoic. In the CAFB, this may be the reason why intrusive bodies are very scarce or not reported in the Yaounde Group schists belt by many previous studies [43] [89] contrarily to the Poli schists in northern Cameroon (far away from the Ntem Complex) which recorded intense intrusive to extrusive activity in Neoproterozoic consistently with a real subduction mechanism, as documented therein by topic related studies [93] [94]. This was justified by some recent works with the existence of a micro plate or a micro continent north of the CC, probably the Adamawa/Yade microcontinent detached from the CC (see, e.g. [88] [95] [96], on this important issue); and validates effective but limited rifting processes at the northern margin of the CC supported by this study and [65]. We further assume that the LP-LT conditions hitherto evoked imply a non or limited reactivation of the Paleoproterozoic faults/fractures which disabled ascent of subcrustal materials.

Despite the lack of data, we propose that the closure of the Yaounde basin in late Neoproterozoic shall be understood as a result of simple compressions between a fixed CC and a moving Adamawa/Yada/East Sahara Block rather than a normal collision as seen worldwide [97] [98] [99] [100] [101]. Therefore, the development of the southern CAFB is a non-collisional orogeny and the consideration of a CC subducted below the CAFB is geodynamically misleading and should be avoided. However, these conclusions are matter of debate and transduce the complexity of the geological history of the northern margin of the CC in particular, as well as enigmas related to the Congo continent in the pre-Gondwana reconstructions. Notwithstanding the lithologic and tectonic links well demonstrated between South America and Africa [57] [102], reassessment of the timing of events could better enlighten the Neoproterozoic evolution of the transition zone at the northern margin of the CC. Another challenge not openly discussed in this work is to investigate the response of this

transition zone to both the ongoing African plate geodynamics.

5.3. Hydrothermal Alteration Mapping and Mining Implications

Landsat 8 OLI data are generally efficient in mapping hydrothermal alteration zones which correspond to areas of clay minerals (with or without some iron oxides) accumulations [16] [19]. Contrarily to most presented studies (mainly carried in open canopy or semi-arid areas), they weakly mapped hydrothermal alteration zones in the study area. This incapability is probably due to the dense vegetation and the thick lateritic cover. In fact, the tropical vegetation produces a high evapotranspiration whose signal is sometimes difficult to remove on satellite data. In another side, Landsat 8 OLI data SWIR region is too broad (only two bands) to enable good mineral characterisation, comparatively to some sensors like ASTER which propose a better sampling in the same domain (five SWIR bands) resulting in a better characterisation of subsurface mineral contents.

However, aeromagnetics overcame that difficulty by mapping porphyry centres like some works [103]. Porphyritic deposits are associated to intrusive or extrusive activity, and require felsic to intermediate magma chamber and/or a cooling pluton; the inter-granular space along bedding planes and fractures in host rocks of enables percolation of hydrothermal fluids that will precipitate ore minerals then leads to the formation of hydrothermal deposits [2] [104] [105]. This is consistent with the close spatial relation between the highlighted porphyry centres and the granitoids and the TTG suites of the Ntem complex (**Figure 10**) in one hand; and in another, location of these mapped porphyry centres at (or close to) faults junctions, in between two subparallel faults or along faults, and at the TTG/granodiorites contact zone. Recalling this study highlighted a major pre-Panafrican NE-SW shear zones, with local NE-SW and NW-SE shear zones (e.g. Sangmelima area), it is clear that faulting played a major role by allowing hydrothermal and oxidising fluids circulations in the Archaean to Paleo/Mesoproterozoic evolution of the Ntem Complex.

Hydrothermal alteration in the Ntem complex has been recognised by recent works at the vicinities of the study area (in areas subject to advanced mineral exploration works) which also showed that hydrothermalism occurred in the Ntem Complex in a shallow seawater, probably in a subduction context [106] [107] [108] [109]. Porphyry as a subclass of hydrothermal deposits, is associated with one or various intrusions of felsic to intermediate rocks [4] [110] [111] as it is the case in this portion of the Ntem Complex made up of TTG granites, granodiorites [41] [47]. Also, some of the porphyry centres from this study coincide or are located in the close proximity of porphyry granites, intrusions and/or known mineral indices mapped by [42]. In the Ntem complex, the indices having Fe-Au (Iron Oxides-Gold; IOG) affiliation are mainly found out of greenstones in TTG, granodiorites and granitoids; they tend to confirm the existence of porphyry and/or IOCG deposits, despite the absence of Cu index in the study area. [112] while confirming the Cu depletion in Akom II southwest of the study area, rather revealed a S, Ni, and Au-PGE enrichment. Regarding the geodynamical,

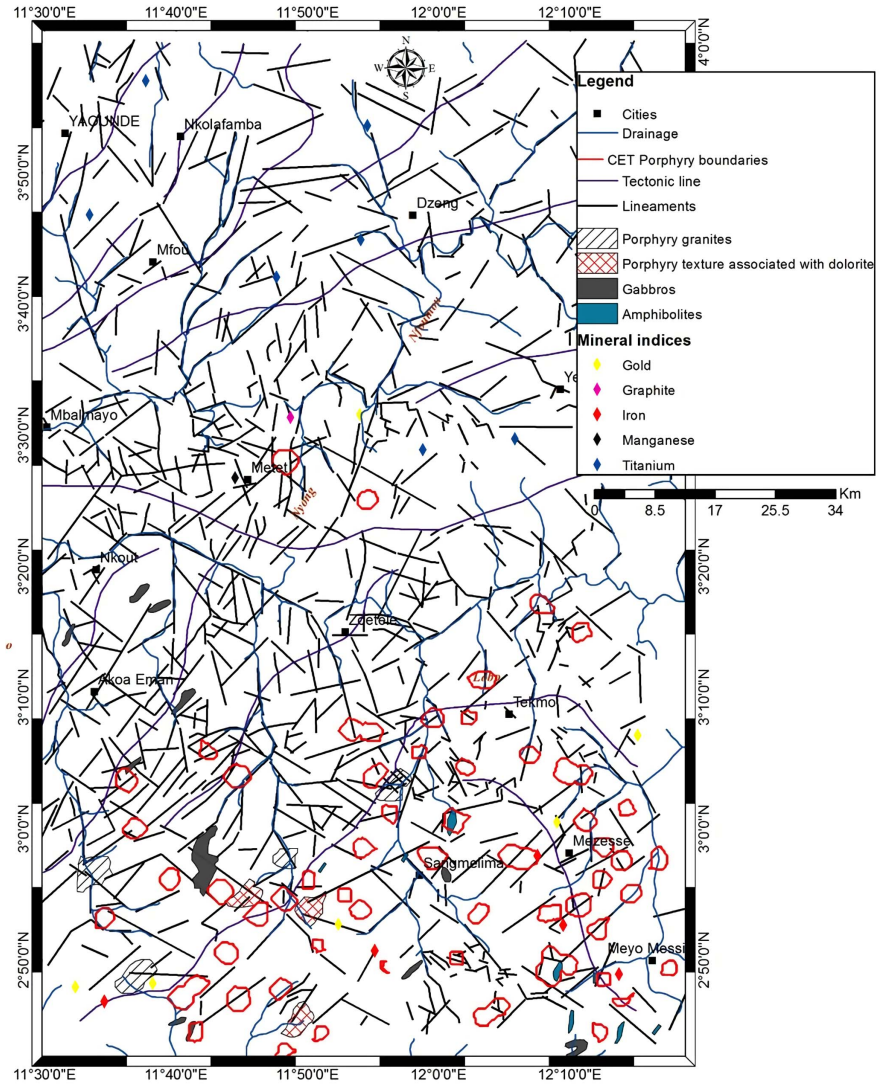

Figure 10. Correlation between highlighted porphyry domains and lineaments with exiting porphyritic textures and mineral indices.

lithological and structural context pertaining to this study area, hydrothermalism and absence of Cu would infer a Kiruma-type deposits [113]. However, [106] evidence of a Ba, Cu, Zn and V enriched iron oxide deposit suggests the existence of skarn or porphyry deposit nearly 45 km west of the study area (Binga project). Our results match with the existence of IOCG and porphyry/skarn ore deposits east and northeast Brazil [3] [4] [114]. Therefore, the Ntem complex in the transition zone at the northern margin of the CC potentially hosts many hydrothermal deposits which need to be explored.

6. Conclusions

An integrated analysis of Landsat 8, legacy aeromagnetic data and geologic maps was implemented as a predictive geological mapping approach in poorly exposed and inaccessible densely vegetated tropical region of southern Cameroon. The

study objective was to revisit the structural and lithological knowledge of the northern margin of the Congo Craton in the Yaounde-Sangmelima area, with the resulting potential mining implications. The main results from the study are:

1) The faults and fractures outline a major SW-NE paleo strike-slips channel or shear zone affecting both the Ntem complex and the CAFB basement.

2) NE and NW trans tensional movements depicted by first and second order faulting, passageways for hydrothermal fluids.

3) Many mapped intrusions and porphyry centres structurally controlled by the regional and local shear zones as imprints of hydrothermal activity.

4) The close proximity of highlighted porphyry centres with mapped faults/fractures junctions, porphyry texture zones and mineral indices includes iron and gold suggest the presence of porphyry deposits in the Ntem complex.

5) Landsat 8 multispectral data are not good enough to predictively map hydrothermal alteration zones in poorly exposed, inaccessible and densely vegetated tropical area. High evapotranspiration from trees, thick lateritic cover, and the width of Landsat-8 SWIR bands may be the reason.

The results show that the mining potential of the Yaounde-Sangmelima in Ntem Complex should be positively reconsidered and more exploration activities shall be encouraged.

Acknowledgements

The authors are grateful to the anonymous reviewers whose remarks and comments will contribute in upgrading the current paper.

Conflicts of Interest

The authors declare no conflicts of interest regarding the publication of this paper.

References

[1] Naslund, H.R., Henríquez, F., Nyström, J.O., Vivallo, W. and Dobbs, F.M. (2002) Magmatic Iron Ores and Associated Mineralisation: Examples from the Chilean High Andes and Coastal Cordillera. *Hydrothermal Iron Oxide Copper-Gold & Related Deposits. A Global Perspective*, **2**, 207-226.

[2] Grooves, D.I., Condie, K.C., Goldfarb, R.J., Hronsky, J.M.A. and Vielreicher, R.M. (2005) Secular Changes in Global Tectonic Processes and Their Influence on the Temporal Distribution of Gold-Bearing Mineral Deposits. *Economic Geology*, **100**, 203-224. https://doi.org/10.2113/gsecongeo.100.2.203

[3] Monteiro, L.V.S., *et al.* (2008) Spatial and Temporal Zoning of Hydrothermal Alteration and Mineralization in the Sossego Iron Oxide-Copper-Gold Deposit, Carajas Mineral Province, Brazil: Paragenesis and Stable Isotope Constraints. *Miners Depo*, **43**, 129-159. https://doi.org/10.1007/s00126-006-0121-3

[4] Lobato, L.M., *et al.* (1998) Styles of Hydrothermal Alteration and Gold Mineralizations Associated with the Nova Lima Group of the Quadrilátero Ferrífero: Part I, Description of Selected Gold Deposits. *Revista Brasileira de Geociências*, **28**, 339-354. https://doi.org/10.25249/0375-7536.1998339354

[5] Zientek, M.L. (2012) Magmatic Ore Deposits in Layered Intrusions—Descriptive Model for Reef-Type PGE and Contact-Type Cu-Ni-PGE Deposits Magmatic Ore Deposits in Layered Intrusions—Descriptive Model for Reef-Type PGE and Contact-Type Cu-Ni-PGE Deposits. https://doi.org/10.3133/ofr20121010

[6] Richard, J.P. (2013) Giant ore Deposits Formed by Optimal Alignments and Combinations of Geological Processes. *Nature Geoscience*, **6**, 911-916. https://doi.org/10.1038/ngeo1920

[7] Al Muntshry, A.N. (2011) Evaluating the Effectiveness of Multi-Spectral Remote Sensing Data for Lithological Mapping in Arid Regions: A Quantitative Approach with Examples from the Makkah Neoproterozoic Region, Saudi Arabia. Missouri University of Science and Technology, Rolla, MO.

[8] Liu, J.G. and Mason, P.J. (2009) Essential Image Processing and GIS for Remote Sensing. https://doi.org/10.1002/9781118687963

[9] Stewart, J.C. (2013) Developing Remote Sensing Methods for Bedrock Mapping of the Front Range Mountains, Colorado.

[10] Oruç, B. and Selim, H.H. (2011) Interpretation of Magnetic Data in the Sinop Area of Mid Black Sea, Turkey, Using Tilt Derivative, Euler Deconvolution and Discrete Wavelet Transform. *Journal of Applied Geophysics*, **74**, 194-204. https://doi.org/10.1016/j.jappgeo.2011.05.007

[11] Ouattara, G., Gnammytchet, B. and Kouakou Yao, A. (2012) Contribution des images satellitales Landsat 7 ETM+ a la cartographie lithostructurale du Centre-Est de la Cote d' Ivoire (Afrique de l' Ouest) to Cite This Version. *International Journal of Innovation and Applied Studies*, **1**, 61-75.

[12] Kiran Raj, S. and Ahmed, S.A. (2014) Lineament Extraction from Southern Chitradurga Schist Belt Using Landsat TM, ASTERGDEM and Geomatics Techniques. *International Journal of Computer Applications*, **93**, 12-20. https://doi.org/10.5120/16266-5993

[13] Mwaniki, M.W., Moeller, M.S. and Schellmann, G. (2015) A Comparison of Landsat 8 (OLI) and Landsat 7 (ETM +) in Mapping Geology and Visualising Lineaments: A Case Study of Central Region Kenya. *International Archives of the Photogrammetry, Remote Sensing and Spatial Information Science*, **XL-7**, 11-15. https://doi.org/10.5194/isprsarchives-XL-7-W3-897-2015

[14] Kayode, J.S., Nawawi, M.N.M., Khiruddin, B.A. and Khalil, A.E. (2016) Integrating Aeromagnetic and Landsat™ 8 Data into Subsurface Structural Mapping of Precambrian Basement Complex. *Journal of African Earth Sciences*, **125**, 202-213. https://doi.org/10.1016/j.jafrearsci.2016.11.010

[15] Crosta, A.P. and Rabelo, A. (1993) Assessing of Landsat TM for Hydrothermal ALteration Mapping in Central Western Brazil. *Proceedings of Ninth Thematic Conference Geologic Remote Sensing Pasadinea*, **3**, 1053-1061.

[16] Amer, R., Kusky, T.M., Reinert, P.C. and Ghulam, A. (2006) Image Processing and Analysis Using Landsat ETM + Imagery for Lithological Mapping at Fawakhir, Central Eastern Desert of Egypt. *ASPRS* 2009 *Annual Conference*, Baltimore, MD, 9-13 March 2009.

[17] Safari, M., Pour, A.B., Maghsoudi A. and Hashim, M. (2013) Targeting Hydrothermal Alterations Utilizing Landsat-8 Andaster Data in Shahr-e-Babak, Iran. *International Archives of the Photogrammetry, Remote Sensing and Spatial Information Sciences-ISPRS Archives*, **42**, 153-157. https://doi.org/10.5194/isprs-archives-XLII-4-W5-153-2017

[18] Pour, A.B. and Hashim M. (2015) Hydrothermal Alteration Mapping from Land-

sat-8 Data, Sar Cheshmeh Copper Mining District, South-Eastern Islamic Republic of Iran. *Journal of Taibah University for Science*, **9**, 155-166. https://doi.org/10.1016/j.jtusci.2014.11.008

[19] Labouré, C., Toledo, B. and De Assis L.M. (2016) Mapping Iron Oxides with Landsat-8/OLI and EO-1/Hyperion Imagery from the Serra Norte Iron Deposits in the Carajás Mineral Province, Brazil. *Brazilian Journal of Geology*, **46**, 331-349. https://doi.org/10.1590/2317-4889201620160023

[20] Pramumijoyo, F.S. and Setijadji, L.D. (2018) Alteration Mineral Mapping to Identify Primary Tin Potential Using Landsat 8 Images and Geographic Information System in Rimba Kulit Area, Southern of Bangka Island. *IOP Conference Series*: *Earth and Environmental Science*, **212**, Article ID: 012021. https://doi.org/10.1088/1755-1315/212/1/012021

[21] Akame, J.M., Mvondo Ondoa, J., Teikeu Assatse, W., Owona, S. and Olinga, J.B. (2014) Apport des images landsat-7 ETM+ a l'etude structurale du socle archeen de sangmelima (SUD CAMEROUN). *Revue Francaise de Photogrammetrie et Teledetection*, **206**, 15-26.

[22] Teikeu, W., Njandjock, P., Tabod, C., Martial, J. and Nshagali, G. (2016) Hydrogeological Activity of Lineaments in Yaoundé Cameroon Region Using Remote Sensing and GIS Techniques. *Egyptian Journal of Remote Sensing and Space Science*, **19**, 49-60.

[23] Didero, J., *et al.* (2016) Use of Landsat 7 ETM + Data for the Geological Structure Interpretation: Case Study of the Ngoura-Colomines Area, Eastern Cameroon. *Journal of Geosciences and Geomatics*, **4**, 61-72.

[24] Mandeng, B., Bondje, L.M., Solange, A., Tchami, L. and Dieudonne, L.B. (2018) Lithologic and Structural Mapping of the Abiete-Toko Gold District in Southern Cameroon, Using Landsat 7 ETM+/SRTM. *Comptes rendus Geoscience*, **350**, 130-140.

[25] Anaba Fotze, Q.M., Djieto Lordon, A., Penaye, J., Sep, J.P. and Neh Frun, M.I. (2019) Mapping Hydrothermal Alteration Targets from Landsat 8 OLI/TIRS and Magnetic Data Using Digital Image Processing Techniques in Garoua, North Cameroon. *Journal of Geosciences and Geomatics*, **7**, 28-41. https://doi.org/10.12691/jgg-7-1-4

[26] Nabighian, M.N., *et al.* (2005) The Historical Development of the Magnetic Method in Exploration. *Geophysics*, **70**, 33-61. https://doi.org/10.1190/1.2133784

[27] Fairhead, J.D., Cooper, G.R.J. and Sander, S. (2017) Advances in Airborne Gravity and Magnetics. In: *Proceedings of Exploration* 17: *Sixth Decennial International Conference on Mineral Exploration*, 113-127.

[28] Keating, P. (1995) A Simple Technique to Identify Magnetic Anomalies Due to Kimberlite Pipes. *Exploration and Mining Geology*, **4**, 121-125.

[29] Blakely, R.J. (1996) Potential Theory in Gravity and Magnetic Applications. Cambridge University Press, Cambridge. https://doi.org/10.1017/CBO9780511549816

[30] Reeves, C.V. (2005) Aeromagnetic Surveys-Principles, Practice & Interpretation. Geosoft.

[31] Reid, A.B., Allsop, J.M., Granser, H., Millett, A.J. and Somerton, I.W. (1990) Magnetic Interpretation in Three Dimensions Using Euler Deconvolution. *Geophysics*, **55**, 80-90. https://doi.org/10.1190/1.1442774

[32] Mushayandebvu, M.F., Lesur, V., Reid, A.B. and Fairhead, J.D. (2004) Grid Euler Deconvolution with Constraints for 2D Structures. *Geophysics*, **69**, 489-496. https://doi.org/10.1190/1.1707069

[33] Prieto, C. (1996) Gravity/Magnetic Signatures of Various Geologic Models-An Exercise in Pattern Recognition. *IGC Footnotes interpretation*, **4**, No. 4.

[34] Noutchogwe Tatchum, C., Koumetio, F. and Manguelle-Dicoum, E. (2010) Structural Features of South-Adamawa (Cameroon) Inferred from Magnetic Anomalies: Hydrogeological Implications. *Comptes rendus Geoscience*, **342**, 467-474. https://doi.org/10.1016/j.crte.2010.03.004

[35] Feumoe, A.N., Ndougsa-Mbarga, T., Manguelle-Dicoum, E. and Fairhead, J.D. (2012) Delineation of Tectonic Lineaments Using Aeromagnetic Data for the South-East Cameroon Area. *Geofizika*, **29**, 175-192.

[36] Som Mbang, M.C., Basseka, C.A., Kamguia, J., Etamè, J., Njiteu Tchoukeu, D.C. and Pemi Mouzong, M. (2018) Mapping of Deep Tectonic Structures of Central and Southern Cameroon by an Interpretation of Surface and Satellite Magnetic Data. *International Journal of Geophysics*, **2018**, 1-11. https://doi.org/10.1016/j.crte.2010.03.004

[37] Haroni, H.A., Erren, H. and Westerhof, P. (2000) Integrated Analysis of Remote Sensing, Aeromagnetic, Geological and Mineral Occurrence Data for the Assessment of a Subduction Setting Along the Zagros Orogenic Belt of Iran 2 Geological Setting of Zagros Orogenic Belt. *International Archives of the Photogrammetry, Remote Sensing*, **33**, 1700-1707.

[38] Opara, A.I., Onyekuru, S.O., Mbagwu, E.C., Emberga, T.T., Ijeomah, K.C. and Nwokocha, K.C. (2015) Integrating Landsat-ETM and Aeromagnetic Data for Enhanced Structural Interpretation over Naraguta Area, North-Central Nigeria. *International Journal of Scientific and Engineering Research*, **6**, 186-195.

[39] Vicat, J. and Moloto-a-Kenguemba, G. (2001) Les granitoides de la couverture protérozoique de la bordure nord du craton du Congo (Sud-Est du Cameroun et Sud-Ouest de la République centrafricaine), témoins d'une activité magmatique panafricaine. *Earth and Planetary Science Letters*, **332**, 235-242. https://doi.org/10.1016/S1251-8050(01)01521-X

[40] Tchameni, R., Mezger, K., Nsifa, N.E. and Pouclet, A. (2001) Crustal Origin of Early Proterozoic Syenites in the Congo Craton (Ntem Complex), South Cameroon. *Lithos*, **57**, 23-42. https://doi.org/10.1016/S0024-4937(00)00072-4

[41] Li, X., Chen, Y., Li, J., Yang, C., Ling, X. and Tchouankoue, J.P. (2016) New Isotopic Constraints on Age and Origin of Mesoarchean Charnockite, Trondhjemite and Amphibolite in the Ntem Complex of NW Congo Craton, Southern Cameroon. *Precambrian Research*, **276**, 14-23. https://doi.org/10.1016/j.precamres.2016.01.027

[42] Champetier de Ribes, G. and Aubague, M. (1956) Carte geologique de reconnaissance a l'echelle 1/500000. Notice explicative sur la feuille Yaounde-Est'.

[43] Maurizot, P., Abessolo, A., Feybesse, J., Johan, L. and Lecomte, P. (1986) Etude et prospection minière du Sud-Ouest du Cameroun. Synthèse des travaux de 1978 à 1985. Orleans, Cameroun.

[44] Nedelec, A., Nsifa, E.N. and Martin, H. (1990) Major and Trace Element Geochemistry of the Archaean Ntem Plutonic Complex South Cameroon): Petrogenesis and Crustal Evolution. *Precambrian Research*, **47**, 35-50. https://doi.org/10.1016/0301-9268(90)90029-P

[45] Shang, C.K., *et al.* (2004) TTG Magmatism in the Congo Craton; A View from Major and Trace Element Geochemistry, Rb-Sr and Sm-Nd Systematics: Case of the Sangmelima Region, Ntem Complex, Southern Cameroon. *Journal of African Earth Sciences*, **40**, 61-79. https://doi.org/10.1016/j.jafrearsci.2004.07.005

[46] Shang, C.K., Siebel, W., Satir, M., Chen, F. and Mvondo Ondoua, J. (2004) Zircon

Pb-Pb and U-Pb Systematics of TTG Rocks in the Congo Craton: Constraints on Crust Formation, Magmatism and Pan-African Lead Loss. *Bulletin of Geosciences*, **79**, 205-219.

[47] Shang, C.K., Liégeois, J.P., Satir, M., Frisch, W. and Nsifa, E.N. (2010) Late Archaean High-K Granite Geochronology of the Northern Metacratonic Margin of the Archaean Congo Craton, Southern Cameroon: Evidence for Pb-Loss Due to Non-Metamorphic Causes. *Gondwana Research*, **18**, 337-355. https://doi.org/10.1016/j.gr.2010.02.008

[48] Houketchang Bouyo, M., Penaye, J., Mouri, H. and Toteu, S.F. (2019) Eclogite Facies Metabasites from the Paleoproterozoic Nyong Group, SW Cameroon: Mineralogical Evidence and Implications for a High-Pressure Metamorphism Related to a Subduction Zone at the NW Margin of the Archean Congo Craton. *Journal of African Earth Sciences*, **149**, 215-234. https://doi.org/10.1016/j.jafrearsci.2018.08.010

[49] Nedelec, A., Macaudiere, J., Nzenti, J.P. and Barbey, P. (1986) Évolution structurale et métamorphique des schistes de Mbalmayo (Cameroun). Implications pour la structure de la zone mobile panafricaine d'Afrique centrale au contact du craton du Congo. *Comptes rendus de l'Académie des Sciences Paris*, **303**, 75-80.

[50] Nzenti, J.P., Barbey, P., Macaudière, J. and Soba, D. (1988) Origin and Evolution of the Late Precambrian High, Grade Yaoundé Gneisses Cameroon. *Precambrian Research*, **38**, 91-109. https://doi.org/10.1016/0301-9268(88)90086-1

[51] Ganwa, A.A., *et al.* (2008) Zircon207Pb/206Pb Evaporation Ages of Panafrican Metasedimentary Rocks in the Kombé-II Area (Bafia Group, Cameroon): Constraints on Protolith Age and Provenance. *Journal of African Earth Sciences*, **51**, 77-88. https://doi.org/10.1016/j.jafrearsci.2007.12.003

[52] Feybesse, J.L., Johan, V., Maurizot, P. and Abessolo, A. (1987) Evolution tectonométamorphique libérienne et eburnéenne de la partie NW du craton zairois (SW Cameroun). In: Matheis, G. and Balkema, S.H., Eds., *Current Research in African Earth Sciences*, Rotterdam, 9-13.

[53] Tchameni, R., *et al.* (2010) Mineralogical Constraint for Metamorphic Conditions in a Shear Zone Affecting the Archean Ngoulemakong Tonalite, Congo Craton (Southern Cameroon) and Retentivity of U-Pb SHRIMP Zircon Dates. *Journal of African Earth Sciences*, **58**, 67-80. https://doi.org/10.1016/j.jafrearsci.2010.01.009

[54] Castaing, C., Feybesse, J.L., Thieblemont, D., Triboulet, C. and Chèvremont, P. (1994) Paleogeographical Reconstructions of the Pan-African/Brasiliano Orogen: Closure of an Oceanic Domain or Intracontinental Convergence between Major Blocks? *Precambrian Research*, **67**, 327-344. https://doi.org/10.1016/0301-9268(94)90095-7

[55] Toteu, S.F., van Schmus, W.R., Penaye, J. and Nyobe, J.B. (1994) U-Pb and Sm-Nd Evidence for Eburnian and Pan-African High-Grade Metamorphism in Cratonic Rocks of Southern Cameroon. *Precambrian Research*, **67**, 321-347. https://doi.org/10.1016/0301-9268(94)90014-0

[56] Toteu, S.F., Van Schmus, W.R. and Penaye, J. (2006) The Precambrian of Central Africa: Summary and Perspectives. *Journal of African Earth Sciences*, **44**, 7. https://doi.org/10.1016/j.jafrearsci.2005.12.002

[57] van Schmus, W.R., Oliveira, E.P., da Silva Filho, A.F., Toteu, S.F., Penaye, J. and Guimarães, I.P. (2008) Proterozoic Links between the Borborema Province, NE Brazil and the Central African Fold Belt. *Geological Society, London, Special Publications*, **294**, 69-99. https://doi.org/10.1144/SP294.5

[58] Fernandez-Alonso, M., Tack, L., Tahon, A. and De Waele, B. (2010) The Protero-

zoic History of the Proto-Congo Craton of Central Africa.

[59] Loose, D. and Schenk, V. (2018) 2.09 Ga Old Eclogites in the Eburnian-Transamazonian Orogen of Southern Cameroon: Significance for Palaeoproterozoic Plate Tectonics. *Precambrian Research*, **304**, 1-11. https://doi.org/10.1016/j.precamres.2017.10.018

[60] Toteu, S.F., Penaye, J. and Djomani, Y.P. (2004) Geodynamic Evolution of the Pan-African Belt in Central Africa with Special Reference Geodynamic Evolution of the Pan-African Belt in Central Africa with Special Reference to Cameroon 1. *Canadian Journal of Earth Sciences*, **41**, 73-85. https://doi.org/10.1139/e03-079

[61] Ngako, V. and Njonfang, E. (2011) Plates Amalgamation and Plate Destruction , the Western Gondwana History. In: Closson, D., Ed., *Tectonics*, InTech, London, 1-36.

[62] Mvondo, H., Owona, S., Ondoa, J.M. and Essono, J. (2007) Tectonic Evolution of the Yaoundé Segment of the Neoproterozoic Central African Orogenic Belt in Southern Cameroon. *Canadian Journal of Earth Sciences*, **44**, 433-444. https://doi.org/10.1139/e06-107

[63] Olinga, J.B., Mpesse, J.E., Minyem, D., Ngako, V., Ndougsa-Mbarga, T. and Ekodeck, G.E. (2010) The Awaé-Ayos Strike-Slip Shear Zones (Southern Cameroon): Geometry, Kinematics and Significance in the Late Pan-African Tectonics. *Neues Jahrbuch für Geologie und Paläontologie*, **257**, 1-11. https://doi.org/10.1127/0077-7749/2010/0042

[64] Mvondo-Ondoa, J., Mvondo, H. and Den Brok, B. (2009) Pan-African Tectonics in Northwestern Cameroon: Implication for the History of Western Gondwana. *Gondwana Research*, **16**, 163-164. https://doi.org/10.1016/j.gr.2008.12.006

[65] Nkoumbou, C., Barbey, P., Yonta-Ngouné, C., Paquette, J.L. and Villiéras, F. (2014) Pre-Collisional Geodynamic Context of the Southern Margin of the Pan-African Fold Belt in Cameroon. *Journal of African Earth Sciences*, **99**, 245-260. https://doi.org/10.1016/j.jafrearsci.2013.10.002

[66] Manguelle Dicoum, E., Bokosah, A.S. and Kwende Mbanwi, T.E. (1992) Geophysical Evidence for a Major Precambrian Schist-Granite Boundary in Southern Cameroon. *Tectonophysics*, **205**, 437-446. https://doi.org/10.1016/j.jafrearsci.2013.10.002

[67] Ndougsa-Mbarga, T., Layu, D.Y., Yene-Atangana, J.Q. and Tabod, C.T. (2014) Delineation of the Northern Limit of the Congo Craton Based on Spectral Analysis and 2.5D Modeling of Aeromagnetic Data in the Akonolinga-Mbama area, Cameroon. *Geofísica Internacional*, **53**, 5-16. https://doi.org/10.1016/S0016-7169(14)71486-2

[68] USGS (2016) Landsat 8 (L8) Data Users Handbook.

[69] Chavez, P.S.J., Berlin, G.L. and Sowers, L. (1982) Statistical Method for Selecting Landsat MSS Ratios. *Journal of Applied Photographic Engineering*, **8**, 23-30.

[70] Crosta, A.P. and Moore, J.M. (1989) Enhancement of Landsat Thematic Mapper Imagery for Residual Soil Mapping in SW Minas Gerais State, Brazil: A Prospecting Case History in Greenstone Belt Terrain. *Proceedings of the 7th Thematic Conference on Remote Sensing for Exploration Geology*, 2-6 October 1989, 1173-1187.

[71] Nabighian, M.N. (1972) The Analytic Signal of Two-Dimensional Magnetic Bodies with Polygonal Cross-Section: Its Properties and Use for Automated Anomaly Inter-Pretation. *Geophysics*, **37**, 507-517. https://doi.org/10.1190/1.1440276

[72] Roest, W.R., Verhoef, J. and Pilkington, M. (1992) Magnetic Interpretation Using the 3-D Analytic Signal. *Geophysics*, **57**, 116-125. https://doi.org/10.1190/1.1443174

[73] Boyd, D.M. and Isles, D.J. (2007) Geological Interpretation of Airborne Magnetic Surveys-40 Years on. *Proceedings of Exploration* 07: *Fifth Decennial International Conference on Mineral Exploration*, Toronto, 9-12 September 2007, 491-505.

[74] Archibald, N., Gow, P. and Boschetti, F. (1999) Multiscale Edge Analysis of Potential Field Data. *Exploration Geophysics*, **30**, 38-44. https://doi.org/10.1071/EG999038

[75] Owona-Angue, M.L., Tabod, C.T., Nguiya, S., Kenfack, J.V. and Tokam Kamga, A.P. (2013) Delineation of Lineaments in South Cameroon (Central Africa) Using Gravity Data. *Open Journal of Geology*, **3**, 331-339. https://doi.org/10.4236/ojg.2013.35038

[76] Kue Petou, M.R., Owona Angue, M.L., Nfor, N., Ndougsa-Mbarga, T. and Manguelle-Dicoum, E. (2017) Determination of Structural and Geometrical Parameters of the Kribi-Campo Sedimentary Sub-Basin Using Gravity Data. *International Journal of Geophysics*, **8**, 1210-1224. https://doi.org/10.4236/ijg.2017.89069

[77] Holden, E., Fu, S.C., Kovesi, P., Dentith, M.C., Bourne, B. and Hope, M. (2011) Automated Identification of Magnetic Responses from Porphyry Systems. *Journal of Applied Geophysics*, **74**, 255-262. https://doi.org/10.1016/j.jappgeo.2011.06.016

[78] Nzenti, J.P., Barbey, P., Jegouzo, P. and Moreau, C. (1984) Un nouvel exemple de ceinture granulitique dans une chaîne protérozoïque de collision: Les migmatites de Yaoundé au Cameroun. *Comptes Rendus de l'Académie des Sciences Paris*, **299**, 1197-1199.

[79] Nedelec, A., Nzenti, J.P. and Barbey, P. (1986) Structural and Metamorphic Evolution of the Mbalmayo Schists (Cameroon). Implications for the Structure of the Pan-African Mobile Belt of Central Africa, Close to the Congo Crat. *Comptes Rendus de l'Académie des Sciences*, **303**, No. 2015.

[80] Shang, C.K., Muharrem, S., Nsifa Nkonguin, E., Liegeois, J.-P., Siebel, W. and Taubald, H. (2007) Archaean High-K Granitoids Produced by Remelting of Earlier Tonalite-Trondhjemite-Granodiorite (TTG) in the Sangmelima Region of the Ntem Complex of the Congo Craton, Southern Cameroon. *International Journal of Earth Sciences*, **96**, 817-841. https://doi.org/10.1007/s00531-006-0141-3

[81] Li, X.-H., Chen, Y., Li, J., Yang, C., Ling, X.-X. and Tchouankoue, J.P. (2016) New Isotopic Constraints on Age and Origin of Mesoarchean Charnockite, Trondhjemite and Amphibolite in the Ntem Complex of NW Congo Craton, Southern Cameroon. *Precambrian Research*, **276**, 14-23.

[82] Akame, J.M., *et al.* (2019) The Sangmelima Granite-Greenstone Belts (South Cameroon): Integration of Remote Sensing and Aeromagnetic Data for Structural Interpretation. *The Egyptian Journal of Remote Sensing and Space Sciences*, **22**, 37-47.

[83] Tadjou, J.M., Njingti-Nfor, Kamguia, J. and Manguelle-Dicoum, E. (2008) Geophysical Prospecting of the Transition Zone between the Congo Craton and the Panafrican Belt in Cameroon. *Earth Sciences Research Journal*, **12**, 169-180.

[84] Meying, A., Ndougsa-Mbarga, T. and Manguelle-Dicoum, E. (2009) Evidence of Fractures from the Image of the Subsurface in the Akonolinga-Ayos Area (Cameroon) by Combining the Classical and the Bostick Approaches in the Interpretation of Audio-Magnetotelluric Data. *Journal of Geology and Mining Research*, **1**, 159-171.

[85] Shandini, N.Y., Tadjou, J.M. and Basseka, C.A. (2011) Delineating Deep Basement Faults in South Cameroon Area. *World Applied Sciences Journal*, **14**, 611-615.

[86] Assembe, S.P., Ndougsa-Mbarga, T., Meying, A., Gouet, D.H., Ngoh, J.D. and Mono, J.A. (2019) Contribution of Geophysics to the Understanding of the Geodynamic Activity at the Northern Margin of the Congo Craton: A Case Study from Aeromagnetic Data Interpretation Over the Metet-Zoetele Region (Southern Ca-

meroon). *European Journal of Scientific Research*, **152**, 286-303.

[87] Takam, T., Makoto, A., Kokonyangi, J., Dunkley, D.J. and Nsifa Nkonguin, E. (2009) Paleoarchaean Charnockite in the Ntem Complex, Congo Craton, Cameroon: Insights from SHRIMP Zircon U-Pb Ages. *Journal of Mineralogical and Petrological Sciences*, **104**, 1-11. https://doi.org/10.2465/jmps.080624

[88] Tchakounte Numbem, J., *et al.* (2018) Reply to Comment by Ngako and Njonfang on "The Adamawa-Yade Domain, a Piece of Archaean Crust in the Neoproterozoic Central African Orogenic Belt (Bafia Area, Cameroon)", by Jacqueline Tchakounté et al., Precambrian Research 299 (2017) 210-229. *Precambrian Research*, **305**, 516-518. https://doi.org/10.1016/j.precamres.2017.12.035

[89] Shandini, Y.N., Tadjou, J.M., Tabod, C.T. and Fairhead, J.D. (2010) Gravity Data Interpretation in the Northern Edge of the Congo Craton, South-Cameroon. *Anuário do Instituto de Geociências*, **33**, 73-82.

[90] Basseka, C.A., Shandini, Y. and Tadjou, J.M. (2011) Subsurface Structural Mapping Using Gravity Data of the Northern Edge of the Congo Craton, South Cameroon. *Geofizika*, **28**, 229-245.

[91] Scotese, C.R. (2009) Late Proterozoic Plate Tectonics and Palaeogeography: A Tale of Two Supercontinents, Rodinia and Pannotia. In: Craig, J., Thurow, J., Thusu, B., Whitham, A. and Abutarruma, Y., Eds., *Global Neoproterozoic Petroleum Systems: The Emerging Potential in North Africa*, 67-83. https://doi.org/10.1144/SP326.4

[92] Goussi, J.F., Bisso, D., Abdelsalam, M.G., Atekwana, E.A., Katumwehe, A.B. and Ekodeck, G.E. (2017) Geophysical Imaging of Metacratonizaton in the Northern Edge of the Congo Craton in Cameroon. *Journal of African Earth Sciences*, **129**, 94-107. https://doi.org/10.1016/j.jafrearsci.2016.12.010

[93] Toteu, S.F. (1990) Geochemical Characterization of the Main Petrographical and Structural Units of Northern Cameroon: Implications for Pan-African Evolution. *Journal of African Earth Sciences*, **10**, 615-624. https://doi.org/10.1016/0899-5362(90)90028-D

[94] Toteu, S.F., Van Schmus, W.R., Penaye, J. and Michard, A. (2001) New U-Pb and Sm-Nd Data from North-Central Cameroon and Its Bearing on the Pre-Pan African History of Central Africa. *Precambrian Research*, **108**, 45-73. https://doi.org/10.1016/S0301-9268(00)00149-2

[95] Tchameni, R., Pouclet, A., Penaye, J., Ganwa, A.A. and Toteu, S.F. (2006) Petrography and Geochemistry of the Ngaoundere Granitoids in Central North Cameroon: Implications for Their Sources and Geological Setting. *Journal of African Earth Sciences*, **44**, 511-529. https://doi.org/10.1016/j.jafrearsci.2005.11.017

[96] Ganwa, A.A., Siebell, W., Shang, K.C., Seguem, N. and Ekodeck, G.E. (2011) New Constraints from Pb-Evaporation Zircon Ages of the Meiganga Amphibole-Biotite Gneiss, Central Cameroon, on Proterozoic Crustal Evolution. *International Journal of Geosciences*, **2**, 138-147. https://doi.org/10.4236/ijg.2011.22014

[97] Han, T. and Nelson, J. (2015) Mapping Hydrothermally Altered Rocks with Landsat 8 Imagery: A Case Study in the KSM and Snow Field Zones, Northwestern British Columbia. Geological Fieldwork 2014, British Columbia Ministry of Energy and Mines, 103-112.

[98] Timm, J. (2001) Subduction and Continental Collision in the Lufilian Arc-Zambesi Belt Orogen: A Petrological, Geochemical and Geochronological Study of Eclogites and Whiteschists (Zambia). University of Kiel, Kiel.

[99] Kröner, A. and Stern, R.J. (2004) Pan-African Orogeny. *Encyclopedia of Geology*, **1**,

1-12. https://doi.org/10.1016/B0-12-369396-9/00431-7

[100] Zhao, Z., Zheng, Y., Zhang, J., Dai, L., Li, Q. and Liu, X. (2012) Syn-Exhumation Magmatism during Continental Collision: Evidence from Alkaline Intrusives of Triassic Age in the Sulu Orogen. *Chemical Geology*, **328**, 70-88. https://doi.org/10.1016/j.chemgeo.2011.11.002

[101] Bouyo Houketchang, M., Zhao, Y., Penaye, J., Zhang, S.H. and Njel, U.O. (2015) Neoproterozoic Subduction-Related Metavolcanic and Metasedimentary Rocks from the Rey Bouba Greenstone Belt of North-Central Cameroon in the Central African Fold Belt: New Insights into a Continental Arc Geodynamic Setting. *Precambrian Research*, **261**, 40-53. https://doi.org/10.1016/j.precamres.2015.01.012

[102] de Wit, M.J., Stankiewicz, J. and Reeves, C. (2008) Restoring Pan-African-Brasiliano Connections: More Gondwana Control, Less Trans-Atlantic Corruption. *The Geological Society of London-Special Publications*, **294**, 399-412. https://doi.org/10.1144/SP294.20

[103] Elkhateeb, S.O. and Abdellatif, M.A.G. (2018) Delineation Potential Gold Mineralization Zones in a Part of Central Eastern Desert, Egypt Using Airborne Magnetic and Radiometric Data. *NRIAG Journal of Astronomy and Geophysics*, **7**, 361-376. https://doi.org/10.1016/j.nrjag.2018.05.010

[104] Boadi, B., Wemegah, D.D. and Preko, K. (2013) Geological and Structural Interpretation of the Konongo Area of the Ashanti Gold Belt of Ghana from Aero-Magnetic and Radiometric Data. *International Research Journal of Geology and Mining*, **3**, 124-135.

[105] Ganno, S., *et al.* (2017) A Mixed Seawater and Hydrothermal Origin of Superior-Type Banded Iron Formation (BIF)-Hosted Kouambo Iron Deposit, Palaeoproterozoic Nyong Series, Southwestern Cameroon: Constraints from Petrography and Geochemistry. *Ore Geology Reviews*, **80**, 860-875. https://doi.org/10.1016/j.oregeorev.2016.08.021

[106] Ngoran, G.N., Suh, C.E., Bowker, D., Verla, R.B. and Bafon, G.T. (2016) Petrochemistry of Two Magnetite Bearing Systems in the Precambrian Belt of Southern Cameroon. *International Journal of Geosciences*, **7**, 501-517. https://doi.org/10.4236/ijg.2016.74038

[107] Soh Tamehe, L., Ganno, S., Nono Kouankap, G.D., Ngnotue, T., Kankeu, B. and Nzenti, J.P. (2014) Stream Sediment Geochemical Survey of Gouap-Nkollo Prospect, Southern Cameroon: Implications for Gold and LREE Exploration. *American Journal of Mining and Metallurgy*, **2**, 8-16.

[108] Teutsong, T., *et al.* (2016) Petrography and Geochemistry of the Mesoarchean Bikoula Banded Iron Formation in the Ntem Complex (Congo Craton), Southern Cameroon: Implications for Its Origin. *Ore Geology Reviews*, **80**, 267-288. https://doi.org/10.1016/j.oregeorev.2016.07.003

[109] Ganno, S., *et al.* (2018) Geochemical Constraints on the Origin of Banded Iron Formation-Hosted Iron Ore from the Archaean Ntem Complex (Congo Craton) in the Meyomessi Area, Southern Cameroon. *Resource Geology*, **68**, 287-302. https://doi.org/10.1111/rge.12172

[110] Faure, S. (2012) Potentiel de mineralisations de type IOCG en contexte intracratonique ou d'arcs continentaux dans les terrains archeens et proterozoiques du Quebec. Project 2010-08.

[111] Seltmann, R., Porter, T.M. and Piranjo, F. (2014) Geodynamics and Metallogeny of the Central Eurasian Porphyry and Related Epithermal Mineral Systems: A Review. *The Journal of Asian Earth Sciences*, **79**, 810-841.

https://doi.org/10.1016/j.jseaes.2013.03.030

[112] Aye, B.A., Sababa, E. and Ndjigui, P. (2017) Geochemistry of S, Cu, Ni, Cr and Au-PGE in the Garnet Amphibolites from the Akom II Area in the Archaean Congo Craton, Southern Cameroon. *Chemie der Erde-Geochemistry*, **77**, 81-93. https://doi.org/10.1016/j.chemer.2017.01.009

[113] Knipping, J.L., Bilenker, L.D., Simon, A.C., Reich, M., Barra, F. and Deditius, A.P. (2015) Giant Kiruna-Type Deposits Form by Efficient Flotation of Magmatic Magnetite Suspensions. *Geology*, **43**, 591-594. https://doi.org/10.1130/G36650.1

[114] Roberto, S., Hühn, B. and Silva, A.M. (2018) Favorability Potential for IOCG Type Deposits in the Riacho do Pontal Belt: New Insights for Identifying Prospects of IOCG-Type Deposits in NE Brazil. *Brazilian Journal of Geology*, **48**, 703-719. https://doi.org/10.1590/2317-4889201820180029

Appendix2: Publications related to the thesis

1. **Assembe, S.P**., Ndougsa-Mbarga, T., and Meying, A., 2016. New structural facts from audio-magnetotelluric (AMT) data interpretation in the Yaoundé-Nkolafamba area (Centre Cameroon). *Journal of Indian Geophysical Union*, **20** (1), 19-32.

2. Akame, J.M., **Assembe, S.P**., Zo'o Zame, P., Owona, S., Ndougsa-Mbarga, T., Azia, G.A., Mvondo-Ondoa, J., 2019. The Sangmelima granite-greenstone belts (South Cameroon): Integration of remote sensing and aeromagnetic data for structural interpretation. *The Egyptian Journal of Remote Sensing and Space Sciences* **22**, 37–47. https://doi.org/10.1016/j.ejrs.2018.11.005.

3. **Assembe, S.P.,** Ndougsa-Mbarga, T., Meying, A., Gouet, D.H., Ngoh, J.D., Mono, J.A., 2019. Contribution of Geophysics to the Understanding of the Geodynamic Activity at the Northern Margin of the Congo Craton : A Case Study from Aeromagnetic Data Interpretation Over the Metet-Zoetele Region (Southern Cameroon). *European Journal of Scientific Research* **152**, 286–303.

4. **Assembe, S.P.,** Ndougsa-Mbarga, T., Enyegue A Nyam, F.M., Ngoumou, P.C., Meying, A., Gouet, D.H., Zanga Amougou, A., Ngoh, J.D., 2020. + − Evidence of Porphyry Deposits in the Ntem Complex: A Case Study from Structural and Hydrothermal Alteration Zones Mapping through Landsat-8 OLI, Aeromagnetic and Geological Data Integration in the Yaounde-Sangmelima Region (Southern Cameroon). *Advances in Remote Sensing* **9**, 53–84. https://doi.org/10.4236/ars.2020.92004.

J. Ind. Geophys. Union (January 2016)
v.20, no.1, pp: 19-32

New structural facts from audio-magnetotelluric (AMT) data interpretation in the Yaoundé-Nkolafamba area (Centre Cameroon)

S. P. Assembe [1], T. Ndougsa-Mbarga *[1,2] and A. Meying [3]

[1] Postgraduate School of Sciences, Technologies & Geosciences, University of Yaoundé I, P.O. Box 8251, Yaoundé, Cameroon
[2]Department of Physics, Advanced Teachers' Training College, University of Yaoundé I, P.O. Box 47 Yaoundé, Cameroon
[3] School of Geology, Mining and Mineral Processing, University of Ngaoundéré, Cameroon
*Corresponding author: theopndougsa@gmail.com

ABSTRACT

Several geological models that explain the tectonic evolution of the Central Africa Pan-African Belt are discussed, each one having both outstanding results and unresolved questions. To improve the knowledge of the Pan-African domain in Cameroon, especially within the Yaoundé series, a geophysical investigation of shallow crustal structures was carried out in Nkolafamba, 26 km away from Yaoundé on the Yaoundé-Akonolinga highway, between the northing latitudes 03°45 and 04°, and easting longitudes 11°30 to 12° area during August 2011. The study combines field geological observations with twenty-three tensor Audio-magnetotelluric/Controlled source audio-magnetotelluric (AMT/CSAMT) experiments along four north 135° trending profiles, using a Geometric's Stratagem EH4 resistivitymeter. The 2D modelling of geophysical data exhibits: (1) That the formations encountered in the area are a mixture of both Pan-African and Congo Craton formations; (2) Many folding patterns and a set of strike-slip conductive faults and fractures that correlate the field observations. From the outcome of the study, we state that the study area belongs to the transition zone between the Congo Craton and the Pan-African belt. We propose that many of these faults form a southwest-northeast shallow tectonic line, seem to be related to the enhancement of the Centre Cameroon Shear Zone within the Yaoundé area. These facts demonstrate that the region has been affected by the collision between the Pan-African and the steady Congo Craton, followed by post Pan-African transpressional evolution characterized by dextral and sinistral strike-slips along the southwest-northeast trend. Therefore, we opine that the indentation tectonics model, earlier proposed through some geological studies, is more suitable in describing the geological evolution. It is also evident that geophysics played significant role in better understanding of the Yaoundé series' structural geology.

Keywords: Tensor audio-magnetotelluric experiment, Controlled source audio-magnetotelluric experiment, 2D modelling, tectonic line, Pan-African belt, Congo Craton, Yaoundé series.

INTRODUCTION

Structural geology divides South-Cameroon into two major sets: (**a**) The Congo Craton (CC)in the Southern part, represented by the Ntem complex, which has not been affected by the Pan-African thermo-tectonic event; (**b**) The central and northern parts that correspond to the Central African mobile zone, where the Pan-African orogeny occurs. This E-W orogenic zone, the Central Africa Pan-African Belt (CAPAB), is sited at the Northern edge of the CC and stretches from Cameroon to Sudan (Poidevin, 1985; Nzenti et al., 1988; Rolin, 1992 and 1995; Penaye et al., 1993).
The study area is located 26 km away from Yaoundé on the Yaoundé-Akonolinga highway, between north-latitudes 03°45 and 04°, and east-longitudes 11°30 to 12°. It belongs to the Yaoundé series, a unit of the Yaoundé Group, which is part of the CAPAB. The Yaoundé series is a Neoproterozoic feature located at the North of the CC, which stretches from west to east. It is made up of gneisses and migmatitic garnets coming from old granitised and metamorphosed sediments in the high pressure granulite facies. It constitutes the heart of the Pan-African thrust (Nzenti et al, 1984 and 1988; Nédelec et al, 1986). The Precambrian basement of the area, as that of the whole Yaoundé series (Figure 1), comprises two geological facies: gneisses associated with micaschists (ectinites), and migmatitic garnetiferous gneisses (migmatites).

The Neoproterozoic Yaoundé series has undergone structurally sub-horizontal tangential tectonics, which is the origin of its position as a sheet on the northern edge of the CC (Bessoles et Trompette, 1980; Nédelec et al 1986; Nzenti et al, 1988; Ngako et al., 2008) .Tectonics in the region can then be described as corresponding to alternative east-west to northwest-southeast contractions and to north-south to northeast-southwest parallel orogenic stretches. Olinga et al. (2010) state that the tectonics corresponds to: the thrusting of the Yaoundé nappe over the CC; and the strike-slip shearing in ductile to brittle-ductile conditions, characterized by penetrative foliation dipping north or south, an associated east-northeast-west-southwest

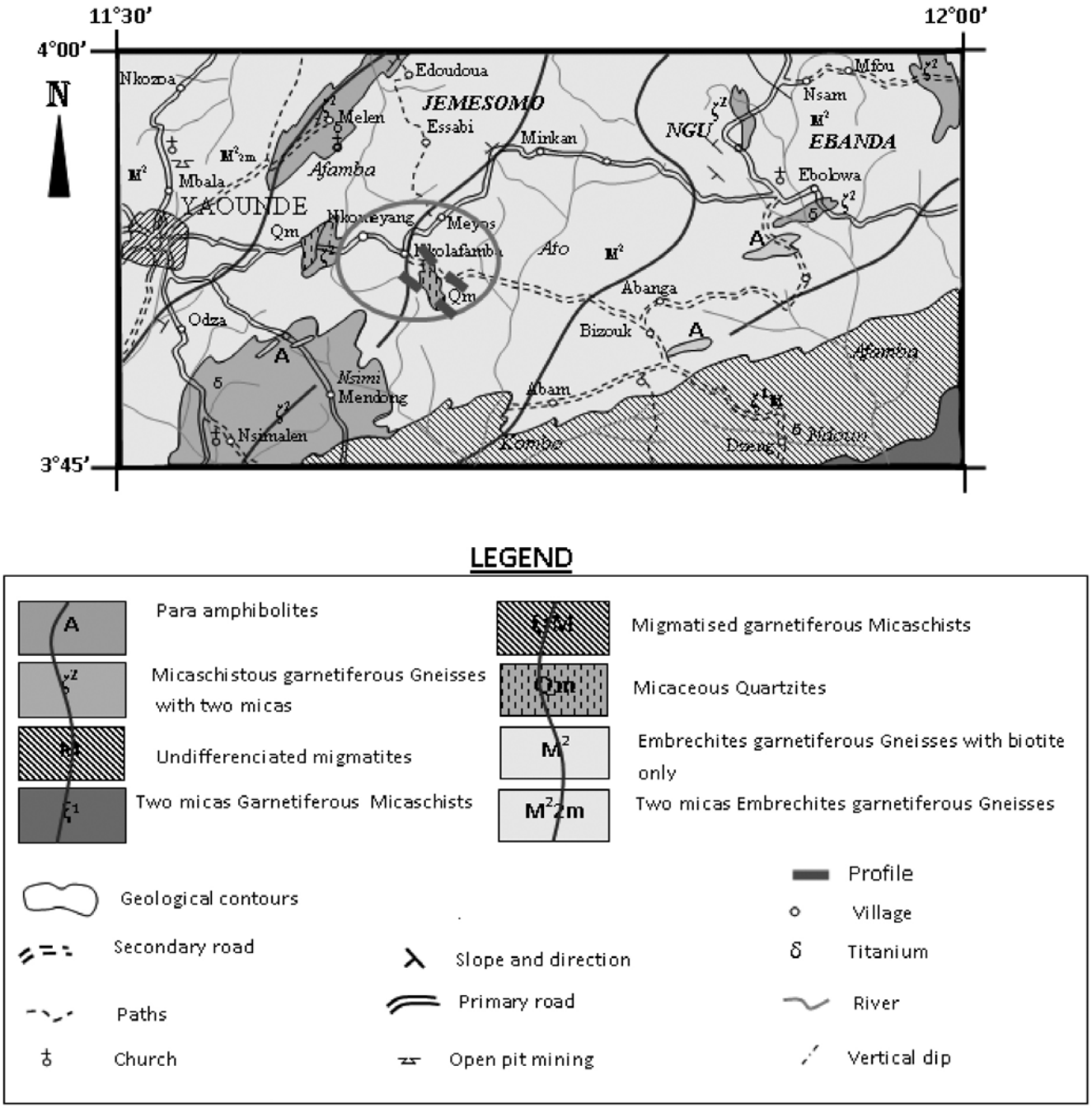

Figure 1. Geologic map of the study area (after Champetier de Ribes & Aubagues, 1956)

stretching lineation and north-south to northeast-southwest folding.

Geophysical inputs involving the CC/CAPAB transition zone are mainly from gravity studies. Early interpretations of gravity anomaly maps (Collignon, 1968) revealed E-W strong anomaly gradients in the Akonolinga/Ayos/Nguelemendouka/Abong-Mbang area, which were interpreted as an E-W tectonic activity along parallel 04°N (Mbom-Abane, 1997), while Ndougsa et al. (2003) suggest an E-W normal fault in the Mengueme/Abong-Mbang area. More recent studies by Shandini et al. (2010 & 2011) confirmed the CC/CAPAB boundary and highlighted NE-SW and NW-SE basement lineaments that Basseka et al. (2011) suggested to be related to faulting associated with the granitic rocks in the upper brittle crust. Hence, crustal faulting in the northern margin of the CC is assumed to be associated with deep-seated structures (Feumoe et al., 2012; Ndougsa et al., 2012; Shandini and Tadjou, 2012) related to the CC/CAPAB collision.

Magnetotellurics (MT) revealed the CAPAB's overthrust line onto the CC corresponding to the Eseka-Dja faults line (Manguelle-Dicoum et al., 1993) and a major E-W (N105°)

general trending lineament corresponding to the CC/CAPAB boundary and secondary ENE-WSW to NNW-SSE lineaments (Meying et al 2009) at Ayos, in the southern edge of the CAPAB. The E-W lineament corresponding to the CC/CAPAB boundary was confirmed by Tadjou et al. (2008), who additionally detailed about subsidence within the basement associated with intrusions of low resistive materials beneath the CAPAB domain in the Abong-Mbang/Akonolinga area, located east of our study area. Recent investigations in the CC/CAPAB transition zone using Audiomagnetotellurics confirmed that the E-W event associated with fault structures is related to the inferred tectonic boundary separating CC and CAPAB ,while NNW-SSE to ENE-WSW structures are related to post-collision tectonics occurring in the area (Meying et al., 2009; Ndougsa et al., 2011; Meying et al., 2013). It is important to state that the area under study has not been clearly subjected to AMT investigations. It is subjected to these geophysical investigations, in the recent past, as detailed above.

Studies of the CAPAB reveal that it collides with the CC. However, to date, in spite of its proximity with the CC/CAPAB limit, finer details of the Yaoundé series could not be obtained due to insufficiency of geophysical studies, to explicitly explain the tectonics. We have interpreted an AMT dataset and found evidences of CC/CAPAB collision in the Yaoundé-Nkolafamba area that belongs to the southern margin of the CAPAB. The results are correlated with geological observations made simultaneously in the area.

METHOD AND DATA ACQUISITION

Method

The Magnetotelluric (MT) method separately developed both by Thikonov (1950) and Cagniard (1953) is applied for geophysical and structural geology prospecting (Bostick, 1977**;** Vozoff, 1972 & 1990; Manguelle-Dicoum et al., 1992 & 1993**;** Meying et al., 2009 and references therein, Meying et al., 2013). It consists of simultaneous measurements of electric and magnetic natural fields at any point on the surface of the Earth, in order to deduce the resistivity of rocks of the homogeneous subsurface. For the real case, subsurface is inhomogeneous and apparent resistivity is determined using the Bostick law (1977) derived from the Cagniard's fundamental formula (Ndougsa et al., 2011).

Data Acquisition

In this work, the high frequency MT or Audio-magnetotelluric (AMT) method was used to image the subsurface structure of the Yaoundé/Nkol-Afamba area using a Geometrics' Stratagem EH4 AMT/CSAMT system. The data were acquired during six days of field work conducted during the first half of August 2011. The method has been chosen because of its reliability and its fast handling even in remote and hostile areas. We lately combined geophysical studies with some field geological levees to strengthen our statements.

The Geometrics Stratagem EH4 unit measures electrical resistivity with orthogonal electrical and magnetic field changes to depths ranging from few meters to more than 1 km in the frequency range of 10 Hz to 92 kHz. Data collected are processed to provide tensor impedance measurements, which allow full complex 2D structures interpretation (Geometrics, 2000). Nevertheless, natural signals are generally weak in the higher frequency range; hence the use of artificial signals (Vozoff, 1972; 1990 and 1991; Strangway et al., 1973; Goldstein and Strangway, 1975; Zonge and Hugues, 1991; Garcia and Jones, 2002; Zhdanov, 2009) produced by a transmitter to strengthen weak background field signals. The Geometrics Stratagem EH4 transmitter, when used, was assembled at least 300 m away from the receiver site to enable the plane wave assumption to be valid. AMT/CSAMT data were collected along four profiles; these profiles were parallel with a two by two recording pattern. They followed a NW-SE (N135°) direction based on the assumption that structural features in the Pan-African are generally E-W and/or NE-SW. The profiles were indexed from 1 to 4. The profile1, profile3 and profile 4 were 500 m in length and contained six sounding stations each, with a station-station spacing of 100 m. Profile 2 was 400 m in length with five stations at a constant separation distance of 100 m. Soundings data were acquired at each station with 25 m dipoles length both in the X and Y directions (however, dipoles length was 25 m in the Y direction and 50 m along the X direction in profile1). The X dipole was parallel to the profiles' trend. Data collected have been initially processed using the Bostick's transform, and then interpreted with Imagem software within the Stratagem EH4. We used Plot2D and Surfer 9.0 software, which provided the geoelectrical sections and pseudo sections, respectively for analyses. The frequencies ranged between 25.12 Hz to 39810 Hz, assuming a penetration depth from 8 m to 10000 m. The details presented below focus only on the upper 1000 m.

While collecting field geophysical data, some geological facts have been observed, according to outcrops available in the area. The formation is of gneissic type. The main structures that appear in are: a sub horizontal east-foliation; with an E-W maximal stretch and a N-S minimal stretch; folds, shears (Figure 2a) and fractures (Figure 2c) that include two major families, the first being NE-SW oriented and the second ESE-WSW. The double boudinage (Figure 2b) enables to highlight an extensive tectonics with a vertical maximal deformation. These structures are imprints of a multiphase deformation.

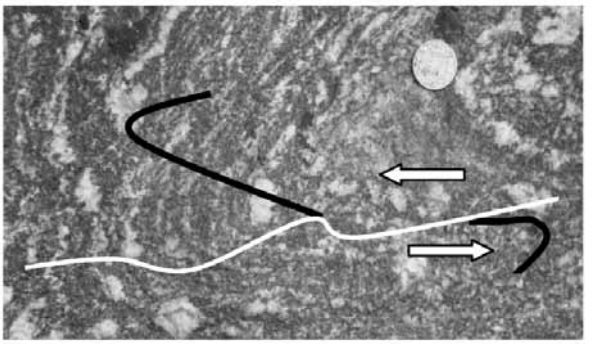

Figure 2a. Recumbent folds crossed by a dextral shear.

Figure 2b. Double boudinage

Figure 2c. ESE-WNW Fracture in the rock

RESULTS

Profile 1:

The pseudo-sections (Figure 3a & 3b) show irregularly shaped iso-contours. They exhibit dislocation patterns of blocks on one hand. They also show that conductive formations are encountered both on surface and at depth. The resistivity pseudo-section particularly presents three concentric anomalies, between OS2 and OS4, from depth to surface with a mean resistivity value of 193.0 Ω.m, forming a conductive channel. This channel may be an up well or intrusion of conductive materials. We also observe that entire near surface is conductive. However, an anomalous resistant structure centred at OS2 is found to continue downwards. The shape of isoresistivity contour

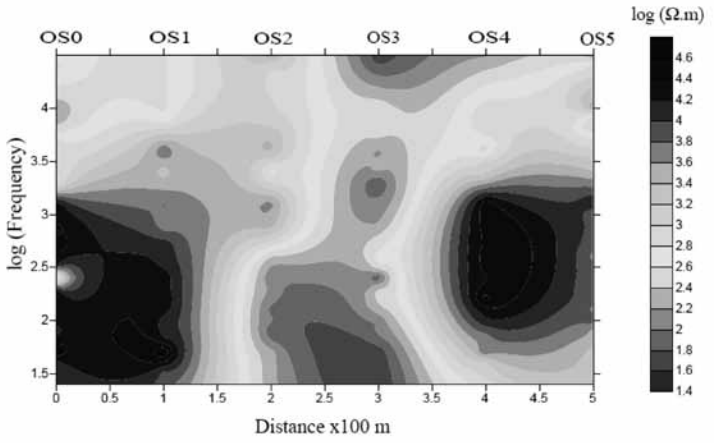

Figure 3a. Resistivity pseudo-section of profile 1

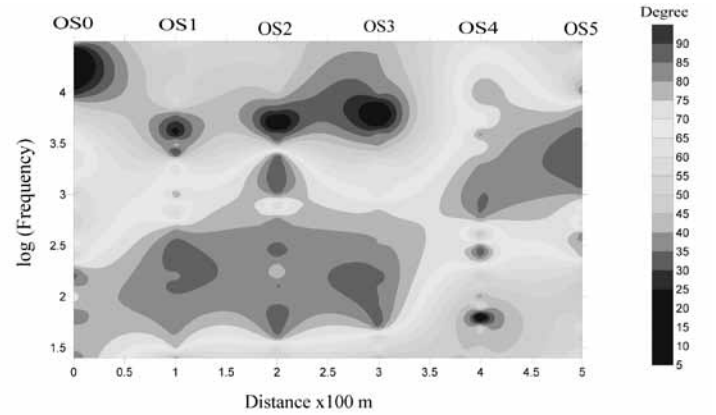

Figure 3b. Phase pseudo-section of profile 1

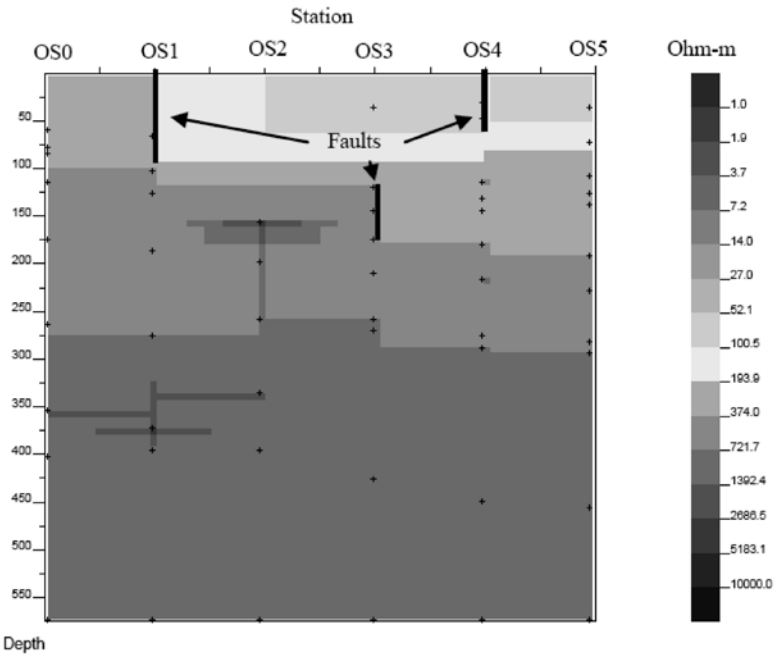

Figure 3c. Geoelectrical section of profile1. Depth in meters

lines suggests that the area might have undergone a folding process. Subvertical isoresistivity lines below OS1 and OS4 suggest the presence of discontinuities that are either faults or contacts.

The geoelectrical section plot (Figure 3c) confirms above observations. It shows two shallow conductive formations of mean resistivity 147.2 Ω.m and 284 Ω.m, respectively. The contacts between these formations are interpreted as faults at OS1 and OS4. The second formation outcrops from station OS0 to OS1. The third formation, with a mean resistivity of 547.9 Ω.m and a variable thickness, is jagged by faults at stations OS1, OS3 and OS4.It shapes like a graben. An intrusion of the underlying material at station OS2 forms a sill of 100 m wide and 25 m thick, near 150 m depth. The fourth formation, with a mean resistivity value of 1057 Ω.m, is marked by faults beneath stations OS2 and OS3. A resistive material embedded at OS0 that splits itself up to OS2, has a mean resistivity value of 3934.8 Ω.m (this fifth formation probably extends beyond 1 km depth and lays on a more resistive structure). This is not shown in the model.

Profile 2:

The apparent resistivity and phase pseudo-sections (Figure 4a & 4b respectively) exhibit a high anomalous zone (both resistivity and phase) from the beginning of the profile until almost the fourth station, where it forms vertical to subvertical contour lines characterizing a major discontinuity. The plot reveals a conductive basin-like feature between stations BE0 and BE1. The near-surface of the whole area seems to be conductive, and it suggests that the area probably experienced a tectonic activity.

The geoelectrical section (Figure 4c) exhibits a subsurface structure comprising some discontinuities, which may be faults or relief scarps. We observe, downward from the top, a conductive layer (mean resistivity 98.9 Ω.m around BE1, and 417.2 Ω.m in almost the whole area until 250 m depth). This formation is marked by many islets of resistive materials at stations BE0, BE2 and around station BE3. Another very thin formation is encountered at around 250 m depth. The fourth formation encountered has a mean thickness of 400 m with a mean resistivity value of 1119.2 Ω.m.It embeds a more resistive formation (1833.1 Ω.m), which seems to correspond to the fifth layer encountered at 725 m depth. The basement lays at 825 m depth with resistivity values ranging between 3728.1 Ω.m and 6105.8 Ω.m. A major discontinuity that seems to be a fault can be observed beneath station BE1, while others may be scarps.

Profile 3:

Analyses from pseudo-sections of profile 3 (Figure 5a & 5b respectively) exhibit two distinctive zones: a very resistive zone at depth (frequencies less than 1200Hz), contrasting with the conductive overburden (frequencies greater than 1200Hz), both separated by a narrow transition zone. Some anomalous isoresistivity values enclosed between stations NK2 and NK4 (with a paroxysmal uplift centred beneath station NK3) may correspond to an uplift of resistive materials in conductive structures. A discontinuity is also highlighted at middle depth below station NK1 and below NK4 by subvertical lines. The shape of isocontours of the overburden formation is an evidence of the folding processes that probably affected the shallow formations.
The geoelectrical section (Figure 5c) presents a first layer of mean resistivity 80.9 Ω.m with an average thickness of 100 m; the second layer has a mean resistivity of 355.5 Ωm; a third thin layer with a mean resistivity of 683.1 Ωm; the fourth layer with a mean resistivity of 1118.9 Ωm is very thick and marked by an intrusion of the underlying material between stations NK3 and NK4; the fifth formation has a mean resistivity of 1832.7 Ωm. It is deformed by the uplift of underlying formations, which have resistivity values ranging between 2275.8 and 10000 Ωm. This uplift can either be seen as an intrusion or channel of resistive materials from the basement. Some discontinuities interpreted as faults or discontinuities are highlighted below NK1 and NK4.

Profile 4:

Data from profile 4 (Figure 6a & 6b respectively) indicate presence of a prominent resistive formation at depth between stations BG1 and BG5; it appears like an intrusion of more resistive materials, compared to the surrounding. This formation is embedded within a less resistive formation covering the entire area, while some very conductive formations appear from station BG0 to station BG1 and between stations BG3 and BG5 on surface; below stations BG0 and BG3 they appear at deeper levels .The intermediate apparent resistivity values dominating the whole pseudo-section, have led us to conclude that the profile is set on an area made up of mixture of both resistive and conductive formations. The phase pseudo-section mainly exhibits a depression or subsidence along the profile from BG0 to BG5. The shape of isocontour lines on the pseudo-sections also show irregular patterns that suggest that formations have been folded.

The geoelectrical section from profile 4 (Figure 6c) outlines a near surface electrical lithology characterized by three main conductive formations. On the top of the plot, we have two formations with mean resistivity 683.4 Ωm and 1119.3 Ωm, respectively, with a fault type contact detected at station BG3; the third formation more conductive than the first two, with a mean resistivity value of 417.2 Ωm is encountered at 75 m depth below BG0.Its roof is jagged by many minor scarps ,which shape

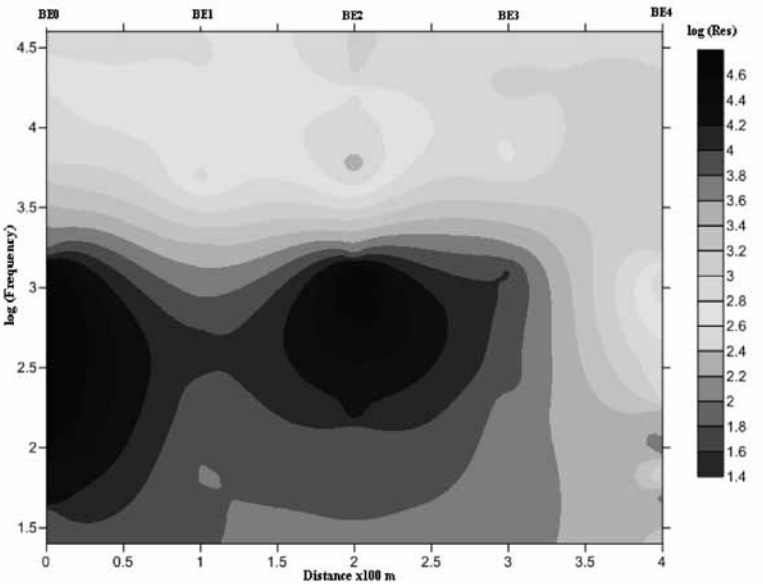

Figure 4a. pseudo-section of profile 2

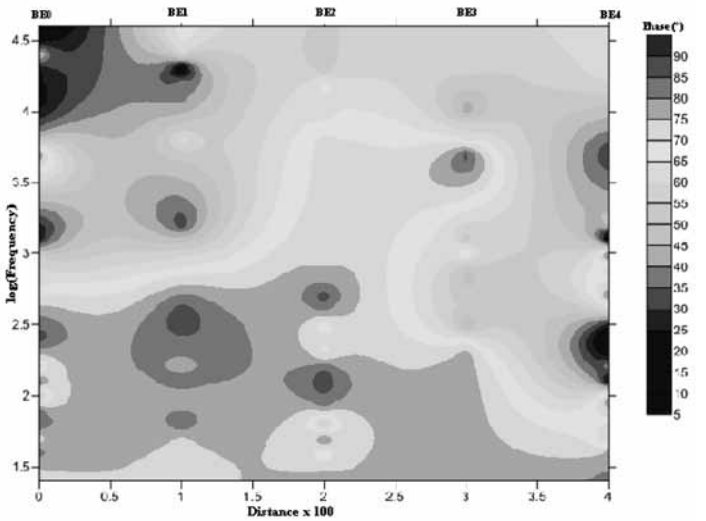

Figure 4b. Phase pseudo-section of profile 2

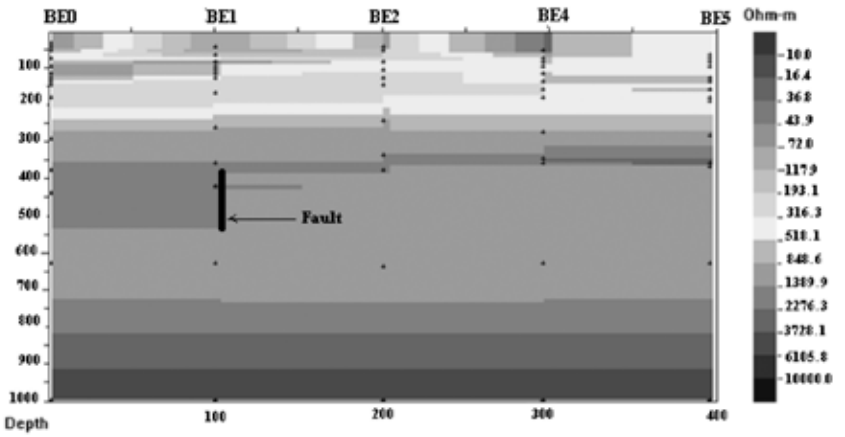

Figure 4c. Geoelectrical section of profile 2. Depth in meters.

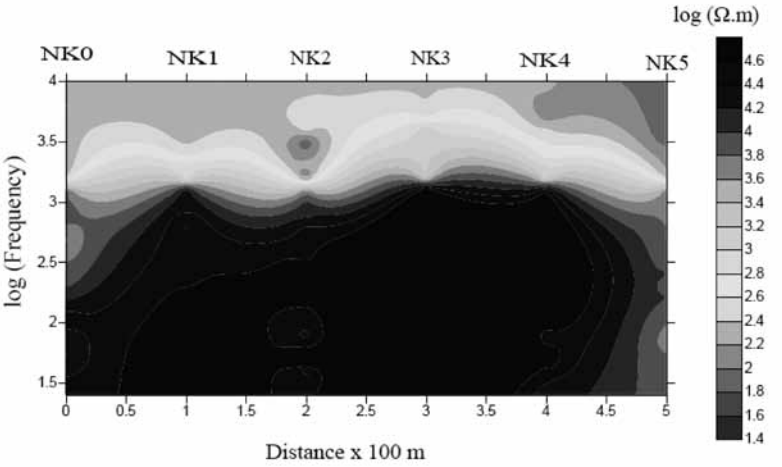

Figure 5a. Resistivity pseudo-section of profile 3

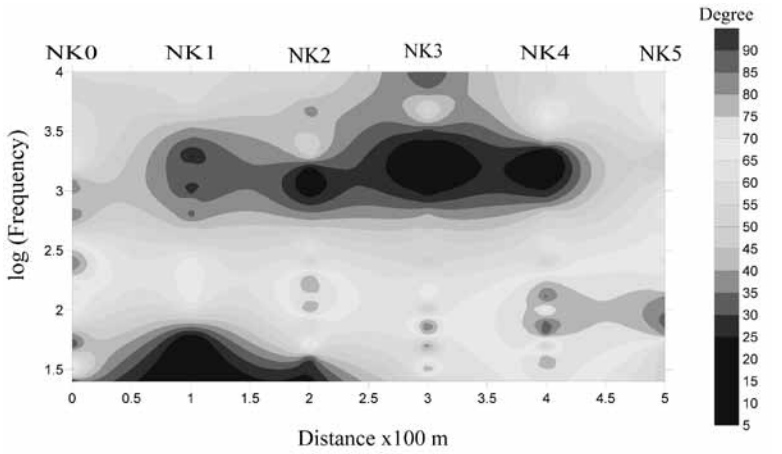

Figure 5b. Phase pseudo-section of profile 3

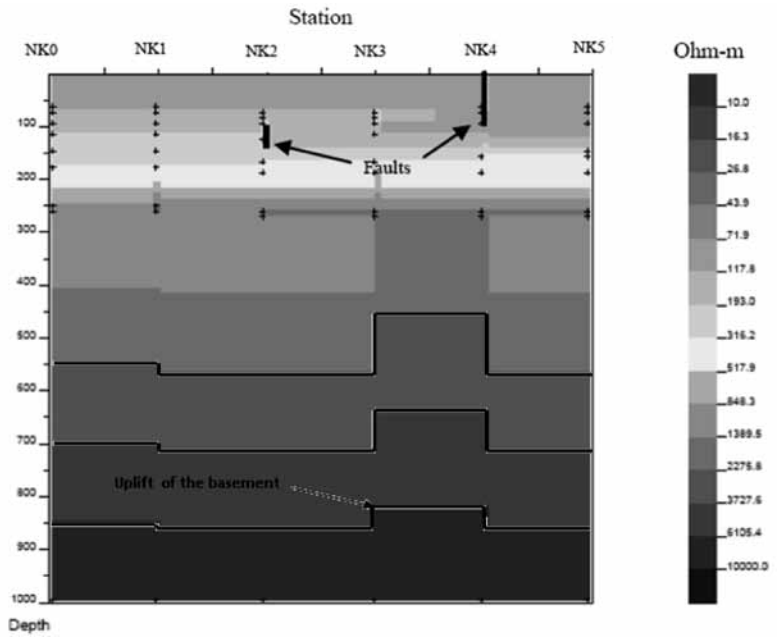

Figure 5c. Figure 5c. Geoelectrical section of profile 3. Depth in meters.

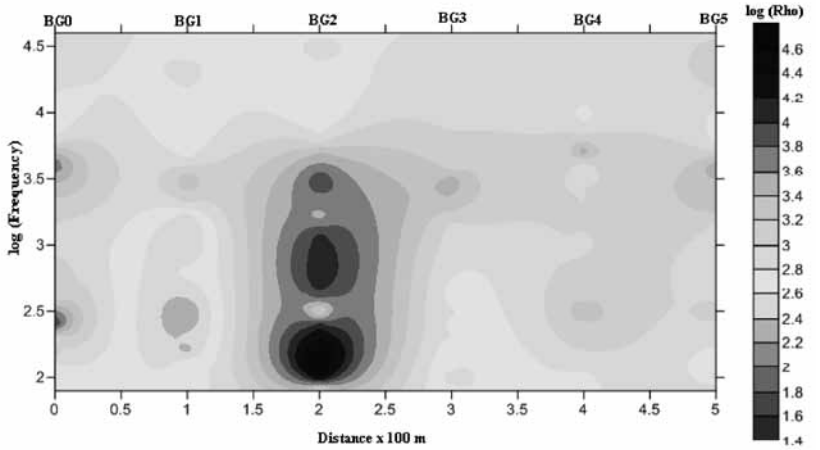

Figure 6a. Resistivity pseudo-section of profile 4

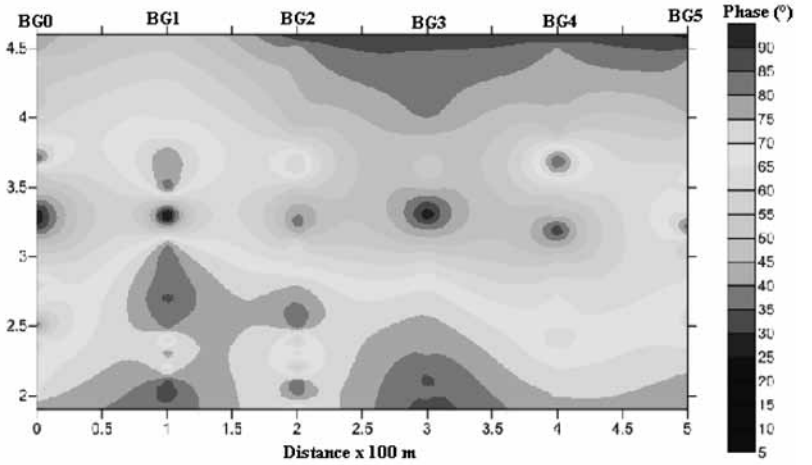

Figure 6b. Phase pseudo-section of profile 4

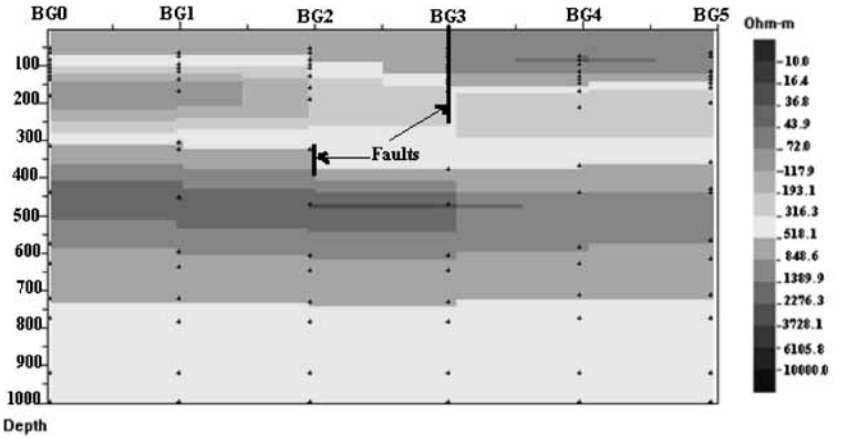

Figure 6c. Figure 6c. Geoelectrical section of profile 4. Depth in meters

it like downstairs from BG2 to BG5 while a fault type discontinuity is identified around 300 m depth under BG2; the first formation is encountered again at 300 m and extends up to 750 m depth enclosing the second formation (350 m to 600 m depth) within which a resistive structure (3002.2 Ωm mean resistivity) is embedded from BG0 to BG3 with a mean thickness of 100 m (from 400 m to 500 m depth). It appears from the geoelectrical section that there is a graben-like structure in near subsurface from BG2 to BG5, as shown in the phase pseudo-section.

DISCUSSION

AMT analyses

Analyses of results from the current study suggest that profiles 1, 2 and 4 are located on the same geological environment, where as profile 3 on a different environ. Soundings from profiles 1, 2 and 4 are made on fairly conductive areas, with a range of resistivity values that correspond to a weathered gneissic environment (Palacky, 1987). Profile 3 seems to be located on micaceous quartzites. It appears that the study area is composed of a mixture of both very resistive and conductive formations. The basement appears at 1400 m in profile 1, 825 m in profile 2, 550 m in profile 3 and deeper (more than 1400 m) in profile 4. This indicates that the basement rises up in some parts, while it collapses in other parts. This in turn might have induced thickening of overlying materials. The observed uplift of the basement may also be attributed to cooled intrusions beneath it. The subsidence and uplift of the basement probably attest the existence of a depressed structure (graben or basin), as evidenced by pseudo-sections. This shows a rugged subsurface structure of the area. The roughness of this subsurface structure is also emphasized by the shape of isocontour lines on all the pseudo-sections, hence suggesting that the formations in the area have been folded. The folding process is originated from a shortening,a priori, parallel to the direction of all the profiles (N135°). This shortening was caused probably by the collision between the CC and the CAPAB. In addition, many faults, scarps and fractures have been inferred in all the profiles. Some of the faults show significant throw (e.g. 150 m below station OS4 in profile1; 50 m and 100 m beneath BG2 and BG3 respectively in profile 4; 175 m below BE1 in profile 3).

As, the general trend of profiles is N135°, faults and fractures highlighted are generally SW-NE to WSW-ENE oriented through other faults with different trends (E-W direction probably). The conductive channel seen on profile 1 (figure 3a) could be either an intrusion or an active fault. The shape of apparent resistivity isocontours, faults and fractures detected by our study suggest that tectonics of the study area occurred in brittle to brittle-ductile conditions, as in the Yaoundé Group. Besides, the geoelectrical section of profile 4 shows that resistive formations alternate with conductive ones, suggesting a reversal phenomenon within superficial formations in the area. This reversal suggests operation of the folding and thrust processes of the Yaoundé series' nappes onto the CC. The investigated area is located near the latitude N04°, the CC/CAPAB limit identified by previous geophysical studies (Tadjou et al., 2008; Ndougsa et al., 2010; Basseka et al., 2011 and Shandini et al., 2012). It is considered as a major discontinuity oriented in E-W direction. This discontinuity limit is assumed to be a suture line between those aforesaid units below the CAPAB. The CC subducts approximately from 50 to 100 km beneath the CAPAB. Resistivity values show the signature of rock mixture from the Pan African (conductive) and the CC (resistive) materials. It is seated at the transition zone between the CC and the CAPAB, as suggested by Meying et al. (2013), over a closed eastward (Ayos-Nguelemendouka) area. The current geophysical analysis could not clearly detect events coeval to the CC/CAPAB limit (E-W faults), compared to the geoelectrical model defined by Tadjou et al. (2008). In Tadjou et al.(2008) model, the CC is a resistive block in the south and the CAPAB a conductive block to the north.

The study has highlighted folding patterns within the Yaoundé-Nkolafamba subsurface at shallower depth. The folding system occurs along profiles strike i.e. they are locally caused by NW-SE to N-S compressional movements of the crustal blocks. This result is consistent with those from previous AMT investigations (Ndougsa et al., 2011 and Meying et al., 2013), which highlighted folding at the scale of the Yaoundé series, but eastward of the present study. The present study shows significant geoelectrical shallow discontinuities. These shallower discontinuities oriented from SW-NE to WSW-ENE (perpendicular to the profiles which are directed NW-SE), are interpreted as faults and folds. These folds may constitute local signatures of deep faults (along the same broad directions). Such signatures were also noticed both by Basseka et al. (2011) and Shandini & Tadjou (2012), through a gravity study that encompassed the present sudy area (from nearly N02° to N05° latitudes and from E11° to 13° longitudes). The aforesaid NE-SW to ENE-WSW events form a NE trending structural lineament (Figure 7).This is coeval to the NE secondary tectonic line suggested by Meying et al. (2013).It is linked to the setup of the Centre Cameroon Shear Zone (CCSZ), at a regional scale. The NE tectonic lineament is assumed to be a strike-slip fault system. This is in agreement with earlier geoelectrical studies by Mbom Abane (1997). It proves the existence of E-W and NE-SW oriented wrench fault sets: (a) the first one extends as far as to the Abong-Mbang area, east of Ayos, and (b) the second one runs parallel to the trend of the Trans-African strike-slip. The finding supports the results from the isoresistivity map analyses , carried out by Njinti-Nfor et al. (2001), over an adjacent area (Akonolinga/Abong-Mbang). The study also brought out presence of, E-W and NE-SW trending wrench faults.

In addition, the study reveals the occurrences of uplifts and collapses of the basement in the Yaoundé-Nkolafamba area. Taking into consideration the importance of the highlighted faults and folds that exhibit vertical to subvertical dips, we infer that the subsurface topography

is probably controlled by grabens and horsts. According to the coverage of the profiles (oriented NW-SE), the basin and horst-like subsurface structures are elongated in the SW-NE direction. Gravity studies (Shandini at al., 2010; Basseka et al., 2011 and Shandini and Tadjou, 2012) highlighted presence of similarly trending features .It is further inferred that the basement collapse occurred during the CC and the CAPAB collision process. We also brought in to light qualitatively presence of a conductive channel from depth to surface on profile 1 pseudo-section, which can be either seen as an intrusion or a signature of an active faulting process. In the case of an intrusion, this result is in agreement at the local scale, with Basseka et al. (2012) who indicated the presence of granitic intrusions in the northern margin of the CC. If the faulting process is admitted, this channel correlated with horizontal movements linked to shearing processes along the NE-SW direction, as seen by Basseka et al. (2012). These NE shears correspond to horizontal trans-current movements occurring in the Yaoundé series coeval to the CCSZ. The NE tectonic lineament (Figure 7) is correlated to the CCSZ and inferred from the conductive channel as previously mentioned by some authors (Ndougsa et al., 2010; Bisso et al., 2004), who predicted the seismic activity generated on the Sanaga fault (SF) in 2005. The Yaoundé series investigated by AMT soundings over the Yaoundé-Nkolafamba area has provided evidence of collapses and uplifts of the basement. The study also helped in imaging near-subsurface folds and faults. The faults span from the SW-NE to WSW-ENE directions and have vertical to subvertical dips (i.e. they are nearly to normal faults).These faults, when considered together and correlated with geological observations, are linked to the NE shallow lineament (Figure 7) coeval to the setup of the CCSZ characterized by the Sanaga Fault, which is passing north of the study area. The results therefore are in agreement, at the local scale, with the previous geophysical studies. The folding and faulting processes bear witness to intense tectonic movement in the brittle to brittle-ductile conditions that have affected the area at shallow depths. These facts support presence of the multistage tectonic activities (including the CC/CAPAB collision) that occurred in the area, as well as in the whole CAPAB or the Mobile belt at the regional scale. The length of profiles (500 m) as well as the use of high frequencies may constitute a critical limitation to the current geophysical analysis. Inspite of this limitation, the study has detected new faults and clearly imaged folds affecting the near subsurface. These results are supported both at the local and the regional scale by previous geophysical studies , namely the gravity and farther located magnetotelluric (MT) studies.

Geological data integration

Geological data collected through direct observations during the field campaign coincides with results obtained from AMT analyses. The interpretation of AMT data suggests that profiles were laid on a terrain of gneissic and quartzite formations. This fact is supported by the presence of gneissic formations outcrops. These gneisses are of three types: clinopyroxene amphibolic gneiss, biotite gneiss and garnetiferous biotite gneiss. The gneissic fabric presents a double boudinage (Figure 2b) with E-W maximal stretch (B_1) and an N-S minimal stretch (B_2). The folding patterns, corresponding to another deformation stage, are also observed. These folds are cross-cut by many shears (Figure 2a). Besides, many veins and families of fractures characterising the fourth deformation stage have been recorded. Among these fractures' families, the most interesting sets follow the NE-SW and ESE-WNW trends with vertical to subvertical dips. The NE-SW set correlates the faults highlighted by the AMT interpretation (Figure 7). The ESE-WNW family may represent faults nearly parallel to the AMT profiles. The folding and faulting underline the presence of medium to high grade conditions experienced by the area .These conditions facilitated the amphibolite and the granulites facies formations, characterized respectively by amphibolic gneisses, and, biotite gneisses and biotite garnetiferous gneisses, which are herein reported. The strength of tectonic forces occurred in the area has been recorded in the surrounding topography. Indeed, the study area topography is very rough with too many undulations .Even rivers like the Afamba and Ato kept those imprints as they flow in the NE direction. The double boudinage helped to bring to light role of an extensive tectonic activity that resulted in the NE-SW tectonic line suggested by the AMT study. The NE-SW line may constitute strike slip system, owing to the shears observed (Figure 2a). At the outcrop scale, the Yaoundé-Nkolafamba area experienced many deformation stages, as reported on the entire PanAfrican belt in southern Cameroon.

In agreement with geological studies, the faulting system proposed correlates at a local scale, with the SW-NE faults within the Yaoundé domain (significant to the Awaé-Ayos strike-slip shear zones in the late Pan-African tectonics)- (Olinga et al., 2010). At the regional scale, the fault system seems to be correlative with the Centre Cameroon Shear Zone, whose local segment is the Sanaga Fault. The strain field that affected the area is on the scale of that of Central African Fold Belt (Olinga et al., 2010) and consistent with the northeast-southwest Trans-Saharan collision system proposed by Mvondo et al. (2007 & 2009). Further, the NE-SW tectonic line proposed by this study

is within the Yaoundé series, imprint of a remarkable extension due to dextral wrenches still occurring in the African plate as witnessed by earthquakes, which struck the Yaoundé region in March, 2005 (Ndougsa et al., 2010). This extension is the modern outcome of the breakup of Gondwana and probably a consequence of the currently occurring NE movements of the African plate towards the Eurasian plate. The NE-SW tectonic line is then correlative to the general NE-SW trending lineaments system running W-E from the Gulf of Guinea to the Aden Gulf (Genik, 1992; Mvondo et al., 2007 & 2009; Olinga et al., 2010).

CONCLUSIONS

The AMT imaging has enabled to highlight folds that affected near subsurface formations. They are assumed to be caused by the Congo Craton/Panafrican collision.

Some geoelectric sections show graben-like topography due to the basement collapses and upward transport of resistive materials to shallow depth, forming basement uplifts.

The analyses have outlined a family of hidden strike-slip normal faults, which form a shallow structural line oriented NE-SW. This faulting network suggests extensive tectonic movement in the Pan African Yaoundé series, and correlates with the Centre Cameroon Shear Zone, while linked to the general NE-SW trending lineaments system running west-east from the Gulf of Guinea to the Aden Gulf.

The fault system, the uplifting of the basement and folding support the intense multistage tectonic activity, including the CC/CAPAB collision that occurs in the Yaoundé-Nkolafamba area, at the regional scale. The seismic activity recorded in Yaoundé in 2005 suggests ongoing tectonic activity. The CC and the CAPAB continue to collide, as part of continent-continent convergence activity.

ACKNOWLEDGEMENTS

The authors respectfully thank Mr Ava Christophe, Country Manager of Harvest Mining Corporation for the logistical support provided to facilitate the AMT survey. Thanks are due to the anonymous reviewer and Editor of JIGU for valuable remarks that enabled to improve the quality of this paper.

REFERENCES

Basseka, C. A., Shandini, Y. and Tadjou, J.M., 2011. Subsurface structural mapping using gravity data of the northern edge of the Congo craton, South Cameroon, Geofizika, v.28, pp: 229-245.

Bessoles, B. & Trompette, M., 1980. Géologie de l'Afrique. La chaîne Pan-Africaine « Zone Mobile » d'Afrique Centrale (partie sud) et zone mobile soudanaise, Mémoires du Bureau de Recherches Géologiques et Minières,Orléans, v.19, pp: 396.

Bisso D., Manguelle-Dicoum E., Ndougsa-Mbarga T., Tabod C. T., Njandjock N. P., Njingti N., Tadjou J. M. and Essono J., 2004.Geophysical Determination of the Sanaga Fault using Audio-magnetotelluric soundings in the Ebebda region, Cameroon, Segmite International, v.1, no.1, pp: 31-34

Bostick, F. X., 1977. A Simple Almost Exact Method of MT Analysis, Workshop on Electrical Methods in Geothermal Exploration, US Geological Survey, Contract No.14080001-8, pp:174-183.

Cagniard, L., 1953. Basic Theory of the Magneto Telluric Method of Geophysical Prospecting, Geophysics, v.18, no.3, pp: 605-635.

Champetier De Ribes, G. and Aubague, M., 1956. Notice explicative sur la feuille Yaoundé-Est (1/500 000), Bulletin Direction des Mines et de la Géologie, Yaoundé, Cameroun, pp: 35.

Feumoe Siyapdje, A.N., Ndougsa Mbarga, T., Manguelle-Dicoum, E. and Fairhead, J. D., 2012. Delineation of tectonic lineaments using aeromagnetic data for the south-east Cameroon area. Geofizika. v.29, pp: 175-192.

Garcia, X. and Jones, A.G., 2002. Atmospheric sources for audio-magnetotelluric (AMT) sounding, Geophysics, v.67, no.2, pp: 448-458.

Genik, G. J., 1992. Regional framework, structural and petroleum aspects of rift basins in Niger, Chad and the Central African Republic (C.A.R.), Tectonophysics, v.213, pp:169-185.

Geometrics, 2000. Operation manual for Stratagem systems running IMAGEM, ver. 2.16, Geometrics Printing Press, San Jose, California, pp: 16.

Goldstein, M.A. and Strangway, D. W., 1975. Audio-frequency magnetotellurics with a grounded electric dipole source, Geophysics, v.40, no.4, pp: 669-683.

Manguelle-Dicoum, E., Nouayou, R., Bokossah, A. S. and Kwende-Mbanwi T. E., 1993. Audio-magnetotelluric Soundings on the Basement-Sedimentary Transition Zone around the Eastern Margin of the Douala Basin in Cameroun, Journal of African Earth Sciences, v.17, no.4, pp: 487-496.

Manguelle-Dicoum, E., Bokossah, A.S., and Kwende-Mbanwi, T.E., 1992. Geophysical evidence for a major Precambrian schist-granite boundary in Southern Cameroon, Tectonophysics, v.205, pp: 437-446.

Mbome Abane, S., 1997. Investigations géophysiques en bordure du Craton du Congo et implications structurales. Thèse de Doctorat es sciences, Université de Yaoundé 1., pp: 180.

Meying, A., Ndougsa-Mbarga, T., and Manguelle-Dicoum, E., 2009. Evidence of fractures from the image of the subsurface in the Akonolinga-Ayos area (Cameroon) by combining the Classical and the Bostick approaches in the interpretation of

The Egyptian Journal of Remote Sensing and Space Sciences 22 (2019) 37–47

HOSTED BY

Contents lists available at ScienceDirect

The Egyptian Journal of Remote Sensing and Space Sciences

journal homepage: www.sciencedirect.com

Research Paper

The Sangmelima granite-greenstone belts (South Cameroon): Integration of remote sensing and aeromagnetic data for structural interpretation

Akame Joseph Martial [a,e,f,*], Assembe Stéphane Pactrick [b], Zo'o Zame Philemon [a], Owona Sébatien [d], Ndougsa Mbarga Théophile [c,e], Azia Giles Abuara [e], Mvondo Ondoa Joseph [a]

[a] Department of Earth Sciences, Faculty of Science, University of Yaoundé I, PO Box 812, Yaoundé, Cameroon
[b] Department of Physics, Faculty of Science, University of Yaoundé I, PO Box 812, Yaoundé, Cameroon
[c] Department of Physics, Advanced Teacher's Training College University of Yaoundé I, PO Box 47 Yaoundé, Cameroon
[d] Department of Earth Sciences, Faculty of Science, University of Douala, P.O. Box. 24157, Cameroon
[e] Department of Geology in the Ministry of Mines Industry & Technological Development of Cameroon, Cameroon
[f] Laboratoire G-Time (Géochimie: Tracage isotopique, minéralogique et élémentaire) Université Libre de Bruxelles 50, Av. F.D. Roosevelt CP 160/02 B-1050 Brussels, Belgium

ARTICLE INFO

Article history:
Received 8 January 2017
Revised 22 November 2018
Accepted 29 November 2018
Available online 13 December 2018

Keywords:
Remote sensing
Aeromagnetic
Lineament
Structural
Archeaen
Sangmelima
Cameroon

ABSTRACT

The integration of geology, geophysics and remote sensing data was used to map the Sangmelima granite-greenstone belt terrain located in the South Cameroon. The region was not easily accessible, because of dense vegetation and thick lateritic overburden. Aeromagnetic data were help in mapping new possible small greenstone belts and structural features in this area. Many of the identified lineaments are interpreted to represent fracture/fault zones, some of strike-slip faults. The NE–SW, NW–SE, N–S and E–W are the main revealed from remote sensing processing; while the NE–SW, E–W to ESE–WNW, NW–SE and N–S are the dominant structural trends revealed from aeromagnetic data. We distinguish three deformation events within the Sangmelima area: D_1 is recorded by a sub-vertical penetrative S_1 foliation bearing steeply plunging stretching lineations. D_2 overprints D_1 structures with tight-to-isoclinal folds with associated foliation, N160°–175°E and N05°–25°E ductile shear zones, indicating ENE–WSW shortening. The D_3 strike slip shearing is likely the result of the Eburnean deformation phase. The mafic dykes are striking NE–SW, N–S and NW–SE, and field evidence and airborne magnetic data suggest that some of them intrude preexisting structures. Many faults/fractures might have originated during previous deformation phases and they were only reactivated during the pan-African events.

1. Introduction

The Sangmelima Archean granite greenstone belt were studied to better understand the evolution of geological structures and their bearing on mineral potential. The Sangmelima region is located in the wet tropical forest on Archean flattened bedrock whose altitude ranges between 600 and 900 m, with a thick weathered overburden, vegetation, and isolated granitic domes (Akame et al., 2014). The integration of airborne geophysics, remote sensing data, and field observations was used to aid geological mapping and ground structural. The efficiency of these integration was demonstrated in Precambrian terrains in Australia, West Africa, and Canada (Betts et al., 2003; Direen et al., 2005; Peschler et al., 2006; Aitken et Betts, 2009; Stewart and Betts, 2010; Metelka, 2011; Pilkington and Keating, 2009). The data integration approach provided efficient results in a recent study involving the Dalema region in West-Senegal (Moussa and Tahar, 2013), or Wadi Allaqi area, South Eastern Desert of Egypt (Eldosouky et al., 2017). The field observations and measures as well as laboratory data were used to constrain and validate the results.

The study also involved investigation of the Ntem Archean Complex that is part of the Congo Craton in South-Cameroon, and occurring in the Sangmelima region (Fig. 1). The Complex was reported to be less understood compared to its Brazilian geologic equivalent, the Sao Francisco Craton as well as the West and the South African cratons (Metelka, 2011; Block et al., 2012; Dabo

Peer review under responsibility of National Authority for Remote Sensing and Space Sciences.

* Corresponding author at: Laboratoire G-Time (Géochimie: Tracage isotopique, minéralogique et élémentaire) Université Libre de Bruxelles 50, Av. F.D. Roosevelt CP 160/02 B-1050 Brussels Belgium

E-mail addresses: akamejosephmartial@gmail.com, akamejosephmartial@yahoo.fr (A. Joseph Martial).

https://doi.org/10.1016/j.ejrs.2018.11.005
1110-9823/

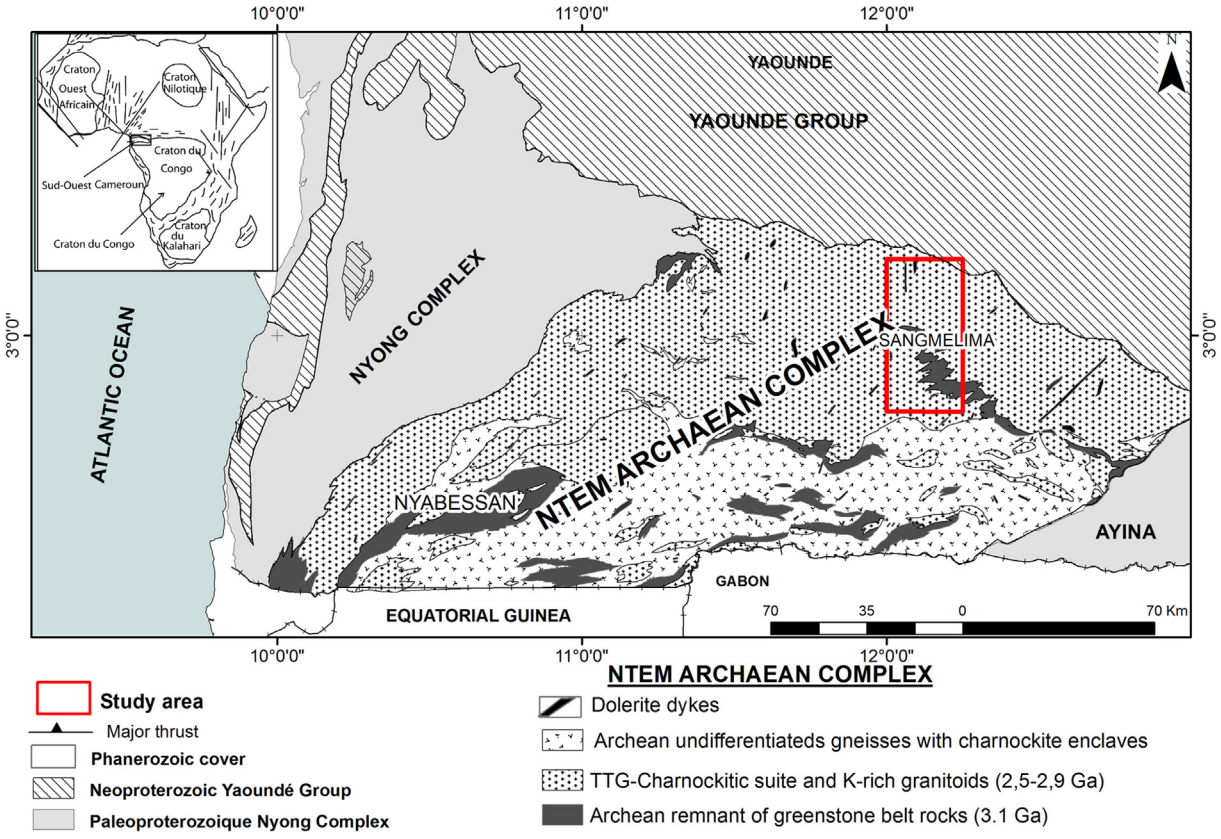

Fig. 1. Simplified geological map of the south-west Cameroon and location of the study area (Maurizot et al., 1986).

and Aïfa, 2013; Teixeira et al., 2017, and references therein). The results of the study highlighted various tectonic structures: fractures, faults, folds, and foliation related to Archean and Precambrian (Eburnean) tectono-magmatic events.

2. Geological setting

The Ntem Complex represents the north-western part of the Congo Craton in Central Africa(Lasserre and Soba, 1976; Maurizot et al., 1986; Caen-Vachette et al., 1988; Tchameni et al., 2000), comprising the Paleoproterozoic Nyong Unit to the north-west and the Archean Ntem Unit to southeast (Fig. 1). It is limited to the north by a major thrust that marks the contact with the Pan-Africanorogenic belt (Yaounde group). The Nyong Unit consists mainly of metasedimentary and metavolcanic rocks as wellas some syn- to late-tectonic intrusive rocks (Toteu et al., 1994). The Ntem Unit includes an Intrusive Series and a Banded Series BandedSeries as well as minor amount of supracrustal rocks (Maurizot et al., 1986; Shang et al., 2004a; Pouclet et al., 2007; Tchameni et al., 2004). The Intrusive Series is essentially exposed in the northern part of the Ntem Complex and is strongly mylonitized and retrogressed along the thrust boundary with the Pan-African Yaounde Group (Takam et al., 2009). It is dominated by a magmatic charnockitic suite and a TTG suite. The Banded Series outcrops over the southern part of the Ntem Complex and is dominated by strongly deformed granitic gneisses. Charnockitic enclaves are found within the gneisses of the Banded Series. Supracrustal rocks include banded iron formations (BIF) and sillimanite-bearing paragneisses occurring as xenoliths in the TTG; they are thought to be the remnants of greenstone belts (Suh et al., 2008; Chombong and Suh, 2013). K-rich granitoid rock sand dolerite dikes intrude the TTG and greenstone belts (Toteu et al., 1994; Tchameni et al., 2000; Shang et al., 2010).

Petro-structural studies suggest two major episodes of deformation in this geological domain. (*1*) The first deformation episode is characterized by vertical foliation, stretching and vertical lineation and isoclinal folds. These structural elements are correlated with successive emplacements of the mid-Archaean granitoids (Shang et al., 2004b), considered to be diapiric by Shang (2001) and Tchameni (1997). (*2*) The second major deformational event is marked by the development of sinistral shear planes of N0°–N45°E and of partial melting of TTG and of the supracrustal country rocks with the generation of various granites. This event is described as post-Archaean and postcharnockitic migmatization by Nsifa and Riou (1990) but is now thought to be late Archaean: 2666 Ma (e.g. Tchameni et al., 2000) and 2721 Ma (e.g. Shang et al., 2007).

3. Methodology

3.1. Processing of remote sensing data

The satellite imageries used were: (1) the 213–906 Landsat 7 ETM+ scene of March 18th, 2001 (Path 185 and Row 058); and (2) SRTM (Shuttle Radar Topography Mission) 90 m (Path: p184/SRTM_ff03_p184r058). The Landsat image was first orthorectified (rectification of the raw image distortion) then directly imported as a georeferenced on a GIS platform.

To enable the detection of lineaments, ETM+ channels 4, 5, and 7 have been chosen because of their spectral and spatial characteris-

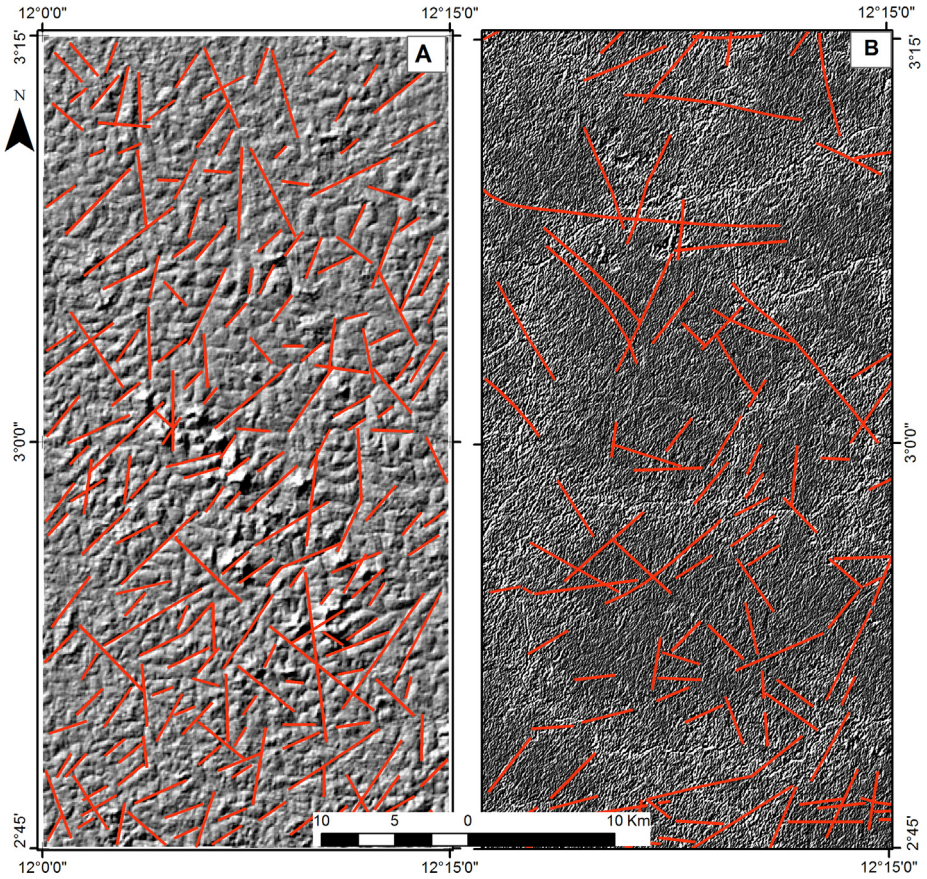

Fig. 2. Images from remote sensing of the study area with the main lineaments identified: (A) A shaded relief of the STRM; (B) A window of the gradient filter (Yésou et al., 1993).

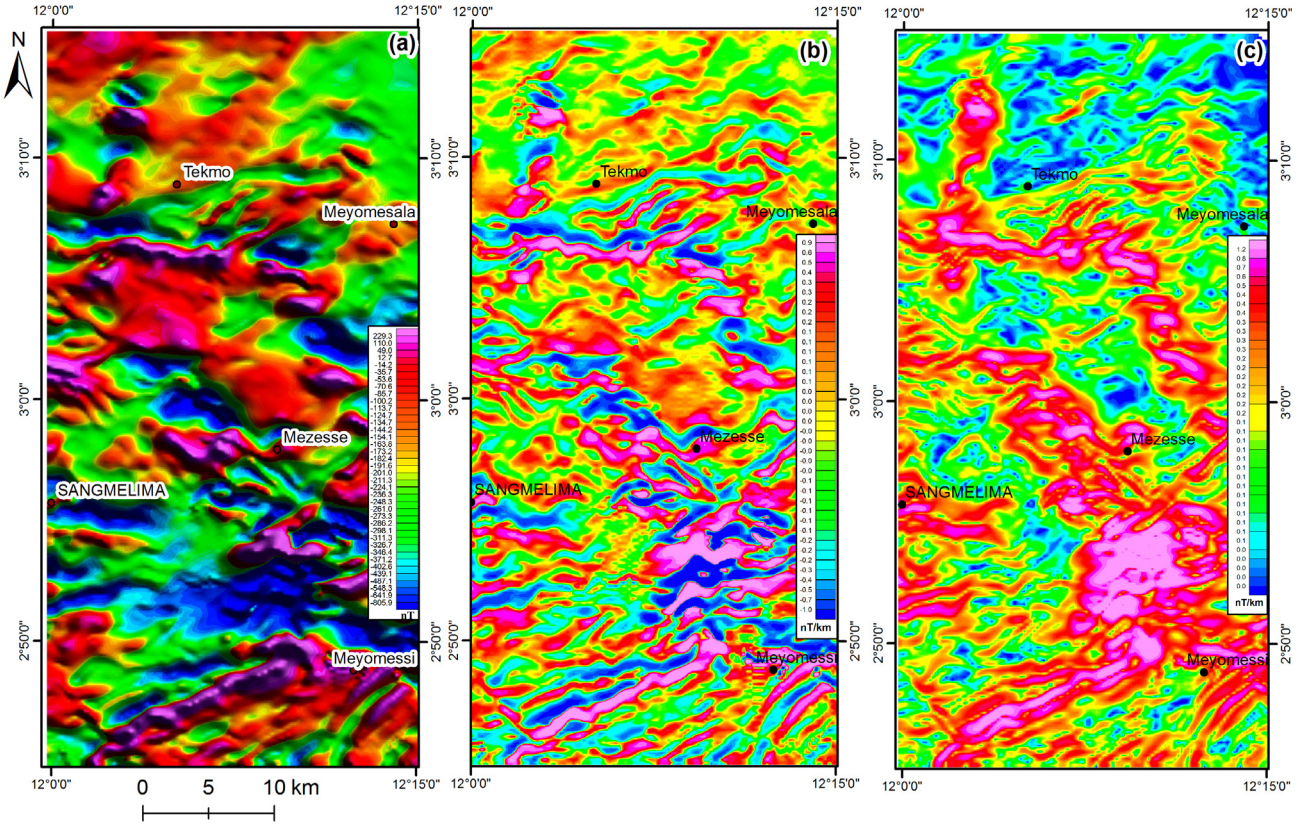

Fig. 3. **(a)** Total magnetic intensity reduced to the equator of the Sangmelima. **(b)** First vertical derivative of the total magnetic intensity reduced to the equator. **(c)** First horizontal derivative of the total magnetic intensity reduced to the equator.

tics (30 m). The principal components analysis (PCA) of pre-processed channels produced new channels for which only the first component could deliver efficient results. Linear structures were most visible on the first principal component (PCA1) than on a multispectral image. The discontinuities were enhanced through the application of both the Sobel filter on a 7×7 window along the N00°, N45° and N315° directions, and the gradient filtering from Yésou *et al.* (1993) to ETM + 5, ETM + 7, ETM + 5/ETM + 4 and PCA1 channels. The study focused on structural lineaments (Fig. 2).

Maps of the shaded relief, of the slope gradient and of the slope orientations were particularly helpful to highlight breaks-in-slope, ideal to detect tectonic features, such as faults characterized by a linear topographic step. Therefore, major lineaments/fractures probably faults, topographic differences are

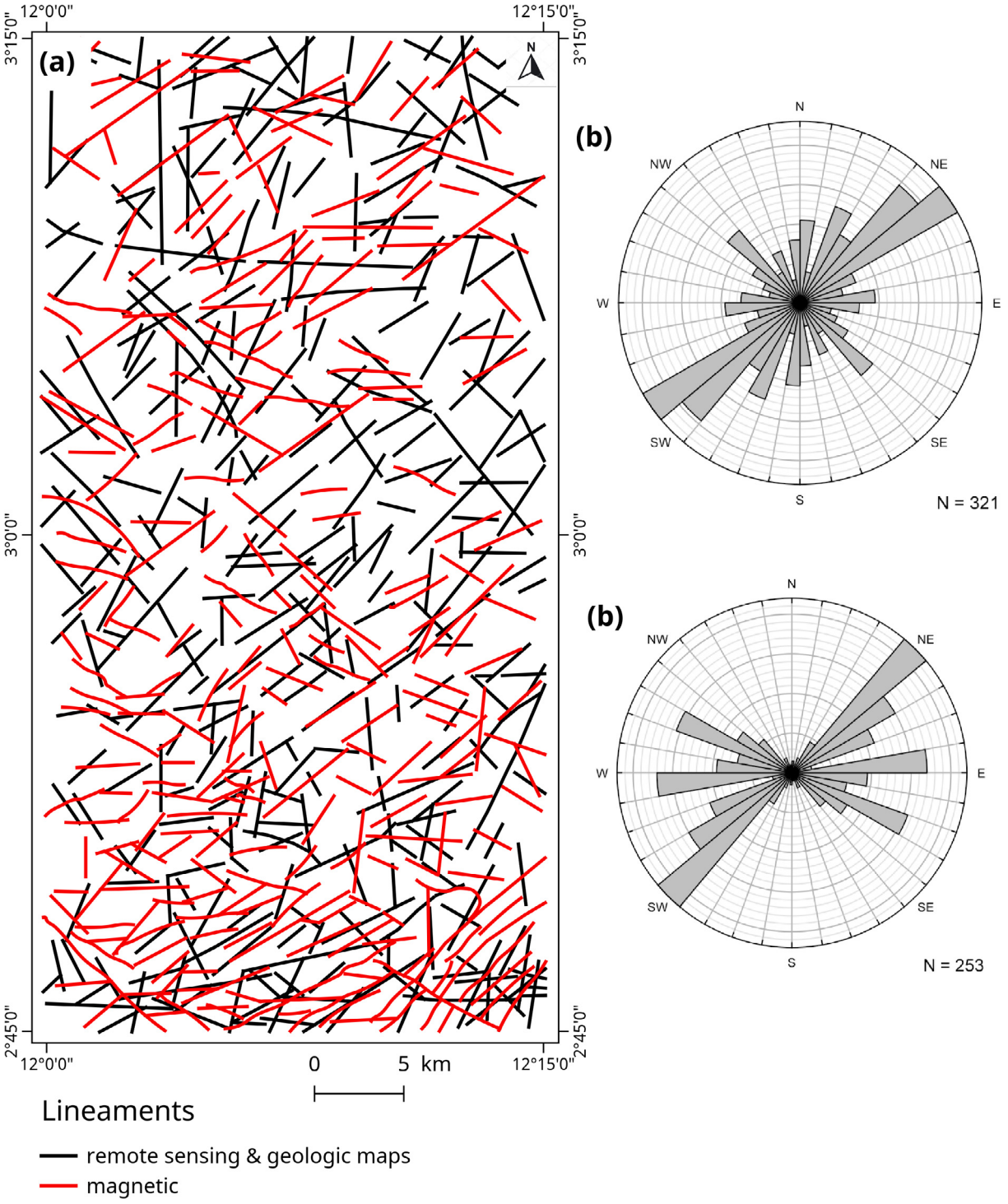

Fig. 4. Lineaments extraction and analysis. (a) Lineaments of Sangmelima revealed from remote sensing, aeromagnetic and geologic data; (b) and (c) rose diagrams show the distribution of the remote sensing and magnetic lineaments.

easily seen on Shuttle Radar Topography Mission; since these features cover large areas (Fig. 2). The lineaments were manually extracted by photo-interpretation and classified using the ArcGis 10. Both the natural and cultural artefacts (roads, power lines, farms and forest boundaries) were removed from the interpreted lineaments. The frequencies of the remote sensed lineaments were analysed to highlight their main directions for comparison with field observations.

3.2. Aeromagnetic data set and processing

The digital aeromagnetic dataset used in this study was a compilation of various digitalised contour maps of wide regional aeromagnetic surveys. The data was collected under taken under a cooperative agreement between the government of Canada and that of the Federal Republic of Cameroon (Patterson and Watson Ltd, 1976). The aeromagnetic survey was flown in the year 1970, with a line spacing of between 750 m and a mean flight height of 235 ± 20 m (Sheet: NA-33-XIII-1 and NA-33-XIX-13. 1971). The data was manually contoured to generate magnetic intensity maps at a scale of 1:50 000 Magnetic intensity values were extracted with ArcGIS. Magnetic data was processed and filtered with Geosoft Oasis Montaj software version 8.2. The residual total field was obtained by subtracting the International Geomagnetic Reference Field (IGRF). Reduction to Equator (RTE) transform was applied to the Total Magnetic Intensity (TMI) grid using an inclination of −18.59°and declination of −6.22° (Milligan and Gunn, 1997). To enhance the magnetic linear features associated with the Precambrian structures, frequency filtering operators were applied on the RTE to create the first vertical derivative image, analytic signal, and Tilt angle maps (Fig. 3). The resulted images were mainly interpreted individually using the ArcGIS.

4. Results

4.1. Remote sensing lineaments

A total of 321 lineaments were identified from the remote sensing data (Fig. 4a). The maximum linear length detected was 12189 m, while the minimum length was 508 m (average 3289 m). Both data sets are characterized by a heterogeneous spatial distribution of the lineaments. In the southern part of the study area an apparent higher lineament density is observed in both data sets. The rose diagram showing their orientations (Fig. 4b) indicates two major trends: NE–SW (035−065°) and NW–SE (120−140°). The N–S and E–W systems are less significant and can be identified throughout the whole domain. In the southern domain, the E–W lineaments do not seem to cross-cut the NE–SW fractures network, but rather to articulate towards them. The N–S network is sharply secant compared to the previous one.

4.2. Interpretation of aeromagnetic data

The total magnetic field map showed heterogeneous variations of the magnetic amplitude which span from −805.9 to 229.3 nT. The prominent variation in magnetic intensity was located at the centre of the map while the other anomalies were set within a NE trending zone. The main zone extended along the NW to SE direction and it corresponds to the greenstone belts and associated granitoids (Fig. 3a). The first vertical derivation (FVD) displays several dominant trends NE–SW and WNW–ESE to NW–SE, the belts zone was outline by NW strike lines boths (Fig. 3b). In the southestern area (Meyomessi) tight folded structures in supracrustal rock are clearly seen on color shaded relief image of FVD (Fig. 3b). The faults/fractures were traced easily along of linear

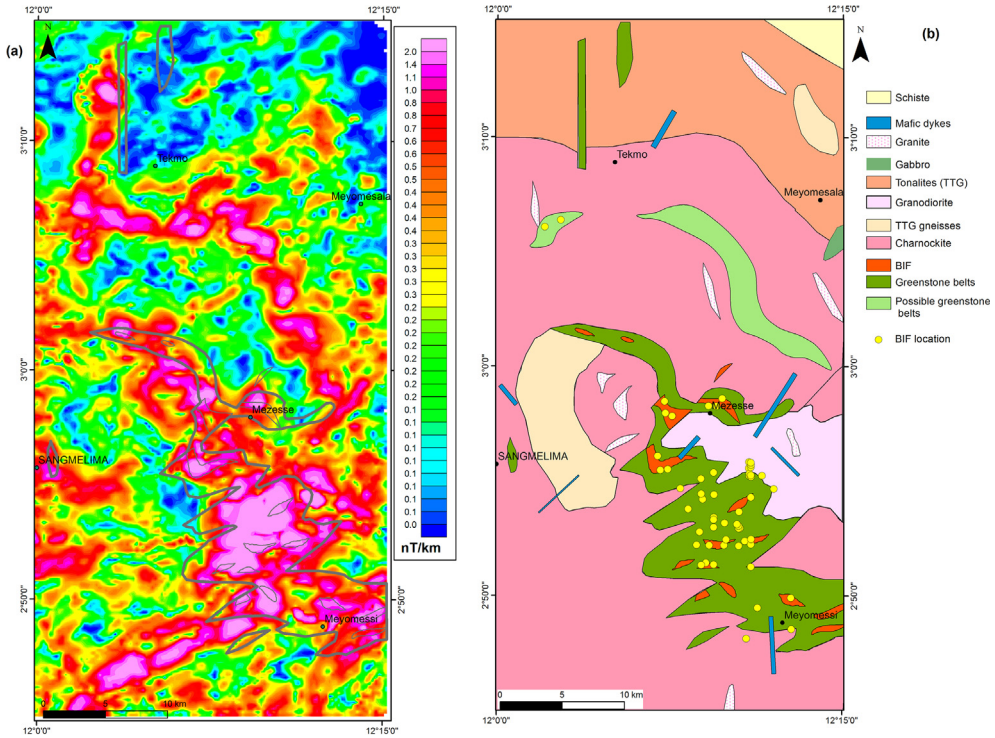

Fig. 5. (a) Greenstone belt and associated iron formation superimpose on the Analytical Signal map. (b). Lithological map, potential target for new green rock belts and iron formation.

features which are related to the trend of faults in the horizontal derivatives map (Fig. 3c). The frequency analysis of the lineaments directions showed a high frequency of NE–SW and E–W to ESE–WNW lineaments followed by the dominance of the NW–SE direction (Fig. 4a–c). The frequencies of N–S lineaments were lower (Fig. 4a–c). The south eastern region exhibited long lineaments trending NE–SW but, in general, lineament of magnetic map where shorter than lineaments extracted from remote sensing data. The maximum linear length detected was 10635 m, while the minimum length was 1045 m. These tectonic structures are comparable with those structures stated in remote sensing data.

The analytical signal can be useful in locating edges of remanently magnetized bodies in areas of low magnetic latitude. The interpretations of the analytical signal map make it possible to identify geophysical anomalies similar to the signature of small known greenstone belts. The method consists in superimposing the known greenstone belts shapefiles on the analytical signal to identify the corresponding anomalies (Fig. 5a). Subsequently, similar anomalies were identified in areas where there is no recent and detailed mapping. As an example, the banded iron formation of Mezesse shows high magnetic amplitudes (Fig. 5a). A total of 57 outcrops of Banded Iron Formation (BIF) were located, so two possible small belts or greenstone belts extensions were interpreted (Fig. 5b).

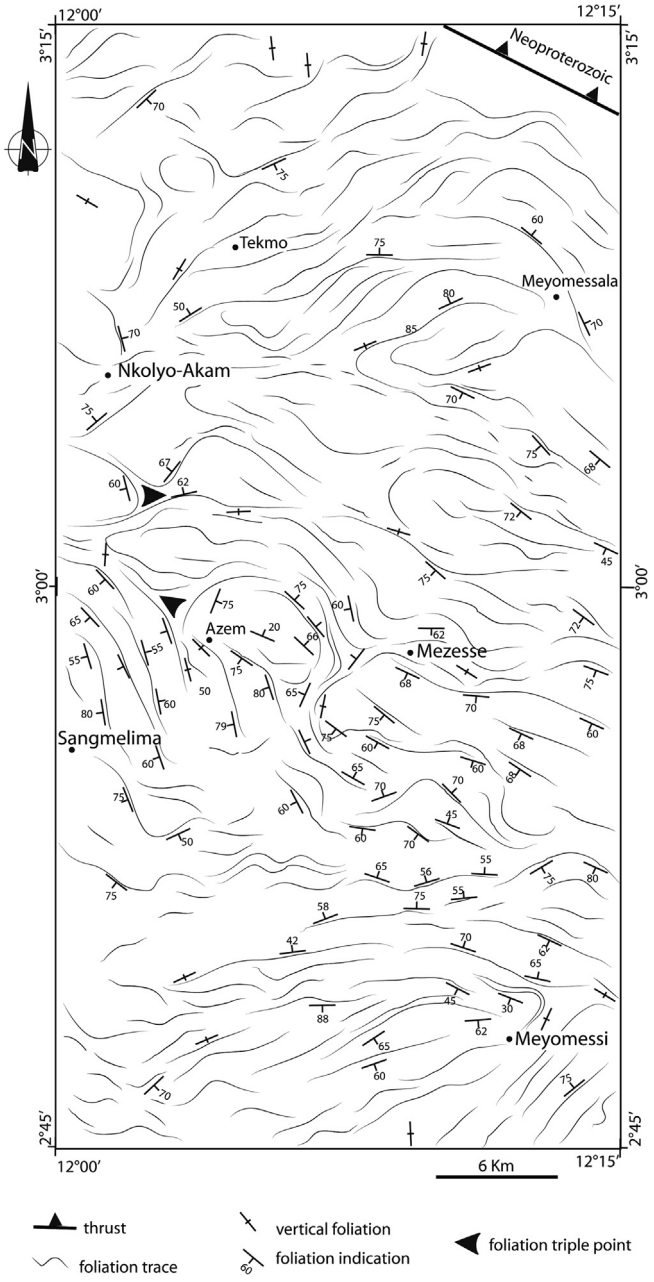

Fig. 6. Associated foliation data and interpreted foliation trajectories in the study area.

4.3. Structural analysis

The main structural features are:

The *metamorphic foliation* (S_1) is a regional structure affected by many folding episodes. Foliation trajectories have been partly drawn from the interpretation of aeromagnetic map in this study (Fig. 6). Foliation trajectories highlight several heterogeneities in the strain pattern. They appear locally folded and tend to define underline domes structures (Fig. 6). But, no conclusive evidence as to domes and basin geometries were observed. S_1 is oriented NW–SE to NNW–SSE or N–S and sometimes E–W; it dips 30° to 70° west (Figs. 6 and 7). Vertical foliations are observed all over the study area. The S_1 planes displayed stretching or mineral *linéations* (L_1), maked by ferromagnesian minerals (biotite, orthopyroxene) and elongation of clasts (quartz, feldspath). Centimetre to metre-scale shear bands are observed in association with the granulitic foliation, but they bear a very variable sense of shear, with both strike-slip components.

Shear zones are frequent in the Sangmelima area. In plane view, N160°−175°E and N05°−25°E striking ductile shear bands (C_2) show components of dextral and sinistral strike slip, respectively (Fig. 8a). They are compatible with a N85°E strike of shortening. Locally, a normal sense of shear is observed but in general no shear bands are recorded. The C_2 shears zones are generally associated with the development of mylonitic foliation and F_2 synmetamorphic folds that display oblique axes (Fig. 8a).

Brittle shear zones C_3 are observed at all scales throughout the belt (Fig. 4 and Fig. 8b and c). At the regional scale, the N40°–N60° structures are clearly outlined by aerial photographs. Locally, C_3 shears are N40°–N60°, N20°−30°, N70°–N80°oriented sinistral strike-slips and associated with some conjugated dextral shear bands (Fig. 9c and d). N20°–N30° and N40–N60° oriented shear bands (C_3) are the most common structures. They indicate sinistral movements. The geometrical of C_3 shear zone of the D_3 deformation compatible with a Riedel system in a wide NE–SW channel setting affected by sinistral movements (Fig. 9c). Therefore, NNE–SSW and ENE–WSW sinistral shear zones correspond to the R and P, respectively. R' is represented by NNW–SSE dextral shear zones.

Abundant faults and fractures were found throughout the study area (Fig. 8d). They display variable strikes from N040−070°E to N120−160°E with sub-vertical dip and low pitch striations oscillating between 10 and 40° (Fig. 10). Faults show occasionally an antagonist movement, being either sinistral or dextral along a similar direction and may correspond to C_3 NNE–SSW and NE–SW sinistral shear bands reactivations, with dextral movements. The intensity of the dextral shear is lower than the sinistral one. The Fig. 10 present the statistical analysis of shear bands using the right-dihedra method (Angelier and Mechler, 1979). The orientation of the deformation's maximal main stress (6_1) is 03°N187, the intermediary (6_2) and the minimal (6_3) stresses are oriented 87°N017 and 01°N087.2, respectively. The reconstitution of these stress axes suggests that the strike-slip component may dominate

at the scale of the study area (R = 0.50, Fig. 10). This horizontal shortening correlates the N–S sinistral transpression that caused the C_3 synthetic sinistral ENE–WSW, NNE–SSW and C_3 antithetic dextral NNW–SSE strike-slips of a main NE–SW shear zone (Fig. 9a).

5. Discussion

Geological structures and lineaments were delineated from satellite imagery and aeromagnetic studies. The regional litho-structural architecture of Sangmelima region was updated based on the use of remote sensing data. Lithological boundaries recognized from image interpretations were supported by available geological maps and field observation datasets. A geodynamic model was built which incorporated the integrated approach, fault-system geometry, and the relative structural kinetics. The NE–SW, NW–SE, N–S and E–W are the main revealed from remote sensing processing; while the NE–SW, E–W to ESE–WNW, NW–SE and N–S are the dominant structural trends revealed from aeromagnetic data (Fig. 4). The structural grain is defined by S_1 regional foliation, F_2 folds, shear zones, brittle bands and Fault/fractures. D_1 is recorded by a sub-vertical penetrative S_1 foliation bearing stee-

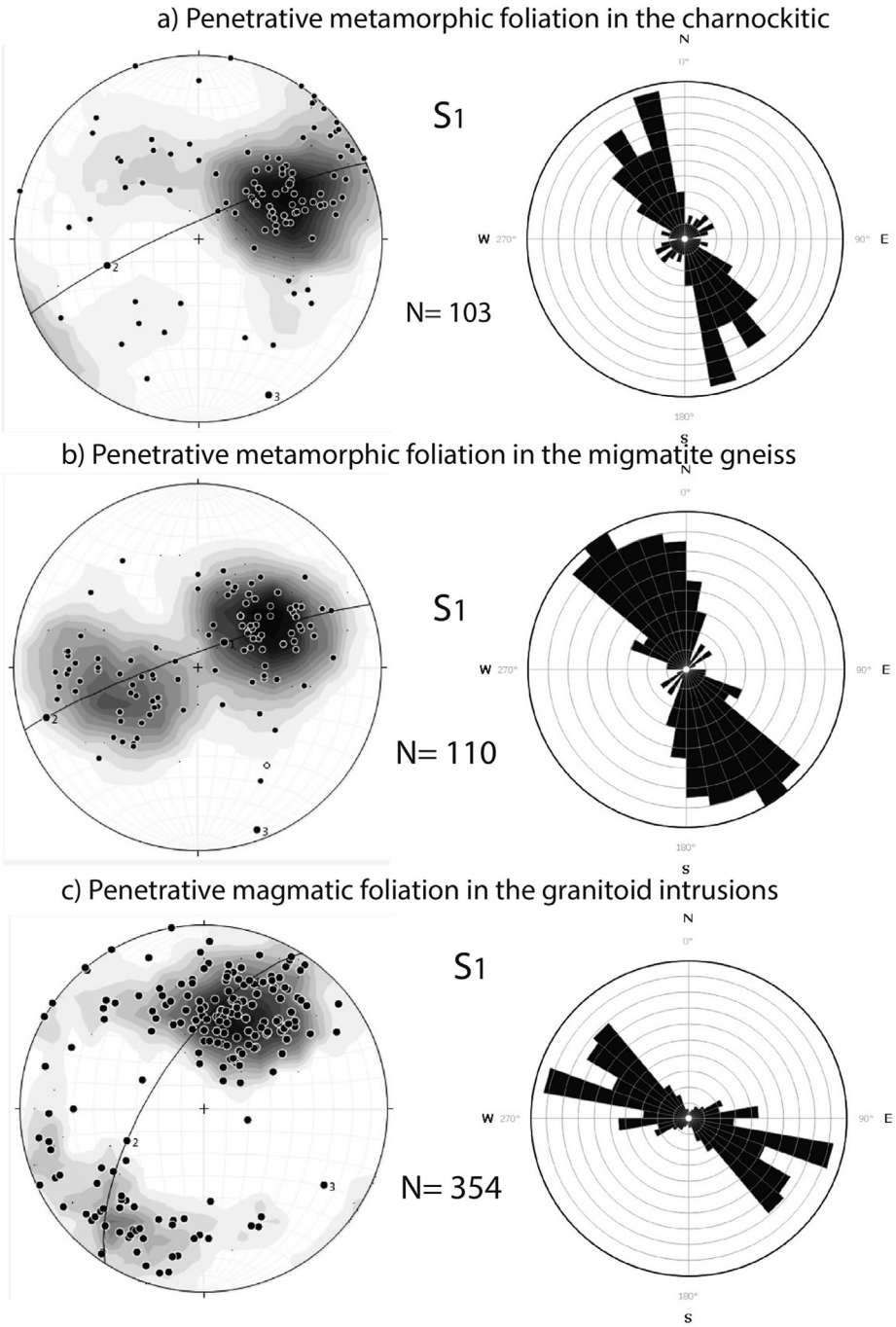

Fig. 7. Equal area lower hemisphere stereoplots showing distribution of foliation poles. Rose diagrams show the distribution of the foliation strikes in the study area.

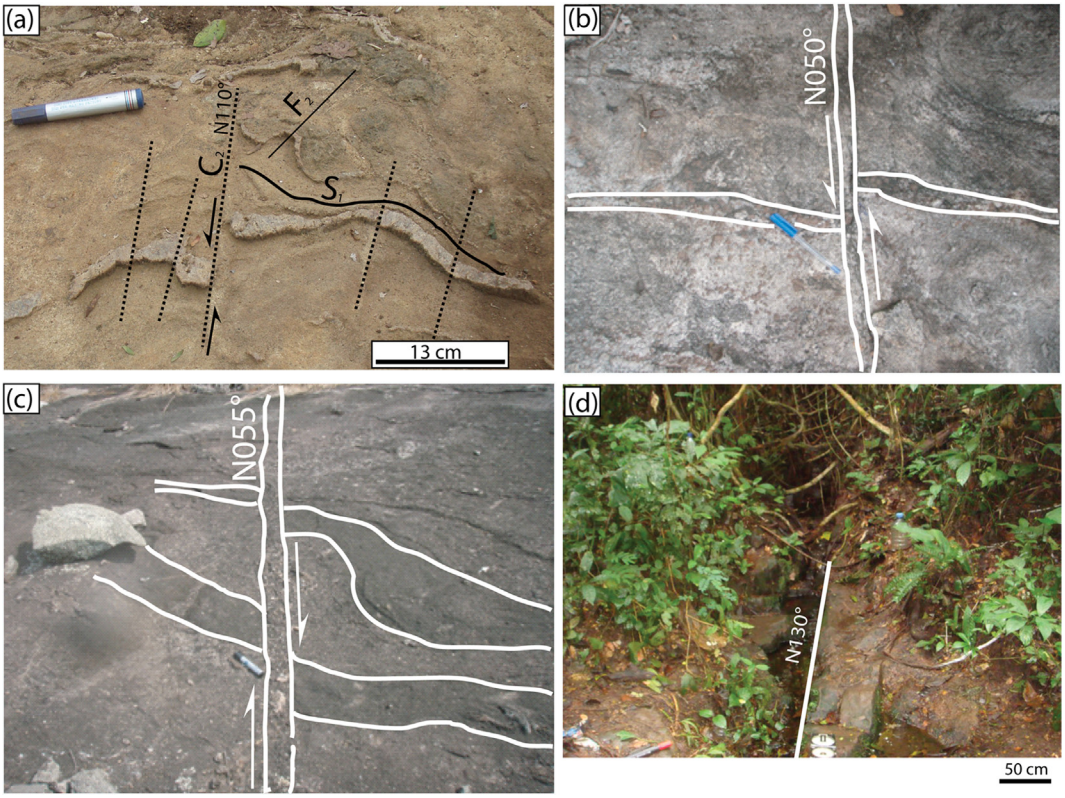

Fig. 8. Field photographs of representative structures**. (a)** Relations between penetrative metamorphic foliation S_1, subvertical NNW-trending shear zone C_2 and F_2 folds in charnockites. **(b)** and **(c)** C_3 Shear zones NE–SW antagonists to motion. (d) Fracture network.

ply plunging stretching lineations (L_1). Kinematics associated with the D_1 events is difficult to assess. However, the distribution of greenstone belts in the lower part of Fig. 5b is characterized by a linear pattern clearly reflects horizontal shortening, similar to other Archean cratons such as North China Craton (Kusky et al., 2016 and references therein), Slave craton of Canada (Card, 1990; Gapais et al., 2005; Bleeker and Hall, 2007; Helmstaedt, 2009; Gerya, 2014 and references therein; Mvondo et al., 2017) and Barberton Greenstone Belt of South Africa (Furnes et al., 2013 and references). D_2 overprints D_1 structures with tight-to-isoclinal folds with associated foliation, N160°−175°E and N05°−25°E ductile shear zones, indicating ENE–WSW shortening. Therefore, we suggest that D1 and D2 should be grouped in a single progressive deformation even. On the other hand, deformation–metamorph ism relationships indicate that all ductile structures, from earliest S_1 foliation to mylonitic foliations in C_2 shear zones, are coeval with migmatisation.

A well-constrained overprinting relationship was observed between the D_2-D_3 shear zones both in the field and in remote sensing/aeromagnetic data. In the Sangmelima belt, many small scales shear zones C_3 cross-cut S_1 foliation and F_2 folds. Most of these shear zones show sinistral displacements and are interpreted to have formed in response to a later phase of deformation that we identify as D_3. Therefore D_3 is attributed to late strike slip shearing affected the Ntem Complex. At the regional scale, satellite, magnetic images and fields observation show at least two syn-D_3 shear zone generations. The first one is oriented N035−65°E lineaments and the kinematic interpretation of brittle shear measured in the area suggest that the tectonic lineaments are controlled by a system of strike-slip faults, more precisely by a system of Riedel shear fractures (Fig. 9 and Fig. 11). This Riedel model show that the principal horizontal stress ($\sigma 1$) is oriented at N–S, and the minimum horizontal stress ($\sigma 3$) is oriented at N085°. N00° E < T < N10°E where T is the direction of tensional fractures. Many of them are intruded by mafic dykes in the study area (Fig. 5b). P and P', have orientations of ∼60−65° and ∼110°, whit an with an extension direction E in E–S. These three directions were also identified by Maurizot et al. (1986) at a regional scale. R and R', which are sets of synthetic and antithetic shear fractures, are oriented at N20−25° and 150°−155°, respectively.

The second is oriented N–S and cross-cuts earlier N045°E shears and the D_3 thrusts within the Nyong Complex (e.g Maurizot et al., 1986; Feybesse et al., 1987; Owona et al., 2011, 2012). This lineament system extends to the southwest of study area, through the Kribi peneplain to the Atlantic coast.

The D_3 strike slip shearing is likely the result of the Eburnean deformation phase (Fig. 11). Our D_3 therefore corresponds to D_2 of Maurizot et al. (1986), Feybesse et al. (1998), Owona et al. (2011). The mafic dykes are striking NE–SW, N–S and NWSE, and field evidence and airborne magnetic data suggest that some of them intrude preexisting structures. The faults/fractures are clearly visible in remote sensing/geophysical data from the Sangmelima belt (Figs. 4 and 11) and we attribute them to the D_4 deformation event. Nevertheless, some of these faults/fractures might have originated during previous deformation phases and they were only reactivated during the D_4.

6. Conclusion

This paper presents the results of a integration of remote sensing, aeromagnetic and field data for mapping structural

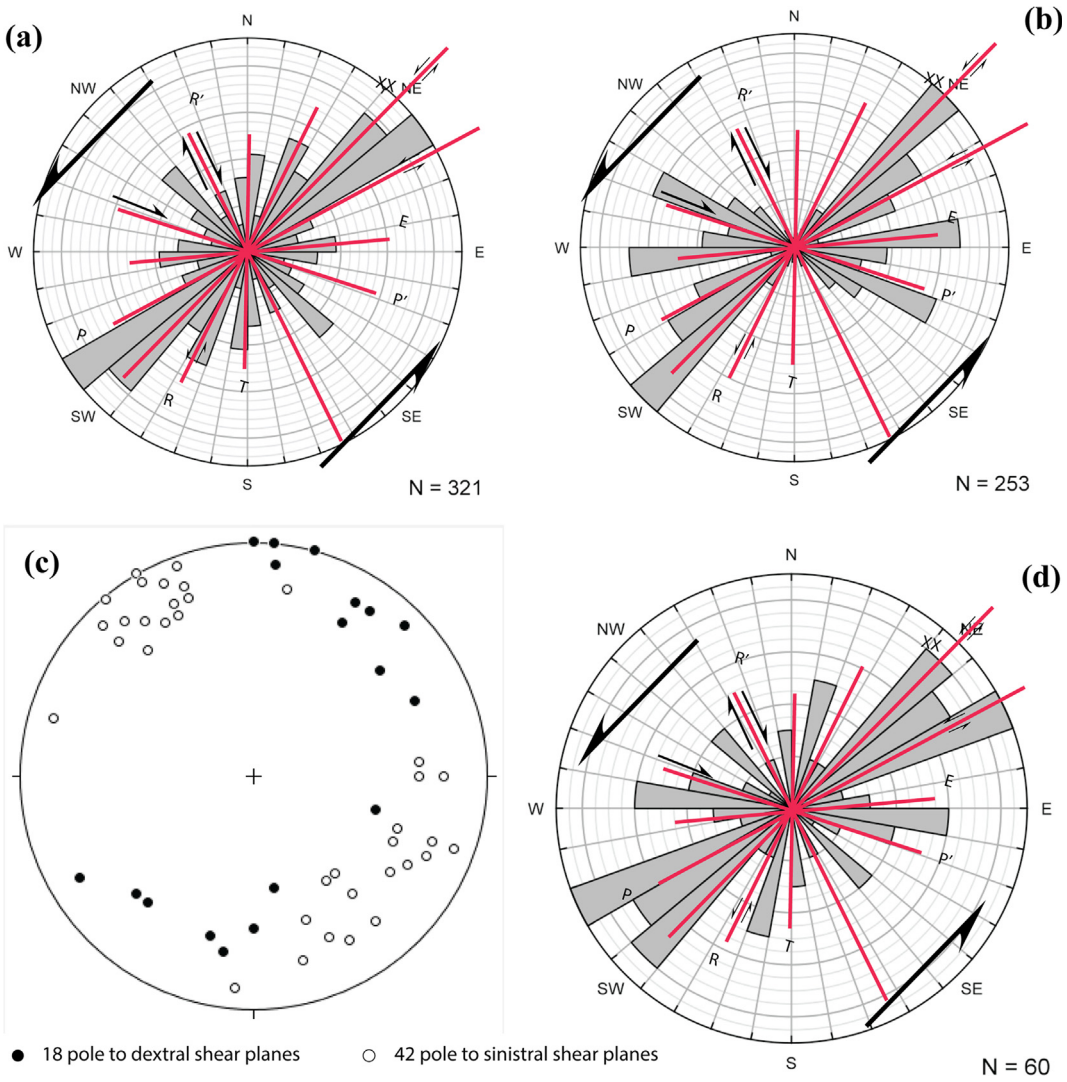

Fig. 9. Schematic Riedel model using a sinistral simple shear associated with rose diagrams.

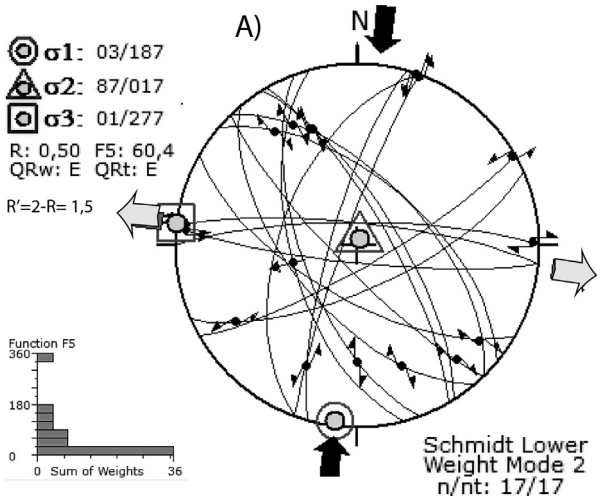

Fig. 10. Stereograms(Equal area, lower hemisphere) showing the fault shear population measured for this study and calculated principal axes for all shear bands (axes 1, 2, and 3).

features and update lithological map in Sangmelima area, South Cameroon. Analytical signal, vertical and horizontal derivatives of total field magnetic also helped in mapping new possible greenstone belts and structural features. Many of the identified lineaments are interpreted to represent fracture/fault zones, some of strike-slip faults. We distinguish three deformation events within the Sangmelima area: D_1 is recorded by a sub-vertical penetrative S_1 foliation bearing steeply plunging stretching lineations. No conclusive evidence as to domes and basin geometries were observed. D_2 overprints D_1 structures with tight-to-isoclinal folds with associated foliation, N160°–175°E and N05°–25°E ductile shear zones, indicating ENE–WSW shortening. According to field data and structural analysis, we suggest that D_1 and D_2 should be grouped in a single progressive deformation even. The D_3 strike slip shearing is likely the result of the Eburnean deformation phase. The mafic dykes are striking NE–SW, N–S and NWSE, and field evidence and airborne magnetic data suggest that some of them intrude preexisting structures. Many faults/fractures might have originated during previous deformation phases and they were only reactivated during the pan-African events.

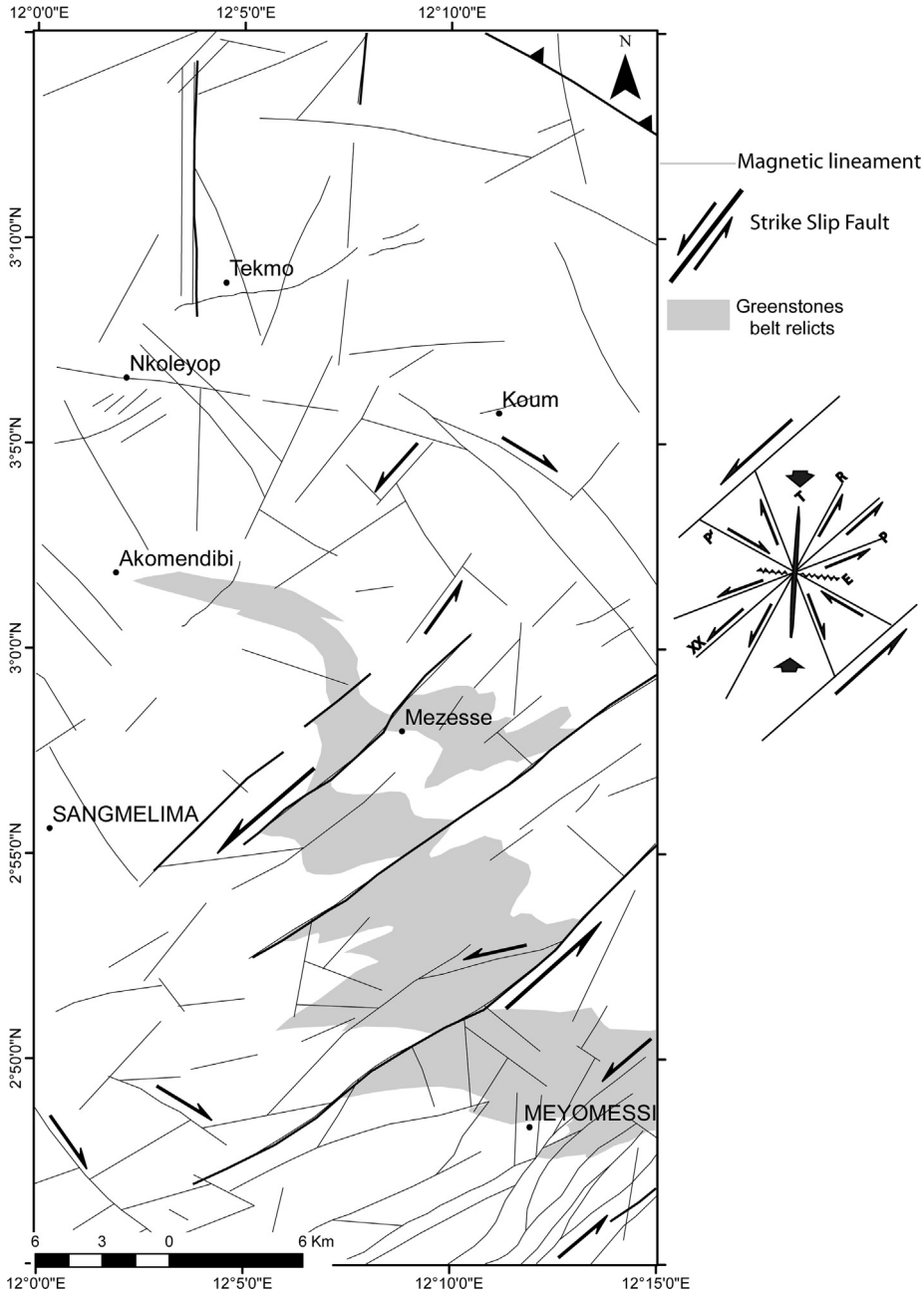

Fig. 11. Tectonic map of the Sangmelima and fractures associated with the Riedel model, showing the relationship between the orientation of the main compressional strain axis and the direction of shearing.

Conflict of interest

None.

Acknowledgements

We thank the anonymous reviewer for kindly contacting us for any data need.

Appendix A. Supplementary data

Supplementary data to this article can be found online at https://doi.org/10.1016/j.ejrs.2018.11.005. These data include Google maps of the most important areas described in this article.

References

Aitken, A.R.A., Betts, P.G., 2009. Constraints on the Proterozoic supercontinent cycle from the structural evolution of the south-central Musgrave Province, central Australia. Precambrian Res. 168, 284–300.

Akame, J.M., Mvondo Ondoa, J., William, Assatse Teikeu, Owona, S., Olinga, J. B., Ottou, E., Messi, J., Ntomba, S.M., 2014. Apport des images Landsat-7 ETM+ a l'étude structurale du socle archéen de Sangmélima (Sud Cameroun). Revue Française de Photogrammétrie et de Télédétection 206, 15–26.

Angelier, J., Mechler, P., 1979. Sur une méthode graphique de recherche des contraintes principales également utilisable en tectonique et en sismologie: La méthode des dièdres droits. Bull. Soc. Geol. Fr. 7, 597–608.

Betts, P.G., Valenta, R.K., Finlay, J., 2003. Evolution of the Mount Woods inlier, northern Gawler Craton, Southern Australia: an integrated structural and aeromagnetic analysis. Tectonophysics 366, 83–111.

Bleeker, W., Hall, B., 2007. The Slave Craton: Geology and metallogenic evolution. In: Goodfellow, W.D. (Ed.), Mineral Deposits of Canada: A Synthesis of Major

Deposit-Types, District Metallogeny, The Evolution of Geological Provinces, and Exploration Methods. Geological 731 Association of Canada, Mineral Deposits Division. Special Publication, pp. 849–879.

Block, S., Moyen, J.F., Zeh, A., Poujold, M., Jaguin, J., Paquette, J.L., 2012. The Murchison Greenstone Belt, South Africa: accreted slivers with contrasting metamorphic conditions. Precambrian Res. 2012. https://doi.org/10.1016/j.precamres.2012.03.005.

Caen-Vachette, M., Vialette, Y., Bassot, J.P., Vidal, P., 1988. Apport de la géochronologie à la connaissance de la géologie gabonaise. Chron. Rech. Min. 491, 35–54.

Card, K.D., 1990. A review of the Superior Province of the Canadian Shield, a product of Archean accretion. Precambrian Res. 48, 99–156.

Chombong, N.N., Suh, C.E., 2013. 2883 Ma commencement of BIF deposition at thenorthern edge of Congo craton, southern Cameroon: new zircon SHRIMP dataconstraint from metavolcanics. Episodes 36, 47–57.

Dabo, Moussa, Aïfa, Tahar, 2013. **A**rchitecture tectonique des formations paleoproterozoïques de la Dalema (Senegal Oriental): apport des lineaments d'images landsat-7 etm+/srtm et aeromagnetique. J. Sci. 13 (1).

Direen, N.G., Cadd, A.G., Lyons, P., Teasdale, J.P., 2005. Architecture of Proterozoic shear zones in the Christie Domain, western Gawler Craton, Australia: geophysical appraisal of a poorly exposed orogenic terrane. Precambrian Res. 142, 28–44.

Eldosouky, A.M., Abdelkareem, M., Sayed, O., Elkhatee, S.O., 2017. Integration of remote sensing and aeromagnetic data for mapping structural features and hydrothermal alteration zones in Wadi Allaqi area, South Eastern Desert of Egypt. J. Afr. Earth Sci. 130, 28–37. https://doi.org/10.1016/j.jafrearsci.2017.03.006.

Feybesse, J.L., Johan, V., Maurizot, P., Abessolo, A., 1987. Evolution tectonométamorphique libérienne et éburnéenne de la de la partie NW du craton zaïrois (SW Cameroun). In: Matheis, J., Schandelmeier, G. (Eds.), Current Research in African Earth Sciences. Balkema, Rotterdam, pp. 9–12.

Feybesse, J.L., Johan, V., Triboulet, C., Guerrot, C., Mayaga-Minkolo, F., Bouchot, V., Eko N'dong, J., 1998. The West Central African belt: a model of 2.5-2.0 Ma accretion and two-phase orogenic evolution. Precamb. Res. 87, 161–216.

Furnes, H., de Wit, M.J., Robins, B., 2013. A review of new interpretations of the tectonostratigraphy, geochemistry and evolution of the Onverwacht Suite, Barberton Greenstone Belt, South Africa. Gondwana Res. 23, 403–428.

Gapais, D., Potrel, A., Machado, N., 2005. Kinematics of long-lasting Paleoproterozoic transpression within the Thompson Nickel Belt, Manitoba, Canada. Tectonics 24. https://doi.org/10.1029/2004TC001700.

Gerya, T., 2014. Precambrian geodynamics: concepts and models. Gondwana Res. 24, 442–463.

Helmstaedt, H., 2009. Crust-mantle coupling revisited: The Archean Slave craton, NWT, Canada. Lithos 112 (S2), 1055–1068.

Kusky, T.M., Polat, A., Windley, B.F., Burke, K.C., Dewey, J.F., Kidd, W.S.F., Maruyama, S., Wang, J.P., Hao, D., Wang, Z.S., Wang, C., Dong, F., Li, X.W., Peng, H.T., 2016. Insights into the tectonic evolution of the North China Craton through comparative tectonic analysis: a record of outward growth of Precambrian continents. Earth-Sci. Rev. 162, 387–432.

Lasserre, M., Soba, D., 1976. Age liberien des granodiorites et des gneiss à pyroxènes du Cameroun Meridional. Bull. BRGM 2 (4), 17–32.

Maurizot, P., Feybesse, J.K., Johan, Lecomte, P., 1985. Etude et prospection minière du Sud-Ouest Cameroun, synthèse des travaux de 1978 à 1985. Rapport du Bureau de Recherche géologique et minière 85, 274. CMR066.

Václav Metelka, 2011. Application des méthodes de géophysique et de télédétection à l'analyse du régolithe et de la géologie du Burkina Faso, Afrique de l'Ouest. (Thèse de doctorat). l'Université Toulouse III - Paul Sabatier, 230P. tel-00670786, version 1 - 17 Feb 2012.

Milligan, P.R., Gunn, P.J., 1997. Enhancement and presentation of airborne geophysical data. AGSO J. Aust. Geol. Geophys. 17, 63–75.

Mvondo, H., Lentz, D., Bardoux, M., 2017. Crustal shortening and thickening in Neoarchean granite-greenstone belts: a case study from the link between the ~2.7 Ga Elu and Hope Bay belts, northeast Slave craton, Canada. J. Struct. Geol. 2017. https://doi.org/10.1016/ j.jsg.2017.10.004.

Nsifa, E.N., Riou, R., 1990. Post Archean migmatization in the charnockitic series of the Ntem complex, Congo craton, Southern Cameroon. 15th colloquium on African Geology. Publications Occasionnelle, CIFEG, pp. 33–36.

Owona, S., Mvondo Ondoa, J., Ratschbacher, L., Mbola Ndzana, S.P., Tchoua, M.F., Ekodeck, G.E., 2011. The geometry of the Archean, Paleo- and Neoproterozoic tectonics in the Southwest Cameroon. Compte. Rendus de Geosci. 343, 312–322.

Owona, S., Ndzana Mbola, S.P., Mvondo Ondoa, J., Nsangou Ngapna, Moussa, Nkabsaah, C., Ratschbacher, L., Ekodeck, G.E., 2012. Geological control of geomorphologic units in the Southwest (SW) Cameroon (Central Africa). J. Geol. Mining Res. 4 (7), 152–167.

Paterson, G., Watson Ltd., 1976. Etudes aeromagnetiques sur certaines Régions de la République Unie du Cameroun. ACDI, Toronto, Canada. 190.

Peschler, A.P., Benn, K., Roest, W.R., 2006. Gold-bearing fault zones related to Late Archean orogenic folding of upper and middle crust in the Abitibi granite-greenstone belt, Ontario. Precambrian Res. 151, 143–159.

Pilkington, M., Keating, P.B., 2009. The utility of potential field enhancements for remote predictive mapping. Can. J. Remote Sens. 35 (Suppl. 1), S1–S11.

Pouclet, A., Tchameni, R., Mezger, K., Vidal, M., Nsifa, N.E., Penaye, P., 2007. Archaeancrustal accretion at the northern border of the Congo Craton (South Cameroon). The charnockite-TTG link. Bull. Soc. Geol. Fr. 178, 3–14.

Shang, C.K., 2001 Unpublished Ph.D. Thesis. In: Geology, Geochemistry and Geochronology of Archaean Rocks from the Sangmelima Region, Ntem complex, NW Congo craton, South Cameroon. University of Tubingen, Germany, p. 313.

Shang C.K, Liégeois J.P, Satir M, Frisch W, Nsifa E.N., 2010. Late Archaean high-K granite geochronology of the northern metacratonic margin of the Archaean Congo craton, Southern Cameroon: Evidence for Pb-loss due to non-metamorphic causes. (article In press) Gondwana Research xxx (2010) xxx–xxx.

Shang, C., Satir, M., Siebel, W., Nsifa, E.N., Taubald, H., Liegeois, J.P., Tchoua, F.M., 2004a. TTG magmatism in the Congo Craton; a view of major and trace element geochemistry, Rb-Sr and Sm-Nd systematics: case of the Sangmelima region, Ntem Complex, Southern Cameroon. J. Afr. Earth Sci. 40, 61–79.

Shang, C.K., Wolfgang, S., Muharrem, S., Funken, C., Mvondo Ondoa, J., 2004b. Zircon Pb-Pb and U-Pb systematics of TTG rocks in the Congo Craton: Constraints on crust formation, magmatism, and Pan-African lead loss. Bull. Geosci. 79 (4), 205–219.

Shang, C.K., Satir, M., Nsifa, E.N., Liegeois, J.P., Siebel, W., Taubald, H., 2007. Archean high-K granitoids produced by remelting of earlier Tonalite-Trondhjemite-Graondiorite (TTG) in the Sangmelima region of the Ntem complex of the Congo craton, Southern Cameroon. Int. J. Earth Sci. (Geol Rundsch) 96, 817–841.

Stewart, J.R., Betts, P.G., 2010. Late Paleo-Mesoproterozoic plate margin deformation in the southern Gawler Craton: insights from structural and aeromagnetic analysis. Precambrian Res. 177, 55–72.

Suh, C.E., Cabral, A.R., Shemang, E.M., Mbinkar, L., Mboudou, G.G.M., 2008. Two contrasting iron deposits in the Precambrian mineral belt of Cameroon, West Africa. Explor. Min. Geol. 17, 197–207.

Takam, T., Arima, M., Kokonyangi, J., Dunkley, D.J., Nsifa, E.N., 2009. Paleoarcheancharnockite in the Ntem Comples, Congo Craton, Cameroon: in sights fromSHRIMP zircon U-Pb ages. J. Mineral. Petrol. Sci. 104, 1–11.

Tchameni, R., 1997. Géochimie et géochronologie des formations de l'archéen et du paléoprotozoïque du Sud-Cameroun (groupe du Ntem Thèse non publiée de l. Université d'Orléans, Craton du Congo), p. 335p.

Tchameni, R., Mezger, K., Nsifa, E.N., Pouclet, A., 2000. Neoarchean evolution in the Congo Craton: evidence from. K rich granitoids of the Ntem complex, Southern Cameroon. J. Earth Sci. 30 (1), 113–147.

Tchameni, R., Pouclet, A., Mezger, K., Nsifa, E.N., Vicat, J.P., 2004. Monozircon and Sm-Nd whole rock ages from the Ebolowa greenstone belts: evidence for the terranes older than 2.9 Ga in the Ntem Complex (Congo craton, South Cameroon). J. Cameroon Acad. Sci. 4, 213–224.

Teixeira, W., Oliveira, E.P., Marques, L.S., 2017. Nature and evolution of the archean crust of the São Francisco Craton. Regional Geol. Rev. https://doi.org/10.1007/978-3-319-01715-0_3.

Toteu, S.M., Van Schmus, W.R., Penaye, J., Nyobe, J.B., 1994. U-Pb and Sm–Nd evidence for Eburnean and Pan-African high grade metamorphism in cratonic rocks of southern Cameroon. Precambrian Res. 67, 321–347.

European Journal of Scientific Research
ISSN 1450-216X / 1450-202X Vol. 152 No 3 April, 2019, pp. 286-303
http://www. europeanjournalofscientificresearch.com

Contribution of Geophysics to the Understanding of the Geodynamic Activity at the Northern Margin of the Congo Craton: A Case Study from Aeromagnetic Data Interpretation Over the Metet-Zoetele Region (Southern Cameroon)

Assembe Stéphane Patrick
Corresponding Author, Postgraduate School of Science Technology and Geosciences
University of Yaounde 1 PO Box 812 Yaounde, Cameroon
Faculty of Science, University of Bamenda, PO Box 39 Bambili, Cameroon
E-mail: assembest@yahoo.fr

Ndougsa Mbarga Théophile
Postgraduate School of Science Technology and Geosciences
University of Yaounde 1 PO Box 812 Yaounde, Cameroon
Higher Teacher Training College, University of Yaounde 1
PO Box 47 Yaounde, Cameroon
E-mail: tndougsa@yahoo.fr

Meying Arsene
School of Geology and Mining Engineering, University of Ngaoundere
PO Box 115 Meiganga, Cameroon

Gouet Daniel Hervé
Faculty of Mining and Petroleum Industries
University of Maroua, PO Box Kaele, Cameroon

Ngoh Jean Daniel
Postgraduate School of Science Technology and Geosciences
University of Yaounde 1 PO Box 812 Yaounde, Cameroon

Mono Jean Aime
Basical Science Department, Advanced Technical Teacher Training School
University of Douala, Cameroon

Abstract

The qualitative and quantitative geophysical investigations involving image enhancement, multiscale edge analysis, Euler's deconvolution and 23/4 D inverse modelling are applied to aeromagnetic data over the Metet-Zoetele area (southern Cameroon), a portion of the Congo Craton (CC)/North Equatorial Fold Belt (NEFB) transition zone. The study investigates the geodynamic evolution of the northern margin of the CC through the detection of lineaments. The geology of the area is made up of the NEFB and the CC both affected by multi-stage tectonics summarised in to alternating compressions and extensions. The analyses highlight a broad NE-SW high amplitudes channel which presumes the dominance of a NE structural direction in the area. The study

differentiated the CC from NEFB by outlining a subvertical boundary at N03º20'; WNW-ESE, W-E, NW-SE, SW-NE and WSW-ENE vertical to sub-vertical lineaments defining shear zones affecting both the CC and the NEFB. These lineaments are interpreted as pre-Neoproterozoic events which experienced syn- to -late and post-Neoproterozoic reactivations. The post-Neoproterozoic events are coeval to, or postdate the Central Cameroon Shear Zone. Therefore, the WSW-ENE to SW-NE fractures form dextral strike-slips corresponding to wrenches related to a SW-NE shear zone overprinted by sinistral NW-SE to WNW-ESE displacements inferring neo-tectonic activity in the CC/NEFB transition zone as a consequence of the on-going movements that affect the African Plate.

Keywords: Aeromagnetic data; Congo Craton; strike-slips; wrenches; neo-tectonic activity

Introduction

Understanding the geological evolution of the transition zone between the North Equatorial Fold Belt (NEFB) in Central Africa and the Congo Craton (CC) remains a great challenge for geoscience researchers despite the recent advances. For example, the geodynamic setting remains discussed although some unifying points exist (Toteu *et al* 2006; Mvondo *et al* 2007; 2009; Ngako and Njonfang 2011; Ngnotue *et al* 2012). One of the major limitations comes from the limited aerial extend of the studied areas from which inferences are made on the regional scale and the limited use of geophysical methods, e.g. airborne magnetic surveying.

Aeromagnetics within few decades, has gained a strong reputation in mapping buried structures and lithology irrespective of the terrain conditions and availability of outcrops (Paterson and Reeves 1985; Nabighian *et al* 2005; Boyd and Isles 2007; Fairhead *et al* 2017), as it is the case for the study area where the vegetation is thick and outcrops scarce. The method has permitted to update the geology of some areas of the Cameroon (Feumoe *et al* 2012; Ndougsa-Mbarga *et al* 2012; Yandjimain *et al* 2017), involving either the NEFB and/or the CC setting. Most of these studies used traditional derivative-based filters (edge detectors) which have proven their efficiency in mapping lineaments, though they are limited to qualitative analyses and accentuate noise [13]. Some edge detectors like the tilt-angle method additionally evaluate the depth-to-the-source but it is limited to shallow subsurface sources; this depth limitation is mitigated by the Euler deconvolution method (Reid *et al* 1990) which provides full location of the source. The need to get maximum geological information from magnetic data has seen the emergence of more robust interpretation approaches involving the combination of edge detectors and depth-to-basement calculations. In order to get updated insights on the geology of the NEFB/CC transition zone, we apply both modern edge detection filters, depth-to basement and inverse modelling methods to aeromagnetic data collected in the Metet-Zoetele region (Southern Cameroon) in a region whose lithology is dominated by Neoproterozoic and Archaean terrains.

Geological Setting

Neoproterozoic Formations and Related Tectonics

The Neoproterozoic terrains in Cameroon corresponds belong to the NEFB herein represented north to south respectively, by the Yaounde and Mbalmayo series (figure 1). *(i)* The Yaounde series is mainly represented by foliated garnetiferous micaschists, high pressure granulitic metasediments made up of quartz, biotite, muscovite and garnets, with various feldspars (Toteu *et al* 2004; Nkoumbou *et al* 2014; references therein). *(ii)* The Mbalmayo Series, made up of schists and quartz-sericite formations with

some volcanic relics, is the southernmost member of the NEFB laying discordantly onto the CC (Toteu *et al*. 2006, *references therein*).

Figure 1: Local geology map (Maurizot *et al* 1986; Ngako and Njongfang 2011, modified)

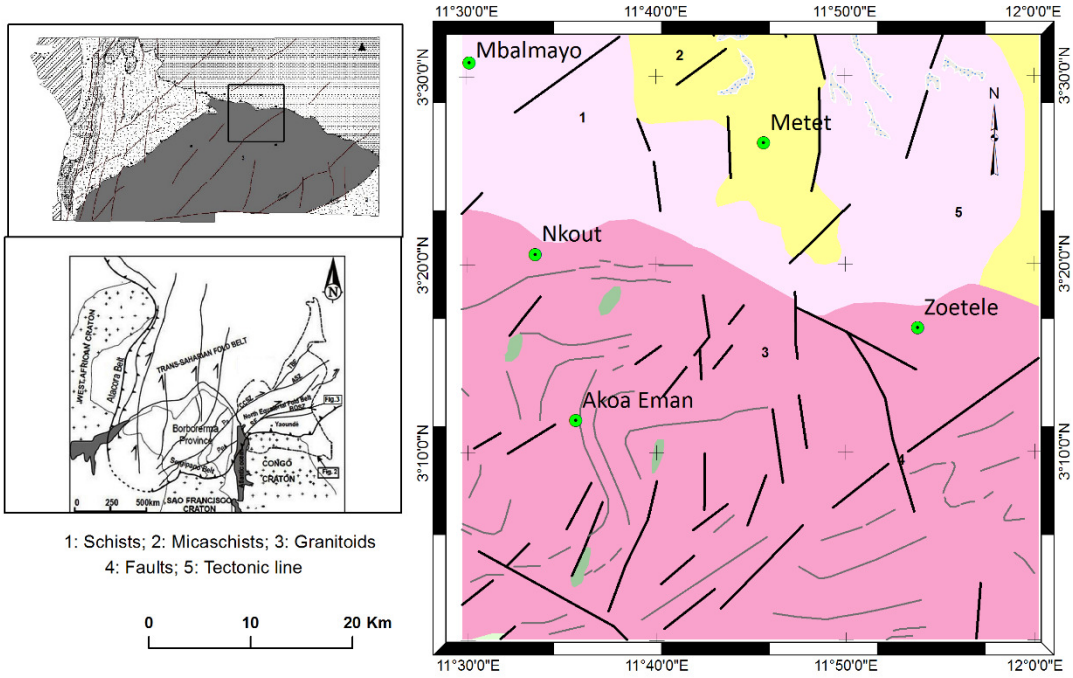

Tectonics in the Yaounde Group corresponds to four deformation stages D1 to D4 exhibited by outcropping metamorphic rocks surrounding Yaounde (Toteu *et al* 2004; 2006; Mvondo *et al* 2007; Mvondo Ondoa *et al* 2009). The D1 event, prior to the calc-alkaline diorites mineralization, is responsible of the nappe formation that led to the granulites facies metamorphism of soft sediments. A great reprint of these nappes during symmetrical extend D2 is probably associated to large scale foliation boudinage and (or) gneissic domes formation along with intensive sub-superficial magmatic deposits. This reprint generated flat regional textures. These formations have been upraised again by unclassified D3 and D4 folding, defining a vertical constriction which occurred with an E-W to NW-SE major narrowing, in the same trend as that of the D1 stage of thrust nappes piling (Olinga *et al* 2010; Mbola-Ndzana *et al* 2014; and references).

The Archaean (Congo Craton) Group and Related Tectonics

The Archaean group referred to as the Ntem complex in Cameroon (Shang *et al* 2007, and references), corresponds to Archaean to Mesoproterozoic terrains dominating the southern part of the study area (figure 1). The Ntem complex is mainly formed by Tonalite-Tronghemite-Granodiorite (TTG) and K-rich granitoids [23]. The tonalites (Soo granites), essentially exposed to the north, is strongly mylonitized and retrogressed along the fault boundary with the NEFB, while granodiorite massifs form distinct bodies within the dominantly charnockitic southern zone (Shang *et al* 2010). Late- to post-tectonic granitoids and syenites with calc-alkaline to alkaline affinity intrude the TTG and clearly postdate the major crust forming episode. This magmatic activity in the Ntem unit ends with post-Archean doleritic dykes affected by Eburnean high-grade metamorphism (Tchameni *et al* 2001, 2010; Shang *et al* 2010).

According to Takam *et al* (2009), the tectonic events in the CC start in the Archaean by the Liberian orogeny related to the development of greenstone belts and late diapiric intrusions of

charnockitic TTG plus late anatexite K-granitoids which was accompanied by high to low-grade metamorphism, associated to a D1-M1 syn-metamorphic deformation characterised by E-W sub-vertical foliation and structures. The Paleo-Proterozoic evolution is dominated by the Eburnean orogeny, a collision between the Sao-Francisco and the Congo Cratons identified by alkaline syenites and dolerites, with a prevalent D2-M2 deformation associated to a prograde metamorphism from amphibolite to granulite facies. Many studies (Toteu *et al* 1994; Akame *et al* 2013; Loose and Schenk 2018) suggest that the deformations witnessed the development of NNE-SSW lineaments (including dextral or sinistral shear zones) NW of the CC which were reactivated during a very diffuse Panafrican episode marked by dolerites (~1000 Ma) and nepheline syenites (~570 Ma) intrusions along with a low grade metamorphism.

Material and Methods

Materials and Data Preparation

The study used the only available data covering the area, acquired under the Cameroon/Canada cooperation. This data has been collected in 1970s with a 0.5 nT sensitive magnetometer, along N-S flight lines with a line spacing of 750 m for a constant fly height of 235 m, monitored by a radar altimeter at ±20 m accuracy. The data were processed by Paterson, Grant and Watson Ltd and delivered as 1/50,000 scaled total intensity contour maps availed to us in a pdf format by the Ministry of Mines (Cameroon). These maps have been georeferenced and digitised using ArcGIS 10.4.1 software. Then, the resulting database was further gridded using a squared 250 m cell to produce the total magnetic field intensity (TMI) anomaly map. The cell size was chosen in accordance with Reeves (2005) and (Hinze *et al* 2013) to avoid noisy cross-track ringing effects. For inversion and geological modelling, three 52 km length S-N parallel profiles have been digitised on the filtered RTE map. Interpolation, processing/filtering and modelling (with GMSYS) were done in Oasis Montaj 8.4 platform.

Methods

The Reduction to the Magnetic Equator, Noise Filtering and RTE Image Enhancement

The reduction to magnetic equator (RTE) transform is applied to the TMI anomaly data. It is an equivalence to the reduction to the poles, which enables to shift the magnetic anomalies above their causative sources in low latitudes areas (Reeves 2005; Hinze *et al* 2013). The operation was conducted considering average values of the inclination -6.2° and declination -18.2° of the geomagnetic magnetic reference field model pertaining when the data were collected, i.e. January 1970 (figure 2).

The RTE map was upward continued to 125 m (comprised between half the flight height -235 m- and the sixth of the lines spacing - 750 m) to suppress noise, often related to high frequency signals in grids (Nabighian *et al* 2005; Reeves 2005; Hinze *et al* 2013). The colour shaded image of RTE draped on a shaded relief image of the digital elevation (figure 3) yielded an enhanced image which favoured the direct detection of regional structures (lineaments) of crustal origin.

The Multiscale Edge Detection

The multiscale analysis (Archibald *et al* 1999) is a processing technique involving the combination of the upward continuation of magnetic field data at several heights and the detection the peaks (Blakely and Simpson, 1986) of their respective horizontal gradient magnitude grids. This modern approach enables to infer the 3D geometry of deep structures. Its main constitutive filters are hereafter described:

The Upward Continuation (UC) Filter

The UC transforms a potential field from a surface it was measured to a field that would had be measured to another surface farther from all sources. It is a low-pass filter which enables to outline deep regional geological sources and basement structural patterns (Reeves *et al* 1997).

The Horizontal Gradient Magnitude (HGM) Filter

The HGM filter uses the two first-order horizontal derivatives of the field to estimate contact locations of bodies at depths; its biggest advantage is its low sensitivity to noise in the data [13,32]. The multiscale analysis map over Metet-Zoetele is obtained overlaying the HGM peaks UC field at respectively, 1, 2, 3 and 4 km.

The 3D Euler Deconvolution Method

The 3D Euler deconvolution (Reid *et al.* 1990, *references therein*) method, applied to gridded data, is based on Euler's homogeneous functions and uses first-order x, y and z derivatives to determine location and depth targets, assuming an a priori information (known as structural index, N, theoretically 0 for contact and fault structures). Applications to field data have enabled to solve geological problems in Cameroon and other settings worldwide (Owona-Angue *et al* 2016; Yandjimain *et al* 2018; references therein). We applied the 3D Euler method using a 9 x9 window, a depth tolerance of 5 % and a structural index (SI) of 0.5 to avoid noisy solutions.

Geophysical Inversion ($2^{3/4}$ Modelling)

The modelling consists in designing and calculating the response of a theoretical model using the GMSYS program on Oasis montaj 8.5. Local known geology is used to constraint models as and we use assumed that both various supra-basement and intrabasement sources caused the observed anomalies; the final models were chosen for RMS error less than 7 % (Prieto 1996).

Results and Discussion

Results

Analysis of Reduced to the Magnetic Equator (RTE) Map

The signal on the RTE map (figure 2) spans from -676 nT to 276 nT, with two clearly outlined main areas. The first area is a small portion located south of Zoetele with a very low magnetic background (down to -676 nT) jagged by nearly E-W very high intensity elongated anomalies corresponding to very high susceptibility materials, probably related to basic to ultramafic intruded rocks, or greenstones relics within charnockites (e.g. dolerites, gabbros or granites) of the CC. The second area forms a NE-SW channel of very high intensity anomalies (peaking at 276 nT) between Abang and Zoetele; with three main blocks of probable old mafic/ultramafic or basic materials intruding the tonalities, as seen at Nkout, Zoetele, and around Metet; and underlying or intruding the Mbalmayo schists west of Metet. By assuming its south continuation between Abang and Nkout, we infer that those materials intruded the Paleoproterozoic crust before the formation of the Yaounde basin. Meanwhile, the anomaly in the east of Metet may be related to garnetiferous micaschists of the Yaounde series.

Figure 2: The reduced to the magnetic equator (RTE) of the TMI map. Evidenced prominent NE high anomaly channel in the centre of the map; yellow lines modelling profiles

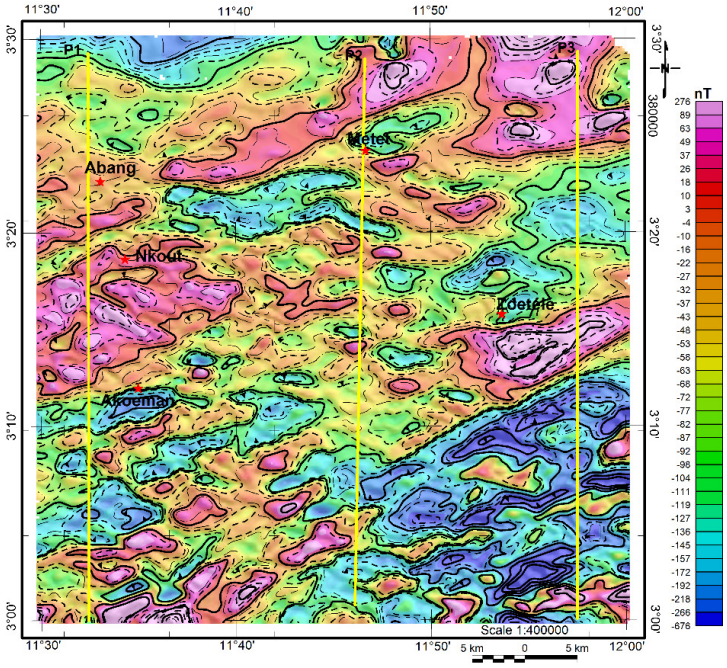

The broad SW-NE orientation of the central domain is a strong indication on the major deformation trend which could have affected the study area's subsurface. Indeed, at first sight, it can be inferred that the basement is controlled by a SW-NE architecture. On Figure 2, the throws and the highs are stretched along the WNW-ESE to NW-SE, E-W or ENE-WSW to NE-SW extensional directions as a consequence of ENE-WSW to NW-SE, N-S and WNW-ESE to NE-SW possible compressions that affected the area. So, the Nkout and Zoetele anomalies seem to have form a unique block tore by relative E-W to ENE-WSW shear movements. This axis is linked to regional ENE-WSW to NE-SW trans-tensions, probably accompanied by the upwells of basic or mafic materials in both the CC and the NEFB as depicted by high susceptibility anomaly blobs within the SW-NE outlined channel.

Analyses of Structures in the Metet-Zoetele Area

The faulting in the Metet-Zoetele area

Lineaments in the Metet-Zoetele area are highlighted by the combined analysis of the RTE enhanced image (figure 3) and the multiscale HGM map (figure 4).

Figure 3: Enhanced RTE image with highlighted faults. The two grey arrows give the direction of the trans-tensional (shear) movements which forcibly corresponds to sinistral strike-slips

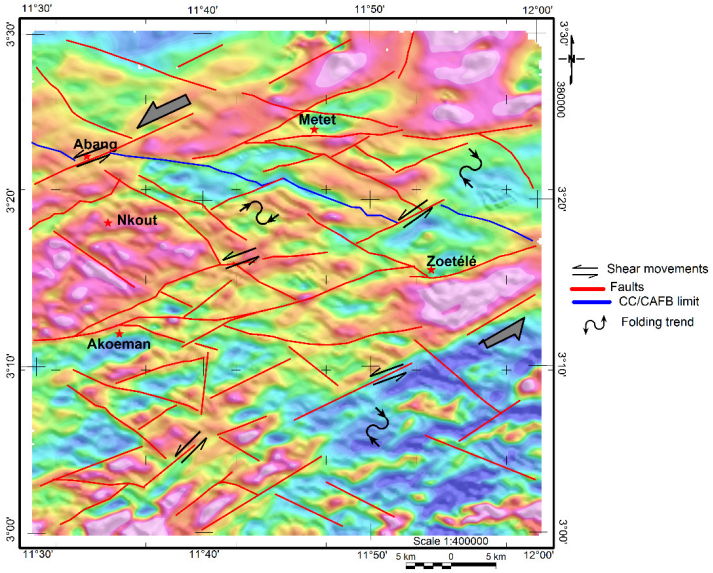

As HGM lineaments (figure 4) are interpretable as faults, fractures, dykes, or simply contacts, a fractures-segregation technique has been done by superimposing the faults from Figure 3 onto the HGM lineaments map (figure 4). On the resulting image (figure 5), only HGM lineaments superimposed by highlighted faults (in red) are interpreted as faults or fractures hereafter. The faults and fractures (Figures 3, and 5) are mainly SW-NE, ENE-WSW, and W-E to NW-SE and WNW-ESE oriented.

Figure 4: Multiscale analysis map of the Metet-Zoetele area. The Lineaments highlighted are mainly vertical to sub-vertical. Dipping either south or north

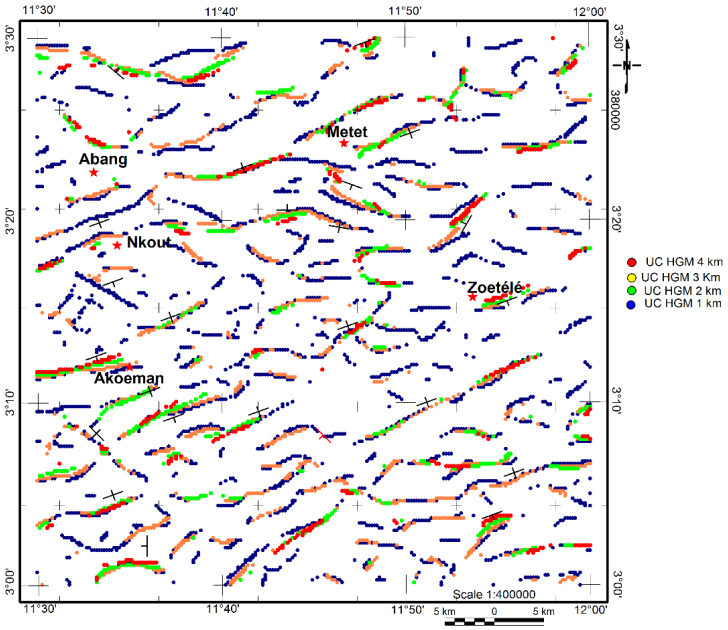

Figure 5: Segregation of faults out of HGM lineaments. Red lines represent early defined faults and the blue line depicts the CC/CAFB limit

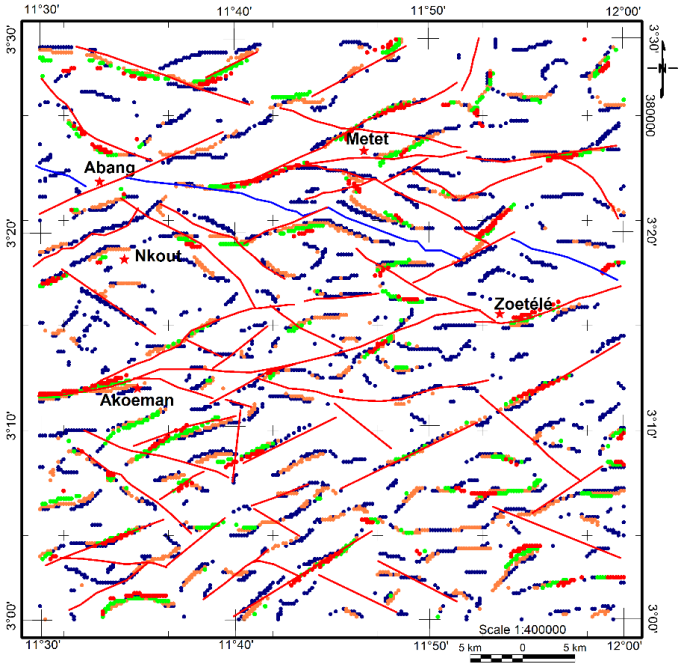

These faults probably guided E-W and NE-SW to NW-SE movements that triggered some compressions herein responsible of the NE-SW and NW-SE folding that occurred in the area. The cross-cutting relationships between those structures show that they either belong to various deformation stages or they are syn- emplaced. Anyhow, the two modes are obvious in regards with the geological history pertaining onto the region. Illustratively in Figure 3, the emplacement of the SW-NE anomaly stretched from Abang to Metet was probably controlled by an early NE-SW structure (Eburnean?), then intersected by a E-W to WNW-ESE (Pan-African?) structure itself post-cut by a NW-SE fault (due to NE-SW sinistral shears) near Abang. The northern area is less fractured, probably the NEFB, in opposition to a southern area, probably the CC (figures 3 and 5). The highlighted nearly E-W set of faults separating those two areas may define the CC/NEFB southernmost limit (blue line on figure 3); hence, NE-SW faults are sinistral strike-slips affecting both the CC and the NEFB.

Attitudes and Depth Range Classification of Faults

The directions and qualitative plunge attitude of lineaments are inferred from Figures 3 and 4 and presented in Table 1. The plunge is assessed by the offset between shallowest (blue) and the deepest (red) peaks. Globally, the lineaments in the area (figure 4) dip north or south and are vertical to sub-vertical. Also, the depth range of fractures has been assessed, depending on their depth perception (presence of peaks levels), yielding three classes (table 1); shallow to the deep (peaks from all levels), middle to deep (peaks from 3 km and 4km only) and deep (4 km peaks).

Table 1: Faults attitudes and depth ranges

Count	Fault's attitude		Depth class	Count	Fault's attitude		Depth class
	Strike	Dip or plunge			Strike	Dip or plunge	
1	SE-NW	North	Middle to deep	16	WSW-ENE	Vertical	Shallow
2	SE-NW	South	Middle to deep	17	WSW-ENE	Subvertical	Shallow
3	SE-NW	South	Shallow	18	WSW-ENE	North	Shallow to middle

Count	Fault's attitude		Depth class	Count	Fault's attitude		Depth class
	Strike	Dip or plunge			Strike	Dip or plunge	
4	SE-NW	Vertical	Shallow to deep	19	WSW-ENE	South	Shallow to deep
5	SE-NW	Subvertical	Shallow to middle	20	WSW-ENE	Vertical	Shallow to middle
6	SE-NW	Subvertical	Shallow	21	WSW-ENE	North	Shallow to deep
7	SE-NW	Vertical	Shallow to deep	22	WSW-ENE	North	Shallow to deep
8	SW-NE	N-Gradational	Shallow to deep	23	WSW-ENE	Subvertical	Shallow to middle
9	SW-NE	South	Shallow to deep	24	W-E	Vertical	Shallow to middle
10	SW-NE	Subvertical	Shallow to deep	25	W-E	Subvertical	Shallow to middle
11	SW-NE	Vertical	Shallow to middle	26	W-E	Subvertical	Shallow to middle
12	SW-NE	Subvertical	Shallow to middle	27	W-E	Subvertical	Shallow to middle
13	WSW-ENE	Subvertical	Shallow to middle	28	W-E	Subvertical	Shallow
14	WSW-ENE	Vertical	Shallow to deep	29	WNW-ESE	Vertical	Shallow to middle
15	WSW-ENE	Vertical	Shallow to deep	30	WNW-ESE	Vertical	Shallow to middle
16	WSW-ENE	Vertical	Shallow	31	WNW-ESE	Vertical	Shallow

The table1 yielded a total of vertical to sub-vertical 31 faults. The main orientations are WNW-ESE (3 counts), W-E (5 counts), NW-SE (7 counts), SW-NE (5 counts) and WSW-ENE (11 counts). Cumulatively, the dominant SW-NE to WSW-ENE cluster (16 counts i.e. 51.61%), followed by the WNW-ESE to NW-SE cluster (10 counts, i.e. 32.25%) are both highlighted in the NEFB and the CC domains, in accordance with previous analyses.

Depth-to-Sources Estimation

The 3D Euler deconvolution provided depth estimates of faults and fractures in the Metet-Zoetele area. The solutions (faults and fractures) are clustered on four depth ranges, from shallow to deep subsurface at [0; 1 km [, [1; 2 km [, [2; 3 km [and more than 3 km intervals, respectively (figure 6). Many solutions match the WNW-ESE, W-E, NW-SE, SW-NE and WSW-ENE directions already highlighted in this study.

Figure 6: Euler 3D solutions underlain by the lineaments map. Depth estimation uses a 9 x 9 window, a depth tolerance of 5% and a structural index of 0.5 for contacts and steep-dipping faults. Solutions correlate with RTE enhanced and HGM faults

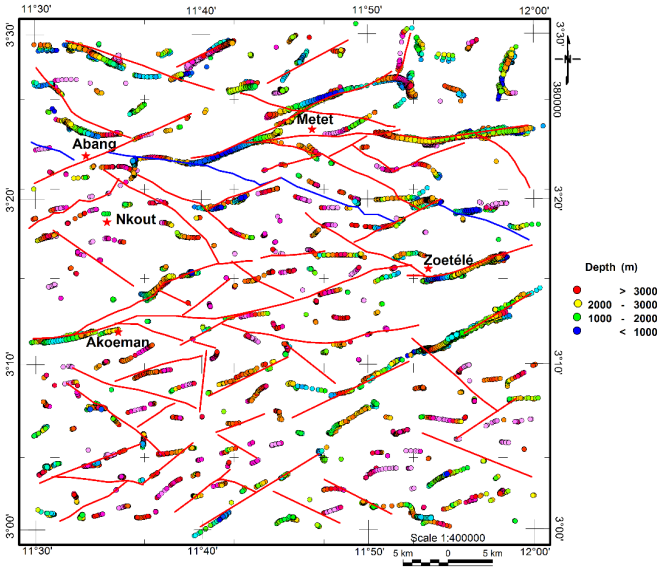

Geological Models

Three profiles (figure 2) were considered for inversion, assuming (1) a uniform basement of magnetic susceptibility $\boldsymbol{k}$ =0.0015. $\boldsymbol{k}$ values in cgs can translated in SI if divided by 4π.

Profile 1

The shape of anomaly profile (figure 7a) suggests the existence of some evident discontinuities interpreted as faults (F1-1 to F1-4) respectively at 3 km, 8.4 km, 22 km and 37 km along profile (figure 7b). The supra-basement effects correspond to a basement's uplift (between F1-2 and F1-4), coupled with an intrabasement N-dipping fracture (F1-3) which separates acidic granulites ($\boldsymbol{k}$ = 0.01977) from syenites overlying the basement between 20 and 38 km. The assumed intrabasement effects are mainly observed between the faults F1-1 and F1-2, which bound a probable gabbro ($\boldsymbol{k}$ = 0.00815) intrusion located at ~2.3 km depth, with ~4 km width, between granulites and tonalites ($\boldsymbol{k}$= 0.00547). Those formations are topped by granodiorites ($\boldsymbol{k}$= 0.01219) and acidic igneous formations ($\boldsymbol{k}$ = 0.00062) left of the F1-4 fault. Right of F1-4, the model yields upward above the basement, quartzites ($\boldsymbol{k}$ = 0.00004), metasediments ($\boldsymbol{k}$= 0.01746), ectinites ($\boldsymbol{k}$=0.00550) and schists ($\boldsymbol{k}$=0.00078).

Figure 7: Modelling along profile 1 (a) Magnetic anomaly profile; (b) Combined geophysical model and geological section. The CC/NEFB limit is represented by the fault F1-4; susceptibility values are in cgs, a division by 4π yields SI values

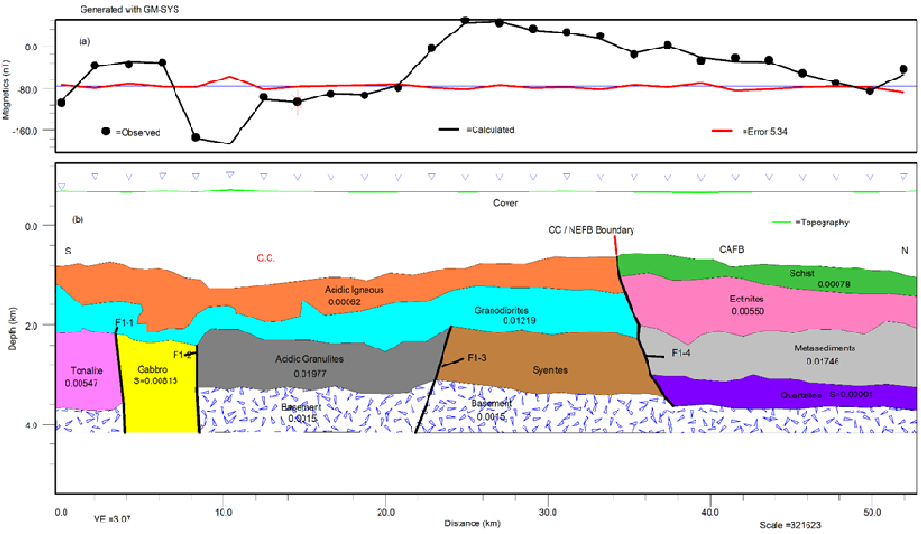

The inversion was performed with a RMS of 5.34%. The geological model (figure 7b) locates the basement nearly at 3.6 km depth from the origin of the profile to F1-1; at 3.2 km from F1-2 to F1-4; then a progressive smooth subsidence from F1-4 to the end of the section. The F1-4 appears to be a north-dipping major discontinuity affecting the basement and separating an igneous complex to the left (south), from a metasedimentary complex to the right (north).

Profile 2

On profile 2, the irregular shape of the curve (figure 8a) testifies the complex geology of the area. The geophysical modelling (figure 8b) assumes only supra-basement effects. The basement is encountered nearly at 3.5 km depth from the origin to 10 km (at F2-1) where it sinks to a nearly constant depth of 4 km up to F2-3; it sinks again therein to nearly 4.4 km depth till position 46 km (F2-10) where it raises again to a constant depth of 4 km. The basement is jagged by faults (F2-1, F2-2, F2-3 and F2-10) which affect partially or totally the overlying formations.

Figure 8: Modelling along profile 2. (a) Magnetic anomaly profile; (b) Combined geophysical model and geological section. The CC/NEFB limit is represented by the fault F2-5 susceptibility values are in cgs, a division by 4π yields SI values

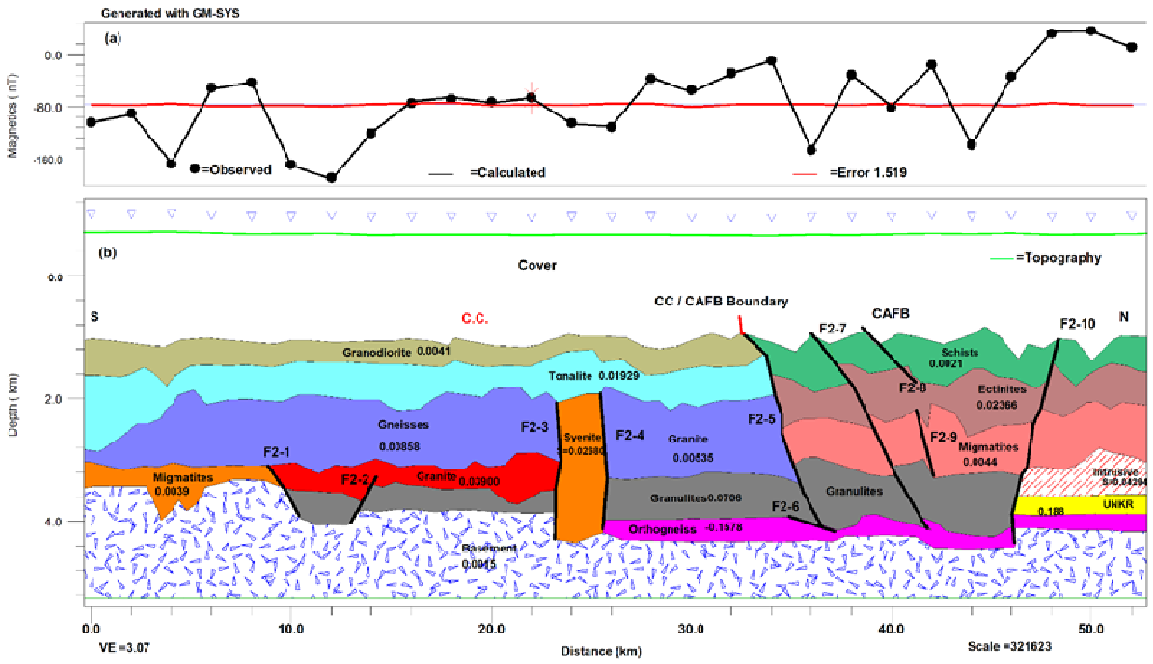

The accepted geological model (RMS error of 1.519 %) shows top-basement formations affected by many faults e.g. F2-1, F2-3 and F2-4 which separate different lithologies: migmatites (***k***=0.0039)/granite (***k***=0.03900), granulites (***k***=0.0706)-granite-gneisses (***k***=0.00858)/syenites (***k***=0.0268) and syenites/granulites-granite (***k***=0.00535). The F2-5 and F2-10 faults seem to limit a basin or syncline stretched in length from 33 km to 48 km; this is supported by their respective geometry, as F2-5 dips north while F2-10 dips south. The faults F2-7, F2-8 and F2-9 seem to outline vertical movements that affect the schists (***k***=0.0021), ectinites (***k***=0.02366), migmatites (***k*** = 0.0044), granulites, orthogneisses (***k*** = -0.0578) and even the basement, in the aforesaid basin. This seems also to be the case for F2-1 and F2-2 regarding the granulites layer and the basement, ~10 km from the origin of the section. Finally, an igneous complex and a metasedimentary complex separated by F2-5 summarises the section (Figure 8b).

Profile 3

The anomaly profile (Figure 9a) starts with a peak (100 nT) attributable to the F3-1 fault (Figure 9b), followed by a general flat low of -220 nT from 4km to 24 km where a new abrupt increase is observed. In the 24-32 km interval the profile peaks at 26.5 km and, then decreases and increases alternatively till the end, shaping the anomaly profile like a valley between 32 and 44 km. The patterns (Figure 9a) at 2 km and in the 24-32km interval, infer discontinuities. Globally, the profile suggests that the subsurface lithology is made up of 2 blocks separated by a major discontinuity at 24 km. The modelling (figure 9b) revealed supra-basement effects witnessed by a collapse of the basement from 11 km to 21 km and from 32 km to the end. The main intrabasement anomaly is interpreted as a syenites intrusion (***k*** = 0.0261).

Figure 9: Modelling along profile 3. (a) Magnetic anomaly profile; (b) Combined geophysical model and geological section. The CC/NEFB limit is represented by the faults F3-6, F3-7, F3-8 and F3-9; susceptibility values are in cgs, a division by 4π yields SI values

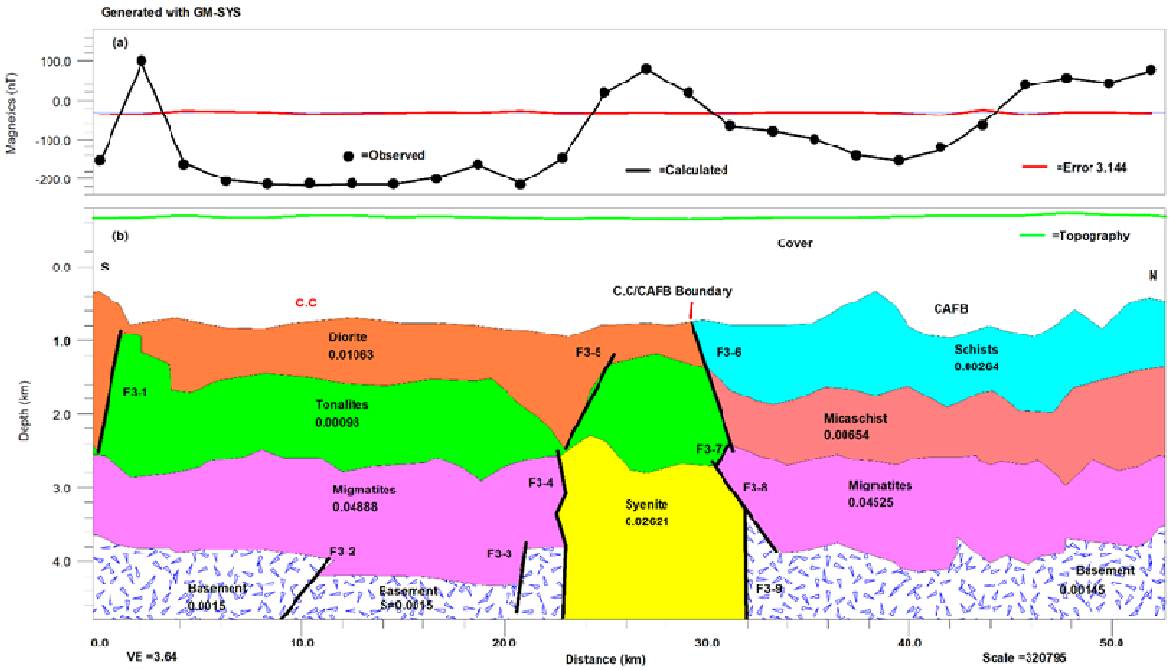

The geological model (obtained for a RMS error of 3.144%) outlines various probable faults, F3-1 to F3-9, which are somewhat hidden on the anomaly profile. Particularly, F3-2 and F3-3 are related to probable vertical movements that may have caused a basement collapse between 10 km and 21 km. Accordingly, F3-4 and F3-9 are related to the modelled intrusion in the basement, in one hand, whereas F3-4 and F3-8 are faulted-contacts separating respectively, the migmatites I (k =0.04888)/syenites and syenites/migmatites II (k =0.04525). In addition, F3-7 and F3-6 seem particular, as F3-6 outlines upward, left to right, gneiss (k = 0.00098)/micaschists (k = 0.00654) and diorite (k = 0.01063)/metasediments (k = 0.00264) contacts; and F3-7 may constitute the gneiss/migmatites boundary. Assuming that F3-6, F3-7, F3-8 and F3-9 faults are relays of a unique fault, they separate a left (south) unit of high susceptibility formations probably of magmatic and origin, to a right (north) group of low susceptibility materials assimilated to detrital metasediments. Also, the zig-zag displayed by NEFB layers infer some probable N-S compressional movements.

Summarily, the three models are consistent with the existence of a low susceptibility block to the north, separated by a sharp discontinuity to a south-high susceptibility block. The high susceptibilities in the left are supposedly due to mafic terrains and low susceptibilities to detrital metasediments. Thus, the study delineates an igneous (equated to the CC) and a metasedimentary (equated to the NEFB) complexes separated by sub-vertical faults, probably the CC/NEFB limit.

Discussion

Validation of the Mapping Methodology

The mapping methodology involved the combined analysis of the multiscale HGM and the Euler 3D methods to detect and locate faults and fractures. The efficiency of these techniques have been proven by various studies including those involving the southern Cameroon context (e.g. Basseka *et al* 2011; Shandini *et al* 2010; Owona Angue *et al* 2016; Yandjimain *et al* 2017). Further, the choice of a depth

tolerance of 5 % and a structural index of 0.5 to recover Euler's solutions enabled to avoid spurious solution and to provide good depth estimates, in accordance with Hinze *et al* (2013). Besides, interpretation of enhanced image of magnetic images are good in locating structures with regional significance (Paterson and Reeves 1985; Reeves 2005). Thus, combining these methods strengthens the validity of the results presented in this paper.

Validation of Highlighted Fractures and Correlation with Previous Studies

The study has revealed the presence of many faults based on qualitative (figures 3 and 4) and quantitative (figure 6) interpretations. The classification of these faults as per the descriptive depth ranges (table 1) matches with the quantitative Euler's depth ranges (figure 6). In regard with the absence of supportive field data, an additional cross-validation between Euler's solutions, RTE enhanced and HGM highlighted faults is done by superimposing those outputs on a same diagram (figure 6) which shows a good fit in between these different results.

The faults orientations are globally WNW-ESE, W-E, NW-SE, SW-NE and WSW-ENE with two dominant outlined clusters (SW-NE to WSW-ENE) and (WNW-ESE to NW-SE). These directions, as well as the vertical to sub-vertical dips observed, are consistent with other geophysical studies in the vicinities of the study area (Shandini *et al* 2010; Basseka *et al* 2011; Ndougsa-Mbarga *et al* 2012; Akame *et al* 2013, 2018; Bikoro-Bi-Alou *et al* 2014; Assembe *et al* 2016; Owona-Angue *et al* 2016). The calculated depth ranges locate these features in the brittle upper crust zone as shown by Basseka *et al* (2011) and Shandini *et al* (2011) over a region that includes the study area. This study emphasised on a dominant WSW-ENE to SW-NE direction's fan which correlates well with the major directions outlined in the CC/NEFB transition zone and within the Ntem complex by previous studies and by Assembe *et al* (*in preparation*), respectively to the east, south-east, the north and within the investigated area. This direction probably corresponds to pre-Neoproterozoic weakness zones which underwent Neoproterozoic and post-Neoproterozoic reactivations, and controlled deposition and metamorphism in the northern margin of the CC as noticed by Nkombou *et al* (2014) in accordance with Katumwehe *et al* (2015).

Clearly, it appears that both in the CC and NEFB domains, WSW-ENE to SW-NE fractures form a major strike-slip line overprinted by sinistral WNW-ESE to NW-SE faults associated to E-W lateral wrenches potentially due to WNW-ESE to NW-SE shears, in accordance with Ngako *et al* (2004). The WSW-ENE strike-slips system hence corresponds to an extensional axis (coeval to the setup of the Central Africa Rift System whose local member is the Centre Cameroon Shear Zone-CCSZ) in a weakness zone set-up during the paleo- to meso-Proterozoic (Ngako *et al* 2004; Mbola Ndzana *et al* 2014). These results are consistent with many geological studies carried out in southern Cameroon (Toteu *et al* 1994; Ngako *et al* 2008; Olinga *et al* 2010; Tchameni *et al* 2010; Mbola-Ndzana *et al* 2014), as well as at the regional scale (Binks and Fairhead 1992; Fairhead *et al* 2013; Kirkpatrick *et al* 2013; Katumwehe *et al* 2015). We assume that the WNW-ESE to NW-SE shears responsible to the E-W wrenches result from the on-going dynamics of the Africa-Eurasia convergence and the rifting in east Africa.

On the Ntem Complex/North Equatorial Fold Belt Limit

The differentiation of the NEFB from the Ntem complex, based on the difference in fracturing density observed on produced maps (figures 3, 4 and 5) of Metet-Zoetele, was linked to the difference in rheology of the in situ materials. That interpretation is supported by the inversion results (figures 7, 8 and 9) which globally define a magmatic complex to south and a metasedimentary complex to the north, and provide a clear location of the CC/NEFB limit on each profile. The location of that limit, measured from the north edge of the map, along each profile is compared to inversion output in table 2.

Table 2: Locations of the CC/NEFB southern limit. The distances are obtained from the north along profiles

Location of the CC/NEFB limit in km (west to east)			
	P1	**P2**	**P3**
Measured on map	19.24	17.87	21.42
From inversion	18.3	16.5	20.45
Stdev.		1.59	

These distances set the average location of the CC/NEFB southern limit at the UTM N370000 (or N03º20') latitude, initially located in the area at N03º30' (Shandini *et al* 2010; Basseka *et al* 2011). Additionally, the models (figures 7, 8 and 9) infer a high susceptibility material beneath the NEFB and a unique basement underlying the Metet-Zoetele area that may reflect the subduction of the Congo Craton under the Yaounde group as evidenced by other studies (Shandini *et al* 2010; Shandini and Tadjou 2012; Meying *et al* 2013; Assembe *et al* 2016). Although the high susceptibility materials beneath the NEFB at the vicinity of the CC/NEFB limit correlate the high density formations outlined and interpreted as a CC/NEFB suture in the area (Tadjou *et al* 2009; Shandini *et al* 2010; Basseka *et al* 2017), the current study suggests that this shall be reviewed in regard to recent studies on the CC northern margin (e.g. Goussi Ngalamo *et al* 2017, 2018). The faults intersecting the CC/NEFB limit (Figure 3) are imprints of the dislocations in the northern margin of the CC (Njingti-Nfor *et al* 2017a.,b). Despite the study correlates past studies, some outstanding points remain; such as the absence of N-S and NNE-SSW fractures reported by other studies. This issue, along with a more detailed quest on the tectonic evolution of the Congo Craton-Panafrican transition zone are still investigated by the authors.

Conclusions

The paper presents an interpretation of aeromagnetic data over a portion of the Congo Craton/Pan-African transition zone in southern Cameroon, in order to improve the understanding of the geological evolution in the northern margin of the Congo Craton. Various fractures have been highlighted mainly along the WNW-ESE, W-E, NW-SE, SW-NE and WSW-ENE directions both in the Congo Craton and the Pan-African domains. The WSW-ENE fractures correspond to a dextral extensional paleo structural network reactivated by NW-SE compressions, coeval to the Central Cameroon Shear Zone, further overprinted by a sinistral WNW-ESE to NW-SE displacement as a response to the on-going general NE convergence of Africa towards Eurasia and the rifting in east Africa. This suggests the existence of on-going wrenches both in the Ntem complex (CC) and the Pan-African (NEFB) system. Additionally, the inverse modelling of the magnetic data corroborates compressions between the CC and the NEFB, clearly defines the southern NEFB/CC limit as a sharp fault-contact line located at latitude N03º20'; and validates the existence of craton materials beneath NEFB. However, further investigations are on-going by the authors towards a consistent geodynamic model northern margin of the Congo Craton that integrates pending tectonics in the African Plate.

Acknowledgement

The authors are thankful to Professor Colin Reeves for his critical remarks and advises; and the anonymous reviewers who will endeavour themselves into the improvement of the quality of this paper through their welcomed critics and remarks.

References

[1] Toteu S F, Schmus W R V and Penaye J 2006a The Precambrian of Central Africa: Summary and perspectives *J. African Earth Sci.* **44**

[2] Mvondo H, Essono J, Mvondo Ondoa J and Yene Atangana J Q 2007 Comment on "U-Pb dating of plutonic rocks involved in the nappe tectonic in southern Cameroon: Consequence for the Pan-African orogenic evolution of the central African fold belt" by Toteu et al. (Journal of African Earth Sciences 44 (2006) 479-493) *J. African Earth Sci.* **48** 49–52

[3] Mvondo Ondoa J, Mvondo H and Den Brok B 2009 Pan-African tectonics in northwestern Cameroon : Implication for the history of western Gondwana *Gondwana Res.* **16** 163–4

[4] Ngako V and Njonfang E 2011 Plates Amalgamation and Plate Destruction , the Western Gondwana History *Tectonics*

[5] Ngnotue T, Ganno S, Nzenti J P, Schulz B, Tchaptchet Tchato D I and Suh Cheo E 2012 Geochemistry and Geochronology of Peraluminous High-K Granitic Leucosomes of Yaound Series (Cameroon): Evidence for a Unique Pan-African Magmatism and Melting Event in North Equatorial Fold Belt *Int. J. Geosci.* **03** 525–48

[6] Paterson N R and Reeves C V 1985 Applications of gravity and magnetic surveys : The state-of-the-art in 1985 *Geophysics* **50** 2558–94

[7] Nabighian M N, Ander M E, Grauch V J S, Hansen R O, LaFehr T R, Li Y, Pearson W C, Peirce J W, Phillips J D and Ruder M E 2005 Historical development of the gravity method in exploration *Geophysics* **70** 63–89

[8] Boyd D M and Isles D J 2007 Geological Interpretation of Airborne Magnetic Surveys - 40 Years On *Proceedings of Exploration 07: Fifth Decennial International Conference on Mineral Exploration* ed B Milkereit pp 491–505

[9] Feumoe A N, Ndougsa-Mbarga T, Manguelle-Dicoum E and Fairhead J D 2012 Delineation of tectonic lineaments using aeromagnetic data for the south-east Cameroon area *Geofizika* **29**

[10] Ndougsa-Mbarga T, Feumoe A N S, Manguelle-Dicoum E and Fairhead J D 2012 Aeromagnetic Data Interpretation to Locate Buried Faults in South- *Geophysica* **48** 49–63

[11] Yandjimain J, Ndougsa-mbarga T, Meying A, Bi-alou M B, Ngoumou P C, Assembe S P, Ngoh J D and Owono-amougou O U I 2017 Combination of Tilt-Angle and Euler Deconvolution Approaches to Determine Structural Features from Aeromagnetic Data Modeling over Akonolinga-Loum Area *Int. J. Geosci.* **8** 925–47

[12] Yandjimain J, Ndougsa-Mbarga T, Bikoro Bi-alou M and Meying A 2018 Aeromagnetic Data Modeling for Geological and Structural Mappings over the DJADOM-ETA Area, in the Southeastern Cameroon *Int. J. Geosci.* **9** 354–70

[13] Blakely R J 1996 *Potential Theory in Gravity and Magnetic* (Cambridge university press)

[14] Reid A B, Allsop J M, Granser H, Millet A J and Somerton I W 1990 Magnetic interpretation in three dimensions using Euler deconvolution **55**

[15] Nkoumbou C, Barbey P, Yonta-Ngouné C, Paquette J L and Villiéras F 2014 Pre-collisional geodynamic context of the southern margin of the Pan-African fold belt in Cameroon *J. African Earth Sci.* **99** 245–60

[16] Toteu S F, Fouateu R Y, Penaye J, Tchakounte J, Mouangue A C S, Van Schmus W R, Deloule E and Stendal H 2006b U-Pb dating of plutonic rocks involved in the nappe tectonic in southern Cameroon: consequence for the Pan-African orogenic evolution of the central African fold belt *J. African Earth Sci.* **44** 479–93

[17] Toteu S F, Penaye J and Djomani Y P 2004 Geodynamic evolution of the Pan-African belt in central Africa with special reference to Cameroon *Can. J. Earth Sci.* **41** 73–85

[18] Toteu S F, Penaye J, Deloule E, Van Schmus W R and Tchameni R 2006 Diachronous evolution of volcano-sedimentary basins north of the Congo craton: Insights from U-Pb ion

microprobe dating of zircons from the Poli, Lom and Yaoundé Groups (Cameroon) *J. African Earth Sci.* **44** 428–42

[19] Mvondo H, Owona S, Ondoa J M and Essono J 2007 Tectonic evolution of the Yaoundé segment of the Neoproterozoic Central African Orogenic Belt in southern Cameroon *Can. J. Earth Sci.* **44** 433–44

[20] Olinga J B, Mpesse J E, Minyem D, Ngako V, Ndougsa-Mbarga T and Ekodeck G E 2010 The Awaé – Ayos strike-slip shear zones (southern Cameroon): Geometry, kinematics and significance in the late Pan-African tectonics *N. Jb. Geol. Paläont. Abh.* **257** 1–11

[21] Mbola-Ndzana S P, Mvondo-Ondoa J, Owona S, Sep-Nlongand J P, Olinga J B and Bilong P 2014 Evidence of the ~NE-SW extension in the Sa'a-Monatélé Region as in the Bafia and Yaounde groups within the Central Africa Fold belt (Cameroon): Implication for the Southern Cameroon Neoproterozoic extension *Sci. Technol. Développement, Technol. Développement* **16** 1–15

[22] Shang C K, Muharrem S, Nsifa Nkonguin E, Liegeois J-P, Siebel W and Taubald H 2007 Archaean high-K granitoids produced by remelting of earlier Tonalite – Trondhjemite – Granodiorite (TTG) in the Sangmelima region of the Ntem complex of the Congo craton, southern Cameroon *Int J Earth Sci (Geol Rundsch)* **96** 817–41

[23] Tchameni R, Lerouge C, Penaye J, Cocherie A, Milesi J P, Toteu S F and Nsifa N E 2010 Mineralogical constraint for metamorphic conditions in a shear zone affecting the Archean Ngoulemakong tonalite, Congo craton (Southern Cameroon) and retentivity of U-Pb SHRIMP zircon dates *J. African Earth Sci.* **58** 67–80

[24] Shang C K, Liégeois J P, Satir M, Frisch W and Nsifa E N 2010 Late Archaean high-K granite geochronology of the northern metacratonic margin of the Archaean Congo craton , Southern Cameroon : Evidence for Pb-loss due to non-metamorphic causes *Gondwana Res.* **18** 337–55

[25] Tchameni R, Mezger K, Nsifa N E and Pouclet A 2001 Crustal origin of Early Proterozoic syenites in the Congo Craton (Ntem Complex), South Cameroon *Lithos* **57** 23–42

[26] Vicat J and Moloto-a-kenguemba G 2013 Les granitoides de la couverture protérozoique de la bordure nord du craton du Congo (Sud-Est du Cameroun et Sud-Ouest de la République centrafricaine), témoins d'une activité magmatique panafricaine

[27] Takam T, Makoto A, Kokonyangi J, Dunkley, Daniel J and Nsifa Nkonguin E 2009 Paleoarchaean charnockite in the Ntem Complex, Congo Craton, Cameroon : insights from SHRIMP zircon U-Pb ages *J. Mineral. Petrol. Sci.* **104** 1–11

[28] Toteu S F, van Schmus W R, Penaye J and Nyobe J B 1994 U-Pb and Sm-Nd evidence for Eburnian and Pan-African high-grade metamorphism in cratonic rocks of southern Cameroon. *Precambrian Res.* **67** 321–47

[29] Akame J M, Mvondo Ondoa J, Olinga J B, Essono J and Kemeng M P 2013 Utilisation des modèles numériques de terrain (MNT) SRTM pour la cartographie des linéaments structuraux : Application à l'Archéen de Mezesse à l'est de Sangmélima *Geo-Eco-Trop.* **37** 71–80

[30] Loose D and Schenk V 2018 2.09 Ga old eclogites in the Eburnian-Transamazonian orogen of southern Cameroon : Significance for Palaeoproterozoic plate tectonics *Precambrian Res.* **304** 1–11

[31] Reeves C 2005 *Aeromagnetic Surveys-Principles, Practice & Interpretation* (Geosoft)

[32] Hinze W J, von Frese R R B and Saad A 2013 *Gravity and magnetic exploration: principles, practices and exploration* (Cambridge university press)

[33] Archibald N, Gow P and Boschetti F 1999 Multiscale edge analysis of potential field data *Explor. Geophys.* **30** 38–44

[34] Blakely J and Simpson R W 1986 Short Note Approximating edges of source bodies from magnetic or gravity anomalies **51** 1494–8

[35] Reeves C V, Reford S W and Milligan P R 1997 Airborne Geophysics : Old Methods , New Images *Proceedings of Exploration 97: Fourth Decennial International Conference on Mineral Exploration* ed A G Gubins pp 13–30

[36] Owona-Angue M L, Assembe S P, Njingti-Nfor, Ngoh J D, Ndougsa-Mbarga T, Kue Petou M R and Bisso D 2016 Determination of the Structural Lineaments in the Kribi-Campo-Ma ' an Area from a Multi-Scale Analysis of Gravity Data Using the HGM and Euler 3D Deconvolution Approaches *Int. J. Geosci.* **7** 1122–43

[37] Fernandez-Alonso M, Tack L, Tahon A and De Waele B 2010 The Proterozoic history of the proto-Congo Craton of Central Africa

[38] Prieto C 1996 Gravity/magnetic signatures of various geologic models-An exercise in pattern recognition *IGC Footnotes Interpret.* **4**

[39] Akame J M, Assembe S P, Zo'o Zame P, Owona S, Ndougsa-Mbarga T, Azia G A and Mvondo-Ondoa J 2018 The Sangmelima granite-greenstone belts (South Cameroon): Integration of remote sensing and aeromagnetic data for structural interpretation *Egypt. J. Remote Sens. Sp. Sci.*

[40] Assembe S P, Meying A and Ndougsa-Mbarga T 2016 New structural facts from audio-magnetotelluric (AMT) data interpretation in the Yaoundé-Nkolafamba area (Centre Cameroon) *J. Ind. Geophys. Union* **20** 19–32

[41] Basseka C A, Shandini Y and Tadjou J M 2011 Subsurface structural mapping using gravity data of the northern edge of the Congo craton , South Cameroon *Geofizika* **28** 229–45

[42] Bikoro-Bi-Alou M, Ndougsa-Mbarga T and Tabod T C 2014 Quantitative Interpretation of Magnetic Anomalies in Ebolowa-Djoum area (Southern Cameroon) *Geophysica* **50** 11–25

[43] Shandini Y N, Tadjou J M, Tabod C T and Fairhead J D 2010 Gravity Data Interpretation in the Northern Edge of the Congo Craton , South-Cameroon *Anuário do Inst. Geociências - UFRJ* **33** 73–82

[44] Katumwehe A B, Abdelsalam M G and Atekwana E A 2015 Tectonophysics The role of pre-existing Precambrian structures in rift evolution : The Albertine and Rhino grabens , Uganda *Tectonophysics* 1–13

[45] Ngako V, Affaton P and Njonfang E 2008 Pan-African tectonics in northwestern Cameroon : Implication for the history of western Gondwana *Gondwana Res.* **14** 509–22

[46] Binks R M and Fairhead J D 1992 A plate tectonic setting for Mesozoic rifts of West and Central Africa *Tectonophysics* **213** 141–51

[47] Fairhead J D, Green C M, Masterton S M and Guiraud R 2013 Tectonophysics The role that plate tectonics , inferred stress changes and stratigraphic unconformities have on the evolution of the West and Central African Rift System and the Atlantic continental margins *Tectonophysics* **594** 118–27

[48] Kirkpatrick J D, Bezerra F H R, Shipton K, Nascimento A F D O, Federal U and Al J D K E 2013 Scale-dependent influence of pre-existing basement shear zones on rift faulting : a case study from NE Brazil *J. Geol. Soc. London.* **170** 237–47

[49] Basseka C A, Eyike Yomba A, Kenfack J V, Njiteu Tchoukeu D C, Som Mbang M C and Shandini Njankouo Y 2017 Magnetic Anomaly Interpretation of the Northern Congo Craton Boundary : Results from Depth Estimation and 2.5D Modeling *J. Geosci. Environ. Prot.* **5** 90–101.

[50] Shandini Y and Tadjou J M 2012 Interpreting gravity anomalies in south Cameroon, central Africa *Earth Sci. Res. J.* **16** 5–9

[51] Goussi Ngalamo J F, Bisso D, Abdelsalam M G, Atekwana E A, Katumwehe A B and Ekodeck G E 2017 Geophysical imaging of metacratonizaton in the northern edge of the Congo craton in Cameroon *J. African Earth Sci.*

[52] Goussi Ngalamo J F, Sobh M, Bisso D, Abdelsalam M G, Atekwana E and Ekodeck G E 2018 Lithospheric structure beneath the Central Africa Orogenic Belt in Cameroon from the analysis of satellite gravity and passive seismic data *Tectonophysics* **745** 326–37

[53] Njingti-Nfor, Owona-Angue M L, Kue Petou M R, Bisso D and Lando Tsakou J A 2017 Application of Coefficient of Anisotropy to the Geophysical Prospecting of Campo — Ma ' an Area of the Ntem Complex in Cameroon *Open J. Geol.* **2017** 1801–18

[54] Njingti-Nfor, Owona Angue M L, Petou Kue M R, Bisso D and Piameu Kwagag J 2017 Magnetotelluric Investigation of the Geo-Tectonic Stability of Campo-Ma ' an Area in South Cameroon *Int. J. Geosci.* 1427–41**.**

Scientific Research Publishing

Advances in Remote Sensing, 2020, 9, 53-84
https://www.scirp.org/journal/ars
ISSN Online: 2169-2688
ISSN Print: 2169-267X

+−Evidence of Porphyry Deposits in the Ntem Complex: A Case Study from Structural and Hydrothermal Alteration Zones Mapping through Landsat-8 OLI, Aeromagnetic and Geological Data Integration in the Yaounde-Sangmelima Region (Southern Cameroon)

Stephane Patrick Assembe[1,2*], Theophile Ndougsa Mbarga[3*], Françoise Enyegue A. Nyam[4], Paul Claude Ngoumou[5], Arsene Meying[5], Daniel Herve Gouet[6], Alain Zanga[7], Jean Daniel Ngoh[1]

[1]Postgraduate School of Technology, Science and Geoscience, University of Yaounde 1, Yaounde, Cameroon
[2]Department of Physics, Faculty of Science, University of Bamenda, Bambili, Cameroon
[3]Department of Physics, Higher Teachers Training College, University of Yaounde 1, Yaounde, Cameroon
[4]Department of Physics, Faculty of Science, University of Yaounde 1, Yaounde, Cameroon
[5]School of Geology and Mining Engineering, University of Ngaoundere, Meiganga, Cameroon
[6]Faculty of Mining and Petroleum Industries, University of Maroua, Kaele, Cameroon
[7]Department of Physics, Faculty of Science, University of Douala, Douala, Cameroon
Email: *assembest@yahoo.fr, *tndougsa@yahoo.fr

How to cite this paper: Assembe, S.P., Mbarga, T.N., Nyam, F.E.A., Ngoumou, P.C., Meying, A., Gouet, D.H., Zanga, A. and Ngoh, J.D. (2020) +−Evidence of Porphyry Deposits in the Ntem Complex: A Case Study from Structural and Hydrothermal Alteration Zones Mapping through Landsat-8 OLI, Aeromagnetic and Geological Data Integration in the Yaounde-Sangmelima Region (Southern Cameroon). *Advances in Remote Sensing*, **9**, 53-84.
https://doi.org/10.4236/ars.2020.92004

Received: January 26, 2020
Accepted: June 5, 2020
Published: June 8, 2020

Abstract

A semi-regional study was carried out in the Yaounde-Sangmelima area, a densely vegetated tropical region of southern Cameroon located in the Central Africa Fold Belt (CAFB)/Congo Craton (CC) transition zone. Towards structural lineaments and predictive hydrothermal porphyry deposits mapping, an integrated analysis of Landsat-8 OLI data, aeromagnetic, geological and mineral indices maps was performed. The Remote sensing using False colour composite images involving bands combinations and Crosta method (features oriented principal components analysis) enabled the mapping of the gneisses and schists domains without a clear differentiation between the Yaounde and Mbalmayo schists; despite the reflectance anomalies evidenced NW of Akonolinga, hydrothermal alterations in the study area failed to be detected. Besides, aeromagnetics depicted a moderately fractured northern zone (the CAFB) contrasting with a high densely fractured zone (the CC,

known as Ntem complex). The Ntem complex displays signatures of a meta-igneous, an intrusive complex, greenstone relics south of Sangmelima and hydrothermal activity. Indeed, CET porphyry analysis tool detected many porphyry centres. In general, the study revealed many lineaments including contacts, fractures faults zones and strike-slips. The major aeromagnetics structures are SW-NE to WSW-ENE and WNW-ESE to NW-SE while those from Landsat-8 are NE-SW, WNW-ESE, NW-SE, WSW-ENE and NW-ESE to NNW-SSE. Together, these structures depict trans-compressions or trans-tensions corresponding to a broad NE-SW strike-slips channel that affect both the CAFB and the Ntem Complex, and they control the intrusions thus confirming a pervasive hydrothermal activity within the Ntem Complex. The proximity or coincidence of these porphyry centres with some mapped Iron-Gold affiliated mineral indices and porphyry granites indicate the possible occurrence of many hydrothermal ore deposits. These results show the high probability for the Ntem complex to host porphyry deposits so they may serve to boost mineral exploration in the Yaounde-Sangmelima region and in the entire southern Cameroon as well.

Keywords

Porphyry Centres, Hydrothermal Ore Deposits, Ntem Complex, Remote sensing, Aeromagnetics, Southern Cameroon

1. Introduction

Hydrothermalism alters rocks and provokes various types of mineralization occurring in general as polymetallic deposits (e.g. (IOCG; porphyry Cu-Au) +/− Ag, U, Mo, Pb, REE, Zn, etc). Most common hydrothermal deposits styles are intrusion related, epithermal, skarns and porphyry [1] [2] [3]. In general, porphyry deposits are hosted in Archaean to Proterozoic terrains in a convergent setting [2] [4] [5] [6]. The CAFB/CC transition zone in southern Cameroon, at the northern margin of the Congo craton (CC), in regards to its geological history, becomes good candidate host of these deposit types. Therefore, a detailed geoscience work needs to be done in this region, to assess this potential and subsequently revamp mineral exploration industry.

Remote sensing (RS) and aeromagnetics are solutions to geoscientific studies in wide and inaccessible regions. in geological RS, surface alteration controls better the reflectance of geologic materials so, high discrimination capabilities of lithology are found in the visible near infrared-VNIR and Shortwave infrared (SWIR) regions *i.e.* 0.7 to 3.0 μm interval [7] [8]. Various pre-processing and processing technique/enhancement workflows exist and are intuitively used to meet desired goals. However, the most common approaches involve whether alone or in combination, bands combination, band rationing, data dimensional reduction and image filtering (e.g. see, [8] [9] for detailed discussions). RS has become a standard tool in geological studies by highlighting faults/fractures in

structural studies [10] [11] [12] [13] [14] and in mapping lithology and/or hydrothermal alteration zones related to mineral ore deposits [15]-[20] in different geological contexts across continents. Some recent pioneer studies involving Landsat suites data have been done in Cameroon to address structural [21] hydrological [22] or lithology and mineral exploration [23] [24] [25] issues.

Aeromagnetics is a premium tool in geological and mineral exploration studies for its high capabilities in mapping structures and lithology irrespective of the terrain conditions and availability of outcrops at any scale [26] [27]. Various filtering and processing techniques have been developed for qualitative, quantitative or both, interpretation. Qualitative interpretation involves mostly the use of edge detection filters for lineaments detection and even specific features like porphyry and kimberlite bodies [27] [28] [29] [30]. Quantitative interpretation involves depth-to-basement (e.g. Euler deconvolution approaches by [31] [32]) and modelling methods which solve either or both the nature, location, shape and susceptibility of the source (e.g. see [33]). Significant contributions from aeromagnetics to update the geology of the CC/CAFB transition zone are being made by many workers [34] [35] [36], but most of these lack field evidences. In geophysics, the adjunction of at least two methods gives more consistent results; thus, we combine the strong mapping capabilities of aeromagnetics, RS so as to yield more accurate and credible results while investigating the Yaounde-Sangmelima region. The consistency of this approach has been proven by several workers (e.g. [14] [25] [37] [38]) who combined Landsat, aeromagnetic and geological data to map both hydrothermal targets, lithology and lineaments as well, in various geological contexts.

2. Geological Setting

The Yaounde-Sangmelima area is located in southern Cameroon, a region entirely dominated by the tropical dense forest with thick lateritic soil at the northern margin of the CC. The main lithological units are, southward, the CAFB and the Ntem complex (**Figure 1(a)**). according to [39] [40] [41], the Ntem complex comprises various Archaean to Paleoproterozoic rocks. Archaean formations are mainly tonalites [42] [43] [44]; calc-alkaline to alkaline granitoids and granodiorites in dominantly occurring charnockites, as well as greenstones relics [40] [45] [46] [47]. Moreover, [40] and [48] identified dolerite dykes, syenites, metabasites and gneisses as in the Nyong series as Paleoproterozoic. The CAFB regroups Neoproterozoic terranes overlying a Paleoproterozoic basement. According to [43] [49] [50] [51] (and references therein), the Neoproterozoic assemblages are: 1) dominantly garnetiferous gneisses and micaschists, amphibolites and some quartzites that form the granulitic Yaounde series; and 2) low-grade schists and quartz-sericite rocks associated with volcanic relics forming the Mbalmayo series discordant to the Ntem complex (**Figure 1(b)**).

The tectonic activity at the northern margin of the CC takes into consideration the difference in its lithological arrangement. Indeed, according to some

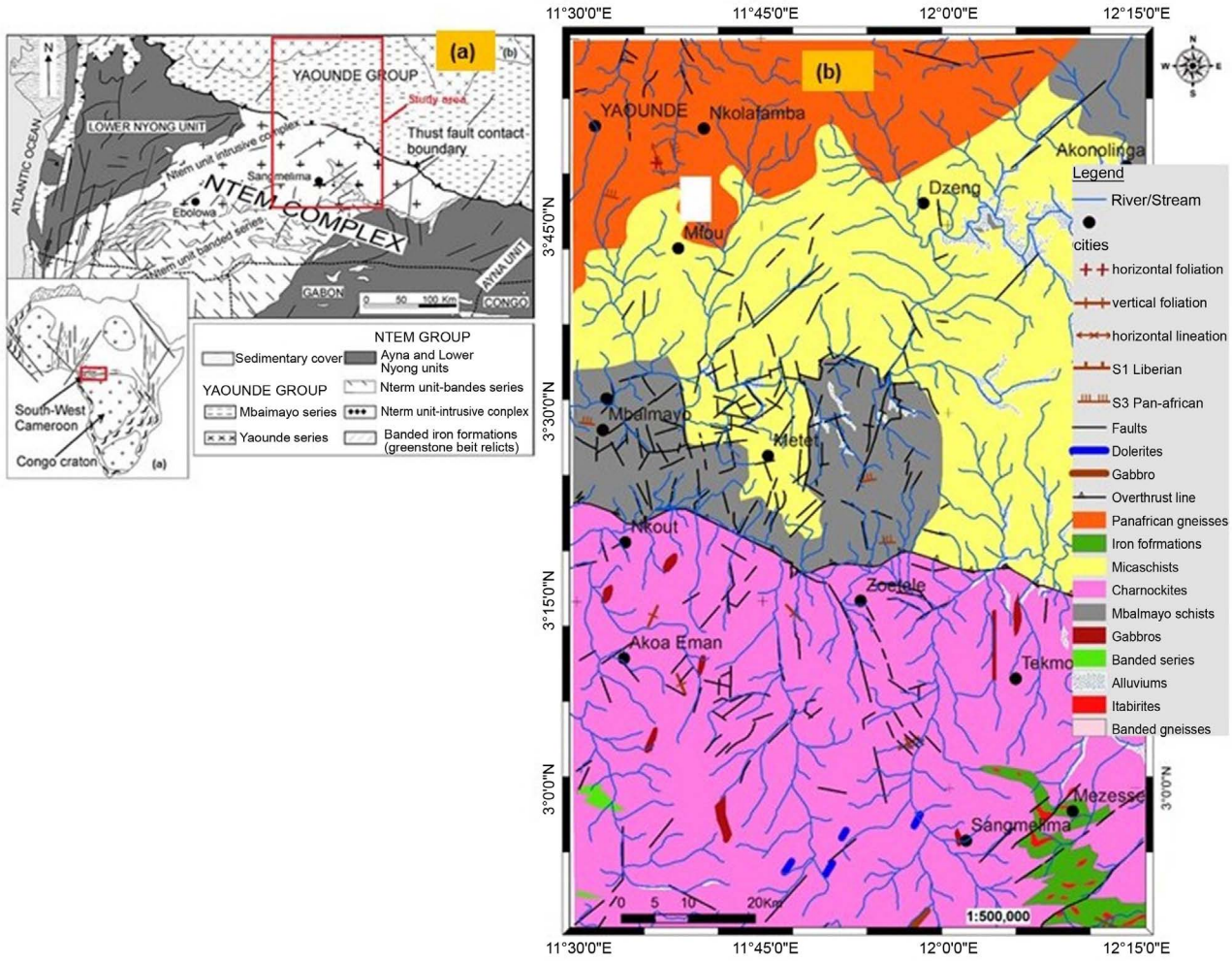

Figure 1. Local geological map of the Yaounde-Sangmelima after [42] [43].

workers the Ntem complex seems to have been first influenced by the Liberian orogeny marked by various folds and brittle structures [52] with an Archaean magmatism [45] [53]. The second main event in the Ntem complex is the Eburnean orogeny marking the Sao-Francisco Craton/Congo Craton collision [54] [55] during which NE–SW, E–W to ESE–WNW, NW–SE and N–S main lineaments formed and the crust rejuvenated at the NW edge of the CC [56] [57] [58] [59]. Obviously, this seems to be the more documented event affecting the cratonic part of the study area.

The CAFB besides is clearly affected by Panafrican and post-Panafrican tectonics. Previous studies identified four Panafrican deformation stages (e.g. [60] [61] [62]). In the Yaounde group, [63] summarised it into the thrusting of the CAFB nappes onto the followed by ENE-WSW strike-slips. These tectonics caused by overall dextral transpressions due to alternating E-W to NW–SE contractions and N-S to NE–SW orogenic-parallel extensions [62] generated N or S penetrative foliation associated with ENE-WSW stretching lineation and a N-S to NE-SW folding. However, this evolution is still debated (see e.g., [50] [64] [65] [66]), regarding the collisional system, the location and direction and the

geodynamic history of the Yaounde domain. Despite some relevant interpretations of the faults/fractures that they discovered (see e.g. [67] [68]), most geophysical studies fail to reconcile the aforesaid matters as they don't propose structural history of the northern margin of the CC based at least on these mapped features. Also, insufficient geophysical works towards predictive mapping of the ore minerals potentialities in the CAFB/CC transition zone have been done. This paper brings contributions to resolve the two above outstanding points through an integrated analysis of remote sensing, aeromagnetic and geological data over the Yaounde-Sangmelima region.

3. Data and Methods

3.1. Geological Datasets

The geological information used for this study comes from the official maps of the Republic of Cameroon that cover the Yaounde-Sangmelima area. To obtain a digital geological database, these maps were initially georeferenced, then warped in Google map for geographical rectification; then lithological, structural and mineral indices information was extracted through ArcGIS desktop 10.6.

3.2. Remote Sensing Method

3.2.1. Data Description and Preparation

The satellite data used are SRTM and Landsat 8 Operational Land Imager (OLI). SRTM are topographic data that model the elevation of a given surface relative to the sea level. They are availed as 1 × 1 degree scenes at a 30 m spatial resolution. OLI is a multispectral sensor on board of the Landsat 8 satellite whose bands characteristics are summarised in Table 1.

These are standard geometrically corrected (L1T1) images projected on the corresponding UTM zone freely available from the Global Land Cover Facility portal (*http://earthexplorer.usgs.gov/*). The current study uses two adjacent scenes whose respective path/row identifications are 185/057 and 185/058, recorded on the 12th January 2015 at approximately 09h 45 min. The two OLI scenes underwent a 3-steps preparation pre-processing stage consisting in:

Table 1. Landsat 8 OLI images characteristics [68].

Band Number	Spectral range (μm)	Spectral band	Resolution
1	0.43 - 0.45	Coastal blue	30 m
2	0.45 - 0.51	Blue	30 m
3	0.53 - 0.59	Green	30 m
4	0.64 - 0.67	Red	30 m
5	0.85 - 0.88	NIR	30 m
6	1.57 - 1.65	SWIR-1	30 m
7	2.11 - 2.29	SWIR-2	30 m
8	0.50 - 0.68	Panchromatic	30 m
9	1.36 - 1.38	Cirrus	30 m

1) The radiometric calibration for atmospheric correction to remove the influence of the atmosphere and haze, and conversion of digital numbers of each individual scene into surface reflectance which is physically meaningful for earth objects investigation. The operation was realised using the Quick atmospheric correction (QUAC®) which determines atmospheric correction parameters directly from the observed pixel spectra in a scene, without ancillary information.

2) Vegetation suppression by removing the signal related to the canopy on each individual scene in order to produce a multispectral image that mimics the surface reflectance without vegetation.

3) the mosaicking of the pre-processed scenes, then spatially subsetting the mosaicked image to the study area and reducing its spectral dimension by removing the coastal band (band 1) which is not useful in geology.

3.2.2. Multispectral Images Processing Methods

Colour composition. Colour composition is an image enhancement technique which consists in combining natural or hybrid bands (e.g. band ratios, eigenvectors, etc.). When using natural bands, the appropriate bands combinations were determined using the optimum index factor (OIF) initially designed by [69] statistically determines the most appropriate combinations represented by the highest OIF ranking as presented in **Table 2**.

These combinations were used to map the lithology of the Yaounde-Sangmelima area, by undelaying the SRTM map to identify changes in texture (**Figure 2(a)**).

Principal components (PC) analysis. The PC transform segregates noise components, decorrelates and reduces the dimensionality of data sets. The dimensionality reduction removes the redundancy in the dataset, yielding uncorrelated hybrids bands (PC bands) which concentrate maximum information from the multispectral data. [70] developed a feature-oriented PC (FPCS) approaches to focus on specific goals (minerals). The principle consists in the calculation of PCs from a specific group of bands containing information on the sought feature then select the most informative FPC band. The FPCS were calculated in the bands (2, 3, 4, 5) for iron oxides and hydroxides detection; and in the bands (4, 5, 6, 7) for clays (OH). The resulting FPCS are presented in **Table 3**.

Lineaments extraction. To map lineaments, the greyscaled standard PC1 image is high-pass filtered using a 3 × 3 window to reduce noise and enhance

Table 2. OIF ranking showing the highest five statistically convenient FCC images.

OIF Highest ranking			
Band 7	Band 6	Band 2	0.51
Band 7	Band 6	Band 3	0.47
Band 7	Band 5	Band 2	0.44
Band 6	Band 5	Band 2	0.42
Band 6	Band 3	Band 2	0.38

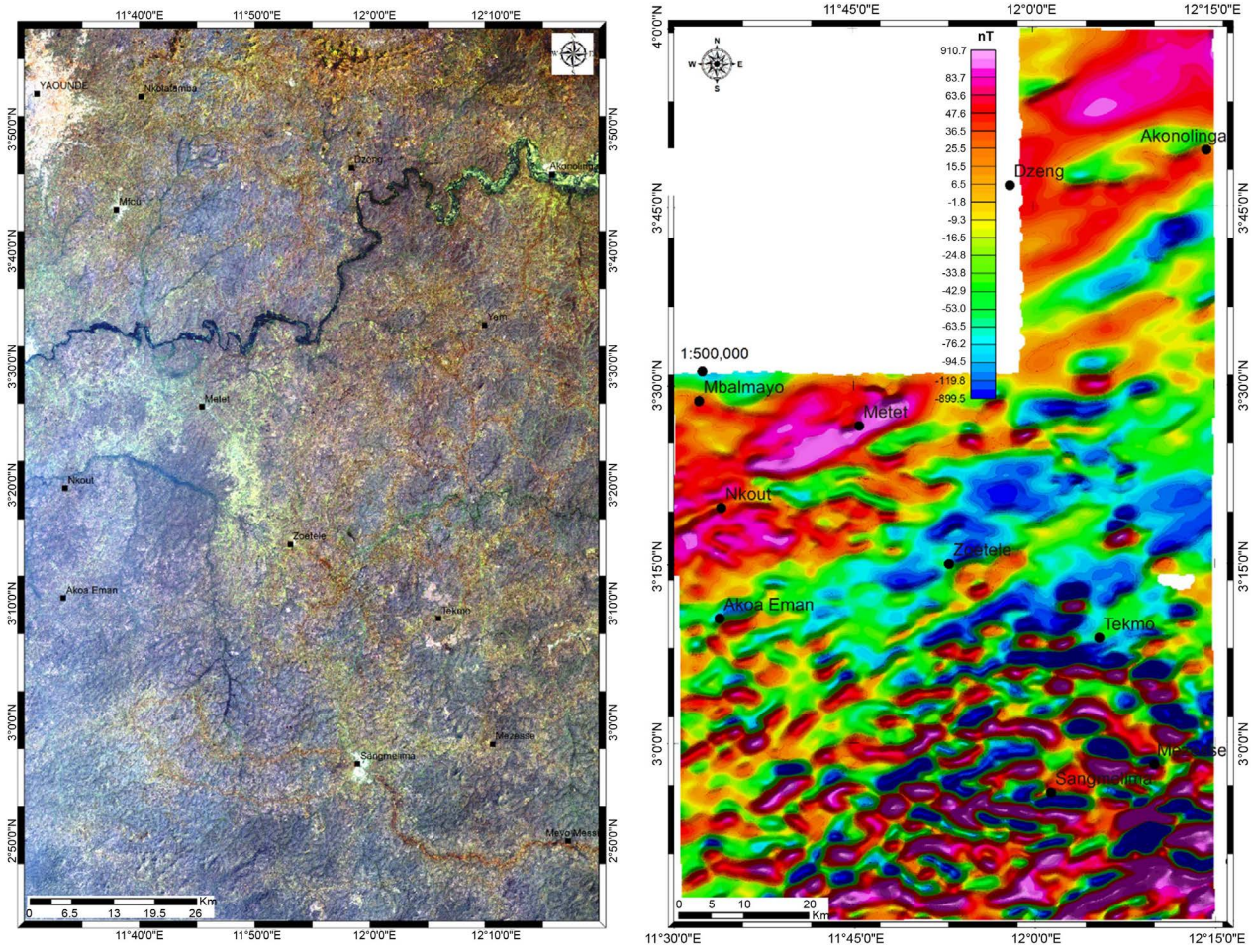

Figure 2. (a) Natural colour composite (RGB432) with the vegetation suppressed. The image mimics the soil surface reflectance. (b) Magnetic anomaly field reduced to the equator. The map has a NE anomaly passing through Metet depicting a discontinuity affecting both the CAFB and the Ntem Complex.

Table 3. Feature-oriented PCs for respectively clays (PCOH) and iron (PCFe) oxides/hydroxide minerals.

(a)

	PCOH			
	Band 2	Band 5	Band 6	Band 7
PCOH1	0.246	0.412	0.578	0.660
PCOH2	0.887	0.259	−0.174	−0.339
PCOH3	0.389	−0.826	−0.042	0.407
PCOH4	−0.036	0.285	−0.796	0.532

(b)

	PCFe			
	Band 2	Band 3	Band 4	Band 5
PCFe1	0.521	0.471	0.501	0.506
PCFe 2	0.763	−0.067	−0.086	−0.638
PCFe 3	0.382	−0.456	−0.555	0.581
PCFe 4	−0.026	−0.752	0.658	0.022

edges. The filtering is performed on Envi 5.3 platform. The features extraction involved a semi-supervised classification that consists in 1) automatically detect lineaments from the high-pass filtered image of PC1 using the Canny edge filter within the LINE module in PCI-Geomatica 9.0 software. Later, 2) the image of the computer extracted features is underlain by the digital elevation model generated from the SRTM data above the area, to manually extract the lineaments using the photo-geological approach.

3.3. The Magnetic Method

3.3.1. Data Description and Preparation

The study utilises aeromagnetic data collected in January 1970 during a nationwide campaign held in Cameroon. The flight paths flown at a nominal altitude of 235 m, were spaced at 750 m and oriented S-N. major equipment consisted in a radar altimeter of 20 m precision. The field data were processed by Paterson Ltd and availed as total field maps at 1/50,000 scale. The total magnetic intensity (TMI) anomaly field was obtained by removing the geomagnetic field that pertained in 1970; assuming a mean declination of −18.2˚ and a mean inclination of −6.2˚, Reduction-to-the magnetic equator (RTE) transform was applied to the anomaly field to shift anomalies on top of their sources [29]. The resultant RTE map (**Figure 2(b)**) served as input for further analyses.

3.3.2. Magnetic Data Processing and Interpretation

Analytic signal method. The analytic signal (AS) is formed through the combination of horizontal and vertical gradients of a potential field [29]. Introduced by [71] to solve the depth and position of the anomaly sources in the 2D case, [72] extended the method to solve 3D problems on gridded data. The AS is used either as a mapping and depth-to source technique and as a way to learn about the nature of the causative magnetization [30].

The horizontal gradient method. The horizontal gradient method (HGM) is in many ways the simplest approach to estimate contact locations of the bodies at depth and it is advantageously less sensitive to the noise in the data because it only requires calculations of the two first-order horizontal derivatives of the field [29]. The HGM function gives a peak anomaly above magnetic sources which will be interpreted as lineaments [30] [73]; HGM peaks can be evaluated at different the upward continued heights, leading to a multiscale analysis [74]. The multiscale HGM is commonly has been used in lineaments mapping by several workers using magnetic or gravity data in structural investigations [27] [75] [76] [77].

CET Porphyry analysis. The CET Porphyry analysis tool was developed by the Centre for Exploration Targeting (CET), an Australian research group addressing mineral exploration industry problems. Developed by [78], this tool relies on the fact that an ideal porphyry hydrothermal mineralisation typically appears as a circular central intrusion surrounded by concentric circular alteration zones. The detection process involves sequentially applying: 1) the circular feature transform which uses a radial symmetry transform algorithm to detect cir-

cular shaped (elevated or depressed) features by identifying where image gradients converge or diverge respectively. 2) Performing central peak detection; and then visualising the feature boundaries using the amplitude contrast transform and the boundary tracing using a spline energy function that specifies porphyry boundaries.

The preparation and processing of Landsat 8 data was done in Envi 5.3 and lineament were automatically extracted with PCI-Geomatica v9.0; all the magnetic data preparation and processing was done in Oasis montaj 8.4. Maps were finalised and edited with ArcGIS 10.6 and Rockworks 16 served to draw lineaments rosaceas.

The work methodology consisted in detecting key lithology, zone of hydrothermal activity and lineaments from remote sensing and aeromagnetics, separately; then making a fusion and cross-validation of the results between the two methods at a first stage, and the final outputs are validated by the available geological data to yield the more plausible map of structural lineaments and porphyry deposits in the study area. This methodology is summarised by the flowchart (**Figure 3**).

4. Results

4.1. Lithology Mapping

4.1.1. Colour Composite Images Analyses

The true colour composition (**Figure 2(a)**) makes it difficult to outline specific

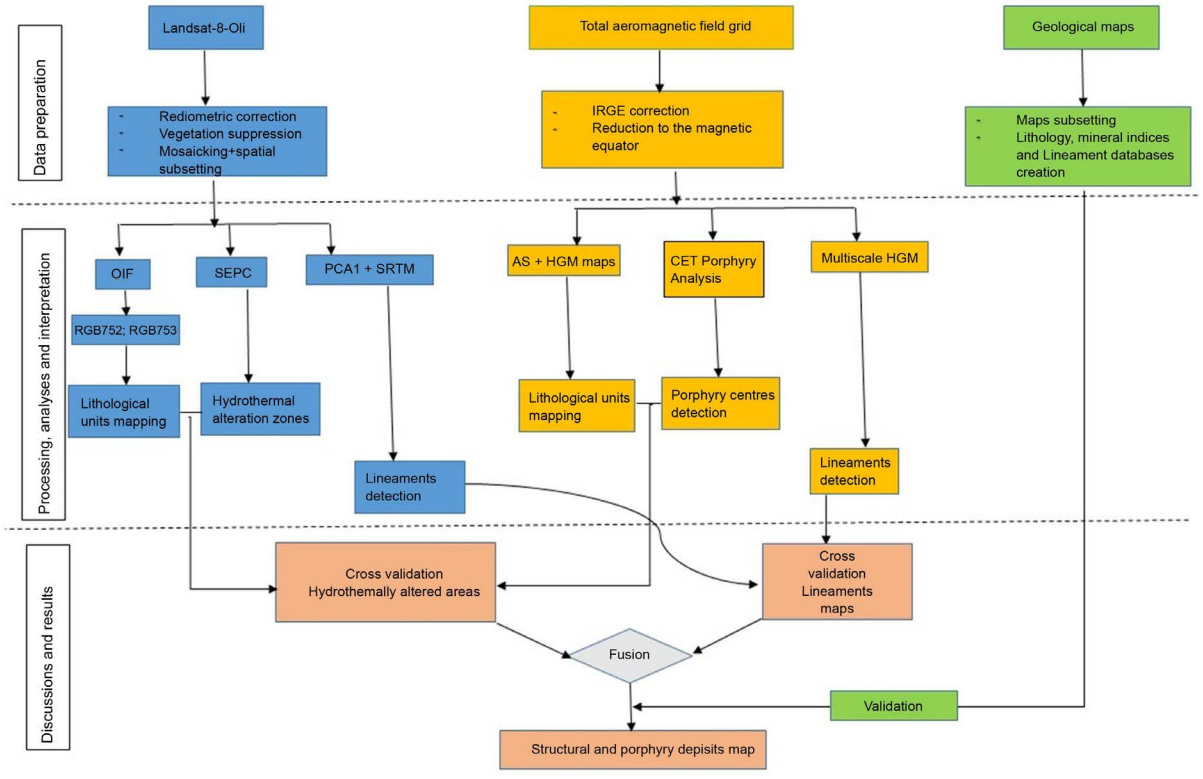

Figure 3. Flow chart summarising the methodology of work.

lithology. The overall coloration is marked by dark tones showing that the lithology is made up of only metamorphic crystalline rocks. The FCC involving the bands 752; 753 in the RGB order (Figure 4) outline well the gneiss formations in the northern part of the study area as a yellow (Figure 4(a)) or a reddish (Figure 4(b)). These colours are due to high absorption of probably iron oxides, micas, feldspars and amphibole minerals in the SWIR bands. These minerals are dominant in gneisses. The gneiss rocks have a south boundary formed by a broad NE-SW line passing south of Yaounde and west of Akonolinga which seems to correspond to the gneiss/schists formations boundary in the Neoproterozoic domain.

The FCC maps (Figure 4) show south and east of gneisses as a mix of dark, dark reddish and dark blue tones with some greyish patchworks. The dark shades of blue may be characteristic to the presence of minerals such as calcite, muscovite, dark minerals, fine grains of pyrite and graphite. Reddish tones may be caused by the presence of ferric oxides, chlorite and amphiboles while the greyish tones throughout the entire map result from the reflection in all the

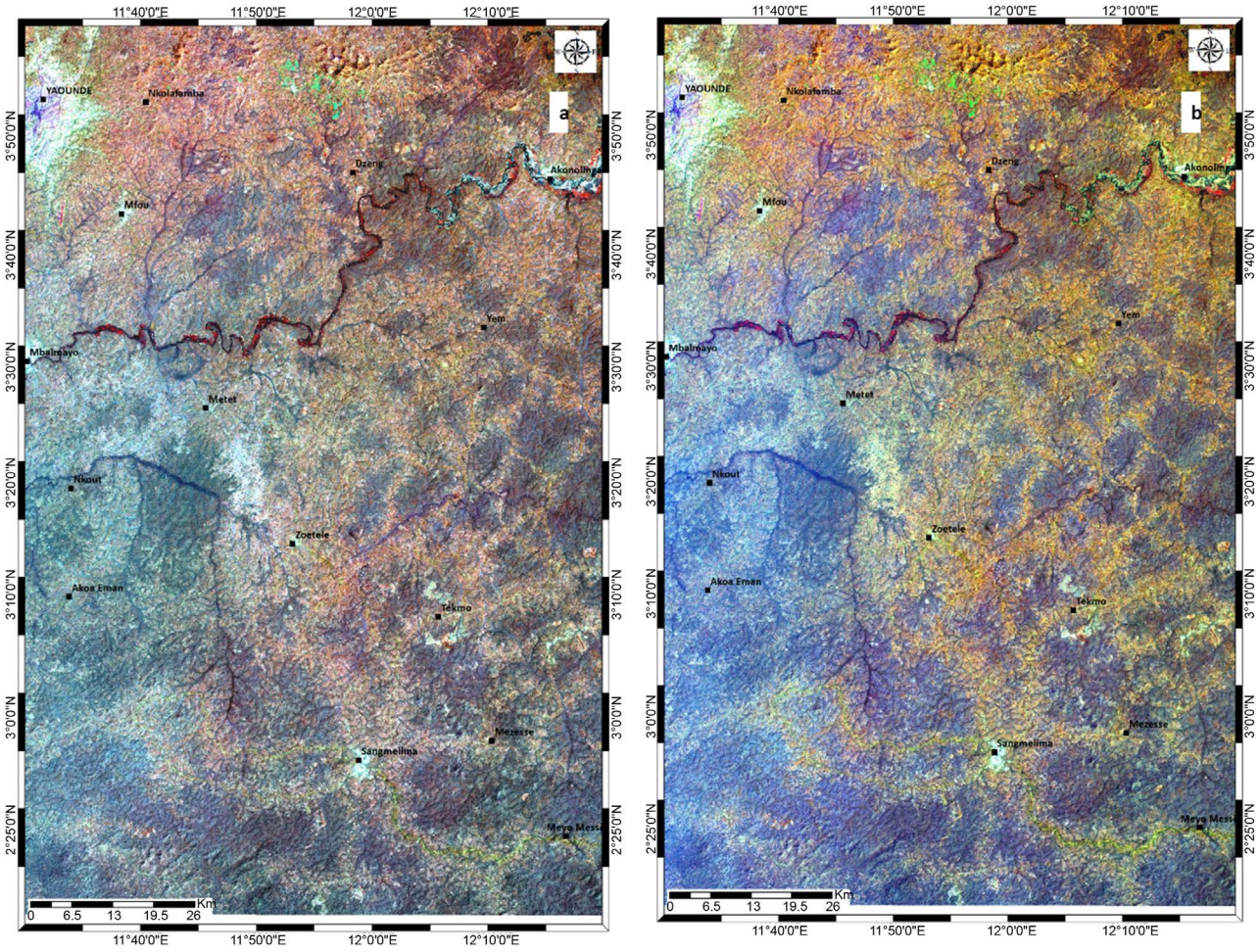

Figure 4. False colour composites (a) RGB752; (b) RGB753. The two images clearly outline the Panafrican gneisses (reddish) and schists (dark red) in the north of the study area.

bands characterising quartz-rich minerals (quartzites). The candidate rocks here are quartz-muscovite schists, pyritic or graphitic schists and quartz-schists. In the schists region, the boundaries between the varieties of schists are diffuse because they are mixed. Thus, they probably form the same schists belt.

South of Nkout (Figure 4), discrimination of the Ntem complex rocks is not obvious. However, the Akoaeman zone, exhibits dark blue tones with patchwork of pale blue to cyan and pale greenish which probably correspond to tonalites. In the Sangmelima zone, the tones are pink to reddish due to high SWIR and medium to low reflectance in bands 5 and 2 or 3 of amphiboles, feldspars, micas, pyroxenes and olivine minerals. This suggests the existence of an igneous or meta-igneous complex, probably the granites/granodiorites and other mafic to ultramafic or subcrustal materials herein. These rocks are better evidenced by magnetic data.

4.1.2. Aeromagnetic Qualitative Analyses

Magnetic data (Figure 5) differentiate Panafrican terranes to the north from CC rocks to the south. The Panafrican domain appears as a quiet magnetic background (low HGM and AS values, Figure 4) with some anomaly peaks around

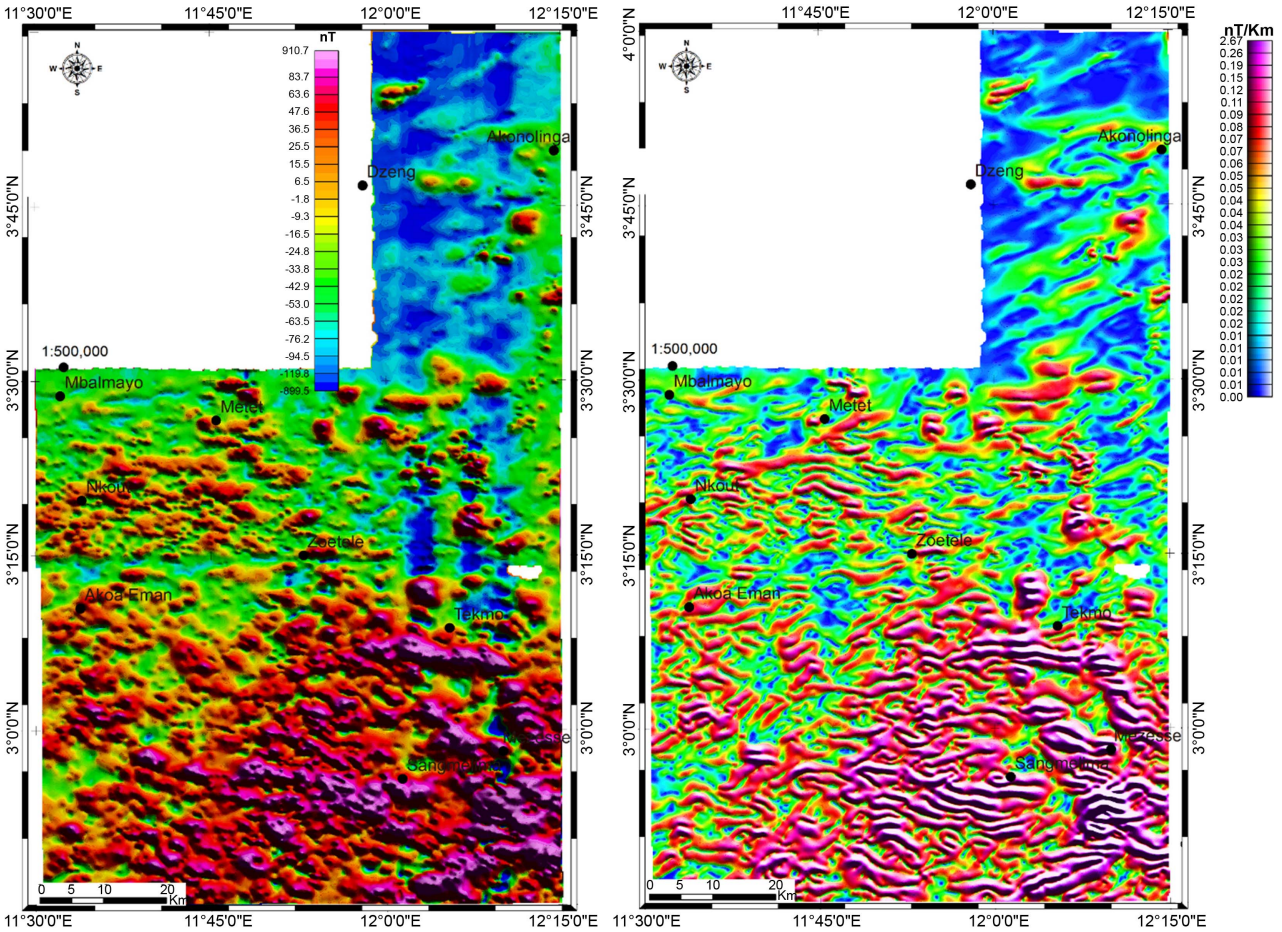

Figure 5. (a) Analytic signal and (b) Horizontal gradient magnitude maps.

Akonolinga, around Metet, probably due to intrusions or deep faults or fractures affecting the Paleoproterozoic basement of the CAFB. Southward from Nkout, an area of HGM intermediate anomalies represents the Ntem complex TTGs, gneisses and other granitoids. The AS and HGM anomaly peaks surrounding Sangmelima (**Figure 5**) possibly charnockites and many other mafic to ultramafic or subcrustal contributions into the local rock budget recognised as greenstones belt relics. The TTG/Charnockites boundary is sub-circular east to north, and NE-SW, west of Sangmelima.

The refinement from the AS map reveals a sparse occurrence of intrusions in the CAFB (except at, and, east of Metet) whereas the Ntem complex has more intrusions (**Figure 5(b)**). The high number of sub-circular anomaly peaks interpreted as various age intrusions is a possible imprint of a hydrothermal activity which was high in charnockites, moderate in the TTG and low in the CAFB. Particularly, we interpret this poor occurrence of intrusions in the schists/TTG boundary as an evidence of a discrete influence of the Panafrican event on the CC.

4.2. Lineaments Detection and Interpretation

Quantitatively, the remotely sensed data analysis (**Figure 6(a)**) enabled to highlight more (863) lineaments than the aeromagnetics. These lineaments make a cumulative length of 3843.90 km, for a minimum length of 0.56 km, a maximum length of 21.73 km and a corresponding average length of 4.67 km. Qualitatively, the major lineaments in the CAFB follow the WNW-ESE to NNW-SSE and NNE-SSW directions in gneisses; and the WNW-ESE and NNE-SSW to NE-SW, directions in schists. In the Ntem complex, the major lineaments are oriented NE-SW and NW-SE. These lineaments describe locally, contacts, faults, folds, dextral (e.g. Yaounde-Mfou area) or sinistral (e.g. Zoetele-Sangmelima) shear zones or strike-slips.

The aeromagnetic data analysis over the Yaounde-Sangmelima area evidenced various lineaments (**Figure 6(b)**). The main directions they follow are NE-SW to ENE-WSW, NW-SE to WNW-ESE and N-S. These probably correspond to folding traces, fracture, faults, dykes or geological contacts between major formations. The continuation of these lineaments clearly shows that some of them are faults affecting both the CAFB and the Ntem complex.

Together, remote sensing and magnetic lineaments (**Figure 9**) highlight the dominance of the NE-SW, NW-SE and N-S directions with some local variations (WNW-ESE, ENE-WSW, NNW-SSE and NNE-SSW). Putting aside all the secondary and minor lineaments, the major lineaments form throughout the whole Yaounde-Sangmelima region a broad NE-SW network of faults that affect the deep basement of both the Ntem complex and the Yaounde Group. Thus it would had formed before the emplacement of the Yaounde Group that it affected through post emplacement reactivations. These NE-SW lineaments intersect or are intersected by N-S and WNW-ESE to NW-SE lineaments which make

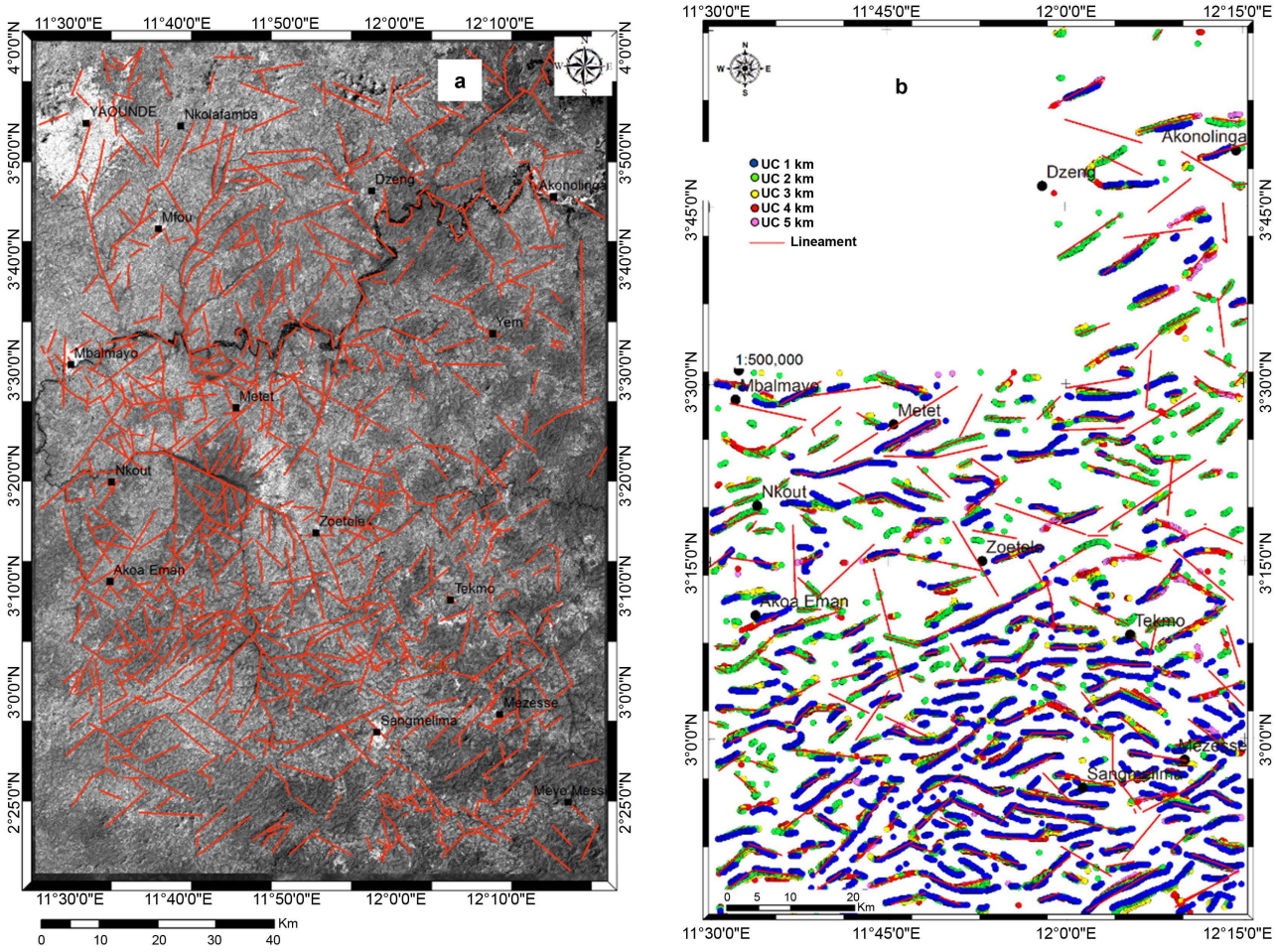

Figure 6. (a) Landsat 8 sensed lineaments; (b) Magnetic lineaments from HGM.

it interpretable as a major sinistral shear concupiscent to transpressional movements both the Ntem complex and the Yaounde Group. Moreover, there is a family of major WNW-ESE and E-W lineaments that form an E-W band between Mbalmayo and Tekmo that can be interpreted as the CAFB/CC southern limit, a faulty contact that represents the thrust line of the CAFB/CC along which visible WNW-ESE to NW-SE strike-slips of shear movements seems to have occurred.

In the CAFB, the subparallel lineaments are relatively widely spaced, as a result of a gentle folding of gneisses and schists probably resulting from a less intense compression in the southern part of the CAFB. The folds and faults as well as other fractures and shear zones (e.g. the area is affected to the north by NE-SW dextral strike-slips-see **Figure 6** and **Figure 9**) observed, suggest that the deformation conditions were ductile to brittle-ductile and the variability in their directions is an imprint of a multi staged and intense tectonics. Indeed, these lineaments in the CAFB result from the Gondwana amalgamation (Neoproterozoic) and breakup (Atlantic Ocean formation), and to the actual Somali Plate individualisation (East African Rift spreading) and the Africa/Eurasia Plates con-

vergence tectonics.

In the Ntem complex, some lineaments are assumed to be Archaean, while other are may be related to:

1) The Eburnean event in Paleoproterozoic causing the development (or reactivation of pre-existing faults) of the SW-NE to WSW-ENE and WNW-ESE to NW-SE faults affecting both the Ntem complex and the Paleoproterozoic basement of the future Yaounde Group. These appeared as a response to pertaining compressional and extensional movements. This would lead to the development of strike-slips that would constitute the paleo senestrial SW-NE shear zone as revealed by this study in the Yaounde-Sangmelima area.

2) The rifting at the northern edge of the Congo Craton caused by the detachment of the Adamawa-Yade block that led to the development of the Yaounde basin. During that rifting the faults above may have acted as a transform faults system where the SW-NE to WSW-ENE faults are in the spreading direction. The WNW-ESE to NW-SE faults and fractures would line up with the rift axis and later become the southern CAFB/Congo Craton limit depicted by the set of WNW-ESE faults that form an E-W lineament around latitudes N03˚20' and N03˚17'.

It is then evident that all the brittle structures outlined in the study area are either newly created or reactivated, depending on the stress and strain regimes upon the northern margin of the CC from Archaean to Cainozoic.

4.3. Hydrothermal Alteration Zones Mapping

4.3.1. Feature Oriented PCs

The application of the Crosta technique for the detection of clays and iron oxides anomalies led to **Table 3**. Clays are traced by the behaviour of the hydroxyl (OH) group in the Clay band (SWIR region) where it has a high reflectance in the SWIR 1 and a strong absorption in SWIR2. Scrutinising the loading of each band for the four FPCs obtained for the OH (**Table 3(a)**), for PCOH4 band 6 contributes at −0.796 and band 7 loading is 0.532, in line with the above comments. By inverting PCOH4, clayey zones will be observable as pale grey to white pixels in the southern part on the PCOH4 grey-scaled image (**Figure 7(a)**). In the north, alluvia in the Nyong River appear bright white in Akonolinga, whereas an anomalous clayey zone is visible west of Akonoloinga.

Regarding the detection of iron-rich minerals, in **Table 3(b)**, PCFe4 is characterised by a high loading from band 4 (0.658) related to a high reflectance and a very low contribution from band 2 (−0.026) corresponding to a very strong absorption. This is characteristic to the presence of iron-rich minerals which generally have a very high reflectance in the red band and a strong absorption in the blue band. Therefore, iron oxide targets will appear as greyish to dark pixels on the grey-scaled image. But the PCFe4 is influenced by the high loading from band 3 (green) due to the dense canopy in the area what makes them almost no detectable (**Figure 7(b)**).

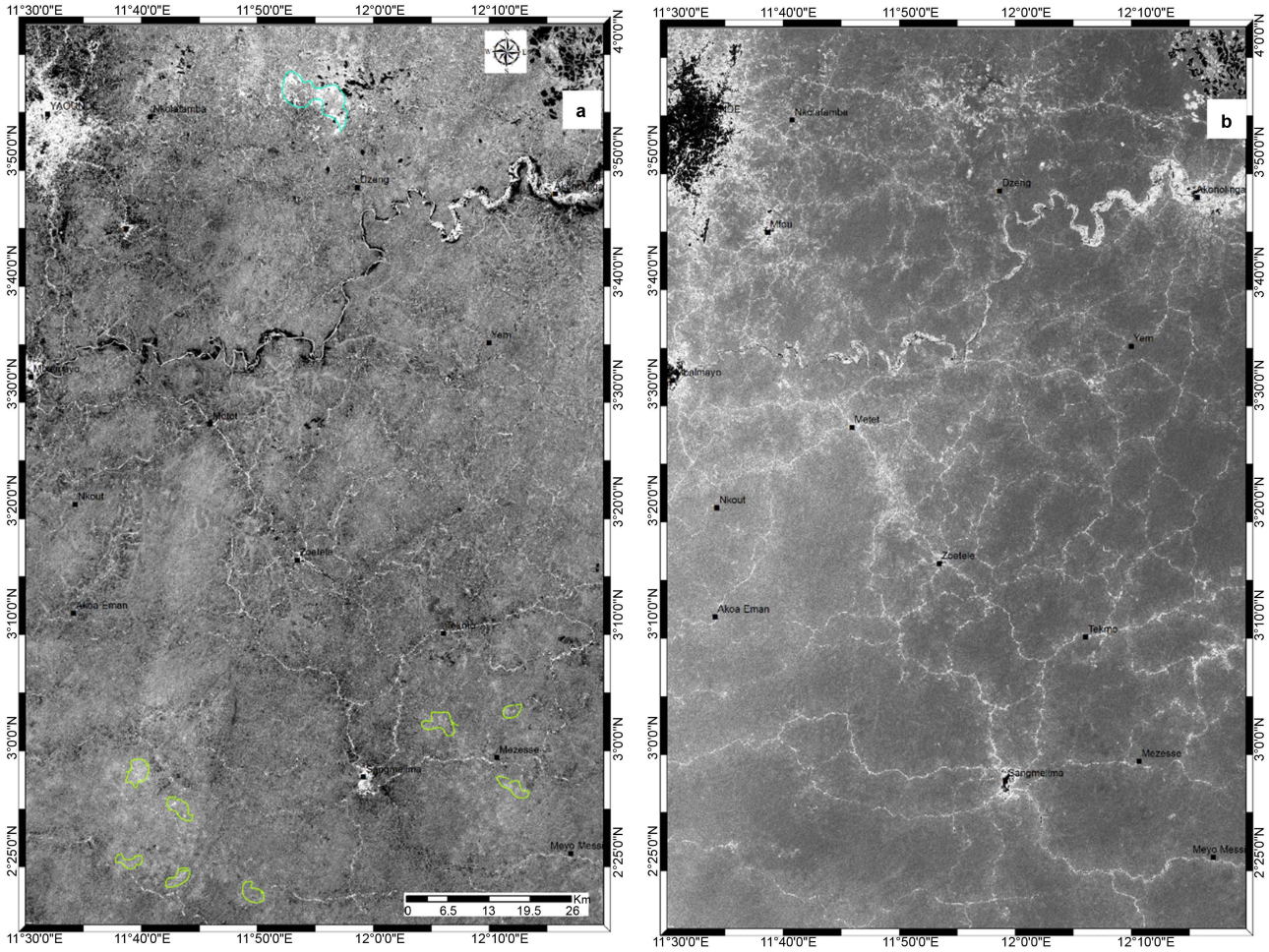

Figure 7. FPCS maps of the study area. (a) FPCOH1 and (b) FPCFe2 highlighting respectively, clays and iron oxides.

4.3.2. Porphyry Centre Detection from Magnetic Data

The application of the CET-porphyry detection tool on magnetic data led to the mapping of a total of 66 centres porphyry centres which correspond to intrusive bodies that occur in the study area (**Figure 8**). The straight visible point is that 61 of these centres are located in the Ntem complex and the remaining 5 centres (*i.e.* 7.58% of the gross total) are located in the Yaounde Group of the CAFB. Of the porphyry centres mapped in the CAFB domain, 3 centres are found in schists, in the vicinity of the schists/TTG boundary while the 2 other centres are located at this boundary. As a result, we interpret this very low occurrence of porphyry centres as an evidence of the absence of magmatic activity within the Yaounde Group in general, suggesting that no hydrothermal alteration of the Neoproterozoic rocks of the Yaounde and Mbalmayo series.

Contrasting with the CAFB domain, the Ntem complex records.92.42% of the porphyry centres of the study area (**Figure 8**) but their variable distribution depends on the change in the nature or composition of its main rocks formations. Indeed, the results enable to distinguish an area of less dense occurrence of porphyry centres (21 centres) from an area of more densely populated (40) porphyry centres which corresponds to what is hitherto regarded as an intrusive

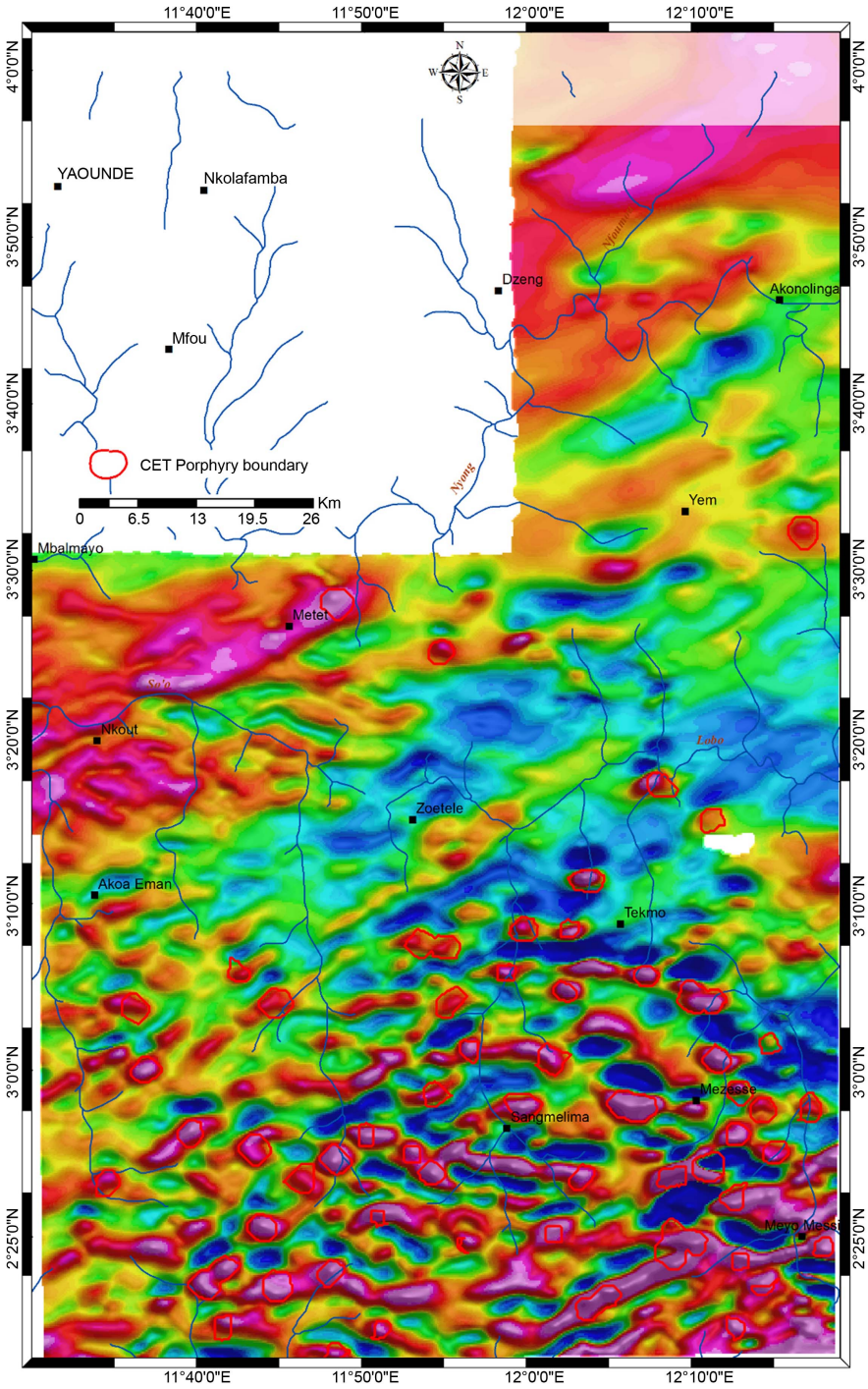

Figure 8. Porphyry domains overlain on the RTE map.

complex, in regards with its dramatically high porphyry centres percentage (60.60% of the gross total). This intrusive complex merely corresponds to the charnockites, whereas the less densely populated area seemingly matches the intrusive TTG of the Ntem complex. This location of intrusive bodies within the TTG and charnockites complex shows that the Panafrican orogeny did not affect or slightly affected the Ntem complex. It can also show that no magmatic events

occurred in the Ntem complex in relation with the Panafrican event but they are rather pre-Panafrican and possibly not tectono-metamorphic.

5. Discussion

5.1. On Lithology Mapping

The lithology mapping from remote sensing confirmed the metamorphic character of the basement lithology as they are generally visible in dark shades in the true colour composition. The reflectance signatures in the north of the study area (**Figure 4(a)**; **Figure 4(b)**) has been interpreted as corresponding to a mixture of garnet, biotite, amphibole, quartz, kyanite, feldspar and chalcopyrite. These minerals are constituents of Panafrican gneisses of the Yaounde Group [42] [79] and various age gneisses worldwide. Besides, mix of dark reddish, dark blue, dark greenish and greyish tones in metamorphic rocks in general indicate the presence of muscovite, calcite, feldspars (orthoclase and albite), garnets, chlorite, quartz along with accessories minerals such as iron oxides, tourmaline or zircon [42] [44] [80] This has been globally interpreted as schists (quartz-muscovite schists, quartz-schists and muscovite schists) and quartzites in accordance with [42] [43] [65]. Moreover, the study was incapable of differentiating the Mbalmayo schists from the schists of the Yaounde series based on the spectral reflectance. This unquestioned differentiation to date, was recognised by pioneer studies (e.g. [43]) on the southern member unit of the CAFB which consider the Yaounde Group as made up of two distinct series: 1) the Yaounde series (gneisses + micaschists) and 2) the Mbalmayo schists. One probable reason of the inability of this study to clearly distinguish the schists of the Yaounde series from the Mbalmayo schists is that they may belong to the same unit, hence differences between them would account for simple variations observed in a same schists belt. Till date, only works by [44] are supportive of this point of view so, more geochemical studies in the schists formations of the Yaounde Group need to be carried out for clarifications.

The discrimination in between the Ntem complex rocks was not evident from the RS analysis (**Figure 2(a)**; **Figure 3(a)**; **Figure 4(b)**). In fact, their close mineralogical content provides them with almost the same signature, possibly because the rocks of the Ntem Complex derive from the same igneous protolith [47] [53]. Thus the igneous nature of these rocks favoured their mapping and differentiation through aeromagnetics. Indeed, the complementary use of aeromagnetic data permitted to segregate Tonalites TTG from an intrusive complex of granodiorites and granites centred on Sangmelima as well as greenstone relics documented from previous works (e.g. [43] and references therein). Moreover, from the HGM and the AS maps (**Figure 5**) and integrating the available geological information in the area [43], the study inferred, other greenstone relics south of Sangmelima in the intrusive complex. The same approach was used by [81] to highlight new greenstone relics northeast of those of the geological map. Highlighting another greenstone relic is a contribution in updating the reference geological map of southern Cameroon and it increases the mineral interest in the

Ntem Complex.

5.2. Structural Mapping and Geodynamic Evolution at the Northern Margin of the Congo Craton

The study highlights in the Yaounde-Sangmelima region, many fractures and faults that affect both the Ntem Complex and the CAFB. The directions of the major structures are mainly SW-NE, WNW-ESE, NW-SE, SSW-NNE, WSW-ENE and N-S. The remote sensing results are consistent with magnetic results (**Figure 9**). These structures and directions are consistent with previous studies [25] [35] [82] [83] [84] [85] in the area and at the vicinities. Indeed, these works have highlighted many faults or fractures interpreted as tectonic accidents affecting the CC, the basement of the CAFB domain without providing a real explanation on the faulting history or kinematics to help understanding geodynamics at the northern margin of the CC.

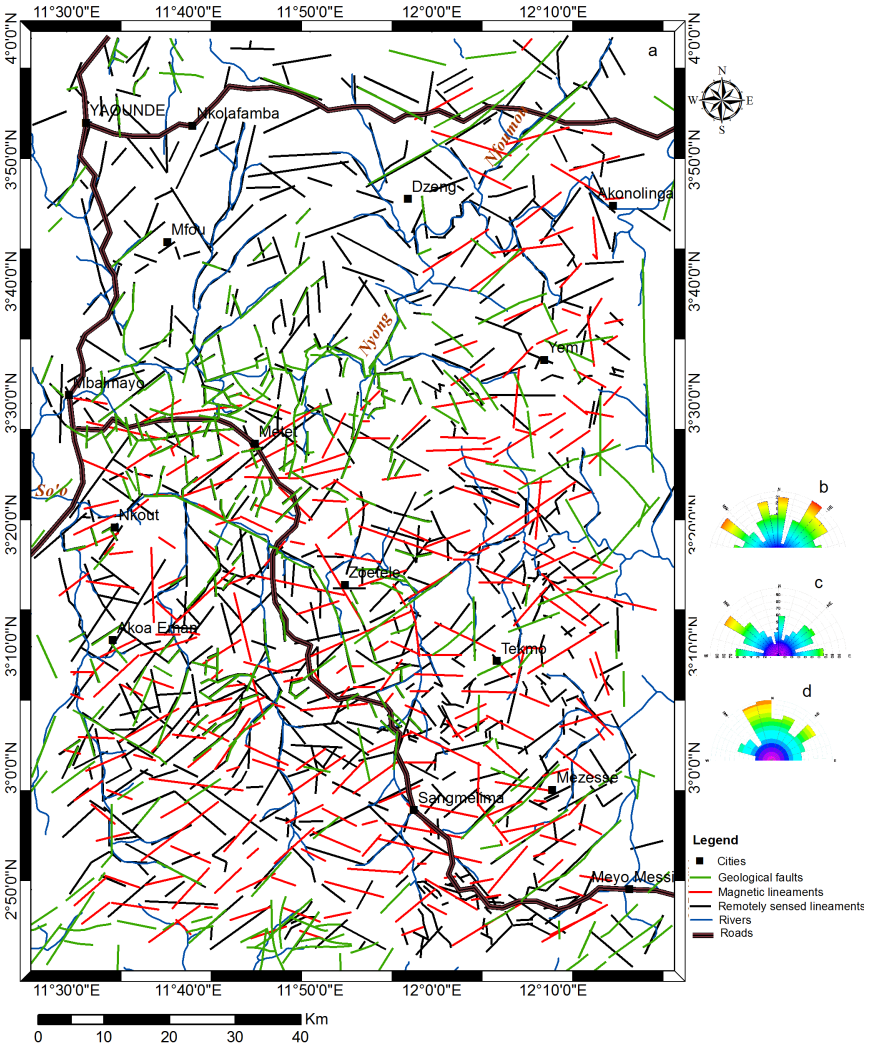

Figure 9. Lineaments map of the study area showing the correlation between previous geological (green lines), the magnetic (red lines) and the remotely sensed (black lines) lineaments. Respective rose diagrams (b, c, d).

This study proposes that the NE-SW to WSW-ENE major faults/fractures affecting both the Ntem complex and the CAFB are within a single paleo shear zone which have controlled deformations at the northern margin of the Congo Craton from the Archaean to the Precambrian and further in the Cenozoic. This confirms the idea recently suggested by [86] and correlates the shear zones highlighted by [82] in the Sangmelima area that we suggest it belongs to the network from this paper. The sinistral shear movements in the Ntem Complex are pre-Panafrican as suggested by the orientation of the greenstone relics (**Figure 1**). The weakening of the Ntem complex crust in response to resurgence of various tectonothermal events [53] [87] may have led to the setting of the NE-SW lineaments during the Eburnean orogeny and the maturation of the ESE-WNW to E-W faults affecting the paleo Proterozoic basement, that would later form a rift at the northern margin of the CC.

Rifting at the northern margin of the CC has been recognised by [65] and [86]. Therefore, the NE-SW to WSW-ENE fractures and faults affecting both the Ntem complex and the Paleoproterozoic basement of the CAFB to the north, would be the structures guiding the spreading direction of the Yaounde basin. Rifting and limited oceanisation was related with the late Paleoproterozoic to early Neoproterozoic detachment of the Adamawa-Yade block from the CC before the Panafrican orogeny [88]. So, the collapse of the basement evidenced by [85] [89] [90] under the Yaounde group are imprints of these extensional processes at the northern and southern margins of the Congo continent due to the circum-Congo subduction zone depicted by [91] in his reconstruction of the Rodinia supercontinent at ca 1000 Ma. Hence, the stress from the northern branch of the circum-Congo subduction zone would cause the opening of the Paleoproterozoic reworked crust at a weakened cratonic zone north of the CC, the metacratonised Ntem Complex [92], to form the Yaounde basin. The ESE-WNW to E-W faults south of Mbalmayo and north of Tekmo define a main E-W lineament corresponding to the southern CAFB/CC boundary (thrust line). The vertical to subvertical geometry of this faults [43] [66] [79] may have been acquired when they development during the rifting and probably remained unchanged thus inherited from the aforesaid rifting. In this case, that would justify the absence of Panafrican schists relics on top of the Ntem Complex (even at the vicinity of the CAFB/CC south boundary) as pointed by [42] [79]. Also, this geometry preservation raises the question on the involvement of the CC during the Panafrican orogeny at its northern margin.

Despite the need of more structural and petrophysical data at the vicinities of the CAFB/CC south limit, this study considers the mentioned faults geometry to back up the assumption that the Ntem Complex and its foreland constituted a passive margin [61], hence the diffuse effects of the Panafrican tectonics onto the Ntem Complex reported by some geological works [79]. [49] observed mylonites in the TTGs south of Mbalmayo along the CAFB/CC boundary that we interpret as imprints of ESE-WNW transpressive movements along the Mbalmayo schists

/CC contact line in response to late to post-Panafrican tectonics (Trans-Saharan orogeny) proving the importance of this tectonic feature. This importance as well as the geodynamic response of the CC and the Central Africa Rift System must be investigated by future works in regards with the ongoing stress related to the East African rifting and the NNE-SSW to NE-SW convergence of Africa towards Eurasia. Whatever, the multiplicity of the directions of the mapped faults shows how difficult it is to reconstruct the tectonic history of the northern margin of the CC.

The use of magnetic data permitted to highlights some intrusions mainly located in granitoids of the Ntem Complex (**Figure 7**) whereas almost no evidence of igneous activity is highlighted north in the CAFB domain. This spatial close relation of these intrusive bodies with granitoids presumed at the regional scale that there is no real Panafrican influence on the Ntem Complex rocks. [41] supposed that the Panafrican was not hot enough *i.e.* that the collision was weak at the margin of the Ntem Complex hence generating LP-LT metamorphic conditions which could only lead to the formation of low grade schists at the CAFB/CC boundary in Neoproterozoic. In the CAFB, this may be the reason why intrusive bodies are very scarce or not reported in the Yaounde Group schists belt by many previous studies [43] [89] contrarily to the Poli schists in northern Cameroon (far away from the Ntem Complex) which recorded intense intrusive to extrusive activity in Neoproterozoic consistently with a real subduction mechanism, as documented therein by topic related studies [93] [94]. This was justified by some recent works with the existence of a micro plate or a micro continent north of the CC, probably the Adamawa/Yade microcontinent detached from the CC (see, e.g. [88] [95] [96], on this important issue); and validates effective but limited rifting processes at the northern margin of the CC supported by this study and [65]. We further assume that the LP-LT conditions hitherto evoked imply a non or limited reactivation of the Paleoproterozoic faults/fractures which disabled ascent of subcrustal materials.

Despite the lack of data, we propose that the closure of the Yaounde basin in late Neoproterozoic shall be understood as a result of simple compressions between a fixed CC and a moving Adamawa/Yada/East Sahara Block rather than a normal collision as seen worldwide [97] [98] [99] [100] [101]. Therefore, the development of the southern CAFB is a non-collisional orogeny and the consideration of a CC subducted below the CAFB is geodynamically misleading and should be avoided. However, these conclusions are matter of debate and transduce the complexity of the geological history of the northern margin of the CC in particular, as well as enigmas related to the Congo continent in the pre-Gondwana reconstructions. Notwithstanding the lithologic and tectonic links well demonstrated between South America and Africa [57] [102], reassessment of the timing of events could better enlighten the Neoproterozoic evolution of the transition zone at the northern margin of the CC. Another challenge not openly discussed in this work is to investigate the response of this

transition zone to both the ongoing African plate geodynamics.

5.3. Hydrothermal Alteration Mapping and Mining Implications

Landsat 8 OLI data are generally efficient in mapping hydrothermal alteration zones which correspond to areas of clay minerals (with or without some iron oxides) accumulations [16] [19]. Contrarily to most presented studies (mainly carried in open canopy or semi-arid areas), they weakly mapped hydrothermal alteration zones in the study area. This incapability is probably due to the dense vegetation and the thick lateritic cover. In fact, the tropical vegetation produces a high evapotranspiration whose signal is sometimes difficult to remove on satellite data. In another side, Landsat 8 OLI data SWIR region is too broad (only two bands) to enable good mineral characterisation, comparatively to some sensors like ASTER which propose a better sampling in the same domain (five SWIR bands) resulting in a better characterisation of subsurface mineral contents.

However, aeromagnetics overcame that difficulty by mapping porphyry centres like some works [103]. Porphyritic deposits are associated to intrusive or extrusive activity, and require felsic to intermediate magma chamber and/or a cooling pluton; the inter-granular space along bedding planes and fractures in host rocks of enables percolation of hydrothermal fluids that will precipitate ore minerals then leads to the formation of hydrothermal deposits [2] [104] [105]. This is consistent with the close spatial relation between the highlighted porphyry centres and the granitoids and the TTG suites of the Ntem complex (**Figure 10**) in one hand; and in another, location of these mapped porphyry centres at (or close to) faults junctions, in between two subparallel faults or along faults, and at the TTG/granodiorites contact zone. Recalling this study highlighted a major pre-Panafrican NE-SW shear zones, with local NE-SW and NW-SE shear zones (e.g. Sangmelima area), it is clear that faulting played a major role by allowing hydrothermal and oxidising fluids circulations in the Archaean to Paleo/Mesoproterozoic evolution of the Ntem Complex.

Hydrothermal alteration in the Ntem complex has been recognised by recent works at the vicinities of the study area (in areas subject to advanced mineral exploration works) which also showed that hydrothermalism occurred in the Ntem Complex in a shallow seawater, probably in a subduction context [106] [107] [108] [109]. Porphyry as a subclass of hydrothermal deposits, is associated with one or various intrusions of felsic to intermediate rocks [4] [110] [111] as it is the case in this portion of the Ntem Complex made up of TTG granites, granodiorites [41] [47]. Also, some of the porphyry centres from this study coincide or are located in the close proximity of porphyry granites, intrusions and/or known mineral indices mapped by [42]. In the Ntem complex, the indices having Fe-Au (Iron Oxides-Gold; IOG) affiliation are mainly found out of greenstones in TTG, granodiorites and granitoids; they tend to confirm the existence of porphyry and/or IOCG deposits, despite the absence of Cu index in the study area. [112] while confirming the Cu depletion in Akom II southwest of the study area, rather revealed a S, Ni, and Au-PGE enrichment. Regarding the geodynamical,

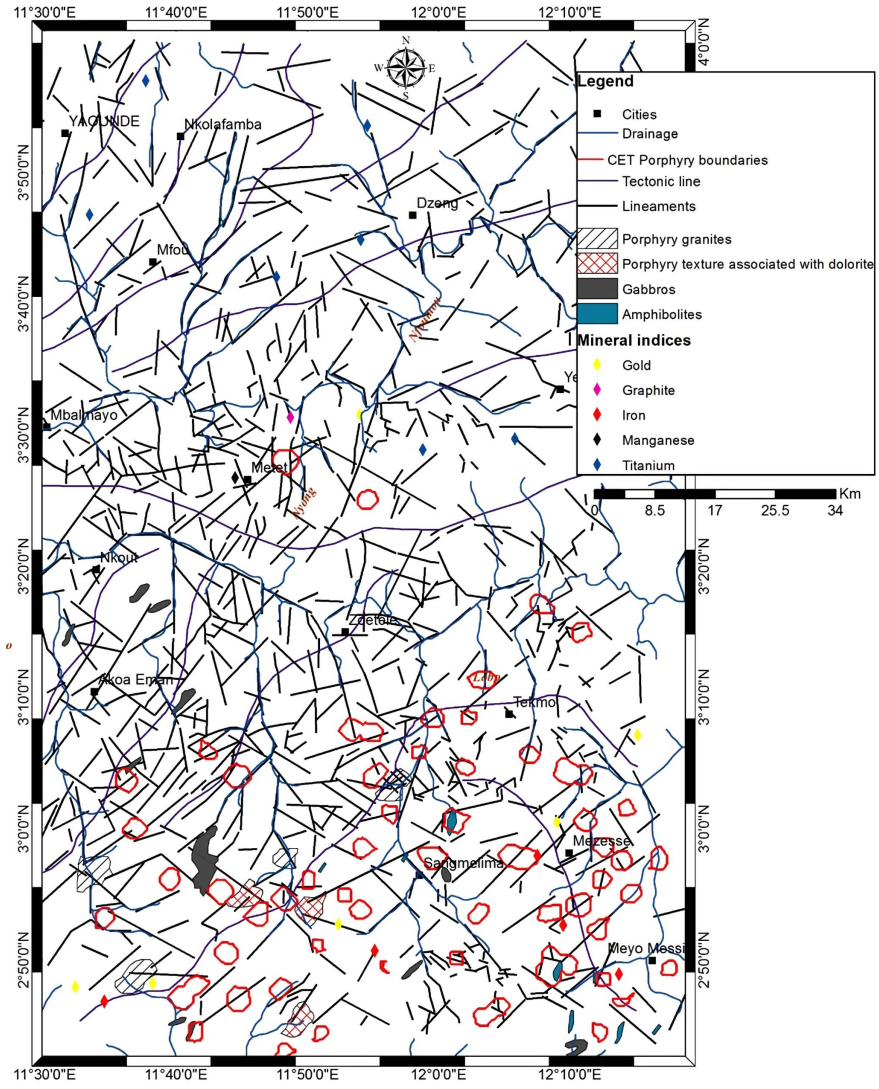

Figure 10. Correlation between highlighted porphyry domains and lineaments with exiting porphyritic textures and mineral indices.

lithological and structural context pertaining to this study area, hydrothermalism and absence of Cu would infer a Kiruma-type deposits [113]. However, [106] evidence of a Ba, Cu, Zn and V enriched iron oxide deposit suggests the existence of skarn or porphyry deposit nearly 45 km west of the study area (Binga project). Our results match with the existence of IOCG and porphyry/skarn ore deposits east and northeast Brazil [3] [4] [114]. Therefore, the Ntem complex in the transition zone at the northern margin of the CC potentially hosts many hydrothermal deposits which need to be explored.

6. Conclusions

An integrated analysis of Landsat 8, legacy aeromagnetic data and geologic maps was implemented as a predictive geological mapping approach in poorly exposed and inaccessible densely vegetated tropical region of southern Cameroon. The

study objective was to revisit the structural and lithological knowledge of the northern margin of the Congo Craton in the Yaounde-Sangmelima area, with the resulting potential mining implications. The main results from the study are:

1) The faults and fractures outline a major SW-NE paleo strike-slips channel or shear zone affecting both the Ntem complex and the CAFB basement.

2) NE and NW trans tensional movements depicted by first and second order faulting, passageways for hydrothermal fluids.

3) Many mapped intrusions and porphyry centres structurally controlled by the regional and local shear zones as imprints of hydrothermal activity.

4) The close proximity of highlighted porphyry centres with mapped faults/fractures junctions, porphyry texture zones and mineral indices includes iron and gold suggest the presence of porphyry deposits in the Ntem complex.

5) Landsat 8 multispectral data are not good enough to predictively map hydrothermal alteration zones in poorly exposed, inaccessible and densely vegetated tropical area. High evapotranspiration from trees, thick lateritic cover, and the width of Landsat-8 SWIR bands may be the reason.

The results show that the mining potential of the Yaounde-Sangmelima in Ntem Complex should be positively reconsidered and more exploration activities shall be encouraged.

Acknowledgements

The authors are grateful to the anonymous reviewers whose remarks and comments will contribute in upgrading the current paper.

Conflicts of Interest

The authors declare no conflicts of interest regarding the publication of this paper.

References

[1] Naslund, H.R., Henríquez, F., Nyström, J.O., Vivallo, W. and Dobbs, F.M. (2002) Magmatic Iron Ores and Associated Mineralisation: Examples from the Chilean High Andes and Coastal Cordillera. *Hydrothermal Iron Oxide Copper-Gold & Related Deposits. A Global Perspective*, **2**, 207-226.

[2] Grooves, D.I., Condie, K.C., Goldfarb, R.J., Hronsky, J.M.A. and Vielreicher, R.M. (2005) Secular Changes in Global Tectonic Processes and Their Influence on the Temporal Distribution of Gold-Bearing Mineral Deposits. *Economic Geology*, **100**, 203-224. https://doi.org/10.2113/gsecongeo.100.2.203

[3] Monteiro, L.V.S., *et al.* (2008) Spatial and Temporal Zoning of Hydrothermal Alteration and Mineralization in the Sossego Iron Oxide-Copper-Gold Deposit, Carajas Mineral Province, Brazil: Paragenesis and Stable Isotope Constraints. *Miners Depo*, **43**, 129-159. https://doi.org/10.1007/s00126-006-0121-3

[4] Lobato, L.M., *et al.* (1998) Styles of Hydrothermal Alteration and Gold Mineralizations Associated with the Nova Lima Group of the Quadrilátero Ferrífero: Part I, Description of Selected Gold Deposits. *Revista Brasileira de Geociências*, **28**, 339-354. https://doi.org/10.25249/0375-7536.1998339354

[5] Zientek, M.L. (2012) Magmatic Ore Deposits in Layered Intrusions—Descriptive Model for Reef-Type PGE and Contact-Type Cu-Ni-PGE Deposits Magmatic Ore Deposits in Layered Intrusions—Descriptive Model for Reef-Type PGE and Contact-Type Cu-Ni-PGE Deposits. https://doi.org/10.3133/ofr20121010

[6] Richard, J.P. (2013) Giant ore Deposits Formed by Optimal Alignments and Combinations of Geological Processes. *Nature Geoscience*, **6**, 911-916. https://doi.org/10.1038/ngeo1920

[7] Al Muntshry, A.N. (2011) Evaluating the Effectiveness of Multi-Spectral Remote Sensing Data for Lithological Mapping in Arid Regions: A Quantitative Approach with Examples from the Makkah Neoproterozoic Region, Saudi Arabia. Missouri University of Science and Technology, Rolla, MO.

[8] Liu, J.G. and Mason, P.J. (2009) Essential Image Processing and GIS for Remote Sensing. https://doi.org/10.1002/9781118687963

[9] Stewart, J.C. (2013) Developing Remote Sensing Methods for Bedrock Mapping of the Front Range Mountains, Colorado.

[10] Oruç, B. and Selim, H.H. (2011) Interpretation of Magnetic Data in the Sinop Area of Mid Black Sea, Turkey, Using Tilt Derivative, Euler Deconvolution and Discrete Wavelet Transform. *Journal of Applied Geophysics*, **74**, 194-204. https://doi.org/10.1016/j.jappgeo.2011.05.007

[11] Ouattara, G., Gnammytchet, B. and Kouakou Yao, A. (2012) Contribution des images satellitales Landsat 7 ETM+ a la cartographie lithostructurale du Centre-Est de la Cote d' Ivoire (Afrique de l' Ouest) to Cite This Version. *International Journal of Innovation and Applied Studies*, **1**, 61-75.

[12] Kiran Raj, S. and Ahmed, S.A. (2014) Lineament Extraction from Southern Chitradurga Schist Belt Using Landsat TM, ASTERGDEM and Geomatics Techniques. *International Journal of Computer Applications*, **93**, 12-20. https://doi.org/10.5120/16266-5993

[13] Mwaniki, M.W., Moeller, M.S. and Schellmann, G. (2015) A Comparison of Landsat 8 (OLI) and Landsat 7 (ETM +) in Mapping Geology and Visualising Lineaments: A Case Study of Central Region Kenya. *International Archives of the Photogrammetry, Remote Sensing and Spatial Information Science*, **XL-7**, 11-15. https://doi.org/10.5194/isprsarchives-XL-7-W3-897-2015

[14] Kayode, J.S., Nawawi, M.N.M., Khiruddin, B.A. and Khalil, A.E. (2016) Integrating Aeromagnetic and Landsat™ 8 Data into Subsurface Structural Mapping of Precambrian Basement Complex. *Journal of African Earth Sciences*, **125**, 202-213. https://doi.org/10.1016/j.jafrearsci.2016.11.010

[15] Crosta, A.P. and Rabelo, A. (1993) Assessing of Landsat TM for Hydrothermal ALteration Mapping in Central Western Brazil. *Proceedings of Ninth Thematic Conference Geologic Remote Sensing Pasadinea*, **3**, 1053-1061.

[16] Amer, R., Kusky, T.M., Reinert, P.C. and Ghulam, A. (2006) Image Processing and Analysis Using Landsat ETM + Imagery for Lithological Mapping at Fawakhir, Central Eastern Desert of Egypt. *ASPRS* 2009 *Annual Conference*, Baltimore, MD, 9-13 March 2009.

[17] Safari, M., Pour, A.B., Maghsoudi A. and Hashim, M. (2013) Targeting Hydrothermal Alterations Utilizing Landsat-8 Andaster Data in Shahr-e-Babak, Iran. *International Archives of the Photogrammetry, Remote Sensing and Spatial Information Sciences-ISPRS Archives*, **42**, 153-157. https://doi.org/10.5194/isprs-archives-XLII-4-W5-153-2017

[18] Pour, A.B. and Hashim M. (2015) Hydrothermal Alteration Mapping from Land-

sat-8 Data, Sar Cheshmeh Copper Mining District, South-Eastern Islamic Republic of Iran. *Journal of Taibah University for Science*, **9**, 155-166. https://doi.org/10.1016/j.jtusci.2014.11.008

[19] Labouré, C., Toledo, B. and De Assis L.M. (2016) Mapping Iron Oxides with Landsat-8/OLI and EO-1/Hyperion Imagery from the Serra Norte Iron Deposits in the Carajás Mineral Province, Brazil. *Brazilian Journal of Geology*, **46**, 331-349. https://doi.org/10.1590/2317-4889201620160023

[20] Pramumijoyo, F.S. and Setijadji, L.D. (2018) Alteration Mineral Mapping to Identify Primary Tin Potential Using Landsat 8 Images and Geographic Information System in Rimba Kulit Area, Southern of Bangka Island. *IOP Conference Series*: *Earth and Environmental Science*, **212**, Article ID: 012021. https://doi.org/10.1088/1755-1315/212/1/012021

[21] Akame, J.M., Mvondo Ondoa, J., Teikeu Assatse, W., Owona, S. and Olinga, J.B. (2014) Apport des images landsat-7 ETM+ a l'etude structurale du socle archeen de sangmelima (SUD CAMEROUN). *Revue Francaise de Photogrammetrie et Teledetection*, **206**, 15-26.

[22] Teikeu, W., Njandjock, P., Tabod, C., Martial, J. and Nshagali, G. (2016) Hydrogeological Activity of Lineaments in Yaoundé Cameroon Region Using Remote Sensing and GIS Techniques. *Egyptian Journal of Remote Sensing and Space Science*, **19**, 49-60.

[23] Didero, J., *et al.* (2016) Use of Landsat 7 ETM + Data for the Geological Structure Interpretation: Case Study of the Ngoura-Colomines Area, Eastern Cameroon. *Journal of Geosciences and Geomatics*, **4**, 61-72.

[24] Mandeng, B., Bondje, L.M., Solange, A., Tchami, L. and Dieudonne, L.B. (2018) Lithologic and Structural Mapping of the Abiete-Toko Gold District in Southern Cameroon, Using Landsat 7 ETM+/SRTM. *Comptes rendus Geoscience*, **350**, 130-140.

[25] Anaba Fotze, Q.M., Djieto Lordon, A., Penaye, J., Sep, J.P. and Neh Frun, M.I. (2019) Mapping Hydrothermal Alteration Targets from Landsat 8 OLI/TIRS and Magnetic Data Using Digital Image Processing Techniques in Garoua, North Cameroon. *Journal of Geosciences and Geomatics*, **7**, 28-41. https://doi.org/10.12691/jgg-7-1-4

[26] Nabighian, M.N., *et al.* (2005) The Historical Development of the Magnetic Method in Exploration. *Geophysics*, **70**, 33-61. https://doi.org/10.1190/1.2133784

[27] Fairhead, J.D., Cooper, G.R.J. and Sander, S. (2017) Advances in Airborne Gravity and Magnetics. In: *Proceedings of Exploration* 17: *Sixth Decennial International Conference on Mineral Exploration*, 113-127.

[28] Keating, P. (1995) A Simple Technique to Identify Magnetic Anomalies Due to Kimberlite Pipes. *Exploration and Mining Geology*, **4**, 121-125.

[29] Blakely, R.J. (1996) Potential Theory in Gravity and Magnetic Applications. Cambridge University Press, Cambridge. https://doi.org/10.1017/CBO9780511549816

[30] Reeves, C.V. (2005) Aeromagnetic Surveys-Principles, Practice & Interpretation. Geosoft.

[31] Reid, A.B., Allsop, J.M., Granser, H., Millett, A.J. and Somerton, I.W. (1990) Magnetic Interpretation in Three Dimensions Using Euler Deconvolution. *Geophysics*, **55**, 80-90. https://doi.org/10.1190/1.1442774

[32] Mushayandebvu, M.F., Lesur, V., Reid, A.B. and Fairhead, J.D. (2004) Grid Euler Deconvolution with Constraints for 2D Structures. *Geophysics*, **69**, 489-496. https://doi.org/10.1190/1.1707069

[33] Prieto, C. (1996) Gravity/Magnetic Signatures of Various Geologic Models-An Exercise in Pattern Recognition. *IGC Footnotes interpretation*, **4**, No. 4.

[34] Noutchogwe Tatchum, C., Koumetio, F. and Manguelle-Dicoum, E. (2010) Structural Features of South-Adamawa (Cameroon) Inferred from Magnetic Anomalies: Hydrogeological Implications. *Comptes rendus Geoscience*, **342**, 467-474. https://doi.org/10.1016/j.crte.2010.03.004

[35] Feumoe, A.N., Ndougsa-Mbarga, T., Manguelle-Dicoum, E. and Fairhead, J.D. (2012) Delineation of Tectonic Lineaments Using Aeromagnetic Data for the South-East Cameroon Area. *Geofizika*, **29**, 175-192.

[36] Som Mbang, M.C., Basseka, C.A., Kamguia, J., Etamè, J., Njiteu Tchoukeu, D.C. and Pemi Mouzong, M. (2018) Mapping of Deep Tectonic Structures of Central and Southern Cameroon by an Interpretation of Surface and Satellite Magnetic Data. *International Journal of Geophysics*, **2018**, 1-11. https://doi.org/10.1016/j.crte.2010.03.004

[37] Haroni, H.A., Erren, H. and Westerhof, P. (2000) Integrated Analysis of Remote Sensing, Aeromagnetic, Geological and Mineral Occurrence Data for the Assessment of a Subduction Setting Along the Zagros Orogenic Belt of Iran 2 Geological Setting of Zagros Orogenic Belt. *International Archives of the Photogrammetry, Remote Sensing*, **33**, 1700-1707.

[38] Opara, A.I., Onyekuru, S.O., Mbagwu, E.C., Emberga, T.T., Ijeomah, K.C. and Nwokocha, K.C. (2015) Integrating Landsat-ETM and Aeromagnetic Data for Enhanced Structural Interpretation over Naraguta Area, North-Central Nigeria. *International Journal of Scientific and Engineering Research*, **6**, 186-195.

[39] Vicat, J. and Moloto-a-Kenguemba, G. (2001) Les granitoides de la couverture protérozoique de la bordure nord du craton du Congo (Sud-Est du Cameroun et Sud-Ouest de la République centrafricaine), témoins d'une activité magmatique panafricaine. *Earth and Planetary Science Letters*, **332**, 235-242. https://doi.org/10.1016/S1251-8050(01)01521-X

[40] Tchameni, R., Mezger, K., Nsifa, N.E. and Pouclet, A. (2001) Crustal Origin of Early Proterozoic Syenites in the Congo Craton (Ntem Complex), South Cameroon. *Lithos*, **57**, 23-42. https://doi.org/10.1016/S0024-4937(00)00072-4

[41] Li, X., Chen, Y., Li, J., Yang, C., Ling, X. and Tchouankoue, J.P. (2016) New Isotopic Constraints on Age and Origin of Mesoarchean Charnockite, Trondhjemite and Amphibolite in the Ntem Complex of NW Congo Craton, Southern Cameroon. *Precambrian Research*, **276**, 14-23. https://doi.org/10.1016/j.precamres.2016.01.027

[42] Champetier de Ribes, G. and Aubague, M. (1956) Carte geologique de reconnaissance a l'echelle 1/500000. Notice explicative sur la feuille Yaounde-Est'.

[43] Maurizot, P., Abessolo, A., Feybesse, J., Johan, L. and Lecomte, P. (1986) Etude et prospection minière du Sud-Ouest du Cameroun. Synthèse des travaux de 1978 à 1985. Orleans, Cameroun.

[44] Nedelec, A., Nsifa, E.N. and Martin, H. (1990) Major and Trace Element Geochemistry of the Archaean Ntem Plutonic Complex South Cameroon): Petrogenesis and Crustal Evolution. *Precambrian Research*, **47**, 35-50. https://doi.org/10.1016/0301-9268(90)90029-P

[45] Shang, C.K., *et al.* (2004) TTG Magmatism in the Congo Craton; A View from Major and Trace Element Geochemistry, Rb-Sr and Sm-Nd Systematics: Case of the Sangmelima Region, Ntem Complex, Southern Cameroon. *Journal of African Earth Sciences*, **40**, 61-79. https://doi.org/10.1016/j.jafrearsci.2004.07.005

[46] Shang, C.K., Siebel, W., Satir, M., Chen, F. and Mvondo Ondoua, J. (2004) Zircon

Pb-Pb and U-Pb Systematics of TTG Rocks in the Congo Craton: Constraints on Crust Formation, Magmatism and Pan-African Lead Loss. *Bulletin of Geosciences*, **79**, 205-219.

[47] Shang, C.K., Liégeois, J.P., Satir, M., Frisch, W. and Nsifa, E.N. (2010) Late Archaean High-K Granite Geochronology of the Northern Metacratonic Margin of the Archaean Congo Craton, Southern Cameroon: Evidence for Pb-Loss Due to Non-Metamorphic Causes. *Gondwana Research*, **18**, 337-355. https://doi.org/10.1016/j.gr.2010.02.008

[48] Houketchang Bouyo, M., Penaye, J., Mouri, H. and Toteu, S.F. (2019) Eclogite Facies Metabasites from the Paleoproterozoic Nyong Group, SW Cameroon: Mineralogical Evidence and Implications for a High-Pressure Metamorphism Related to a Subduction Zone at the NW Margin of the Archean Congo Craton. *Journal of African Earth Sciences*, **149**, 215-234. https://doi.org/10.1016/j.jafrearsci.2018.08.010

[49] Nedelec, A., Macaudiere, J., Nzenti, J.P. and Barbey, P. (1986) Évolution structurale et métamorphique des schistes de Mbalmayo (Cameroun). Implications pour la structure de la zone mobile panafricaine d'Afrique centrale au contact du craton du Congo. *Comptes rendus de l'Académie des Sciences Paris*, **303**, 75-80.

[50] Nzenti, J.P., Barbey, P., Macaudière, J. and Soba, D. (1988) Origin and Evolution of the Late Precambrian High, Grade Yaoundé Gneisses Cameroon. *Precambrian Research*, **38**, 91-109. https://doi.org/10.1016/0301-9268(88)90086-1

[51] Ganwa, A.A., *et al.* (2008) Zircon207Pb/206Pb Evaporation Ages of Panafrican Metasedimentary Rocks in the Kombé-II Area (Bafia Group, Cameroon): Constraints on Protolith Age and Provenance. *Journal of African Earth Sciences*, **51**, 77-88. https://doi.org/10.1016/j.jafrearsci.2007.12.003

[52] Feybesse, J.L., Johan, V., Maurizot, P. and Abessolo, A. (1987) Evolution tectonométamorphique libérienne et eburnéenne de la partie NW du craton zairois (SW Cameroun). In: Matheis, G. and Balkema, S.H., Eds., *Current Research in African Earth Sciences*, Rotterdam, 9-13.

[53] Tchameni, R., *et al.* (2010) Mineralogical Constraint for Metamorphic Conditions in a Shear Zone Affecting the Archean Ngoulemakong Tonalite, Congo Craton (Southern Cameroon) and Retentivity of U-Pb SHRIMP Zircon Dates. *Journal of African Earth Sciences*, **58**, 67-80. https://doi.org/10.1016/j.jafrearsci.2010.01.009

[54] Castaing, C., Feybesse, J.L., Thieblemont, D., Triboulet, C. and Chèvremont, P. (1994) Paleogeographical Reconstructions of the Pan-African/Brasiliano Orogen: Closure of an Oceanic Domain or Intracontinental Convergence between Major Blocks? *Precambrian Research*, **67**, 327-344. https://doi.org/10.1016/0301-9268(94)90095-7

[55] Toteu, S.F., van Schmus, W.R., Penaye, J. and Nyobe, J.B. (1994) U-Pb and Sm-Nd Evidence for Eburnian and Pan-African High-Grade Metamorphism in Cratonic Rocks of Southern Cameroon. *Precambrian Research*, **67**, 321-347. https://doi.org/10.1016/0301-9268(94)90014-0

[56] Toteu, S.F., Van Schmus, W.R. and Penaye, J. (2006) The Precambrian of Central Africa: Summary and Perspectives. *Journal of African Earth Sciences*, **44**, 7. https://doi.org/10.1016/j.jafrearsci.2005.12.002

[57] van Schmus, W.R., Oliveira, E.P., da Silva Filho, A.F., Toteu, S.F., Penaye, J. and Guimarães, I.P. (2008) Proterozoic Links between the Borborema Province, NE Brazil and the Central African Fold Belt. *Geological Society, London, Special Publications*, **294**, 69-99. https://doi.org/10.1144/SP294.5

[58] Fernandez-Alonso, M., Tack, L., Tahon, A. and De Waele, B. (2010) The Protero-

zoic History of the Proto-Congo Craton of Central Africa.

[59] Loose, D. and Schenk, V. (2018) 2.09 Ga Old Eclogites in the Eburnian-Transamazonian Orogen of Southern Cameroon: Significance for Palaeoproterozoic Plate Tectonics. *Precambrian Research*, **304**, 1-11. https://doi.org/10.1016/j.precamres.2017.10.018

[60] Toteu, S.F., Penaye, J. and Djomani, Y.P. (2004) Geodynamic Evolution of the Pan-African Belt in Central Africa with Special Reference Geodynamic Evolution of the Pan-African Belt in Central Africa with Special Reference to Cameroon 1. *Canadian Journal of Earth Sciences*, **41**, 73-85. https://doi.org/10.1139/e03-079

[61] Ngako, V. and Njonfang, E. (2011) Plates Amalgamation and Plate Destruction , the Western Gondwana History. In: Closson, D., Ed., *Tectonics*, InTech, London, 1-36.

[62] Mvondo, H., Owona, S., Ondoa, J.M. and Essono, J. (2007) Tectonic Evolution of the Yaoundé Segment of the Neoproterozoic Central African Orogenic Belt in Southern Cameroon. *Canadian Journal of Earth Sciences*, **44**, 433-444. https://doi.org/10.1139/e06-107

[63] Olinga, J.B., Mpesse, J.E., Minyem, D., Ngako, V., Ndougsa-Mbarga, T. and Ekodeck, G.E. (2010) The Awaé-Ayos Strike-Slip Shear Zones (Southern Cameroon): Geometry, Kinematics and Significance in the Late Pan-African Tectonics. *Neues Jahrbuch für Geologie und Paläontologie*, **257**, 1-11. https://doi.org/10.1127/0077-7749/2010/0042

[64] Mvondo-Ondoa, J., Mvondo, H. and Den Brok, B. (2009) Pan-African Tectonics in Northwestern Cameroon: Implication for the History of Western Gondwana. *Gondwana Research*, **16**, 163-164. https://doi.org/10.1016/j.gr.2008.12.006

[65] Nkoumbou, C., Barbey, P., Yonta-Ngouné, C., Paquette, J.L. and Villiéras, F. (2014) Pre-Collisional Geodynamic Context of the Southern Margin of the Pan-African Fold Belt in Cameroon. *Journal of African Earth Sciences*, **99**, 245-260. https://doi.org/10.1016/j.jafrearsci.2013.10.002

[66] Manguelle Dicoum, E., Bokosah, A.S. and Kwende Mbanwi, T.E. (1992) Geophysical Evidence for a Major Precambrian Schist-Granite Boundary in Southern Cameroon. *Tectonophysics*, **205**, 437-446. https://doi.org/10.1016/j.jafrearsci.2013.10.002

[67] Ndougsa-Mbarga, T., Layu, D.Y., Yene-Atangana, J.Q. and Tabod, C.T. (2014) Delineation of the Northern Limit of the Congo Craton Based on Spectral Analysis and 2.5D Modeling of Aeromagnetic Data in the Akonolinga-Mbama area, Cameroon. *Geofísica Internacional*, **53**, 5-16. https://doi.org/10.1016/S0016-7169(14)71486-2

[68] USGS (2016) Landsat 8 (L8) Data Users Handbook.

[69] Chavez, P.S.J., Berlin, G.L. and Sowers, L. (1982) Statistical Method for Selecting Landsat MSS Ratios. *Journal of Applied Photographic Engineering*, **8**, 23-30.

[70] Crosta, A.P. and Moore, J.M. (1989) Enhancement of Landsat Thematic Mapper Imagery for Residual Soil Mapping in SW Minas Gerais State, Brazil: A Prospecting Case History in Greenstone Belt Terrain. *Proceedings of the 7th Thematic Conference on Remote Sensing for Exploration Geology*, 2-6 October 1989, 1173-1187.

[71] Nabighian, M.N. (1972) The Analytic Signal of Two-Dimensional Magnetic Bodies with Polygonal Cross-Section: Its Properties and Use for Automated Anomaly Inter-Pretation. *Geophysics*, **37**, 507-517. https://doi.org/10.1190/1.1440276

[72] Roest, W.R., Verhoef, J. and Pilkington, M. (1992) Magnetic Interpretation Using the 3-D Analytic Signal. *Geophysics*, **57**, 116-125. https://doi.org/10.1190/1.1443174

[73] Boyd, D.M. and Isles, D.J. (2007) Geological Interpretation of Airborne Magnetic Surveys-40 Years on. *Proceedings of Exploration* 07: *Fifth Decennial International Conference on Mineral Exploration*, Toronto, 9-12 September 2007, 491-505.

[74] Archibald, N., Gow, P. and Boschetti, F. (1999) Multiscale Edge Analysis of Potential Field Data. *Exploration Geophysics*, **30**, 38-44. https://doi.org/10.1071/EG999038

[75] Owona-Angue, M.L., Tabod, C.T., Nguiya, S., Kenfack, J.V. and Tokam Kamga, A.P. (2013) Delineation of Lineaments in South Cameroon (Central Africa) Using Gravity Data. *Open Journal of Geology*, **3**, 331-339. https://doi.org/10.4236/ojg.2013.35038

[76] Kue Petou, M.R., Owona Angue, M.L., Nfor, N., Ndougsa-Mbarga, T. and Manguelle-Dicoum, E. (2017) Determination of Structural and Geometrical Parameters of the Kribi-Campo Sedimentary Sub-Basin Using Gravity Data. *International Journal of Geophysics*, **8**, 1210-1224. https://doi.org/10.4236/ijg.2017.89069

[77] Holden, E., Fu, S.C., Kovesi, P., Dentith, M.C., Bourne, B. and Hope, M. (2011) Automated Identification of Magnetic Responses from Porphyry Systems. *Journal of Applied Geophysics*, **74**, 255-262. https://doi.org/10.1016/j.jappgeo.2011.06.016

[78] Nzenti, J.P., Barbey, P., Jegouzo, P. and Moreau, C. (1984) Un nouvel exemple de ceinture granulitique dans une chaîne protérozoïque de collision: Les migmatites de Yaoundé au Cameroun. *Comptes Rendus de l'Académie des Sciences Paris*, **299**, 1197-1199.

[79] Nedelec, A., Nzenti, J.P. and Barbey, P. (1986) Structural and Metamorphic Evolution of the Mbalmayo Schists (Cameroon). Implications for the Structure of the Pan-African Mobile Belt of Central Africa, Close to the Congo Crat. *Comptes Rendus de l'Académie des Sciences*, **303**, No. 2015.

[80] Shang, C.K., Muharrem, S., Nsifa Nkonguin, E., Liegeois, J.-P., Siebel, W. and Taubald, H. (2007) Archaean High-K Granitoids Produced by Remelting of Earlier Tonalite-Trondhjemite-Granodiorite (TTG) in the Sangmelima Region of the Ntem Complex of the Congo Craton, Southern Cameroon. *International Journal of Earth Sciences*, **96**, 817-841. https://doi.org/10.1007/s00531-006-0141-3

[81] Li, X.-H., Chen, Y., Li, J., Yang, C., Ling, X.-X. and Tchouankoue, J.P. (2016) New Isotopic Constraints on Age and Origin of Mesoarchean Charnockite, Trondhjemite and Amphibolite in the Ntem Complex of NW Congo Craton, Southern Cameroon. *Precambrian Research*, **276**, 14-23.

[82] Akame, J.M., *et al.* (2019) The Sangmelima Granite-Greenstone Belts (South Cameroon): Integration of Remote Sensing and Aeromagnetic Data for Structural Interpretation. *The Egyptian Journal of Remote Sensing and Space Sciences*, **22**, 37-47.

[83] Tadjou, J.M., Njingti-Nfor, Kamguia, J. and Manguelle-Dicoum, E. (2008) Geophysical Prospecting of the Transition Zone between the Congo Craton and the Panafrican Belt in Cameroon. *Earth Sciences Research Journal*, **12**, 169-180.

[84] Meying, A., Ndougsa-Mbarga, T. and Manguelle-Dicoum, E. (2009) Evidence of Fractures from the Image of the Subsurface in the Akonolinga-Ayos Area (Cameroon) by Combining the Classical and the Bostick Approaches in the Interpretation of Audio-Magnetotelluric Data. *Journal of Geology and Mining Research*, **1**, 159-171.

[85] Shandini, N.Y., Tadjou, J.M. and Basseka, C.A. (2011) Delineating Deep Basement Faults in South Cameroon Area. *World Applied Sciences Journal*, **14**, 611-615.

[86] Assembe, S.P., Ndougsa-Mbarga, T., Meying, A., Gouet, D.H., Ngoh, J.D. and Mono, J.A. (2019) Contribution of Geophysics to the Understanding of the Geodynamic Activity at the Northern Margin of the Congo Craton: A Case Study from Aeromagnetic Data Interpretation Over the Metet-Zoetele Region (Southern Ca-

meroon). *European Journal of Scientific Research*, **152**, 286-303.

[87] Takam, T., Makoto, A., Kokonyangi, J., Dunkley, D.J. and Nsifa Nkonguin, E. (2009) Paleoarchaean Charnockite in the Ntem Complex, Congo Craton, Cameroon: Insights from SHRIMP Zircon U-Pb Ages. *Journal of Mineralogical and Petrological Sciences*, **104**, 1-11. https://doi.org/10.2465/jmps.080624

[88] Tchakounte Numbem, J., *et al.* (2018) Reply to Comment by Ngako and Njonfang on "The Adamawa-Yade Domain, a Piece of Archaean Crust in the Neoproterozoic Central African Orogenic Belt (Bafia Area, Cameroon)", by Jacqueline Tchakounté et al., Precambrian Research 299 (2017) 210-229. *Precambrian Research*, **305**, 516-518. https://doi.org/10.1016/j.precamres.2017.12.035

[89] Shandini, Y.N., Tadjou, J.M., Tabod, C.T. and Fairhead, J.D. (2010) Gravity Data Interpretation in the Northern Edge of the Congo Craton, South-Cameroon. *Anuário do Instituto de Geociências*, **33**, 73-82.

[90] Basseka, C.A., Shandini, Y. and Tadjou, J.M. (2011) Subsurface Structural Mapping Using Gravity Data of the Northern Edge of the Congo Craton, South Cameroon. *Geofizika*, **28**, 229-245.

[91] Scotese, C.R. (2009) Late Proterozoic Plate Tectonics and Palaeogeography: A Tale of Two Supercontinents, Rodinia and Pannotia. In: Craig, J., Thurow, J., Thusu, B., Whitham, A. and Abutarruma, Y., Eds., *Global Neoproterozoic Petroleum Systems: The Emerging Potential in North Africa*, 67-83. https://doi.org/10.1144/SP326.4

[92] Goussi, J.F., Bisso, D., Abdelsalam, M.G., Atekwana, E.A., Katumwehe, A.B. and Ekodeck, G.E. (2017) Geophysical Imaging of Metacratonizaton in the Northern Edge of the Congo Craton in Cameroon. *Journal of African Earth Sciences*, **129**, 94-107. https://doi.org/10.1016/j.jafrearsci.2016.12.010

[93] Toteu, S.F. (1990) Geochemical Characterization of the Main Petrographical and Structural Units of Northern Cameroon: Implications for Pan-African Evolution. *Journal of African Earth Sciences*, **10**, 615-624. https://doi.org/10.1016/0899-5362(90)90028-D

[94] Toteu, S.F., Van Schmus, W.R., Penaye, J. and Michard, A. (2001) New U-Pb and Sm-Nd Data from North-Central Cameroon and Its Bearing on the Pre-Pan African History of Central Africa. *Precambrian Research*, **108**, 45-73. https://doi.org/10.1016/S0301-9268(00)00149-2

[95] Tchameni, R., Pouclet, A., Penaye, J., Ganwa, A.A. and Toteu, S.F. (2006) Petrography and Geochemistry of the Ngaoundere Granitoids in Central North Cameroon: Implications for Their Sources and Geological Setting. *Journal of African Earth Sciences*, **44**, 511-529. https://doi.org/10.1016/j.jafrearsci.2005.11.017

[96] Ganwa, A.A., Siebell, W., Shang, K.C., Seguem, N. and Ekodeck, G.E. (2011) New Constraints from Pb-Evaporation Zircon Ages of the Meiganga Amphibole-Biotite Gneiss, Central Cameroon, on Proterozoic Crustal Evolution. *International Journal of Geosciences*, **2**, 138-147. https://doi.org/10.4236/ijg.2011.22014

[97] Han, T. and Nelson, J. (2015) Mapping Hydrothermally Altered Rocks with Landsat 8 Imagery: A Case Study in the KSM and Snow Field Zones, Northwestern British Columbia. Geological Fieldwork 2014, British Columbia Ministry of Energy and Mines, 103-112.

[98] Timm, J. (2001) Subduction and Continental Collision in the Lufilian Arc-Zambesi Belt Orogen: A Petrological, Geochemical and Geochronological Study of Eclogites and Whiteschists (Zambia). University of Kiel, Kiel.

[99] Kröner, A. and Stern, R.J. (2004) Pan-African Orogeny. *Encyclopedia of Geology*, **1**,

1-12. https://doi.org/10.1016/B0-12-369396-9/00431-7

[100] Zhao, Z., Zheng, Y., Zhang, J., Dai, L., Li, Q. and Liu, X. (2012) Syn-Exhumation Magmatism during Continental Collision: Evidence from Alkaline Intrusives of Triassic Age in the Sulu Orogen. *Chemical Geology*, **328**, 70-88. https://doi.org/10.1016/j.chemgeo.2011.11.002

[101] Bouyo Houketchang, M., Zhao, Y., Penaye, J., Zhang, S.H. and Njel, U.O. (2015) Neoproterozoic Subduction-Related Metavolcanic and Metasedimentary Rocks from the Rey Bouba Greenstone Belt of North-Central Cameroon in the Central African Fold Belt: New Insights into a Continental Arc Geodynamic Setting. *Precambrian Research*, **261**, 40-53. https://doi.org/10.1016/j.precamres.2015.01.012

[102] de Wit, M.J., Stankiewicz, J. and Reeves, C. (2008) Restoring Pan-African-Brasiliano Connections: More Gondwana Control, Less Trans-Atlantic Corruption. *The Geological Society of London-Special Publications*, **294**, 399-412. https://doi.org/10.1144/SP294.20

[103] Elkhateeb, S.O. and Abdellatif, M.A.G. (2018) Delineation Potential Gold Mineralization Zones in a Part of Central Eastern Desert, Egypt Using Airborne Magnetic and Radiometric Data. *NRIAG Journal of Astronomy and Geophysics*, **7**, 361-376. https://doi.org/10.1016/j.nrjag.2018.05.010

[104] Boadi, B., Wemegah, D.D. and Preko, K. (2013) Geological and Structural Interpretation of the Konongo Area of the Ashanti Gold Belt of Ghana from Aero-Magnetic and Radiometric Data. *International Research Journal of Geology and Mining*, **3**, 124-135.

[105] Ganno, S., *et al.* (2017) A Mixed Seawater and Hydrothermal Origin of Superior-Type Banded Iron Formation (BIF)-Hosted Kouambo Iron Deposit, Palaeoproterozoic Nyong Series, Southwestern Cameroon: Constraints from Petrography and Geochemistry. *Ore Geology Reviews*, **80**, 860-875. https://doi.org/10.1016/j.oregeorev.2016.08.021

[106] Ngoran, G.N., Suh, C.E., Bowker, D., Verla, R.B. and Bafon, G.T. (2016) Petrochemistry of Two Magnetite Bearing Systems in the Precambrian Belt of Southern Cameroon. *International Journal of Geosciences*, **7**, 501-517. https://doi.org/10.4236/ijg.2016.74038

[107] Soh Tamehe, L., Ganno, S., Nono Kouankap, G.D., Ngnotue, T., Kankeu, B. and Nzenti, J.P. (2014) Stream Sediment Geochemical Survey of Gouap-Nkollo Prospect, Southern Cameroon: Implications for Gold and LREE Exploration. *American Journal of Mining and Metallurgy*, **2**, 8-16.

[108] Teutsong, T., *et al.* (2016) Petrography and Geochemistry of the Mesoarchean Bikoula Banded Iron Formation in the Ntem Complex (Congo Craton), Southern Cameroon: Implications for Its Origin. *Ore Geology Reviews*, **80**, 267-288. https://doi.org/10.1016/j.oregeorev.2016.07.003

[109] Ganno, S., *et al.* (2018) Geochemical Constraints on the Origin of Banded Iron Formation-Hosted Iron Ore from the Archaean Ntem Complex (Congo Craton) in the Meyomessi Area, Southern Cameroon. *Resource Geology*, **68**, 287-302. https://doi.org/10.1111/rge.12172

[110] Faure, S. (2012) Potentiel de mineralisations de type IOCG en contexte intracratonique ou d'arcs continentaux dans les terrains archeens et proterozoiques du Quebec. Project 2010-08.

[111] Seltmann, R., Porter, T.M. and Piranjo, F. (2014) Geodynamics and Metallogeny of the Central Eurasian Porphyry and Related Epithermal Mineral Systems: A Review. *The Journal of Asian Earth Sciences*, **79**, 810-841.

https://doi.org/10.1016/j.jseaes.2013.03.030

[112] Aye, B.A., Sababa, E. and Ndjigui, P. (2017) Geochemistry of S, Cu, Ni, Cr and Au-PGE in the Garnet Amphibolites from the Akom II Area in the Archaean Congo Craton, Southern Cameroon. *Chemie der Erde-Geochemistry*, **77**, 81-93. https://doi.org/10.1016/j.chemer.2017.01.009

[113] Knipping, J.L., Bilenker, L.D., Simon, A.C., Reich, M., Barra, F. and Deditius, A.P. (2015) Giant Kiruna-Type Deposits Form by Efficient Flotation of Magmatic Magnetite Suspensions. *Geology*, **43**, 591-594. https://doi.org/10.1130/G36650.1

[114] Roberto, S., Hühn, B. and Silva, A.M. (2018) Favorability Potential for IOCG Type Deposits in the Riacho do Pontal Belt: New Insights for Identifying Prospects of IOCG-Type Deposits in NE Brazil. *Brazilian Journal of Geology*, **48**, 703-719. https://doi.org/10.1590/2317-4889201820180029